

ACCEPTED

FACULTY

8 JUN 94

ELECTROMAGNETIC INDUCTION IN THE NEW ZEALAND REGION

Jie Chen
M.Sc., University of Victoria, 1988

A DISSERTATION SUBMITTED IN PARTIAL FULFILLMENT
OF THE REQUIREMENTS FOR THE DEGREE OF
DOCTOR OF PHILOSOPHY
in the Department
of
Physics and Astronomy

We accept this dissertation as conforming
to the required standard

Dr. H.W. Dosso, Supervisor (Dept. of Physics and Astronomy)

Dr. J.T. Weaver, Departmental Member (Dept. of Physics and Astronomy)

Dr. A. Watton, Departmental Member (Dept. of Physics and Astronomy)

Dr. D.E. Hewgill, Outside Member (Dept. of Mathematics)

Dr. F.W. Jones, External Examiner (University of Alberta)

© Jie Chen, 1994

UNIVERSITY OF VICTORIA

1994

All rights reserved. This dissertation may not be reproduced
in whole or in part, by mimeograph or other means,
without permission of the author.

Supervisor: Dr. H. W. Dosso

ABSTRACT

A laboratory analogue model of New Zealand was constructed and magnetic field measurements carried out for a detailed grid of traverses for simulated periods of 5-120 min. The model includes a simulation of the North and South Island coastlines, the surrounding ocean bathymetry in a region 2800 km x 2800 km, and a horizontal conductive asthenosphere at a depth of 100 km. In the analogue model studies, the ocean bathymetry, the irregular coastlines, as well as Cook Strait between the North and South Islands, are seen to lead to a wide range of geomagnetic coast effects both at coastal and inland sites for these relatively narrow islands. In addition, the geological and tectonic structure of New Zealand (not included in the simulation) is rather complex in that in the North Island the Pacific Plate subduction leads to a belt of active volcanism, a zone of crustal and mantle earthquake activity, numerous faults, and large negative gravity anomalies, while in the South Island, as well as numerous faults, the zones of subduction occurring at the northern and southern tips, are joined by the Alpine Fault along the length of the island.

To aid the interpretation of field site measurements in this complex New Zealand region containing numerous conductive major and minor faults, electromagnetic induction studies of idealized analogue models of single and pairs of parallel conductive faults near an ocean coastline are carried out, and empirical curves of

induction arrow responses for a range of parameters (e.g. fault depths, ocean-fault separation distances, inducing field periods, etc) provided. Further, measurements carried out for the responses of the model ocean and the model fault separately, are used to examine and demonstrate the validity of removing by vector subtraction the response of the ocean from that of the ocean and an on shore fault to yield the induction arrow response of the fault alone. In a similar fashion, the New Zealand model induction arrow responses, being those of the ocean alone, are used to remove the coast effect components present in geomagnetic field site measurements, to yield difference induction arrow responses of any anomalous conductors present at that site but not simulated in the analogue model. The resulting difference arrows at 96 sites (both coastal and inland New Zealand) are then interpreted in terms of the responses of a range of conductive structures (conductive faults, sedimentary basins, geology, and subducting plate structure) in the field site survey region.

Examiners:

Dr. H.W. Dosso, Supervisor (Dept. of Physics and Astronomy)

Dr. J.T. Weaver, Departmental Member (Dept. of Physics and Astronomy)

Dr. A. Watton, Departmental Member (Dept. of Physics and Astronomy)

Dr. D.E. Hewgill, Outside Member (Dept. of Mathematics)

Dr. F.W. Jones, External Examiner (University of Alberta)

CONTENTS

| | |
|--|-------------|
| Abstract | ii |
| Contents | iv |
| Figures | vi |
| Acknowledgements | xiii |
| | |
| Chapter I: INTRODUCTION | 1 |
| 1.1 Regional Electromagnetic Induction Studies | 2 |
| 1.1.1 Magnetotelluric (MT) Studies | 3 |
| 1.1.2 Geomagnetic Depth Sounding (GDS) Studies | 6 |
| 1.1.3 Controlled Source Methods | 9 |
| 1.1.4 Electromagnetic Analogue Model Studies | 11 |
| 1.2 The Geomagnetic Coast Effect | 13 |
| 1.3 Previous EM Induction Studies in New Zealand | 15 |
| 1.4 Summary of the Work in This Dissertation | 16 |
| | |
| Chapter II: LABORATORY ANALOGUE ELECTROMAGNETIC MODELLING | 19 |
| 2.1 Model Scaling Conditions and Scaling Factors | 19 |
| 2.2 The Laboratory Analogue Model Facility | 22 |
| 2.3 Chapter Summary | 27 |
| | |
| Chapter III: EM RESPONSES OF OCEAN AND FAULT LABORATORY ANALOGUE MODELS | 28 |
| 3.1 Introduction | 28 |
| 3.2 The Responses of a Constant Depth Ocean | 29 |
| 3.3 The Responses of an Ocean and an on Shore Fault Parallel to the Coastline | 44 |
| 3.4 Removal of the Coast Effect From the Response of an Ocean and an on Shore Fault Parallel to a Coastline | 68 |
| 3.4.1 The Effect of the Fault Depth for a Small Ocean-Fault Separation Distance | 68 |
| 3.4.2 The Effect of Fault Depth for a Large Ocean-Fault Separation Distance | 72 |
| 3.5 Chapter Summary | 76 |

| | |
|---|------------|
| Chapter IV: EM RESPONSES OF SINGLE AND MULTIPLE-FAULT LABORATORY ANALOGUE MODELS | 79 |
| 4.1 Introduction | 79 |
| 4.2 The Responses of a Single Fault | 80 |
| 4.3 The Responses of a Pair of Parallel Faults | 92 |
| 4.4 Removal of a Single Fault Response From the Response of a Pair of Parallel Faults | 115 |
| 4.5 Chapter Summary | 119 |
| | |
| Chapter V: TECTONIC AND GEOLOGICAL SETTING OF THE NEW ZEALAND REGION | 122 |
| 5.1 Tectonic and Geological Setting | 122 |
| 5.2 Chapter Summary | 138 |
| | |
| Chapter VI: ANALOGUE MODEL EM RESPONSES IN THE NEW ZEALAND REGION | 139 |
| 6.1 The Analogue Model of the New Zealand Region | 139 |
| 6.2 Analogue Model Magnetic Field Components in the New Zealand Region | 141 |
| 6.3 Induction Arrows in the New Zealand Region | 146 |
| 6.3.1 Induction Arrows Along the North Island Model Traverses | 149 |
| 6.3.2 Induction Arrows Along the South Island Model Traverses | 155 |
| 6.4 Chapter Summary | 161 |
| | |
| Chapter VII: INTERPRETATION OF ANALOGUE MODEL AND FIELD SITE INDUCTION ARROWS IN NEW ZEALAND | 162 |
| 7.1 The Midha (1979) and Ingham (1985a, 1985b, 1987, 1988b) Field Sites | 163 |
| 7.1.1 In-phase Induction Arrows | 165 |
| 7.1.2 Quadrature Induction Arrows | 168 |
| 7.2 The Kellett et al. (1988) Eyrewell Field Site | 170 |
| 7.2.1 Analogue Model and Field Site Induction Arrows at EYR | 171 |
| 7.2.2 Difference Induction Arrows at EYR | 173 |
| 7.3 The Bromley (1979) Field Sites | 175 |
| 7.3.1 In-phase Difference Arrows | 176 |
| 7.3.2 Quadrature Difference Arrows | 180 |
| 7.4 The New Zealand Array (Chamalaun and McKnight, 1993) Field Sites | 185 |
| 7.4.1 Difference Induction Arrows on North Island | 196 |
| 7.4.2 Difference Induction Arrows on South Island | 205 |
| 7.5 Chapter Summary | 216 |

| | |
|--|-----|
| Chapter VII: SUMMARY AND CONCLUSIONS | 220 |
| REFERENCES | 222 |
| Appendix A: Model induction arrow responses for faults parallel to an ocean coastline | 245 |
| Appendix B: Model induction arrow responses for single faults | 252 |
| Appendix C: Model induction arrow responses for pairs of parallel faults ... | 255 |
| Appendix D: Model B_x, B_y and B_z components for X- and Y-polarizations ... | 262 |
| Appendix E: Model induction arrow V_x and V_y response curves | 286 |
| Appendix F: Field site (Chamalaun and McKnight, 1993) Induction Arrow Components as a Function of Period at 34 Sites | 301 |
| Appendix G: Analogue Model Induction Arrow Components as a Function of Period at 34 Sites. | 313 |
| Appendix H: Difference Induction Arrow Components (D_x and D_y) as a Function of Period at the 34 Sites of Chamalaun and McKnight, 1993 | 325 |
| Appendix I: Analogue Model and Field site (Chamalaun and McKnight, 1993) Induction Arrows at 34 Sites | 337 |
| Appendix J: Difference Induction Arrows at the 34 Sites of Chamalaun and McKnight (1993) | 344 |

FIGURES

| | | |
|------|---|----|
| 2.1 | Inducing source field and tank containing salt solution. | 23 |
| 2.2 | The detectors and recording equipment. | 25 |
| 3.1 | The cross-section of the model ocean (a) in a resistive host earth, all underlain by a conductive substratum (c). | 30 |
| 3.2 | The in-phase and quadrature induction arrow responses V along a traverse perpendicular to the coastline for periods of 2 and 20 min. | 31 |
| 3.3 | The in-phase and quadrature induction arrow responses V along a traverse perpendicular to the coastline at the characteristic period T_C . The quadrature response curves for 1.5 and 5 min are also shown. | 33 |
| 3.4 | The in-phase and quadrature induction arrow responses V along a traverse perpendicular to the coastline for periods of 1-90 min. | 35 |
| 3.5 | The amplitude and phase angle response curves along a traverse perpendicular to the coastline for periods of 1-90 min. | 38 |
| 3.6 | a) The in-phase response maximum V_m (and the quadrature response at the same location), b) the amplitude response maximum (and the phase angle) as a function of period for the 5 km depth ocean. | 40 |
| 3.7 | The in-phase response maximum V_m (and the corresponding quadrature) as a function of period for the 5 km depth ocean underlain by a conductive substratum at depths $Z_C=50, 100, 200$ km. | 42 |
| 3.8 | The cross-section of the model ocean (a) with the straight coastline parallel to an elongated conductive fault (b), all underlain by a conductive substratum (c). | 45 |
| 3.9 | The in-phase and quadrature induction arrow responses V along a traverse perpendicular to the ocean (a), coastline and the fault (b) for periods of 2 and 20 min. | 46 |
| 3.10 | The in-phase and quadrature induction arrow responses V along a traverse perpendicular to the coastline and the fault for periods of 1-90 min. | 49 |
| 3.11 | The in-phase induction arrow maximum responses V_{ma} (at the | |

| | | |
|------|---|----|
| | coastline) and V_{mb} (just to the left of the fault) as a function of period for fault depths $Z_b=5, 25, 50, 75$ km for $S=50, 100, 200$ km. | 50 |
| 3.12 | The quadrature induction arrow maximum responses V_{ma} (at the coastline) and V_{mb} (just to the left of the fault) as a function of period for fault depths $Z_b=5, 25, 50, 75$ km for $S=50, 100, 200$ km. | 52 |
| 3.13 | The zero in-phase response period T_0 as a function of the distance Y from the coastline. The induction arrows for 3 and 10 min are also shown. | 54 |
| 3.14 | The zero quadrature response period T_0 as a function of the distance Y from the coastline. The induction arrows for 3 and 10 min are also shown. | 55 |
| 3.15 | Empirical plots of the zero in-phase response period T_0 as a function of the distance Y from the coastline for $Z_b=5, 25, 50, 75$ km and for $S=50, 100, 200$ km. | 57 |
| 3.16 | Empirical plots of the zero quadrature response period T_0 as a function of the distance Y from the coastline for $Z_b=5, 25, 50, 75$ km and for $S=50, 100, 200$ km. | 59 |
| 3.17 | Empirical plots of T_m (the upper limit to the zero in-phase response period T_0) as a function of the fault depth Z_b for ocean-fault separation distances $S=50, 100, 200$ km. | 62 |
| 3.18 | The in-phase and quadrature induction arrow responses as a function of period for selected locations at distances $Y=15-45$ km from the coastline for $S=50$ km for fault depth $Z_b=5$ km. | 64 |
| 3.19 | The in-phase and quadrature induction arrow responses as a function of period for selected locations at distances $Y=15-45$ km from the coastline for $S=50$ km for fault depth $Z_b=25$ km. | 66 |
| 3.20 | The in-phase and quadrature induction arrow responses as a function of period for selected locations at distances $Y=15-45$ km from the coastline for $S=50$ km for fault depth $Z_b=50$ km. | 67 |
| 3.21 | The in-phase and quadrature induction arrow responses V at 2 and 20 min for the ocean, the fault, the ocean and the fault parallel to the coastline, and the sum of the ocean and the fault responses for $S=50$ km and $Z_b=5$ km. | 69 |
| 3.22 | The in-phase and quadrature induction arrow responses V at 2 | |

| | | |
|------|--|----|
| | and 20 min for the ocean, the fault, the ocean and the fault parallel to the coastline, and the sum of the ocean and the fault responses for $S=50$ km and $Z_b=75$ km. | 71 |
| 3.23 | The in-phase and quadrature induction arrow responses V at 2 and 20 min for the ocean, the fault, the ocean and the fault parallel to the coastline, and the sum of the ocean and the fault responses for $S=100$ km and $Z_b=5$ km. | 73 |
| 3.24 | The in-phase and quadrature induction arrow responses V at 2 and 20 min for the ocean, the fault, the ocean and the fault parallel to the coastline, and the sum of the ocean and the fault responses for $S=100$ km and $Z_b=5$ km. | 75 |
| 4.1 | The cross-section of the model of a conductive fault (a) in a resistive host earth underlain by a conductive substratum (c). | 81 |
| 4.2 | The in-phase and quadrature induction arrow responses V along a traverse perpendicular to the fault for periods of 2 and 20 min for a 5 km depth fault. W is the width of the response curve at half maximum. | 82 |
| 4.3 | The in-phase and quadrature induction arrow responses along a traverse perpendicular to the fault for 1-90 min for a 5 km depth conductive fault underlain by a conductive substratum. | 84 |
| 4.4 | The in-phase and quadrature induction arrow responses along a traverse perpendicular to the fault for 1-90 min for a 50 km depth conductive fault underlain by a conductive substratum. | 86 |
| 4.5 | Empirical plots of the in-phase and quadrature maximum responses V_m as a function of period for the fault depths $Z_a=5, 25, 50, 75$ km underlain by a conductive substratum. | 87 |
| 4.6 | The period T at which the quadrature V_m is maximum as a function of the fault depth Z_a for the conductive substratum depths $Z_c=100$ and 200 km. | 89 |
| 4.7 | The width W of the fault response curves at half maximum (as shown in Fig. 4.2) as a function of period for the fault depths $Z_a=5, 25, 50$ km. | 91 |
| 4.8 | The cross-section of the model of parallel major (a) and minor (b) conductive faults in a resistive host earth, all underlain by a conductive substratum (c). | 93 |
| 4.9 | The in-phase and quadrature induction arrow responses V along | |

| | | |
|------|---|-----|
| | a traverse perpendicular to the faults for periods of 2 and 20 min. | 94 |
| 4.10 | The in-phase and quadrature induction arrow responses V along a traverse perpendicular to the faults for 1-90 min for a pair of parallel major and minor faults separated by a distance S | 97 |
| 4.11 | Empirical plots of the in-phase response V_{ma} and V_{mb} as a function of period for the major fault depth $Z_a=75$ km and the minor fault depths $Z_b=5, 25, 50$ km for $S=50, 100, 200$ km. | 99 |
| 4.12 | Empirical plots of the quadrature response V_{ma} and V_{mb} as a function of period for the major fault depth $Z_a=75$ km and the minor fault depths $Z_b=5, 25, 50$ km for $S=50, 100, 200$ km. | 100 |
| 4.13 | Empirical plots of the period T at which the quadrature V_{mb} is maximum as a function of the minor fault depth Z_b for three separation distances $S=50, 100, 200$ km. | 102 |
| 4.14 | The zero in-phase response period T_0 as a function of the distance Y from the major fault. The induction arrows for 2 and 10 min are also shown. | 104 |
| 4.15 | The zero quadrature response period T_0 as a function of the distance Y from the major fault. The induction arrows for 2 and 10 min are also shown. | 105 |
| 4.16 | Empirical plots of the zero in-phase response period T_0 as a function of the distance Y from the major fault for $Z_b=5, 25, 50$ km and for $S=50, 100, 200$ km. | 107 |
| 4.17 | Empirical plots of the zero quadrature response period T_0 as a function of the distance Y from the major fault for $Z_b=5, 25, 50$ km and for $S=50, 100, 200$ km. | 109 |
| 4.18 | The in-phase and quadrature induction arrow responses as a function of period for selected locations at distances $Y=15-45$ km from the major fault ($Z_a=75$ km) for $S=50$ km for $Z_b=5$ km. | 111 |
| 4.19 | The in-phase and quadrature induction arrow responses as a function of period for selected locations at distances $Y=15-45$ km from the major fault ($Z_a=75$ km) for $S=50$ km for $Z_b=25$ km. | 113 |
| 4.20 | The in-phase and quadrature induction arrow responses as a function of period for selected locations at distances | |

| | | |
|------|---|-----|
| | Y=15-45 km from the major fault ($Z_a=75$ km) for S=50 km for $Z_b=50$ km. | 114 |
| 4.21 | The in-phase and quadrature induction arrow responses V at 2 and 20 min for the major fault, the minor fault, the pair of parallel faults, and the sum of the responses of the major and minor faults for $Z_b=5$ km and S=50 km. | 116 |
| 4.22 | The in-phase and quadrature induction arrow responses V at 2 and 20 min for the major fault, the minor fault, the pair of parallel faults, and the sum of the responses of the major and minor faults for $Z_b=5$ km and S=100 km. | 118 |
| 5.1 | Reconstructed tectonic history of New Zealand (adapted from Thornton, 1993). | 123 |
| 5.2 | The tectonic configuration 130 Ma ago as compared with that of the present (adapted from Thornton, 1993). The rock types indicated were formed in the period 300-130 Ma. | 124 |
| 5.3 | A possible tectonic history of New Zealand during the last 30 Ma (adapted from Thornton, 1993). | 126 |
| 5.4 | Earthquakes in New Zealand in 1992, magnitudes 3.0 and greater, provided by Smith (1994). | 128 |
| 5.5 | The tectonic setting in the New Zealand region. | 130 |
| 5.6 | a) The subducted Pacific Plate as viewed from the west (adapted from Robinson, 1986). b) Possible segmentation (dashed lines) of the subducted Pacific Plate (adapted from Reyners, 1983). | 133 |
| 5.7 | a) The New Zealand physiography. b) Fault distribution of New Zealand (adapted from Suggate, 1978, Campbell, 1992, Thornton, 1993, Beanland, 1994, Cowan, 1994). For profiles AA' and BB' see Fig. 5.6. | 135 |
| 5.8 | Sedimentary basins of New Zealand (adapted from Czochanska et al., 1987). | 137 |
| 6.1 | Simplified map of the modelled New Zealand region including the ocean bathymetry and showing the model traverses for which model measurements were carried out. | 140 |
| 6.2 | Simplified map of New Zealand showing the selected traverses N1-N8 on North Island and S1-S8 on South Island. | 143 |
| 6.3 | The in-phase and quadrature B_z along traverses over the model at 10 min for X-polarization. | 144 |

| | | |
|------|---|-----|
| 6.4 | The in-phase and quadrature V_x (x-component of the induction arrow V) response curves at 10 min for traverses over the model. | 147 |
| 6.5 | The in-phase and quadrature V_y (y-component of the induction arrow V) response curves at 10 min for traverses over the model. | 148 |
| 6.6 | Simplified map of the New Zealand North Island showing the location of the model traverses (N1-N8) for which model induction arrows are provided. | 150 |
| 6.7 | The in-phase induction arrows for traverses N1-N8 on North Island for periods of 5-120 min. | 151 |
| 6.8 | The quadrature induction arrows for traverses N1-N8 on North Island for periods of 5-120 min. | 154 |
| 6.9 | Simplified map of the New Zealand South Island showing the location of the model traverses (S1-S8) for which model induction arrows are provided. | 156 |
| 6.10 | The in-phase induction arrows for traverses S1-S8 on South Island for periods of 5-120 min. | 157 |
| 6.11 | The quadrature induction arrows for traverses S1-S8 on South Island for periods of 5-120 min. | 159 |
| 7.1 | Map of the North Island of New Zealand showing the 35 field site locations where geomagnetic measurements were carried out by Midha (1979) andingham (1985a,b, 1987, 1988b). | 164 |
| 7.2 | Analogue model and field site in-phase induction arrows for five periods at the 35 locations (given in Fig. 7.1) on the North Island of New Zealand. | 166 |
| 7.3 | Analogue model and field site quadrature induction arrows for five periods at the 35 locations (given in Fig. 7.1) on the North Island of New Zealand. | 169 |
| 7.4 | The in-phase and quadrature model (solid arrows) and field site (dashed arrows), and the in-phase and quadrature difference arrows (dotted arrows) at Eyrewell (Kellett et al., 1988), for periods of 5, 10, 15, 20, 35, and 80 min. | 172 |
| 7.5 | The in-phase difference induction arrows (field site arrows (Bromley, 1979) minus analogue model arrows) in the Southern Alps region of South Island. | 177 |

| | | |
|------|---|-----|
| 7.6 | The quadrature difference induction arrows (field site arrows (Bromley, 1979) minus analogue model arrows) in the Southern Alps region of South Island. | 181 |
| 7.7 | The Chamalaun and McKnight (1993) magnetometer array field sites. | 186 |
| 7.8 | The analogue model and thin sheet numerical model (Chamalaun and McKnight, 1993) in-phase induction arrow amplitudes at selected coastal and inland sites in the New Zealand region. | 187 |
| 7.9 | The x and y-components of the field site induction arrows, the analogue model induction arrows, and the difference induction arrow responses at field site EYR (see Figs. 7.4 and 7.7). | 190 |
| 7.10 | The in-phase and quadrature analogue model and field site (Chamalaun and McKnight, 1993) induction arrows at 10 min period. | 191 |
| 7.11 | Geological and tectonic features on the North Island of New Zealand. The geomagnetic field sites are indicated as black dots. | 193 |
| 7.12 | Geological and tectonic features on the South Island of New Zealand. The geomagnetic field sites are indicated as black dots. | 195 |
| 7.13 | The in-phase difference arrows on North Island at 10 min period. | 198 |
| 7.14 | The quadrature difference arrows on North Island at 10 min period. | 199 |
| 7.15 | The in-phase difference arrows on North Island at 50 min period. | 200 |
| 7.16 | The quadrature difference arrows on North Island at 50 min period. | 201 |
| 7.17 | The in-phase difference arrows on South Island at 10 min period. | 206 |
| 7.18 | The quadrature difference arrows on South Island at 10 min period. | 207 |
| 7.19 | The in-phase difference arrows on South Island at 50 min period. | 209 |

| | | |
|------|--|-----|
| 7.20 | The quadrature difference arrows on South Island at 50 min period. | 210 |
| A.1 | The in-phase and quadrature induction arrow responses as a function of period for selected locations at distances $Y=35-95$ km from the coastline for $S=100$ km for the fault depth $Z_b=5$ km. | 246 |
| A.2 | The in-phase and quadrature induction arrow responses as a function of period for selected locations at distances $Y=35-95$ km from the coastline for $S=100$ km for the fault depth $Z_b=25$ km. | 247 |
| A.3 | The in-phase and quadrature induction arrow responses as a function of period for selected locations at distances $Y=35-95$ km from the coastline for $S=100$ km for the fault depth $Z_b=50$ km. | 248 |
| A.4 | The in-phase and quadrature induction arrow responses as a function of period for selected locations at distances $Y=60-180$ km from the coastline for $S=200$ km for the fault depth $Z_b=5$ km. | 249 |
| A.5 | The in-phase and quadrature induction arrow responses as a function of period for selected locations at distances $Y=60-180$ km from the coastline for $S=200$ km for the fault depth $Z_b=25$ km. | 250 |
| A.6 | The in-phase and quadrature induction arrow responses as a function of period for selected locations at distances $Y=60-180$ km from the coastline for $S=200$ km for the fault depth $Z_b=50$ km. | 251 |
| B.1 | The in-phase and quadrature induction arrow responses V along a traverse perpendicular to the fault for periods of 1-90 min for a 25 km depth conductive fault underlain by a conductive substratum. | 253 |
| B.2 | The in-phase and quadrature induction arrow responses V along a traverse perpendicular to the fault for periods of 1-90 min for a 75 km depth conductive fault underlain by a conductive substratum. | 254 |
| C.1 | The in-phase and quadrature induction arrow responses as a function of period for selected locations at distances $Y=30-90$ km from the major fault ($Z_a=75$ km) for $S=100$ km for $Z_b=5$ km. | 256 |
| C.2 | The in-phase and quadrature induction arrow responses as a function of period for selected locations at distances | |

| | | |
|-----|--|-----|
| | Y=30-90 km from the major fault ($Z_a=75$ km) for S=100 km for $Z_b=25$ km. | 257 |
| C.3 | The in-phase and quadrature induction arrow responses as a function of period for selected locations at distances Y=30-90 km from the major fault ($Z_a=75$ km) for S=100 km for $Z_b=50$ km. | 258 |
| C.4 | The in-phase and quadrature induction arrow responses as a function of period for selected locations at distances Y=60-180 km from the major fault ($Z_a=75$ km) for S=200 km for $Z_b=5$ km. | 259 |
| C.5 | The in-phase and quadrature induction arrow responses as a function of period for selected locations at distances Y=60-180 km from the major fault ($Z_a=75$ km) for S=200 km for $Z_b=25$ km. | 260 |
| C.6 | The in-phase and quadrature induction arrow responses as a function of period for selected locations at distances Y=60-180 km from the major fault ($Z_a=75$ km) for S=200 km for $Z_b=50$ km. | 261 |
| D.1 | The in-phase and quadrature B_z along traverses over the model at 25 min for X-polarization. | 263 |
| D.2 | The in-phase and quadrature B_z along traverses over the model at 50 min for X-polarization. | 264 |
| D.3 | The in-phase and quadrature B_z along traverses over the model at 80 min for X-polarization. | 265 |
| D.4 | The in-phase and quadrature B_y along traverses over the model at 10 min for X-polarization. | 266 |
| D.5 | The in-phase and quadrature B_y along traverses over the model at 25 min for X-polarization. | 267 |
| D.6 | The in-phase and quadrature B_y along traverses over the model at 50 min for X-polarization. | 268 |
| D.7 | The in-phase and quadrature B_y along traverses over the model at 80 min for X-polarization. | 269 |
| D.8 | The in-phase and quadrature B_x along traverses over the model at 10 min for X-polarization. | 270 |
| D.9 | The in-phase and quadrature B_x along traverses over the model at 25 min for X-polarization. | 271 |

| | | |
|------|--|-----|
| D.10 | The in-phase and quadrature B_x along traverses over the model at 50 min for X-polarization. | 272 |
| D.11 | The in-phase and quadrature B_x along traverses over the model at 80 min for X-polarization. | 273 |
| D.12 | The in-phase and quadrature B_z along traverses over the model at 10 min for Y-polarization. | 274 |
| D.13 | The in-phase and quadrature B_z along traverses over the model at 25 min for Y-polarization. | 275 |
| D.14 | The in-phase and quadrature B_z along traverses over the model at 50 min for Y-polarization. | 276 |
| D.15 | The in-phase and quadrature B_z along traverses over the model at 80 min for Y-polarization. | 277 |
| D.16 | The in-phase and quadrature B_x along traverses over the model at 10 min for Y-polarization. | 278 |
| D.17 | The in-phase and quadrature B_x along traverses over the model at 25 min for Y-polarization. | 279 |
| D.18 | The in-phase and quadrature B_x along traverses over the model at 50 min for Y-polarization. | 280 |
| D.19 | The in-phase and quadrature B_x along traverses over the model at 80 min for Y-polarization. | 281 |
| D.20 | The in-phase and quadrature B_y along traverses over the model at 10 min for Y-polarization. | 282 |
| D.21 | The in-phase and quadrature B_y along traverses over the model at 25 min for Y-polarization. | 283 |
| D.22 | The in-phase and quadrature B_y along traverses over the model at 50 min for Y-polarization. | 284 |
| D.23 | The in-phase and quadrature B_y along traverses over the model at 80 min for Y-polarization. | 285 |
| E.1 | The in-phase and quadrature V_x (x-component of the induction arrow V) response curves at 5 min for traverses over the model. | 287 |
| E.2 | The in-phase and quadrature V_x (x-component of the induction arrow V) response curves at 15 min for traverses over the model. | 288 |

| | | |
|------|--|-----|
| E.3 | The in-phase and quadrature V_x (x-component of the induction arrow V) response curves at 20 min for traverses over the model. | 289 |
| E.4 | The in-phase and quadrature V_x (x-component of the induction arrow V) response curves at 25 min for traverses over the model. | 290 |
| E.5 | The in-phase and quadrature V_x (x-component of the induction arrow V) response curves at 50 min for traverses over the model. | 291 |
| E.6 | The in-phase and quadrature V_x (x-component of the induction arrow V) response curves at 80 min for traverses over the model. | 292 |
| E.7 | The in-phase and quadrature V_x (x-component of the induction arrow V) response curves at 120 min for traverses over the model. | 293 |
| E.8 | The in-phase and quadrature V_y (y-component of the induction arrow V) response curves at 5 min for traverses over the model. | 294 |
| E.9 | The in-phase and quadrature V_y (y-component of the induction arrow V) response curves at 15 min for traverses over the model. | 295 |
| E.10 | The in-phase and quadrature V_y (y-component of the induction arrow V) response curves at 20 min for traverses over the model. | 296 |
| E.11 | The in-phase and quadrature V_y (y-component of the induction arrow V) response curves at 25 min for traverses over the model. | 297 |
| E.12 | The in-phase and quadrature V_y (y-component of the induction arrow V) response curves at 50 min for traverses over the model. | 298 |
| E.13 | The in-phase and quadrature V_y (y-component of the induction arrow V) response curves at 80 min for traverses over the model. | 299 |
| E.14 | The in-phase and quadrature V_y (y-component of the induction arrow V) response curves at 120 min for traverses over the model. | 300 |
| F.1 | The x- and y-components of the field site induction arrows as a function of period at BAL, BIR and CAR. | 302 |

| | | |
|------|--|-----|
| F.2 | The x- and y-components of the field site induction arrows as a function of period at CLA, COO and EYR. | 303 |
| F.3 | The x- and y-components of the field site induction arrows as a function of period at FAI, GIS and GLE. | 304 |
| F.4 | The x- and y-components of the field site induction arrows as a function of period at HAM, HOK and INC. | 305 |
| F.5 | The x- and y-components of the field site induction arrows as a function of period at INV, MAN and MAS. | 306 |
| F.6 | The x- and y-components of the field site induction arrows as a function of period at MIL, MOU and MUR. | 307 |
| F.7 | The x- and y-components of the field site induction arrows as a function of period at NAP, NEW and OAM. | 308 |
| F.8 | The x- and y-components of the field site induction arrows as a function of period at OHA, OXF and PUP. | 309 |
| F.9 | The x- and y-components of the field site induction arrows as a function of period at RAN, RIV and TAU. | 310 |
| F.10 | The x- and y-components of the field site induction arrows as a function of period at TEK, TIM and WES. | 311 |
| F.11 | The x- and y-components of the field site induction arrows as a function of period at WHG, WHK, WHP and WOO. | 312 |
| G.1 | The x- and y-components of the analogue model induction arrows as a function of period at BAL, BIR and CAR. | 314 |
| G.2 | The x- and y-components of the analogue model induction arrows as a function of period at CLA, COO and EYR. | 315 |
| G.3 | The x- and y-components of the analogue model induction arrows as a function of period at FAI, GIS and GLE. | 316 |
| G.4 | The x- and y-components of the analogue model induction arrows as a function of period at HAM, HOK and INC. | 317 |
| G.5 | The x- and y-components of the analogue model induction arrows as a function of period at INV, MAN and MAS. | 318 |
| G.6 | The x- and y-components of the analogue model induction arrows as a function of period at MIL, MOU and MUR. | 319 |
| G.7 | The x- and y-components of the analogue model induction arrows as a function of period at NAP, NEW and OAM. | 320 |

| | | |
|------|---|-----|
| G.8 | The x- and y-components of the analogue model induction arrows as a function of period at OHA, OXF and PUP. | 321 |
| G.9 | The x- and y-components of the analogue model induction arrows as a function of period at RAN, RIV and TAU. | 322 |
| G.10 | The x- and y-components of the analogue model induction arrows as a function of period at TEK, TIM and WES. | 323 |
| G.11 | The x- and y-components of the analogue model induction arrows as a function of period at WHG, WHK, WHP and WOO. | 324 |
| H.1 | The x- and y-components of the difference induction arrows as a function of period at sites BAL, BIR and CAR. | 326 |
| H.2 | The x- and y-components of the difference induction arrows as a function of period at sites CLA, COO and EYR. | 327 |
| H.3 | The x- and y-components of the difference induction arrows as a function of period at sites FAI, GIS and GLE. | 328 |
| H.4 | The x- and y-components of the difference induction arrows as a function of period at sites sites HAM, HOK and INC. | 329 |
| H.5 | The x- and y-components of the difference induction arrows as a function of period at sites INV, MAN and MAS. | 330 |
| H.6 | The x- and y-components of the difference induction arrows as a function of period at sites MIL, MOU and MUR. | 331 |
| H.7 | The x- and y-components of the difference induction arrows as a function of period at sites sites NAP, NEW and OAM. | 332 |
| H.8 | The x- and y-components of the difference induction arrows as a function of period at sites OHA, OXF and PUP. | 333 |
| H.9 | The x- and y-components of the difference induction arrows as a function of period at sites RAN, RIV and TAU. | 334 |
| H.10 | The x- and y-components of the difference induction arrows as a function of period at sites sites TEK, TIM and WES. | 335 |
| H.11 | The x- and y-components of the difference induction arrows as a function of period at sites WHG, WHK, WHP and WOO. | 336 |
| I.1 | The in-phase and quadrature model and field site (Chamalaun and McKnight, 1993) induction arrows at 5 min. | 338 |
| I.2 | The in-phase and quadrature model and field site (Chamalaun | |

| | | |
|-----|--|-----|
| | and McKnight, 1993) induction arrows at 15 min. | 339 |
| I.3 | The in-phase and quadrature model and field site (Chamalaun and McKnight, 1993) induction arrows at 20 min. | 340 |
| I.4 | The in-phase and quadrature model and field site (Chamalaun and McKnight, 1993) induction arrows at 25 min. | 341 |
| I.5 | The in-phase and quadrature model and field site (Chamalaun and McKnight, 1993) induction arrows at 50 min. | 342 |
| I.6 | The in-phase and quadrature model and field site (Chamalaun and McKnight, 1993) induction arrows at 80 min. | 343 |
| J.1 | The in-phase and quadrature difference induction arrows at 34 sites at 5 min period. | 345 |
| J.2 | The in-phase and quadrature difference induction arrows at 34 sites at 15 min period. | 346 |
| J.3 | The in-phase and quadrature difference induction arrows at 34 sites at 20 min period. | 347 |
| J.4 | The in-phase and quadrature difference induction arrows at 34 sites at 25 min period. | 348 |
| J.5 | The in-phase and quadrature difference induction arrows at 34 sites at 80 min period. | 349 |

ACKNOWLEDGEMENTS

I am greatly indebted to my supervisor, Dr. H.W. Dosso, for encouraging me in my studies and for suggesting this research problem. His generous support and valuable guidance in conducting the research and the writing of this dissertation are very much appreciated.

I would also like to thank Dr. W. Nienaber, Dr. Z. Meng, Dr. A.K. Agarwal, and my fellow graduate students S. Kang and X. Pu for helpful assistance and useful discussions in the various stages of my research.

The financial support in the form of a University of Victoria Fellowship, the Charles S. Humphrey Graduate Student Award, and a research assistantship provided by my supervisor Dr. H. W. Dosso is gratefully acknowledged.

Last but not least, I would like to thank my wife Ping, my son Brandon, and my parents for their encouragement, patience and understanding throughout the time of this research.

Chapter I

INTRODUCTION

Electrical conductivity is one of the physical properties of the rock constituting the crust and mantle. The conductivity distribution within the earth has been studied for decades employing the principle of electromagnetic induction. It is now well understood that geomagnetic variations observed at the earth's surface are associated with electric currents induced in the conducting medium of the earth by external time-varying electromagnetic fields that originate in the ionosphere and magnetosphere. Upon striking the earth's surface, most of the incident energy of the electromagnetic fields is reflected. The small portion of energy transmitted travels vertically downward. As the field propagates into the earth, its amplitude is reduced. The depth at which the field has decreased to $1/e$ (37%) of its value at the surface is called the skin depth:

$$\delta(T) = [T/(\pi\mu\sigma)]^{1/2} \text{ m}, \quad (1.1)$$

where T is the period in seconds, μ is the magnetic permeability in Henrys/m (H/m) and σ is the conductivity in Siemens/meter (S/m). The magnetic permeability is generally taken as the free space value, $\mu_0 = 4\pi \times 10^{-7}$ H/m. Electromagnetic (EM) methods respond to an integration of the electrical conductivity distribution from the surface to the depth of penetration, normally taken as several skin depths. Geomagnetic fields at short periods are primarily sensitive to the conductivity distribution near the site, whereas at long periods the fields are also

influenced by the distant conductivity distribution. EM methods are more sensitive to conductance S (conductivity-thickness product, in Siemens) than to the conductivity or thickness of a zone of enhanced conductivity (Jones, 1992). On a global scale, the geomagnetic field observed at the surface of the earth can be separated into inducing external, and induced internal parts. The ratio of the induced to inducing fields yields information on the nature of both the external field and the global conductivity structure within the earth. Roberts (1986) has given a critical review of global electromagnetic induction.

1.1 Regional Electromagnetic Induction Studies

Regional electromagnetic induction studies deal with a limited region of the earth, usually of the order of several hundred km in depth and in horizontal range. On this scale the curvature of the earth can be neglected. An external field originating in the ionosphere and magnetosphere can be treated as being approximately spatially uniform within an area of local extent. On a regional scale, the observed field usually can not be separated into inducing and induced parts, but the variation of the total fields observed on the earth's surface should contain some information on the subsurface conductivity structure. Recent reviews of regional electromagnetic induction studies have been provided by Haak and Hutton (1986), Kaikkonen (1986), Chave and Booker (1987), Jones (1987, 1992, 1993), Campbell and Schiffmacher (1988), Hjelt (1988), Gough (1989, 1992), Schwarz (1990), Hjelt and Korja (1993).

1.1.1 Magnetotelluric (MT) Studies

Cagniard's (1953) magnetotelluric method is well known for studying regional conductivity distributions in the earth's crust and upper mantle. In the MT method, large scale naturally-occurring electromagnetic source fields of long period (a few seconds to a few hours) are used to probe the earth up to depths of a few hundred km. The principal reason for this is that natural fields can be considered to be essentially plane waves in the mid-latitudes and to have sufficient energy at long periods to generate a detectable response from very deep structure. In this period range displacement currents, compared with the conduction currents, can be neglected. Thus the problem may be treated as diffusion of the electromagnetic field into the conducting medium. A collection of fifty-five papers on the MT method up to the early 1980's is given by Vozoff (1986). In MT studies the horizontal electric field components (E_x and E_y in V/m) and the horizontal magnetic induction (B_x and B_y in Teslas) are measured simultaneously at a field site. Usually x denotes north (or along a strike for a 2-dimensional body), y denotes east (or perpendicular to a strike), and thus z is directed vertically downwards. The fields are normally measured in the time domain and then transformed into the frequency domain through Fourier transformations. The amplitude and phase relationship between $E(\omega)$ and $B(\omega)$ at a particular frequency ω , are indicative of the conductivity distribution. The horizontal field components are related by the frequency dependent complex MT impedance tensor:

$$\begin{pmatrix} E_x \\ E_y \end{pmatrix} = \frac{1}{\mu} \begin{pmatrix} Z_{xx} & Z_{xy} \\ Z_{yx} & Z_{yy} \end{pmatrix} \begin{pmatrix} B_x \\ B_y \end{pmatrix}. \quad (1.2)$$

The principal impedances Z_{xy} and Z_{yx} are converted to apparent resistivities (ρ_a in Ωm) and phases (ϕ) using:

$$(\rho_a)_{xy} = (1/\omega\mu)[Z_{xy}(\omega)]^2, \text{ and} \quad (1.3)$$

$$\phi_{xy}(\omega) = \tan^{-1}[\text{Imag } Z_{xy}(\omega)/\text{Real } Z_{xy}(\omega)]. \quad (1.4)$$

Expressions similar to Eq.(1.3) and Eq.(1.4) determine $(\rho_a)_{yx}$ and $\phi_{yx}(\omega)$. For a uniform earth, the apparent resistivities are the true resistivity of the half-space, and the phase ϕ_{xy} is 45° .

In a one-dimensional (1D) structure where the conductivity varies only with depth, the impedance tensor reduces to the simple form:

$$Z_{1D} = \begin{pmatrix} 0 & Z_{xy} \\ -Z_{xy} & 0 \end{pmatrix}. \quad (1.5)$$

Because of the symmetry, the impedance for a layered earth does not depend on the orientation of the measuring axes at the earth's surface. So in this case $Z_{xy} = -Z_{yx}$. The negative sign for the lower off-diagonal element indicates that the sign convention is such that the phases of this element are in the third rather than the first phase angle quadrant. In a layered earth, the phase varies with the conductivity of the layers. For a 1D model in which the conductivity increases with increasing depth, the phase lies between 45° and 90° , and conversely for the model in which the conductivity decreases with increasing depth, the phase lies between 0° and 45° . Mathematical modelling for 1D geoelectric structure has been greatly advanced and the analytical solutions and many inversion schemes have been widely used (e.g., Niblett and Sayn-Wittgenstein, 1960; Parker, 1980; Fischer and LeQuang, 1981; Schmucker, 1983; Constable et al., 1987; Dosso and Oldenburg, 1991; Weaver and Agarwal, 1993).

In a two-dimensional (2D) environment where the axes of the co-ordinate frame are aligned parallel (x) and perpendicular (y) to the strike, the impedance tensor becomes:

$$Z_{2D} = \begin{pmatrix} 0 & Z_{xy} \\ Z_{yx} & 0 \end{pmatrix}. \quad (1.6)$$

The techniques of 2D forward modelling and 2D inversion are widely used (e.g., Brewitt-Taylor and Weaver, 1976; Jones and Craven, 1990; Kurtz et al., 1990; Smith and Booker, 1991; Oldenburg and Ellis, 1993; Agarwal and Weaver, 1993; Agarwal et al., 1993).

In a fully three-dimensional (3D) earth model, MT data are not as well understood. The apparent resistivity curves giving ρ_a as a function of period are found in many cases to demonstrate a strongly anisotropic earth due to lateral inhomogeneities. Much effort has gone into calculating the distortion of the apparent resistivity curves for 2-D and 3-D conductivity structures (e.g., Groom and Bailey, 1989; Cerv and Pek, 1990; Jiracek, 1990; Groom and Bahr, 1992; Singer, 1992). Due to prohibitively high computational costs, 3D modelling is usually undertaken only for representative structure, and 3D inversions for arbitrarily-shaped realistic structures continue to pose a challenge (Raiche, 1993; Pu et al., 1993). Approximate 3D solutions, such as thin-sheet methods, have been developed and used for modelling continent-ocean boundaries (e.g., Vasseur and Weidelt, 1977; Dawson and Weaver, 1979; Weaver, 1982, McKirdy et al., 1985; Agarwal and Weaver, 1989; Fainberg et al., 1993; Heinson and Lilley, 1993).

1.1.2 Geomagnetic Depth Sounding (GDS) Studies

Geomagnetic depth sounding (GDS) is based on the ratio of the vertical to horizontal magnetic field responses. In GDS, similar to MT, the natural source is used. The vertical (B_z') and the two horizontal (B_x' and B_y') components are measured at the same site on the surface of the earth, usually in the time domain. These components are then transformed into the frequency domain through Fourier transformation, for example:

$$B_z(\omega) = \int_{-\infty}^{\infty} B_z'(t) \exp(-i\omega t) dt, \quad (1.7)$$

where $B_z(\omega)$ is the transform of the time series $B_z'(t)$ at angular frequency ω . The correlation of the vertical component with the horizontal components in the frequency domain for a uniform inducing field is assumed to be:

$$B_z = aB_x + bB_y + \Delta, \quad (1.8)$$

where B_z , B_x and B_y are the Fourier transformations of the vertical and two horizontal components. The coefficients a and b are complex numbers and are generally frequency dependent (Schmucker, 1970). To determine the complex coefficients a and b , magnetic field components for two independent polarizations of the regional source field are required. If Δ is negligible, and thus not included, it follows from Eq.(1.8) that

$$a = \frac{B_{z1}B_{y2} - B_{z2}B_{y1}}{B_{x1}B_{y2} - B_{x2}B_{y1}}, \quad (1.9)$$

$$b = \frac{B_{z2}B_{x1} - B_{z1}B_{x2}}{B_{x1}B_{y2} - B_{x2}B_{y1}}. \quad (1.10)$$

Statistical methods are used in the field data processing to minimize the error Δ (e.g., Everett and Hyndman, 1967). Lateral conductivity variations cause defor-

mation in the induced current system which in turn yields an anomalous field. The coefficients a and b characterize the frequency-dependent response at the field site. The pairs $\text{Real}(-a, -b)$ and $\text{Imaginary}(-a, -b)$ are defined respectively as the in-phase and quadrature induction arrows (Parkinson, 1959, 1962; Wiese, 1962; Schmucker, 1970), with the signs of both the in-phase and quadrature a and b reversed. This follows the sign convention of Lilley and Arora (1982) for time-varying fields of the form $\exp(i\omega t)$, so that both the in-phase and quadrature arrows at long periods point towards current concentrations. In the present work, the symbol to be used for the induction arrow is V , with in-phase and quadrature parts. In the Cartesian coordinate system used throughout, it will be convenient in some cases to discuss the V_x and V_y components of each the in-phase and quadrature parts.

Induction arrows are commonly used to display anomalous geomagnetic variations associated with lateral conductivity inhomogeneities. The magnitudes and directions, as well as the components of the induction arrows, can readily be calculated and displayed on geographical maps. Since the magnitudes and directions of the induction arrows do not change under a rotation of the coordinate systems, B_x and B_y in Eq. 1.8 need not necessarily be northward and eastward. Gregori and Lanzerotti (1980, 1982), Jones (1981a) and Wolf (1982) have discussed in detail the different methodologies and arrow conventions and their relationships. In general, at a given site the in-phase induction arrow associated with a conductivity anomaly points in the direction of the horizontal field which is most efficient in inducing the anomalous vertical magnetic field observed at that site. In a 2-D case, this arrow usually points towards current concentration in the conductive body. How-

ever, at periods for which the depth of burial of the conductive body is more than one skin depth in the resistive host, the in-phase arrows (though small in amplitude) may point away from a buried conductor (e.g., Jones, 1986; Hu et al., 1989).

The properties of the quadrature induction arrow appear to be more complex than those of the in-phase arrow (e.g., Rokityansky, 1982; Nienaber et al., 1983; Chen and Fung, 1985, 1987; Agarwal and Dosso, 1990, 1993). At sufficiently short periods, in numerical studies of an ocean model, the quadrature arrow near the coast is seen to point away from (rather than towards) the conductive ocean, then with increasing period, the arrow magnitude decreases to become zero at a period (T_C) characteristic of the model. With further increase in period, the quadrature arrow reverses direction (to point towards the current concentrations) and increases in magnitude to some maximum value, then again decreases. The characteristic period (T_C) of the ocean model is the period at which the in-phase arrow amplitude is maximum and the quadrature arrow amplitude is zero (Rokityansky, 1982; Agarwal and Dosso, 1990, 1993). In a recent 2D numerical model study of the induction arrow spatial behaviour for a conductor in a resistive host, Agarwal and Dosso (1993) suggested that the characteristic period could be used to delineate the boundaries of an anomalous conductor, such as a buried conductive sill, and to provide information on the depth of the conductive substratum when the conductivity of the host is known. The analytic calculations of Weaver (1987), in studying the geomagnetic coast effect both at short (1 min) and long (60 min) periods, showed a sign reversal in the quadrature vertical magnetic field in the vicinity of maximum conductivity contrast. The sign reversal of the quadrature induction arrow at the conductive-resistive interface has also frequently been observed

in earlier analogue model experiments at the University of Victoria (Hebert et al. (1983a) for the Newfoundland coastal region, Hu et al. (1989) for a seamount, and Meng and Dosso (1990) for the Japan-China region). In field studies, DeLaurier et al. (1983) noted that for periods less than 35 min the quadrature induction arrow reversed direction at sea floor sites crossing the continental margin off Vancouver Island. The seemingly erratic behavior of reversing direction over a short period range, combined with the often rather small magnitudes of the quadrature induction arrows, has resulted in this component often being ignored in the interpretation of field site measurements. With improved methods of measurements and analysis of data, the behaviour of the quadrature arrow should aid the interpretation when its characteristics are fully understood.

1.1.3 Controlled Source Methods

Controlled source EM methods are alternative to natural source soundings in some circumstances (e.g., Nekut and Spies, 1989; Kurtz et al., 1990). Unlike natural source EM methods, artificial EM source methods can be used to optimize resolution and minimize interactions with local conductive structures. The source characteristics are precisely known and are controllable in time or frequency. Examples of the conventional controlled source techniques include LOTEM (Long Offset Transient ElectroMagnetic system: Keller et al., 1984; Strack, 1984; Skokan, 1991), CSAMT (Controlled Source Audio MagnetoTellurics: Boerner et al., 1990), and UTEM (University of Toronto ElectroMagnetic system: Kurtz et al., 1989). Controlled source EM methods are used in land-based petroleum exploration to a typical depth of a few km for mapping geological structures (e.g., Trevino and Edwards, 1983), stratigraphy (e.g., Macnae and Lamontagne, 1987),

hydrocarbon-induced alteration (e.g., Duckworth, 1987), and in some application to enhance the interpretation of other geophysical data such as MT and seismic reflection. The MT method of exploring the upper few kilometers of the seafloor has severe limitations due to the overlying conductive seawater that attenuates the natural source signal. However, seafloor controlled source methods can be used very effectively, since the EM source is placed on the seafloor. Examples of seafloor studies are those of the EMSLAB project (the EMSLAB Group, 1988; EMSLAB, 1989), and the Tasman project (Lilley et al., 1989). Constable (1990) provided a review of marine EM induction studies using controlled sources. Controlled source EM methods can also be used for exploration to depths on the order of 20 km, if the measurements are made on a relatively uniform resistive surface (e.g., Ward, 1983). Devices developed for other purposes can also be used to carry out large scale experiments to probe the lower crust of the earth, such as power transmission lines (e.g., Towle, 1980), decommissioned telephone lines (Constable et al., 1984), and the Kola Peninsula Magneto-hydrodynamic Generator (Velikhov et al., 1986). Simulated controlled source EM induction studies can also be carried out in laboratory using analogue models, for example, line currents (Dosso, 1966c; Dosso and Jacobs, 1968; Ogunade and Dosso, 1981), vertical and horizontal magnetic dipoles (Dosso, 1969; Ramaswamy et al., 1972; Thomson et al., 1972; Ramaswamy and Dosso, 1973, 1975, 1978; Hibbs et al., 1978). The major restrictions of controlled source EM methods include limited depth penetration and the limited number of modelling algorithms. Reviews of controlled source EM soundings were presented by Ward (1983), Keller (1989), and more recently by Boerner (1992).

1.1.4 Electromagnetic Analogue Model Studies

The theory of scaling in the simulation of electromagnetic systems and the applications to geophysical problems were introduced by Sinclair (1948), and further developed by many others employing laboratory modelling techniques for studying electromagnetic problems (e.g., Rankin et al., 1965; Dosso, 1966a; Ward, 1967; Brjunelli et al., 1969; Frischknecht, 1971; Morrison et al., 1982; Olm and Frischknecht, 1982).

The validity of laboratory analogue modelling in MT and GDS interpretations has long been recognized, particularly for 3D cases. Dosso (1966a), at the University of Victoria, developed a laboratory analogue modelling facility employing graphite plate to simulate conductive structures, and brine solution to simulate a resistive host earth. The graphite-brine conductivity contrast is of the correct order for modelling a wide range of realistic induction problems. An interesting range of induction problems has been modelled in the University of Victoria Geophysics Laboratory. These include the studies of idealized conductive structures such as vertical faults and dykes (Dosso, 1966b; Charters et al., 1989), conductive spheres and cylinders embedded in a resistive host earth (Ogunade et al., 1974; Ogunade and Dosso, 1977, 1980, 1981; Ramaswamy and Dosso, 1977), islands surrounded by an ocean (Ramaswamy et al., 1975, 1977), island-continent-ocean channels (Nienaber et al., 1976, 1977a, 1977b), cape and bay coastlines (Chan et al., 1981a; Dosso et al., 1986), and seamounts (Hu et al., 1984, 1986, 1989). Inducing source fields that have been employed in the laboratory electromagnetic induction studies include approximately uniform fields (Dosso, 1966a; Nienaber et al., 1976), non-uniform fields of line currents (Dosso, 1966c; Dosso and Jacobs,

1968; Ogunade and Dosso, 1981), fields of vertical and horizontal magnetic dipoles (Dosso, 1969; Ramaswamy et al., 1972; Thomson et al., 1972; Ramaswamy and Dosso, 1973, 1975, 1978; Hibbs et al., 1978), and a vertical line current source to simulate lightning induced Schumann Resonances (Heard et al., 1985). Magnetic field variations induced by ocean waves have also been simulated using mercury as a conductive fluid (Miles et al., 1977; Miles and Dosso, 1979, 1980). As well, 3D models of realistic coastal conductivity structures have been used to examine the effects of complex continental coastlines, for example, in the Vancouver Island region (Nienaber et al., 1979a, 1979b, 1980, 1982; Ramaswamy et al., 1980), in the San Juan Bay region of Vancouver Island (Chan et al., 1981a), in the eastern coastal region of North America (Dosso et al., 1980b), in the British Isles region (Dosso et al., 1980a; Nienaber et al., 1981), in the Assistance Bay region (Heard et al., 1983), in the Queen Charlotte Islands region (Chan et al., 1981b, 1983), in the Newfoundland region (Hebert et al., 1983a, b), in the Hainan Island region of the south China sea (Hu et al., 1983, 1984), in the Tasmania region (Dosso et al., 1985; Parkinson et al., 1988), in the Bohai Bay region of China (Meng et al., 1990), and the Japan-Korea-China region (Meng and Dosso, 1990; Dosso and Meng, 1992).

As part of the LITHOPROBE project (Clowes et al., 1984; Kurtz et al., 1986; Clowes et al., 1992) and EMSLAB (EMSLAB, 1989; Kurtz et al., 1990), an analogue model of the subducting Juan de Fuca plate region, including a simulation of conductive substructure associated with the subducting plate was constructed at the University of Victoria and measurements were used to aid in the interpretation of field measurements (Dosso and Nienaber, 1986, Chen et al., 1989; Dosso et al., 1989, 1990, 1992). These analogue model results, when compared with field site

measurements, clearly demonstrated the importance of the dipping conductive substructures on the observed electromagnetic field responses in regions of lithospheric plate subduction.

1.2 The Geomagnetic Coast Effect

The ocean-continent interface can influence the geomagnetic field observation since the conductivity of both seawater and the material beneath the ocean differs considerably from that of the continents. Near most coastlines the vertical/horizontal magnetic field ratio is greatly enhanced as the coast is approached from the landward side. This phenomenon is known as the geomagnetic coast effect and has been studied extensively since it was noted by Parkinson (1959). Induction arrows, characterizing induced current concentrations, have been widely used through the years to study this coast effect. Examples of the coast effect field studies include those of Parkinson (1962), Wiese (1962), Everett and Hyndman (1967), Schmucker (1970), Parkinson and Jones (1979), Gough and Ingham (1983), Jones (1983), Gough (1989). Numerical EM modelling techniques have also been widely used to study the coast effect, for example, Jones (1981b), DeLaurier et al., (1983), Fischer and Weaver (1986), Weaver (1987), Agarwal and Weaver (1989), Dosso and Meng (1992), Agarwal and Dosso (1993). In a thin sheet numerical model study of the coast effect, Fischer and Weaver (1986) examined induction for lateral variations in lithospheric conductivity in the presence of the strong ocean response. They concluded that MT methods do not perform very well in these circumstances, but GDS experiments are well suited to the detection of lateral conductivity changes. Analogue model studies of the ocean coast effect

have been carried out in many interesting coastal regions (as referred to in the previous section). Dosso (1973) provided a review of analogue model studies of the coast effect. Some recent analogue model studies of the coast effect are those of the Vancouver Island region (Dosso et al., 1989, 1990, 1992) and the Japan-China region (Meng et al., 1990; Meng and Dosso, 1990; Dosso and Meng, 1992). However, the coast effect component tends to mask any induction arrow component associated with a local anomalous conductor. In a region such as that of New Zealand (to be studied in the present work), where the coast effect is expected to be important for all inland sites, the interpretation of geomagnetic measurements would be much simplified if the coast effects could simply be removed before interpretation.

If the mutual coupling between the ocean and the anomalous conductor is small, it can readily be argued that in principle, the ocean response components can approximately be removed from the field measurements to yield the response of the anomalous conductor alone. Wolf (1983) investigated the mutual coupling effect for what he termed the additive case in which the anomalous conductor was located some distance from the ocean and underlain by a conductive layer, and the coupled case in which the anomalous conductor was overlain by the ocean and underlain by a conductive layer. His results indicated that simple subtraction for the additive case may be promising if the separation distance of the anomalous conductor and the ocean were sufficiently large, but for the coupled case, strong mutual induction effects would lead to erroneous interpretation. Weaver and Agarwal (1991) employed a thin sheet numerical model to study electromagnetic induction in a rectangular surface conductive anomaly near a coastline, and con-

cluded that in certain regions the induction arrow is not simply the resultant of the component for the ocean and the component for the anomalous conductor individually, unless the region is sufficiently far from the ocean so as to have negligible coupling through mutual induction and the redistribution of the charge accumulations on their boundaries. Dosso and Meng (1992) carried out calculations for 2-D numerical models of electromagnetic induction for anomalous conductors in continental and island coastal regions to determine empirical criteria for conductive structures that would permit such a subtraction. The anomalous conductors were in the form of upwellings and depressions in the conductive substratum. Their empirical curves provided the anomalous conductor - ocean separation distances required to permit a valid subtraction. As an application, they used analogue model measurements (Meng and Dosso, 1990) to subtract coast effects from field measurements in the Japan-China region. The interpretation of the resulting difference arrows supported the 2-D model of Utada et al. (1986) for Japan, a model that proposed a coastal 2-D conductor at moderate depth, and a second parallel subsurface conductor somewhat inland. Many other authors have also used difference induction arrows to interpret field observations (e.g. Bapat et al., 1993; Chamalaun and McKnight, 1993; Kang et al., 1993).

1.3 Previous EM Induction Studies in New Zealand

The present study of EM induction in New Zealand has been preceded by others. Lawrie (1965) discussed the geomagnetic fluctuations near coastlines on the North Island of New Zealand. Gill and MacDonald (1967) used a signal obtained by switching a major dc power transmission line to make large scale earth resistivity

measurements. MT and GDS studies have been carried out on the North Island of New Zealand by Christoffel and Linford (1968), Hurst (1974), Midha (1979), Ingham (1985a, 1985b, 1988a, 1988b, 1991), Boteler (1987), and on the South Island by Bromley (1979), Kellett et al. (1988). A review of the North Island measurements was provided by Ingham (1987). Much of the North Island work has centred around the Taupo Volcanic Zone which is the main area of geothermal activity in New Zealand. Midha (1979) undertook a major study in this area to investigate the geological structure beneath. However, the magnetovariational measurements over a wide range of periods produced induction arrows that pointed in the same north-east direction, for sites on either side of the Taupo Volcanic Zone. Midha (1979) reported that these induction arrow responses could not be explained by a simple coast effect, but could be caused by a conductor at depth. It has been suggested that such a conducting structure could be related to a fracture of the subducting plate. More recently, Chamalaun and McKnight (1993) carried out a magnetometer array study for 34 sites on New Zealand. An attempt was made to remove the ocean effect by means of a thin sheet numerical model.

1.4 Summary of the Work in This Dissertation

The motivation for the present analogue model measurements for the New Zealand coastal region is to delineate the coast effect, and to remove this component from the observed responses at field sites before interpretation. Laboratory EM responses of analogue models of a simple ocean, conductive fault, and combined ocean and conductive fault are used to demonstrate how the geomagnetic coast effect can be removed, and how the residue can be used to interpret field responses in terms of the many conductive faults present in New Zealand.

EM induction for pairs of elongated parallel conductors in a resistive host earth underlain by a conductive substratum for both continental and coastal regions is studied with the aid of laboratory analogue models. Magnetic field measurements for a wide range of periods are obtained for models of elongated conductors parallel to an ocean coastline, and for models that vary the separation distance and depth extent of the elongated conductors. It is demonstrated that in certain cases the coast effect induction arrows can be subtracted from those of the ocean-elongated conductors to yield the responses of the elongated conductors alone. The behaviour of the induction arrows at locations between pairs of simulated major-minor conductive faults is examined in detail in order to obtain empirical plots that show the dependence of the arrow magnitudes and directions on the relative distances from the faults, the fault separations, the depth extent of the minor fault, and the period of the inducing field.

The construction of a laboratory analogue model of the New Zealand region, that includes a simulation of the North and South Islands and the expansive surrounding oceans, and the methods to carrying out detailed model field measurements are discussed. Model measurements of the in-phase and quadrature electromagnetic field components are carried out for the simulated period range of 5-120 min for X- and Y-polarizations for an approximately uniform horizontal inducing source field. Traverses are selected to provide detailed measurements of the model ocean coast effects in the North and South Island regions where field site measurements are available. The geomagnetic field measurements studied at over ninety onland sites throughout New Zealand are from a recent array experiment (Chamalaun and McKnight, 1993), and from earlier work in local regions (Ingham,

1985a, 1985b, 1987, 1988b; Bromley, 1979; Midha, 1979; Kellett et al., 1988). Since the model simulates only the effects of the oceans and a conductive substratum at depth, the resulting difference arrows, after the coast effects have been removed, are expected to be indicative of anomalous conductive structures not included in the model simulation. The empirical results obtained in the model study of simulated major-minor faults described above are used to interpret the difference arrow responses in terms of the geological faults at given sites in the surveyed regions of New Zealand.

Chapter II

LABORATORY ANALOGUE ELECTROMAGNETIC MODELLING

2.1 Model Scaling Conditions and Scaling Factors

Electromagnetic scale modelling involves the use of a laboratory analogue model to study large-scale geoelectromagnetic problems. In the laboratory, only linear and isotropic media are considered. The validity of constructing a model of a given electromagnetic system is based on the linearity of Maxwell's equations (SI units)

$$\nabla \times \mathbf{E} = - \partial \mathbf{B} / \partial t, \quad (2.1)$$

$$\nabla \times \mathbf{B} = \mu \mathbf{j} + \mu \epsilon \partial \mathbf{E} / \partial t, \quad (2.2)$$

$$\nabla \cdot \mathbf{E} = \rho / \epsilon, \quad (2.3)$$

$$\nabla \cdot \mathbf{B} = 0, \quad (2.4)$$

where \mathbf{E} , \mathbf{B} , \mathbf{j} , ρ , μ and ϵ are electric field vector, magnetic induction vector, the electric current density, the volume charge density, the magnetic permeability and the electrical permittivity respectively. For most materials in the earth, μ does not differ significantly from the free space value, and thus in regional geophysical studies is chosen to be $\mu \approx \mu_0 = 4\pi \times 10^{-7}$ H/m. Materials within the upper regions of the earth have conductivities ranging from 10^{-4} S/m for some rocks to 4 S/m for seawater. Since at low frequencies $\sigma \gg \epsilon\omega$, displacement currents can be neglected, and thus the last term of (2.2) can be ignored. Physically this means that only quasi-static electromagnetic fields are considered and the

free space wavelength of the electromagnetic field is much longer than the typical geophysical linear dimension.

To obtain the scaling conditions, the principle of electromagnetic similitude is applied to Maxwell's equations, by relating the field variables and parameters in the model and geophysical systems through the linear transformations,

$$\mathbf{E}_g = K_E \mathbf{E}_m, \quad (2.5)$$

$$\mathbf{B}_g = K_B \mathbf{B}_m, \quad (2.6)$$

$$\epsilon_g = K_\epsilon \epsilon_m, \quad (2.7)$$

$$\mu_g = K_\mu \mu_m, \quad (2.8)$$

$$\sigma_g = K_\sigma \sigma_m, \quad (2.9)$$

$$L_g = K_L L_m, \quad (2.10)$$

$$t_g = K_t t_m, \quad (2.11)$$

where the subscripts g and m refer to the geophysical and analogue model values respectively. The dimensionless constants K_E , K_B , K_ϵ , K_μ , K_σ , K_L , K_t are the scaling factors for the electric field, magnetic field, electric permittivity, magnetic permeability, conductivity, length and time respectively. Since only non-ferromagnetic media are considered, it is reasonable to choose $\mu_m = \mu_g$. By comparing Maxwell's equations in the two systems, it is readily shown that under these assumptions, a valid simulation requires the two necessary and sufficient conditions

$$(\sigma_g/\sigma_m)(L_g/L_m) = 1/K, \quad (2.12)$$

$$(f_g/f_m)(L_g/L_m) = K, \quad (2.13)$$

where f is the frequency of the time harmonic field, and $K = K_E / K_B$ is the impedance scaling factor. In cases where impedance scaling is not of interest, K can be eliminated by combining (2.12) and (2.13), and the scaling condition becomes

$$(\sigma_g/\sigma_m)(f_g/f_m)(L_g/L_m)^2 = 1. \quad (2.14)$$

Equations (2.12) and (2.13) consist of four unknowns, thus any two of the four scaling factors can be chosen arbitrarily. In practice, the conductivity scaling factor σ_g/σ_m , and the length scaling factor L_g/L_m for the geophysical problem, are restricted by the model materials and the size of the laboratory. Thus the frequency scaling factor f_g/f_m and the impedance scaling factor K are determined respectively by (2.14) and (2.12) or (2.13).

The modeling materials used in the previous analogue model studies carried out at the University of Victoria, and also used in the present work, are graphite plate (1.2×10^5 S/m) to simulate the conductivity of an ocean (3.6 S/m), and saturated salt solution (21 S/m) in a large tank to simulate the conductivity of a resistive host earth (6.3×10^{-4} S/m). Using these materials, the conductivity scaling σ_g/σ_m is 3×10^{-5} . Two different sets of length and frequency scaling are used in the present work. In the case of the simulated ocean and fault models, the length scaling was chosen to be $L_g/L_m = 10^6$, so that the frequency and impedance scaling by Eqs. 2.12 and 2.13 are constrained to be $f_g/f_m = 3.3 \times 10^{-8}$ and $K = 30$ respectively. Thus 1 cm simulates 10 km in the geophysical scale, and a frequency of 100 kHz in the laboratory corresponds to a geomagnetic variation period of 5 minutes. In the case of the analogue model of the New Zealand region, the length scaling was chosen to be $L_g/L_m = 2 \times 10^6$, so that the frequency and impedance scaling factors are $f_g/f_m = 10^{-8}/1.2$ and $K = 60$ respectively. In this model 1 cm simulates 20 km in the geophysical scale, and a frequency of 40 kHz in the laboratory corresponds to a geomagnetic variation period of 50 minutes. This latter length scaling was chosen to permit modeling a very large region, that of New Zealand and the surrounding oceans in an area of 2800 km x 2800 km.

2.2 The Laboratory Analogue Model Facility

The analogue model facility in the University of Victoria geophysics laboratory has been described earlier in detail by Dosso (1966a, 1973) and Nienaber et al. (1976). The sketch of the model tank and the source field used in analogue model experiments is shown in Fig. 2.1. Saturated salt water ($\sigma = 21 \text{ S/m}$) in a large wooden tank ($2.44 \text{ m} \times 1.90 \text{ m} \times 0.76 \text{ m}$ deep) filled to a depth of 0.64 m simulates a uniform resistive earth. Graphite ($\sigma = 1.2 \times 10^5 \text{ S/m}$) plate of scaled shape can be used to simulate conductive oceans, sediments, anomalous conductors, and conductive substructures. A thick graphite plate lining the bottom of the tank reduces the effects of the concrete floor of the laboratory. In certain model induction problems, this graphite plate is used to simulate a highly conductive lower layer in the earth.

The inducing source field for a wide period range is provided by oscillating currents in two parallel wires. The horizontal separation of the horizontal current lines is 2.4 m , twice the height above the surface of the salt solution. This configuration provides a reasonably uniform horizontal inducing field and is used to simulate an ionospheric source of large extent (Ramaswamy et al., 1975; Nienaber et al., 1976). The current for the source field is supplied by a sine-wave signal generator and a power amplifier. In the laboratory coordinates (Fig. 2.1), source electric currents are parallel to the x -axis while the source magnetic fields are mainly horizontal and parallel to the y -axis. The walls of the tank perpendicular to the inducing electric field of the source are lined with stainless steel plates which are electrically connected by a thick copper wire outside the tank. This permits electric currents induced in the model materials to flow in the direction

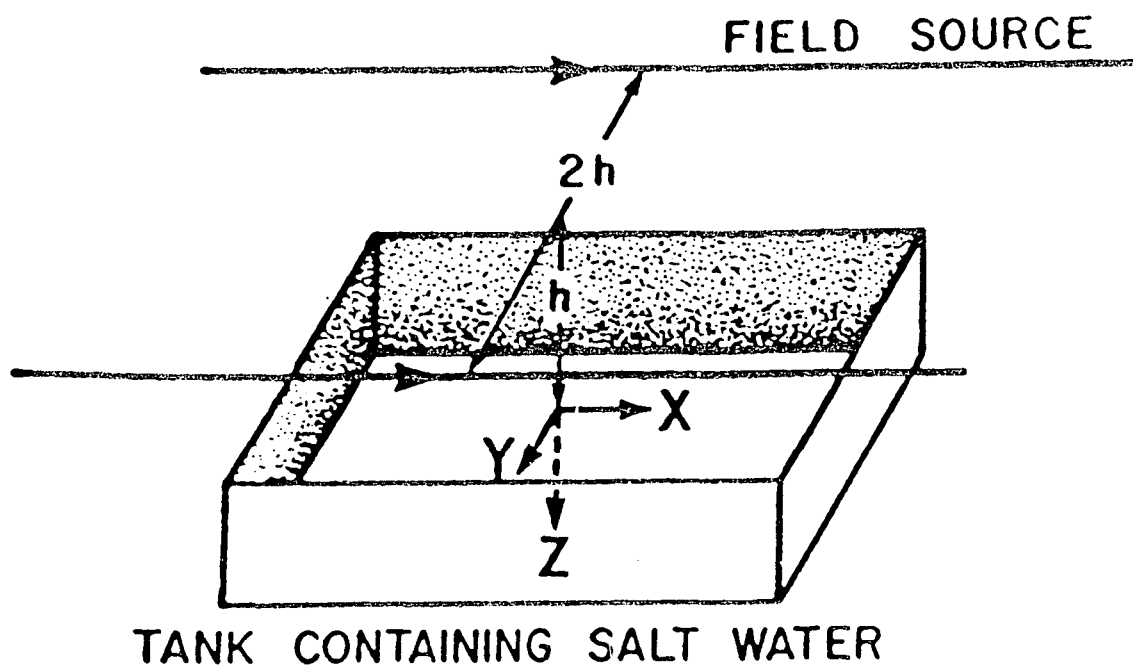


Figure 2.1: Inducing source field and tank containing salt solution.

of the source electric field right to the edge of the tank and thus decrease the edge effects of the two walls. A current transformer is used to monitor the magnitude and stability of the current, as well as to provide a reference signal for the lock-in analyzers employed in carrying out the model measurements.

The detecting and recording equipment used is schematically illustrated in Fig. 2.2. Each field detecting sensor is mounted at the end of a lucite tube. The magnetic field detectors each employ a hand-wound coil of 250 turns of No.42 wire. The horizontal and vertical magnetic field detectors are similar in construction, with the coil length in each detector 0.1 cm and the inside and outside diameters 0.235 cm and 0.635 cm respectively. The coil axis is horizontal in the horizontal magnetic field detector and vertical in the vertical magnetic field detector. The horizontal electric field detector consists of three electrodes in a straight line with the two outer electrodes having a 1.48 cm separation. The centre electrode is connected to the common ground of the differential input pre-amplifier. These three electrodes just protrude through the flat sealed end of the lucite tube and thus when in use make contact with the salt solution. The horizontal electric field components along the surface of the salt solution are determined by measuring the voltage difference between the two outer electrodes. Noise common to the outer electrodes and the cable leads are removed employing a differential pre-amplifier which is mounted on the detector carriage. The magnetic field components (B_x , B_y , B_z) are measured with the magnetic probes just above the surface of the salt solution while the horizontal electric field components (E_x , E_y) are measured with the electric probe just touching the salt solution. The calibration of the magnetic and electric field detectors has been discussed by Dosso

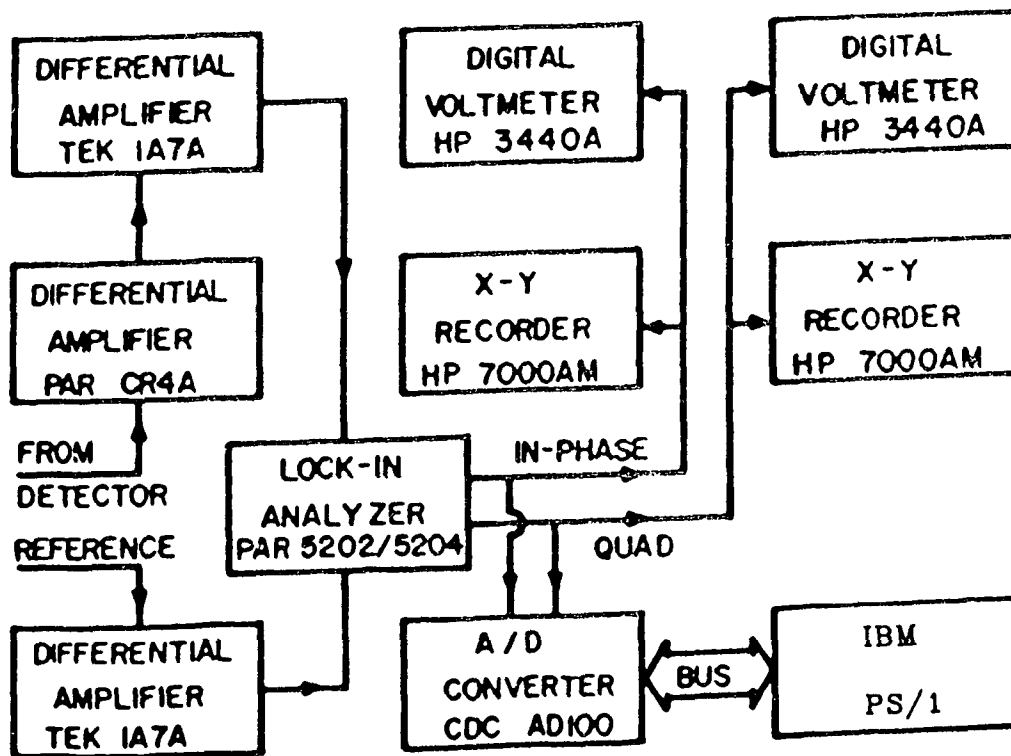
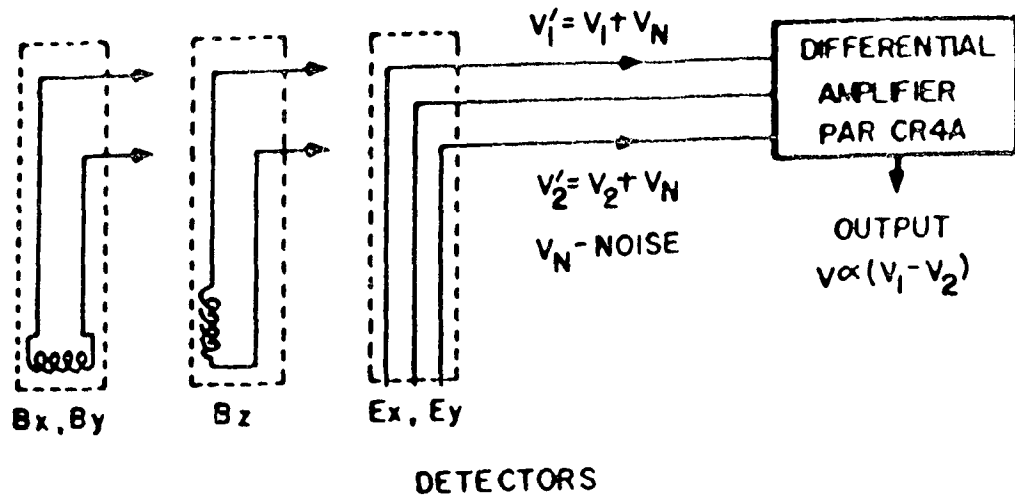


Figure 2.2: The detectors and recording equipment.

(1966a). In the present work, the calibration of the electric field detector was extended to higher model frequencies than used previously by comparing measured fields with numerically calculated fields for the model frequency range of 1 kHz - 400 kHz.

When measuring the field components, the appropriate probe is mounted on the motor driven carriage that moves along the horizontal wooden beam that rests on the two edges of the tank walls. A wiper mounted on the probe carriage slides along a resistive nichrome wire embedded in the vinyl track. The voltage of the wiper contact defines the horizontal position of the detector as it traverses the model tank. The detector signal amplified by the differential pre-amplifier mounted on the carriage is transmitted to the analyzing and recording equipment shown in Fig. 2.2. The in-phase and quadrature components are monitored on digital voltmeters, recorded in analogue form on X-Y plotters, and in digital form using a computer.

Model measurements along traverses over the model can be carried out for two perpendicular polarizations (X and Y) of the source field. The X- and Y-polarizations of the source field are defined as the inducing electric field respectively along the x- and y-axes of the model structure. The horizontal magnetic field is normalized for each frequency at a model land reference point well removed from the model structure and tank edges. For X-polarization the analyzing equipment is adjusted so that in-phase $B_y = 1$ nT and quadrature $B_y = 0$, while for Y-polarization, in-phase $B_x = 1$ nT and quadrature $B_x = 0$. The model field measurements are processed using the University of Victoria Mainframe Computing System IBM 3090 (model 180S), as well as an IBM PS/1 computer. In-phase and

quadrature electromagnetic field components can then be plotted for traverses over the model at given periods. As well, model induction arrow responses can readily be calculated using the measured field components. Computer programs are used to plot the in-phase and quadrature induction arrows V on a map of the region, and also in the form of V_x and V_y (x - and y -components of V) in-phase and quadrature response curves along traverses over the model map.

2.3 Chapter Summary

In this Chapter, a brief description of the electromagnetic model scaling conditions and a general description of the laboratory analogue model facility used in the present work are presented. The modeling materials used are graphite plate to simulate the ocean and conductive structures, and saturated salt solution in a large wooden tank to simulate the resistive host earth. In the case of the idealized ocean and fault models, the scaling factors were chosen so that 1 cm in the analogue model simulated 10 km in the geophysical scale, and a frequency of 100 kHz in the laboratory corresponded to a geomagnetic variation period of 5 min. In order to include a large ocean region surrounding New Zealand, length scaling for this model was chosen so that 1 cm in the analogue model simulated 20 km in the geophysical scale, and thus a frequency of 40 kHz in the laboratory corresponded to a geomagnetic variation period of 50 min.

Chapter III
EM RESPONSES OF OCEAN AND FAULT LABORATORY
ANALOGUE MODELS

3.1 Introduction

The interpretation of geomagnetic field observations can be aided by studies of various types of conductivity structures, which then may permit an approximate determination of true geoelectric structures within the earth. The understanding of the effects of oceans, the responses of conductive faults, as well as the electromagnetic coupling between them, is of crucial importance. As discussed in Chapter I, induction arrows, characterizing induced current concentrations, are useful indicators of lateral conductivity variations in the earth. However, for the case of a local conductor in a coastal region, the ocean coast effect is a major component in the geomagnetic responses, and thus complicates the interpretation of the induction arrow responses. The interpretation would be much simplified if the coast effects were known and could be removed before interpretation.

The motivation for the work in this chapter is to delineate these coast effects, and to examine the possible removal of the coast effects for cases of parallel conductive faults near coastlines. The approach used is to vectorially subtract the induction arrow responses of a model ocean from the responses of a model of a conductive fault near an ocean coastline. This study has application to

the interpretation of geomagnetic field measurements in the New Zealand region, where major conductive faults, for example, the Alpine and Wellington Faults, are roughly parallel to the ocean coastlines.

3.2 The Responses of a Constant Depth Ocean

Figure 3.1 shows the schematic cross-section of a model ocean (a) of 5 km depth and dimensions $X=1000$ km and $Y=500$ km in a resistive host earth, all underlain by a conductive substratum (c) at depth Z_C . The origin of the coordinate system is at the ocean coastline with Y towards the right and Z vertically downward. Model magnetic field B_Z and B_Y measurements for the case of X -polarization (inducing electric field in the X -direction and parallel to the ocean coastline) for a period range 1-90 min were carried out for a traverse in the Y -direction along a profile perpendicular to the straight coastline for a range of depths Z_C . The field measurements were used to calculate model in-phase and quadrature induction arrow responses along the profile. These induction arrow responses of the model ocean as a function of the period, as well as the effect of the depth Z_C of the conductive substratum, are examined here.

Figure 3.2 shows the in-phase and quadrature induction arrow responses V as a function of the distance Y from the coastline at periods $T=2$ and 20 min for a conductive substratum depth $Z_C = 200$ km. In the response curves shown, negative values of V represent induction arrows pointing to the left (negative Y -direction), while positive values of V represent arrows pointing to the right (positive Y -direction). Both the in-phase and quadrature responses show the typically large coast effect near an ocean-land interface. The in-phase responses for both peri-

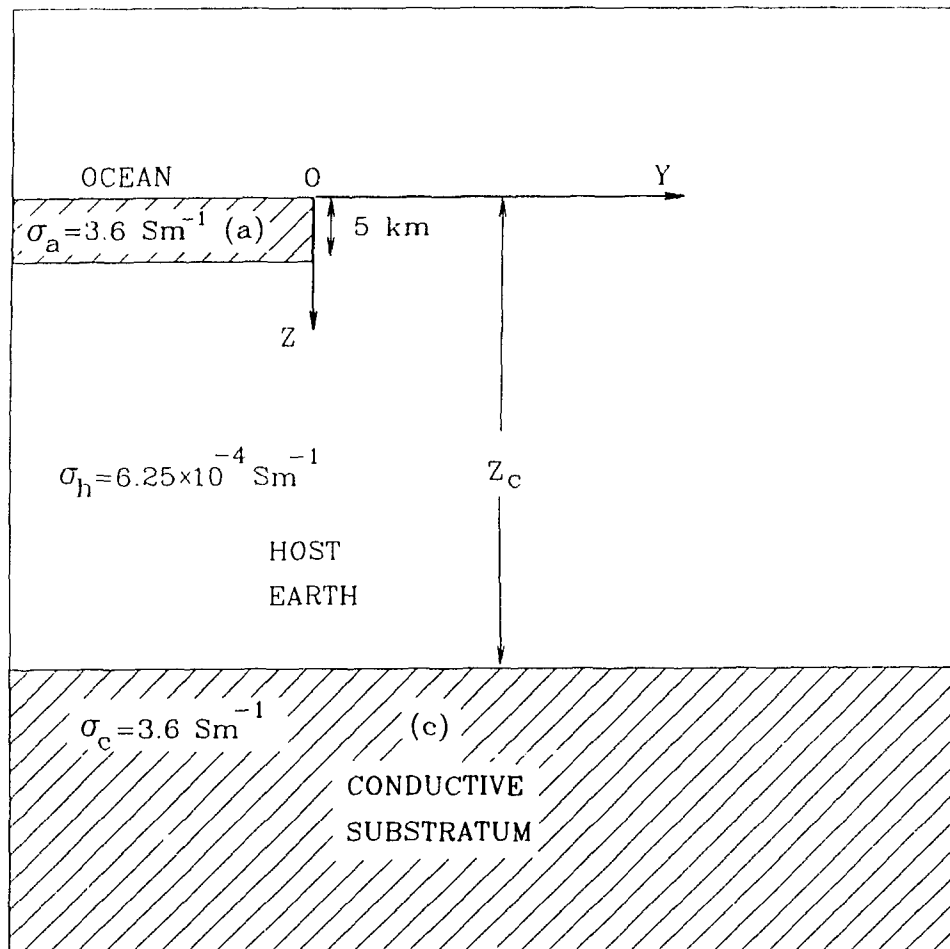


Figure 3.1: The cross-section of the model ocean (a) in a resistive host earth, all underlain by a conductive substratum (c).

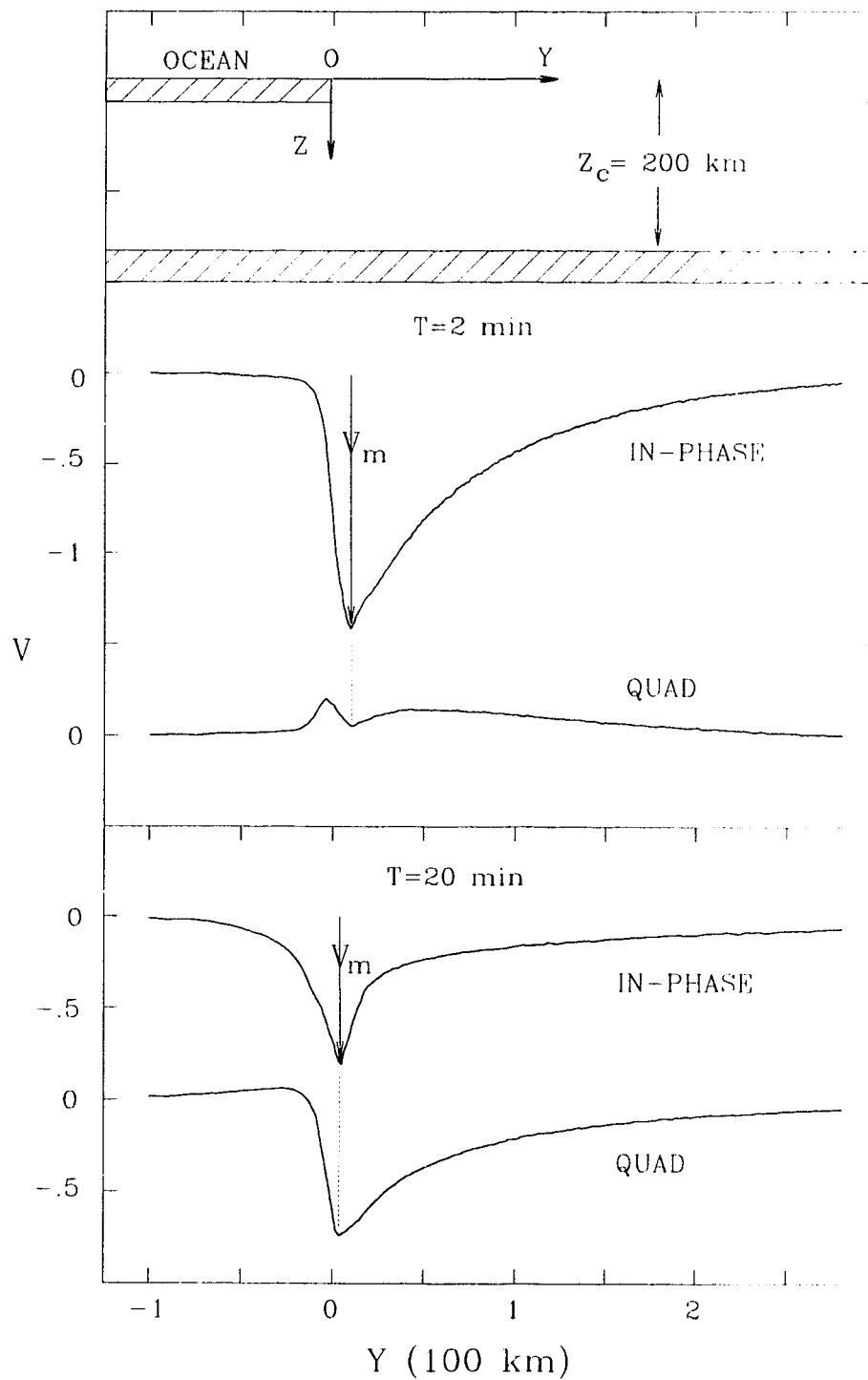


Figure 3.2: The in-phase and quadrature induction arrow responses V along a traverse perpendicular to the coastline for periods of 2 and 20 min.

ods are everywhere negative, and, thus the arrows at all locations point towards the bulk of the ocean, as expected. The maximum in the in-phase response at the coastline (labelled as V_m) clearly depends on period, with the maximum at 2 min being roughly a factor of two greater than at 20 min. The in-phase response seaward shows a larger spatial gradient at 2 min than at 20 min, while landward near the coast the opposite is the case. At 20 min the spatial gradient of the in-phase response seaward is much smaller than that of the quadrature response, but over land near the coast, the in-phase response curve shows the greater spatial gradient. The quadrature responses at 2 min are positive everywhere indicating arrows pointing away from the bulk of the ocean, while at 20 min the response over land and about 25 km seaward are negative, indicating arrows pointing towards the bulk of the ocean as expected. These results show that the in-phase arrows for points both over land and sea point towards the bulk of the ocean at both short and long periods, while the quadrature arrow reverses its direction from pointing away from the ocean at short periods to pointing towards the ocean at long periods. Such a reversal of the quadrature arrow direction near a conductive-resistive interface has also been noted earlier by other authors (e.g., Hebert et al., 1983a; Nienaber et al., 1983; DeLaurier et al., 1983; Weaver, 1987; Hu et al., 1989; Agarwal and Dosso, 1990, 1993).

The periods $T=1.5, 2.6, 5$ min for the induction arrow responses shown in Fig. 3.3, were selected from the range of model measurements carried out, in order to demonstrate the behaviour of the ocean responses at the characteristic period T_C . As described in Chapter 1, T_C is that period at which the ocean in-phase response as a function of period is maximum, and the quadrature response at the same loca-

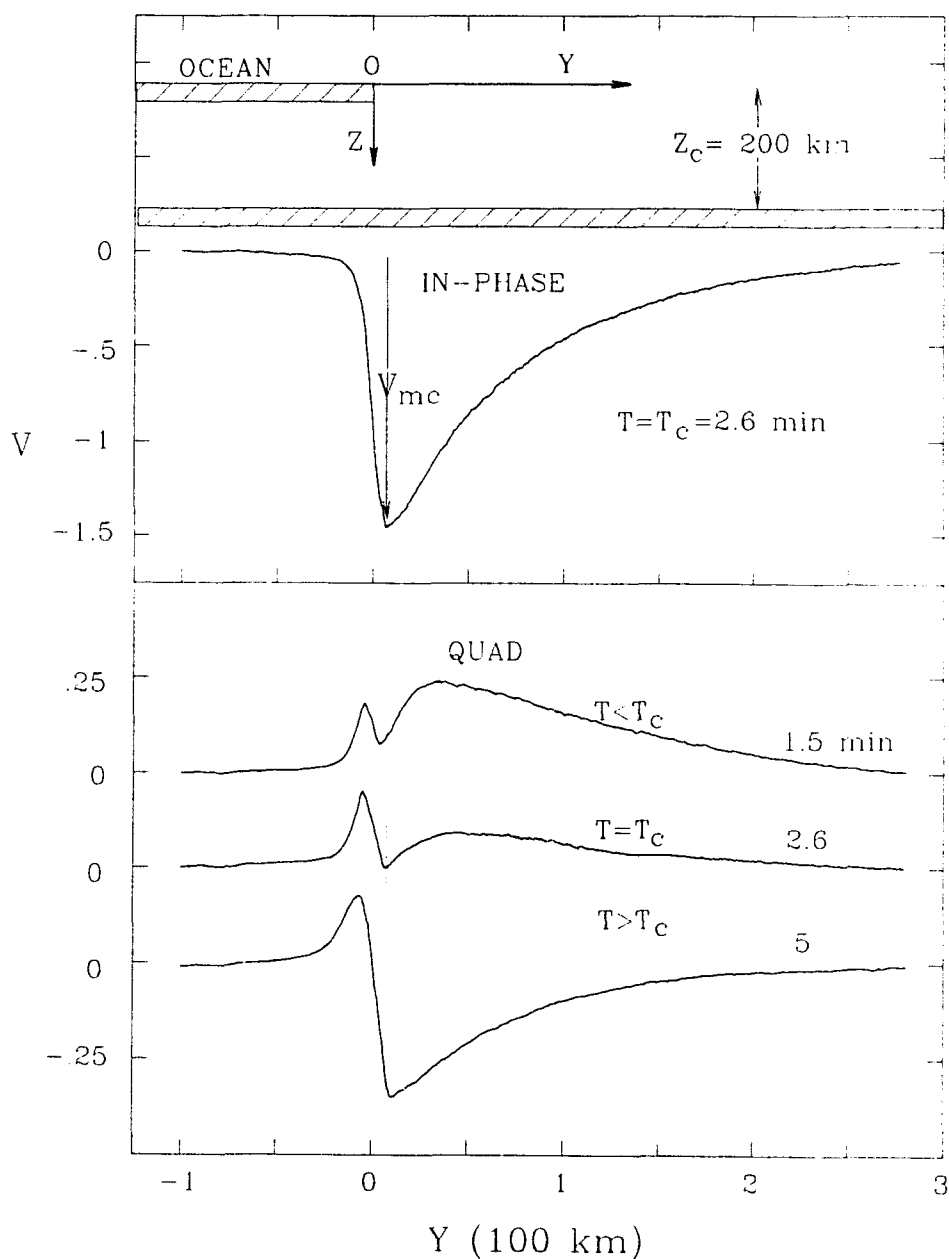


Figure 3.3: The in-phase and quadrature induction arrow responses V along a traverse perpendicular to the coastline at the characteristic period T_c , the period at which the in-phase V_m (as defined in Fig.3.2) is maximum (labelled V_{mc}) and the corresponding quadrature response at the same location is zero. The quadrature response curves for 1.5 and 3 min, periods slightly smaller and larger than T_c respectively, are also shown to demonstrate the behaviour of the quadrature response near the characteristic period.

tion is zero (and does not reverse sign along the profile). In the period range included in the analogue model measurements, it was found that at $T=2.6$ min the in-phase V_m (as introduced in Fig. 3.2) was maximum (labelled as V_{mC} in Fig. 3.3) and the quadrature response was zero, as required for the responses at the characteristic period. In order to demonstrate the quadrature response behaviour at periods $T < T_C$ and $T > T_C$, the responses at periods $T=1.5$ and 5 min are included in Fig. 3.3. These responses clearly show that for $T < T_C$ the quadrature induction arrows everywhere along the profile point away (positive Y-direction) from the ocean, while for $T > T_C$ the reversed sign over land indicates arrows pointing towards the ocean, the same as observed for the in-phase arrows.

To show the period dependence in some detail, the in-phase and quadrature coast effect responses V for a range of periods (1-90 min) are presented in Fig. 3.4. It is apparent that both the in-phase and quadrature responses are strongly period dependent. The in-phase V_m is seen first to increase with an increase in period, to attain a maximum between 2 and 3 min (more precisely 2.6 min, the characteristic period described in Fig. 3.3), and then to decrease with a further increase in period. The corresponding quadrature response, however, positive at short periods ($T < 2$ min), decreases with an increase in period to approach zero at T_C (2-3 min), changes sign to become negative at 3 min, and then increases in magnitude with a further increase in period. After reaching a maximum response at roughly 10 min, (a period roughly a factor of 4 greater than the period T_C at which the in-phase response is maximum), the quadrature response gradually decreases with a further increase in period.

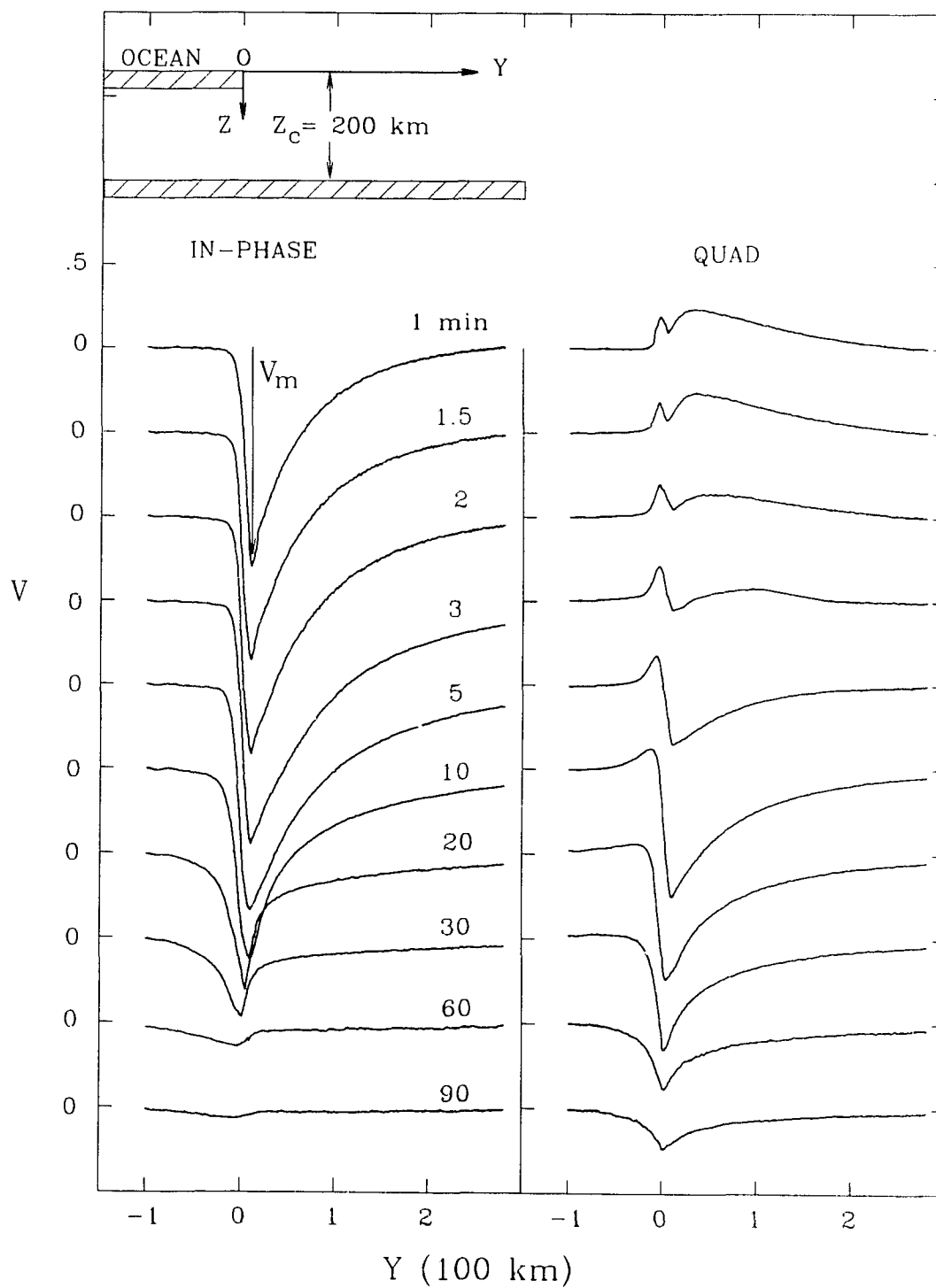


Figure 3.4: The in-phase and quadrature induction arrow responses V along a traverse perpendicular to the coastline for periods of 1–90 min.

If the in-phase curves in Fig. 3.4 (for example, the curves for 5, 10, and 30 min) were normalized to all have the same maximum response V_m at the coast, it would readily be seen that seaward the spatial gradient near the coast decreases with an increase in period. Another way of stating this behaviour is that over the ocean (near the coast) the response curves are steeper at short periods than they are at long periods. For example, at 5 min period the in-phase response over the ocean 10 km from the coast is about 20% of that observed at the coast, while at 20 min period the distance from the coast for such a decreased response is seen to be about 25 km. It is noted that the distances of 10 and 25 km are roughly equal to 2δ (ocean conductivity skin depths) at 5 and 20 min periods respectively. Over the land, the opposite trend to that over the ocean is noted, with the in-phase response as a function of distance decreasing more rapidly at long periods than at short periods, so that the distances for attenuation to 20% of the response at the coast are 180 km and 115 km at 5 and 20 min periods respectively. The quadrature component shows a more complex behaviour, partly due to the sign change in the neighborhood of the characteristic period. But if the curves were normalized as described for the in-phase component, it would be seen that over the ocean, at periods somewhat greater than T_C , the quadrature response curves are steeper than those of the in-phase curves. For example, at 20 min the distance seaward at which the response is decreased to 20% of that at the coast is roughly 10 km (or 1δ), compared with 20 km (or 2δ) for the in-phase component. The spatial gradients of the quadrature response curves landward as a function of period do not change much for periods greater than 5 min. Thus, the spatial gradients landward are smaller for the quadrature than for the in-phase responses, indicating that

over land the quadrature component of the coast effect attenuates less rapidly with distance than does the in-phase component.

Figure 3.4 also shows that for periods somewhat greater than T_C , the quadrature arrows on either side of the coastline, but near the coast, point towards each other, thus point towards the conductive-resistive interface. It is noted that differing from the quadrature arrow response behaviour, the in-phase arrows at all locations along the profile point towards the bulk of the conductive ocean at all periods. The reversal of the quadrature arrow near the conductor-land interface, as well as the oppositely directed arrows observed on either side of the interface for $T > T_C$, agree with the results of the numerical calculations of Agarwal and Dosso (1993). They suggested that since these oppositely directed arrows define the location of the conductive-resistive interface, such oppositely directed arrows observed in geomagnetic studies could be an aid in locating the boundary of a buried conductive sill in a resistive host.

Figure 3.5 shows the induction arrow responses (of Fig. 3.4) plotted in the form of amplitude and phase angle. In examining the amplitude maximum at the coast as a function of period, it is seen that the maximum occurs at 3 min (as was also the case for the in-phase response curves in Fig.3.4). The phase angle at the same location is roughly 180° at 3 min, agreeing with the minimal quadrature response seen at this period in Fig. 3.4. It is noted that over the ocean the response as a function of distance from the coast decreases more rapidly at short periods than at long periods. For example, at 5 min the response observed over the ocean 10 km from the coast is approximately 20% of that at the coast, while at 20 min the distance for such a decreased response is about 20 km, a distance

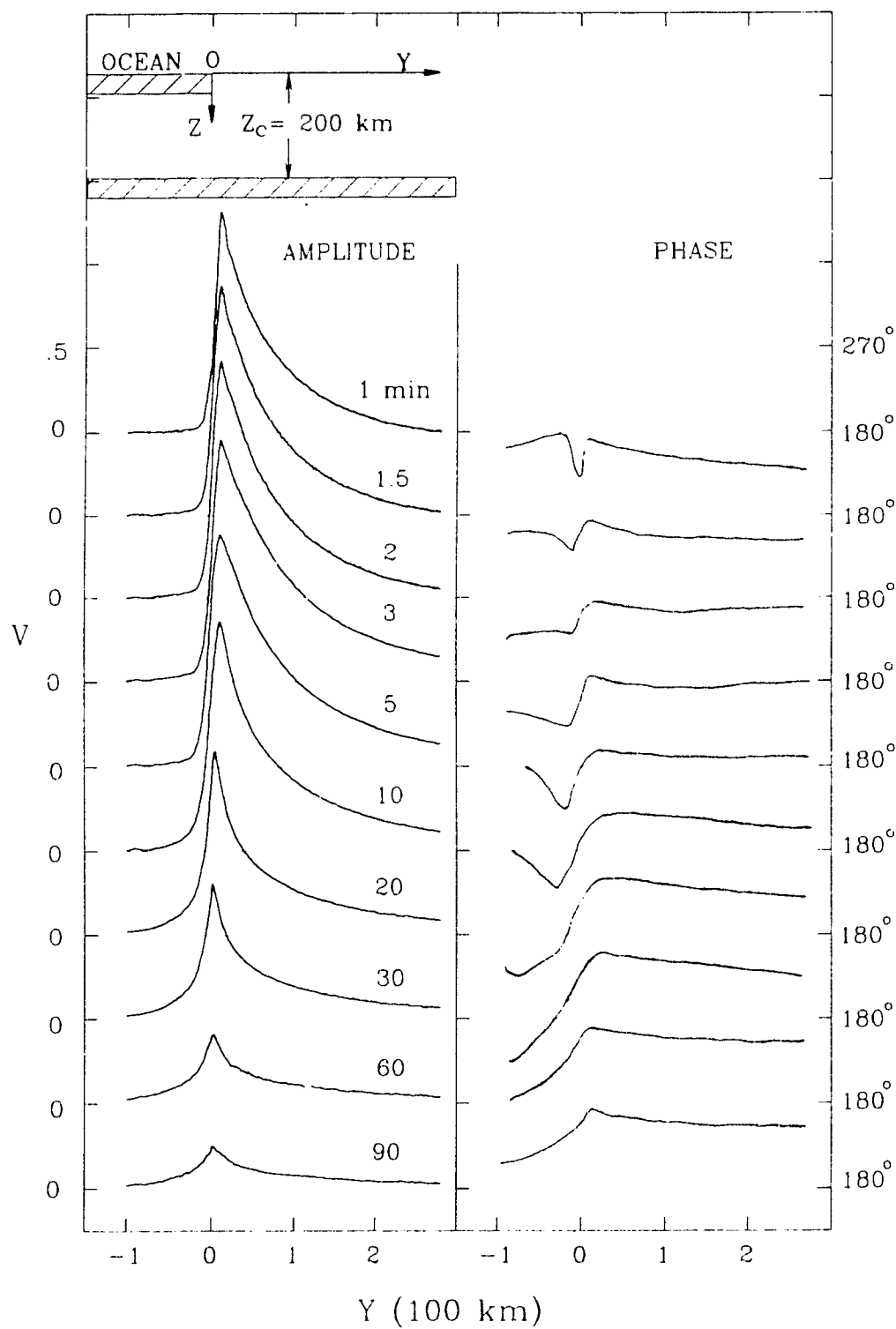


Figure 3.5: The amplitude and phase angle response curves along a traverse perpendicular to the coastline for periods of 1–90 min.

roughly equal to 2δ (ocean conductivity skin depths at this period), similar to that for the in-phase response of Fig. 3.4. On shore, the response at all periods falls off gradually as a function of distance from the coast, with the exception that very near the coast the decrease is very rapid. The general form of the amplitude response curves is that of being broader at long periods than at short periods.

The phase angle at all locations (Fig. 3.5) is less than 180° for $T < 3$ min, while on shore for $T > 3$ min (i.e., $T > T_C$), it is greater than 180° and is seen to increase with an increase in period. At long periods (60 and 90 min) the phase angles both on land and over the ocean are in the third phase angle quadrant, indicating that both the in-phase and quadrature arrows everywhere point towards the bulk of the ocean. At these long periods, the phase angles over the land are greater than 225° , thus agreeing with the responses shown in Fig. 3.4, that the quadrature component is dominant in the ocean response. Over the land, the broad phase angle curves at long periods show the persistence of the quadrature response a great distance inland.

The ocean in-phase response maximum V_m and the corresponding quadrature (both from Fig. 3.4) are shown in the upper portion of Fig. 3.6, while the induction arrow amplitude and the phase angle (both from Fig. 3.5) are shown in the lower portion. The in-phase response curve shows a maximum (V_{mC}) at roughly 2.6 min (the characteristic period T_C), while the corresponding quadrature value is zero. At this characteristic period for $Z_C = 200$ km, the skin depth δ (in the host conductivity) is 260 km, and thus $\delta \approx 1.3 Z_C$, a value that is in agreement with the calculations of Agarwal and Dosso (1990) (who determined δ at the characteristic period to be in the range of $1.1 Z_C$ to $1.3 Z_C$ for single station induction arrows).

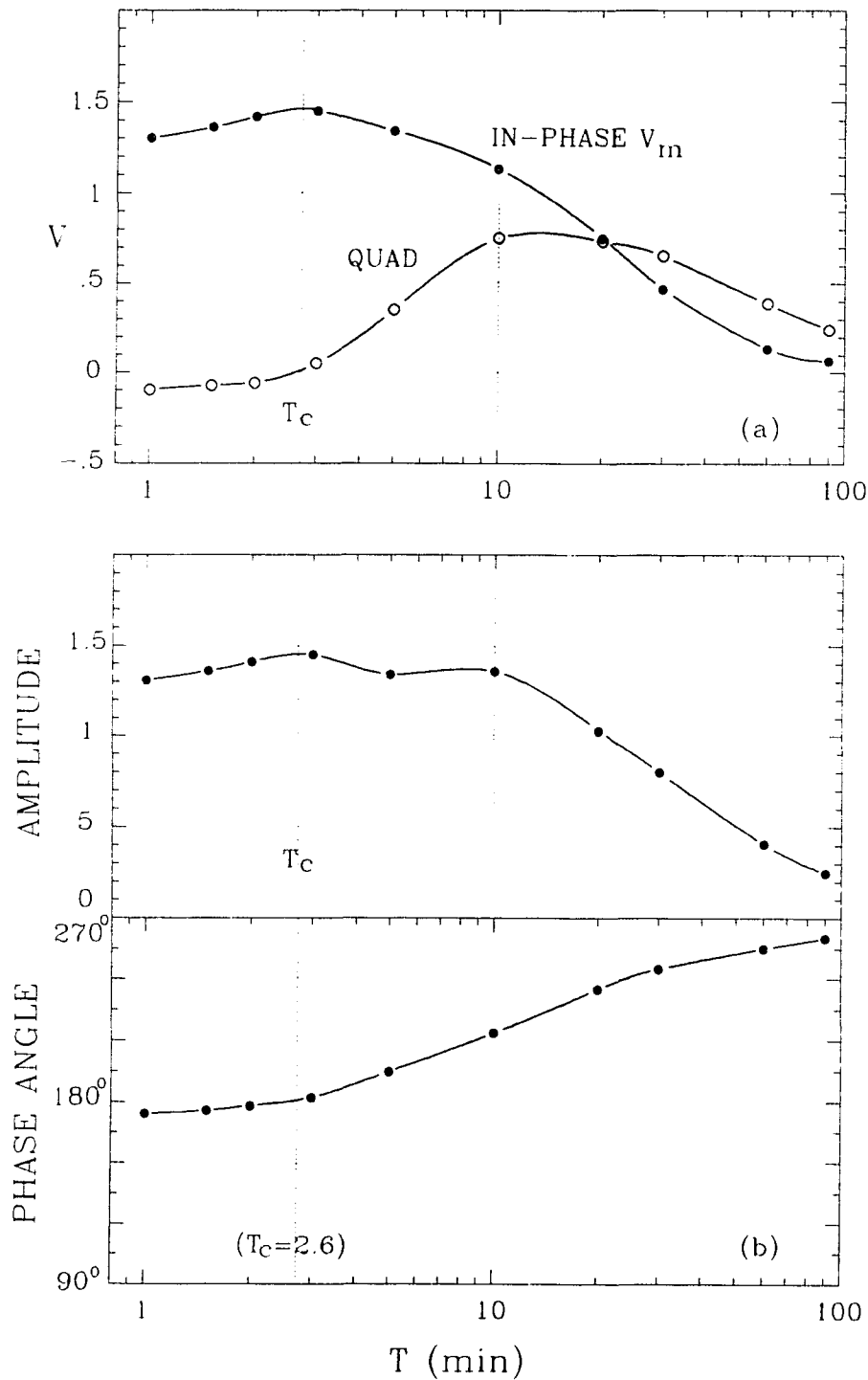


Figure 3.6: a) The in-phase response maximum V_m (and the quadrature response at the same location), b) the amplitude response maximum (and the phase angle) as a function of period for the 5 km depth ocean underlain by a conductive substratum at depth $Z_c = 200$ km.

Again (as was noted in the curves shown in Fig. 3.4), the quadrature response in Fig. 3.6a as well reaches a maximum at approximately 10 min, a period roughly a factor of four greater than the 2.6 min (T_C) period at which the in-phase response is maximum.

As is the case for the in-phase response curve, the amplitude response (Fig. 3.6a) also reaches a maximum at roughly 2.6 min. The amplitude curve shows a second maximum at roughly 10 min, obviously due to the maximum in the quadrature component at this period. The phase angle increases with increasing period, from less than 180° for $T < T_C$ to greater than 180° for $T > T_C$. At short periods $T < 5$ min the phase angle is roughly 180° , and thus the major response is that of the in-phase component, while at long periods (say $T=60-90$ min) the phase angle approaches 270° , indicating that at long periods the major response is that of the quadrature component. Clearly the results of Fig. 3.6b are consistent with those of Fig. 3.6a, and a knowledge of T_C , delineated by the period for in-phase arrow maximum (and the accompanying zero quadrature), or the amplitude maximum (and the accompanying 180° phase angle) used in $\delta(T_C) \approx 1.3 Z_C$, could aid in determining the depth Z_C if the conductivity of the host were known.

In order to show the dependence on substratum depth Z_C , the in-phase response maximum V_m (and the corresponding quadrature) as a function of period for conductive substratum depths $Z_C=50, 100$ and 200 km are shown in Fig. 3.7 (the curve labels are the same as those in Fig. 3.6a). As shown by the curves in Figs. 3.3 and 3.6 for the case of $Z_C=200$ km, the skin depth (in the host conductivity) at the characteristic period $T_C=2.6$ min could be expressed as $\delta(T_C) \approx 1.3 Z_C$. This expression indicates that T_C decreases with decreasing substratum depth Z_C , so

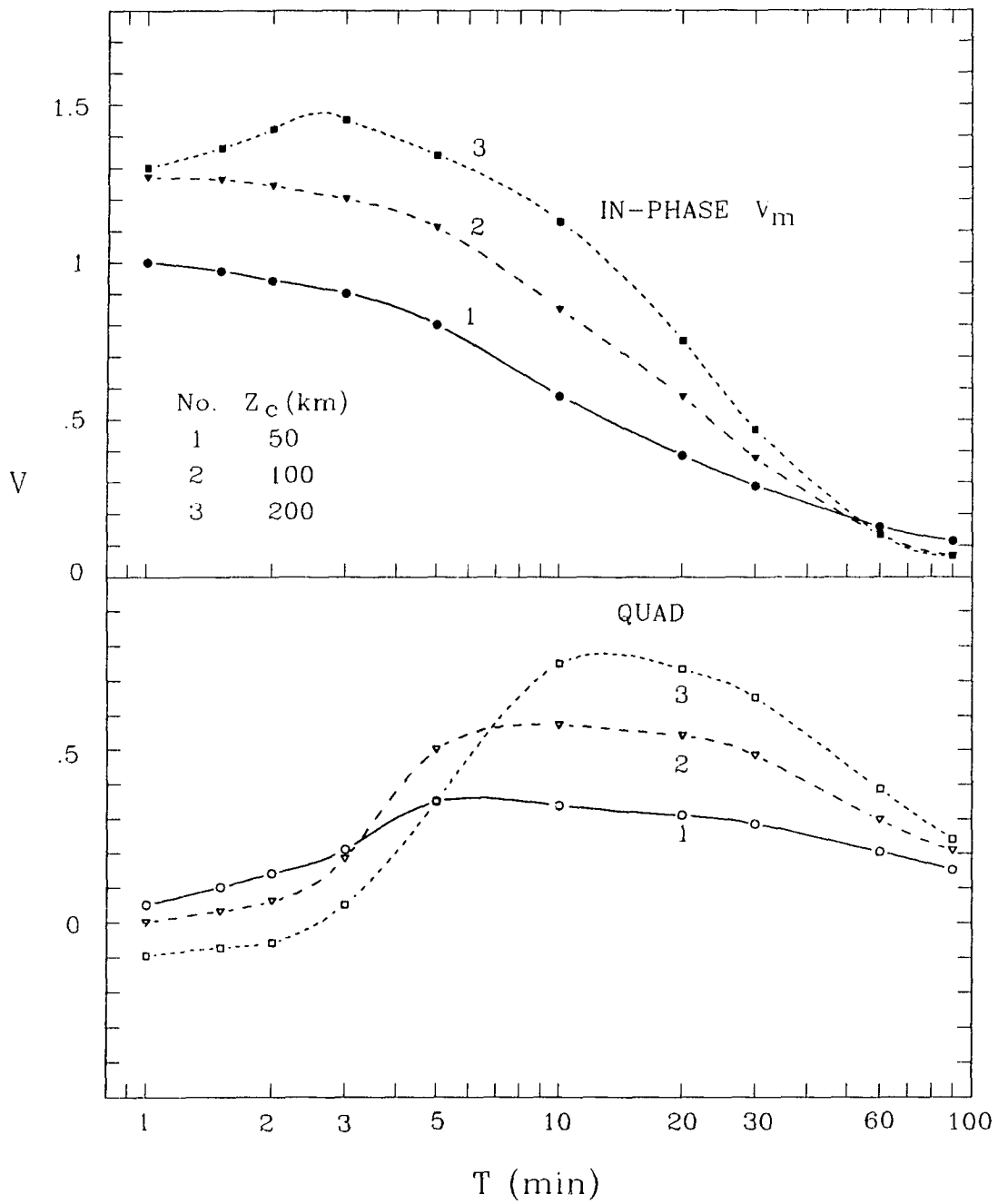


Figure 3.7: The in-phase response maximum V_m (and the corresponding quadrature) as a function of period for the 5 km depth ocean underlain by a conductive substratum at depths $Z_c = 50, 100, 200$ km.

that for a smaller depth, say $Z_C=100$ km, T_C should be decreased by a factor of four. It should be stated that the analogue model equipment did not permit measurements below simulated periods of 1 min, and thus it was not possible to show characteristic periods T_C for the cases of $Z_C=50$ km and 100 km. However, two-dimensional numerical model calculations carried out confirmed the period of $T_C \approx 0.7$ min for the case of $Z_C=100$ km, thus indicating that the quadrature arrow which reverses direction for $T > T_C$, should do so at a shorter period for the decreased substratum depth $Z_C=100$ km.

The in-phase and quadrature responses over most of the period range in Fig. 3.7 are clearly seen to be highly dependent on the substratum depth Z_C . For example, at 10 min both the in-phase and quadrature responses are each about a factor of two smaller for $Z_C=50$ km than for the case of $Z_C=200$ km. This can be attributed to the effect of current induced in the underlying conductive substratum, since the induced current has the effect of both attenuating B_z and enhancing B_y much more when the current is induced in a conductive substratum nearer the surface than for one at greater depth, thus leading to the smaller induction arrow responses for $Z_C=50$ km. At the shorter periods ($T < 10$ min) the in-phase response shows a much stronger dependence on Z_C than does the quadrature response, while for periods $T > 10$ min, the opposite is the case. The somewhat complex behaviour of the quadrature curve at short periods can be attributed to the sign reversals at the characteristic periods, differing for each depth Z_C . However, at the long period of 90 min, a period at which the skin depth (for the host earth conductivity) is approximately 1500 km (a depth much greater than all the Z_C depths studied), the responses for both components show little dependence on Z_C .

3.3 The Responses of an Ocean and an on Shore Fault Parallel to the Coastline

Figure 3.8 shows the schematic cross-section of a 5 km depth ocean (a), and at a distance S from the coastline, a parallel conductive fault (b) in a resistive host earth, all underlain by a conductive substratum (c) at depth Z_C , that was simulated in the laboratory analogue model. Model magnetic field components along a profile normal to the coastline were measured for the case of X -polarization (electric field of the inducing source parallel to the ocean coastline and the fault strike) for a range of periods ($T=1-90$ min) and fault depths ($Z_b=5, 25, 50, 75$ km) for each ocean-fault separation distance ($S=50, 100, 200$ km). These field components were used to calculate in-phase and quadrature induction arrow responses for various models.

Figure 3.9 shows the 2 and 20 min in-phase and quadrature induction arrow responses V as a function of the distance Y from the coastline for $Z_b = 5$ km, $Z_C=100$ km, and $S=100$ km. This figure is provided to introduce the labels of the response maximum V_{ma} (at the coastline), and the response maximum V_{mb} (just to the left of the fault). From the curves for the 2 and 20 min periods it is obvious that the responses along the traverse are strongly period dependent, and that the period dependence is not the same for the in-phase and quadrature components. For example, the changes in the magnitudes and the signs of V_{ma} and V_{mb} for the 2-20 min period interval for the quadrature response differ in a complex manner from those for the in-phase response. Other examples are the sign reversal (at 75 km) seen in the in-phase response at 2 min (but not at 20 min), and a similar sign reversal (at 80 km) in the quadrature component at 20 min (but not at 2 min).

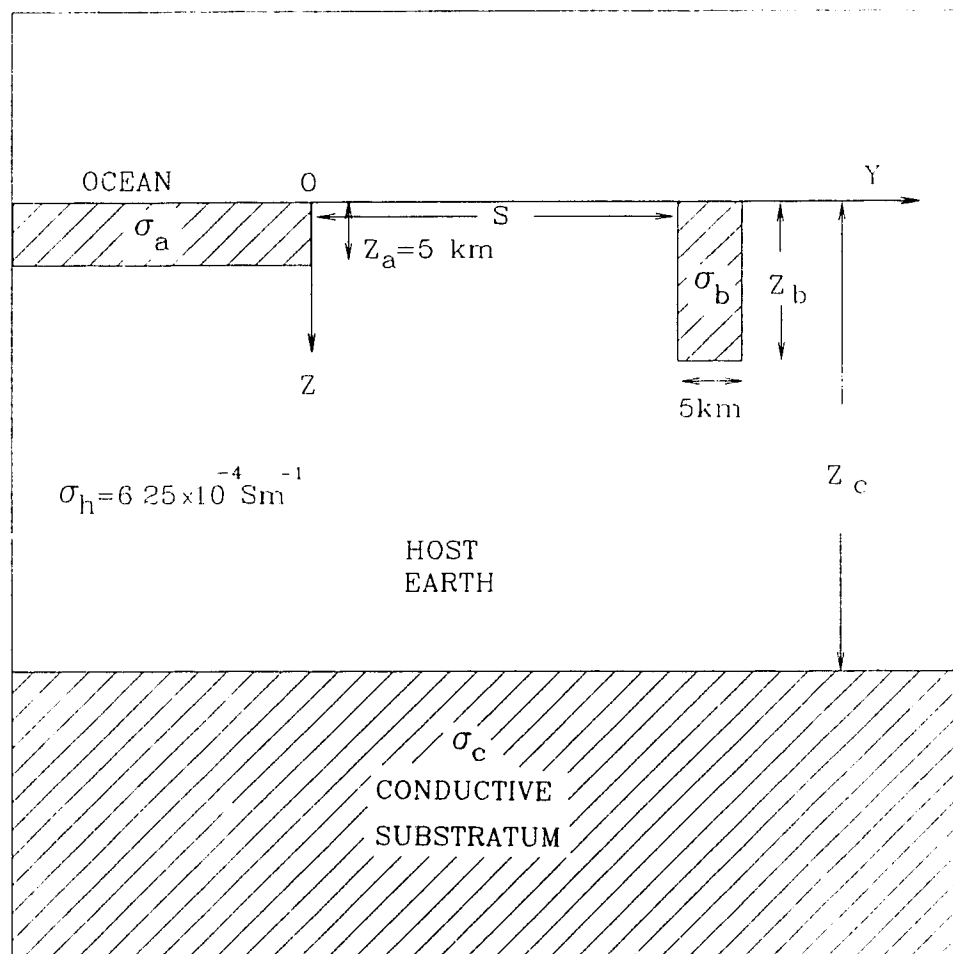


Figure 3.8: The cross-section of the model ocean (a) with the straight coastline parallel to an elongated conductive fault (b), all underlain by a conductive substratum (c). The conductivities for the ocean, the fault, and the conductive substratum are $\sigma_a = \sigma_b = \sigma_c = 3.6 \text{ Sm}^{-1}$.

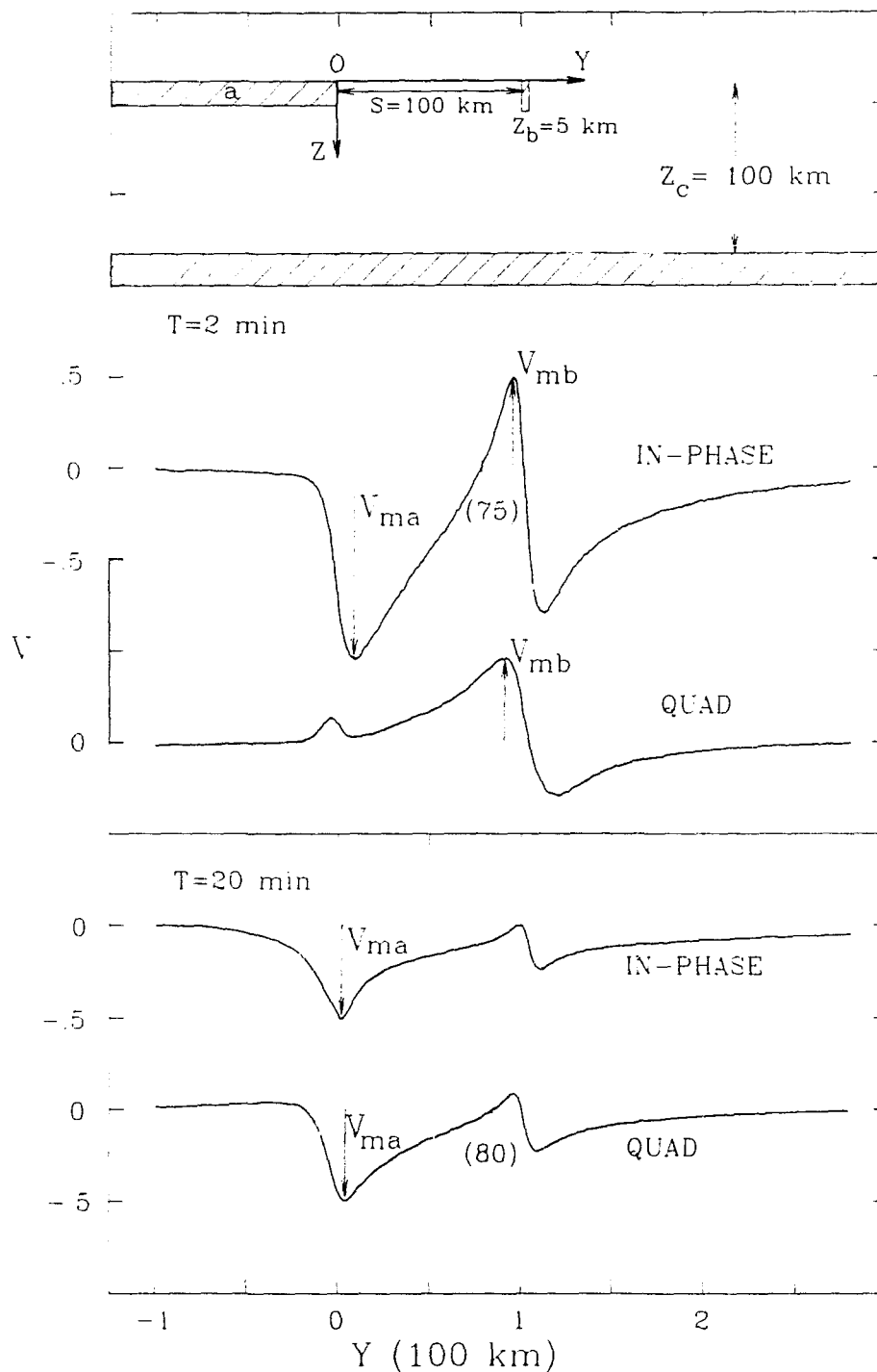


Figure 3.9: The in-phase and quadrature induction arrow responses V along a traverse perpendicular to the ocean (a) coastline and the fault (b) for periods of 2 and 20 min.

To show the dependence on period in some detail the in-phase and quadrature induction arrow responses along the profile for a range of periods (1-90 min) for the ocean-fault model are shown in Fig. 3.10 (it should be noted that the response curves for 2 and 20 min are the same as those shown in Fig. 3.9). It is seen that both the in-phase and quadrature responses are strongly period dependent over the entire period range. The in-phase V_{ma} (as introduced in Fig. 3.9) at the coastline for $T < 3$ min increases gradually with period to its maximum value at about 3 min, and then decreases with further increasing period, while the in-phase V_{mb} (also introduced in Fig. 3.9) just to the left of the fault decreases rapidly with increasing period to become zero at 20 min. It is noted that at 1 min the in-phase response reverses sign at a distance of approximately 75 km from the coastline, while at 10-20 min this distance is increased to approximately 100 km. To the left of this response reversal along the profile, the in-phase induction arrows point towards the ocean (negative Y direction), while to the right they point towards the fault (positive Y direction and away from the ocean). Since at periods $T \geq 20$ min the in-phase response is seen to be negative over the entire profile, the in-phase induction arrow at these longer periods everywhere points towards the ocean. The quadrature response, however, due to the characteristic period behaviour of the ocean response, shows a more complex behaviour. For periods $T \leq 2$ min, it is positive pointing towards the fault at all locations between the ocean and the fault, while for periods $T \geq 3$ min it shows a behaviour similar to that of the in-phase arrow, reversing direction at distances from the coastline that increase with increasing period. However, at the short period of 3 min, the quadrature response reverses direction at $Y \approx 30$ km, a location much nearer the coastline than that for

the in-phase response. Thus, for $T=3$ min the quadrature arrows at distances less than $Y \approx 30$ km point towards the ocean, and at distances $Y > 30$ km point towards the fault, while at very long periods (say 60-90 min), both the quadrature and the in-phase arrows at all locations point towards the ocean. The arrows (in-phase and quadrature), everywhere at long periods pointing towards the ocean, together with the ocean showing the larger responses, indicate that the induction responses at long periods are predominantly those of the ocean. In contrast, at short periods ($T < 3$ min in Fig. 3.10) the major quadrature response is clearly that of the fault.

Figure 3.11 shows the response maximums V_{ma} and V_{mb} (as defined in Fig. 3.9) for the in-phase component as a function of period for fault depths $Z_b = 5, 25, 50, 75$ km for each ocean-fault separation distance ($S = 50, 100, 200$ km). Both V_{ma} and V_{mb} at a given period for a given Z_b increase with an increase in the separation distance S . The V_{ma} response curves show that the effect of increasing the fault depth, though small, is the largest for the $S = 50$ km ocean-fault separation distance, and is negligible at the largest separation distance of $S = 200$ km. It is interesting to note that for each separation distance $S = 50$ and 100 km the maximum in the V_{ma} response curve occurs at roughly 3 min, the same period at which the V_{mb} curves for four fault depths intersect. For the $S = 200$ km separation, the V_{ma} response curve does not show such a maximum, since the fault response would be expected to provide only a negligible component to the response at the distant ocean, and the ocean response alone would be expected to show a maximum at the characteristic period $T_c \approx 0.7$ min, a period outside the range shown in Fig. 3.11. For periods $T \approx 3$ min for all three separation distances ($S = 50, 100, 200$ km), the largest V_{mb} responses are observed for the shallowest fault, and the

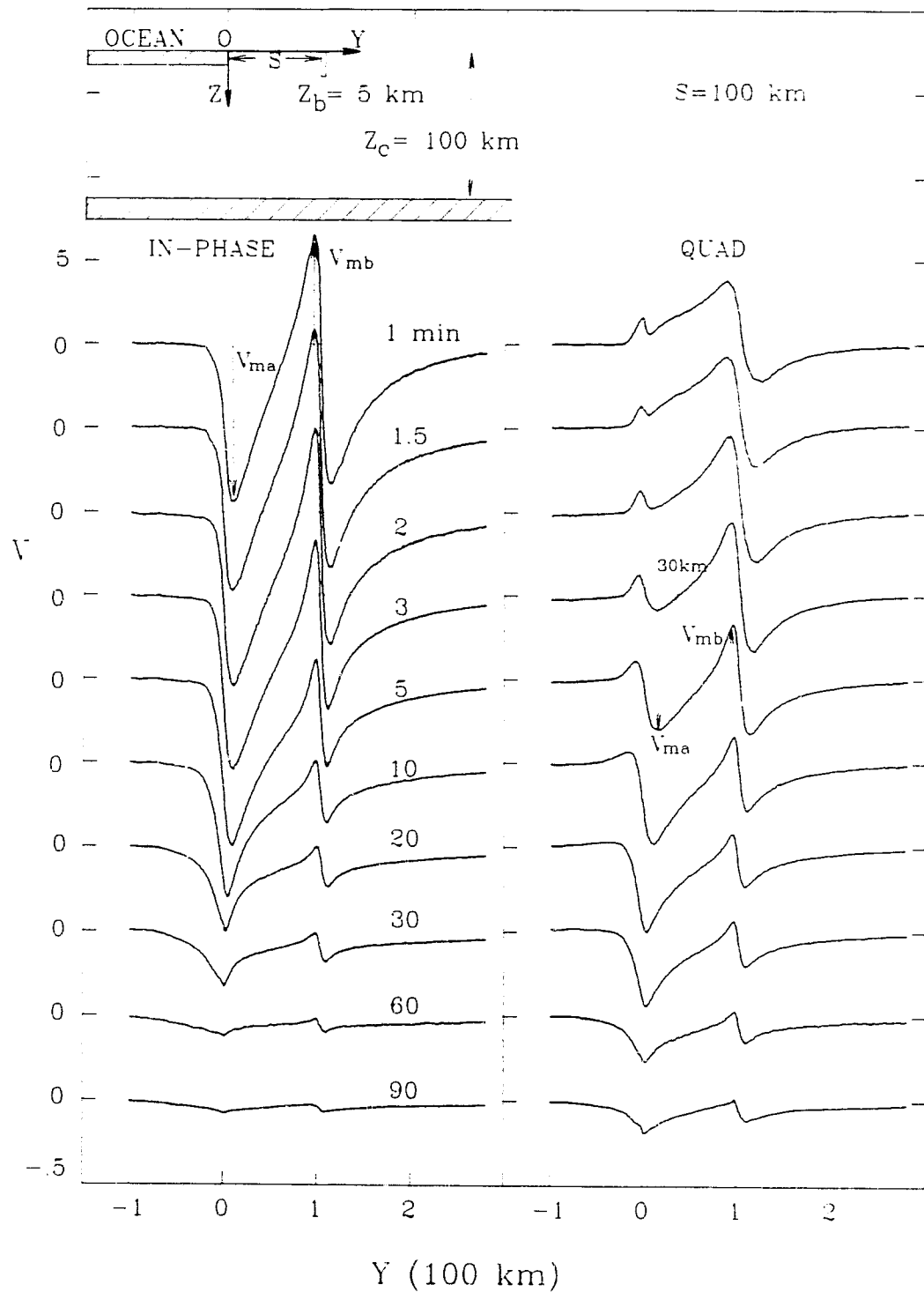


Figure 3.10: The in-phase and quadrature induction arrow responses V along a traverse perpendicular to the coastline and the fault for periods of 1–90 min.

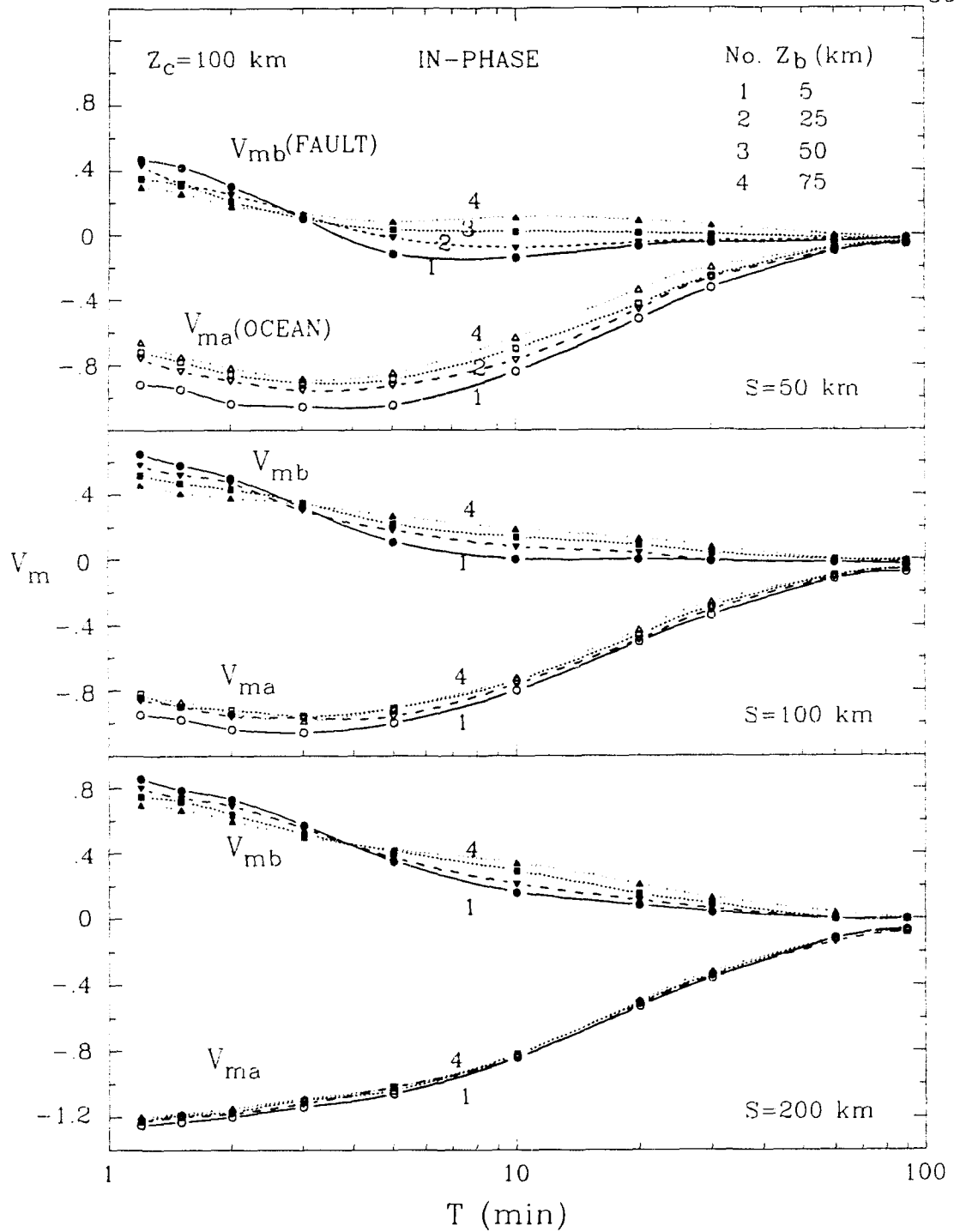


Figure 3.11: The in-phase induction arrow maximum responses V_{ma} (at the coastline) and V_{mb} (just to the left of the fault), as a function of period for fault depths $Z_b=5, 25, 50, 75$ km for each of three ocean-fault separation distances $S=50, 100, 200$ km. The dotted horizontal lines indicate the zero response reference.

magnitudes of the responses decrease with increasing fault depth. For periods $T > 3$ min, the opposite is observed, except for the case of $S = 50$ km which shows the responses for the shallow fault depths ($Z_b = 5, 25$ km) to be of sign opposite to those for the larger fault depths ($Z_b = 50$ and 75 km). In general, both V_{ma} and V_{mb} show strong dependence on period.

Figure 3.12 shows the response maximums V_{ma} and V_{mb} for the quadrature component as a function of period (as for the in-phase component in Fig. 3.11). The change in the fault depth is seen to have even a smaller effect on the quadrature ocean response V_{ma} than was observed for the in-phase component (Fig. 3.11). In fact, except for the smallest separation distance ($S = 50$ km) for $T > 3$ min, the quadrature V_{ma} appears to be insensitive to the fault depth. Similar to the results for the in-phase component, the quadrature V_{mb} is the largest for the shallowest fault at short periods for all separation distances, with the opposite being the case at long periods. A major difference is that this cross-over from the behaviour at short periods to the opposite behaviour at long periods occurs at roughly 10-12 min, a period approximately a factor of 3-4 greater than the lower period of roughly 3 min observed for the in-phase component (Fig. 3.11).

The cross-over in the dependence on fault depth at short periods, where the shallower fault results in the larger response, to the opposite dependence on fault depth at long periods, observed at different periods for the in-phase (Fig. 3.11) and in the quadrature (Fig. 3.12) components, could have application in determining the depth of a fault in a coastal region.

Figure 3.13 shows the zero response period T_0 for the in-phase component as a function of the distance Y from the coastline for the ocean-fault separation dis-

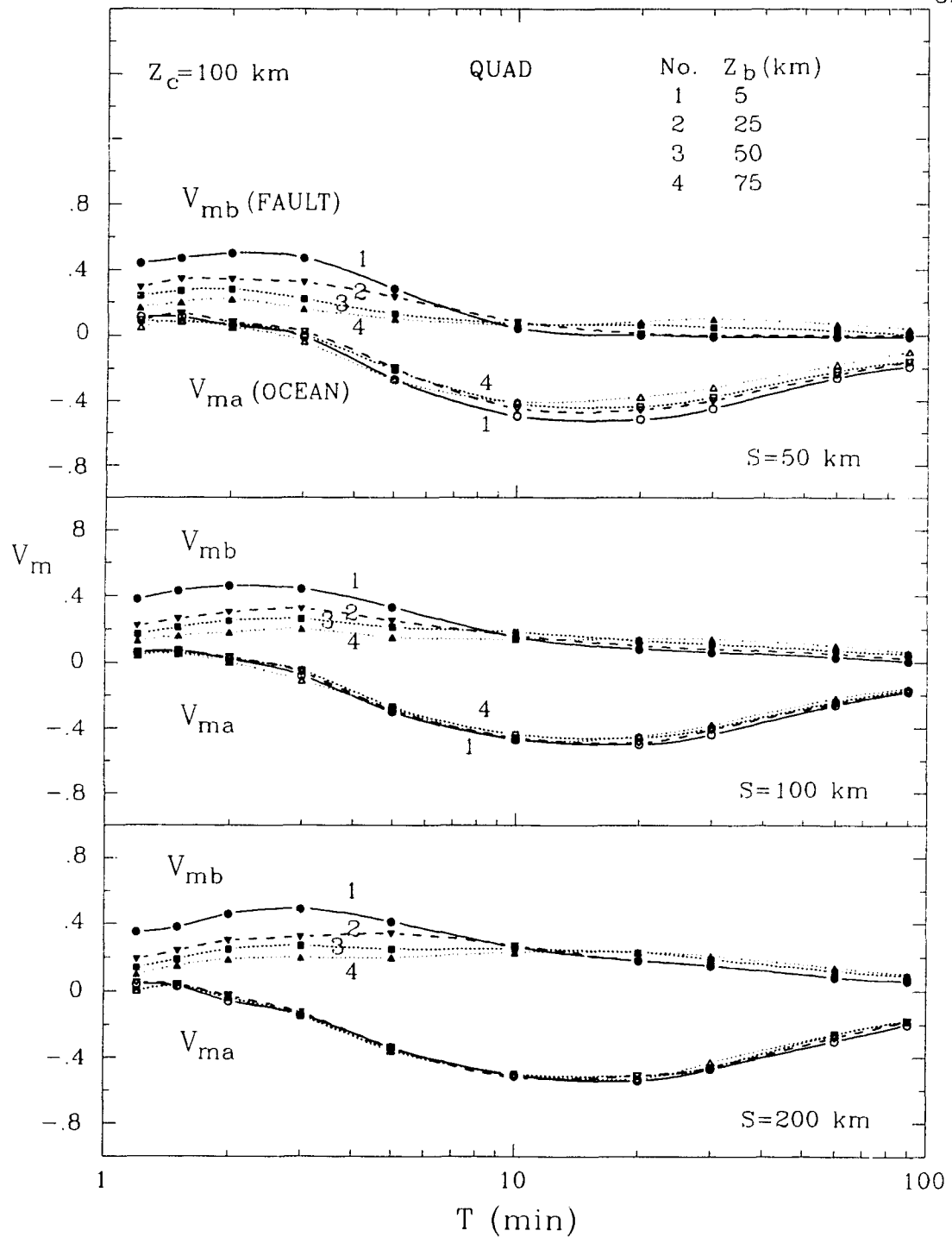


Figure 3.12: The quadrature induction arrow maximum responses V_{ma} (at the coastline) and V_{mb} (just to the left of the fault), as a function of period for fault depths $Z_b = 5, 25, 50, 75$ km for each of three ocean-fault separation distances $S = 50, 100, 200$ km. The dotted horizontal lines indicates the zero response reference.

tance $S=100$ km and the fault depth $Z_b=5$ km. The zero response period T_0 is that period at which the response, at a given distance from the coastline, is zero, and for $T>T_0$ is of sign opposite to that for $T<T_0$. The induction arrows for 3 and 10 min are included to demonstrate arrow reversals and magnitude changes along the profile. At roughly 85 km from the ocean the in-phase response is zero at 3 min (T_0), then for $T>3$ min the arrow points towards the ocean, while for periods $T<3$ min the arrow points towards the fault (or away from the ocean). Further, at this 3 min period, the arrows at sites $Y<85$ km point towards the ocean, and at sites $Y>85$ km point towards the fault (or away from the ocean). The zero response curve (T_0 as a function of Y) divides the region between the ocean and the fault into two zones in which the induction arrows to the left of the curve point towards the ocean and to the right of the curve point away from the ocean (or towards the fault). It is noted that the points on the zero response curve lie well to the right of mid-way ($S/2$) between the ocean and the fault, and move towards the fault with increasing period.

The zero response curve for the quadrature component, similar to that for the in-phase component (Fig. 3.13), is shown in Fig. 3.14 (it should be noted that the arrow scale differs by a factor of two from that for the in-phase component). Differing from the in-phase arrow at 3 min, which reverses direction near the fault at $Y\approx 85$ km (Fig. 3.13), the quadrature arrow over land reverses sign at $Y\approx 35$ km, a location much nearer to the ocean than to the fault. As was the case for the in-phase component (Fig. 3.13), the zero response curve for the quadrature component also divides the region between the ocean and the fault into two zones in which the arrows to the left of the curve point towards the ocean, and to the

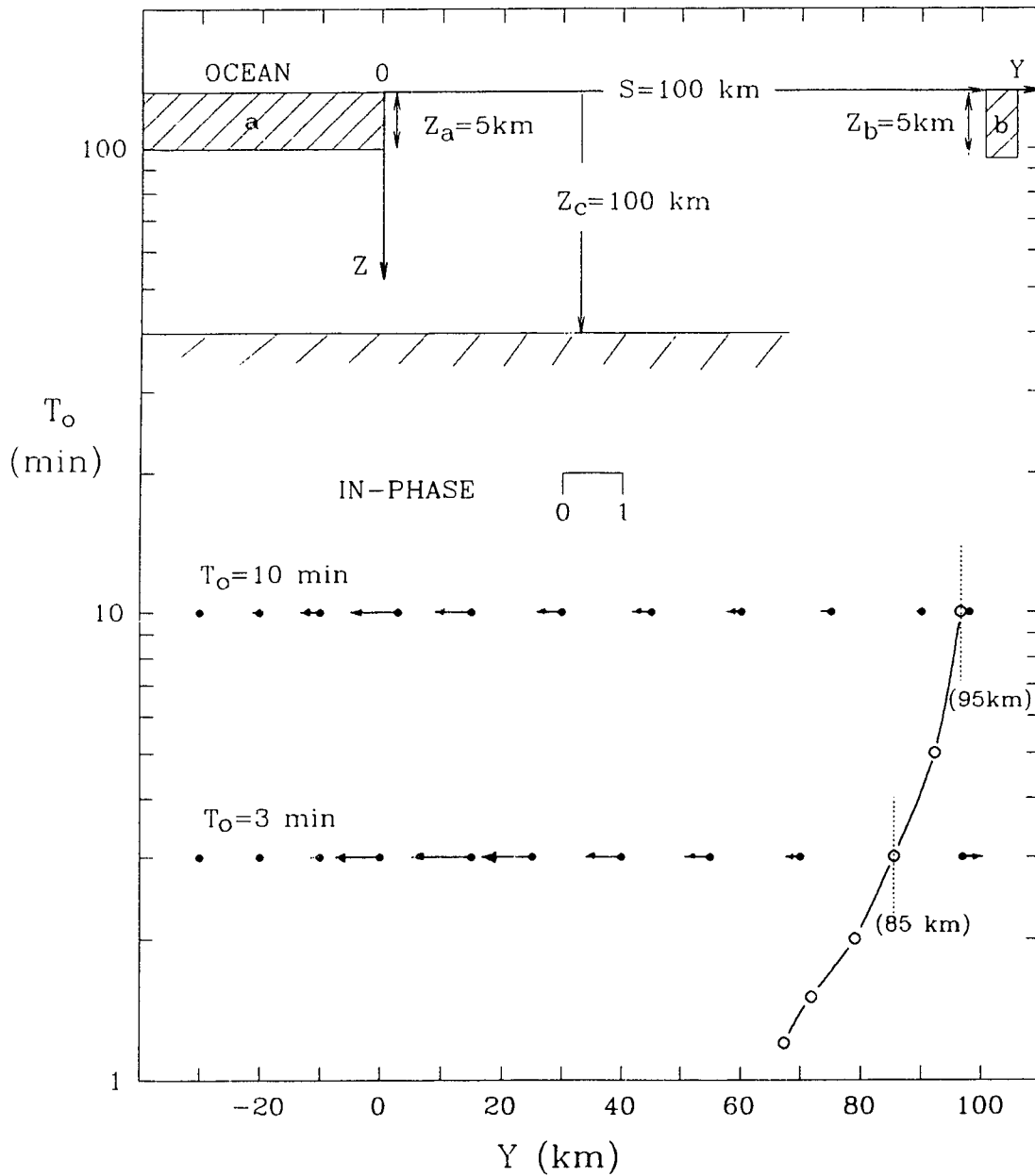


Figure 3.13: The zero in-phase response period T_0 as a function of the distance Y from the coastline. The induction arrows for 3 and 10 min are shown to demonstrate that at a given site the arrow directions for periods larger than T_0 are opposite to those for periods smaller than T_0 .

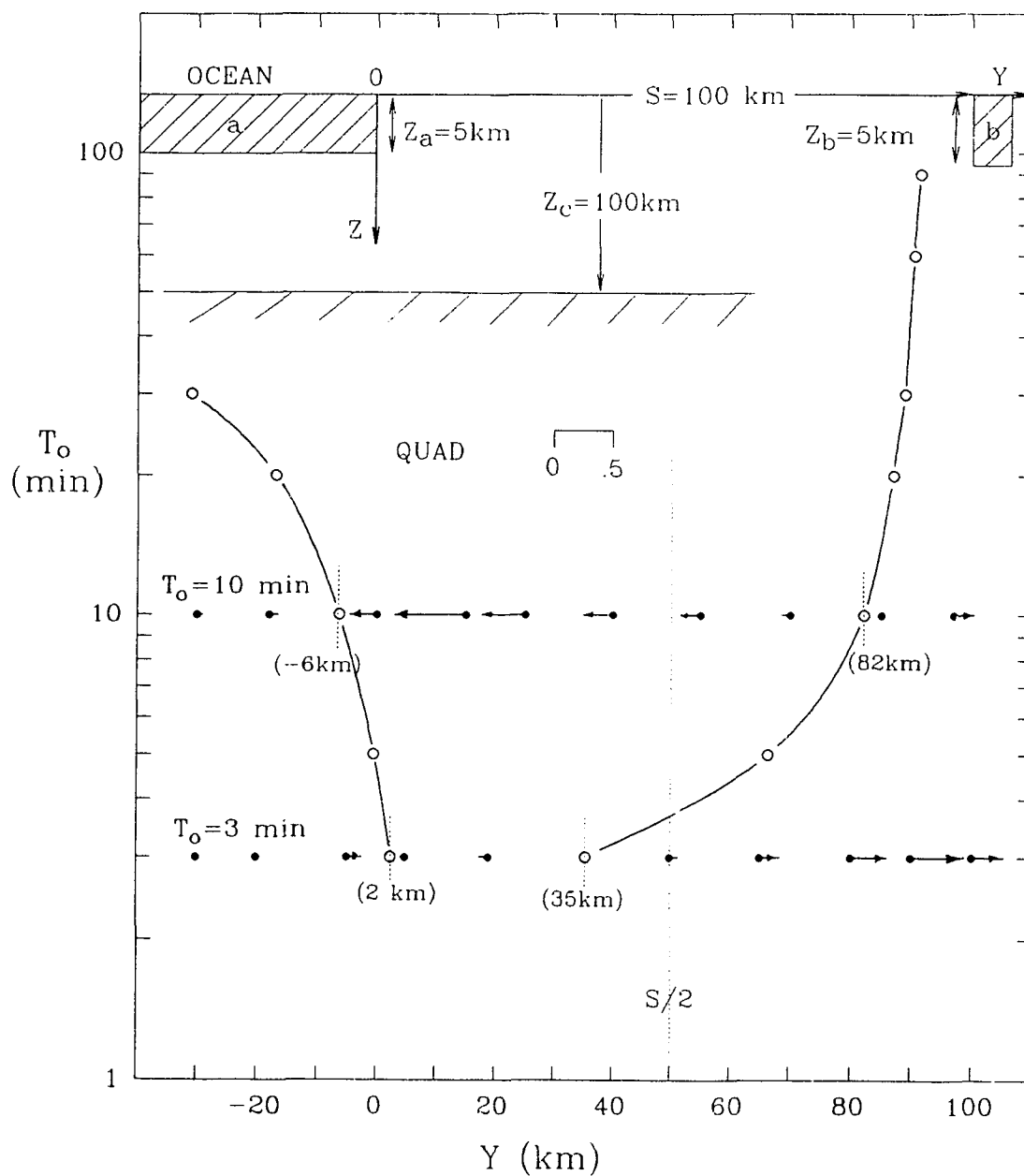


Figure 3.14: The zero quadrature response period T_0 as a function of the distance Y from the coastline. The induction arrows for 3 and 10 min are shown to demonstrate that at a given site the arrow directions for periods larger than T_0 are opposite to those for periods smaller than T_0 .

right of the curve point towards the fault. A second zero quadrature response curve (to the left in Fig. 3.14) lies completely over the ocean, with the arrows to the left of the curve pointing to the right and those to the right of the curve pointing to the left, so that the arrows on opposite sides point towards each other. This differs from the quadrature arrow behaviour on land (zero response curve to the right in Fig. 3.14) where the arrows on opposite sides of the zero response curve are also oppositely directed, but point away from each other. In general, the zero response periods T_0 for both the in-phase and quadrature components increases with distance from the coastline.

Figure 3.15 shows in detail the zero response curves (T_0 as a function of Y) for the in-phase component for fault depths $Z_b=5, 25, 50, 75$ km for each ocean-fault separation distance $S=50, 100, 200$ km. It is seen that for all three separation distances ($S=50, 100, 200$ km), the zero response curves shift to smaller values of Y (towards the ocean) with increasing fault depth Z_b . This is expected due to the increasing positive fault response with increasing fault depth, a response that is of sign opposite to that of the negative ocean response (see Fig. 3.10). At short periods ($T_0 \leq 5$ min) the zero response period T_0 increases with increasing distance Y from the ocean (or decreasing distance from the fault) for all fault depths and separation distances. This is also the case at longer periods for fault depths $Z_b=5$ and 25 km for separation distances $S=100$ and 200 km. However, for the very large fault depths $Z_b=50$ and 75 km, the zero response curves show an inflection in the neighborhood of $T_0=5$ min, so that for the period range $T_0=5-20$ min, T_0 increases with decreasing distance from the coastline for all three separation distances. At the longer periods (say, for $T_0 > 20$ min) for these large fault depths, T_0

IN-PHASE

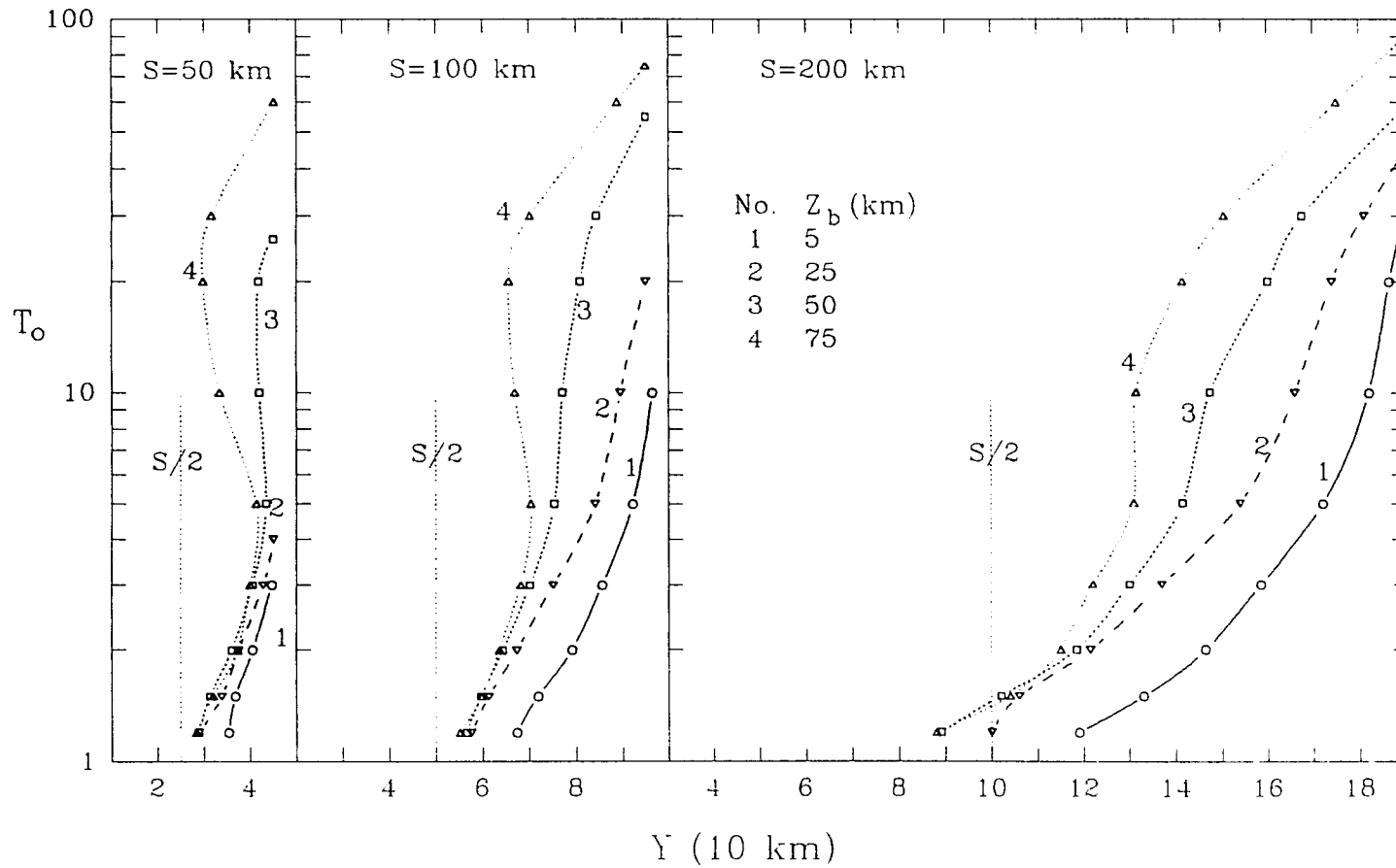


Figure 3.15. Empirical plots of the zero in-phase response period T_0 as a function of the distance Y from the coastline for a range of fault depths ($Z_b = 5, 25, 50, 75$ km) and for each of three ocean-fault separation distances ($S=50, 100, 200$ km).

again increases with distance from the coastline. This is expected since at very long period the response of the massive ocean should be larger than that of the fault. These inflections in the zero response curves observed for the large fault depths draw attention to the rather interesting feature that at certain distance from the coastline the in-phase response could be zero at two or even three different periods T_0 . For example, in the case of $Z_b=75$ km for $S=50$ km, curve 4 shows zero response periods T_0 of approximately 1.2, 15, and 30 min at $Y=30$ km. It is apparent that the fault depth and the proximity of the ocean are important parameters in determining the zero response period at a given location. It is interesting to note that T_0 , in the proximity of the fault, is very sensitive to the fault depth, increasing sharply with increasing Z_b , and that there is an upper limit to the zero response period at the fault edge for each ocean-fault separation distance. This feature has application to delineate a fault location and depth in a field survey carried out along a profile in a coastal region. For example, if in a linear array of field sites such a cut-off period (say $T_0=10$ min) was observed at a site $Y=95$ km from the coastline, curve 1 for $S=100$ km would suggest that the site may be roughly at the edge of a 5 km depth fault.

The curves for the zero quadrature response periods T_0 are shown in Fig. 3.16. Compared with the observations for the in-phase component (in Fig. 3.15), the zero quadrature response locations (say for given periods $T_0 < 5$ min) are much nearer the ocean at short periods than was the case for the in-phase component. Further, as was the case for the in-phase component (Fig. 3.15), the zero quadrature response curves (T_0 as a function of Y) shift towards the ocean (or away from the fault) for increasing fault depth for all ocean-fault separation distances S .

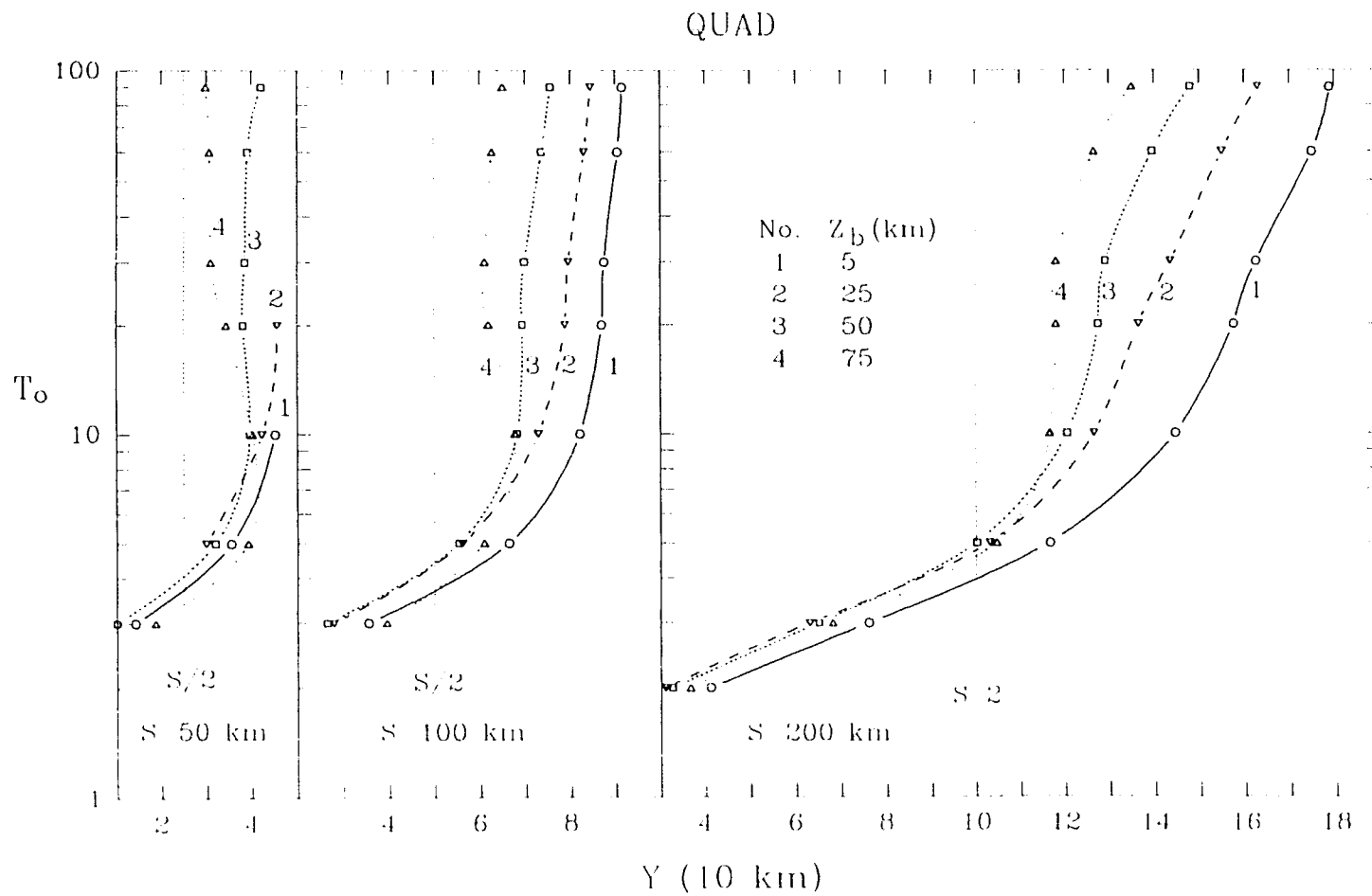


Figure 3.16 Empirical plots of the zero quadrature response period T_0 as a function of the distance Y from the coastline for a range of fault depths ($Z_b = 5, 25, 50, 75$ km) and for each of three ocean fault separation distances ($S = 50, 100, 200$ km).

For example, in Fig. 3.16 for the case of $S=200$ km and $Z_b=5$ km (curve 1), Y (at $T_0=10$ min) decreases from roughly 145 km for $Z_b=5$ km, to approximately 115 km for $Z_b=75$ km. Again, as for the in-phase component (Fig. 3.15), the zero quadrature response curves at intermediate periods (roughly 10-40 min) for the deep faults also show multiple T_0 values at certain distances from the coastline. The zero response period T_0 depends more strongly on Z_b at long periods than it does at short periods. For example, for $S=200$ km and $Z_b=5$ km, the zero response periods at $Y=40$ and 120 km are $T_0=2$ and 5 min respectively, while for $Z_b=75$ km at the same two sites they are $T_0=2.2$ and 50 min respectively. The zero in-phase and zero quadrature response curves in Figs. 3.15 and 3.16 could aid in determining a fault location as well as its depth for the case of a fault near a coastline. For example, if at a distance $Y=80$ km from the coastline, the in-phase response were found to be zero at 4 min period, the curves in Fig. 3.15 would suggest the ocean-fault separation distance S to be roughly 100 km and the fault depth to be approximately 25 km. This would be confirmed by the zero quadrature response observed at a period of roughly 20-30 min (Fig. 3.16) at the same site ($Y=80$ km), with the sign negative at sites $Y<80$ km, and positive at $Y>80$ km.

As was pointed out in the discussion for the in-phase component (Fig. 3.15), for each ocean-fault separation distance there exists an upper limit (T_m) to the zero response period (T_0) observed at the fault edge. For example, for the fault depth $Z_b=5$ km for the case of $S=200$ km (curve 1 in Fig. 3.15), the upper limit period T_m is 30 min, a period beyond which no zero in-phase response is observed (and thus no reversal in sign at any site) between the ocean and the fault. This period $T_m=30$ min for the shallow fault $Z_b=5$ km, increases to 60 min for $Z_b=50$

km, and to 90 min for $Z_b=75$ km. For a decreasing ocean-fault separation distance ($S=100, 50$ km) the cut off period T_m shifts to shorter periods for a given fault depth Z_b . For example, the $T_m=30$ min period observed for the shallow fault ($Z_b=5$ km) for the case of $S=200$ km (curve 1), is decreased to 10 min for $S=100$ km, and to 3 min for $S=50$ km. It is noted that the zero response curves for the quadrature component (Fig. 3.16) do not show an upper limit to the zero response period as is observed for the in-phase component.

An empirical plot of the cut-off period T_m as a function of the fault depth Z_b for the three ocean-fault separation distances $S=50, 100,$ and 200 km is shown in Fig. 3.17. It is noted that these curves show the relationship between the cut-off period and the fault depth only approximately, since some extrapolation was required in view of the spacing of the periods studied. Nevertheless, the curves in Fig. 3.17 do show that in principle a knowledge of the cut-off period could provide information on the fault location and depth. For example, a cut-off period T_m of roughly 20 min at a site roughly 100 km from the ocean coastline could suggest an ocean-fault separation distance $S=100$ km and a fault depth of approximately 25 km.

If the sites in a geomagnetic field study were in a coastal region that included conductive faults, zero in-phase and/or quadrature induction arrow responses at some sites might be expected at periods T_0 , periods that on the basis of the models studied in this section should be characteristic of the ocean-fault model geometry. Further, comparing the magnitudes and the signs of the responses for a spectrum of periods (including those for $T < T_0$ and $T > T_0$), normally available at each site, with those for a range of models should in principle permit an interpre-

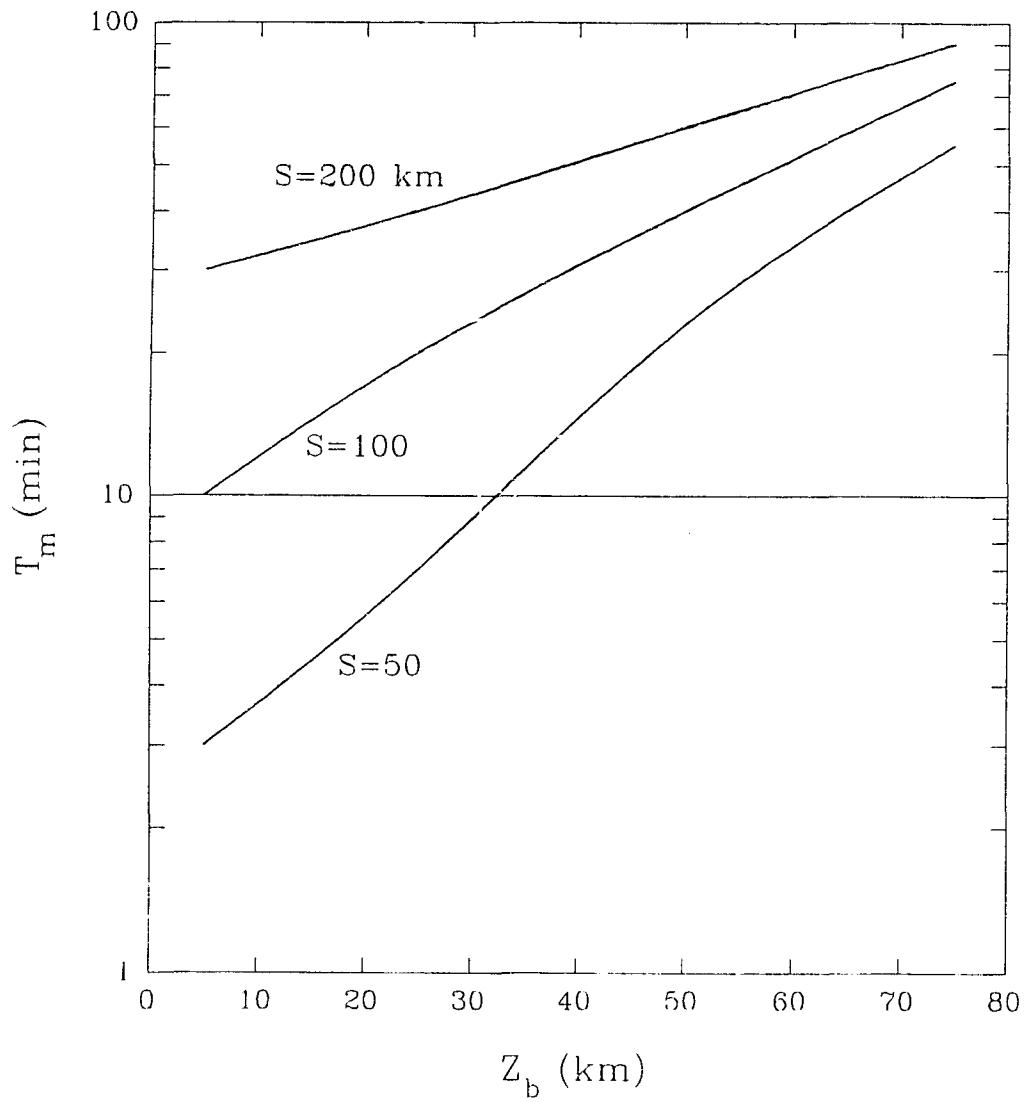


Figure 3.17: Empirical plots of T_m (the upper limit to the zero in-phase response period T_0) as a function of the fault depth Z_b for ocean-fault separation distances $S=50, 100, 200$ km.

tation of the field site measurements. In the following, figures 3.18-3.20 are presented to provide such model responses over a spectrum of periods at specific sites between the fault and the ocean coastline.

The in-phase and quadrature induction arrow responses at selected distances $Y=15-45$ km from the coastline for an ocean-fault separation distance $S=50$ km are shown as a function of period for fault depths $Z_b=5, 25, 50$ km in Figs. 3.18, 3.19, 3.20 respectively. The response curves for a shallow fault $Z_b=5$ km in Fig. 3.18 show that for locations $Y<35$ km the in-phase responses are negative at all periods, indicating that the in-phase arrows point towards the ocean. Nearer the fault, at sites $Y>35$ km, the in-phase responses reverse sign at T_0 (closed circles), from positive for $T<T_0$ to negative for $T>T_0$. This zero in-phase response period T_0 increases for sites near (increasing Y) the fault, for example, T_0 increases from roughly 1 min at $Y=35$ km to 3 min at $Y=45$ km. The quadrature response shows a sign reversal at T_0 (open circles) over a much larger distance range ($Y=15-45$ km) than that for the in-phase response. Again, as is the case for the in-phase response, the zero quadrature response period T_0 also increases with increasing Y . At a location very near the fault ($Y=45$ km), the quadrature response becomes negligible for periods $T>T_0$ (but the in-phase response remains significant). It is noted that at short periods ($T<5$ min), while one of the components (say in-phase) is zero at the period T_0 , the other component (say quadrature) shows a broad maximum at roughly the same period. For example, at $Y=35$ km the in-phase response is zero at 1 min while the corresponding quadrature response is roughly maximum; and at 5 min period, the quadrature response is zero while the in-phase response shows a maximum. The zero response periods T_0 for the in-

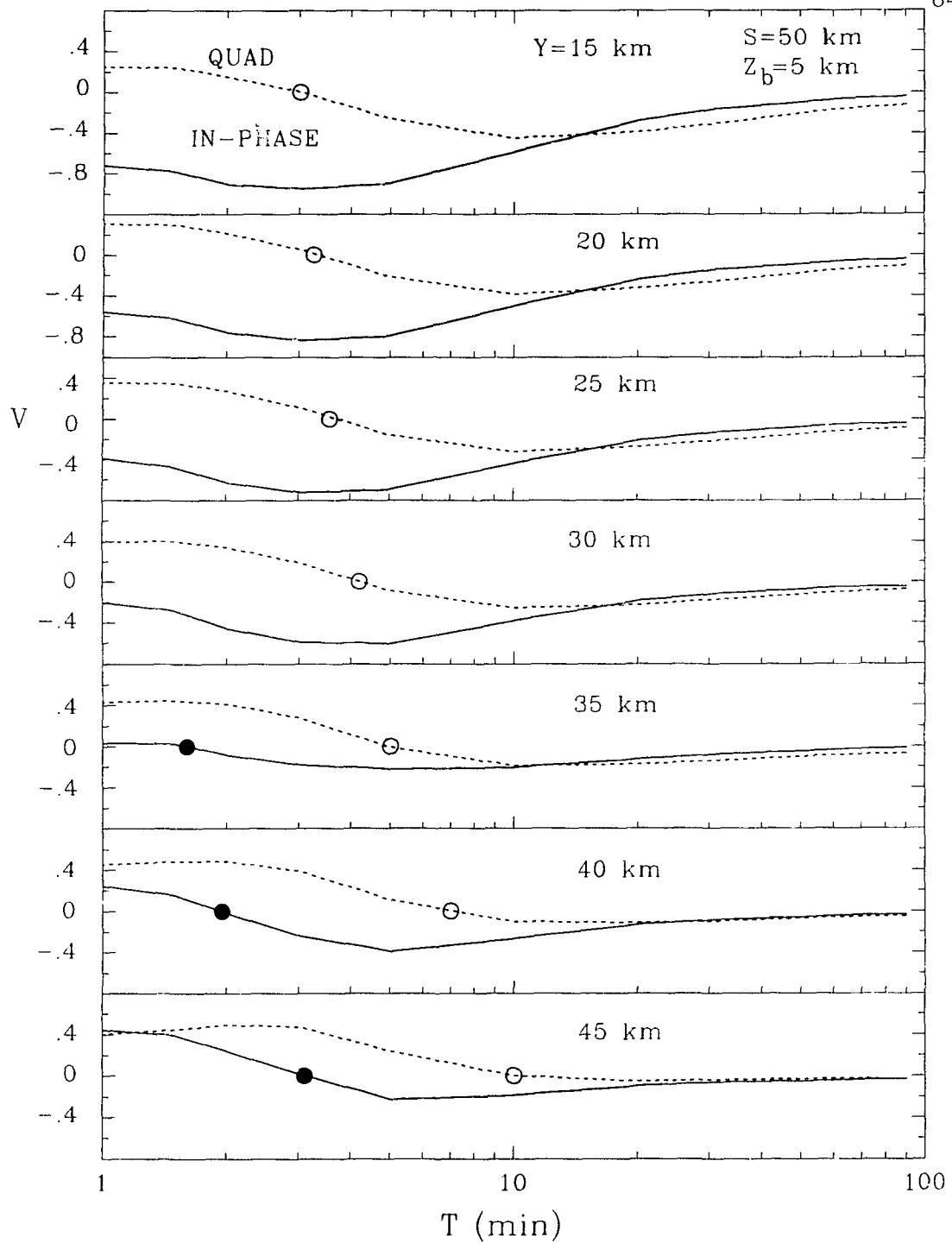


Figure 3.18: The in-phase and quadrature induction arrow responses as a function of period for selected locations at distances $Y=15-45$ km from the coastline for $S=50$ km for fault depth $Z_b=5$ km. The closed and open circles indicates the zero response periods T_0 for the in-phase and quadrature components respectively.

phase and quadrature components are seen to be confined to the period range of 1-10 min for this ocean-fault model. For periods $T > 10$ min, both the in-phase and quadrature responses are negative, indicating that the arrows for both components at all sites point towards the ocean at the longer periods.

To show the effect of increasing the fault depth, the in-phase and quadrature responses at the same sites ($Y=15-45$ km) as those in Fig. 3.18 are provided for fault depths $Z_b=25$ km and 50 km in Figs. 3.19 and 3.20 respectively. In comparing the responses in Fig. 3.19 for the fault depth $Z_b=25$ km with those for the shallower fault depth $Z_b=5$ km in Fig. 3.18, the main changes are a shift to larger T_0 at each site Y , and a generally attenuated response at periods $T < T_0$ and $T > T_0$ for the increased fault depth. The zero in-phase and zero quadrature response periods T_0 are now confined to the increased period ranges 1-4 min and 3-20 min respectively, as compared with the ranges 1-3 min and 3-10 min for the shallower fault depth $Z_b=5$ km. Signs reversals (at T_0) in the in-phase response (in the period range shown) occur at locations $Y \geq 30$ km, as compared with $Y \geq 35$ km for the shallower fault. The quadrature response shows sign reversals (at periods T_0) at all sites. However, the quadrature response for periods $T > T_0$ is negligible at sites $Y \geq 40$ km, compared with the similar small responses at $Y=45$ km for the case of $Z_b=5$ km.

In comparing the responses for the further increased fault depth of $Z_b=50$ km (Fig. 3.20) with those for the $Z_b=25$ km depth (Fig. 3.19), it can be seen that the zero response periods T_0 (characteristic of the model parameters) for the in-phase component are again shifted to somewhat longer periods (for example, from 4 to 8 min at $Y=45$ km), while for the quadrature component they are shifted to slightly

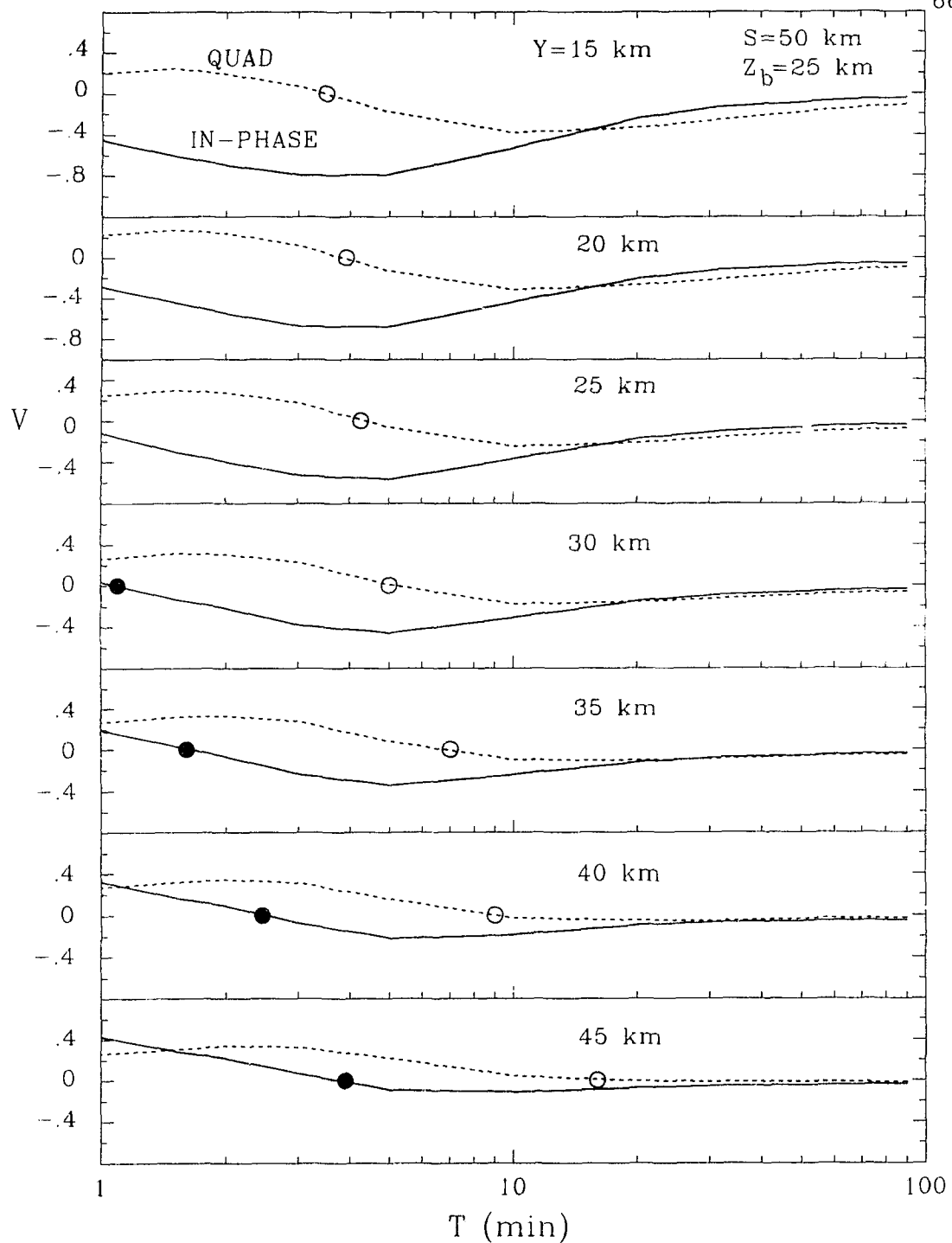


Figure 3.19: The in-phase and quadrature induction arrow responses as a function of period for selected locations at distances $Y=15-45$ km from the coastline for $S=50$ km for fault depth $Z_b=25$ km. The closed and open circles indicates the zero response periods T_0 for the in-phase and quadrature components respectively.

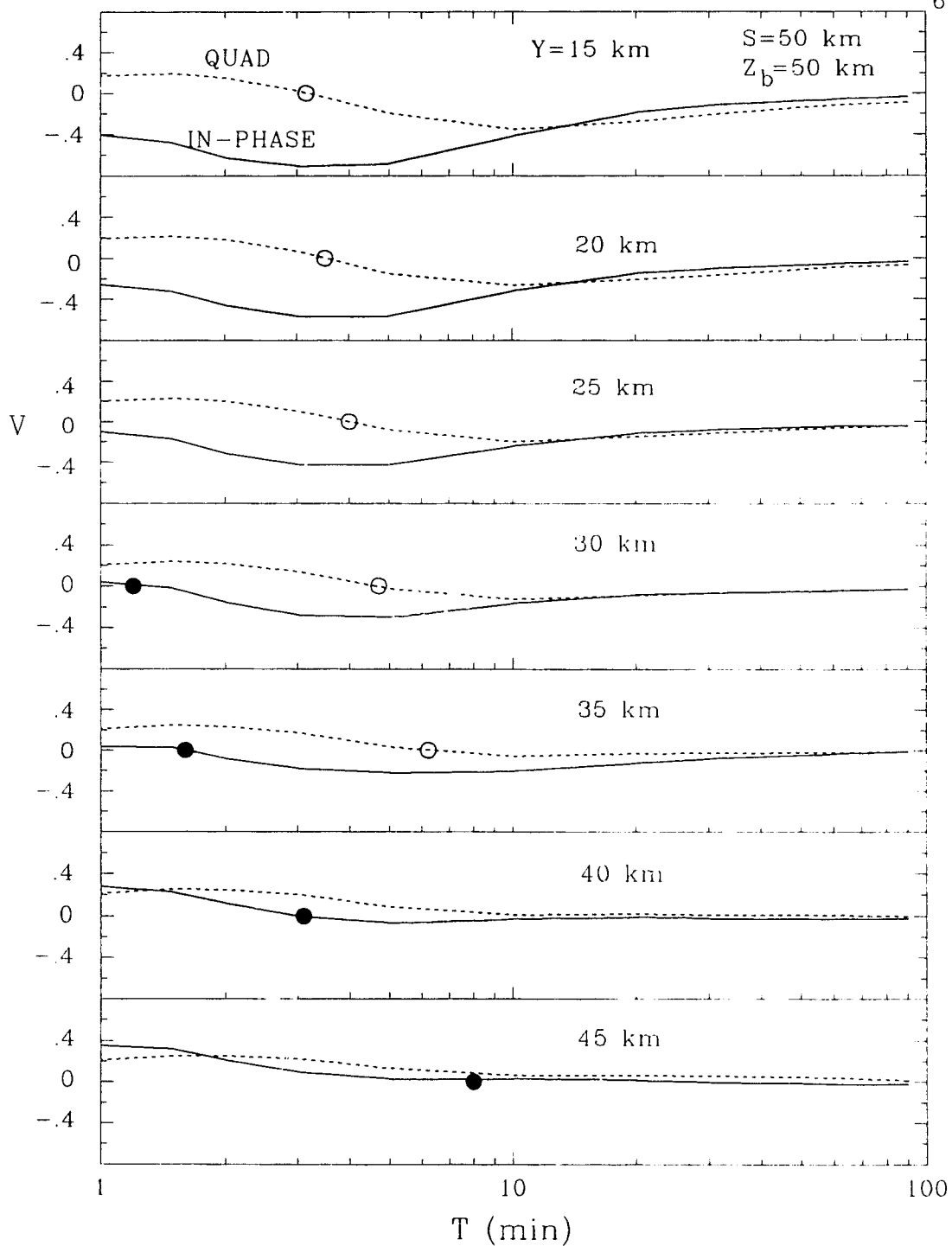


Figure 3.20: The in-phase and quadrature induction arrow responses as a function of period for selected locations at distances $Y=15-45$ km from the coastline for $S=50$ km for fault depth $Z_b=50$ km. The closed and open circles indicates the zero response periods T_0 for the in-phase and quadrature components respectively.

shorter periods for $Y \leq 35$ km, and to longer periods for $Y > 35$ km. The increased fault depth also has the effect of further attenuating the responses for both components, with the quadrature response for $T > T_0$ being negligible for $Y \geq 35$ km. Additional response curves, similar to those in Fig. 3.18-3.20, but for increased ocean-fault separations of $S=100$ and 200 km are given in Appendix A.

3.4 Removal of the Coast Effect From the Response of an Ocean and an on Shore Fault Parallel to a Coastline

In order to examine if the sum of the individual responses of a model ocean and a model fault would yield the response of a model of an ocean and an on shore fault parallel to the coastline, laboratory measurements were carried out for models of each of an ocean, an elongated conductive fault, and an ocean and an elongated conductive fault parallel to the coastline, each in a resistive host earth. The parameters for these models are shown in the upper parts of Figs. 3.21-3.24, the figures that show the in-phase and quadrature induction arrow responses at 2 and 20 min for models of the ocean (V_a), the elongated conductive fault (V_b), the fault parallel to a straight ocean coastline (V_{ab}), as well as the sum (dashed curve) of the ocean and the fault responses (V_a+V_b).

3.4.1 The Effect of the Fault Depth for a Small Ocean-Fault Separation Distance

The in-phase and quadrature responses for each of the ocean, the fault, and the ocean and an on shore fault parallel to the coastline, as well as the sum of the ocean and the fault responses for a small ocean-fault separation distance ($S=50$ km) are shown for the cases of a shallow fault ($Z_b=5$ km) in Fig. 3.21 and for a

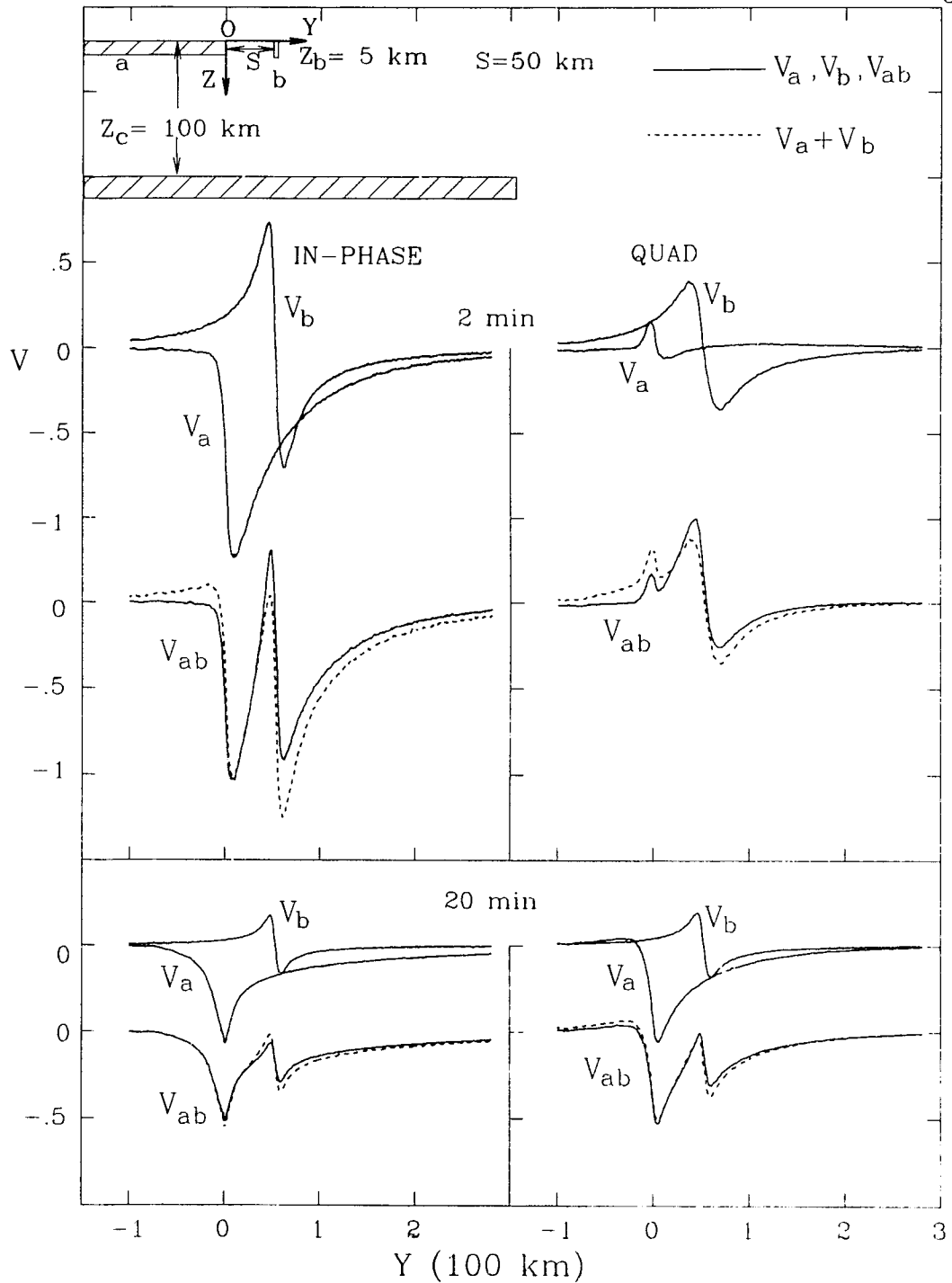


Figure 3.21: The in-phase and quadrature induction arrow responses V at 2 and 20 min for each of: the ocean (V_a); the fault (V_b); the ocean and the fault parallel to the coastline (V_{ab}); and the sum of the ocean and the fault responses ($V_a + V_b$) for the ocean-fault separation distance $S = 50$ km and for the fault depth $Z_b = 5$ km.

very deep fault ($Z_b=75$ km) in Fig. 3.22. The in-phase responses V_a (ocean) at 2 and 20 min are seen to be negative at all locations, indicating arrows pointing towards the bulk of the ocean as expected. The quadrature response V_a at 2 min reverses sign near the ocean coastline as well as at a location further inland, indicating that the 2 min period shown is greater than the characteristic period (T_c) for this ocean underlain by a conductive substratum at 100 km depth. At 20 min the ocean quadrature response V_a is negative everywhere on land, the same as is the case for the in-phase response. This agrees with the ocean coast effect observed at long periods in a previous section (3.2). Both the in-phase and quadrature responses V_b (fault) at 2 and 20 min are positive to the left of the fault but negative to the right of the fault, again indicating that the arrows at either side of the fault point towards the fault as expected. At 2 min the in-phase response V_b is considerably larger than the quadrature response V_b , but at 20 min the two responses are roughly the same. The in-phase response V_{ab} (ocean and the fault parallel to the coastline) reverses sign (at a location very near the fault) at 2 min, but not at 20 min. The quadrature response V_{ab} however, at 2 min does not show a reversal but is positive between the ocean and the fault. At 20 min the quadrature response V_{ab} , as is the case for the in-phase response, is negative everywhere. Thus the observations of the induction arrow behaviour for models of the ocean, the fault, and the ocean and the fault, are consistent with the results in the previous sections.

The sum of the individual responses V_a+V_b are shown in the dashed curves in Fig. 3.21. For the in-phase response at 2 min very good agreement is seen between the dashed line curve (V_a+V_b) and solid line curve (V_{ab}) in the region

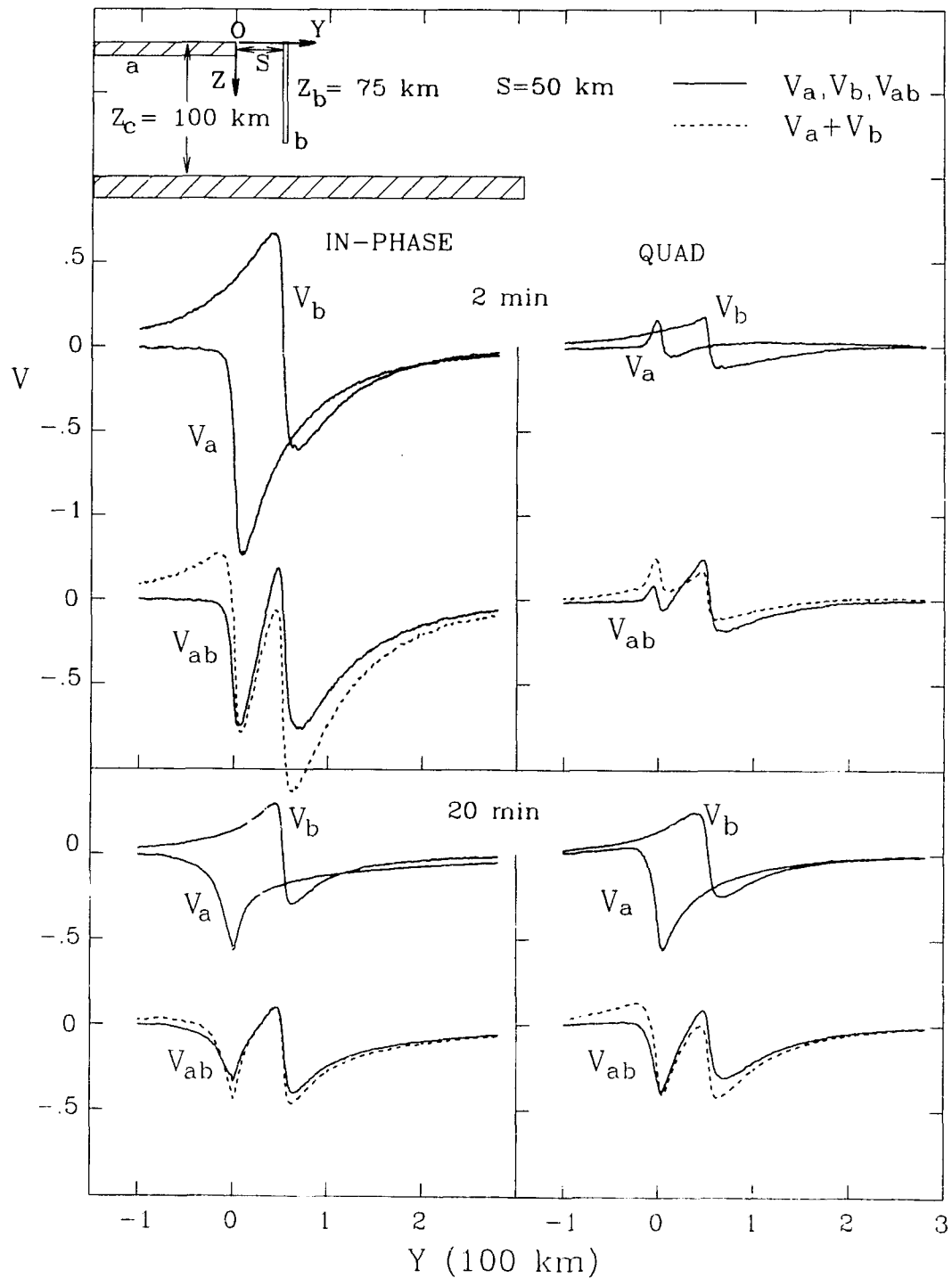


Figure 3.22: The in-phase and quadrature induction arrow responses V at 2 and 20 min for each of: the ocean (V_a); the fault (V_b); the ocean and the fault parallel to the coastline (V_{ab}); and the sum of the ocean and the fault responses ($V_a + V_b$) for the ocean-fault separation distance $S = 50$ km and the fault depth $Z_b = 75$ km.

between the ocean and the fault. The agreement for the quadrature component at 2 min is also very good, except right at the coastline and at the fault. A comparison of the results (not presented here) for periods greater than 20 min for the 5 km depth fault, as well as for the 25 km and 50 km depth faults also showed good agreement. In general, Fig. 3.21 shows that the agreement between V_{ab} (the induction arrow response of an ocean and a conductive fault parallel to the coastline) and V_a+V_b (the sum of the individual ocean and fault responses), though very good at the short period of 2 min, is even better at the longer period of 20 min.

The curves in Fig. 3.22 show that for an unrealistically deep fault ($Z_b=75$ km, rather than $Z_b=5$ km as in Fig. 3.21) the agreement between V_{ab} and V_a+V_b at 2 min has deteriorated somewhat, compared with the results for the shallower 5 km depth fault (Fig. 3.21). However, very good agreement in the region between the ocean and the fault for both components is seen at 20 min. Thus, for the responses of the conductive fault parallel to the coastline for the case of a small ocean-fault separation distance ($S=50$ km), the sum of the responses V_a+V_b shows good agreement with the response V_{ab} in the region between the ocean and the fault for shallow and intermediate depth faults at both short and long periods (periods as long as 90 min were also studied, but not shown here).

3.4.2 The Effect of Fault Depth for a Large Ocean-Fault Separation Distance

Figures 3.23 and 3.24 show the in-phase and quadrature responses for the same models as those of Figs. 3.21 and 3.22 except that the ocean-fault separation distance has been increased to $S=100$ km. It is apparent that for this increased separation distance both for the shallow fault ($Z_b=5$ km in Fig. 3.23), and the very deep fault ($Z_b=75$ km in Fig. 3.24), the agreement between V_{ab} and V_a+V_b is excellent

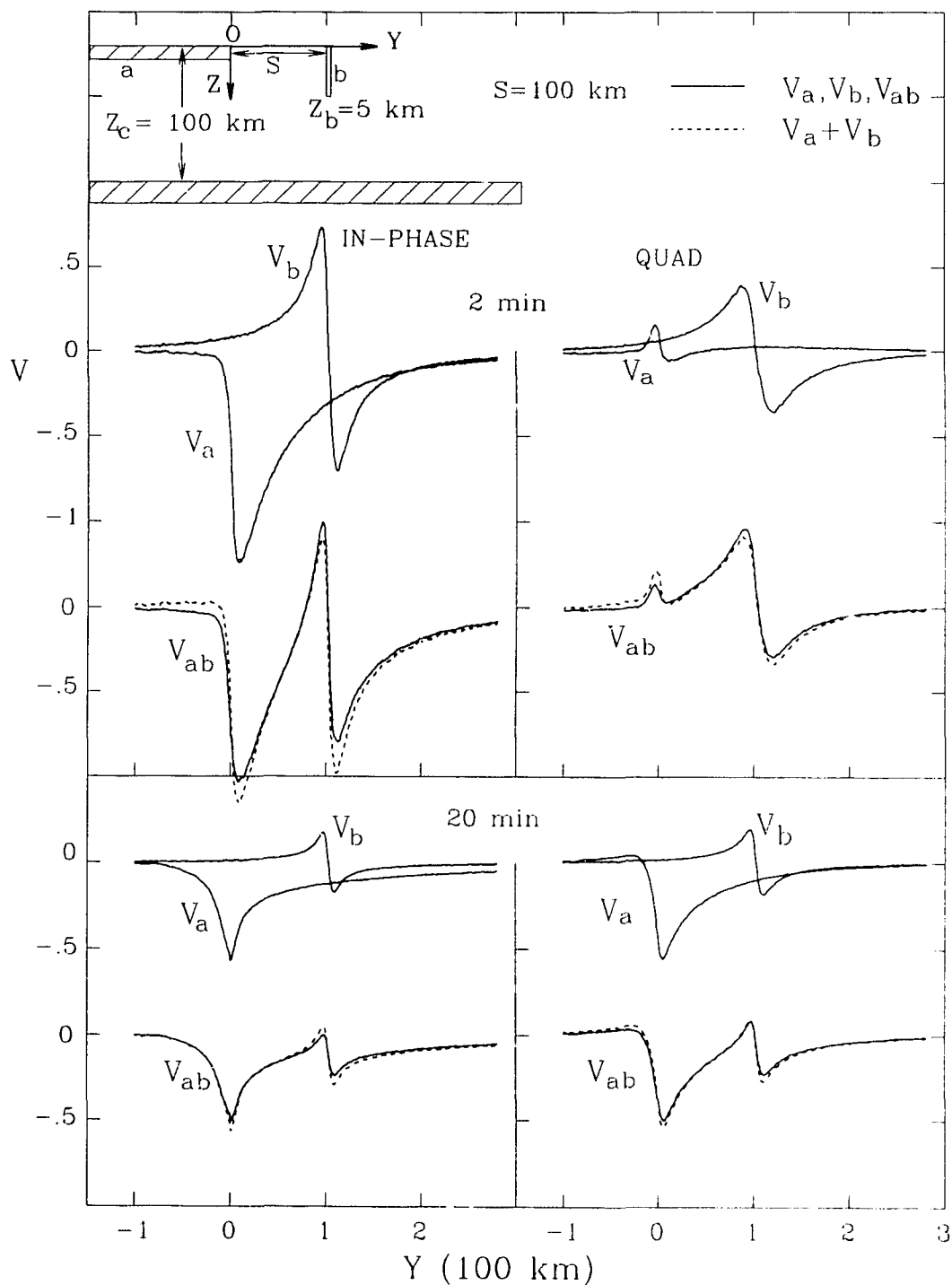


Figure 3.23: The in-phase and quadrature induction arrow responses V at 2 and 20 min for each of: the ocean (V_a); the fault (V_b); the ocean and the fault parallel to the coastline (V_{ab}); and the sum of the ocean and the fault responses ($V_a + V_b$) for the ocean-fault separation distance $S = 100$ km and the fault depth $Z_b = 5$ km.

at both short and long periods along the entire profile (except very near the conductive-resistive interfaces). As expected, this agreement for the larger ocean-fault separation distance of $S=100$ km is even better than that for the smaller separation of $S=50$ km (in Fig. 3.21), since the electromagnetic mutual coupling of the ocean and the fault is reduced with the increased separation distance.

Thus for an ocean-fault separation distance as small as $S=50$ km, the coupling between the ocean and the fault is seen to be sufficiently small, so that the sum of the response of the ocean and the response of the fault yields (within reasonable accuracy) that of the ocean and the fault. This indicates that in geomagnetic field studies of faults in coastal regions, the coast effects (if known) could be subtracted from the measurements to yield the responses of the fault alone, and thus simplify the interpretation of the measurements.

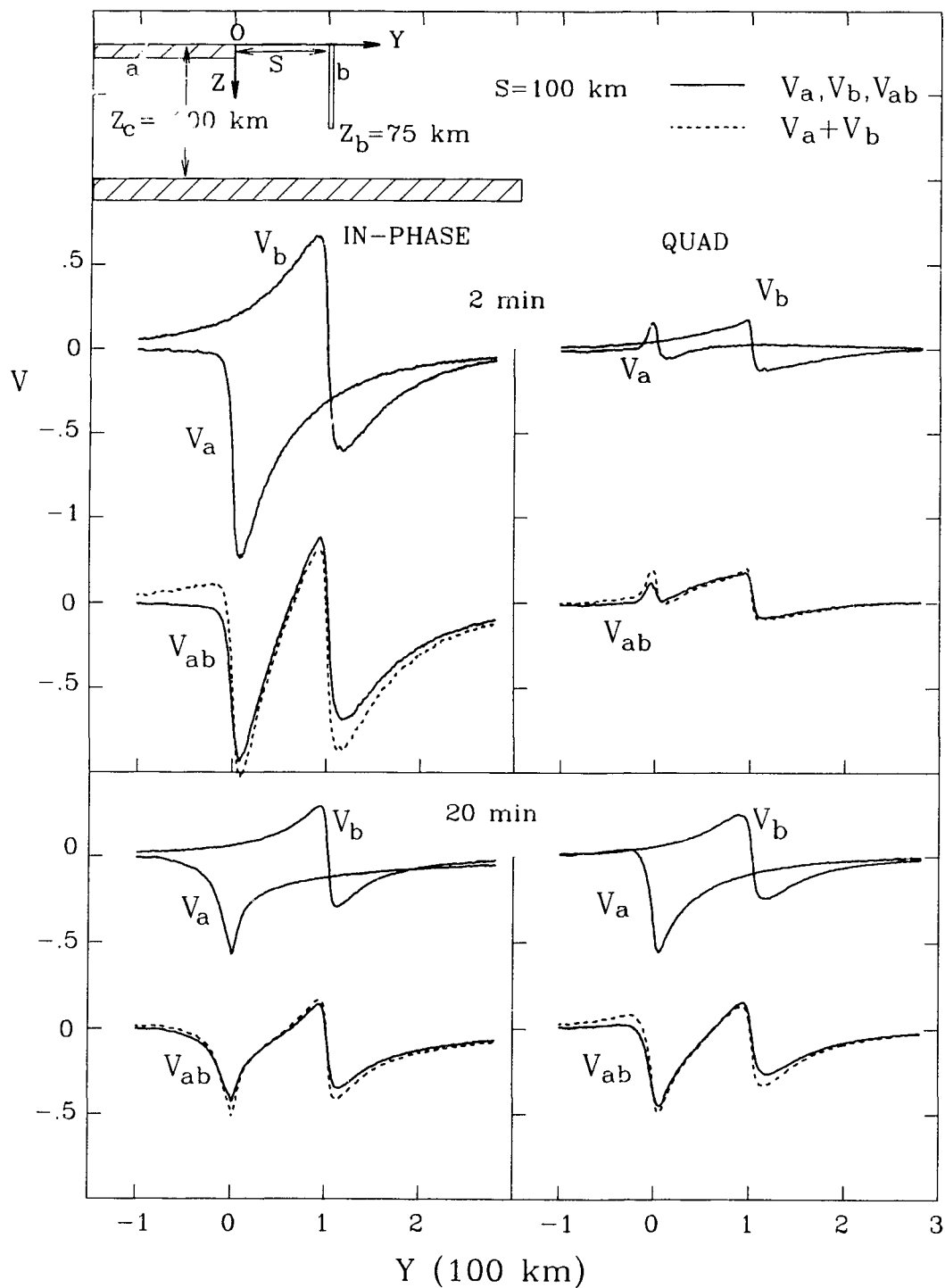


Figure 3.24: The in-phase and quadrature induction arrow responses V at 2 and 20 min for each of: the ocean (V_a); the fault (V_b); the ocean and the fault parallel to the coastline (V_{ab}); and the sum of the ocean and the fault responses (V_a+V_b) for the ocean-fault separation distance $S=100$ km and the fault depth $Z_b=75$ km.

3.5 Chapter Summary

In this chapter, analogue model measurements are used to study induction arrow responses for two basic models: i) a simple 5 km depth ocean for a range of conductive substratum depths; and ii) an elongated conductive fault parallel to the ocean coastline for a range of periods, fault depths, and ocean-fault separation distances. These results are then used to examine the removal of coast effect responses from those of a fault near an ocean coastline.

The Responses of a Constant Depth Ocean

The induction arrow in-phase and quadrature responses (as well as the amplitudes and phase angles) along a profile perpendicular to the ocean coastline are studied for a wide period range (1-90 min) for three conductive substratum depths ($Z_C=50, 100, 200$ km). These model responses depend strongly on the depth of the conductive substratum as well as on the period. The characteristic period T_C (the period at which the in-phase induction arrow response near the coastline is maximum, and the corresponding quadrature response at the same location is zero) for the model ocean underlain at depth by a conductive substratum, is seen to increase with increasing substratum depth. The corresponding quadrature response at the same location shows a maximum at a period roughly a factor of four larger than the period at which the in-phase response is maximum. The empirical relationship between the host skin depth δ (at the characteristic period T_C) and the depth (Z_C) of the conductive substratum, $\delta(T_C) \approx 1.3 Z_C$, could be used as an aid in determining the conductive substratum depth if the conductivity of the host were known.

The Responses of an Ocean and an on Shore Fault

The in-phase and quadrature induction arrow responses of an ocean and an elongated conductive fault parallel to the coastline are studied for a range of periods (1-90 min) and fault depths ($Z_b=5, 25, 50, 75$ km) for each of three ocean-fault separation distances ($S=50, 100, 200$ km). Due to the opposite signs of the ocean and fault responses at locations between the ocean and the fault, the resultant responses for both the in-phase and quadrature components are zero and reverse sign at periods T_0 that are seen to depend on the ocean-fault separation distance, the fault depth, and the distance from the ocean (location between the ocean and the fault). Empirical response curves for the in-phase and quadrature induction arrows are provided to show this dependence. A knowledge of the magnitudes and the signs of the induction arrow responses for a spectrum of periods (including those for $T < T_0$ and $T > T_0$), as well as a knowledge of the periods for maximum and zero responses along a profile for a catalogue of ocean-fault analogue models, should have application to the interpretation of induction arrow responses along a profile in coastal regions that included conductive faults.

Removal of the Coast Effect from the Responses of a Fault Near an Ocean

The possible removal of the geomagnetic coast effect from the response of an ocean and an on shore fault parallel to the coastline is studied by comparing the model induction arrow response of the ocean and an on shore fault with the sum of the ocean and the fault responses for a range of fault depths ($Z_b=5, 25, 50, 75$ km) and ocean-fault separation distances ($S=50, 100, 200$ km). It is demonstrated that a simple vector subtraction of the ocean responses from those of the ocean and the on shore fault does yield (within reasonable accuracy) the in-phase and quadra-

ture induction arrow responses of the fault alone. Thus in geomagnetic field studies in coastal regions that include faults parallel to the coastlines, the ocean coast effect could be removed from the field site measurements by a simple vectorial subtraction, and hence simplify the interpretation of the measurements.

Chapter IV
EM RESPONSES OF SINGLE AND MULTIPLE-FAULT
LABORATORY ANALOGUE MODELS

4.1 Introduction

The interpretation of geomagnetic field observations can be complicated in the vicinity of faults. Vertical thrust faults in some regions of the world have been suggested to penetrate the entire crust (e.g., Clowes et al., 1984, 1992; McCaig, 1988; McGeary, 1989). Some of these faults could be highly conductive because of the presence of water or solution in a large zone of high porosity. EM induction in elongated conductors, a topic of major interest in geophysics, has seen some study in numerical models (e.g., Rankin, 1962; Chouteau, 1985; Schnegg et al., 1986), as well as in some geomagnetic field studies (e.g., Schnegg et al., 1983; Rooney and Hutton, 1987; Arora and Adam, 1992; Jones et al., 1992; Hjelt and Korja, 1993).

In this chapter, analogue model measurements are used to examine the induction responses of a single and a pair of elongated conductive faults for a range of fault depths. The results of this study of the induction response behaviour of faults should have general application to the interpretation of field measurements in regions that include single and multiple conductive faults, as are common in many regions of New Zealand.

4.2 The Responses of a Single Fault

Figure 4.1 shows the schematic cross-section of a model fault (a) 5 km wide, 5 km deep, and 500 km long in a resistive host earth, underlain by a conductive substratum (c) at depth $Z_c=100$ km. Analogue model magnetic field components were measured for the case of X-polarization (the inducing magnetic field in the Y direction) for periods of 1-90 min for fault depths $Z_a=5, 25, 50, 75$ km. These field components were used to calculate in-phase and quadrature induction arrow responses along a profile perpendicular to the fault strike.

Figure 4.2, showing the in-phase and quadrature induction arrow responses V along a traverse perpendicular to the fault for periods of 2 and 20 min, is provided to introduce the labels V_m and W , the response maximum and the curve width at half maximum for each component. The in-phase and quadrature responses along the profile are seen to be positive to the left of the fault and negative to the right of the fault, indicating that the arrows at either side of the fault point towards the conductive fault as expected. The responses for both components, reversing sign directly over the mid-point of the fault, clearly depend on period. For example, the in-phase maximum (V_m) is roughly a factor of 3 smaller at 20 min than at 2 min, and the quadrature maximum (also labelled as V_m) is roughly a factor of 2 smaller at 20 min than at 2 min. Further, at 20 min the in-phase V_m and the quadrature V_m are essentially equal, while at 2 min, the in-phase V_m is a factor of approximately 1.5 larger than the quadrature V_m . Near the fault the spatial gradient of the in-phase response is greater at 20 min than at 2 min. For example, at 2 min the response has been attenuated to 20% of its maximum value V_m at a distance of 65 km from the fault, while for the same attenuation at 20 min the dis-

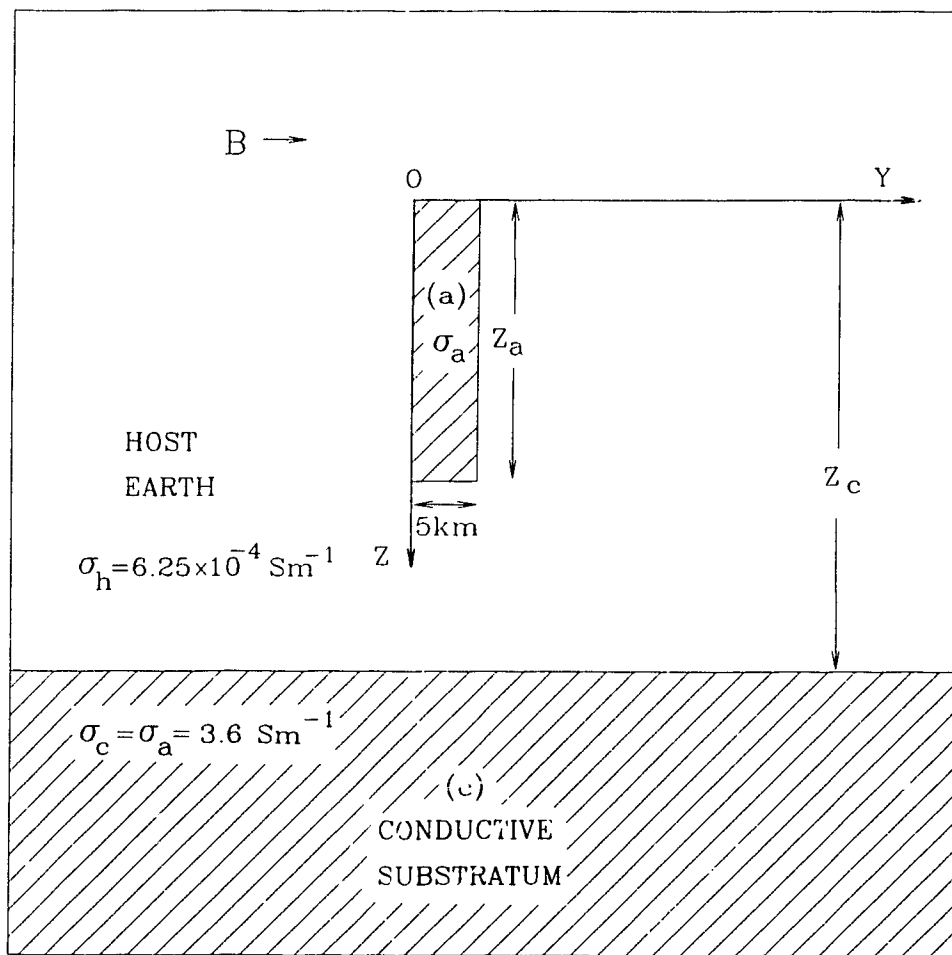


Figure 4.1: The cross-section of the model of a conductive fault (a) in a resistive host earth underlain by a conductive substratum (c).

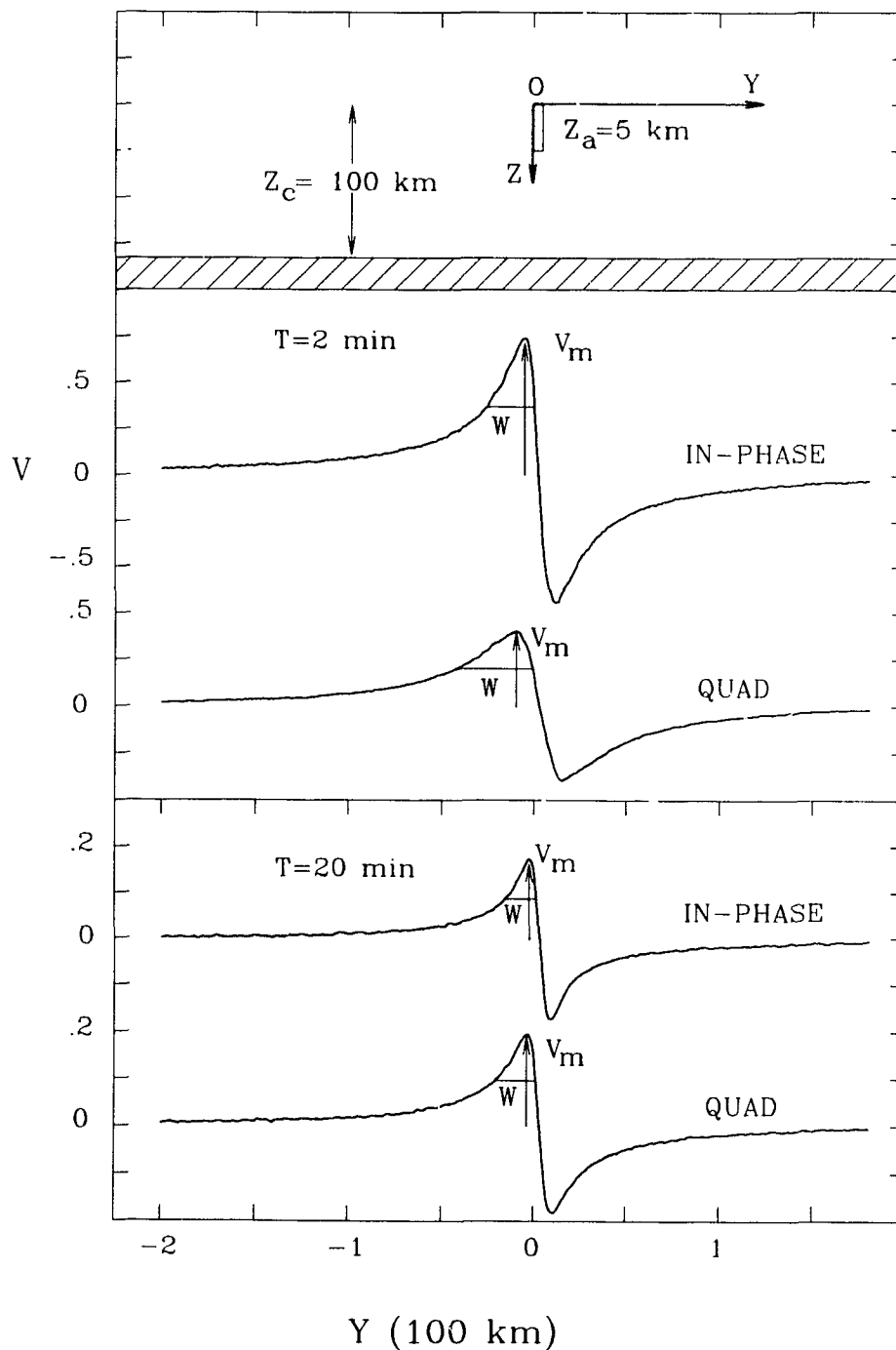


Figure 4.2: The in-phase and quadrature induction arrow responses V along a traverse perpendicular to the fault for periods of 2 and 20 min for a 5 km depth fault underlain by a conductive substratum. W is the width of the response curve at half maximum.

tance is roughly 40 km. For the quadrature component, the spatial gradient of the response is also greater at 20 min than at 2 min, with distances for attenuation to 20% of the maximum values being 55 km and 87 km respectively. Thus, for both the in-phase and quadrature responses the spatial gradients are greater at long periods than at short periods, and the spatial gradient of the in-phase response is greater than that of the quadrature response.

Another parameter of interest in the response curves in Fig. 4.2 is the width W of the curve at half maximum (or half height). As examples, the widths W of the fault response curves for the in-phase components are roughly 22 and 16 km at 2 and 20 min respectively, while for the quadrature components these widths W are approximately 42 and 20 km at 2 and 20 min respectively. Thus at 2 min W for the quadrature component is roughly a factor of two larger than for the in-phase component, while at 20 min W is roughly the same for both components. Further, for each component W is smaller at 20 min than at 2 min. The period dependence of W will be shown in detail in a later figure (Fig. 4.7).

To show the dependence on period in some detail the in-phase and quadrature induction arrow responses along the profile for a range of periods (1-90 min) for the fault ($Z_a=5$ km) are shown in Fig. 4.3. The in-phase response V_m for the fault (defined in Fig. 4.2) decreases with increasing period, while the quadrature V_m first increases with increasing period, reaching a maximum at roughly 3 min, then decreases with a further increase in period. At short periods ($T < 5$ min) the in-phase response is greater than the quadrature response, while for periods $T > 10$ min the quadrature response is greater than the in-phase response. At a very long period of 90 min the in-phase response becomes negligible while the quadrature response is still measurable near the fault.

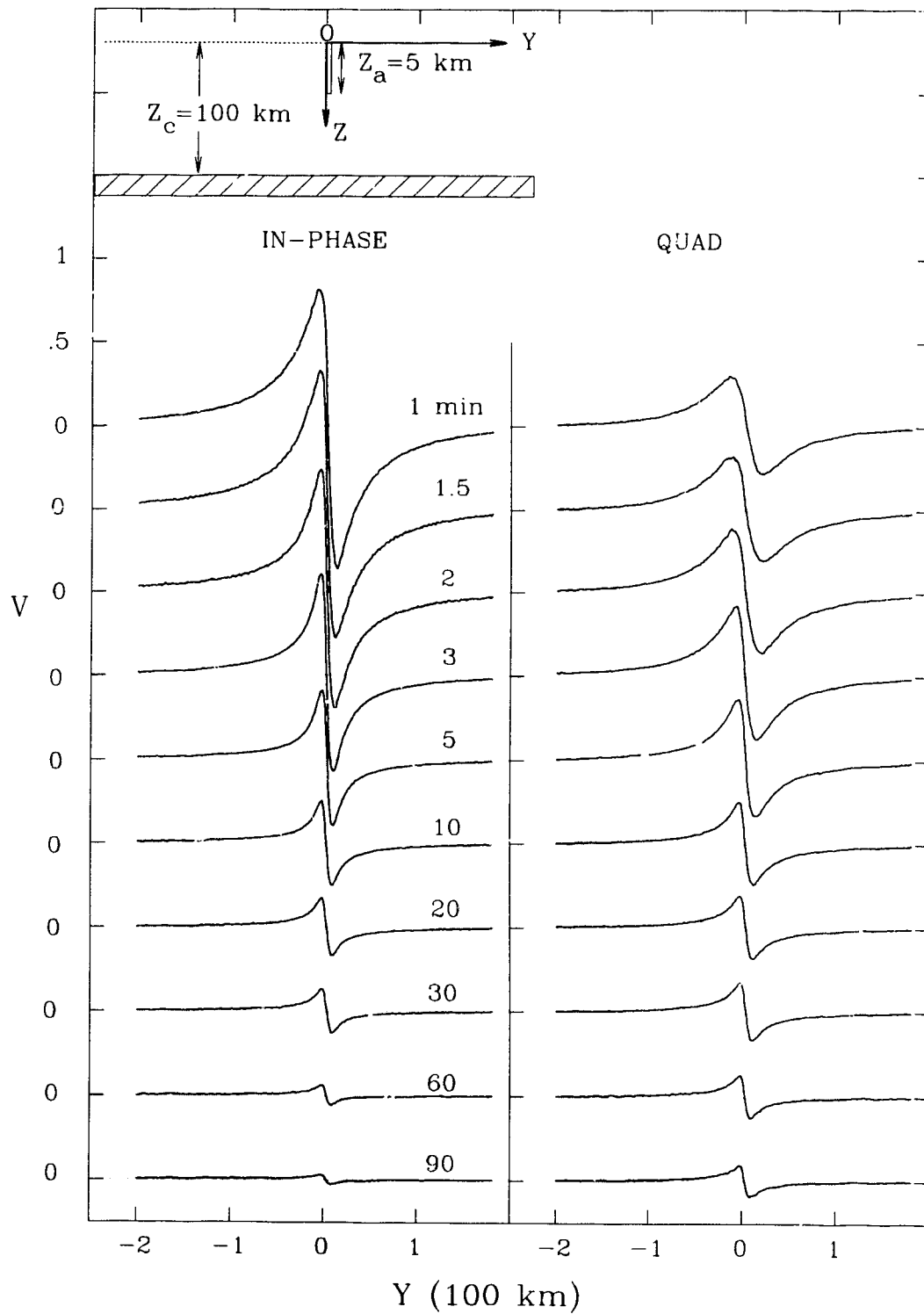


Figure 4.3: The in-phase and quadrature induction arrow responses V along a traverse perpendicular to the fault for periods of 1–90 min for a 5 km depth conductive fault underlain by a conductive substratum.

To demonstrate the effect of increasing the fault depth Z_a , Fig. 4.4 provides the induction arrow responses for a fault of $Z_a=50$ km depth. (Model measurements for fault depths $Z_a=25, 75$ km were also carried out, and the results are provided in Appendix B). It is seen that the response curves are broader for this deep fault than those for the shallow fault ($Z_a=5$ km in Fig. 4.3). This indicates that the induction arrow response is more localized for a shallow fault than for a deep fault, as expected. The in-phase response V_m for the deep fault also decreases with an increase in period. The quadrature response V_m is maximum at roughly 10 min, compared with the 3 min period for the case of $Z_a=5$ km (Fig. 4.3). It is interesting to note that at short periods (1-3 min) the in-phase V_m and quadrature V_m are each smaller for this deep fault $Z_a=50$ km than the corresponding ones for the shallow fault $Z_a=5$ km (Fig. 4.3).

Figure 4.5 shows in detail empirical plots of the in-phase and quadrature responses V_m (introduced in Fig. 4.2) as a function of period for the fault depths $Z_a=5, 25, 50, 75$ km. The response curves for both the in-phase and quadrature components show a strong dependence on period, and a somewhat complex dependence on the fault depth Z_a . For the in-phase component V_m decreases sharply with increasing period for each fault depth, and the V_m curves for four fault depths intersect at roughly 3 min period. For periods $T \lesssim 3$ min the in-phase V_m is the largest for the shallowest fault, and V_m decreases with an increase in fault depth. For example, at 2 min for the shallow fault ($Z_a=5$ km) the in-phase V_m is roughly 0.75 and for the deep fault ($Z_a=75$ km) is decreased to approximately 0.65. For periods $T > 3$ min, however, the opposite is generally the case with the largest in-phase V_m observed for the deepest fault. The period of roughly 3 min where

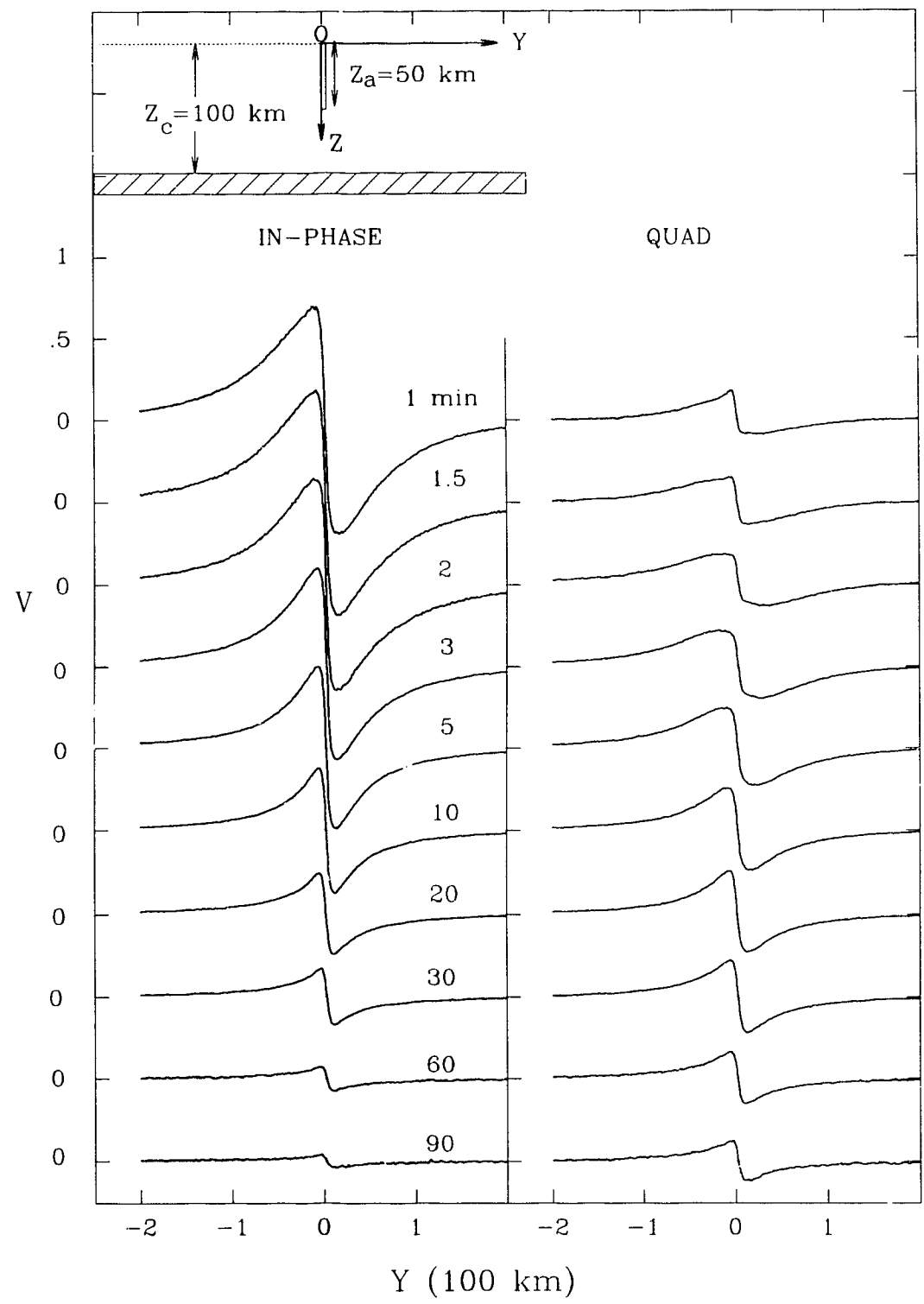


Figure 4.4: The in-phase and quadrature induction arrow responses V along a traverse perpendicular to the fault for periods of 1–90 min for a 50 km depth conductive fault underlain by a conductive substratum.

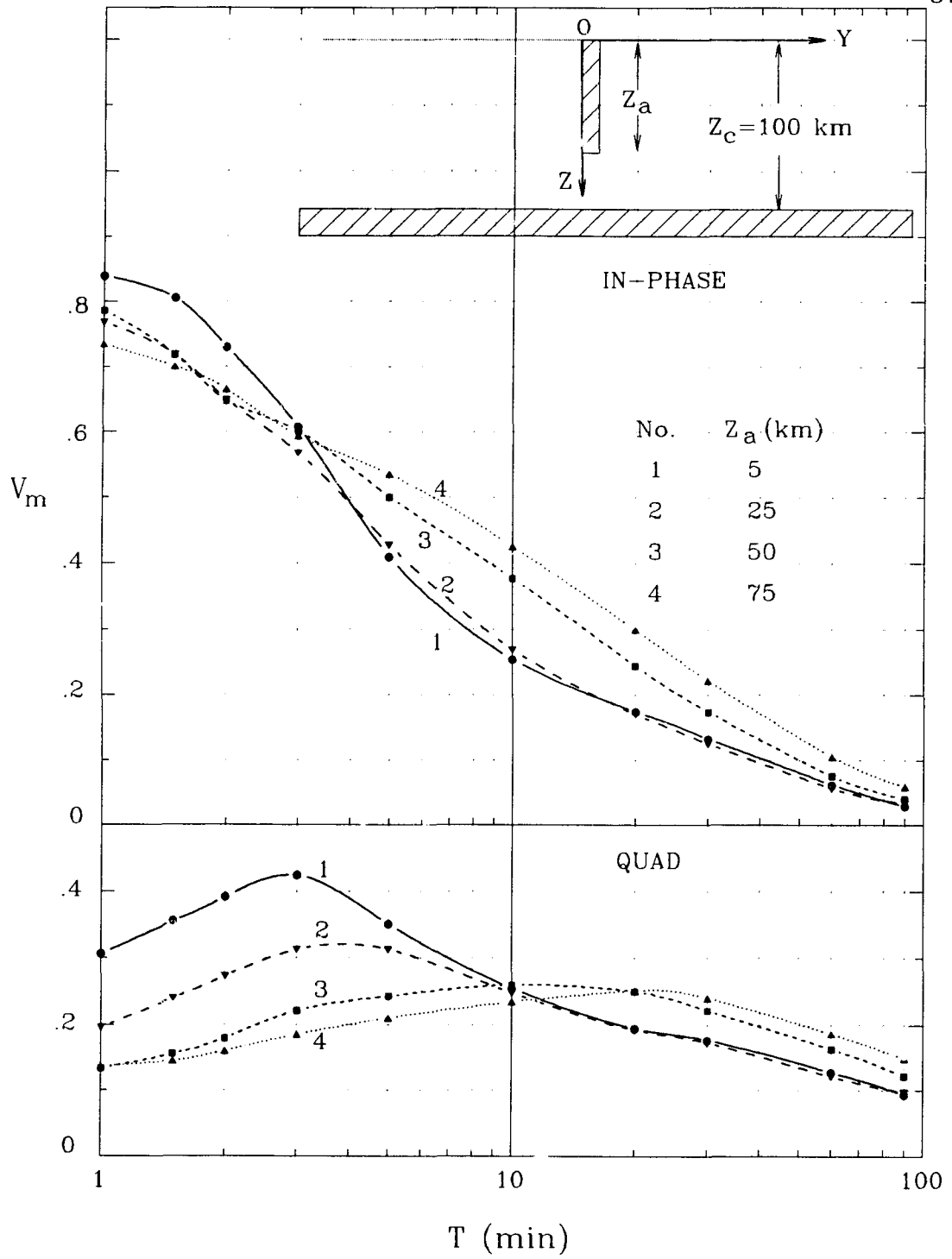


Figure 4.5: Empirical plots of the in-phase and quadrature maximum responses V_m as a function of period for the fault depths $Z_a=5, 25, 50, 75$ km underlain by a conductive substratum.

the in-phase response curves intersect, is the period at which the quadrature responses show the strongest dependence on fault depth. Similar to the behaviour of the in-phase component, V_m for the quadrature component is also seen to be the largest for the shallowest fault at short periods, with the opposite being the case at long periods. This cross-over in the behaviour at long periods opposite to that at short periods, occurs in the neighborhood of 10 min where the four quadrature response curves roughly intersect. This 10 min period is a factor of 3-4 greater than the period at which the in-phase curves intersect. Further, the in-phase component shows its strongest dependence on fault depth Z_a at this 10 min period, the period at which the quadrature component shows negligible dependence on fault depth. Varying the fault depth affects the in-phase V_m most in the intermediate period range ($T=5-30$ min), and affects the quadrature V_m most at short periods ($T=1-5$ min). Differing from the in-phase response V_m which decreases with increasing period, the quadrature response V_m shows a broad maximum at a period which increases with an increase in the fault depth. For example, V_m for the quadrature response shows maximum values at roughly 2.5 and 25 min for fault depths $Z_a=5$ km and 75 km respectively.

Analogue model measurements were also carried out for an increased substratum depth ($Z_c=200$ km) to examine the effect of varying the substratum depth. Figure 4.6 shows an empirical plot of the period at which the quadrature V_m is maximum as a function of the fault depth Z_a for the substratum depths $Z_c=100$ and 200 km. It is seen that for a given Z_c the quadrature V_m is maximum at increasing periods for increasing fault depth. Except for very large fault depths, the curve is shifted towards longer periods for the increased Z_c . This feature has

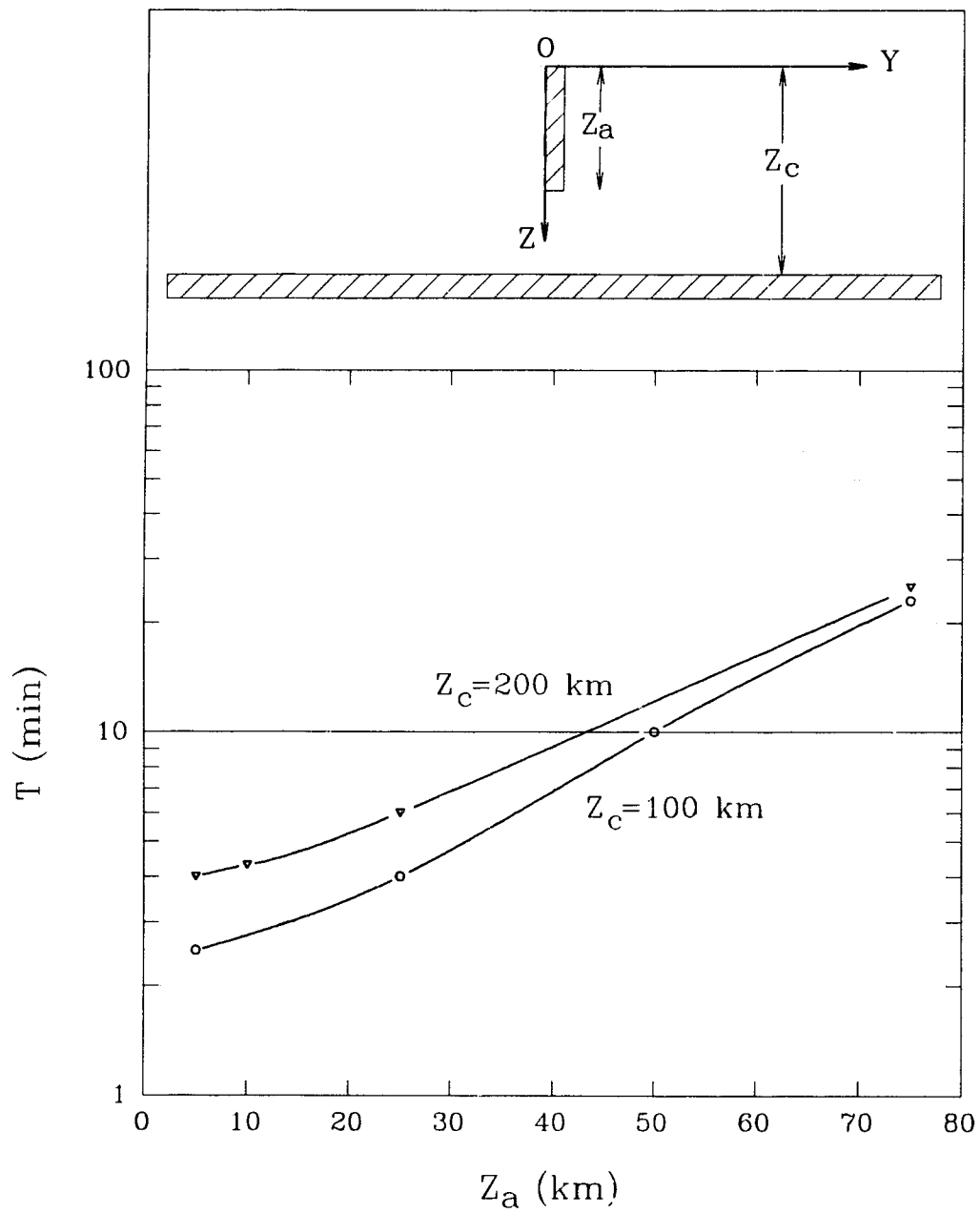


Figure 4.6: The period T at which the quadrature V_{II} is maximum as a function of the fault depth Z_a for the conductive substratum depths $Z_c=100$ and 200 km.

application in determining the depth of the fault if the depth of the underlying conductive substratum (asthenosphere) is known. For example, a maximum quadrature V_m observed at $T \approx 4$ min at a site near a fault would suggest a fault depth of approximately 25 km, if Z_c was known as 100 km.

Figure 4.7 shows empirical plots of the width W of the fault response curves at half maximum (introduced in Fig. 4.2) as a function of period for the fault depths $Z_a = 5, 25, 50$ km. It is seen that for the in-phase component this width W decreases smoothly with increasing period for each fault depth. For the quadrature component, however, W is maximum at a period which increases with increasing fault depth, but for $T > 3$ min decreases with increasing period for each fault depth, similar to that observed over the entire period for the in-phase component. For both the in-phase and quadrature components the widths W increase with an increase in the fault depth, indicating that the response curves are broader for a deep fault than those for a shallow fault. The curves for a range of fault depths ($Z_a = 5, 25, 50$ km) in Fig. 4.7 show that a knowledge of the width of the fault response curves at half maximum could lead to useful information on the fault depth. For example, if the width W for the in-phase response observed along a profile over a fault were roughly 40 km at a short period $T = 1$ min, 20 km at $T = 5$ min, and roughly 15 km for $T > 10$ min, a shallow fault of depth 5 km would be indicated (see curve 1 in Fig. 4.7). Further support for this interpretation would be provided, if the quadrature component measurements yielded $W \approx 30$ km at 5 min, and the W values were generally somewhat larger for the quadrature component than for the in-phase component.

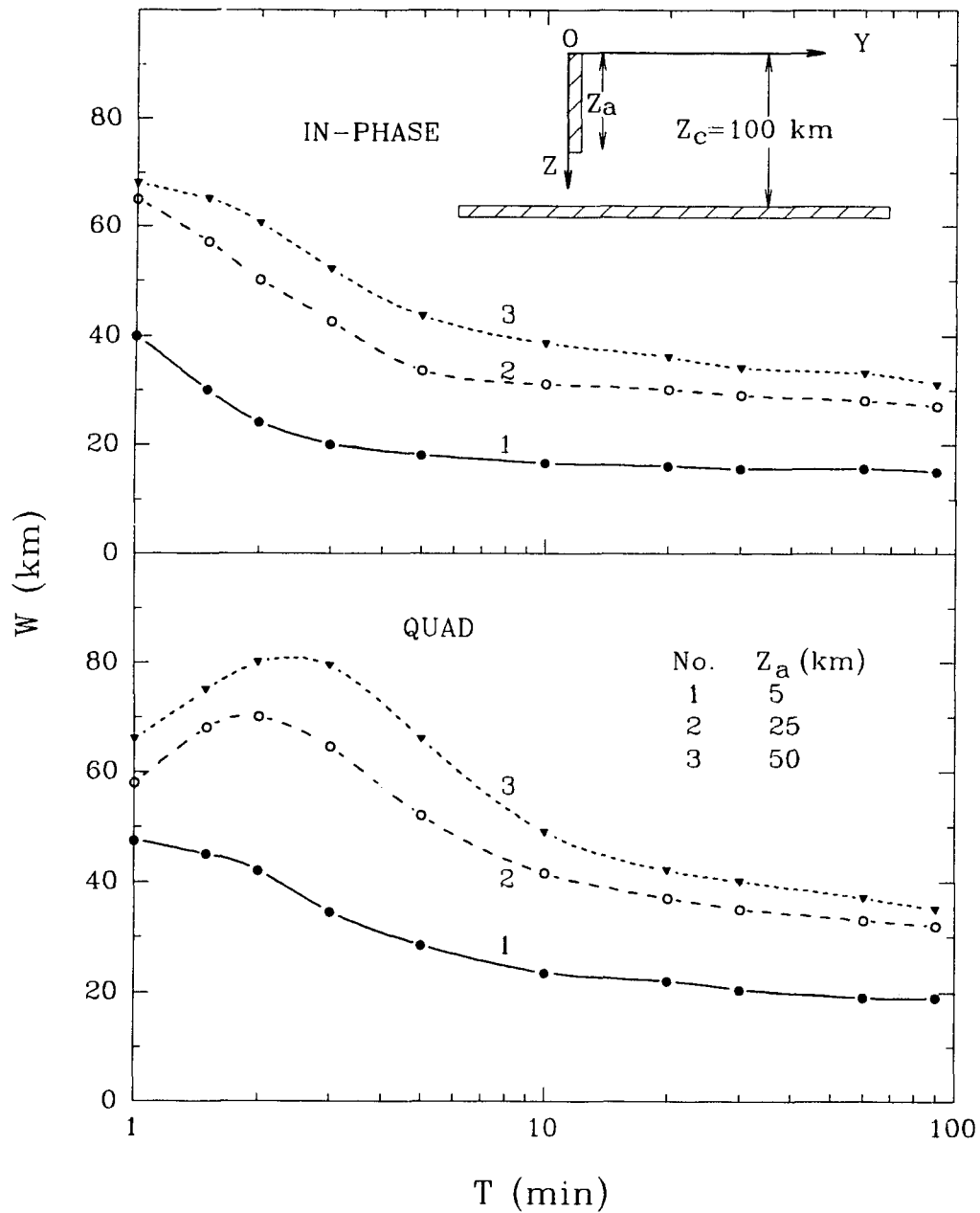


Figure 4.7: The width W of the fault response curves at half maximum (as shown in Fig. 4.2) as a function of period for the fault depths $Z_a=5, 25, 50$ km.

The results for the single fault discussed in this section show that both the in-phase and quadrature induction arrows at either side of a fault point towards the fault at all periods, with the maximum responses observed at either edge of the fault. Further, the behaviour of the maximum responses V_m as a function of period for various fault depths, the cross-over in the behaviour of the V_m curves, with the shallow fault at short periods showing the larger V_m , and at long periods showing the smaller V_m , the quadrature V_m period dependence on the fault depth, as well as the width of the response curve at half maximum should aid the depth determination of a fault in a geomagnetic field study.

4.3 The Responses of a Pair of Parallel Faults

Figure 4.8 shows the schematic cross-section of a pair of parallel major (a) and minor (b) faults separated by a distance S in a resistive host earth, all underlain by a conductive substratum. The depth of the major fault is fixed to be $Z_a = 75$ km, while the depth of the minor fault takes the values of $Z_b = 5, 25, 50$ km. Model measurements were again carried out along a traverse perpendicular to the parallel faults for a range of periods (1-90 min), minor fault depths ($Z_b = 5, 25, 50$ km), and separation distances ($S = 50, 100, 200$ km). The responses in the region between the parallel faults are of major interest in the present section.

Figure 4.9 shows the induction arrow in-phase and quadrature responses V along the traverse for periods of 2 and 20 min for the case of $Z_b = 5$ km and $S = 100$ km. Both the in-phase and quadrature responses to the left of the major fault are positive (arrows pointing towards the major fault), and to the right of the minor fault are negative (arrows pointing towards the minor fault), similar to those of a

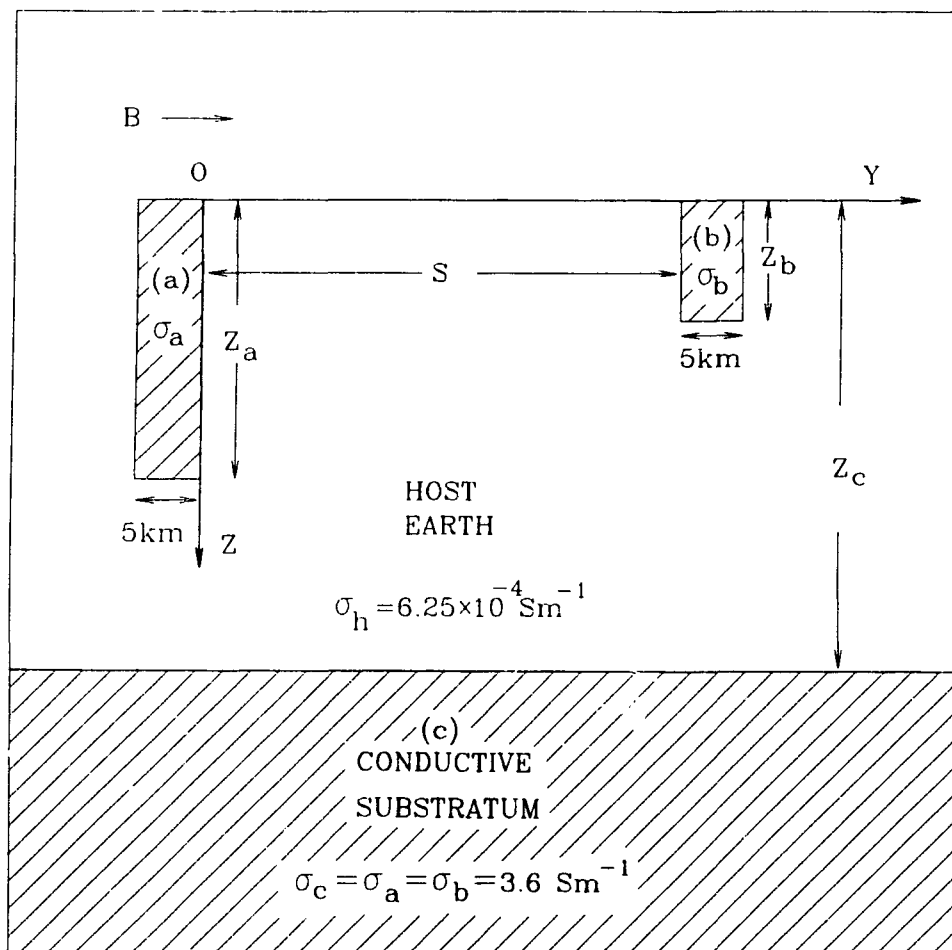


Figure 4.8: The cross-section of the model of parallel major (a) and minor (b) conductive faults in a resistive host earth, all underlain by a conductive substratum (c).

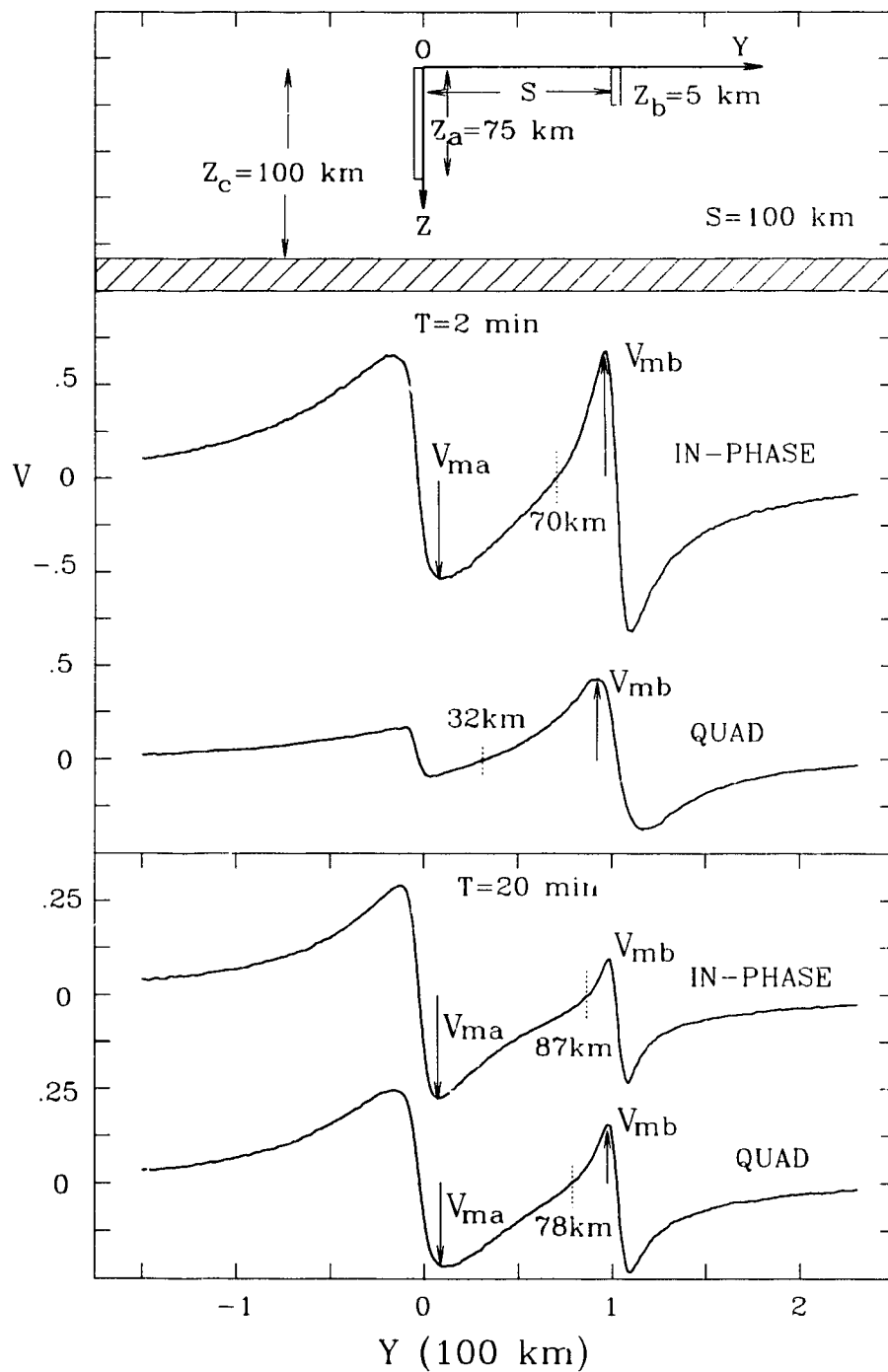


Figure 4.9: The in-phase and quadrature induction arrow responses V along a traverse perpendicular to the faults for periods of 2 and 20 min.

single fault discussed in detail in the previous section (Figs. 4.3 and 4.4). In this figure the response maximum just to the right of the major fault is labelled as V_{ma} and the response maximum just to the left of the minor fault is labelled as V_{mb} . From the model results for a single fault in the previous section, it is expected that in the region between the faults the responses of the two faults should be of opposite sign, and thus the induction arrows along a profile would be expected to decrease to zero and reverse direction at periods (T_0) that would depend on the locations and the geometries of the faults. For example, at 2 min the in-phase response along the traverse is zero at $Y \approx 70$ km and reverses sign, while at 20 min it reverses sign at $Y \approx 87$ km. To the left of these sites the in-phase arrows point towards the major fault, while to the right they point towards the minor fault. The 2 and 20 min periods are thus the zero response periods (T_0) for the sites at $Y = 70$ and 87 km respectively. For the in-phase responses, at 2 min V_{ma} is smaller than V_{mb} , while at 20 min V_{ma} is at least a factor of 2 greater than V_{mb} . The spatial gradient of the in-phase response curve near the minor fault is greater than that near the major fault at 2 min, resulting in the zero in-phase response at a location nearer to the minor fault than to the major fault. At 20 min the major fault shows the dominant (negative) response, leading to the zero in-phase response at a site ($Y \approx 87$ km) very near the minor fault. However, at 2 min the minor fault shows the dominant response, resulting in the zero quadrature response at a site ($Y \approx 32$ km) near the major fault. At the longer period of 20 min, however, the major fault shows the greater (negative) quadrature response, and thus at this period results in the zero quadrature response at a site ($Y \approx 78$ km) again near the minor fault, as is also the case for the in-phase component.

To show the dependence on period in some detail the in-phase and quadrature induction arrow responses along the profile for a range of periods (1-90 min) for the case of $S=100$ km and $Z_b=5$ km are shown in Fig. 4.10. Both the in-phase V_{ma} and V_{mb} (introduced in Fig. 4.9) are seen to decrease smoothly with increasing period. For the in-phase component, V_{mb} at very short periods ($T \leq 2$ min) is slightly larger than V_{ma} , while for periods $T > 2$ min the opposite is the case, with V_{mb} decreased to negligible values at long periods. The quadrature response curves show maximum V_{ma} and V_{mb} values at approximately 25 and 2.5 min respectively. At short periods $T \leq 10$ min the minor fault shows the larger quadrature response, while at longer periods $T > 10$ min the major fault shows the larger response (as discussed for Fig. 4.9). Both the in-phase and the quadrature response curves show zero responses at locations Y (distance from the major fault) that shift towards the minor fault with increasing period. For a pair of identical faults, zero responses at all periods would be expected at the site mid-way ($S/2$) between the faults, with the responses for $Y < S/2$ of sign opposite to those for $Y > S/2$. For the periods studied here, the zero in-phase responses along the traverse are confined to distances $Y > S/2$ from the major fault, while the zero quadrature responses are confined to distances $Y < S/2$ for $T < 5$ min, and to $Y > S/2$ for periods $T > 5$ min. At longer periods ($T > 20$ min) both the in-phase and quadrature responses are generally negative at all sites (arrows pointing towards the major fault) except for locations very near the minor fault, indicating again that the major fault dominates the induction arrow response in this region. This characteristic of the zero response period (T_0) increasing with decreasing distance from the minor fault, could have application to delineating the location of a minor fault parallel to a nearby major fault in a geomagnetic field study.

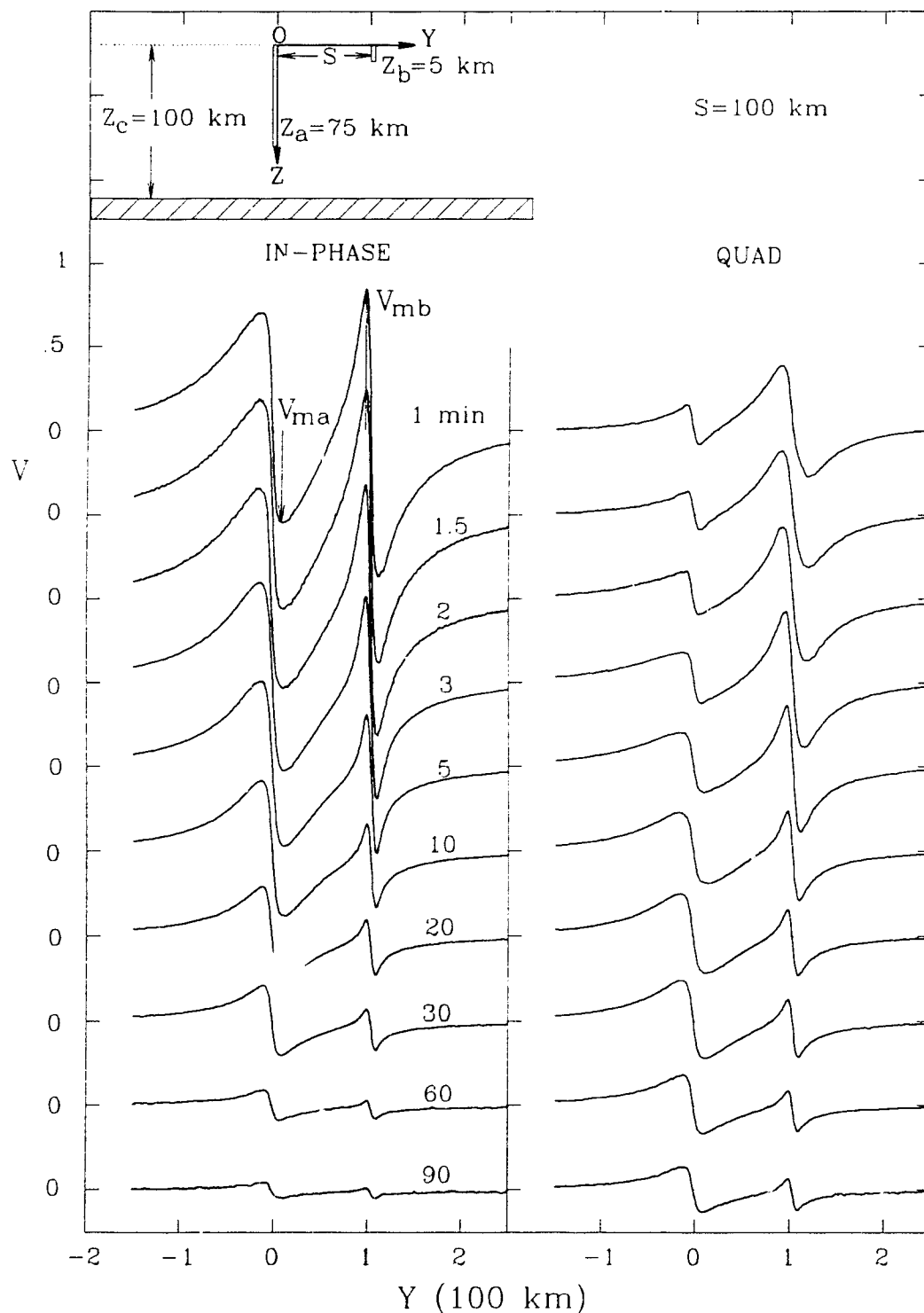


Figure 4.10: The in-phase and quadrature induction arrow responses V along a traverse perpendicular to the faults for periods of 1–90 min for a pair of parallel major and minor faults separated by a distance S .

Figure 4.11 presents in detail the response maximums V_{ma} and V_{mb} for the in-phase component as a function of period for the minor fault depths $Z_b=5, 25, 50$ km (the major fault depth is fixed to be 75 km) for separation distances $S=50, 100, 200$ km. In general, both V_{ma} and V_{mb} decrease with increasing period for all fault depths and for each separation distance. For a given S the V_{mb} curves for three minor fault depths intersect at roughly $T=2-3$ min, so that for $T < 2$ min the largest V_{mb} response is observed for the shallowest fault, and the magnitude of V_{mb} decreases with increasing Z_b , while for periods $T > 2$ min the opposite is observed with the largest V_{mb} observed for the deepest fault. The V_{ma} curves do not show such a cross-over, but V_{ma} does decrease with an increase in Z_b , due to the increasing positive response of the minor fault, a response which is of sign opposite to that of the major fault in the region between the faults. The V_{ma} response curves show that the effect of increasing the minor fault depth, though small, is the largest for the $S=50$ km case, and is negligible at the largest separation distance of $S=200$ km, as expected. At a fixed period for a given fault depth, the increase in both V_{ma} and V_{mb} for an increased separation distance S can be contributed to the decreased mutual electromagnetic coupling between the faults, since the responses for the two faults are of opposite sign in the region between the faults, leading to a cancellation of fields.

Figure 4.12 shows the response maximums V_{ma} and V_{mb} as a function of period for the quadrature component (as for the in-phase component in Fig. 4.11, except that the scale differs by a factor of two). The change in the minor fault depth is seen to have even a smaller effect on the quadrature V_{ma} curves than was observed for the in-phase component (Fig. 4.11). In fact, except for the

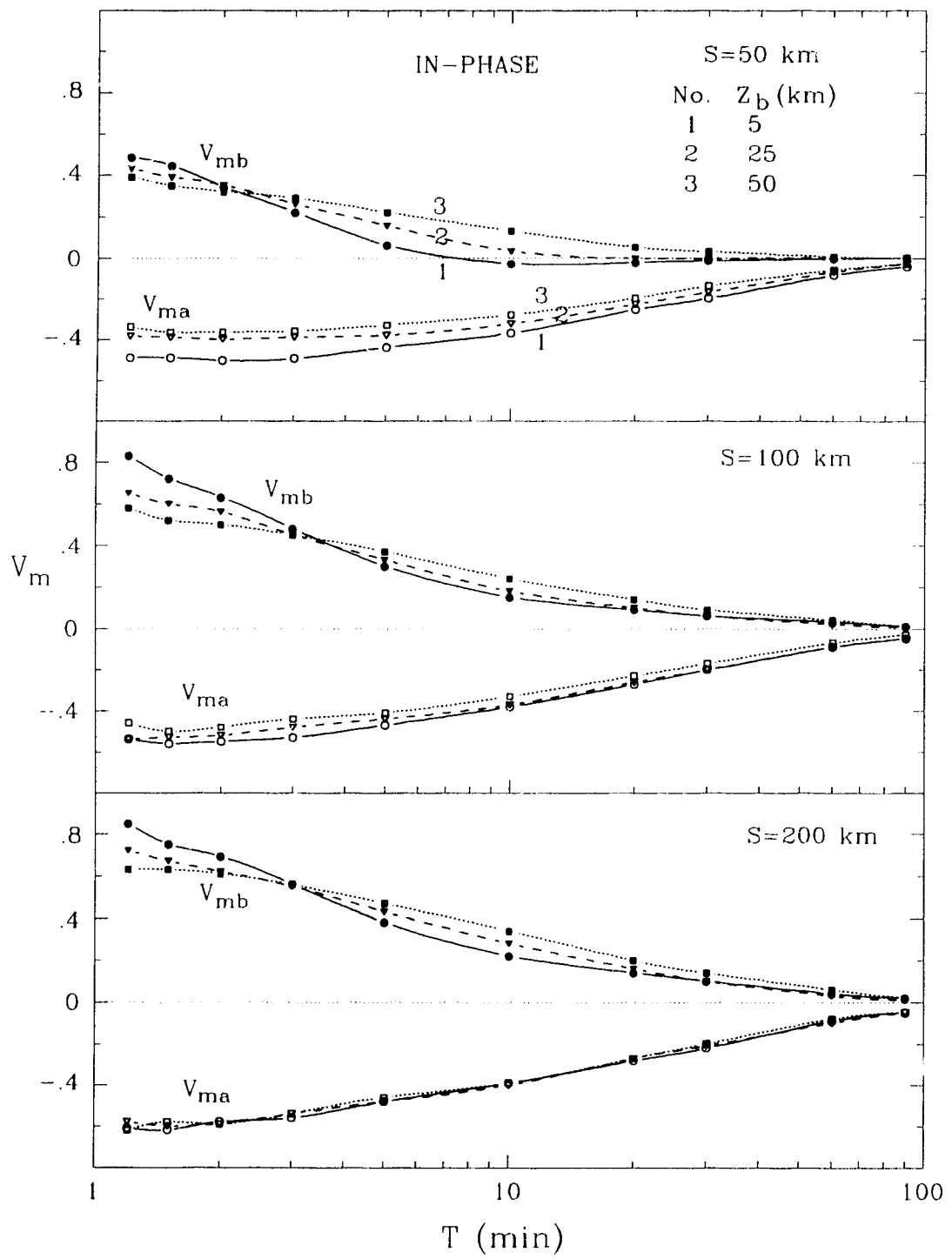


Figure 4.11: Empirical plots of the in-phase response V_{ma} and V_{mb} as a function of period for the major fault depth $Z_a=75$ km and the minor fault depths $Z_b=5, 25, 50$ km for $S=50, 100, 200$ km.

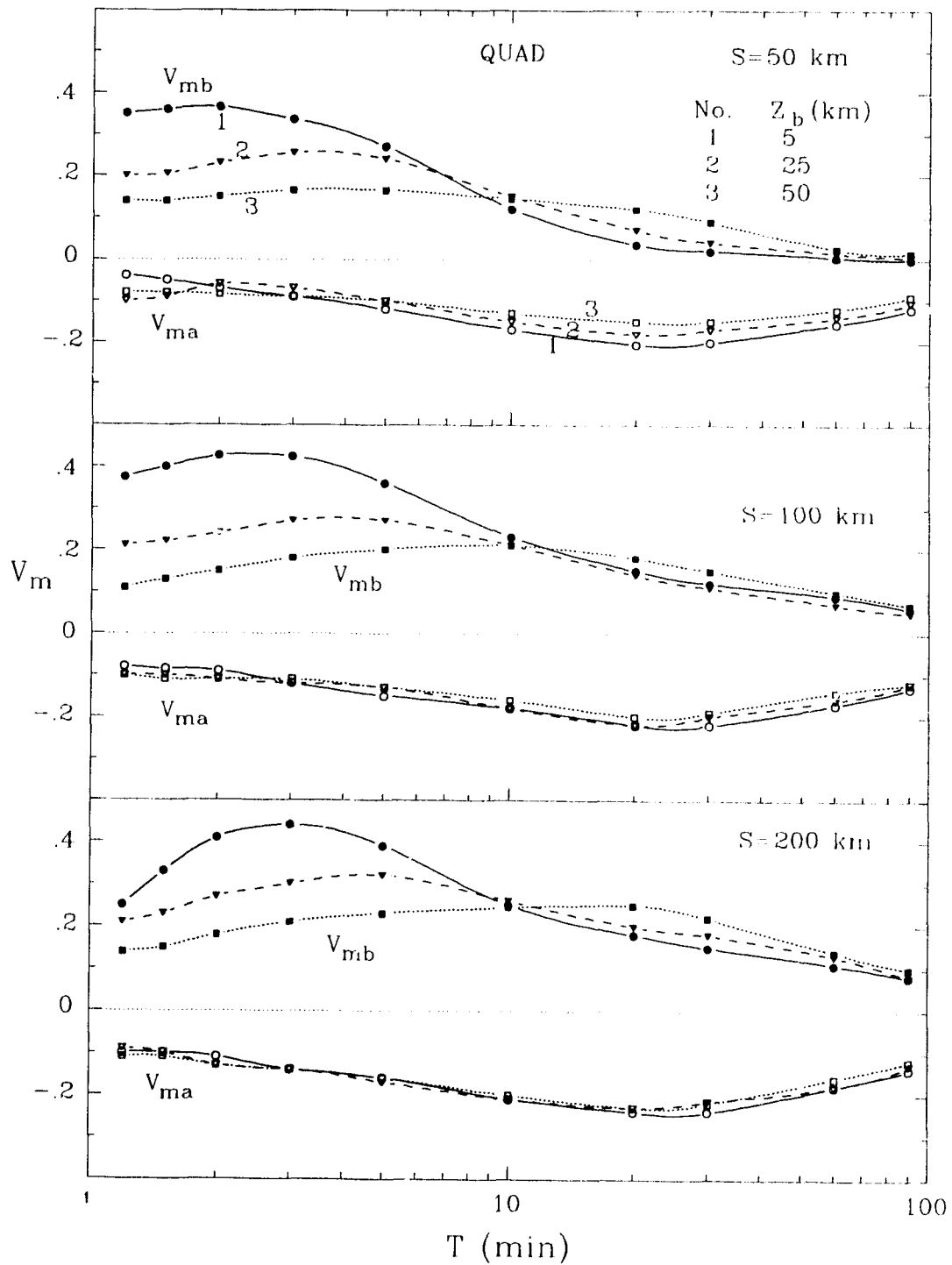


Figure 4.12: Empirical plots of the quadrature response V_{ma} and V_{mb} as a function of period for the major fault depth $Z_a=75$ km and the minor fault depths $Z_b=5, 25, 50$ km for $S=50, 100, 200$ km.

smallest separation distance ($S=50$ km), the quadrature V_{ma} appears to be insensitive to the change of the minor fault depth. Similar to the results for the in-phase component, the quadrature V_{mb} is the largest for the shallowest fault ($Z_b=5$ km) at short periods ($T<10$ min) for all separation distances, with the opposite being the case at periods $T>10$ min. A major difference is that this cross-over from the behaviour at short periods to the opposite behaviour at long periods occurs at roughly 10 min, a period roughly a factor 3-4 greater than that for the in-phase component (Fig. 3.10). This cross-over behaviour for both the in-phase and quadrature V_{mb} is consistent with the observation for a single fault in the previous section (Fig. 4.5). The roughly 25 min period of the broad quadrature V_{ma} maximum for all Z_b and S is characteristic of the major fault ($Z_a=75$ km underlain by a conductive substratum at $Z_c=100$ km), agreeing with the period for the quadrature maximum shown in Fig. 4.5 for a single fault. The quadrature V_{mb} curves each show a broad maximum at a period which increases with increasing Z_b and S . As examples, for the separation distances $S=50, 100, 200$ km the periods for maximum V_{mb} response for $Z_b=5$ km are approximately 1.5, 2.5 and 3 min respectively, and for $S=200$ km the periods for fault depths $Z_b=5, 25, 50$ km are approximately 3, 5, and 20 min respectively.

Figure 4.13 shows an empirical plot of the period at which the quadrature V_{mb} is maximum (from Fig. 4.12) as a function of fault depth Z_b for three separation distances. It is seen that for each major-minor fault separation distance S , this period increases with increasing fault depth Z_b , and with increasing S the curve is shifted to longer periods. The curves in Fig. 4.13 show that in principle, a knowledge of the quadrature V_{mb} period dependence could provide information on the

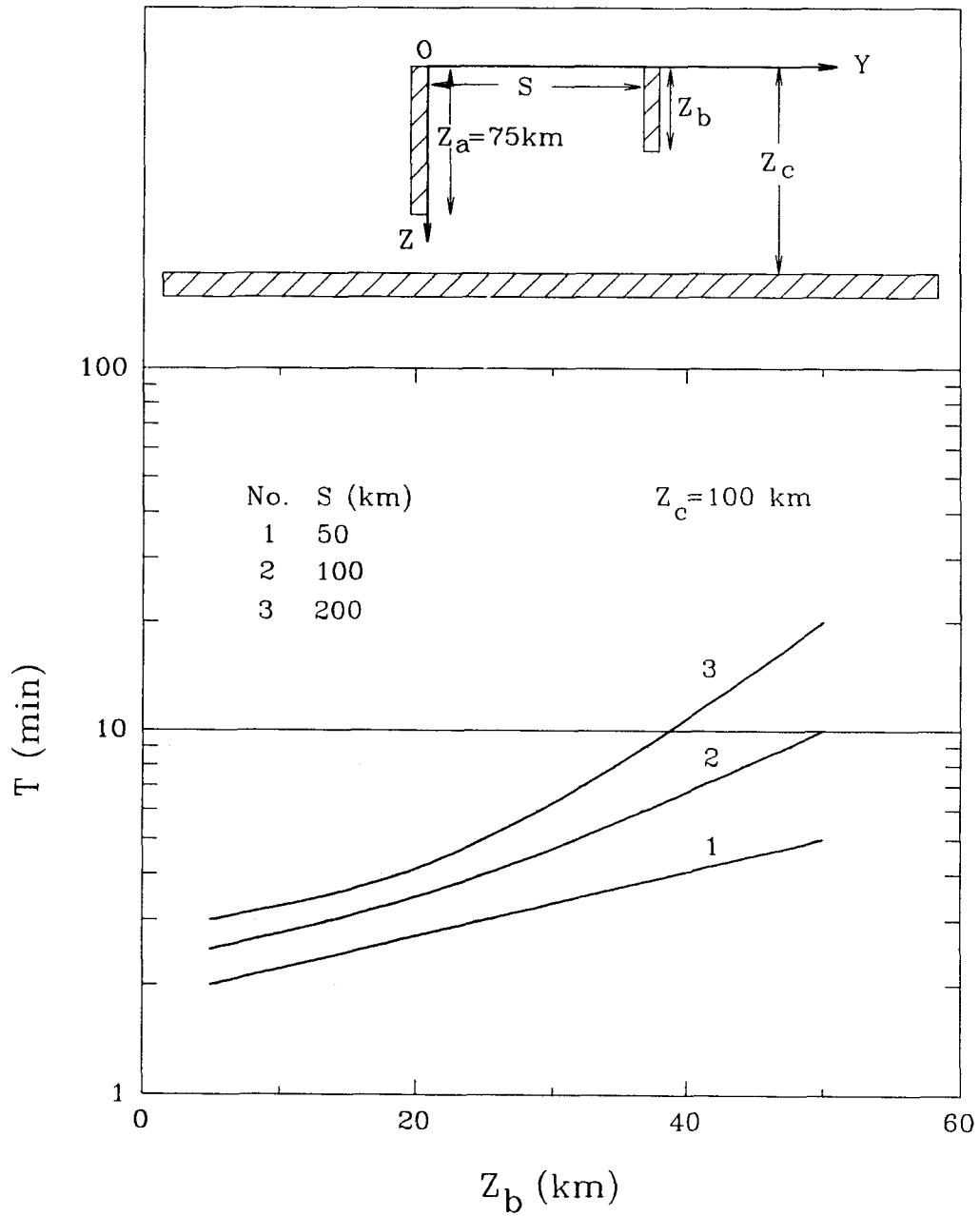


Figure 4.13: Empirical plots of the period T at which the quadrature V_{mb} is maximum as a function of the minor fault depth Z_b for three separation distances $S=50, 100, 200$ km.

minor fault depth if the separation distance between the faults were known. For example, if the separation distance between the faults were known as 100 km, a maximum quadrature V_{mb} observed at $T=2$ min at a site near the minor fault would suggest a minor fault depth of approximately 15 km.

Figure 4.14 shows the zero in-phase response period T_0 (obtained from Fig. 4.10) as a function of distance Y from the major fault. As described earlier, the zero response period T_0 is that period at which the response, at a given distance from the major fault, is zero, and for $T > T_0$ is of sign opposite to that for $T < T_0$. A profile of the induction arrows for 2 and 10 min is also shown in the figure to demonstrate the arrow magnitude change and direction reversals along the profile. At roughly 70 km from the major fault the in-phase response is zero at 2 min (T_0), then for periods greater than 2 min the arrow points towards the major fault, while for periods less than 2 min the arrow points away from the major fault (or towards the minor fault). At this $T_0=2$ min period, the arrows at sites $Y < 70$ km point towards the major fault, while at sites $Y > 70$ km the arrows point away from the major fault (or towards the minor fault). The zero response curve (T_0 as a function of Y) divides the region between the major and minor faults into regions in which the induction arrows to the left of the curve point towards the major fault and to the right of the curve point away from the major fault (or towards the minor fault). As was the case for the earlier ocean-fault model, the points on the zero response curve lie well to the right ($Y > S/2$) of mid-way between the faults, and moves towards the minor fault with increasing period.

The zero quadrature response curve, similar to that for the in-phase component (Fig. 4.14) is shown in Fig. 4.15 (it should be noted that the arrow scale dif-

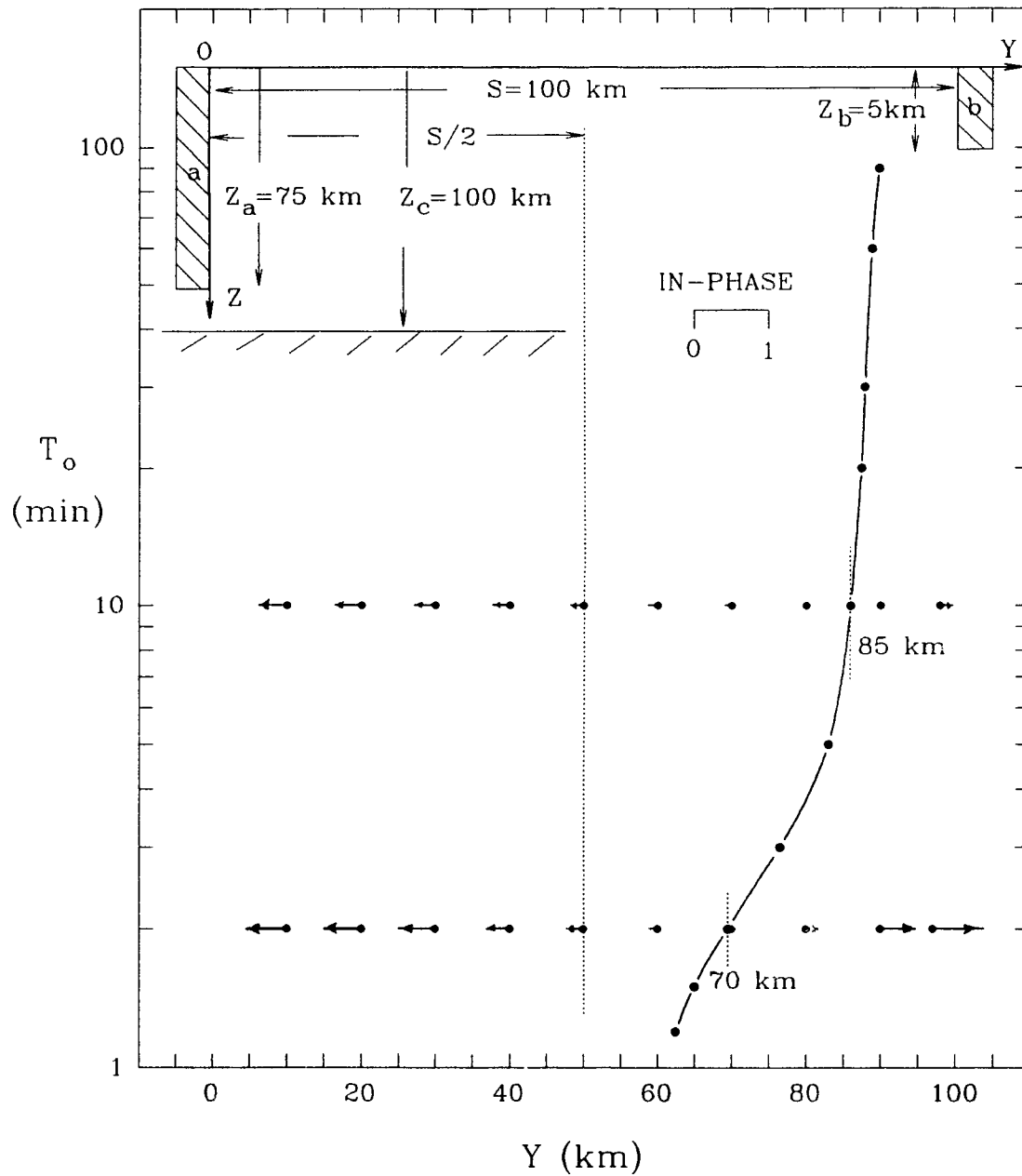


Figure 4.14: The zero in-phase response period T_0 as a function of the distance Y from the major fault. The induction arrows for 2 and 10 min are shown to demonstrate that at a given site the arrow directions for periods larger than T_0 are opposite to those for periods smaller than T_0 .

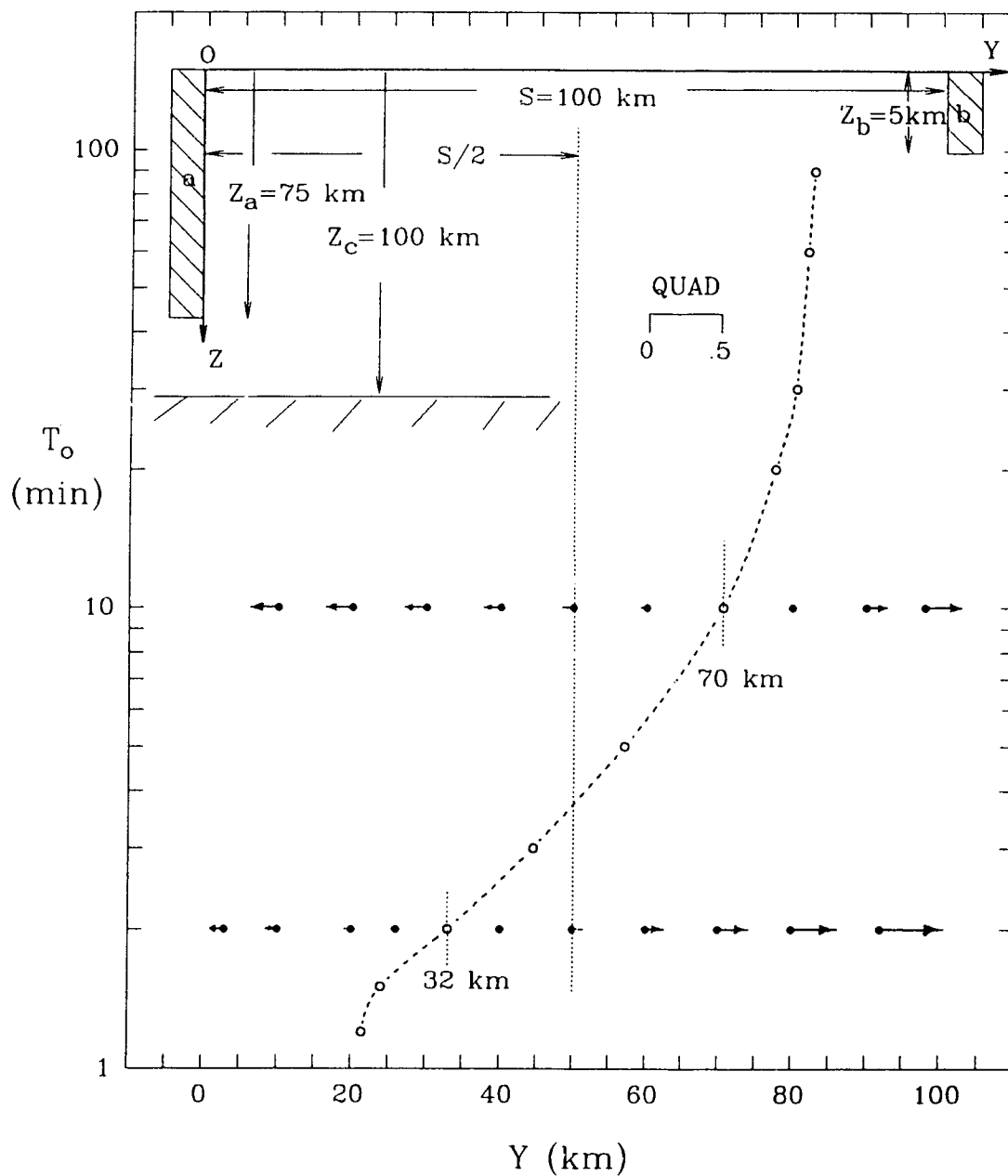


Figure 4.15: The zero quadrature response period T_0 as a function of the distance Y from the major fault. The induction arrows for 2 and 10 min are shown to demonstrate that at a given site the arrow directions for periods larger than T_0 are opposite to those for periods smaller than T_0 .

fers by a factor of two from that for the in-phase component in Fig. 4.14). It is seen, that differing from the in-phase arrow at 2 min, which reverses direction near the minor fault ($Y \approx 70$ km in Fig. 4.14), the quadrature arrow reverses sign much nearer the major fault ($Y \approx 32$ km). Again, the zero response curve divides the region between the major fault and the minor fault into regions in which the quadrature arrows to the left of the curve point towards the major fault, and to the right of the curve point towards the minor fault.

Figure 4.16 shows in detail the zero response curves for the in-phase component for the parallel major ($Z_a = 75$ km) and minor ($Z_b = 5, 25, 50$ km) faults separated by distances $S = 50, 100, 200$ km. Again, as was the case for the earlier ocean-fault model, the zero response curves shift to decreased values of Y (towards the major fault) with increasing fault depth Z_b , and the response curves are restricted to sites at distances $Y > S/2$. At a given distance Y from the major fault, the zero response period T_0 increases with increasing minor fault depth Z_b . For example, at $Y = 70$ km ($S = 100$ km), $T_0 \approx 2$ and 5 min for fault depths $Z_b = 5$ and 25 km respectively. Or if Y is considered to be a function of T_0 , then Y decreases with increasing Z_b . For example, for $S = 100$ km and $T_0 = 10$ min, $Y \approx 85$ and 60 km for $Z_b = 5$ and 50 km respectively. This is expected, since as Z_b increases to 75 km (the case for identical faults $Z_a = Z_b = 75$ km), zero responses would be observed at all periods at the same site, namely mid-way ($Y = S/2$) between the two identical faults. With increasing period the zero in-phase response curves shift towards the minor fault (increasing Y) for all fault depths ($Z_b = 5, 25, 50$ km) and separation distances ($S = 50, 100, 200$ km). It is apparent that the minor fault depth and the proximity of the major fault are important parameters that lead to a zero response

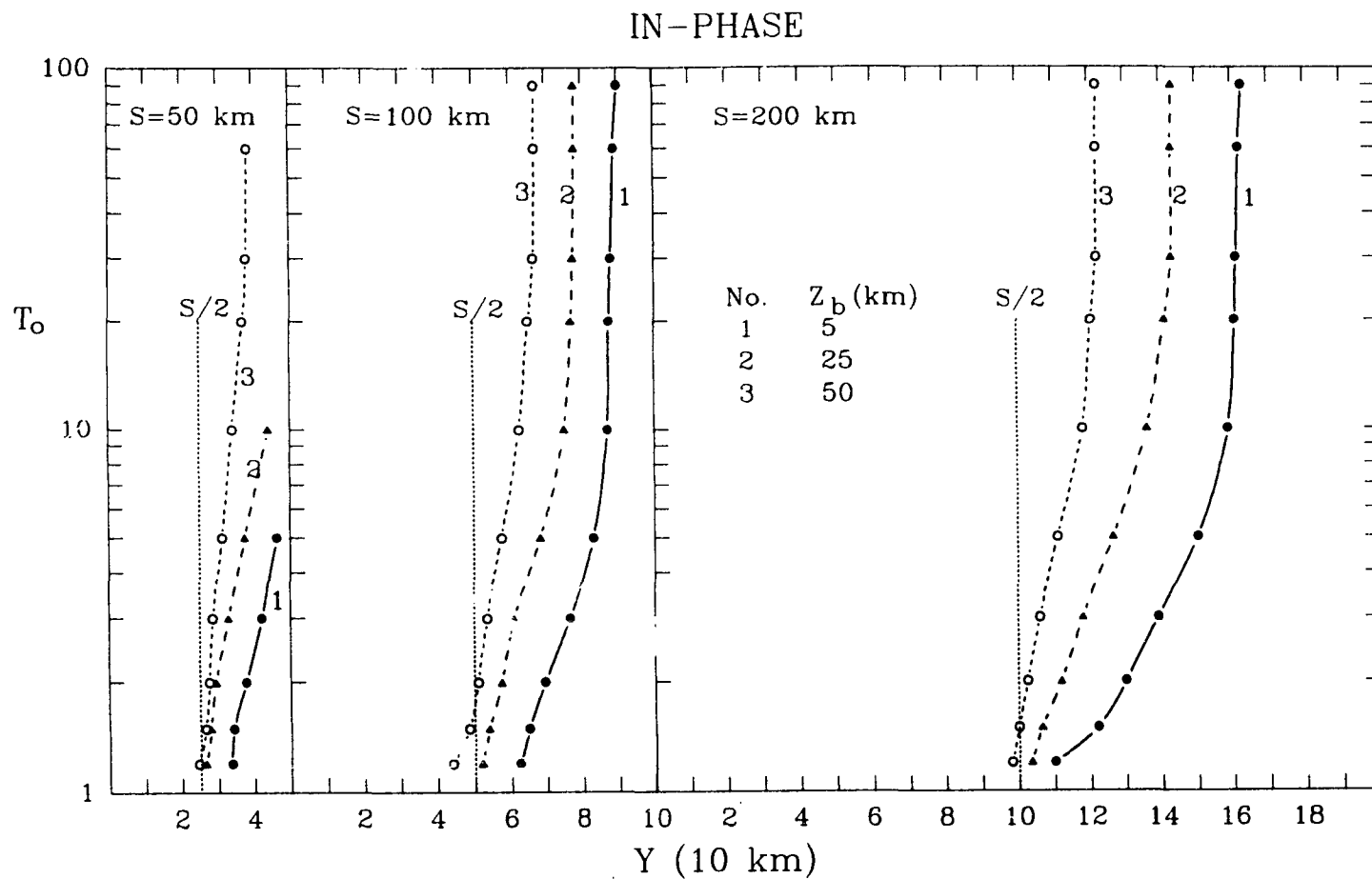


Figure 4.16: Empirical plots of the zero in-phase response period T_0 as a function of the distance Y from the major fault for a range of the minor fault depths ($Z_b=5, 25, 50$ km) and for each of three separation distances ($S=50, 100, 200$ km) between the faults.

period at a given site (and hence to a reversal in sign of the response at that site along the profile), since in the case of a single fault (as discussed in the previous section) no reversals in sign are observed at any site on the profile, except at a site directly over the fault.

The curves for the zero quadrature response period T_0 as a function of Y are shown in Fig. 4.17. Compared with the zero response curves for the in-phase component (in Fig. 4.16), the curves for the quadrature component for all periods and minor fault depths for each of the separation distances ($S=50, 100, 200$ km) are shifted to smaller values of Y (i.e., nearer the major fault). In fact, at short periods ($T_0 < 4$ min) $Y < S/2$. It is interesting to note that differing from the observations for the in-phase component, the zero quadrature response curves for changing Z_b (for all S) intersect at a period of roughly 2-3 min, with Y increasing with increasing Z_b at shorter periods, and decreasing with increasing Z_b at longer periods. This observation could also be stated as, at a given distance Y from the major fault, T_0 for the quadrature component decreases with increasing Z_b for very short periods ($T < 2-3$ min), while the opposite is observed for longer periods.

The zero response curves in Figs. 4.16 and 4.17 for models of parallel conductive faults could be used as an aid to the interpretation of field observations if field measurements were carried out at sites along a linear profile over faults. For example, if the in-phase induction arrows at sites along a profile were observed to reverse direction at $T=5$ min at a site 40 km from a known major fault, and for periods $T < 5$ min the arrows pointed towards the major fault, but for $T > 5$ min arrows pointed towards the major fault, a minor fault ($Z_b=25$ km) located 10 km from the site (roughly $Y=50$ km from the major fault) would be indicated

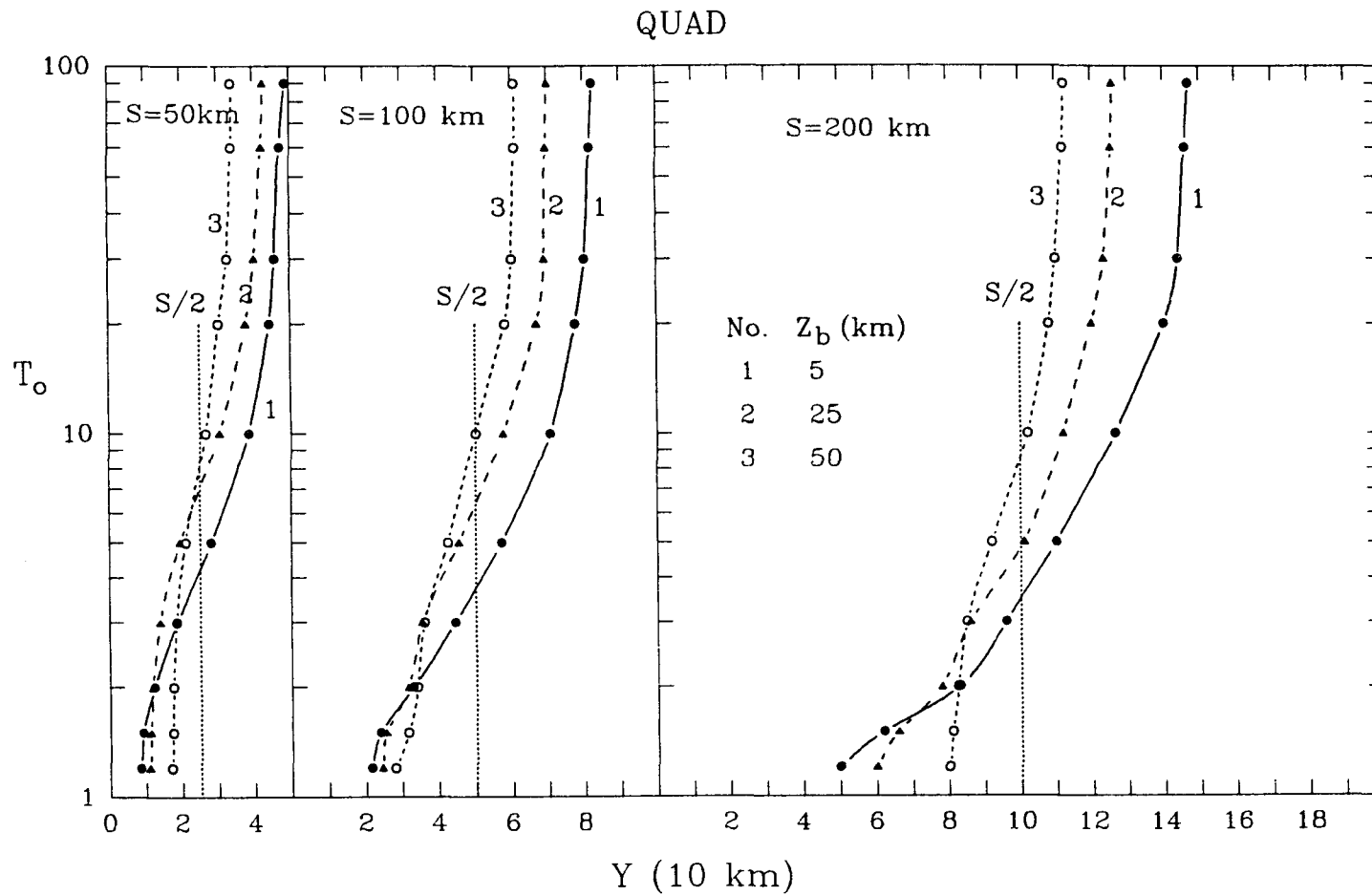


Figure 4.17: Empirical plots of the zero quadrature response period T_0 as a function of the distance Y from the major fault for a range of the minor fault depths ($Z_b=5, 25, 50$ km) and for each of three separation distances ($S=50, 100, 200$ km) between the faults.

(see curve 2 for $S=50$ km in Fig. 4.16). A zero quadrature response period of approximately 20-30 min at the same site would support the interpretation of a nearby minor fault.

If the sites in a geomagnetic field study were in a region including parallel faults, zero in-phase and/or quadrature induction arrow responses at some sites might be expected at periods T_0 , periods that on the basis of the models studied in this section should be characteristic of the major-minor fault geometry. Further, comparing the magnitudes and the signs of the responses for a spectrum of periods with those for a range of models should in principle aid the interpretation of field site measurements. In the following, figures 4.18-4.20 are presented to provide such model responses over a spectrum of periods at specific sites between the faults.

The in-phase and quadrature induction arrow responses at selected distances $Y=15-45$ km from the major fault ($Z_a=75$ km) for the separation distance $S=50$ km are shown as a function of period for the minor fault depths $Z_b=5, 25, 50$ km in Figs. 4.18-4.20 respectively. The response curves for a shallow fault $Z_b=5$ km in Fig. 4.18 show that for locations $Y \leq 35$ km, the in-phase responses are negative at all periods, indicating that the in-phase arrows point towards the major fault. Near the minor fault, at sites $Y > 35$ km, the in-phase response reverses sign at T_0 (closed circles) from positive for $T < T_0$ to negative for $T > T_0$. This zero in-phase response period T_0 increases from roughly 1.5 min at $Y=35$ km to 3.5 min at $Y=45$ km. The quadrature response shows a sign reversal at T_0 (open circles) over a much larger distance range ($Y=15-45$ km) than that for the in-phase response. Again, as is the case for the in-phase response, the zero quadrature response peri-

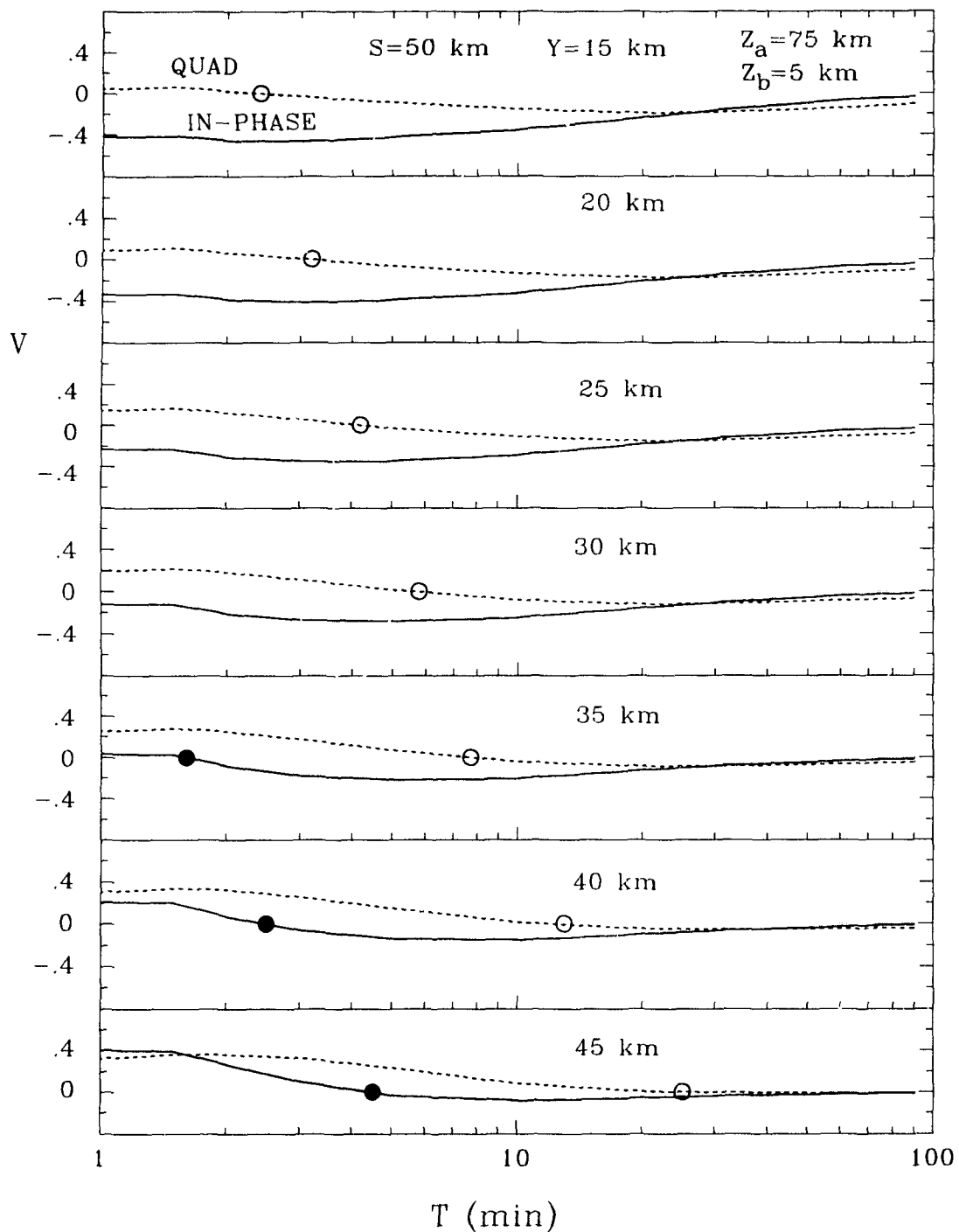


Figure 4.18: The in-phase and quadrature induction arrow responses as a function of period for selected locations at distances $Y=15-45$ km from the major fault ($Z_a=75$ km) for $S=50$ km for $Z_b=5$ km. The closed and open circles indicates the zero response periods T_0 for the in-phase and quadrature components respectively.

od T_0 also increases with increasing Y . The zero response periods for the quadrature component are approximately a factor of 4-5 longer than those for the in-phase component. At a site very near the fault ($Y=45$ km), both the in-phase and quadrature responses become negligible for periods $T > T_0$. It is noted that at short periods ($T < 5$ min), while one of the components (say in-phase) is zero at the period T_0 , the other component (quadrature) shows a broad maximum at roughly the same period. For example, At $Y=15$ km the quadrature response is zero at roughly 2.5 min while the corresponding in-phase response is roughly maximum; and at $Y=35$ km the in-phase response is zero at 1.5 min while the quadrature response is roughly maximum. The zero response periods T_0 are seen to be confined to the period ranges of 1-5 min and 2-25 min for the in-phase and quadrature components respectively for this major-minor fault model.

To show the effect of increasing the fault depth Z_b , the in-phase and quadrature responses at the same sites ($Y=15-45$ km) as those in Fig. 4.18 are provided for $Z_b=25$ km and 50 km in Figs. 4.19 and 4.20 respectively. In comparing the responses in Fig. 4.19 for $Z_b=25$ km with those for the shallower fault depth $Z_b=5$ km in Fig. 4.18, the main changes are a shift of T_0 to longer periods at each site Y , and a generally attenuated response for increased fault depth. Sign reversals in the in-phase response occur at sites $Y=30-40$ km, as compared with $Y=35-45$ km for the shallower fault.

In comparing the responses for the further increased minor fault depth of $Z_b=50$ km in Fig. 4.20 with those for the $Z_b=25$ km (Fig. 4.19), it can be seen that the in-phase and quadrature responses for $Z_b=50$ km are further attenuated, due to the increased minor fault response, which is of sign opposite to that of the major

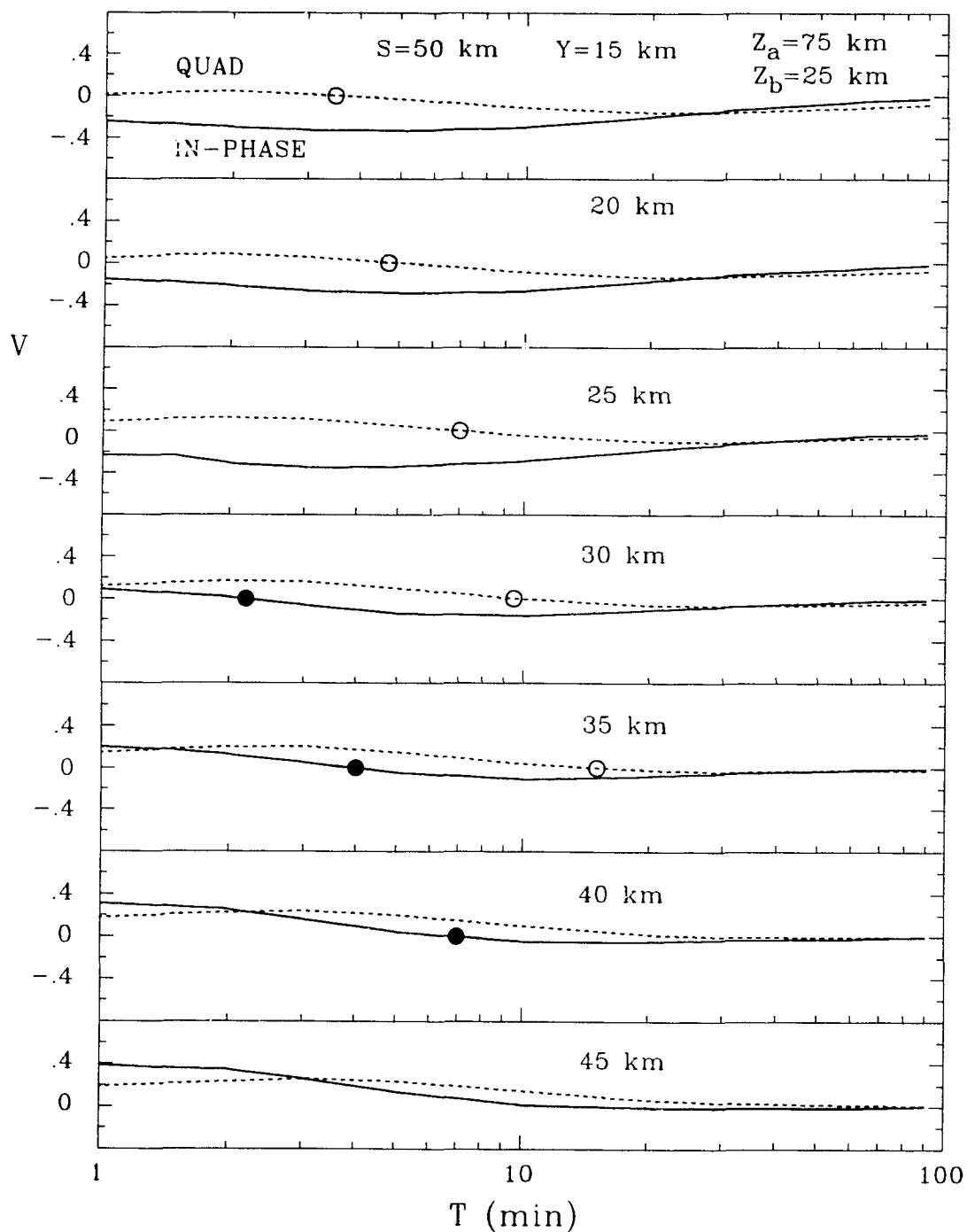


Figure 4.19: The in-phase and quadrature induction arrow responses as a function of period for selected locations at distances $Y=15-45$ km from the major fault ($Z_a=75$ km) for $S=50$ km for $Z_b=25$ km. The closed and open circles indicates the zero response periods T_0 for the in-phase and quadrature components respectively.

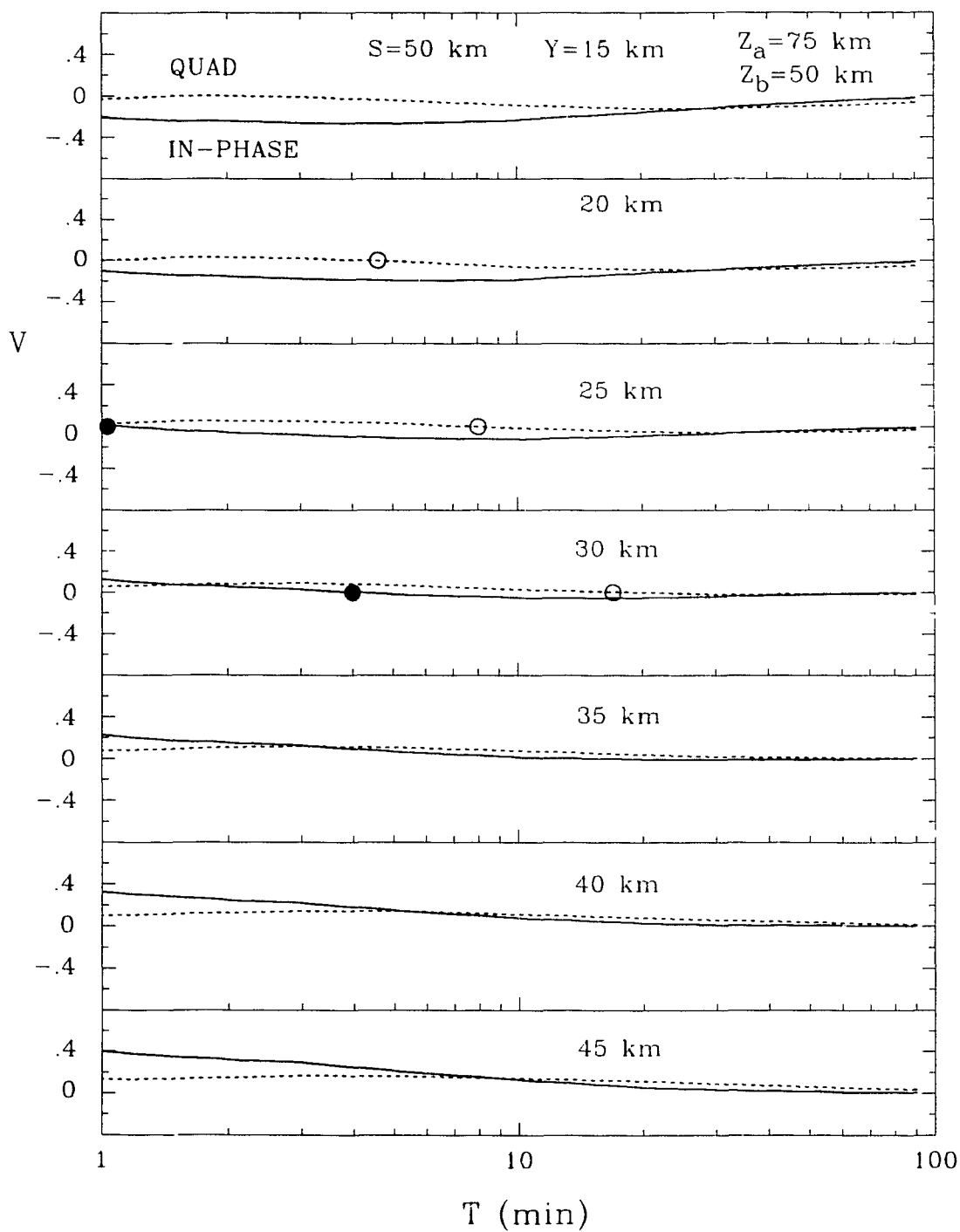


Figure 4.20: The in-phase and quadrature induction arrow responses as a function of period for selected locations at distances $Y=15-45$ km from the major fault ($Z_a=75$ km) for $S=50$ km for $Z_b=50$ km. The closed and open circles indicates the zero response periods T_0 for the in-phase and quadrature components respectively.

fault. For the increased Z_b , the zero in-phase and quadrature responses are now confined to the distance range $Y=20-30$ km (in the neighborhood of $S/2$). This is expected since if Z_b is increased to 75 km, the zero response would be at the same central site ($Y=S/2$) at all periods. Additional model response curves, similar to those in Fig. 4.18-4.20, but for increased separation distances of $S=100$ and 200 km are given in Appendix C.

4.4 Removal of a Single Fault Response From the Response of a Pair of Parallel Faults

In order to examine if the sum of the individual responses of a major and a minor fault would yield the response of a pair of parallel faults, laboratory measurements were carried out for models of each fault, and of the pair of parallel faults, embedded in a resistive earth underlain by a conductive substratum. The parameters for these models are shown in the upper parts of Figs. 4.21 and 4.22, the figures that show the in-phase and quadrature induction arrow responses at 2 and 20 min for models of the major fault (V_a), the minor fault (V_b), the pair of parallel faults (V_{ab}), as well as the sum (dashed curve) of the responses (V_a+V_b) of the major and of the minor fault.

The in-phase and quadrature responses for each of the major fault, the minor fault, and the major and minor faults, as well as the sum of the responses of the major and minor fault, for a small separation distance $S=50$ km are shown for the case of $Z_a=75$ km and $Z_b=5$ km in Fig. 4.21. For each fault, both the in-phase and quadrature responses at the two periods shown are positive to the left of the fault but negative to the right of the fault, again indicating that the single fault induc-

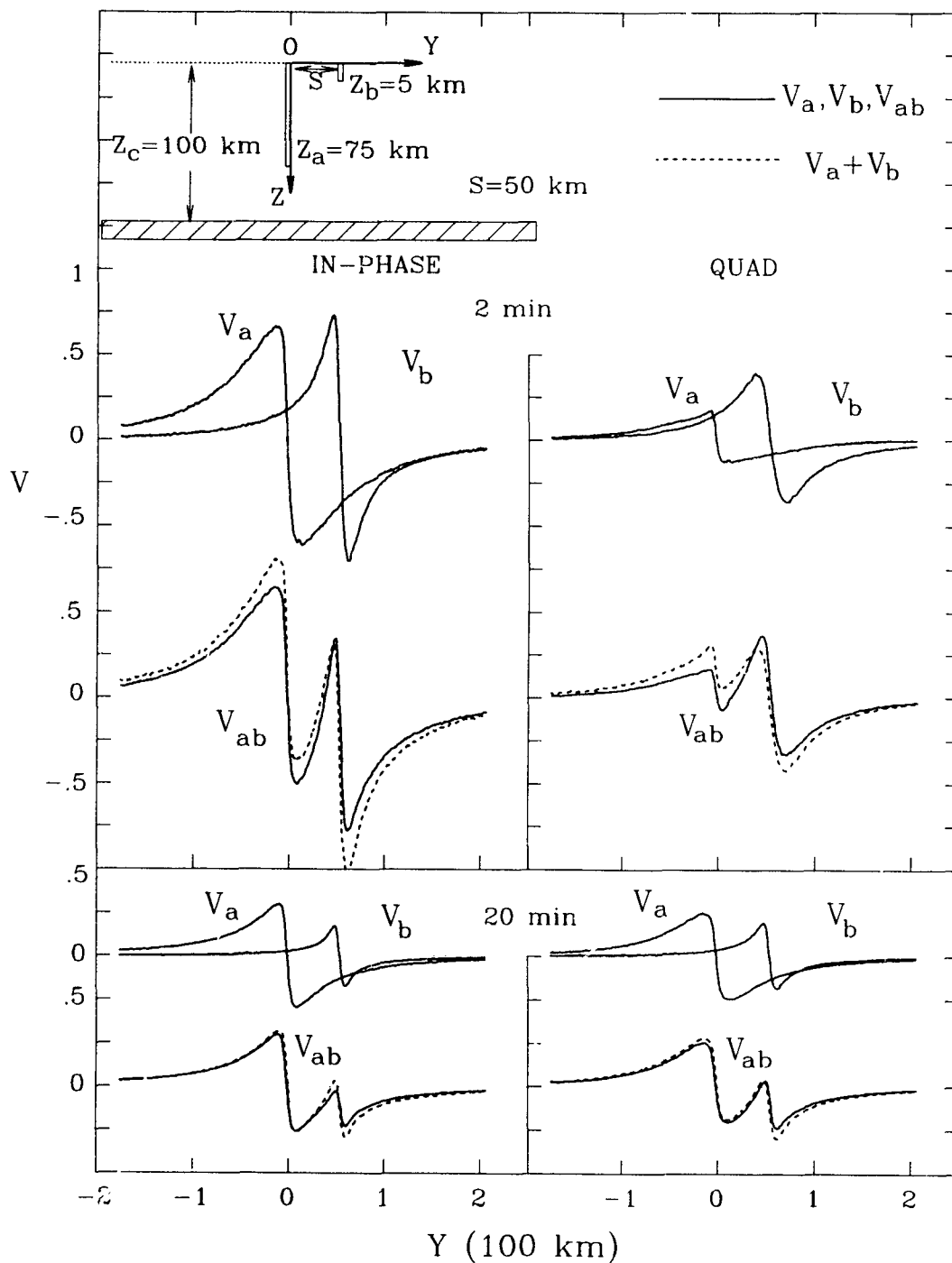


Figure 4.21: The in-phase and quadrature induction arrow responses V at 2 and 20 min for each of: the major fault (V_a); the minor fault (V_b); the pair of parallel faults (V_{ab}); and the sum of the responses of the major and minor faults ($V_a + V_b$) for $Z_b = 5$ km and $S = 50$ km.

tion arrows point towards the fault. The in-phase response V_{ab} along the profile reverses sign (at a location near the minor fault) at 2 min, but not at 20 min. The quadrature response V_{ab} however, shows a reversal at both periods, near the major fault at 2 min, and near the minor fault at 20 min.

The sum of the individual fault responses (V_a+V_b) are shown in the dashed line curves in Fig. 4.21. At 2 min period the in-phase response shows very good agreement between the dashed curve (V_a+V_b) and solid line curve (V_{ab}) in the region between the major and minor faults. The agreement at this period is also very good for the quadrature component, except for sites near the faults. In general, Fig. 4.21 shows that the agreement between V_{ab} and V_a+V_b , though good at 2 min, is even better at the longer period of 20 min.

Figure 4.22 shows the in-phase and quadrature responses for the same faults as those of Fig. 4.21 except that the separation distance has been increased to $S=100$ km. It is apparent that for this increased separation distance, the agreement between V_{ab} and V_a+V_b is excellent at both short and long periods along the entire profile (except right at the fault). As expected, this agreement for the larger separation distance of $S=100$ km is even better than that for the smaller separation of $S=50$ km (in Fig. 4.21), since the electromagnetic mutual coupling of the major and minor faults is reduced with increased separation distance. Model measurements (not shown here), carried out for periods as long as 90 min for both $S=50$ and 100 km confirmed the observation of good agreement at long periods, as well as at short periods. Thus, for a separation distance as small as $S=50$ km, the coupling between the major and minor faults is seen to be sufficiently small, so that the sum of the responses of the individual faults, yields (within reasonable

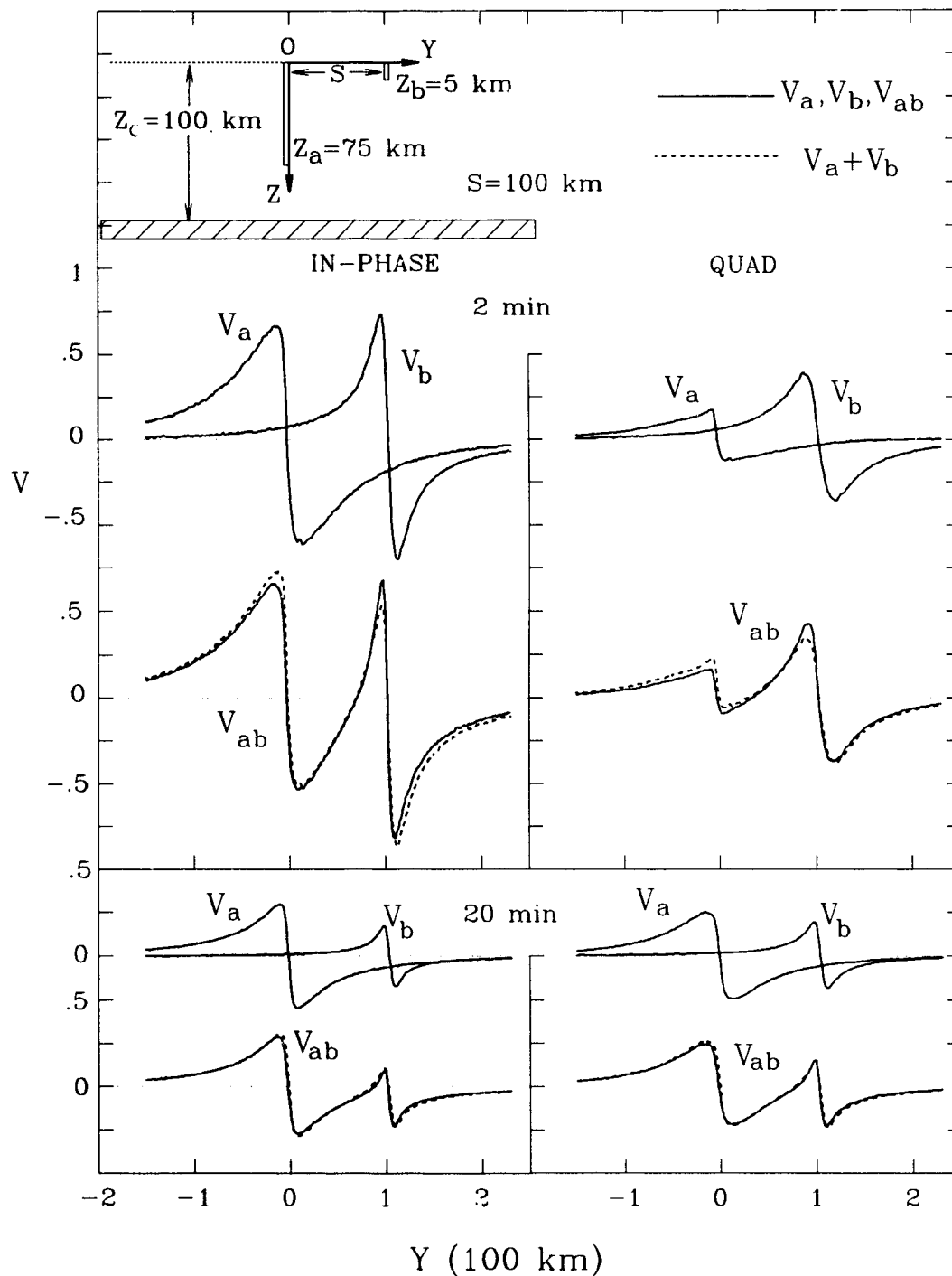


Figure 4.22: The in-phase and quadrature induction arrow responses V at 2 and 20 min for each of: the major fault (V_a); the minor fault (V_b); the pair of parallel faults (V_{ab}); and the sum of the responses of the major and minor faults (V_a+V_b) for $Z_b=5$ km and $S=100$ km.

accuracy) the response of the pair of parallel faults. This indicates that in geomagnetic field studies in regions that included multiple faults, the responses of one fault (if known) could be subtracted from the measurements to yield the responses of the second unknown parallel fault alone, and thus simplify the interpretation of the measurements.

4.5 Chapter Summary

In this chapter, analogue model measurements are used to study induction arrow responses for two basic models: i) a single elongated conductive fault for a range of fault depths, and ii) a pair of parallel faults, for a range of fault depths and separation distances. These results are then used to examine the removal of the responses of one fault from those of a pair of parallel faults.

The Responses of a Single Fault

The induction arrow in-phase and quadrature responses along a profile perpendicular to a single conductive fault are studied for a wide period range (1-90 min) for four fault depths ($Z_b=5, 25, 50, 75$ km). Both the in-phase and quadrature arrows at either side of the fault point towards the fault at all periods, with the maximum responses (V_m) observed at either edge of the fault. The in-phase and quadrature V_m depend strongly on the depth of the fault as well as on the period, with the shallow fault at short periods showing the larger V_m , and at long periods showing the smaller V_m . The quadrature response shows a broad V_m maximum at a period which increases with an increase in the fault depth. The empirical plots of the widths W of the response curves along a profile and the maximum responses V_m as a function of period for a range of the fault depths, as well the period for

quadrature V_m maximum as a function of fault depth should have application to the depth determination of a fault in a geomagnetic field study carried out near a fault.

The Responses of a Pair of Parallel Faults

The in-phase and quadrature induction arrow responses of a pair of parallel faults are studied for a range of periods and fault depths for each of three separation distances. Due to the opposite signs of the major and minor fault responses at locations between the faults, the resultant responses for both the in-phase and quadrature components along a profile are zero at certain periods T_0 (and reverse sign), periods that depend on the major-minor faults separation distance, the minor fault depth, and the distance from the major fault. Empirical curves for the zero response periods as a function of distance from the major fault, as well as the maximum responses near the faults as a function of period for both the in-phase and quadrature components are provided. A knowledge of the magnitudes and the signs of the induction arrow responses for a spectrum of periods, as well as a knowledge of the periods for maximum and zero responses along a profile for a catalogue of major-minor faults models, should have application to the interpretation of induction arrow responses along a profile in regions that include parallel conductive faults.

Removal of a Fault Response From the Responses of a Pair of Parallel Faults

The possible removal of the induction arrow response of a fault from those of a pair of parallel faults is studied by comparing the model induction arrow responses of the pair of parallel faults with the sum of the separate responses of a major and a minor fault for two separation distances. It is concluded that a simple vec-

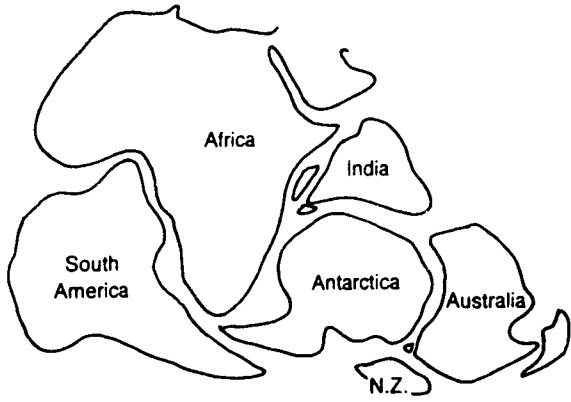
tor subtraction of the response of the major (or minor) fault from that of the pair of faults, does yield (within reasonable accuracy) the response of the minor (or major) fault alone in regions between the faults, and thus in the case of parallel faults, the responses of a known fault (say from analogue model results of a single fault) could be removed from the field site measurements by a simple vectorial subtraction to yield the response of a unknown fault, and thus aid in the interpretation of the measurements.

Chapter V
TECTONIC AND GEOLOGICAL SETTING OF THE NEW
ZEALAND REGION

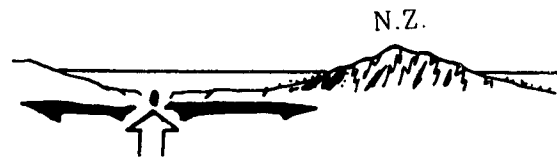
5.1 Tectonic and Geological Setting

It is now generally believed that New Zealand developed as part of the border of Antarctica and Australia when those two continents were part of the great southern super-continent, Gondwana. Figure 5.1 shows an abbreviated tectonic history of New Zealand (adapted from Thornton, 1993). It is interesting to see how South America and Africa fitted together prior to the break-up of Gondwana. New Zealand began its formation as sediments and volcanoes on the borders of Gondwana, and for most of its history was subjected to collision and uplift. About 85 million years ago (as shown in diagram (c) in Fig. 5.1), New Zealand split away from Gondwana (Australia and Antarctica) and became established as a small continent. This rifting by 60 Ma ago (d) resulted in the fully opened Tasman Sea, followed by the healed rift at about 25 Ma ago, at a period when New Zealand was mostly below sea level. During the last 20 million years, renewed uplift (f) through collision has occurred and sediments have been deposited over the older submerged rocks.

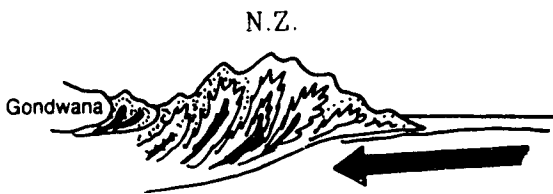
Figure 5.2 shows the postulated geological structure of New Zealand 130 Ma ago and at present (adapted from Thornton, 1993). The rocks can be divided roughly into two groups, one group on either side of the Alpine Fault. Both groups



a) 200 Ma (Gondwana).



d) 60 Ma (opened Tasman Sea).



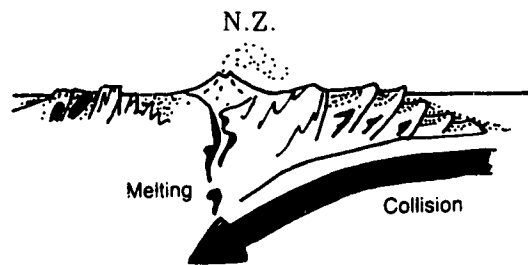
b) 130 Ma (collision and uplift).



e) 25 Ma (healed rift).



c) 85 Ma (break up of Gondwana).



f) 20-0 Ma (renewed uplift).

Figure 5.1: Reconstructed tectonic history of New Zealand (adapted from Thornton, 1993)

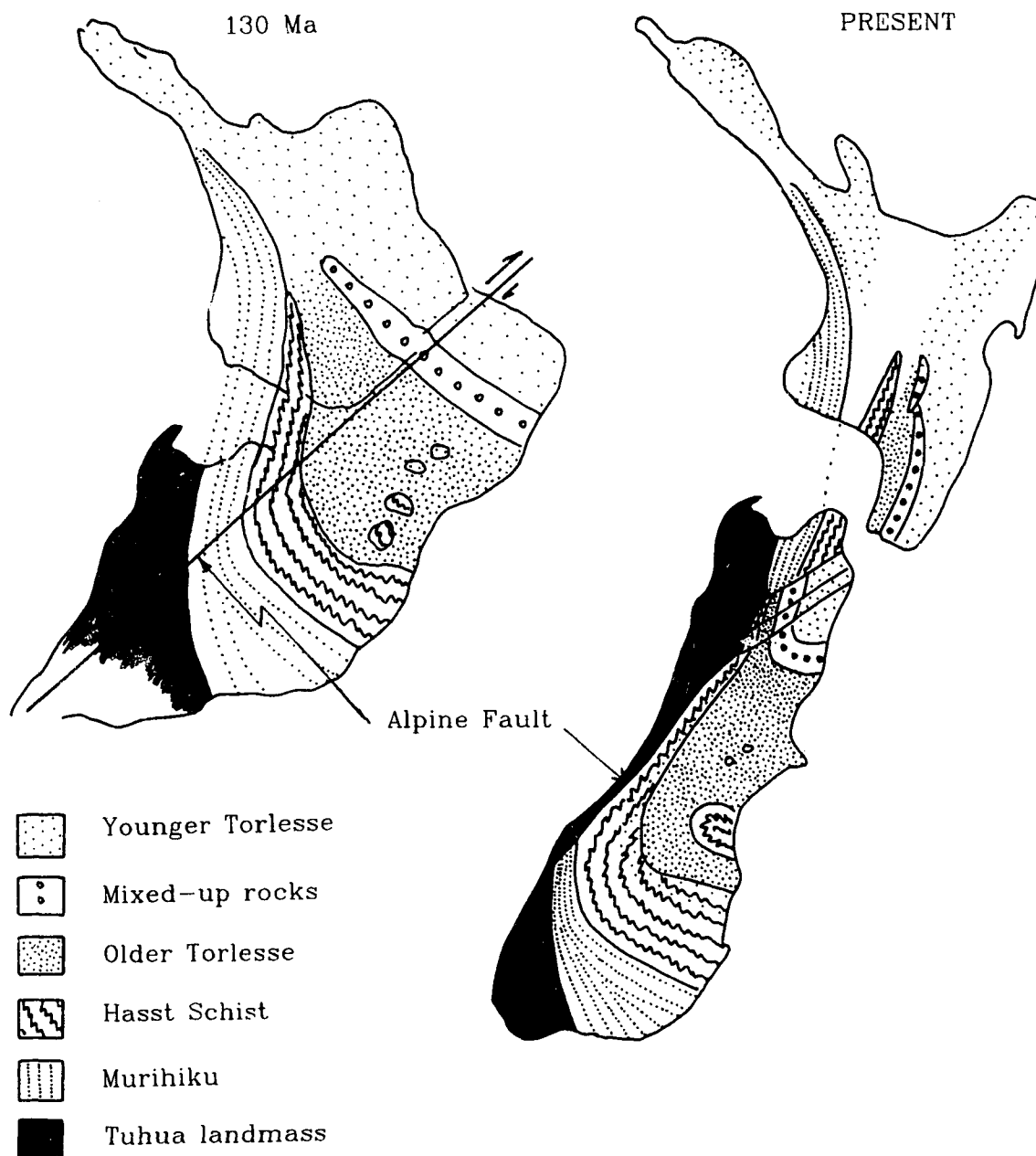


Figure 5.2: The tectonic configuration 130 Ma ago as compared with that of the present (adapted from Thornton, 1993). The rock types indicated were formed in the period 300–130 Ma.

were formed before the movement along the Alpine Fault wrenched some parts of the rocks to locations at the present southern tip of South Island roughly 500 km from the corresponding rocks at the northern tip of the same Island as shown in Fig. 5.2.

The Torlesse rocks in Fig. 5.2 are believed to have been formed 170 Ma ago in great, long trenches in the ocean, into which vast masses of sediments were dumped, and which were later uplifted to form new mountains. The Murihiku rocks were formed in the period 345-170 Ma ago, and the Tuhua landmass is dated as greater than 345 Ma. The schists (345-170 Ma) are sedimentary rock that has been altered by pressure and heat. It is well known that as temperature and pressure increases, various minerals become unstable and their atoms move to regroup and form new minerals. This occurs in the solid state. The formation of the schists on South Island, covering many hundreds of hectares, could not be explained as due to localised heat and pressure, but it is now understood (Thornton, 1993) that the schists in this area were originally deposited as sediment at depth and buried under a sediment pile 345-167 Ma ago, and thus subjected to high temperatures and pressures. Such deep burial results in the high electrical conductivity of schists. Movement along a break in the crust, namely the Alpine Fault dipping to the east at an angle of roughly 45° , and acting as a plow share, has resulted in these rocks at depth turned over and brought to surface zones.

Figure 5.3 illustrates the tectonic development of the two islands of New Zealand during the last 30 million years (adapted from Thornton, 1993). The subduction of the Pacific Plate resulted in the ocean floor slowly being lost during the last 30 million years, while the continental mass of the Chatham Rise was being

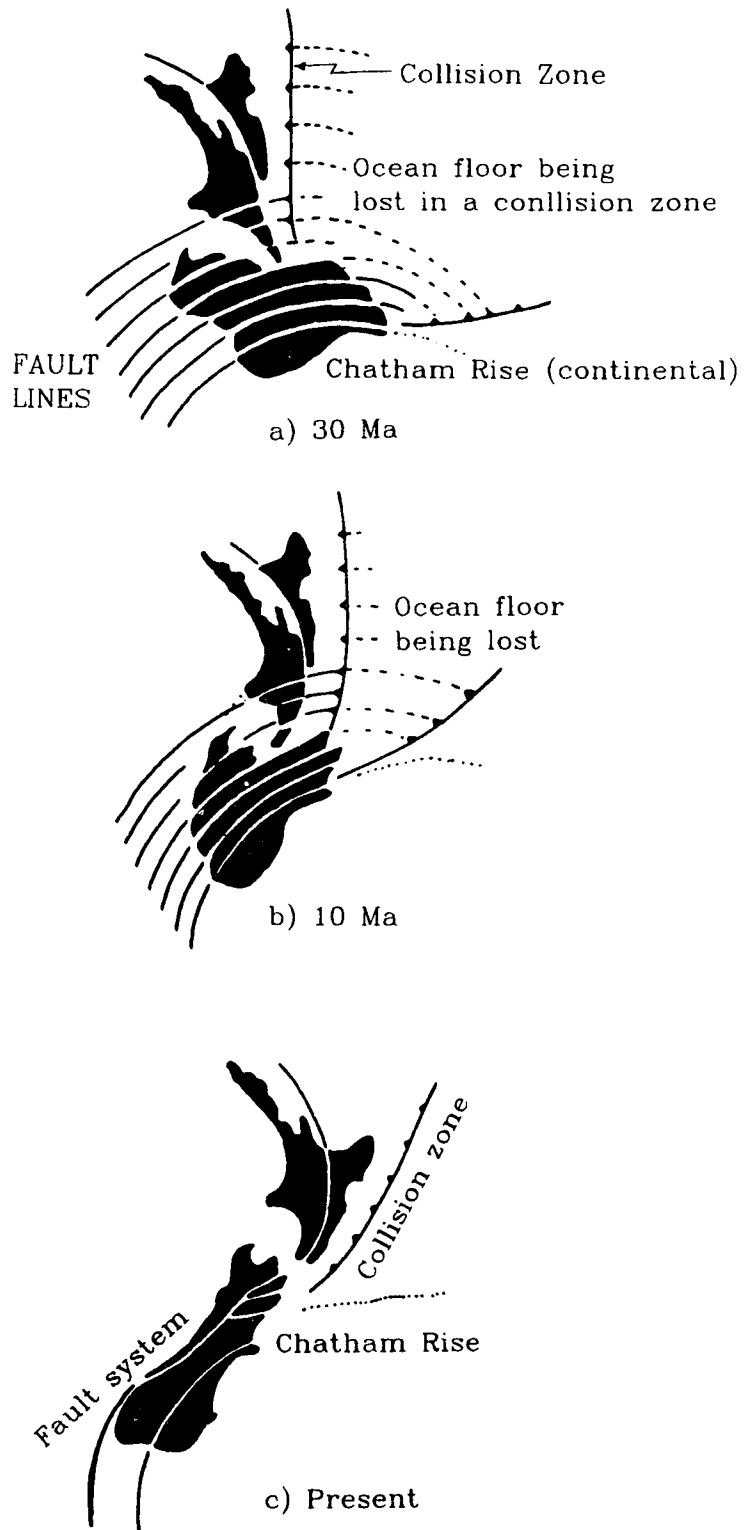


Figure 5.3: A possible tectonic history of New Zealand during the last 30 Ma (adapted from Thornton, 1993).

compressed as it slid along the fault lines. The present-day coastlines shown on the reconstructions in Fig. 5.3 have meaning only as far as locations, since the sea was covering most of New Zealand 25 million years ago (Fig. 5.1). As ocean floor was being lost at the collision zone, horizontal movement of the land mass east of the Alpine Fault continued southward, and New Zealand began to approach its present configuration. It is noted that the fault system extends offshore north of North Island, as well as south of South Island. Walcott (1987) has also reconstructed the plate boundary zone for New Zealand up to 40 million years ago, using knowledge of the transform faults and magnetic anomalies in the Australia, Antarctic, and Pacific Plates. He concluded that the Pacific Plate has been progressively subducted under the Indian Plate over the last 40 million years, with particularly rapid subduction occurring in the time periods of 35-25 Ma and 5-0 Ma.

New Zealand today lies across the convergent boundary between the Indian and the Pacific Plates. The distribution of crustal (0-15 km) and deep (16-40 km, and greater than 40 km) earthquakes of magnitude greater than 3.0 during 1992 is shown in Fig. 5.4 (provided by Smith, 1994). The occurrence of shallow earthquakes is indicative of active crustal deformation over most of New Zealand due to compression and uplift and lateral motion along faults. Earthquakes at depths of 16-40 km, as well as at depths greater than 40 km, indicate subduction of the Pacific Plate under North Island and the northern tip of South Island, and subduction of the Indian Plate under the south-western tip of South Island. The termination of the deep earthquakes at the northern end of South Island indicates the location of the edge of the subducting Pacific Plate, and the shallow earthquakes (0-15 km) cutting diagonally across to the south-western tip of South Island gener-

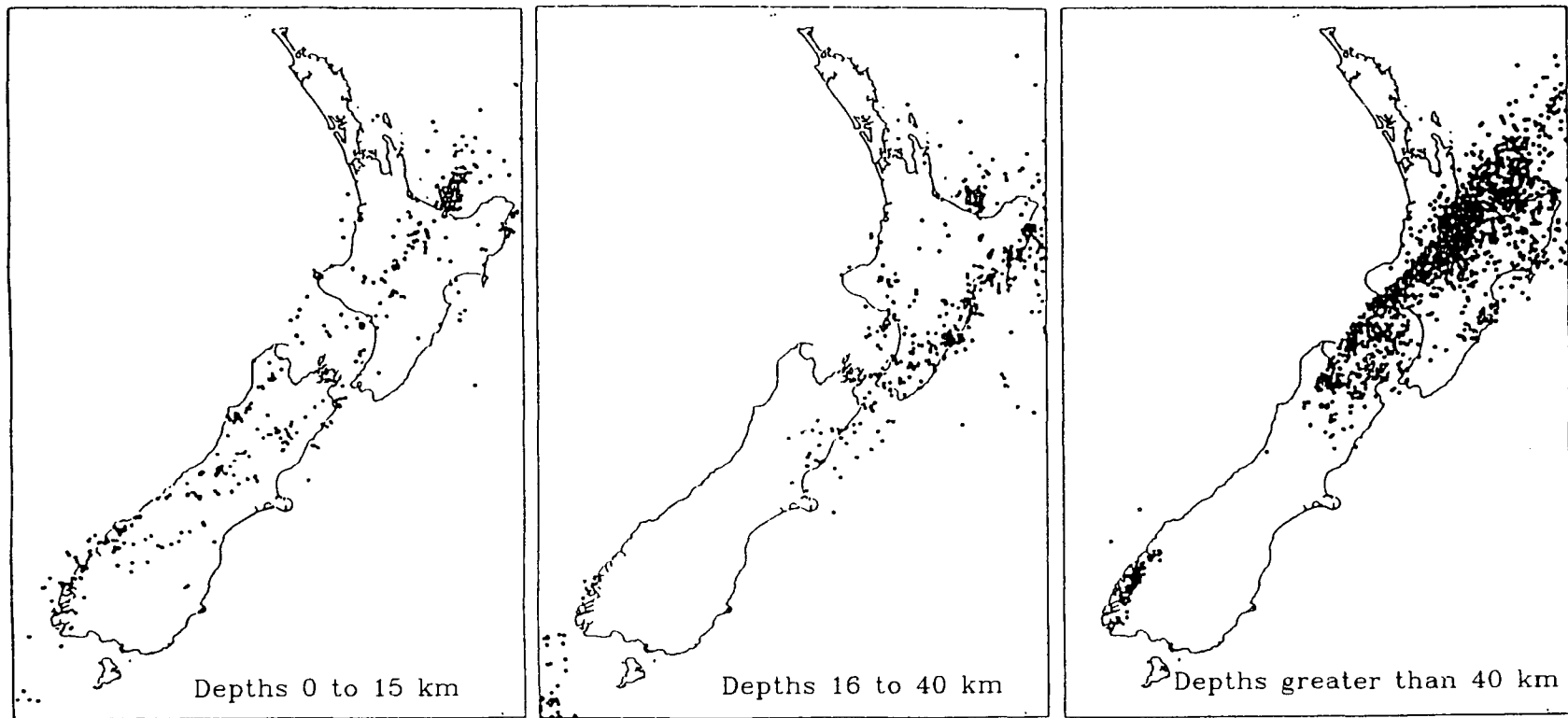


Figure 5.4: Earthquakes in New Zealand in 1992, magnitudes 3.0 and greater, provided by Smith (1994).

ally define the faulted boundary between the Pacific and Indian Plates. Crustal earthquakes during the period 1956-1974 (Walcott, 1978), and earthquakes deeper than 40 km during the period 1964-1987 (Reyners, 1989), also show a similar distribution pattern.

Figure 5.5 shows the present accepted tectonic setting in the New Zealand region. Along Hikurangi Trench, eastward of North Island, the Pacific Plate is subducting under the Indian Plate at a rate of 5 cm/year (Kamp, 1984; Walcott, 1987; Bannister, 1988; Smith et al., 1989; Cashman et al., 1992). Between the Hikurangi Trench and the east coast, the plate dips at $3-5^{\circ}$, so that at the east coast the plate has reached depths of 20-30 km. At these depths, the plate begins to dip more steeply (Smith et al., 1989), and it may well bend at a continuously increasing dip to depths of at least 400 km beneath the North Island. Plate reconstructions for the last 40 million year period (e.g., Walcott, 1987) suggest that subduction of the Pacific Plate lithosphere to this depth is possible. The observed low seismic velocities obtained by Bannister (1988) appear to indicate the presence of an appropriate thickness of subducted sediment at the depth of about 20 km. Such sediment would be expected to have an effect on the mechanical coupling between the overlying and subducted plates. Broad-scale uplift observed by Pillans (1986) along the east coast of North Island may in part result from underplating of the overlying plate by the sediments as they become detached from the subducted plate.

At the south-western tip (Fiordland) of South Island, as shown in Fig. 5.5, the Indian Plate is known to subduct beneath the Pacific Plate along the Puysegur Trench (Davey and Smith, 1983; Kamp and Hegarty, 1989; Reyners et al., 1991).

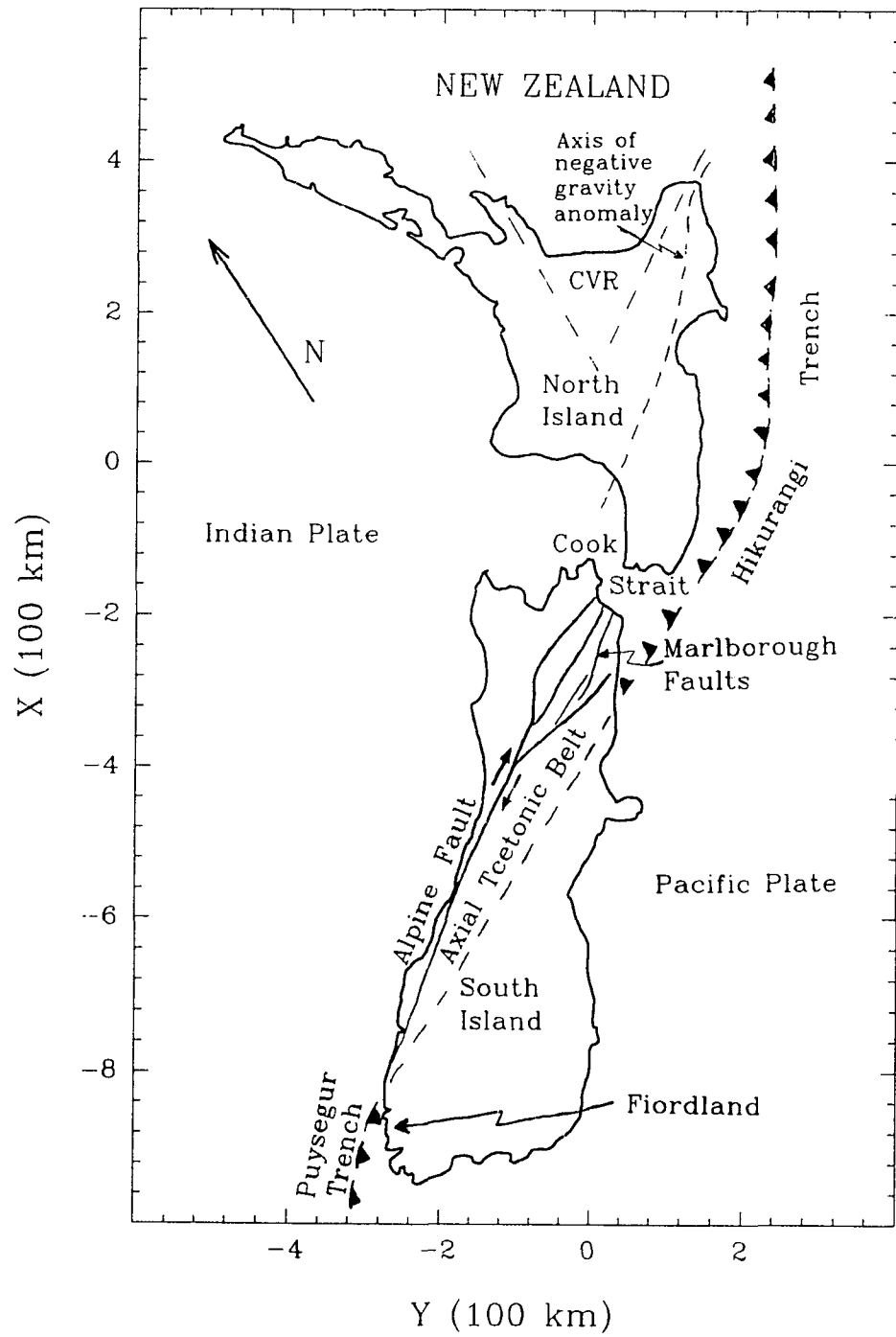


Figure 5.5: The tectonic setting in the New Zealand region.

Subduction here (Fiordland) is believed to have occurred only during the last 7 million years, while the oceanic lithosphere of the Indian Plate has been in contact with the continental lithosphere of the Fiordland region (Davey and Smith, 1983). Seismicity at depths greater than 15 km (see Fig. 5.4) is indicative of this subduction in this south-western region of New Zealand. Opposite to the subduction to the east of North Island, where the Pacific Plate subducts beneath the Indian Plate, a small section of the Indian Plate in the Fiordland region (southern tip of South Island) is subducting under the Pacific Plate. Davey and Smith (1983) delineated a steeply dipping ($>60^{\circ}$) planar zone of intermediate depth earthquakes, that indicated subduction of the Indian Plate at this approximate angle under the Pacific Plate.

Between the North and South Island subduction zones, and through the centre of South Island, the Indian and the Pacific Plates are both continental in nature, and are compressing the terrain and sliding past each other to form the Alpine and Marlborough Faults system (Arabasz and Robinson, 1976). Relative motion between the boundaries of the Pacific and Indian Plates through New Zealand is currently 30-50 mm/year (Walcott, 1978). The area between the Pacific Plate boundary and the Alpine-Marlborough Faults comprises the axial tectonic belt (Walcott, 1978) in which the deformation due to the differential motion between the plates is accommodated. The relative movement between the plates is absorbed to a very large extent by distributed movement within the axial tectonic belt. The shallow depth seismic activity (Fig. 5.4) supports the premise that the boundary between the Pacific and Indian Plates in the New Zealand region is a wide zone of distributed deformation.

The Central Volcanic Region (CVR), and the axis of negative gravity anomaly, on North Island are also shown in Fig. 5.5. The Central Volcanic Region (CVR), a triangular area on North Island, and extending off shore, is an active region of intensive volcanism, with very high heat flow, and with a thin crust (Smith et al., 1989). The CVR is generally considered to be an active back-arc basin associated with the Hikurangi convergent margin and formed within continental lithosphere (Stern and Davey, 1987). The volcanic rocks of the Central Volcanic Region are very young, being less than 1 million years old (Walcott, 1987). Heat flow in the eastern part of the CVR is as high as 700 mW/m^2 , or about 12 times the continental average (Walcott, 1987). This region contains the majority of the important geothermal fields in New Zealand. Reilly (1978) showed negative Bouguer anomalies along an axis diagonally across the central regions of North and South Island. One of the interpretations associates the North Island negative gravity anomaly with a crustal down-warping at depth (Hatherton, 1970; Kayal, 1984).

Lateral segmentation (or tears) in the subducting Pacific Plate has been indicated by seismological data. For example, Robinson (1986) has suggested that a tear in the plate exists at the southern end of North Island. Figure 5.6a shows a sketch of the plate interface configuration as seen from the west (adapted from Robinson, 1986). The plate interface appears to be disrupted along a NW-SE line through Cook Strait (see profile AA' in Figs. 5.6a and 5.6b), with the plate interface believed to be offset vertically by 7 km on average. Other down-dip tears in the subducted Pacific Plate have been suggested by Reyners (1983) 200 km to the northeast of Wellington, and in the northern Hawke Bay region, as well as in the northern region of South Island, as shown in Fig. 5.6b. The termination of deep

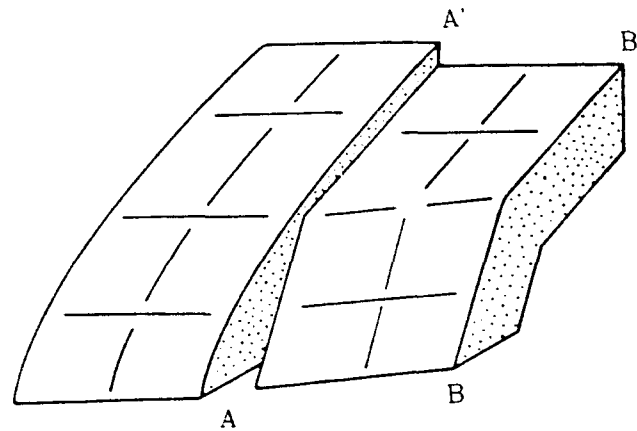


Figure 5.6a: The subducted Pacific Plate as viewed from the west (adapted from Robinson, 1986). See also profiles AA' and BB' in Fig. 5.6b.

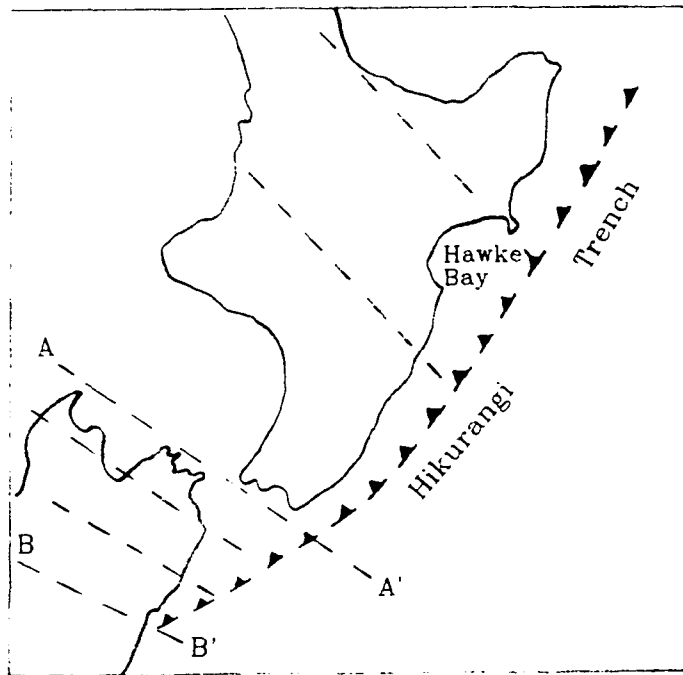


Figure 5.6b: Possible segmentation (dashed lines) of the subducted Pacific Plate (adapted from Reyners, 1983). The AA' and BB' profiles refer to Fig. 5.6a above.

earthquakes near the northern end of South Island (as seen in Fig. 5.4), supports the premise of a tear (see profile BB' in Figs. 5.6a and 5.6b) in the subducting plate that defines the edge of the down-going plate. These tears and offsets would affect the electrical conductivity of the New Zealand substructure, and thus be expected to lead to anomalous geomagnetic responses at appropriate periods.

Figure 5.7 shows the New Zealand physiography, emphasised by the 1-2 km altitude range (shown in black), and fault locations (adapted from Suggate, 1978; Campbell, 1992; Thornton, 1993; Beanland, 1994; Cowan, 1994). It is seen that faults occur generally along the mountain ridges, and thus many of the larger faults have strikes roughly parallel to the coastlines. Most of the recent faults show both vertical and lateral displacement. The fault depths are believed to vary considerably, with some extending to moho depths, and others of shallow depth extents. Some examples are: the Wellington and Wairarapa Faults are believed to extend to depths of 20-30 km (Darby and Beanland, 1992) and both dipping to the west; the Alpine Fault (boundary between the Pacific and Indian Plates) would extend to depths of 20-50 km and is thought to dip to the east at angles of up to about 45° (Grindley, 1978) in the central regions of South Island. While many major faults are roughly parallel to the coastlines, the short faults have strikes at all directions, even perpendicular to the coastlines. This is particularly true on South Island, where the rate of relative motion between the Pacific Plate and the Indian Plate decreases southward. It is understood that many faults could be highly conductive because of the presence of water or solution in a zone of high porosity. Thus, anomalous geomagnetic fields are expected in New Zealand due to the presence of conductive faults in a survey region.

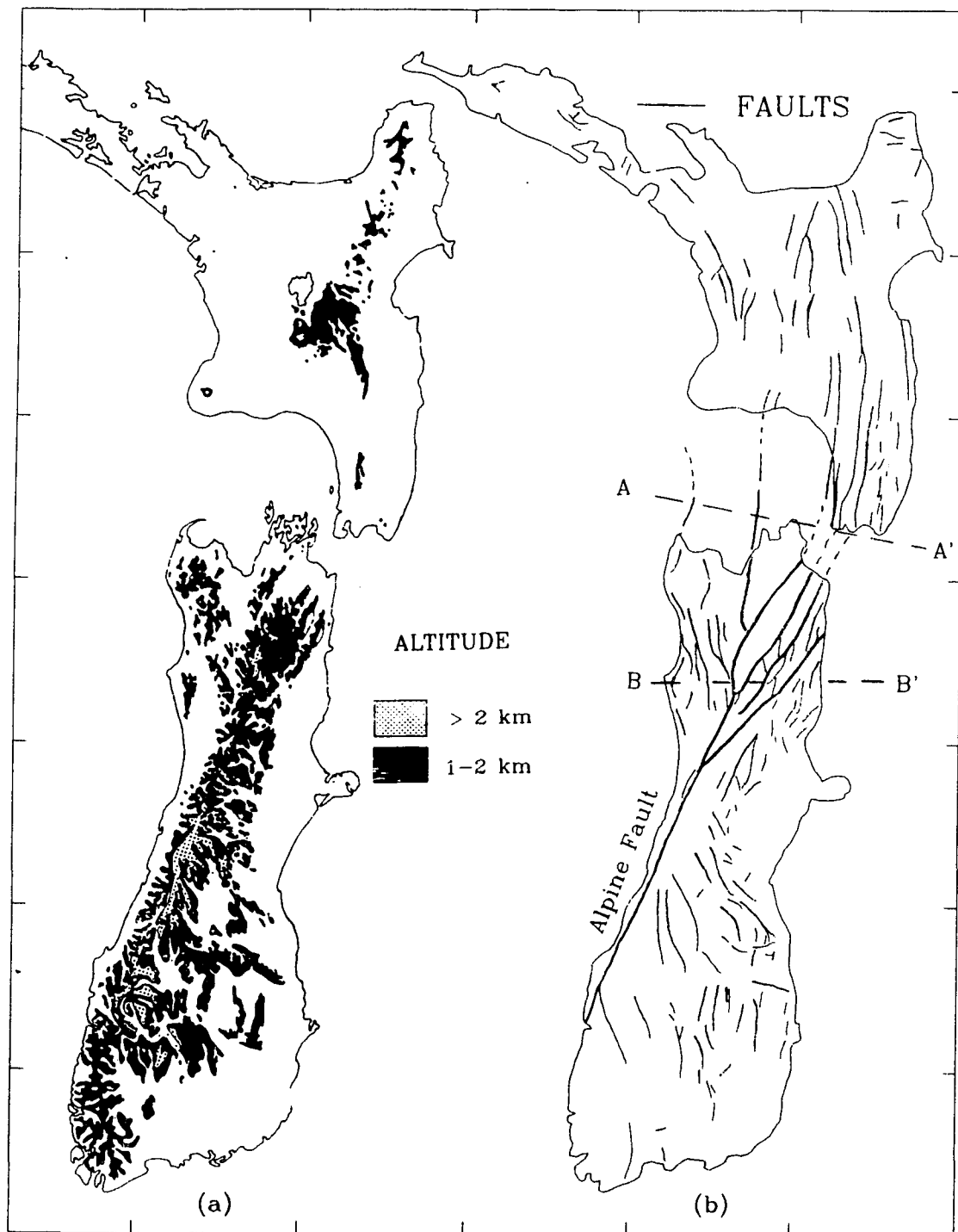


Figure 5.7: a) The New Zealand physiography. b) Fault distribution of New Zealand (adapted from Suggate, 1978; Campbell, 1992; Thornton, 1993; Beanland, 1994; Cowan, 1994). For profiles AA' and BB' see Fig.5.6.

Figure 5.8 shows the many sedimentary basins in offshore and onland regions of New Zealand (adapted from Czochanska et al. 1987). The dotted lines in Fig. 5.9 are 200 m ocean depth contours. The sedimentary basins in New Zealand have a wide range of depths. Walcott (1987) and Barnes (1990) have suggested that a sedimentary wedge of up to 18 km thick has been formed between the east coast of North Island and the Hikurangi Trench. It is likely that a substantial part of the accumulated sediments has been transported below the crust on top of the subducted Pacific Plate. Some of the basins, such as the Taranaki Basin of North Island and the Westland Basin off the west coast of South Island, have petroleum potential. It is well known that sediments with fluid content are conductive materials, and thus sedimentary basins (and their boundaries) are expected to result in anomalous geomagnetic field responses.

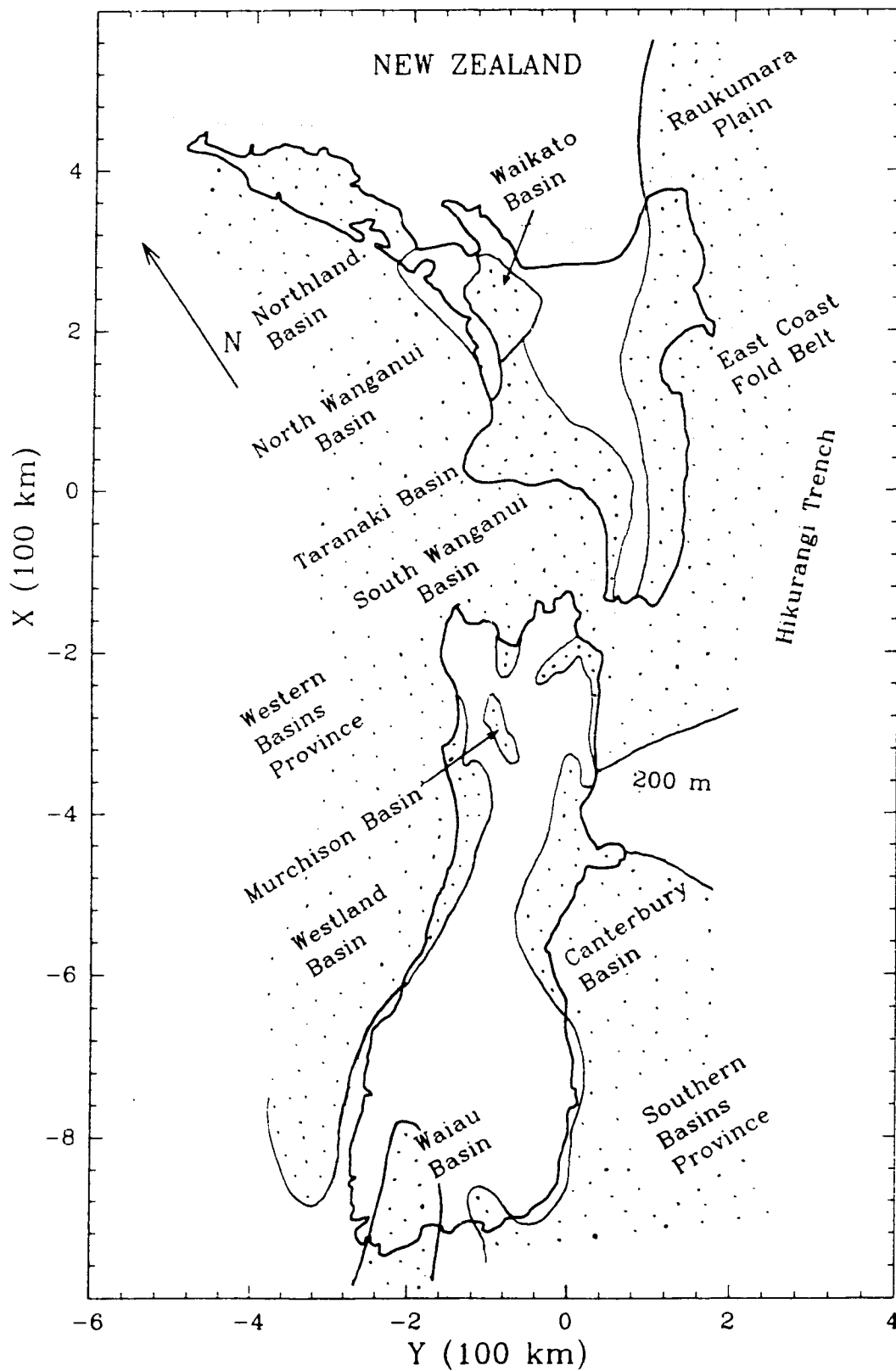


Figure 5.8: Sedimentary basins of New Zealand (adapted from Czochedanska et al., 1987).

5.2 Chapter Summary

The geological and tectonic structure of the North Island of New Zealand is typical of that found in active continental margins and island arcs. It includes an offshore oceanic trench (Hikurangi Trench), a belt of active volcanism, a zone of crustal and mantle earthquake activity, numerous faults, and large negative gravity anomalies. The geological structure of South Island is quite different in that active subduction occurs only at the northern and southern tips, with the transcurrent Alpine Fault (extending to Moho depth) at the boundary between the Indian and Pacific Plates joining the two regions of subduction. The region throughout much of South Island is mountainous and highly faulted.

The electrical conductivities associated with the complex geological and tectonic structure, the two oppositely directed subduction zones, numerous faults, active volcanoes, sedimentary basins, Cook Strait between the North and South Islands, and the proximity of the oceans for all sites would be expected to lead to a wide range of onland anomalous geomagnetic responses. The present work of employing analogue model electromagnetic measurements to aid the interpretation of geomagnetic measurements in the New Zealand region supplements other geophysical studies, and should aid our understanding of the geological structure of the region.

Chapter VI
ANALOGUE MODEL EM RESPONSES IN THE NEW ZEALAND
REGION

6.1 The Analogue Model of the New Zealand Region

Figure 6.1 shows a simplified map of the New Zealand region (2800 x 2800 km²), including the surrounding ocean with its depth contours used as a pattern to construct the analogue model in the present work. In the map, the coastlines have been smoothed to eliminate the extremely shallow inlets.

In the laboratory model of the New Zealand region, graphite plate (1.4 x 1.4 m²) and grafoil (laminated graphite foil) of appropriate scaled thicknesses and shaped according to the contour map in Fig. 6.1 were used to simulate the ocean and a horizontal conductive asthenosphere at a depth of 100 km. Although restricted by model materials, the geophysical model conserves the integrated conductance (σz) as nearly as possible. The ocean model was supported on a fibreglass screen mounted on a plywood frame suspended at the surface of the salt solution in the tank. The model conductive substratum was constructed as a separate unit and suspended at a simulated depth of 100 km below the model ocean.

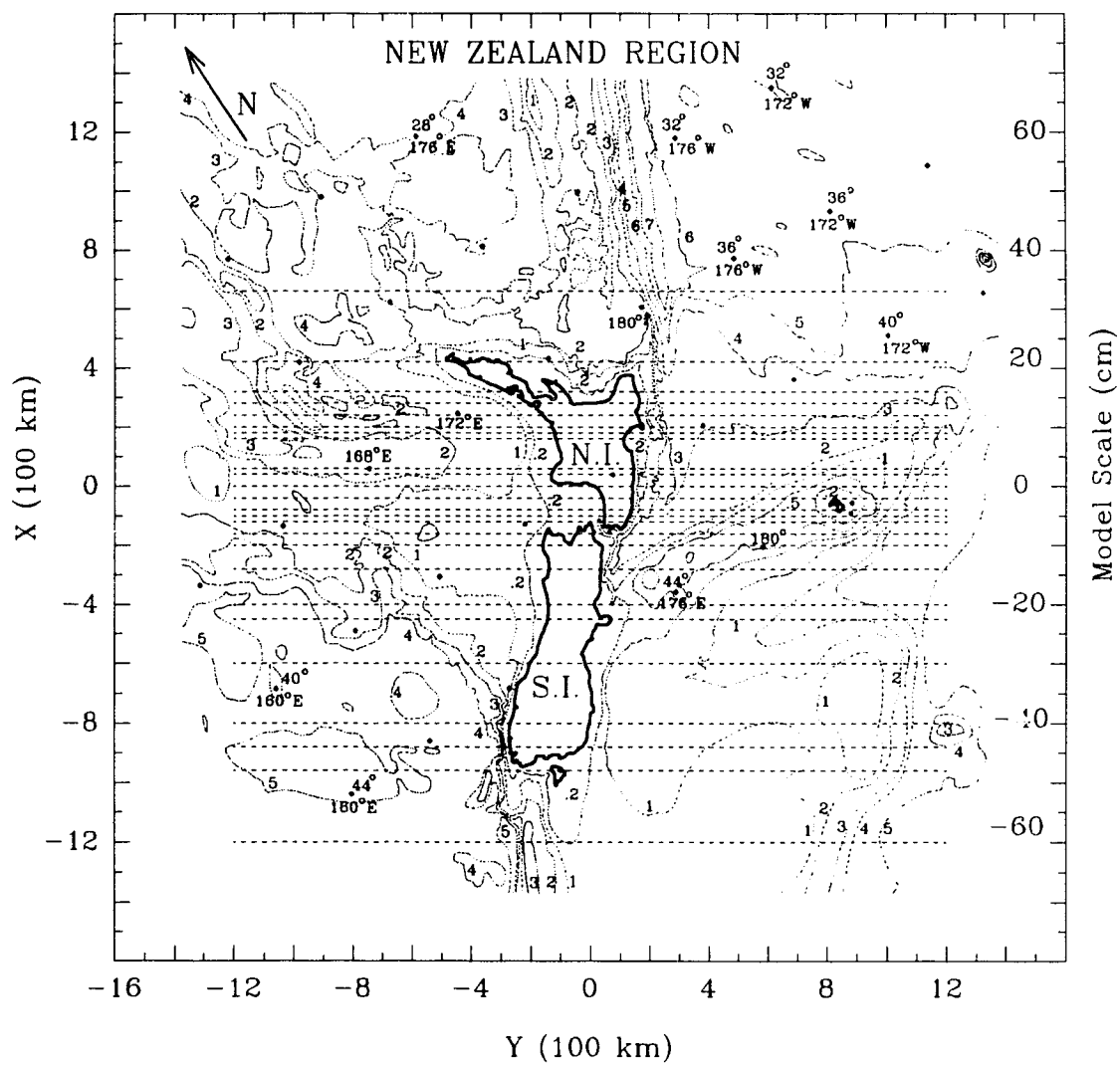


Figure 6.1: Simplified map of the modelled New Zealand region including the ocean bathymetry and showing the model traverses for which model measurements were carried out.

6.2 Analogue Model Magnetic Field Components in the New Zealand Region

The in-phase and quadrature magnetic field components (B_x , B_y and B_z) for the simulated period range 5-120 min were measured for a grid of 25 traverses (horizontal dashed lines in Fig. 6.1) over the New Zealand model for two perpendicular source field polarizations. The field polarizations relative to the model in Fig. 6.1 are here chosen as X- and Y-polarizations for the electric field of the source in the X- and Y-directions respectively. For each polarization the source field was held constant at each period for all measurements (in-phase $B_y = 1$ nT and quadrature $B_x = 0$ nT for X-polarization, and in-phase $B_x = 1$ nT and quadrature $B_y = 0$ nT for Y-polarization) at a simulated land reference location in the model tank well away from the model ocean. In the present work, the time variation of the field is taken to be described by $\exp(i\omega t)$ and thus the quadrature component leads the in-phase component by 90° .

The oceans surrounding both North Island and South Island are expected to play an important role in the geomagnetic field responses due to the proximity of the ocean for all onland locations. In addition, the effect of coastal bays and capes, as well as the Cook Strait separating the two islands, will add to the complexities of the responses. Cook Strait links the Pacific Ocean with the Tasman Sea and is a highly three dimensional structure. The analogue model results should readily delineate these anomalous coastal responses. Although detailed measurements were carried out for periods of 5, 10, 15, 20, 25, 50, 80 and 120 min for 25 traverses over the entire laboratory model of the New Zealand region, only the results for 16 selected traverses will be discussed here. These traverses were chosen in order to examine the coast effect responses onland near a variety of coastal

features, such as the ocean strait, capes, bays, and a range of near shore ocean bathymetries.

Figure 6.2 shows the coastal features in the New Zealand region, traverses N1 to N8 on North Island, and traverses S1 to S8 on South Island. For X-polarization, as described earlier, electric current is induced in the X-direction, and thus on the north-east coast, flows roughly parallel to the coastline. As a consequence, the coast effect expected inland for this polarization is expected to be approximately that for a simple straight coastline. The responses inland on the opposite coast (north-west of North Island) should be somewhat modified by the greater complexities of the coastline contour due to current deflection where the local coastline forms some non-zero angle relative to the inducing electric field. Some part of the current induced in the regions north of the North Island will be deflected eastward to flow along the Hikurangi Trench, and some part will be deflected to flow along the opposite coast. This deflection of current to either side of the islands will lead to increased current density along the two coasts, and thus lead to enhanced electromagnetic fields for coastal as well as inland sites.

As an example of the vertical field B_z responses along traverses over the New Zealand model, Fig. 6.3 shows the in-phase and quadrature B_z components (in unit of nT) at a simulated period of 10 min for traverses N1-N8 and S1-S3 on the North and South Island respectively. This 10 min period example is chosen to demonstrate changes in coast effect responses from traverse to traverse over the model. It is seen that the in-phase B_z responses change from positive on the westerly coast to negative on the easterly coast, reversing sign roughly mid-way between the two coastlines. In general, the maxima in the in-phase B_z responses do not

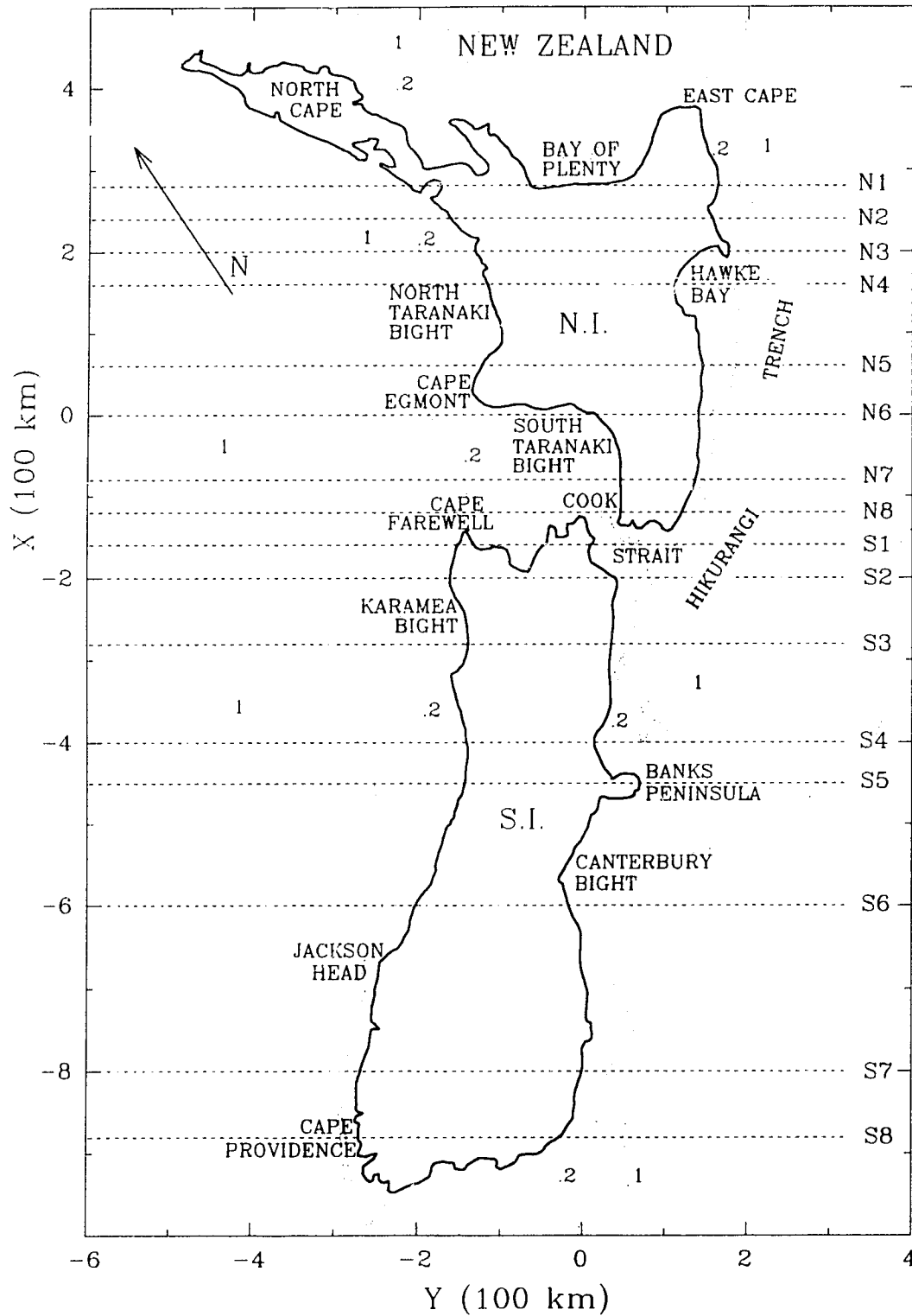


Figure 6.2: Simplified map of New Zealand showing the selected traverses N1–N8 on North Island and S1–S8 on South Island.

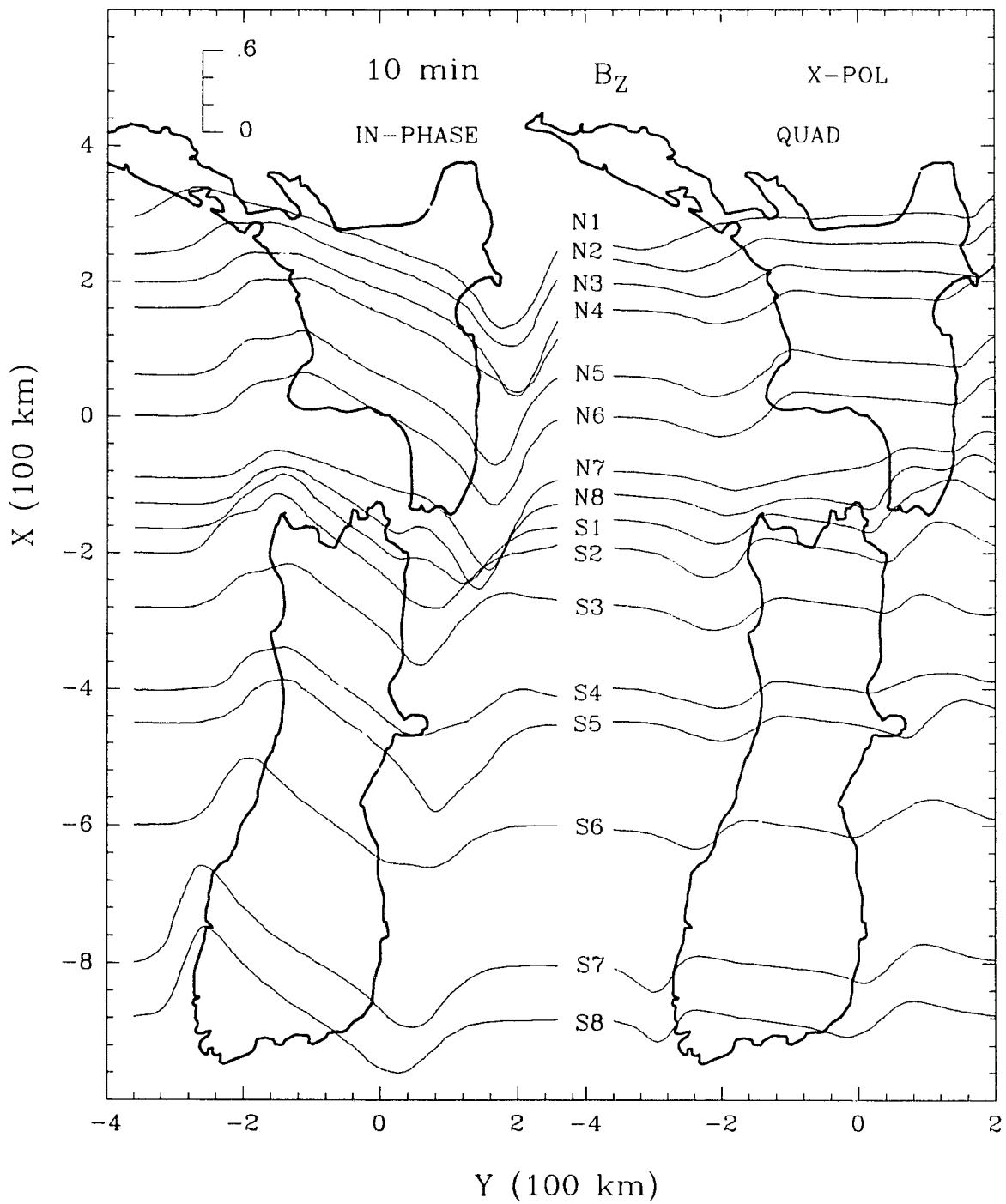


Figure 6.3: The in-phase and quadrature B_z along traverses over the model at 10 min for X-polarization.

occur right at the coastline, but rather some distance offshore where the ocean depth is increasing rapidly. For example, for traverses N3-N6 at the shallow ocean west coast region, the ocean depth gradient at roughly $Y=-200$ km (see Fig. 6.2) leads to the broad offshore coast effect-like responses observed in both the in-phase and quadrature B_z . On the east coast of North Island the coast effect response maximum occurs very much nearer the coastline in response to the nearby sharp ocean depth gradient. For the North Island, the maxima in the B_z response curves are greater on the easterly coast than those on the westerly coast, due to the strong current induced in the Hikurangi Trench east of the North Island (see Fig. 6.2). On the south-west of South Island, however, the ocean is much deeper off the west coast than it is off the east coast, resulting in the larger B_z responses observed at the west coast for S7 and S8 than those at the east coast. It is interesting to note that, although only a small portion of the traverse S1 crosses land (Cape Farewell) at the west coast, the B_z response for S1 at the west coast is almost identical to the corresponding responses observed for N8 and S2. This could be anticipated since the ocean depth in the South Taranaki Bight is very shallow, so that induction in the offshore deeper ocean (also roughly parallel to the west coast of South Island) plays a larger role in the response for X-polarization. Over the Banks Peninsula (see Fig. 6.2) along S4, the in-phase B_z response shows a large maximum due to the current concentration around the peninsula (cape effect). As is typical for induction at short periods, the B_z quadrature component is seen to show a smaller response than that of the in-phase component at this 10 min period. Over the North Island the quadrature B_z responses are everywhere positive, while over the South Island the responses reverse sign at

some points along the traverse, again from positive on the westerly coast to negative on the easterly coast. (The field response curves for other periods will not be discussed further here, but response curves for all three components B_z , B_y and B_x for periods $T=10, 25, 50, 80$ min for X- and Y-polarizations are provided in the Appendix D).

6.3 Induction Arrows in the New Zealand Region

The in-phase and quadrature magnetic field components discussed briefly for B_z at 10 min in the previous section, and for the other components and periods provided in Appendix D, were used in equations 1.9 and 1.10 to calculate the in-phase and quadrature parts of the V_x (x-component) and V_y (y-component) induction arrow components at detailed points along the many traverses over the New Zealand analogue model. As an example, the in-phase and quadrature V_x and V_y response curves are shown in Figs. 6.4 and 6.5 respectively for the 16 traverses at 10 min period. The signs of both the in-phase and quadrature responses have been reversed following the convention of Lilley and Arora (1982) for time-varying fields of the form $\exp(i\omega t)$, so that both the in-phase and quadrature arrows point towards current concentrations. Values along a response curve that are positive relative to the dotted zero base line indicate components in the positive direction (+X for V_x and +Y for V_y), while values negative relative to the base line indicate induction arrow components in the negative direction (-X for V_x and -Y for V_y). Thus, each of the in-phase and quadrature induction arrows at a given site along the traverse can be formed by using the appropriate V_x and V_y component values given for that site. The induction arrow response curves to be used for determin-

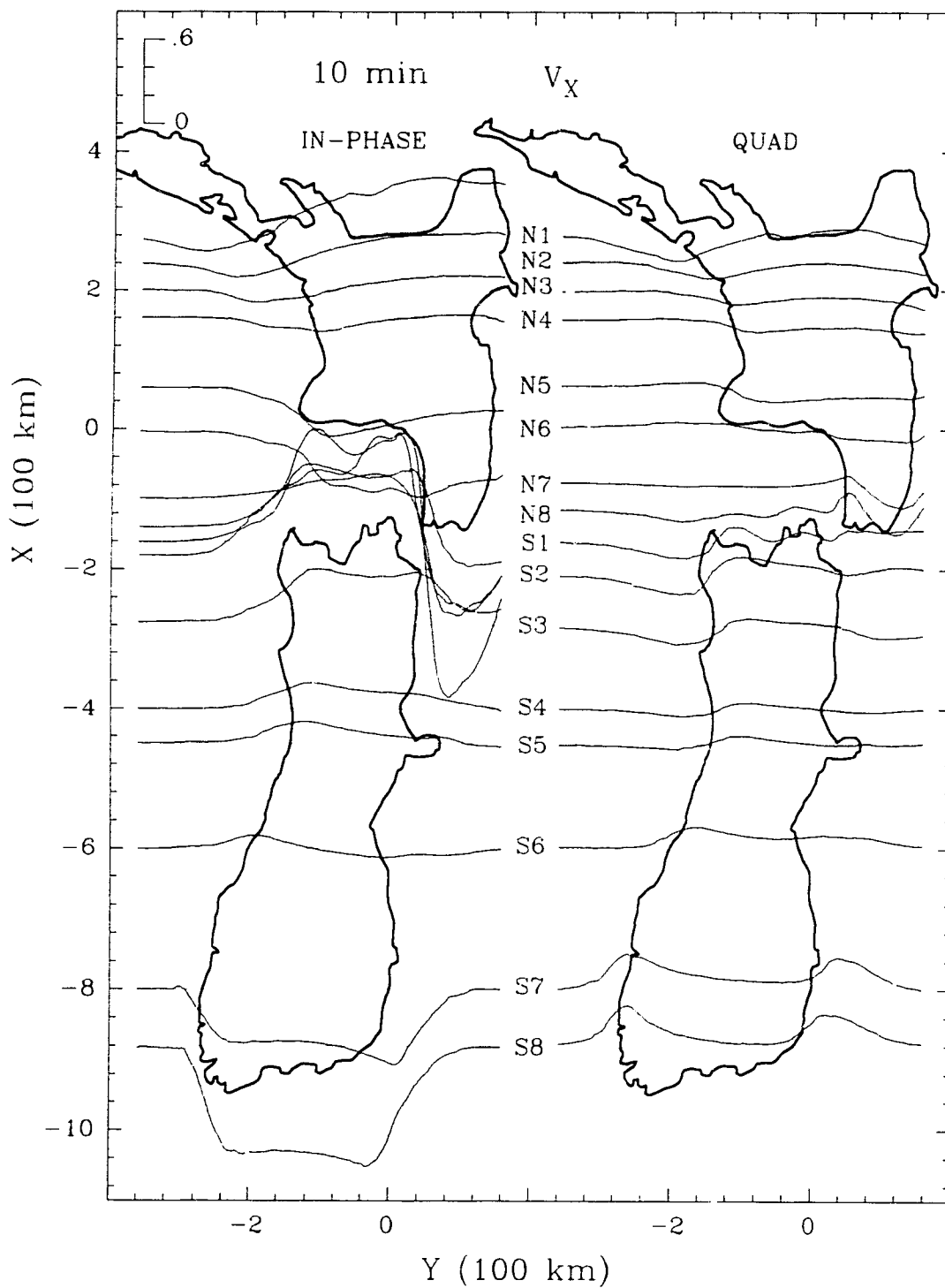


Figure 6.4: The in-phase and quadrature V_x (x-component of the induction arrow V) response curves at 10 min for traverses over the model.

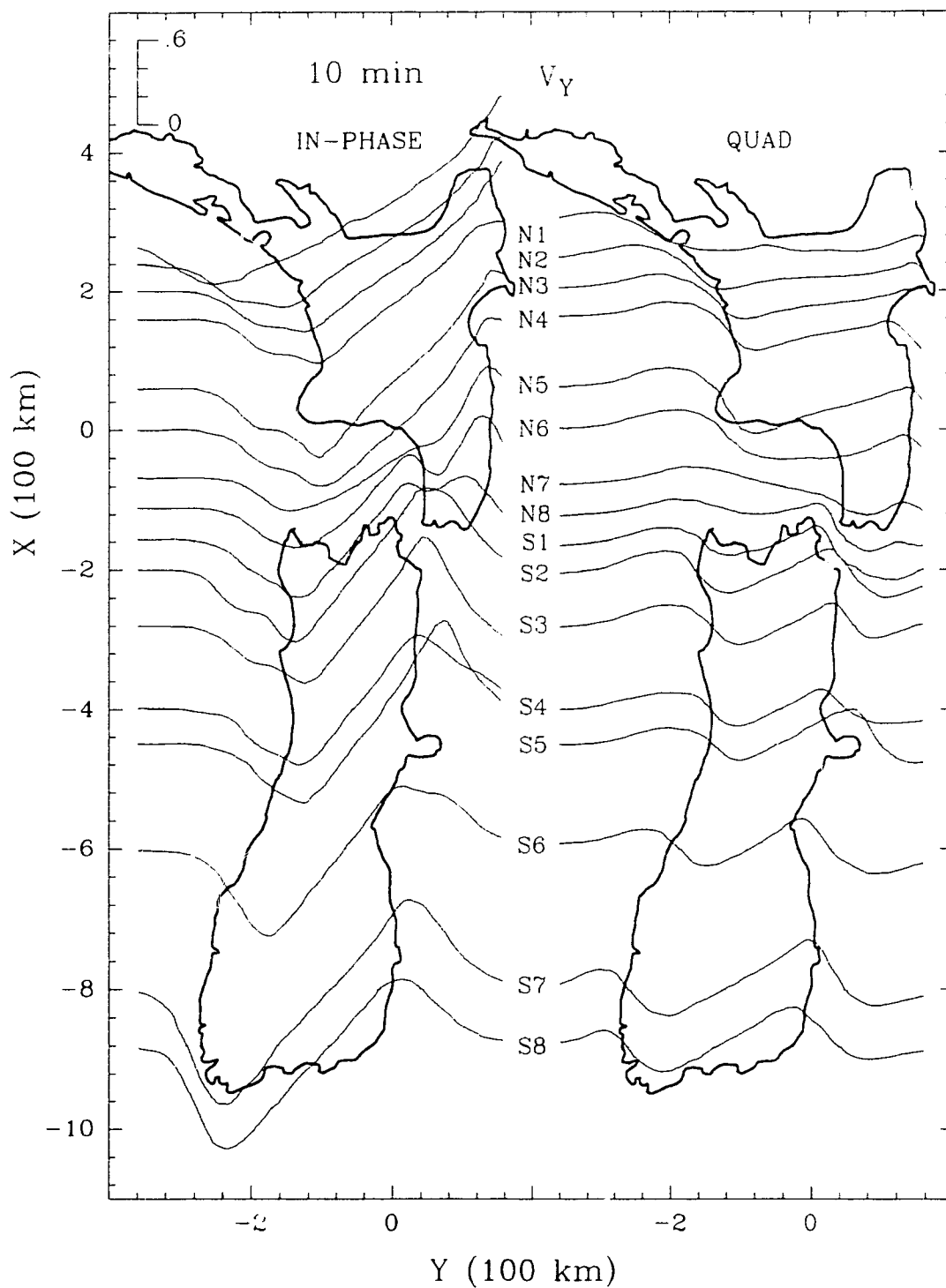


Figure 6.5: The in-phase and quadrature V_y (y-component of the induction arrow V) response curves at 10 min for traverses over the model.

ing the induction arrows for given sites for additional periods (5, 15, 20, 25, 50, 80, 120 min) are provided in Appendix E. Induction arrows determined using these responses curves will be discussed in some detail in sections 6.3.1 and 6.3.2.

6.3.1 Induction Arrows Along the North Island Model Traverses

Figure 6.6, to be used for reference in discussing the model induction arrows in detail, shows the North Island map with ocean bathymetry and labelled coastal features, as well as the location of traverses N1 to N8. The in-phase induction arrows along traverses N1 to N8 on North Island for $T=5, 10, 20, 50, 80$ and 120 min are shown in Fig. 6.7. In the northern regions (N1-N4) the in-phase arrows at coastal sites for the short periods of 5-20 min generally point directly towards the nearest ocean, with the largest induction arrow lengths observed at the easterly coast due to the cape effect (enhanced response due to current concentrations as a result of induced current deflected around the East Cape). The shortest length (or zero) arrows found at the central regions along N3 and N4, are due to the sum of opposite sign coast effects of the easterly and westerly coasts. The location for zero response (with accompanying reversal) is seen to shift towards the west coast with increasing period, due to increasing current density on the east coast due to the cape effect of the East Cape, and the decreasing current density off the west coast due to the bay effect of the North Taranaki Bight. This shift westward with increasing period is also in part due to greater current induction in the deeper ocean off the east coast as compared with induction in the much shallower ocean off the west coast. With increasing period, the arrows in the northern regions of North Island are seen to reach maximum magnitudes at 20-50 min and then decrease in length with further increasing period. The arrow directions at

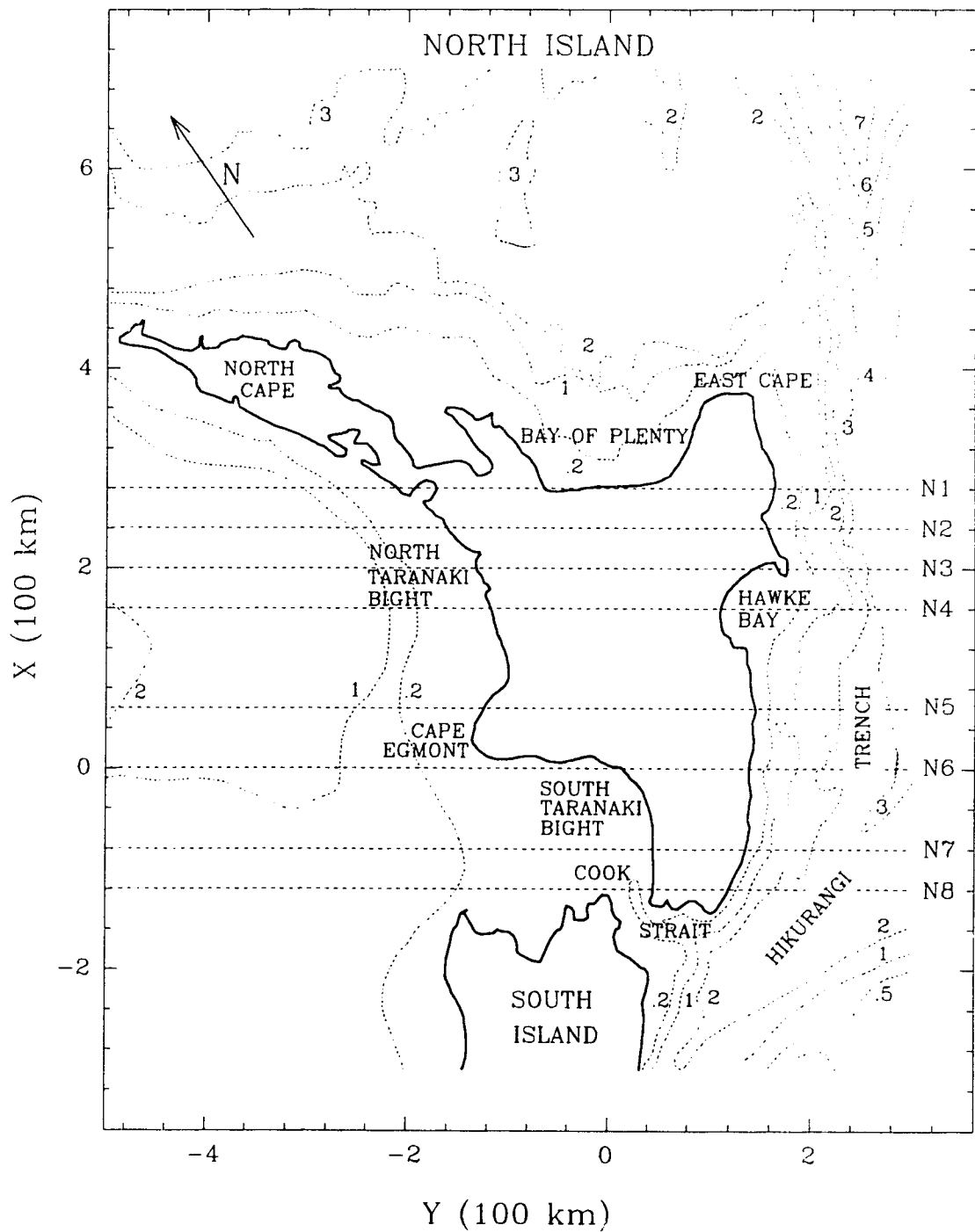


Figure 6.6: Simplified map of the New Zealand North Island showing the location of the model traverses (N1–N8) for which model induction arrows are provided.

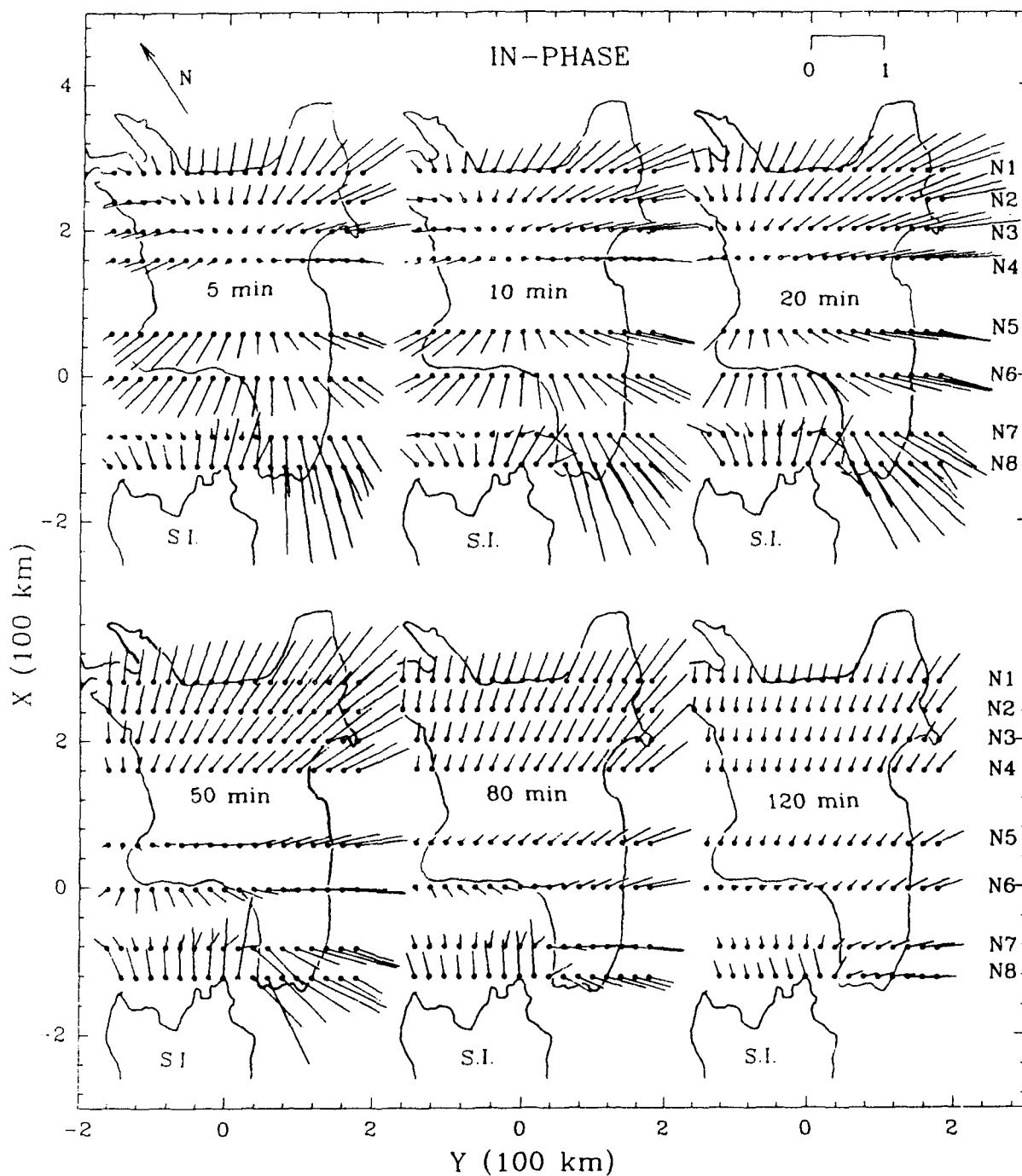


Figure 6.7: The in-phase induction arrows for traverses N1-N8 on North Island for periods of 5-120 min.

T=20-120 min rotate northwards with increasing period to point more towards the deep ocean north-east of North Island. At the long periods of 80-120 min, the arrows along N1-N4 (including the west coast sites) point in the north-east direction towards the deep ocean off the East Cape (see Fig.6.6), due to decreased induction in the west coast shallow oceans at long periods.

As was the case for the northern regions, the arrows in the southern regions of the island (N5-N8 in Fig. 6.7) also point towards the nearest ocean at the short periods of 5-20 min. Electrical currents induced in the oceans east or west of the island for the Y-polarization are forced, as they approach the island, to flow around the much more resistive land masses, or to channel through the narrow Cook Strait. The channelling of current through Cook Strait, as well as the deflection of current by the South Taranaki Bight coastline (see Fig. 6.6), results in the large current concentrations in the Cook Strait region at short periods. The long arrows at points along traverse N8 over the Strait and the southern tip of the island clearly show this channelling effect at short periods, with the arrows pointing towards current concentrations in Cook Strait. With increasing period the arrows in the southern region (N7-N8) of the island are seen to generally rotate counter-clockwise to point more directly towards the deep ocean in the Hikurangi Trench (see Fig. 6.6) as expected. At the east coast N4 region the arrows at 5 min are roughly parallel to the traverse, indicating equal current deflection northward and southward. This region of equal current deflection shifts to N6 at 50 min and N8 at 120 min, indicating increased current deflection around the northern end of the island, and decreased current channelling through Cook Strait at the southern end, with increasing period. In coastal regions, the arrow lengths, generally large

at short periods, are much decreased at long periods, as expected for the typical coast effect.

Figure 6.8 shows the quadrature arrows for North Island. At the short periods of 5-10 min, the quadrature arrows at coastal sites for all traverses are seen to generally point away from the oceans, in the directions which are roughly opposite to those of the in-phase arrows (Fig. 6.7). With increasing period these arrows rotate to roughly reverse directions so as to point towards the ocean at periods greater than 20 min, in directions similar to those of the in-phase arrows. For example, the quadrature arrows at the west coast and offshore in the shallow North Taranaki Bight (N2-N4) and Cape Egmont (N5-N6) regions point landward at 5 min, are roughly zero at 10 min and have reversed directions to point seaward at 20 min. This type of reversal, expected at short periods, and being characteristic of the coast effect response for an ocean underlain by a conductive layer at depth, is discussed in some detail in the next section (6.3.2). The quadrature arrows for N1-N4 at the east coast and offshore (East Cape and Hawke Bay regions), tend to reverse directions at periods greater than 20 min, probably due to the cape effect (N3), the bay effect (N4), and the increasing induction in the deep oceans off the east coast. At 50 min, the arrows for traverse N4 at the east coastal region point roughly perpendicular to the coast, with the arrows at sites north of N4 (N1-N3) pointing northward, and arrows at sites south of N4 (N5-N8) pointing southward. Again, as was the case for the in-phase arrows (Fig. 6.7), this dividing line with increasing period moves southward to N5 at 120 min, due to sustained quadrature phase current channelled through Cook Strait and decreased quadrature phase current in the shallow Bay of Plenty to the north. Differing from the in-phase arrows

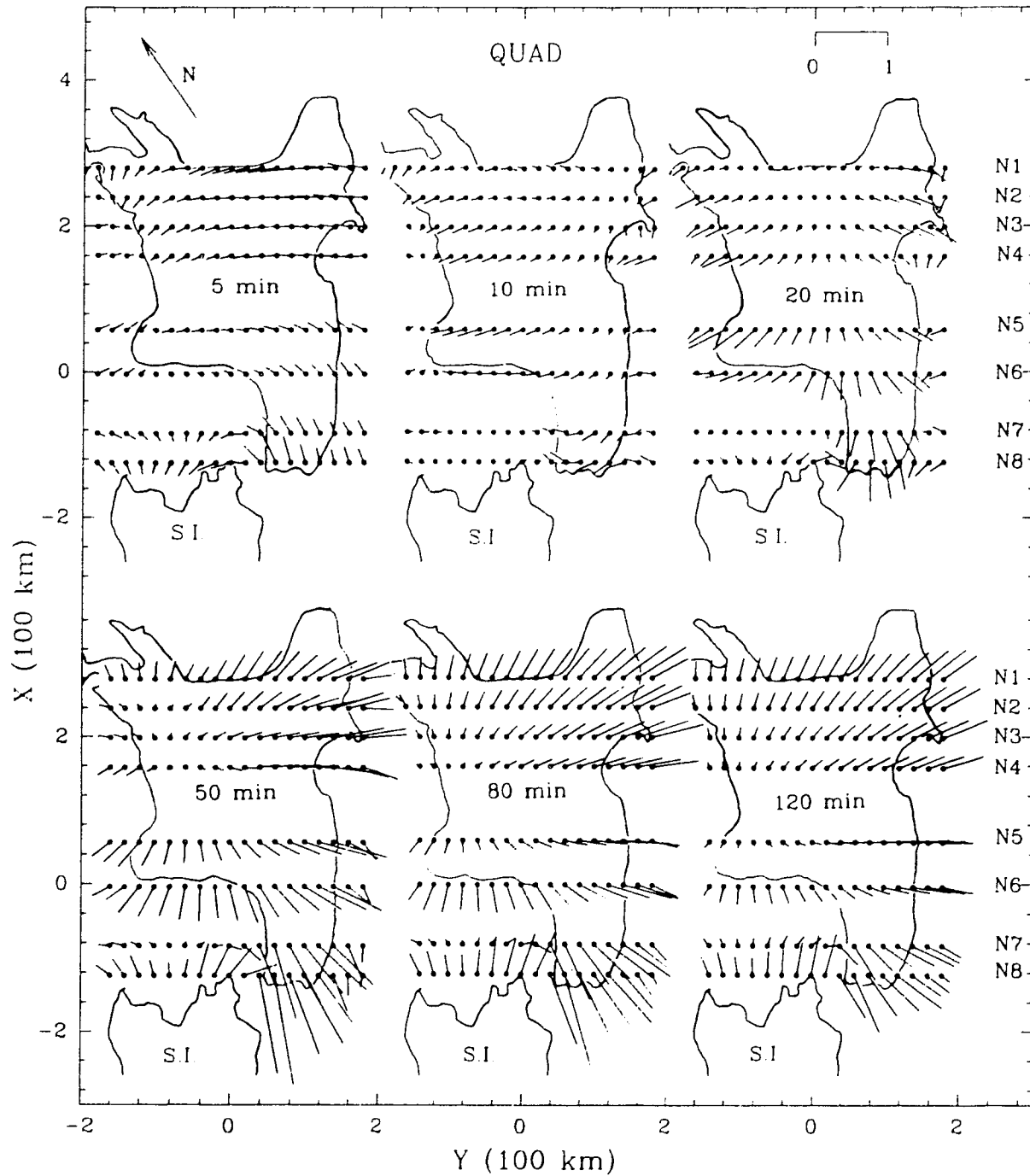


Figure 6.8: The quadrature induction arrows for traverses N1-N8 on North Island for periods of 5-120 min.

(Fig. 6.7), the quadrature arrows for N7 and N8 at the southern end of North Island show significant current channelling effect at the long periods of 50-120 min, due to the current induced in the deepest distant oceans (say to the east or west) being deflected vertically in the shallow sea while approaching land, then in part being channelled to flow through the shallow Cook Strait. This quadrature phase current induced at depth and channelled through Cook Strait leads to the sustained significant quadrature responses in the Cook Strait region. In general, the quadrature responses for the North Island are small at short periods (5-20 min) and significant at longer periods (50-120 min), with the responses at these longer periods being very similar to the responses seen for the in-phase responses (Fig. 6.7) at the shorter periods.

6.3.2 Induction Arrows Along the South Island Model Traverses

Figure 6.9, to be used for reference in discussing the model induction arrows in detail, shows the map of South Island with ocean contours and labelled coastal features, as well as the location of traverses S1-S8. The in-phase induction arrows along traverses S1-S8 across the South Island for periods $T=5, 10, 20, 50, 80$ and 120 min are shown in Fig. 6.10. At all coastal sites the in-phase arrows point seaward, a direction that is perpendicular to the induced current flow in the local oceans. The arrows for S1 and S2 show the effect of current channelling through Cook Strait very dramatically. As discussed for the North Island in section 6.3.1, the sustained responses over the large period range are due to currents induced in the deep ocean being deflected by the off-shore bathymetry and easterly coastline, and funnelled into Cook Strait. This channelling effect would be expected to decrease at the very long periods, as seen for the in-phase arrows for S1 and S2 at

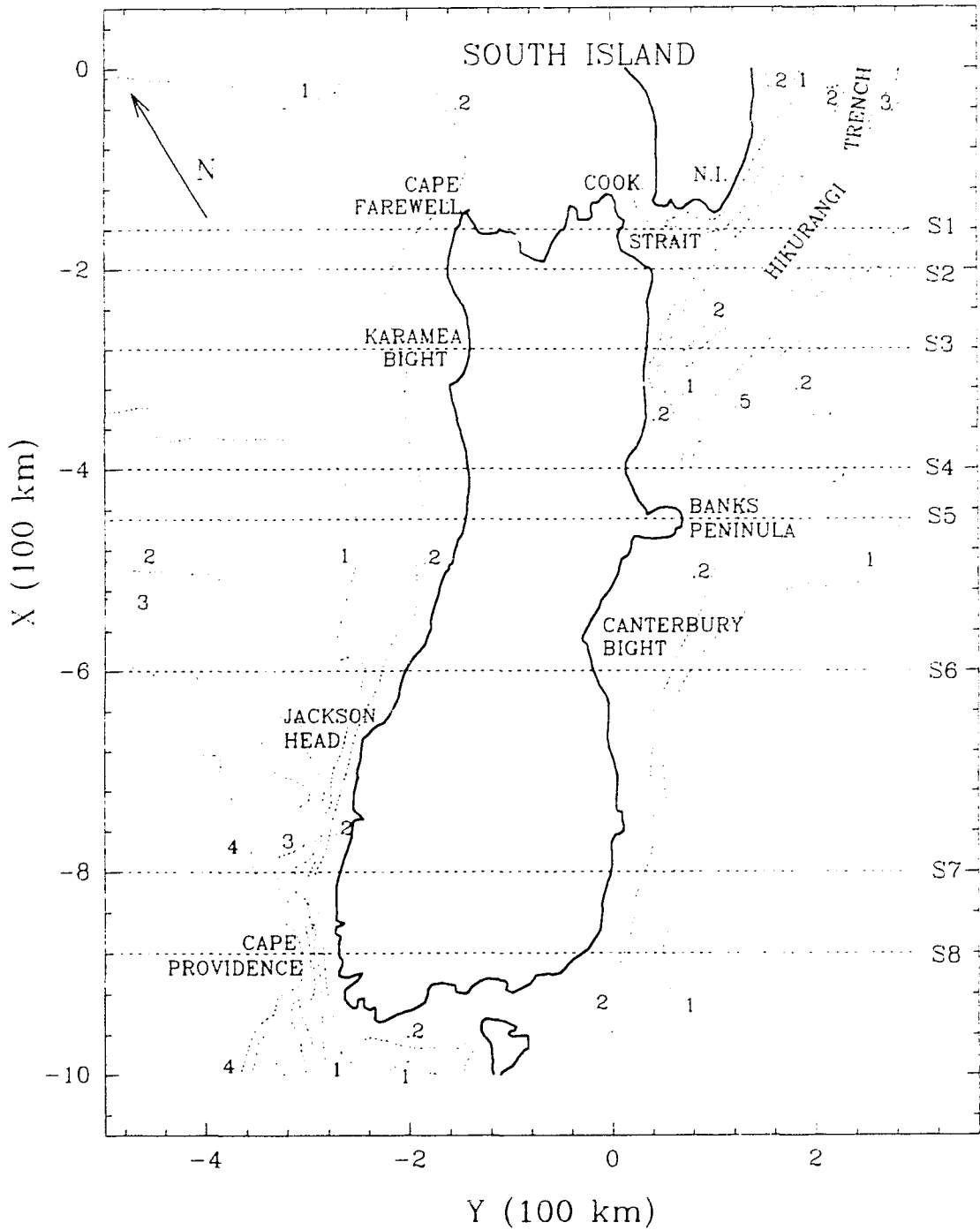


Figure 6.9: Simplified map of the New Zealand South Island showing the location of the model traverses (S1–S8) for which model induction arrows are provided.

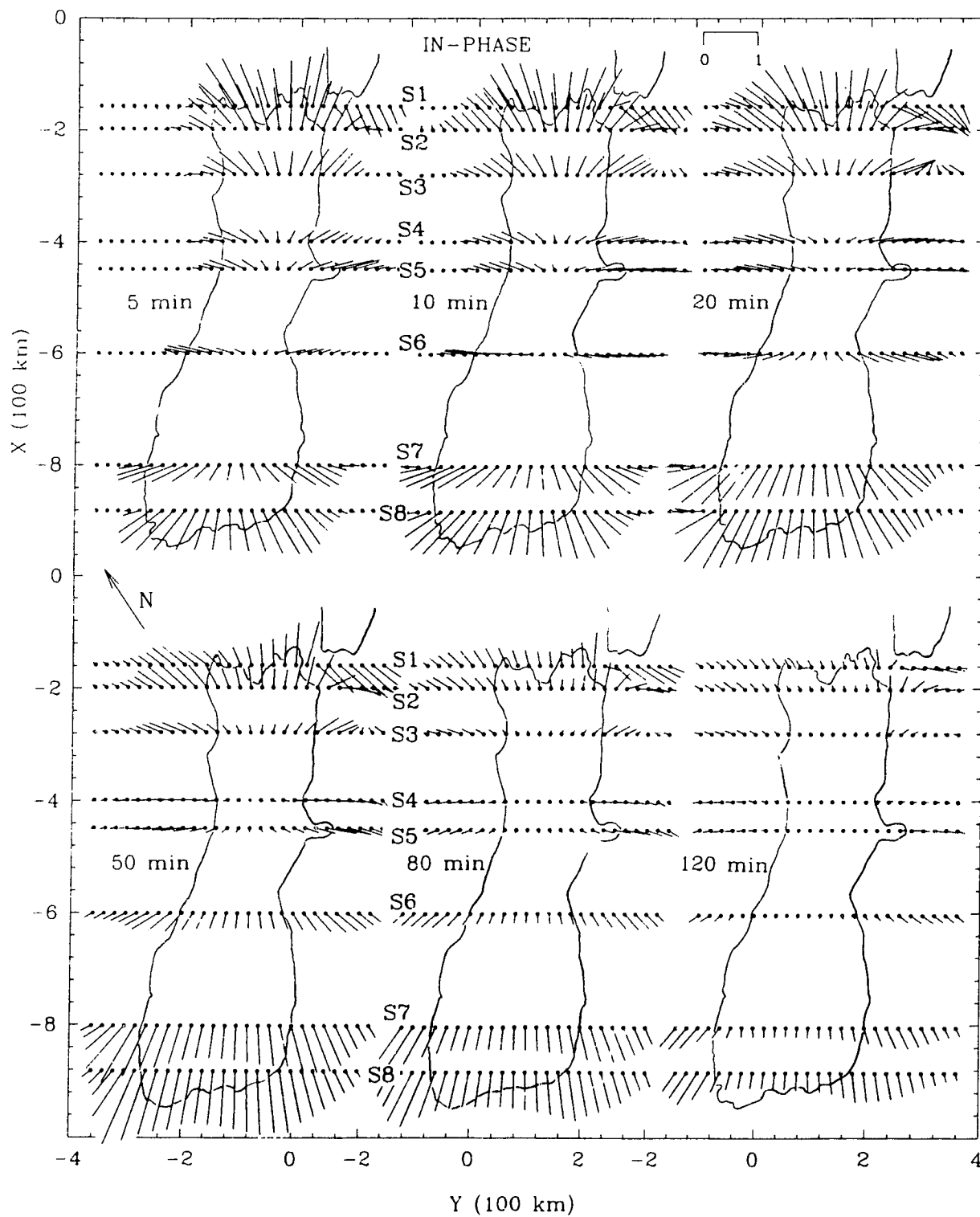


Figure 6.10: The in-phase induction arrows for traverses S1–S8 on South Island for periods of 5–120 min.

120 min, since the currents induced at increasing depth in the deepest ocean would in part be deflected by the ocean bottom depth profile to flow northward or southward, and thus less would be funnelled into Cook Strait. For each traverse the in-phase components at the coast show maximum responses at periods that vary somewhat from site to site. This could be expected on the basis of changes in current densities from site to site in the local ocean due to changes in current deflection and channelling with period. The in-phase response maxima for S1-S6 near the east or west coast occur at 10-20 min, while for S7-S8 the maxima occur at 50 min, showing increased current deflection southward with increasing period. At the east coast S1-S5 regions the in-phase arrows at 5 min indicate significant current deflection northward to the shallow Cook Strait, while at 10 min, the arrows parallel to the traverse S5 indicate equal current deflection northward and southward. At 50 min, this region of equal current deflection in opposite directions has shifted northward to S4. The in-phase responses are much diminished at all coastal sites (except at the southern tip) at 120 min.

The coastal quadrature arrows at 5 min shown in Fig. 6.11 for all traverses generally point landward (almost opposite to the direction of the in-phase arrow), while at 20 min the arrows have rotated to point seaward. Such a quadrature arrow direction reversal is observed, for example, in the S5 west coast region with the arrow pointing landward at 5 min and seaward at 20 min. It is noted that on the west coast at S5 (a region that is approximately 2-D), the quadrature response is minimum and the corresponding in-phase response (Fig. 6.10) is maximum at 10 min. Since the island can approximately be described as 2-D structure at short periods for regions somewhat remote from the northern and southern ends, such as



Figure 6.11: The quadrature induction arrows for traverses S1-S8 on South Island for periods of 5-120 min.

S5 region, these quadrature arrow reversals could be expected on the basis of the Agarwal and Dosso (1990) 2-D ocean-land numerical results which suggested a 5-10 min characteristic period (T_C). (T_C is the period for maximum in-phase and minimum quadrature response at a given coastal site, and for $T < T_C$ the quadrature arrow points landward, while for $T > T_C$ it points seaward.) At periods greater than 20 min ($T > T_C$) the quadrature responses generally mimic the short period in-phase responses. For example, the quadrature responses for all traverses at 50 min are very similar to the in-phase responses at 10-20 min (Fig. 6.10). For all sites on the island, the largest quadrature responses are seen to occur at the southern tip, and at a period of 80 min. For comparison with the in-phase component, the largest responses also occur at the southern tip, but at the shorter period of 50 min (Fig. 6.10). The quadrature responses continue to be significant over a large period range. The strong quadrature arrow responses for S1 and S2 at long periods correspond to currents induced at depth being deflected vertically to be channelled through the shallow Cook Strait. The significant quadrature responses at the southern and northern ends at long periods, attest to the importance of currents induced at depth in the deep oceans at long periods. This quadrature phase current approaching the island (say in the Y-direction) is deflected upward to shallower depths at the coast where it may divide to flow both northward and southward, as well as in part channelled through Cook Strait. Additionally, some of the current is deflected by the more distant ocean depth contours (see Fig. 6.1) to flow southward, resulting in the large quadrature responses shown for S7 and S8. Clearly the induction arrows observed for S1 at the northern tip of South Island and N8 at the southern tip of North Island show rather complex induction arrow responses in this Cook Strait region.

6.4 Chapter Summary

A scaled laboratory analogue model of the New Zealand region was constructed using graphite plate, machined to simulate the ocean bathymetry and the conductive substratum, and salt solution in a wooden tank to simulate the resistive host earth. Thus, the analogue model simulated the New Zealand coastlines and the surrounding oceans, as well as a horizontal conductive substratum at 100 km depth. Model magnetic field measurements were carried out along 25 traverses over the New Zealand model. These magnetic field components were used to calculate the in-phase and quadrature induction arrows for simulated geomagnetic variations of 5-120 min for 16 traverses over the North and South Islands. The V_x and V_y (x- and y-components of the induction arrow V) response curves are provided along these traverses.

Since New Zealand is relatively narrow, the model induction arrow responses for most onland locations show large effects of the surrounding oceans. The ocean bathymetry, the irregular coastlines, as well as Cook Strait between the North and South Island, lead to onland field anomalies due to induced currents in the ocean being deflected and channelled to produce local off shore anomalous current densities. The model induction arrows at short periods show the importance of current channelling in the shallow Cook Strait, while at longer periods show that an increasing proportion of the current induced in the deep ocean is deflected to the south of South Island and to the north of North Island. These complex coast effects for onland sites would clearly pose a difficulty in interpreting geomagnetic field measurements.

Chapter VII
INTERPRETATION OF ANALOGUE MODEL AND FIELD SITE
INDUCTION ARROWS IN NEW ZEALAND

Magnetotelluric (MT) and geomagnetic depth sounding (GDS) surveys have been conducted in the New Zealand region by several authors. Midha (1979) carried out extensive GDS measurements at 15 sites in the central region of North Island. Ingham (1985a, b, 1987, 1988b) carried out measurements at an additional 20 sites in the south-western (Cape Egmont) and southern regions of North Island. In the Southern Alps region of South Island, Bromley (1979) carried out measurements at short periods of up to 10 min at 26 sites, while Kellett et al. (1988) carried out measurements over a period of time at the Eyrewell Observatory (EYR). More recently, between November 1991 and April 1992, Chamalaun and McKnight (1993) operated an array of three-component magnetometers at 34 sites across New Zealand. Thus geomagnetic field data are available at 96 sites on North and South Island.

The analogue model induction arrow response curves (discussed in the previous Chapter and given in Appendix E) can be used to provide ocean effect reference values at the 96 sites, with some sites near the coasts and others inland. For cases of negligible electromagnetic mutual coupling of the ocean and any inland conductors, such as conductive faults and other geological structures, the difference arrows (field site induction arrows minus the analogue model arrows) should pro-

vide approximate responses of the anomalous conductors alone, and simplify the interpretation of the geomagnetic field data.

7.1 The Midha (1979) and Ingham (1985a, 1985b, 1987, 1988b) Field Sites

Midha (1979) has provided induction arrows for periods $T=5-6.5, 12.5, 25, 50,$ and $83-100$ min at 15 sites (BDL, GLT, KGF, KPR, MKI, MKN, MMK, OPP, PRR, RTH, THT, TKR, TPO, WPG, WTP) in the central part of North Island as shown in Fig. 7.1. The 20 sites from the work of Ingham (1985a, b, 1987, 1988b) (Cape Egmont and southern regions of North Island) also shown in Fig. 7.1 are AKA, AWA, EAS, GOL, GOW, HOP, KAH, KAI, KAR, MAK, MOR, NGA, NGM, REI, TEA, TEW, TUR, WAI, WES, WIO. To aid the discussion it is appropriate to place the field sites into three groups (A-the central region; B-the Cape Egmont region; C-the southern tip region of North Island).

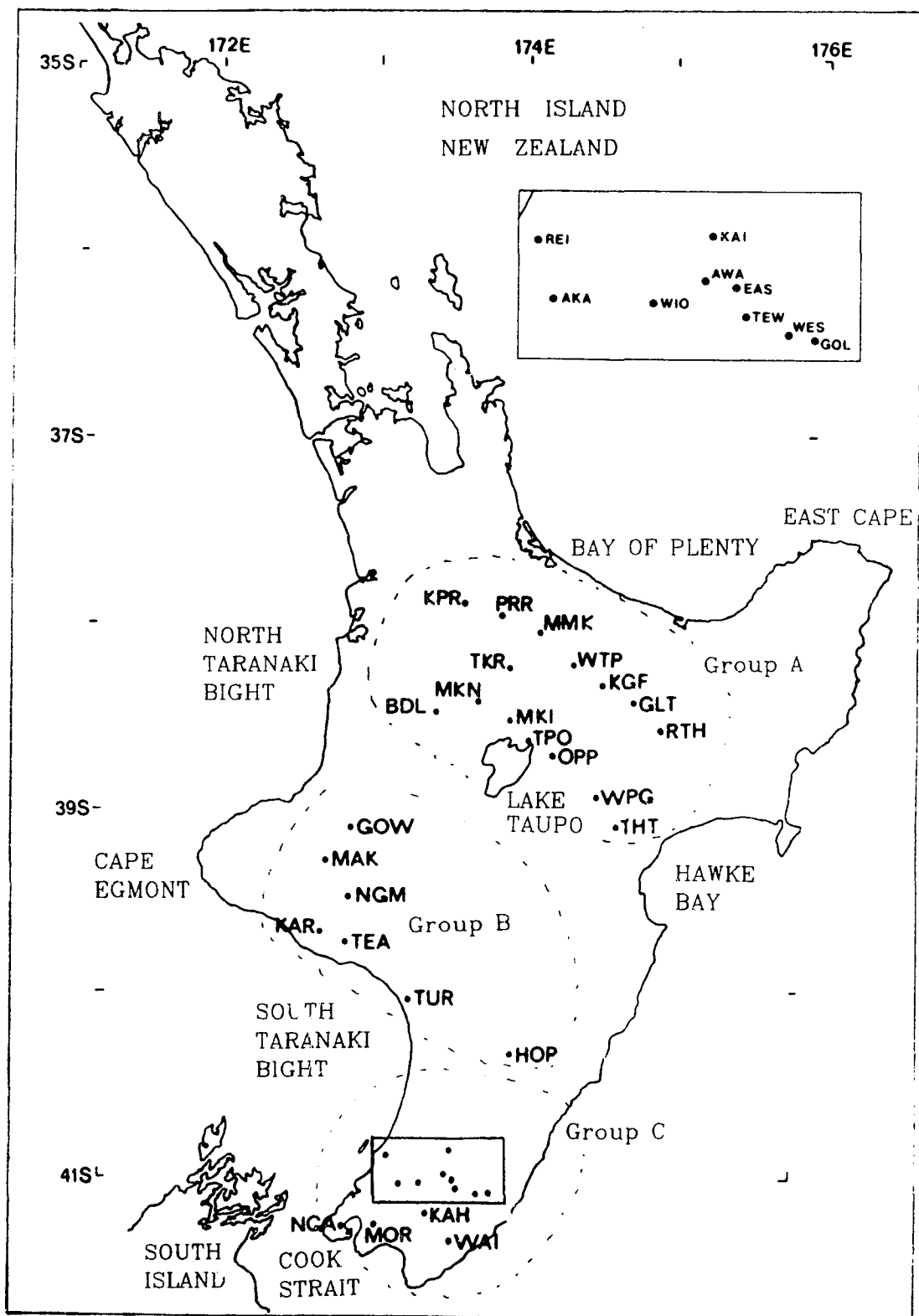


Figure 7.1: Map of the North Island of New Zealand showing the 35 field site locations where geomagnetic measurements were carried out by Midha (1979) and Ingham (1985a, b; 1987; 1988b).

7.1.1 In-phase Induction Arrows

Figure 7.2 shows analogue model and field site in-phase induction arrows at 5, 10, 25, 50 and 80 min at the 35 site locations shown in Fig. 7.1. At 5 min the in-phase model arrows at coastal sites are seen to generally point towards the nearest ocean. At 80 min the model arrows at most sites, including those well-inland and even those near the west coast, have rotated (or are rotating) from pointing towards the local shallow ocean at short periods so as to point towards the more distant deep oceans (generally to the northeast or southeast) at long periods. For periods greater than 10 min, the in-phase model arrows of group A (central region) consistently point in the northeast direction and have very uniform magnitudes. With a few exceptions, the group B arrows and the arrow at BDL, which are all relatively near the shallow ocean of the North and South Taranaki Bights (Fig. 7.1), point towards the nearest shallow ocean off the west coast at short periods, and at the 50 and 80 min periods point north-eastward towards the deep ocean some distance off the east coast. The exceptions at long periods are the arrows at the coastal sites KAR and TEA. The essentially zero magnitude at each of these sites indicates roughly equal and oppositely directed responses of the nearby shallow ocean to the west and the distant deep ocean to the east. The group C in-phase arrows at the southern tip of North Island, generally pointing to the south towards Cook Strait at 5 min, are seen to be gradually rotating counter-clockwise with increasing period so as to point in the south-east direction, more directly towards the deep ocean in the Hikurangi Trench off the east coast. The magnitudes of the group C arrows are much attenuated at 80 min due to decreased current channelling through Cook Strait at long periods. Thus the model in-phase arrows behave much as would be expected due to the ocean effect alone.

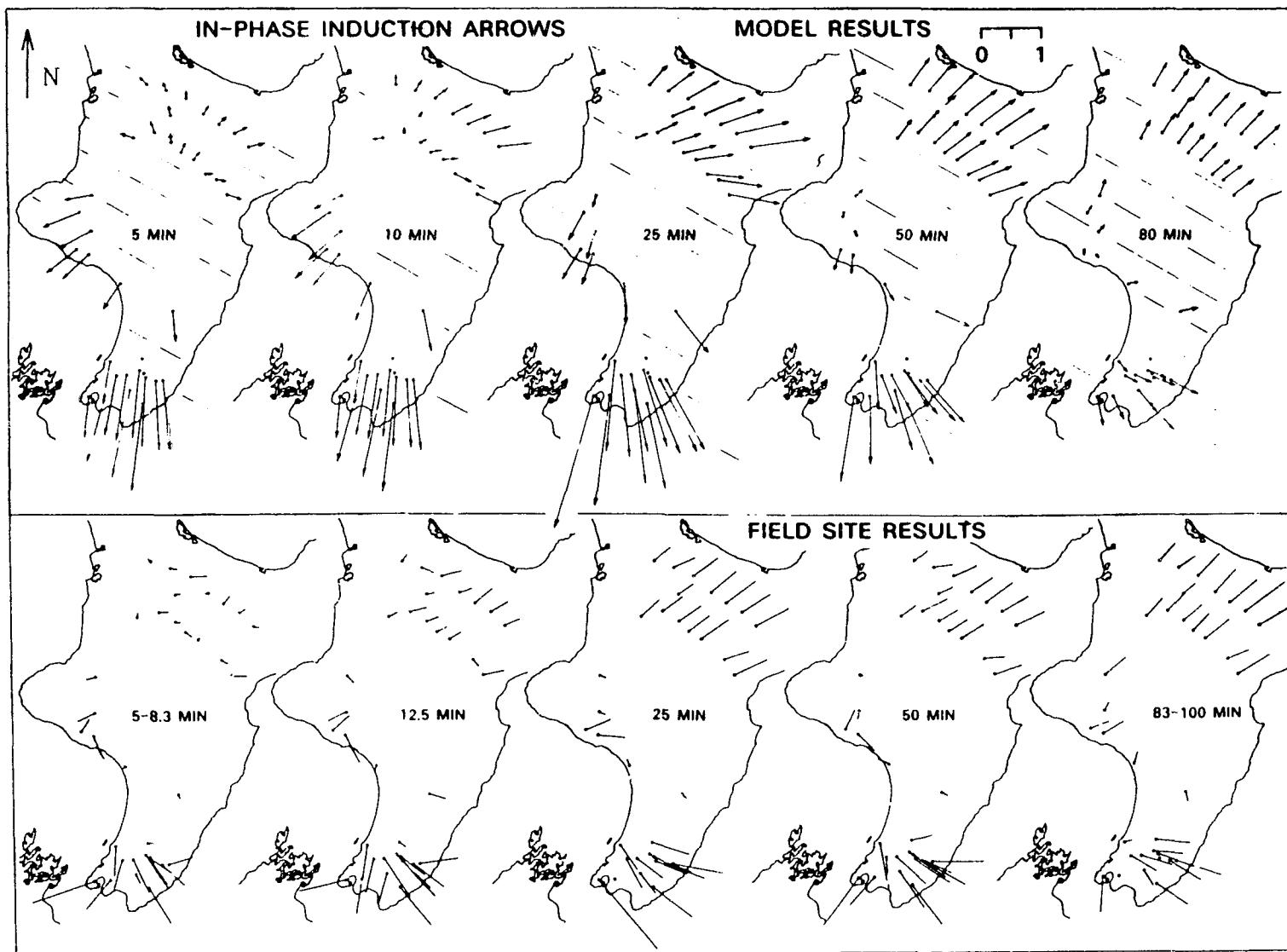


Figure 7.2: Analogue model and field site in-phase arrows for five periods at the 35 locations (given in Fig. 7.1) on the North Island of New Zealand.

The directions of the field site in-phase arrows in group A, with the exception of those at 5-8.3 min (and 12.5 min at several sites), agree very closely with those of the analogue model arrows, indicating that for this region the ocean plays the major role in the in-phase induction arrow responses. The generally smaller magnitudes of the field site arrows than those of the analogue model at all periods, together with the discrepancy in direction at the short periods, could be attributed mainly to geological structure not simulated in the analogue model. In particular the largely conductive structure of the Central Volcanic Region, postulated to be the back-arc basin of the subduction zone to the east of the North Island (Smith et al., 1989), can be expected to have a significant effect on the field site in-phase arrows at short periods. Further, the discrepancies between the model and field site results could support the hypothesis put forward by Midha (1979) of a NW-SE trending conductive structure, associated with the volcanic region both onland and off the north coast beneath the Bay of Plenty.

The behaviour of the in-phase field site arrows for most sites in group B is generally in agreement with that of the analogue model arrows, with the exceptions that the field site arrows are generally shorter at all periods, and they rotate from pointing to the local ocean off the westerly coast, to point to the more distant deep ocean off the easterly coast at a shorter period than is the case for the model arrows. These differences in behaviour too could be attributed to conductive structure in the central region. The conductive structure postulated by Ingham (1987) to lie at around 40 km depth beneath the northwestern part of the North Island would have a significant effect on the group B arrows. The behaviour of the field arrows at sites TEA and TUP is also likely to be strongly influenced by

the deep sediments of the Wanganui Basin (see Fig. 5.6) which were not included in the model simulation.

As was the case for the model arrows, the in-phase field site arrows in group C (southern tip of the island) also gradually rotate with increasing period from pointing towards the shallow Cook Strait at the shortest periods, to pointing more towards the deeper ocean off the east coast at longer periods. As is the case for the group B arrows, the field arrows in group C again tend to show rotation at a shorter period than do the model arrows. The scatter in the directions of the field arrows for adjacent sites (of small separation) may in part be explained by the responses of localized complex geological structure and conductive faults not included in the model, and in part by the responses of coastal features which cannot be accurately simulated in the analogue model.

7.1.2 Quadrature Induction Arrows

Figure 7.3 shows analogue model and field site in-phase induction arrows at 5, 10, 25, 50 and 80 min at the 35 site locations shown in Fig. 7.1. The group A model arrows are small and generally point inland at 5 min. With increasing period, these arrows are seen to rotate counter-clockwise, and at the long period of 80 min the arrows have roughly reversed direction so as to point towards East Cape in response to the cape effect and the distant deep ocean eastward. The group B arrows, also small at short periods, rotate counter-clockwise with increasing period so as to point towards the South Taranaki Bight, in response to current channelling through Cook Strait. The group C arrows at 5 min are also seen to point away from local current concentrations, that is, concentrations due to channelling through Cook Strait. With increasing period, the group C model arrows also rotate

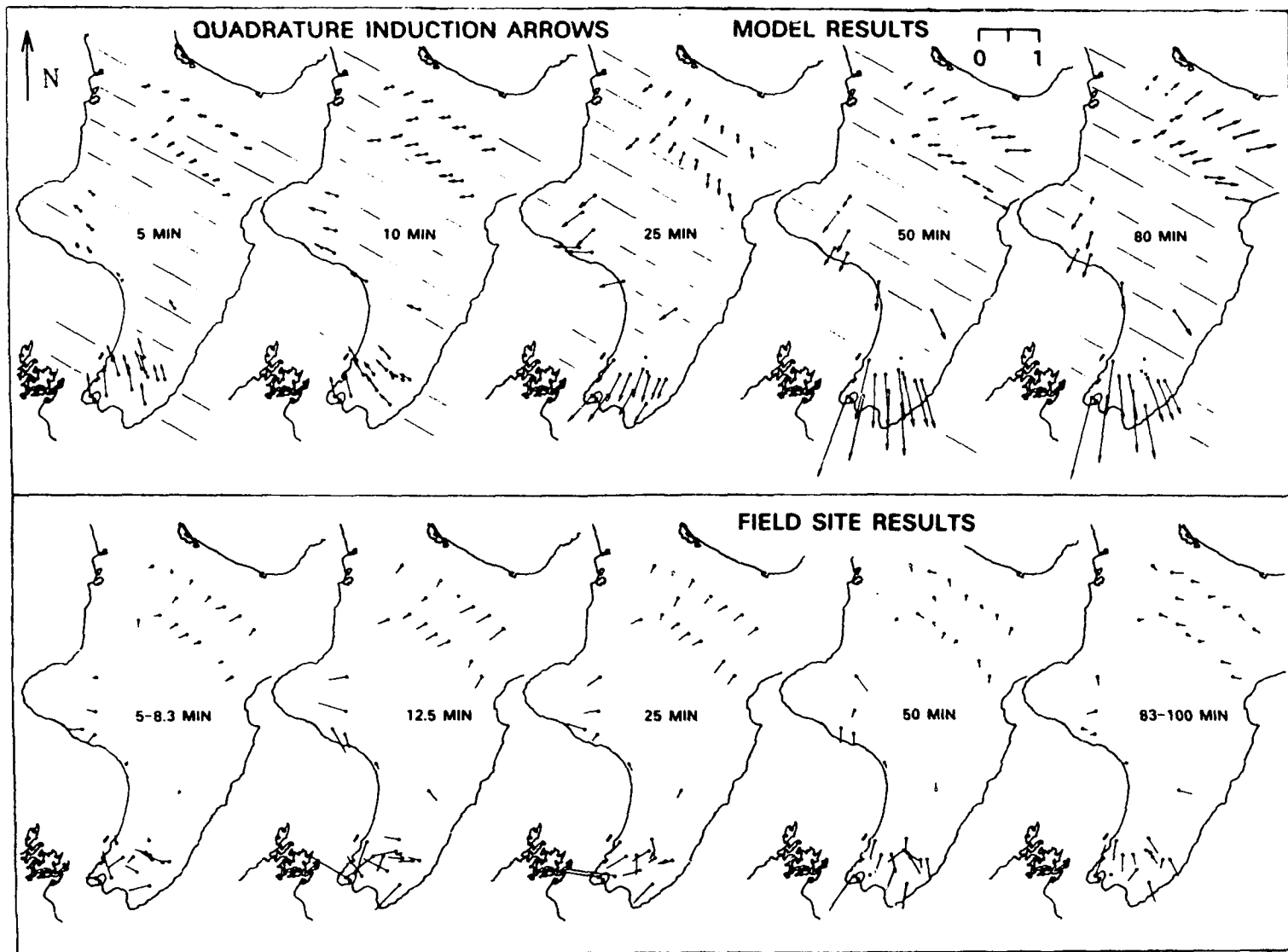


Figure 7.3: Analogue model and field site quadrature arrows for five periods at the 35 locations (given in Fig. 7.1) on the North Island of New Zealand.

counter-clockwise so as to point towards these current concentrations at the long periods. Thus, current channelling through Cook Strait clearly plays an important role in the model induction arrow responses at both the group B and C sites.

The behaviour of the group A field site quadrature arrows (Fig. 7.3) as a function of period is very similar to that of the model arrows, with the differences that the model arrows generally have larger magnitudes, and rotate at a shorter period to point eastward towards the deep ocean. These observations generally also apply in the comparisons for the arrows at the group B sites. The field site quadrature arrows in group C are scattered in direction, particularly at short periods, but at a number of sites reasonable agreement in direction with model observations exists. A dipping subducting tectonic plate, together with tears and offsets as described in Fig. 5.6, as well as the conductive structure of the Central Volcanic Region, and the numerous faults in North Island could readily account for the discrepancies between the model and field site arrows. Such discrepancies will be examined in greater detail in sections 7.2 and 7.3. Suffice it to say, the observations in the present section do indicate the importance of the coast effect throughout the entire North Island region.

7.2 The Kellett et al. (1988) Eyrewell Field Site

Kellett et al. (1988) digitised and analysed four months of magnetic records from the Eyrewell Observatory (EYR) near Christchurch on the South Island of New Zealand. Thus, in-phase and quadrature induction arrows at this site are available for a range of periods. The difference induction arrows at EYR (obtained by subtracting the model arrows from the field site arrows), as well as

the model and the field site induction arrows for periods of 5, 10, 15, 20, 35 and 80 min are shown in Fig. 7.4.

7.2.1 Analogue Model and Field Site Induction Arrows at EYR

The model in-phase arrows at EYR (solid arrows in Fig. 7.4) generally point eastward at all periods, showing the coast effect. At 15 min, the model in-phase arrow is maximum and points directly towards the peninsular cape in response to the cape effect, while at shorter periods the arrows are slightly rotated counter-clockwise in response to the increasing importance of current deflection northward so as to be channelled through the shallow Cook Strait. At longer periods, the arrows are slightly rotated clockwise in response to a greater component of the current induced at depth in the distant ocean being deflected southward. Compared with the model in-phase arrows, the field arrows are roughly 20-50% shorter and are rotated 20-30° counter-clockwise. This could be accounted for by the presence of an anomalous conductor northward of EYR.

Both the model and field site quadrature arrow magnitudes in Fig. 7.4, when compared with the corresponding in-phase arrows, are smaller at short periods ($T < 20$ min), are roughly equal at 35 min, and are longer at 80 min. This increasing quadrature response is due to current in the ocean being induced at increased depth at longer periods. The model quadrature arrow, though small, points away from the ocean at 5 min, is essentially zero at 10 min, and at 15 min has roughly reversed its direction to point eastward towards the local ocean, while the field site quadrature arrow at 5 min is essentially zero, at 10 min has increased in length to point roughly northward, then at 15 min has rotated to point eastward towards the local ocean. With further increase in period, the model and field site

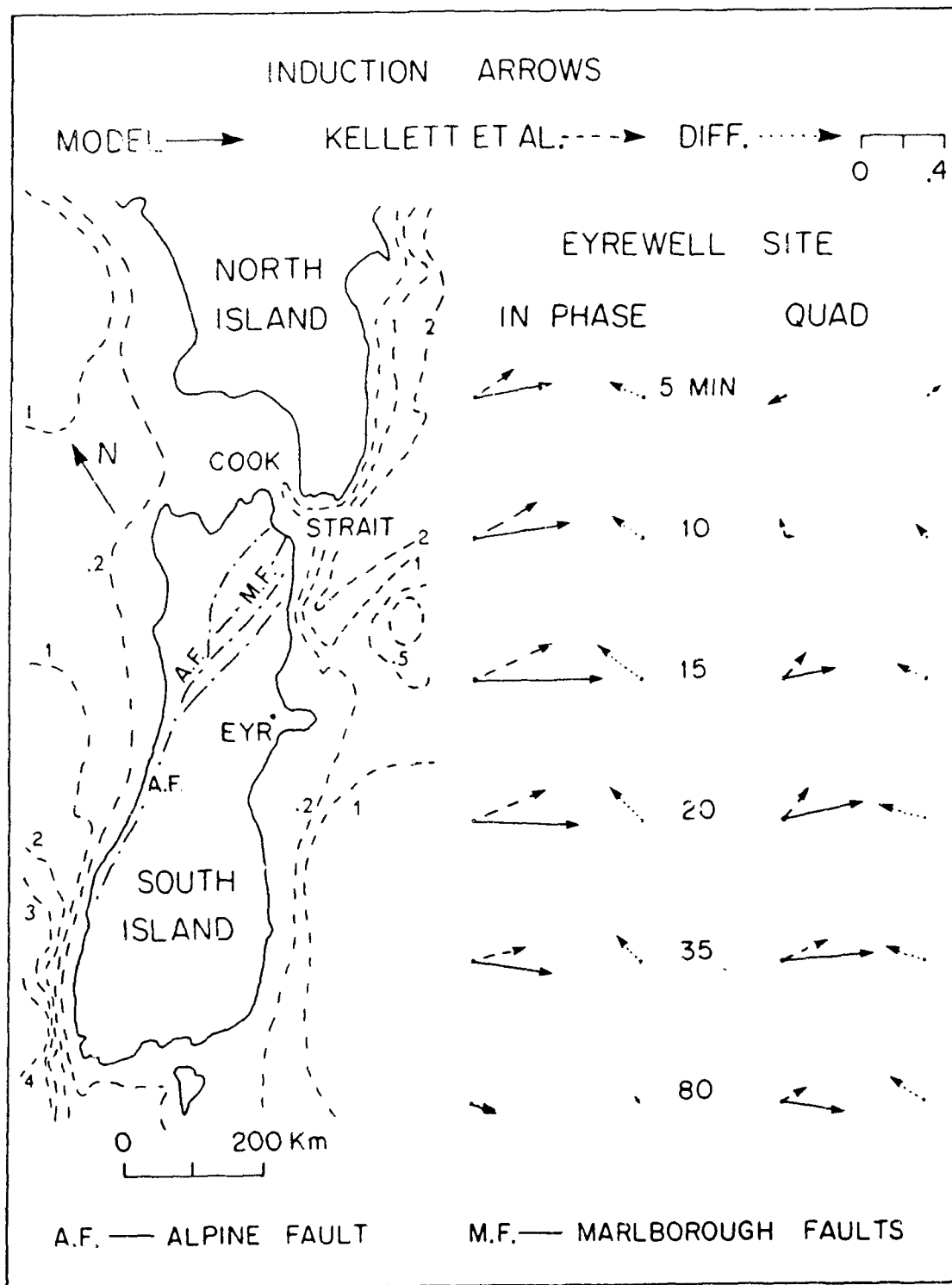


Figure 7.4: The in-phase and quadrature model (solid arrows) and field site (dashed arrows) induction arrows, and the in-phase and quadrature difference induction arrows (dotted arrows) at field site Eyrewell (Kellett et al., 1988) for periods of 5, 10, 15, 20, 35 and 80 min.

quadrature arrows each show a further small rotation clockwise. The magnitudes of both are maximum at 35 min, then much decreased at 80 min.

As was the case for the in-phase components, the field site quadrature arrows also show a 20-30° angle counter-clockwise relative to the model arrows. Kellett et al. (1988) have attributed the observed directions of the quadrature arrows to large quadrature phase currents being channelled through Cook Strait. The model quadrature arrow direction does not indicate such a large current channelling component, but rather supports the premise of an anomalous conductor north of EYR.

7.2.2 Difference Induction Arrows at EYR

The observed field site responses at EYR could be explained as the sum of the responses of the ocean eastward and an anomalous conductor northward. To examine this, difference induction arrows are shown in Fig. 7.4 (dotted arrows). The empirical model results of Dosso and Meng (1992) indicated that for a 200 km wide 2-D island, with an embedded anomalous conductor, the coast effect response could be removed by simple subtraction at short periods if the conductor-ocean separation was at least 30 km, and at long periods (say 80 min) if the separation was at least 10 km. The bulk of the faulted region (Alpine and Marlborough Faults in Fig. 7.4) north of EYR, taken to be the anomalous conductor, should be sufficiently far from the oceans to meet the criteria for negligible coupling, and thus a simple vector subtraction of the model coast effect arrows from the field site arrows should yield a valid response of the faults alone.

The in-phase difference arrows (shown as dotted arrows in Fig. 7.4) consistently point northward at all periods studied. This can be interpreted as largely

that of the induction arrow response of the Alpine and Marlborough Faults in the northern region of South Island, particularly at long periods. The period dependent small rotation (clockwise) of the in-phase difference arrow can be attributed to increased importance of induction in the more distant faulted region (near Cook Strait) at long periods. There are numerous short faults also to the north (near EYR as shown in Fig. 5.7b and in a later Fig. 7.12), and these faults are expected to be particularly important at short periods. Further, the Alpine Fault is believed to extend to depths of 25-50 km and to dip to the east at an angle of roughly 45° (e.g. Suggate, 1978). The combined effects of the nearby short faults, the long major dipping Alpine Fault, and the more distant complex Marlborough Fault regions can readily account for the significant and relatively constant in-phase responses over a wide period range.

The quadrature difference arrows show negligible response at 5 and 10 min, but the magnitudes and arrow directions at 15-80 min support the in-phase difference arrow interpretation as the responses of the nearby minor faults (Fig. 5.7b) and the more distant major Alpine and Marlborough Faults. The slight rotation clockwise of the quadrature arrow at 80 min also agrees with the behaviour of the in-phase arrow. The significant quadrature response at 80 min (while the in-phase response is negligible) indicates induction at considerable depth in the more distant faulted region.

The analogue model results of an idealized single vertical fault discussed in Chapter 4 (Fig. 4.4) would indicate significant in-phase and quadrature responses over the period range 5 to 30 min for, say, a 50 km fault-site distance, with the quadrature responses as a function of period showing a broad maximum. The EYR

site region, with its multiple nearby minor and distant major faults, cannot be simulated by so idealized a fault as that of Fig. 4.4, but the directions and the magnitudes of the difference arrows in Fig. 7.4 are of the order to be expected based on the information of responses of the idealized model faults studied in Chapter 4.

Both the in-phase and quadrature difference arrows clearly indicate the responses at EYR to be those of the faults in the region to the north. The technique used here to remove the coast effects can be seen to simplify the interpretation of geomagnetic field measurements, and in the present work leads to an obvious re-interpretation of the measurements of Kellett et al. (1988). Expanding on their interpretation that current channelling could account for the observed geomagnetic fields, the present work shows that in addition to the effect of current channelling, induction in the conductive faulted region to the north provides an important component.

7.3 The Bromley (1979) Field Sites

Bromley (1979) carried out geomagnetic depth sounding measurements and obtained induction arrows for short periods (up to 10 min) at 26 sites in the Southern Alps region of South Island. As described in the previous section the coast effect components in his measurements are in the present work removed by subtracting the analogue model induction arrows from the field site induction arrows at each of the 26 sites. The resulting in-phase and quadrature difference arrows at 10 min are shown in Figs. 7.5 and 7.6 respectively. Also shown in these figures are the known faults (solid lines), the older fault (dotted lines), and the sedimentary basins (dashed lines) in the Southern Alps region as provided in Bromley (1979).

7.3.1 In-phase Difference Arrows

The in-phase difference arrows at 10 min in Fig. 7.5 clearly show considerable correlation with the expected responses of the known conductive geological features. Excellent examples are those of the in-phase induction arrows at either side of the White Creek Fault (at sites REE and INA) pointing in roughly opposite directions and towards the fault between the two sites. This is supported by the observed responses in the analogue model study of a conductive fault in Chapter 4 (Figs. 4.4 and 4.5), which showed the induction arrow response to reverse sign directly over the fault, with the arrows on either side pointing towards each other and towards the conductive vertical interface. In the following discussion, an attempt is made to interpret the difference arrows at each site in terms of the responses of the numerous faults and many sedimentary basins throughout the survey region.

The site WHI (located roughly on the White Creek Fault in the upper left region of Fig. 7.5) appears to be located directly over the fault, and thus the arrow could be expected to show the observed small response. At site BUL (near the west coast) the in-phase arrow points southward towards the bulk of the nearby sedimentary valley S_1 (dashed contour), with a small component towards the short fault to the right nearby. The arrow at the nearby HEA clearly points towards the sedimentary basin S_1 and to a possible extension of the Glasgow Fault. The arrows at ROT and NEW, situated directly over the upper and lower ends of the basin S_1 respectively, are very small in magnitude as would be expected for responses at sites directly over good conductors. This is also seen to be the case for the arrows at GOE (upper right) over the sedimentary basin S_3 , and at

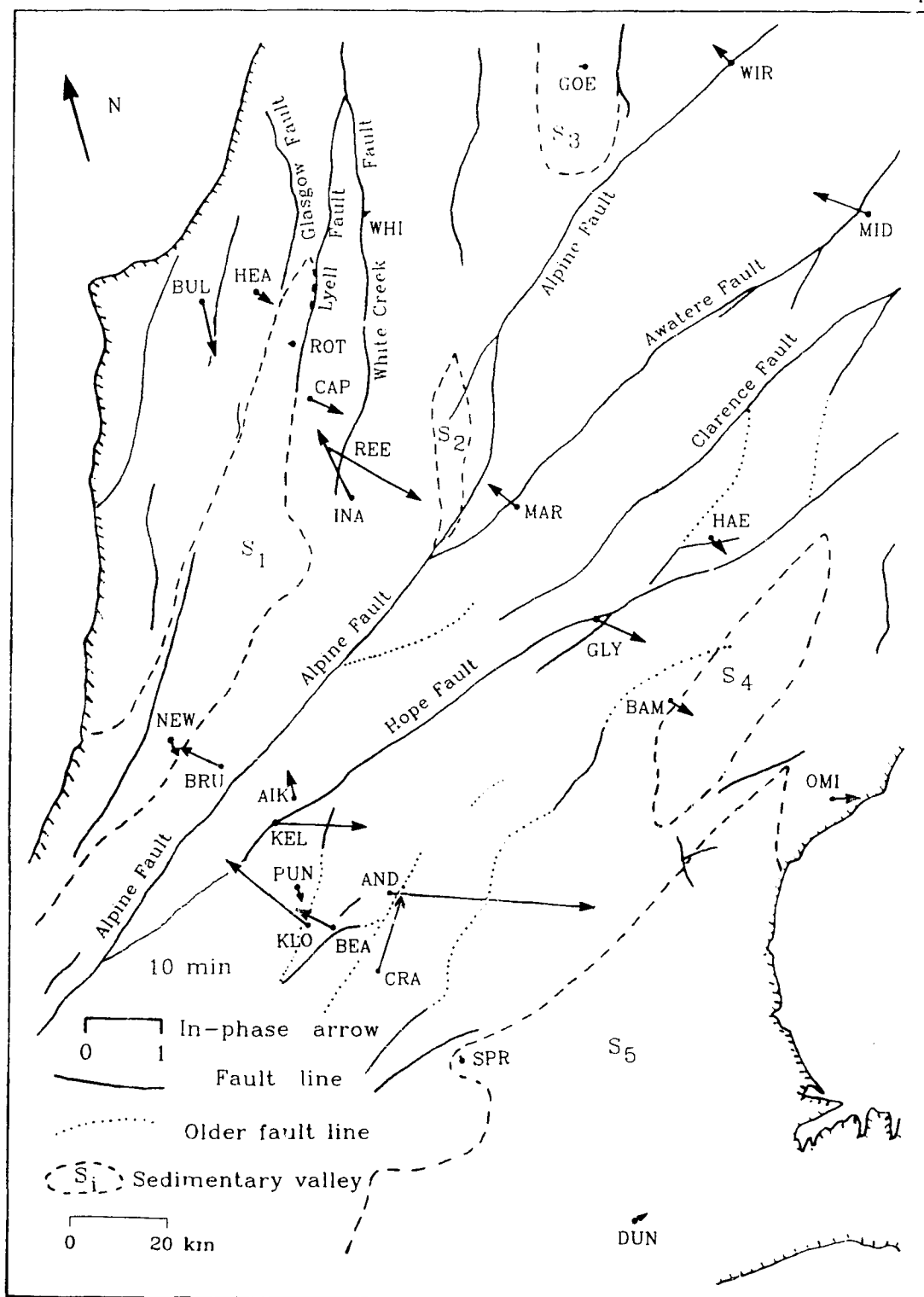


Figure 7.5: The in-phase difference induction arrows (field site arrows (Bromley, 1979) minus analogue model arrows) in the Southern Alps region of South Island.

SPR and DUN, both over basin S₅ at the lower right. At CAP, a site between the roughly parallel Lyell and White Creek Faults (upper left region), the arrow points towards the White Creek Fault at this 10 min period. Analogue model induction arrow response for a pair of major-minor faults discussed in Chapter 4 would support the interpretation that the White Creek Fault is a major fault compared with the Lyell Fault which is shown as coinciding with the S₁ sedimentary basin edge and terminating near CAP. The arrow at WIR (upper right region) is perpendicular to the Alpine Fault, and clearly shows the response expected for a site roughly on the edge of a major fault. At MID and MAR, both just to the east of the Awatere Fault (upper right), the arrow directions also clearly show the major components of the responses to be those of the fault. The somewhat smaller response at MAR than that at MID might be accounted for by differing distances from the fault, and by differing responses of the local faults to the left and to the right of the two sites. At HAE, the site between the Hope and Clarence Faults, it is seen that the arrow points towards the Hope Fault (major fault), as well as towards a nearby minor fault. Here too, the small magnitude of the response could be accounted for by the resultant of the responses of the old fault and the Clarence Fault to the left, and the oppositely directed responses of the local minor fault and the Hope Fault to the right of the site. At GLY, a site that would be over complex fractured structure where the Hope Fault and a short branch fault intersect, the arrow points roughly perpendicular to the strike of the branching fault, and the old fault line and the sedimentary basin S₄ to the south-east. The arrow at BAM, a site just outside the boundary of the basin S₄, points towards the bulk of the conducting basin as would be expected. The arrow at OMI (very near the east coast), seen to

be pointing seaward, could be interpreted as the response of the edge of the subducting Pacific Plate near the east coast (see Fig. 5.6).

Sites in the southwestern (lower left in Fig. 7.5) part of the survey region, too, are expected to show rather complex resultant responses due to the close proximity of numerous faults, young and old, minor and major. The in-phase arrow at BRU, a site that has the major Alpine and Hope Faults to the east, and the large sedimentary basin S_1 , as well as several faults to the west, points towards the sedimentary basin. This can be accounted for as the combined responses of the conductive sediments and the faults to the west of BRU, being significantly greater than the combined responses of the Alpine and Hope Faults to the east at this short 10 min period. At AIK, a site nearer to the Alpine than to the Hope Fault, the arrow is of small magnitude and points towards the Alpine Fault (and away from the Hope Fault). The analogue model study of a pair of parallel major-minor faults (Chapter 4) with separation distance $S=50$ km (see Fig. 4.18, $Y=40$ or 45 km), suggests that at a site near a minor fault, the in-phase arrow could very well point towards the major fault at 10 min, while at the same period the quadrature arrow might be oppositely directed (pointing away from the major fault). It will be seen in the next figure (Fig. 7.6, for the quadrature arrows) that the quadrature arrow at AIK does in fact have a direction opposite to that of the in-phase arrow, pointing away from the Alpine Fault. These oppositely directed responses would support the premise of the Alpine Fault having the greater depth extent of the two faults. In this region, however, the resultant responses of the sedimentary basin S_1 to the left and the faulted region to the right and to the left, would be expected to be more complex than that of a pair of faults alone. At nearby KEL,

the large in-phase arrow is very different from that at AIK, now pointing to the right and showing a large response, probably primarily that of the Hope Fault. The very small response at the nearby site PUN could be accounted for by the combined responses of the surrounding multiple faults roughly adding to zero. The large response at KLO could indicate the importance of the old fault situated just to the left. Further, the added effects of the Hope and Alpine Faults would also contribute so as to enhance the arrow response. The response at BEA, too, might suggest that the old fault near KLO is a major contributor to the local response in this complex region. The very long arrow at AND is puzzling, but if valid, might suggest a nearby major local conductor to the right, as well as indicate the importance of the two nearby old faults and the somewhat more distant large sedimentary basin S₅ to the right. The long in-phase arrow at CRA, seen to be roughly parallel to the strikes of the local faults and the sedimentary basin boundary, can only be accounted for as due to some unknown localised conductors to the north in this geologically complex survey region.

7.3.2 Quadrature Difference Arrows

The quadrature difference induction arrows at the same sites as those of Fig. 7.5 are shown in Fig. 7.6. Field site quadrature arrows were not available at CAP, MID, HAE and HEA, and thus the quadrature difference arrows are not known at these sites. In general, the behaviour of the quadrature arrows at most sites supports the interpretations presented for the in-phase arrows. As is typically the case at short periods, the quadrature responses at many sites are smaller than the in-phase responses. As was the case for the in-phase arrows, the quadrature arrows at REE and INA, on opposite sides of the White Creek Fault, also point in

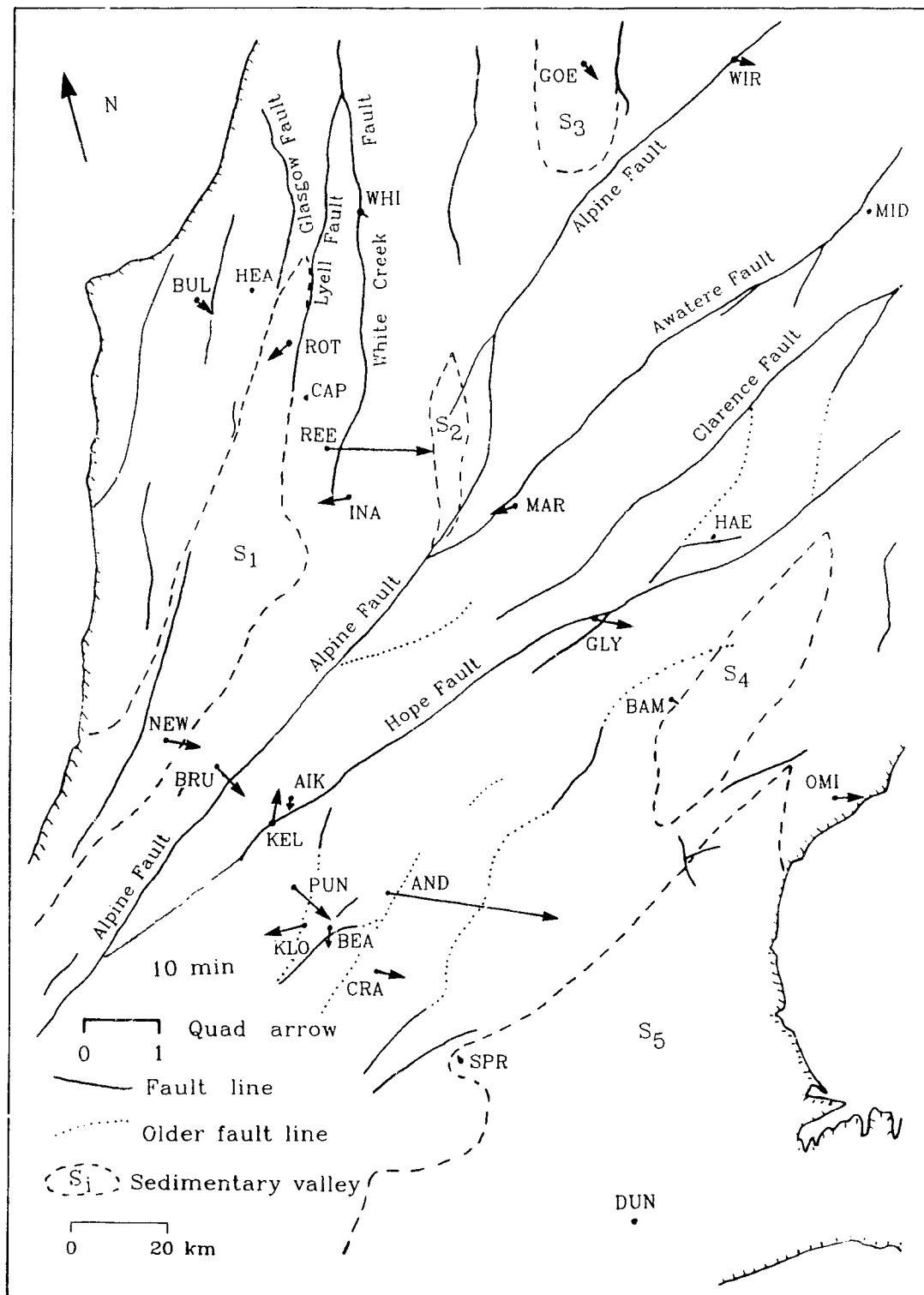


Figure 7.6: The quadrature difference induction arrows (field site arrows (Bromley, 1979) minus analogue model arrows) in the Southern Alps region of South Island.

opposite directions, each pointing directly towards the fault. The response at INA is smaller than that at REE, since INA is very near the termination of the fault. The quadrature arrow at WHI (roughly on the White Creek Fault) is also negligible, as was the case for the in-phase arrow (Fig. 7.5), again as expected for the response at a site directly over a conductive fault. The arrow at BUL (near the west coast) points towards the nearby fault to the right, similar to that observed for the in-phase arrow. Differing from the in-phase arrows, the quadrature arrows at ROT and NEW, both over the sedimentary basin S_1 near the west coast, are not negligible at this 10 min period. The arrow at ROT, pointing to the west, could indicate a possible extension of the Glasgow Fault along the S_4 basin boundary. At long periods, the arrow might very well rotate counter-clockwise to a direction normal to the basin boundary. At NEW (lower left), the arrow points away from the nearby fault and the bulk of the sedimentary basin S_1 , and points towards the major Alpine and Hope Faults to the right of the site. This is another example of the response between pairs of faults as studied in Chapter 4. At this site (NEW), the in-phase response in Fig. 7.5 was seen to be essentially zero, while the quadrature component is significant and points away from the nearby fault. If induction arrows were available for longer periods, the quadrature arrow would probably be seen to rotate with increasing period so as to point directly towards the local fault to the left at long periods. Further, the sedimentary basin too would affect the response, particularly at this short period. Similar to that observed at NEW, the quadrature arrow at GOE (upper right) directly over the sedimentary basin S_3 , has significant length, showing the responses of a minor fault along the basin boundary and the Alpine Fault to the right. These zero in-phase and non-

zero quadrature responses at short periods for sites over sedimentary basins (S_1 and S_3) may indicate that the sedimentary basins are relatively shallow. On the other hand, the negligible responses for both the in-phase and quadrature arrows at sites SPR and DUN over the large sedimentary basin S_5 (at the lower right in Fig. 7.6), would suggest that the basin is relatively deep. As has been noted for the responses at a number of sites, the small quadrature arrow at WIR (upper right) also is oppositely directed to that of the in-phase arrow (Fig. 7.5) at this short 10 min period. With increasing period the arrow would be expected to reverse its direction so as to point in the same direction as the in-phase arrow. At MAR, the quadrature arrow which would typically be expected to rotate counter-clockwise with increasing period, from pointing away from a local conductor at short periods, to pointing towards the conductor at long periods, shows an angle oblique to the strike of the Awatere Fault, as compared with the perpendicular direction for the in-phase arrow. At long periods the quadrature arrow would be expected to also point directly towards the fault. At GLY (junction of the Hope Fault and a branch fault), the quadrature arrow also shows a small angle relative to that of the in-phase arrows at this short 10 min period. The very small quadrature arrow at BAM, near the edge of the sedimentary basin S_4 , supports the interpretation of the competing responses of the basin to the right and the old fault to the left. The quadrature arrow at OMI right at the east coast, though of small magnitude, does have the same direction as observed for the in-phase arrow in Fig. 7.5. As stated for the in-phase arrow (Fig. 7.5) at this site, the quadrature arrow too could be attributed to the response of the subducting Pacific Plate that is believed to terminate just offshore (see Fig. 7.12 to be discussed later).

At BRU, in the southwestern part of the survey region, the quadrature arrow again (Fig. 7.6) is seen to be oppositely directed to that observed for the in-phase arrow (Fig. 7.5). The fact that the in-phase arrow points away from the nearby major fault (Alpine) while the quadrature arrow points in the opposite direction and towards the major fault, might be attributed to the effect of the fault at depth dipping towards the east coast. Further examination of responses for models of dipping conductors, together with field site data for a wide range of periods, would be needed to more fully interpret the observed responses. At AIK, a site very near BRU, the quadrature arrow points towards the nearest minor fault (Hope Fault), while the in-phase arrow was seen to point in the opposite direction, and towards the major Alpine Fault. The quadrature arrows at KEL, PUN, KLO, BEA and CRA, appearing to have somewhat random directions relative to those of the corresponding in-phase arrows, and being situated within a complex array of nearby local faults, as well as being relatively near (10-40 km) the major faults to the left, and the sedimentary basin S₅ to the right, are impossible to interpret without additional field data at both shorter and longer periods. As was discussed for the long in-phase arrow at AND, the similarly long same direction arrow for the quadrature component could be best attributed to a nearby major local conductor in addition to the responses of the two old faults and the large sedimentary basin S₅ to the right of the site.

Although the 10 min period results discussed in this section do clearly show the expected responses at many sites, a much more detailed period coverage would be required to permit a fuller interpretation in terms of the geological structure in this complex Southern Alps region.

7.4 The New Zealand Array (Chamalaun and McKnight, 1993) Field Sites

Figure 7.7 shows the locations of the 34 field sites on the North and South Islands where Chamalaun and McKnight (1993) carried out geomagnetic measurements. At each site, they showed field site induction arrows, as well as difference arrows (field site arrows minus thin sheet numerical model coast effect arrows) in an attempt to determine any induction effects that might be attributed to subduction zones. In their thin sheet numerical model they used 50 by 50 cells each 38 km square to represent New Zealand and the surrounding oceans. The New Zealand analogue model (simulating an area of 2800km x 2800 km) included the bathymetry of the surrounding expansive ocean, as well as the complex coastline contours, in much greater detail than was possible in the thin sheet model. Thus considerable discrepancies between the analogue model and the thin sheet model responses would be expected.

Figure 7.8 shows the analogue model and the thin sheet numerical model (Chamalaun and McKnight, 1993) in-phase induction arrow amplitudes as a function of period at six coastal sites (WES, PUP, EYR, WHK, GIS, INV) and one inland site (TEK) on New Zealand. At the inland site TEK, small essentially constant amplitude responses would be expected due to the result of opposite sign responses of the east and west coast oceans. Both the analogue model and the thin sheet numerical model responses show this expected behaviour. At coastal sites, however, the in-phase arrow responses are known (Parkinson and Jones, 1979) to show considerably variation with period, and to generally show amplitude maxima in the 15-30 min period range. The analogue model responses (Fig. 7.8) at the coastal sites, except for WES located in a bay coastal region of Karamea Bight (west

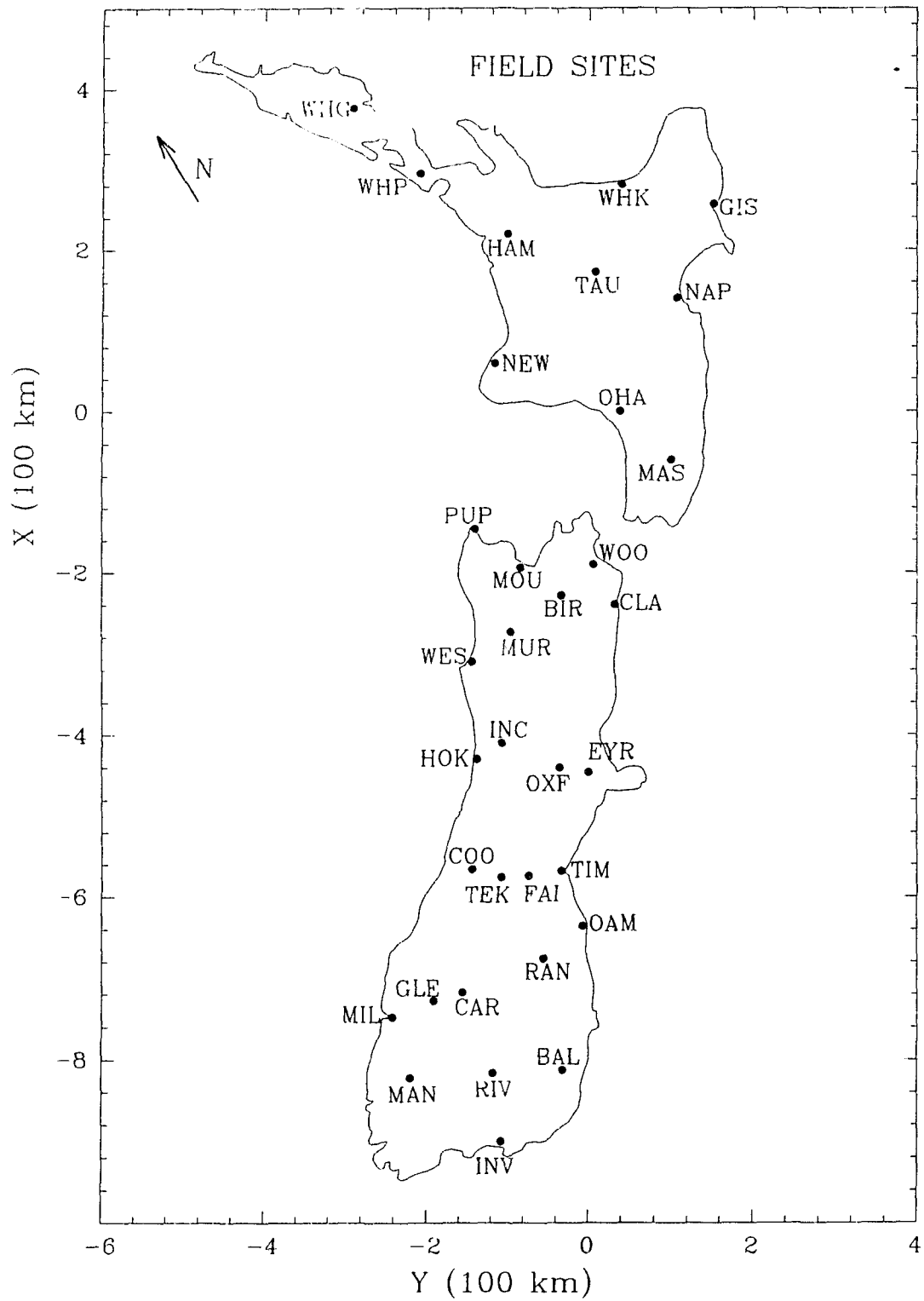


Figure 7.7: The Chamalaun and McKnight (1993) magnetometer array field sites.

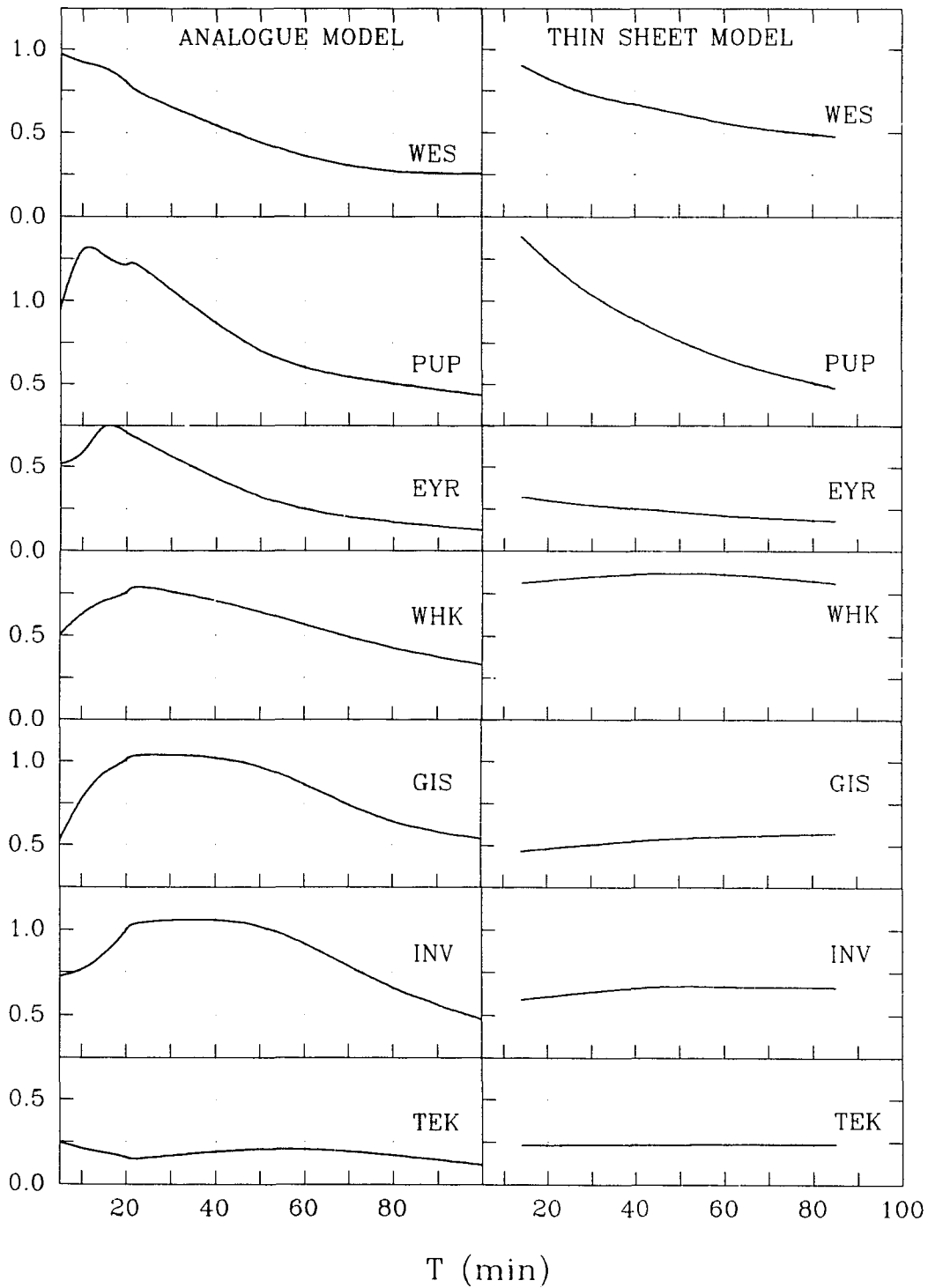


Figure 7.8: The analogue model and the thin sheet numerical model (Chamalaun and McKnight, 1993) in-phase induction arrow amplitude responses at selected coastal and inland sites in the New Zealand region.

coast), do show these expected response maxima, whereas the thin sheet model responses do not. Thus difference arrows as determined using the analogue model coast effects would be expected to differ considerably from those using the thin sheet model coast effects (Chamalaun and McKnight, 1993).

Chamalaun and McKnight (1993) attributed their resultant difference arrows as mainly resulting from the inadequacy of the numerical model in representing the ocean, and thus were unable to demonstrate any evidence of arrow responses attributable to the subduction zone under North Island, or for that matter attributable to any other conductive structure. They have suggested that a numerical model with considerably smaller grid size and much more accurate bathymetric data including offshore sedimentary basins is needed to more accurately obtain the ocean effect responses. The coast effect induction arrow responses obtained using the New Zealand analogue model in the present work have proven to be a realistic representation of the coast effect components expected at sites in New Zealand. Thus, by subtracting these realistic analogue model ocean effects from the field site observations, the difference arrows (to be discussed in the present section) should successfully show the responses of conductive geological and tectonic structures.

Figure 7.9 provides an example of the field site, the analogue model, and the difference (field site responses minus analogue model responses) induction arrow x- and y-component responses at a given site (EYR) where the coast effects would be expected to be significant. Clearly, considerable differences in the field site (F) and analogue model (M) induction arrow (x- and y-component) response curves are seen to exist at EYR. With the coast effects removed, the resultant differ-

ence (D) response curves in the lower section of Fig. 7.9 are taken to be indicative of the responses of actual conductive structures that were not included in the analogue model simulation. The field site, analogue model, as well as the difference induction arrow response curves, provided in Appendixes F, G, and H respectively for the 34 site locations, can readily be used to calculate the induction arrows and the difference arrows at any period at each site.

Figure 7.10 shows the analogue model and field site induction arrows at the 34 sites at 10 min period. An immediate appreciation of the main features of the induction arrow responses can be gained by examining the arrow responses even at one short period. The analogue model arrows show the coast effects alone, since only the oceans, and no anomalous conductors, are included in the simulation. Thus, if the field site arrow and the model arrow are in close agreement at a given site, then the ocean provides the main response at that field site. But if there are considerable differences in the amplitudes and/or the directions in the field site and analogue model arrows, then a responding anomalous conductor in the neighborhood of the site is indicated. An example of a site where almost identical arrows are observed is that of INV (southern tip of South Island), while examples of sites (among many) where considerable differences exist are EYR and WHK (Bay of Plenty coast). In general, at this short 10 min period both the in-phase analogue model and the field site induction arrows show strong coast effects at all coastal sites, and also show considerable variation from site to site due to the irregular coastlines that lead to cape, bay, and channelling effects. The oppositely directed responses of the coast effects from the east and west coasts lead to cancelled coast effects at some inland sites.

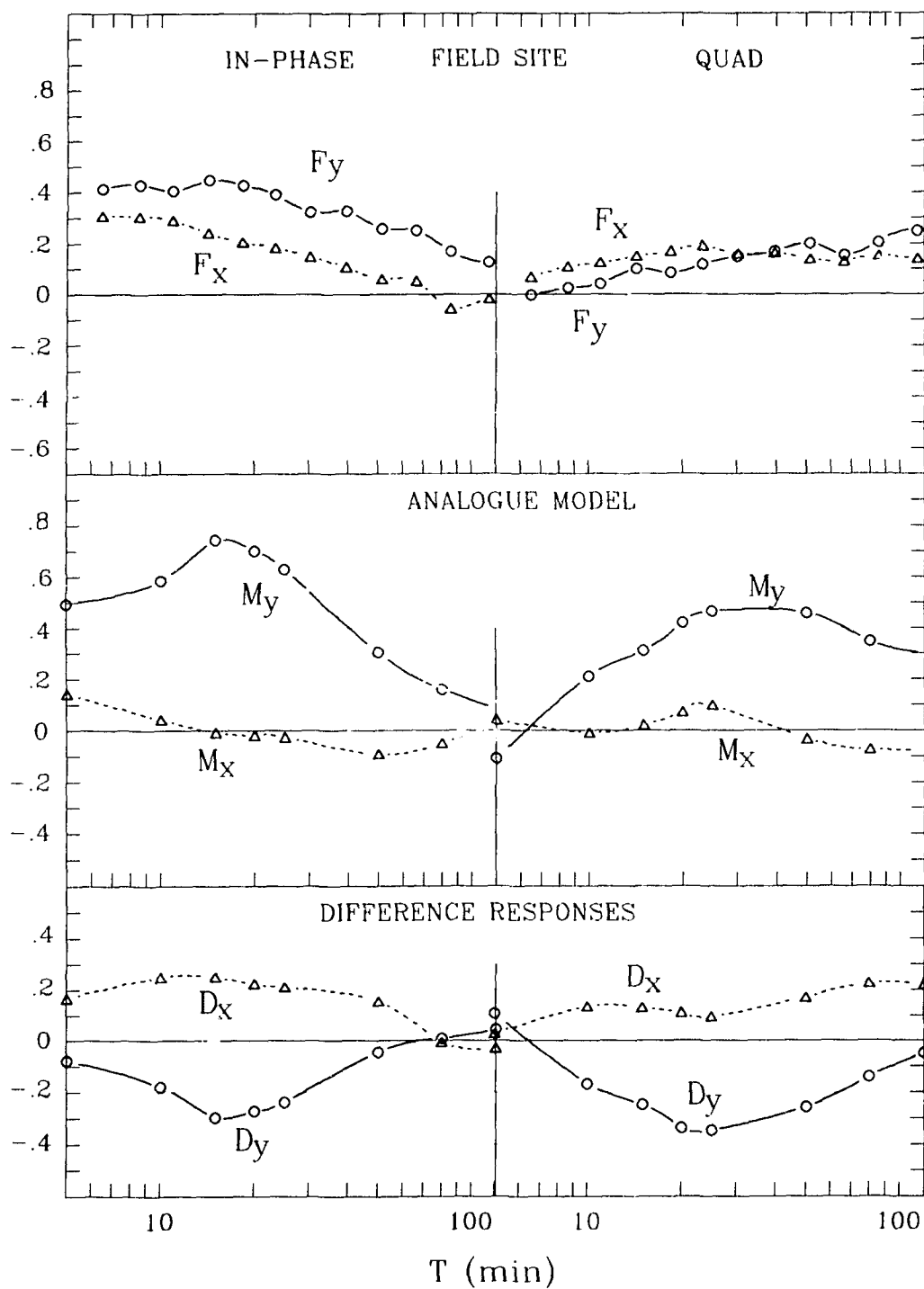


Figure 7.9: The x- and y-components of the field site induction arrows, the analogue model induction arrows, and the difference induction arrow responses at field site EYR (see Figs. 7.4 and 7.7).

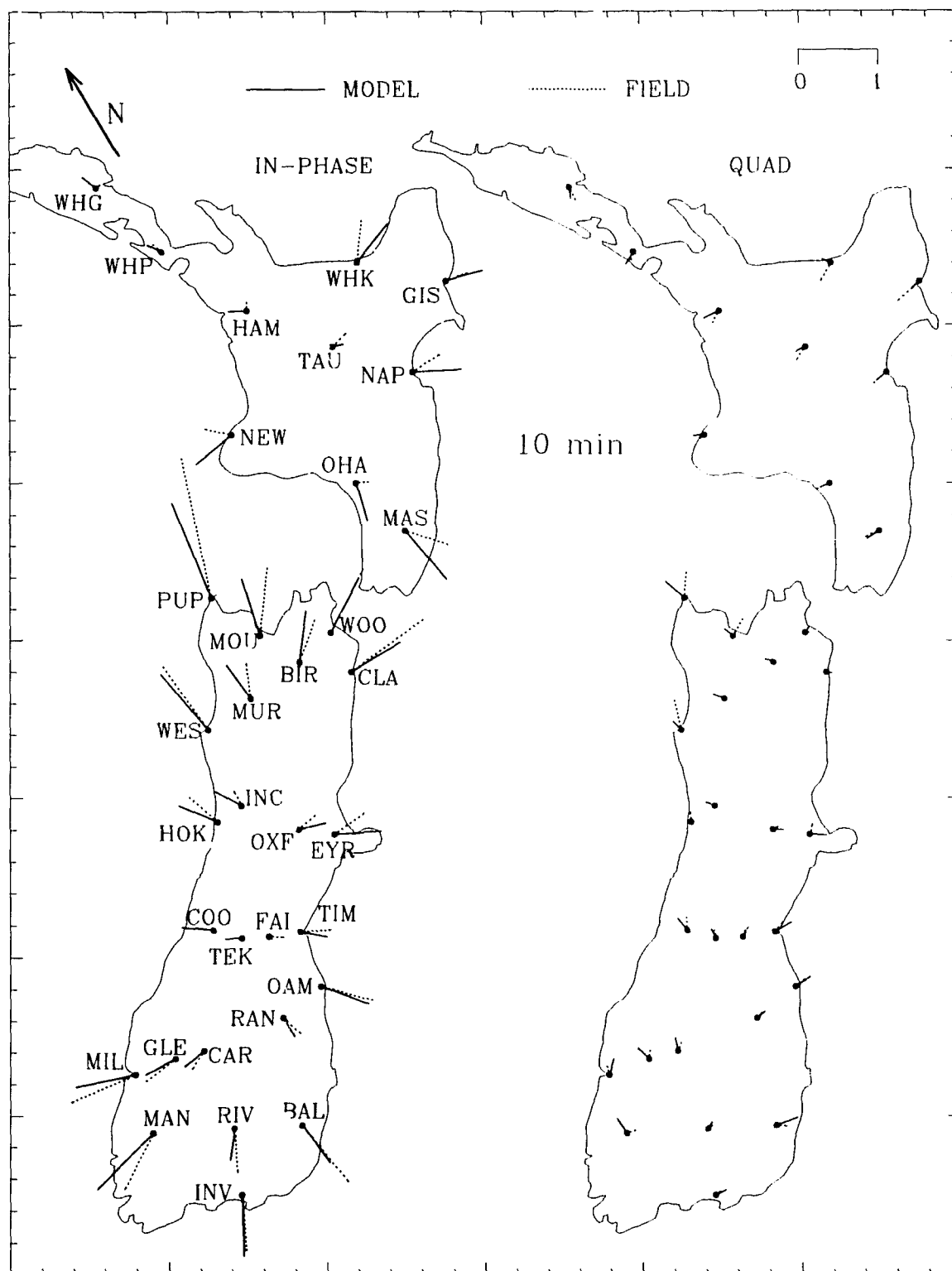


Figure 7.10: The in-phase and quadrature analogue model and field site (Chamalaun and McKnight, 1993) induction arrows at 10 min period.

The quadrature arrows in Fig. 7.10 are significantly smaller than the in-phase arrows, but their patterns do show several consistent features. For example, with a few exceptions, both the model and field site quadrature arrows on North Island consistently point to the west, away from the deep ocean off the east coast as expected at sufficiently short periods. The model and field site induction arrows at each of the 34 sites for $T=5, 15, 20, 25, 50,$ and 80 min period are provided in Appendix I.

Since the difference induction arrow responses at a given site are taken to be indicative of anomalous conductors in the region, any valid interpretation of these responses should permit a rationalization of the effects of many of the known conductive geological and tectonic structures. In some cases, an interpretation might be possible only if the response of some unknown conductor is postulated. Thus, such studies could lead to advances in the knowledge of regional geological structures.

Figure 7.11 and 7.12 are provided to show in considerable detail the currently known (in some cases not fully proven) geological features of the North and South Islands. These two figures will be used for reference in discussing and interpreting the difference induction arrows at each of the 34 sites (locations indicated by black dots) of Chamalaun and McKnight (1993). The solid lines in these figures are the locations of the major and minor faults (Suggate, 1978; Campbell, 1992; Thornton, 1993; Beanland, 1994; Cowan, 1994). The majority of the faults show strikes roughly parallel to the east and west coastlines. It has generally been accepted that a number of the major faults are continuous across Cook Strait (e.g., Suggate, 1978). For example, the Wellington and the Wairarapa Faults on

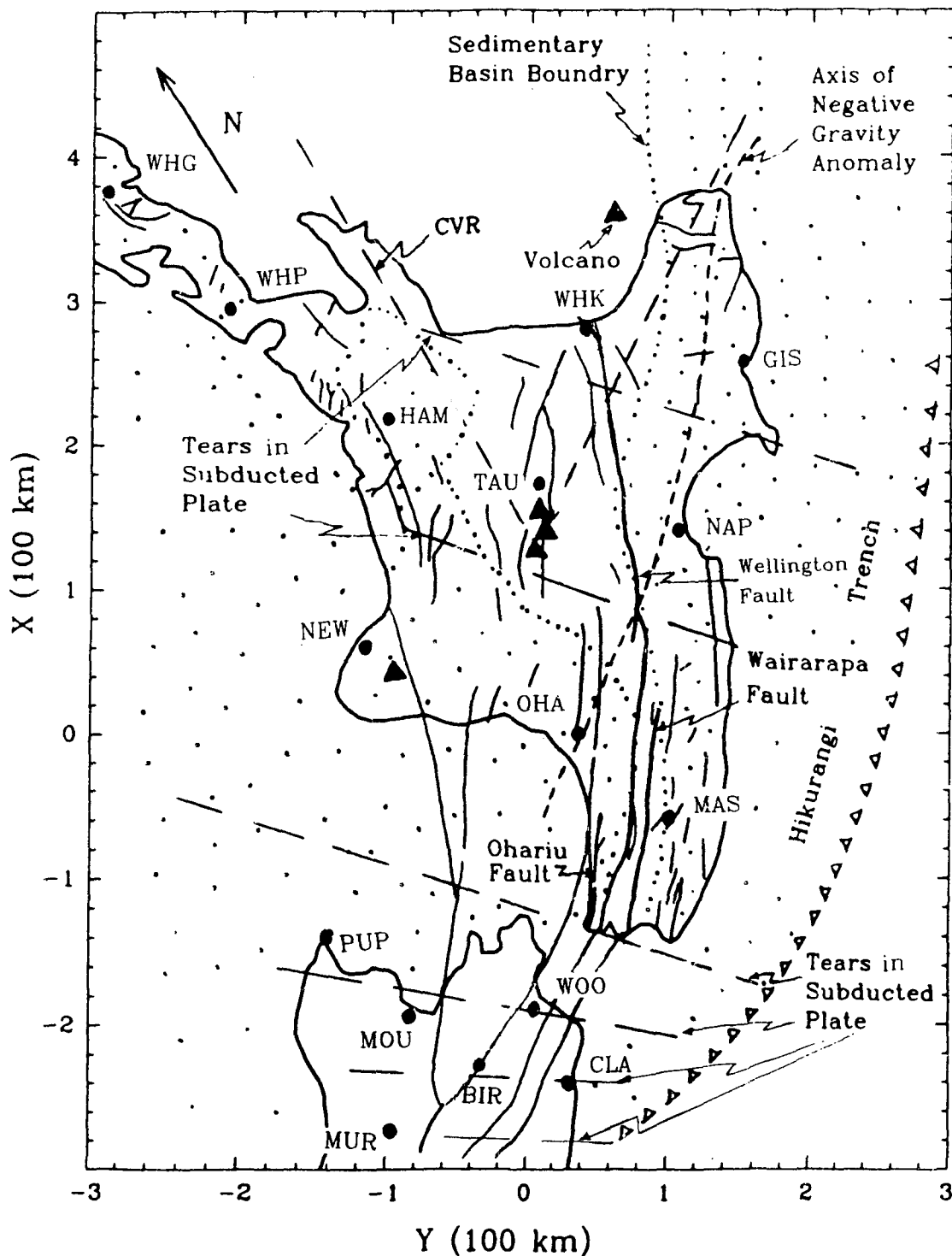


Figure 7.11: Geological and tectonic features on the North Island of New Zealand. The geomagnetic field sites are indicated as black dots (\bullet).

North Island (Fig. 7.11) are usually shown to be linked across to the Awatere and Clarence Faults (Fig. 7.12) respectively on South Island (e.g., Katz, 1979). However, the continuity of the faults across Cook Strait is still under some debate (e.g., Carter et al., 1988). As discussed in Chapter 5 (Fig. 5.6), the dashed straight lines show the postulated segmentation (or tears) of the subducted Pacific Plate (Robinson, 1986; Reyners, 1983). On the North Island map in Fig. 7.11, the triangular region outlined by dashed lines is the Central Volcanic Region (CVR), the region where extensive heat flow and active volcanoes (solid triangles ▲) are observed. The dashed curve on North Island extending from East Cape to the South Taranaki Bight is an axis of negative gravity anomaly, which has been interpreted as associated with the subduction of the Pacific Plate, as discussed in Chapter 5 (Fig. 5.5). The dotted areas bounded by closely spaced dots show the sedimentary basins (Czochanska et al., 1987) which are expected to be more conductive than the continental rock and, thus to lead to anomalous induction arrow responses at some sites.

On the South Island map shown in Fig. 7.12, the Alpine Fault diagonally across the central region of the island is believed (as described in Chapter 5) to extend to moho depths (20-50 km) and in some regions to slope eastward at depth at an angle of up to 45° relative to the vertical. The axial tectonic belt (Walcott, 1978) on South Island (region between the dashed straight line and the Alpine Fault) is an area of active crustal earthquakes (Fig. 5.4), due to crustal deformation along the boundary between the Pacific and the Indian Plates. Simplified geological structures (EOS, 1993) are also shown on the South Island map. These are: the black area, consisting of Dun Mountain rock; the horizontal lined area, consisting of the

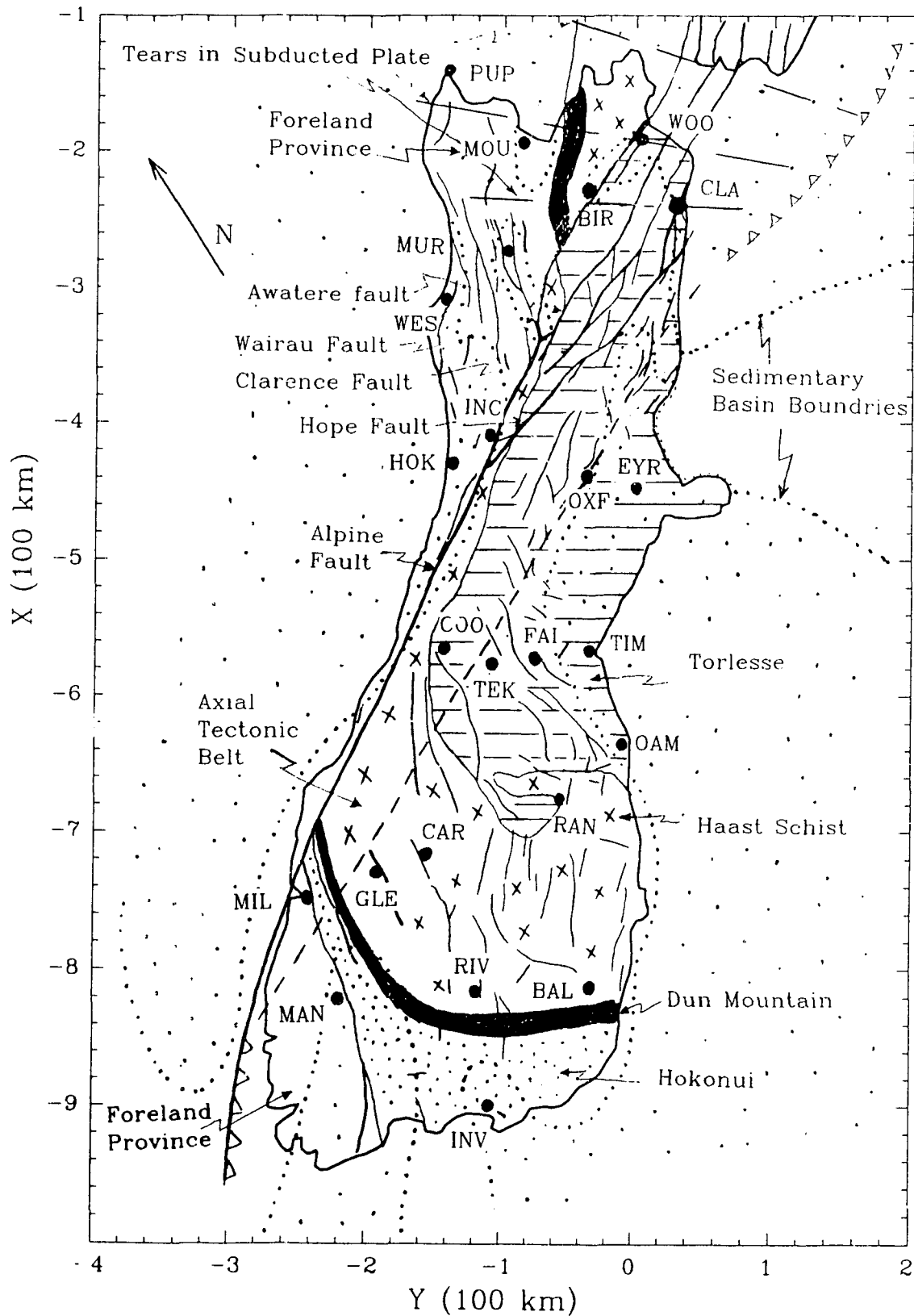


Figure 7.12: Geological and tectonic features on the South Island of New Zealand. The geomagnetic field sites are indicated as black dots (•).

relatively young (170 Ma) Torlesse rock; and the blank areas (at the northern and southern ends of the island), consisting of the relatively old (>345 Ma) Foreland Province rock. The schist rock (indicated by crosses (x) in a small area at the northern tip and linked by a narrow strip to a large region at the south end) is believed to be lower crust rock that has been pushed up from depth, and thus more conductive than the adjacent upper crust materials (see Chapter 5, Fig. 5.2). These geological and tectonic structures, together with the complex North and South Island coastlines, would be expected to lead to a wide range of anomalous geomagnetic field responses.

7.4.1 Difference Induction Arrows on North Island

In discussing the difference induction arrow responses shown in Figs. 7.13-7.16 at 10 and 50 min periods, frequent reference to features shown in the North Island map of Fig. 7.11 will be required. In addition, some reference to the figures in Appendix J showing responses at other periods will also prove helpful. Figures 7.13 and 7.14 show respectively the in-phase and quadrature difference arrows at 10 sites on North Island for a period of 10 min. It is normally expected that, for an embedded conductive anomaly the quadrature responses would be significantly smaller than the in-phase responses at short periods. This is certainly seen to be the case for all sites on North Island, with the quadrature arrows at all but a few sites being of negligible length. Further, as discussed earlier, the quadrature arrow responses for a conductive anomaly increase with period, and if the arrows are directed oppositely to the in-phase arrows at short periods, they tend to rotate counter-clockwise to become aligned with the in-phase arrows. However, at sites in the neighborhood of multiple conductors with various strike direc-

tions, the resultant in-phase and quadrature arrow frequency responses may very well show a more complex behaviour. Further, as was shown in Chapter 3, the difference arrows, for sites right at the coast, and also to a lesser extent for sites on the edge of a fault, will show the effects of mutual coupling and thus be somewhat in error. Fortunately, in most coastal regions of New Zealand, the coastal oceans are shallow and thus the mutual coupling of a fault and the ocean would be less pronounced at the coast than it would be for the deep coastal ocean of the depths employed in the idealized model studies of Chapters 3 and 4.

In Figs. 7.13 and 7.14 both the in-phase and quadrature arrows at WHG (upper left near North Cape) point towards a pair of nearby short faults to the right of the site, then at 50 min in Figs. 7.15 and 7.16 both arrows have rotated counter-clockwise through an angle of about 45° so as to point in part towards a third nearby fault that has a strike roughly perpendicular to the first mentioned pair of parallel faults. The site WHP, somewhat to the south of WHG, is located over a sedimentary basin which could in part account for the negligible responses at 10 min for both the in-phase and quadrature components. At 50 min (Figs. 7.15 and 7.16) both components show some response, but an interpretation is probably not meaningful, since the analogue model could not adequately simulate the ocean effect in this complex Bay of Islands northern coastal region.

The in-phase arrow at HAM, just to the right of a 100 km long fault and a number of short parallel faults, points away from the faults, but towards the Central Volcanic Region (CVR). With increasing period (see Figs. J.1-J.5 in Appendix J), the arrow rotates clockwise (in this case) very gradually so that at 80 min it points roughly north-east towards a postulated tear in the subducting plate (see

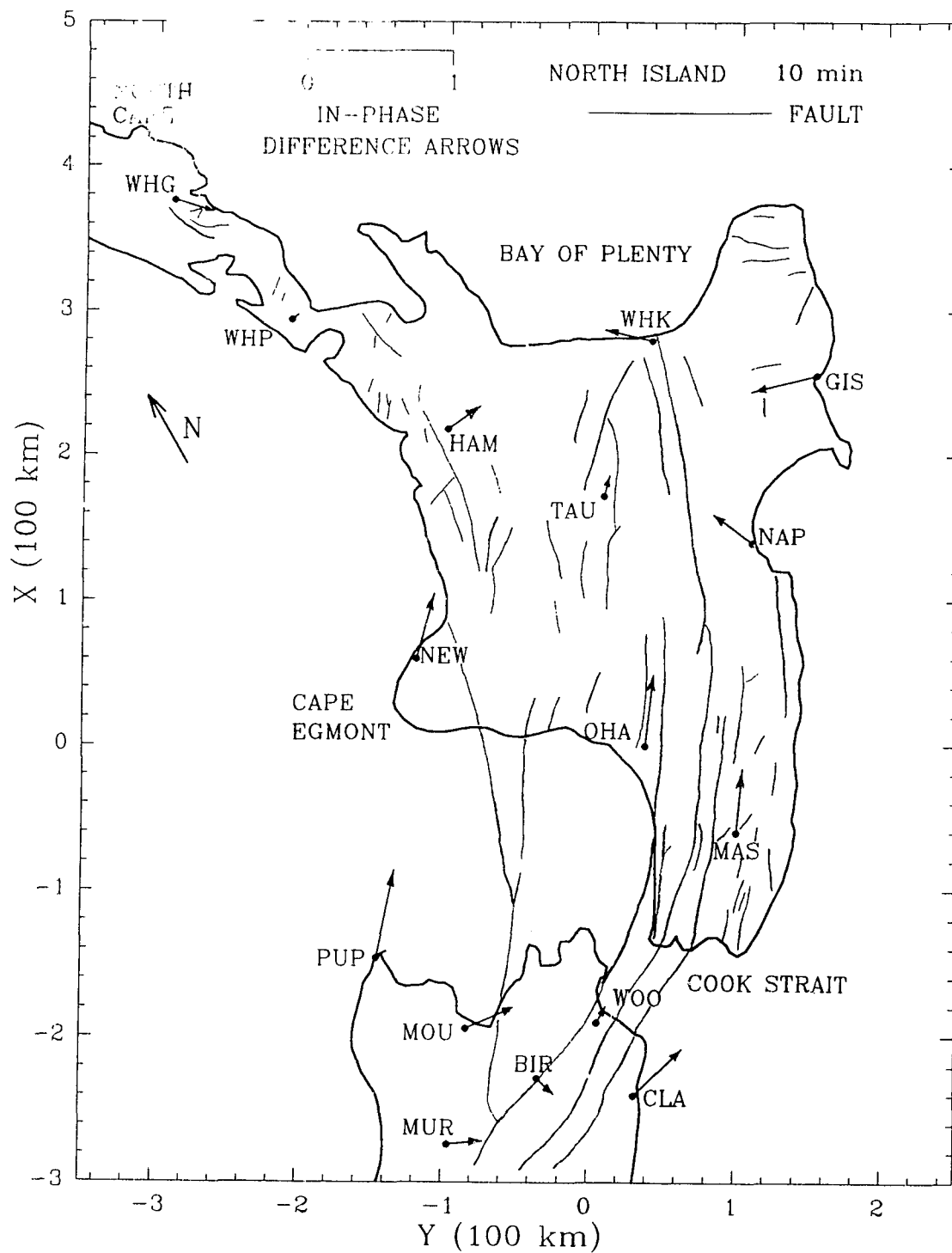


Figure 7.13: The in-phase difference arrows on North Island at 10 min period.

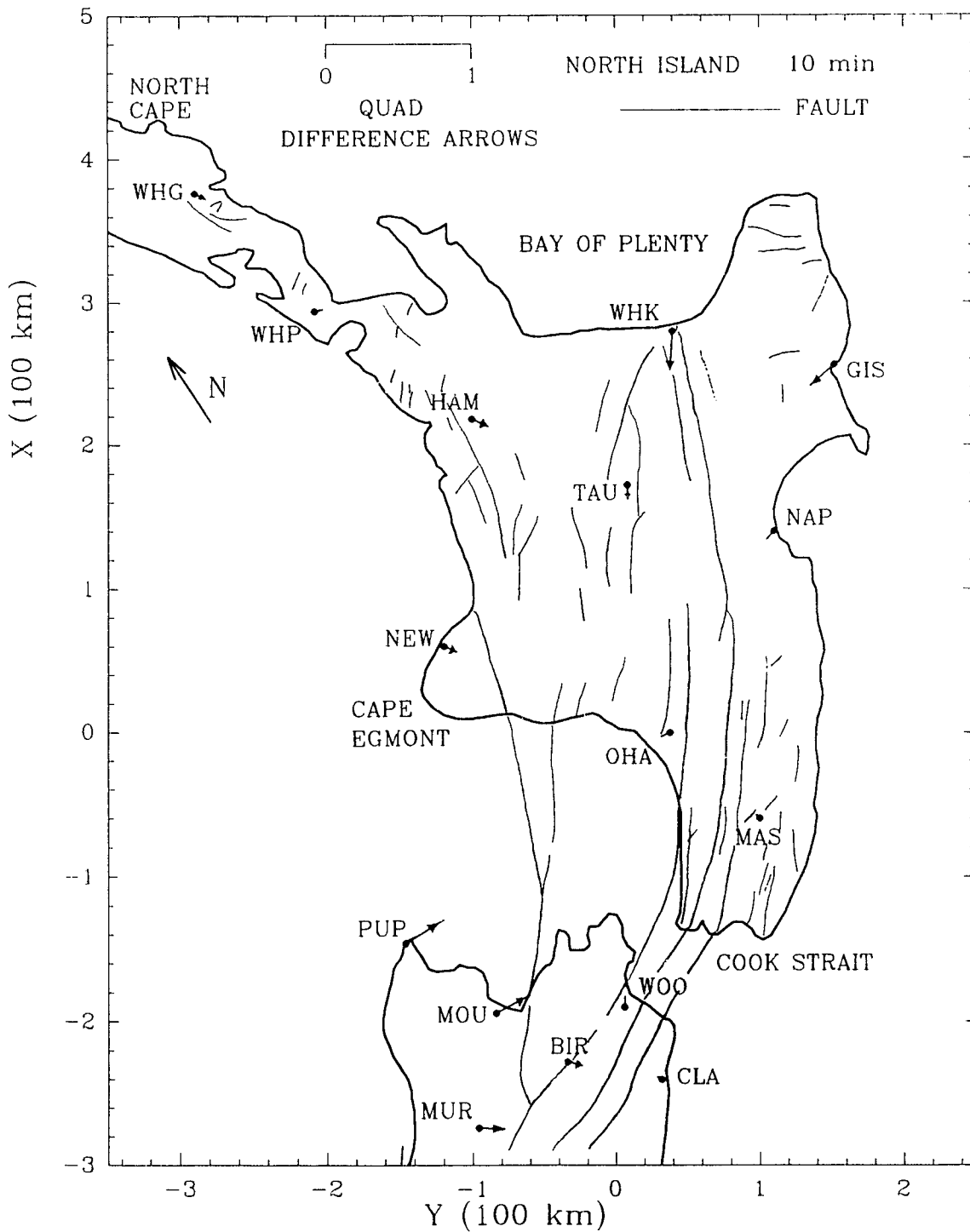


Figure 7.14: The quadrature difference arrows on North Island at 10 min period.

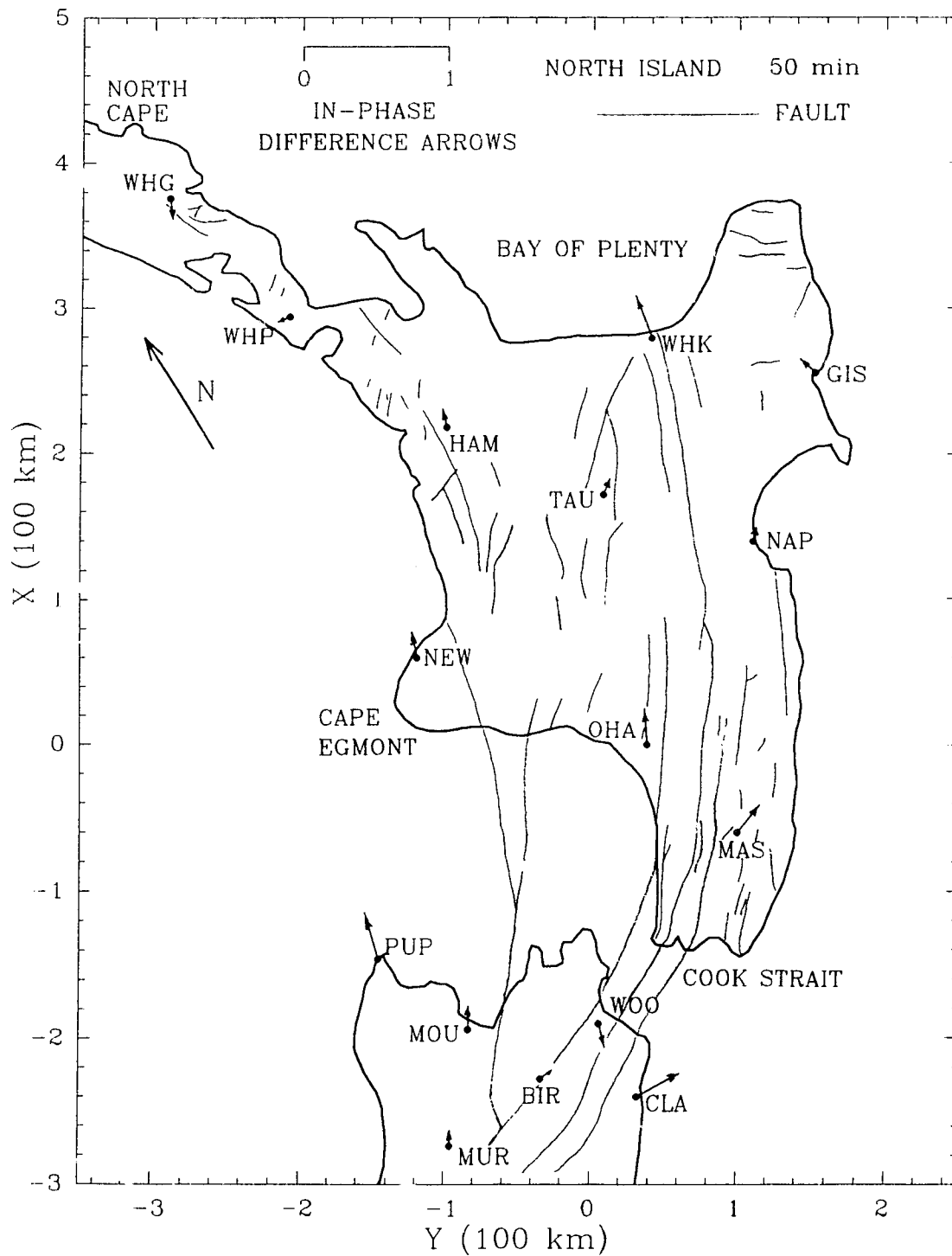


Figure 7.15: The in-phase difference arrows on North Island at 50 min period.

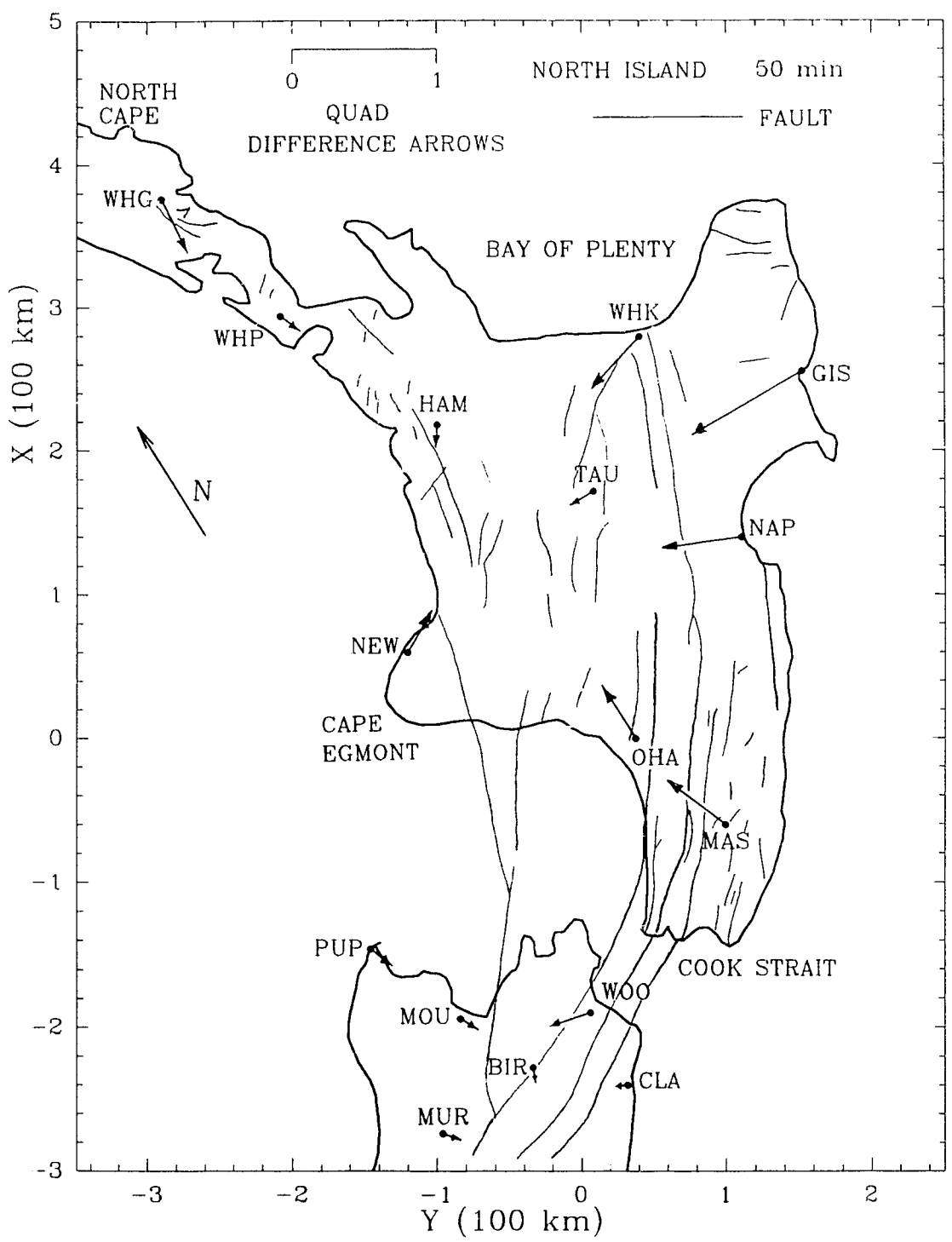


Figure 7.16. The quadrature difference arrows on North Island at 50 min period.

Fig. 7.11). The quadrature arrow, also pointing roughly towards the CVR at 10 min (Fig. 7.14), however rotates counter-clockwise with increasing period so that at 50 min (Fig. 7.16) it is pointing obliquely towards the fault to the left of the site, and in a direction almost directly opposite to that of the in-phase arrow. This unusual behaviour of the arrows pointing in opposite directions at long periods can be accounted for by the resultant of responses of multiple conductors with differing depth extent.

At WHK (near the Bay of Plenty coast line) the in-phase arrow at 10 min (Fig. 7.13) has a direction roughly normal to the strike of a number of fault lines that may very well continue into the Bay of Plenty. With increasing period the arrow rotates counter-clockwise so that at 80 min (see Figs. J.1-J.5) the arrow points roughly towards the off-shore Volcano (Fig. 7.11) in the Bay of Plenty. The quadrature arrow, however rotates little with increasing period, but at 50 min (Fig. 7.16) does attain a direction roughly normal to the parallel faults to the left of the site, and also towards the postulated tear in the subducting plate (Fig. 7.11). At this site, as was the case at HAM, in-phase and quadrature arrows again have roughly opposite directions at long periods.

Both the in-phase and quadrature arrows at GIS (east coast) at 10 min (Figs. 7.13 and 7.14) point inland towards the axis of negative gravity anomaly shown in Fig. 7.11 (believed associated with the subducting plate), and towards the somewhat more distant parallel faults. The quadrature arrow, maintaining this direction, is much enhanced at 50 min (Fig. 7.15), whereas the in-phase arrow at this longer period is much attenuated and has rotated counter-clockwise to point towards the volcanic region in the Bay of Plenty.

At the site TAU (in the lower CVR), the in-phase and quadrature arrows at all periods remain small, with the quadrature arrows pointing almost directly towards the group of volcanoes (Fig. 7.11), while the in-phase arrows now at all periods tend to point in a direction roughly opposite to that of the quadrature arrow, and towards the more central regions of the CVR.

The behaviour of the arrows at NAP (coast bay region on the east coast) is very similar to that observed at GIS, with the in-phase arrow large and the quadrature arrow very small at 10 min (Figs. 7.13 and 7.14), and the in-phase arrow very small and the quadrature arrow large at 50 min (Figs. 7.15 and 7.16). Further, as was the case at GIS, the in-phase arrow at 10 min and the quadrature arrow at 50 min at site NAP, also both point inland towards the axis of negative gravity anomaly (Fig. 7.11), and towards the inland faults (including the Wellington Fault). The large quadrature responses at long periods would be accounted for by induction at great depths, perhaps both in the conductive structure beneath the subducting plate (region beneath the axis of negative gravity anomaly) and in the deeper part of the Wellington Fault to the left of the site.

The difference arrows at site NEW (Cape Egmont) might be expected to include unwanted mutual coupling effects of the nearby fault and the major local ocean current concentrations due to the cape effect. The difference arrows would then not be those of the anomalous conductors alone, and the arrow magnitudes and directions would be in error. However, the quadrature arrow does at 10 min (Fig. 7.14) and at 50 min (Fig. 7.16) generally point inland towards the fault to the right of the site. Having rotated from pointing seaward at 5 min (Figs. J.1-J.5) to pointing inland at 10 min, its magnitude increases gradually with increasing peri-

od. The in-phase arrow at all periods is rotated somewhat clockwise relative to the quadrature arrow, as though responding to the same fault, but perhaps more to an off shore component. However, mutual coupling effects are expected to be problematic at this particular site.

At sites OHA and MAS (lower North Island) the quadrature responses are essentially zero at 10 min, then at 50 min (Fig. 7.16) and at intermediate periods (Figs. J.1-J.5), generally have directions roughly normal to both the axis of negative gravity anomaly (Fig. 7.11) and the multiple parallel faults in the region. The in-phase arrow at OHA at these periods maintains a direction nearly parallel to the local faults, as though pointing more towards the Central Volcanic Region. At MAS the in-phase arrows at short periods also have directions roughly parallel to the local major faults, then at 50 and 80 min have rotated somewhat clockwise. The quadrature arrow at long periods have lengths about a factor of two greater than those of the corresponding in-phase arrows.

Clearly, the interpretations of the induction arrow responses for this structurally complex North Island must be somewhat tentative. However, it does appear that in addition to the expected anomalies due to the numerous faults, the CVR, and the tears in the subducting plate (postulated), as well as the structures at depth (indicated by the negative gravity regions), do play a role in the observed geomagnetic responses.

7.4.2 Difference Induction Arrows on South Island

In the discussion of the induction arrow responses shown in Figs. 7.17 to 7.20, frequent reference will be made to the South Island map of Fig. 7.12. The induction arrow responses at sites on South Island are expected to show the effects of the major Alpine Fault traversing the island and joining the zones of subduction at the two ends, as well as the effects of the numerous more minor faults throughout the entire island. Further, the effects of the electrical conductivity contrasts between adjoining diverse rock types too should prove important in the observed responses.

Due to major current (induced) channelling through Cook Strait, it might be expected that at sites near Cook Strait mutual coupling between this current concentration and the conductive faults would pose a serious problem in the determination of valid difference arrows. However, conductive faults that have strikes roughly perpendicular to the direction of current channelled through Cook Strait, will be much less coupled than if the fault lines were parallel to the current flow direction. In the cases of significant coupling, as explained earlier for some sites on North Island, the difference arrows will show a considerable departure from the responses that would result for an anomalous conductive structure alone. This fact would lead to less reliable interpretations of the responses in terms of the local conductive structures. An example of a site where the difference arrows will have very limited validity is that of PUP at the tip of Cape Farewell, where current concentration due to the cape effect will result in mutual coupling of the ocean and any onland conductive fault. The quadrature arrow directions at 10 min (Fig. 7.18) and at longer periods up to 50 min (Fig. 7.20), might still be interpreted

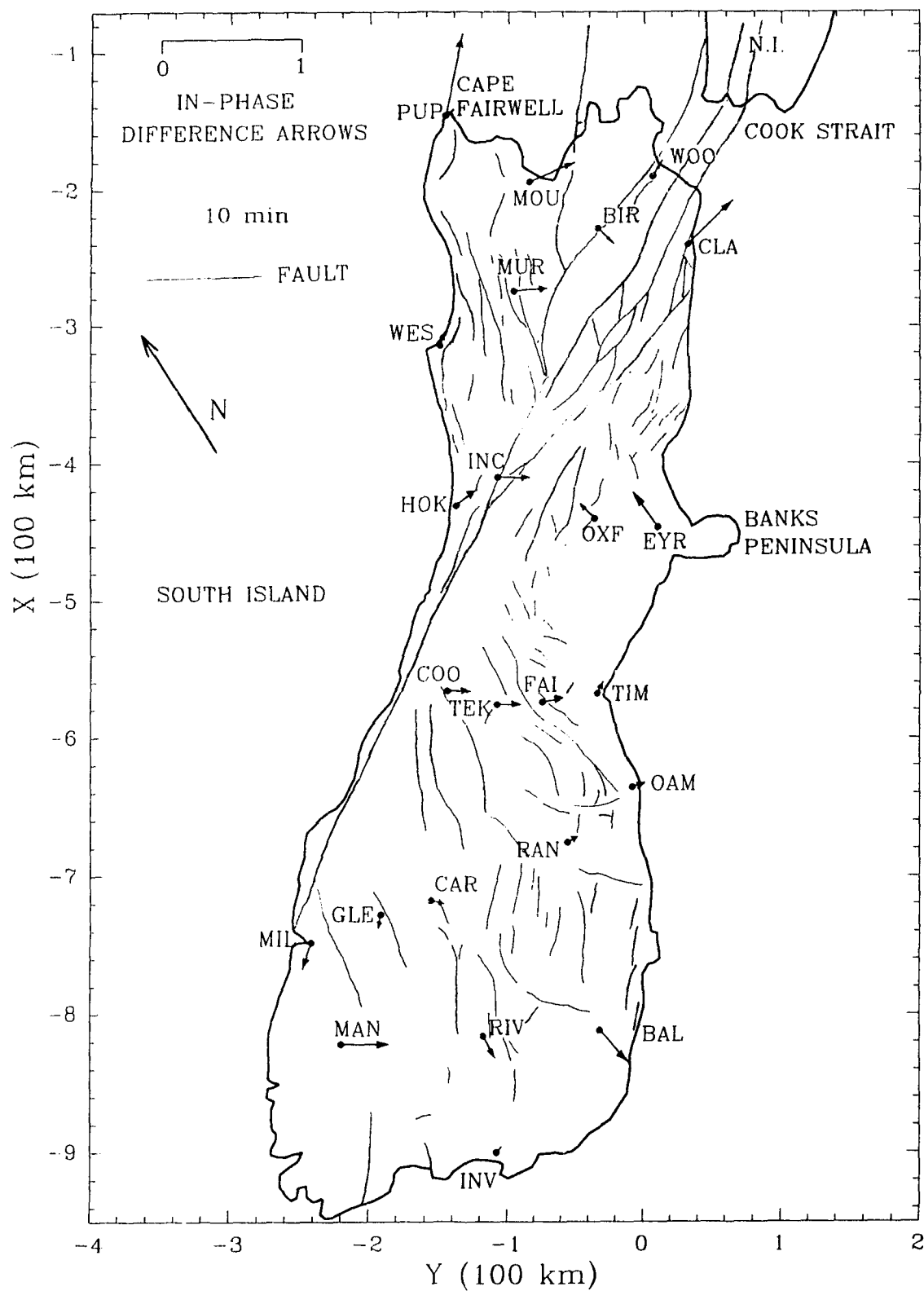


Figure 7.17: The in-phase difference arrows on South Island at 10 min period.

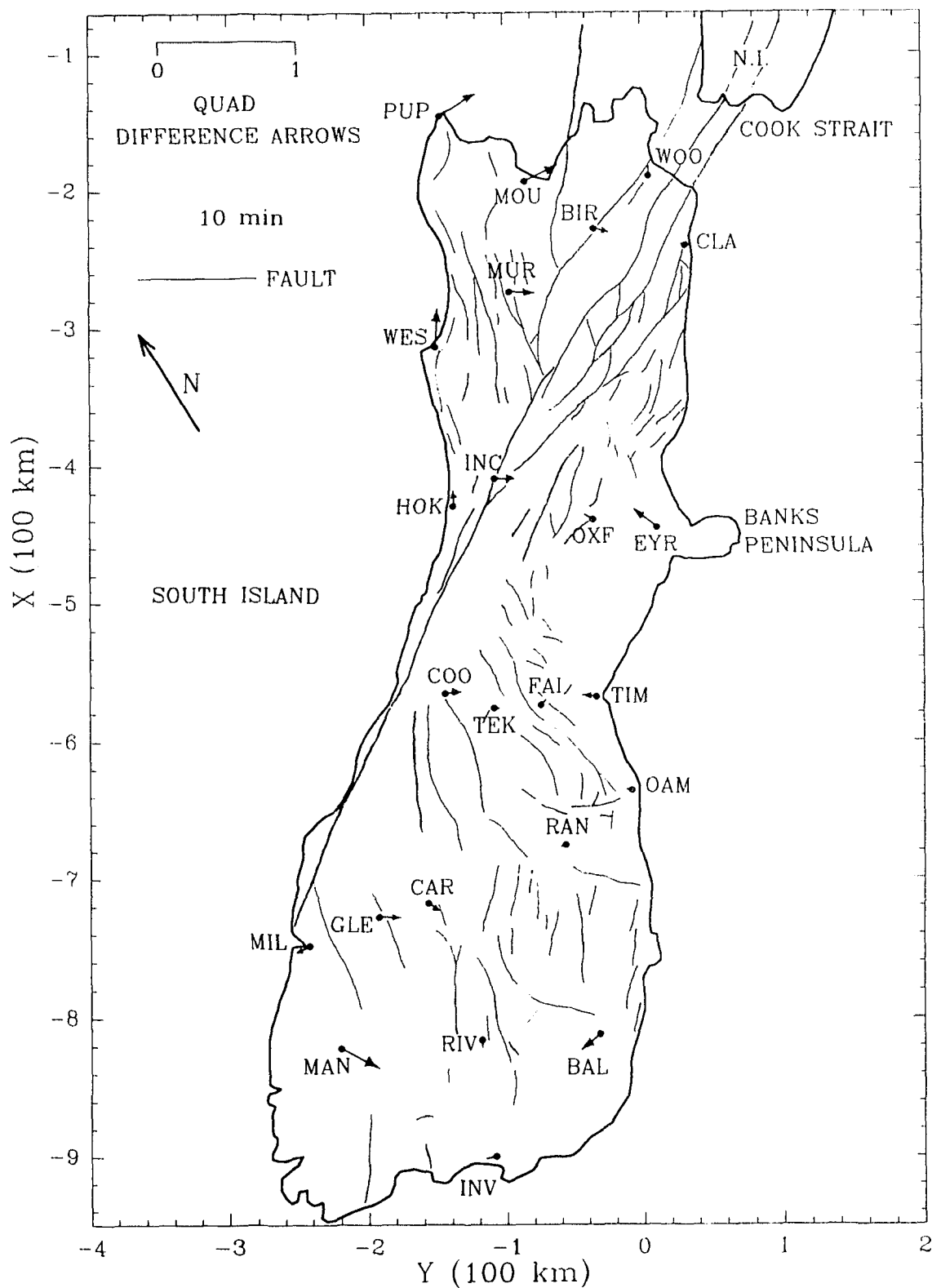


Figure 7.18: The quadrature difference arrows on South Island at 10 min period.

as the responses of the onland fault at PUP continuing out to sea in the South Taranaki Bight as shown in some geological maps. The inconsistent behaviour of the in-phase and quadrature arrows (Figs. 7.17, 7.19, and J.1-J.5) as function of period, does not, however, support such an interpretation, but might suggest a conductive anomaly offshore to the north.

At site MOU (near PUP), also right on the coast where the current channelling through Cook Strait is of importance, the quadrature arrows at all periods (Figs. 7.18, 7.20, and J.1-J.5) would indicate the responses to be those of the nearby (and more distant) faults to the east, and perhaps conductive structures associated with the narrow strip of Don Mountain rock (Fig. 7.12). The in-phase arrow at periods up to 15 min would support this interpretation, but at 20 min and longer periods, the arrow rotates clockwise to eventually point in a direction perpendicular to postulated tear in the subducting plate (dashed line in Fig. 7.12) just off shore near MOU.

The three sites BIR, WOO, and CLA (also very near Cook Strait) are situated in an extremely complex array of conductive structures in the form of a number of parallel faults (and thus a highly disturbed area), a series of parallel tears in the subducting plate, and a variety of rock types with possible conductive interfaces (Fig. 7.12). The sites BIR and WOO, to the left and to the right of the Wairau Fault respectively, tend to show the response of this fault to be the dominant component at some periods for both the in-phase and quadrature responses, and at other periods attest to the additional competing responses of the structures associated with the tears in the subducting plate and the local geology (various nearby rock types). The changing responses with period result in complete cancellation of

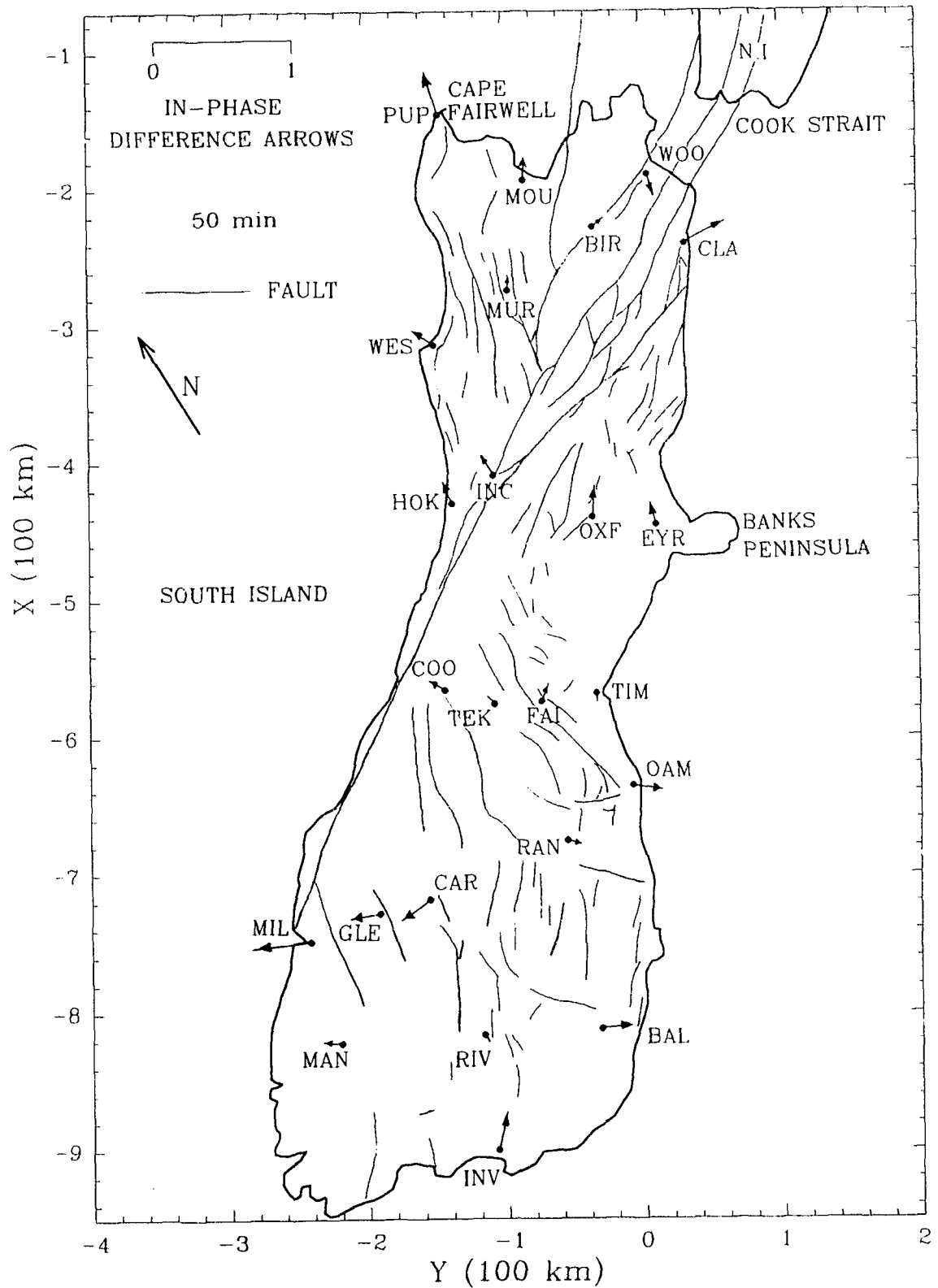


Figure 7.19: The in-phase difference arrows on South Island at 50 min period

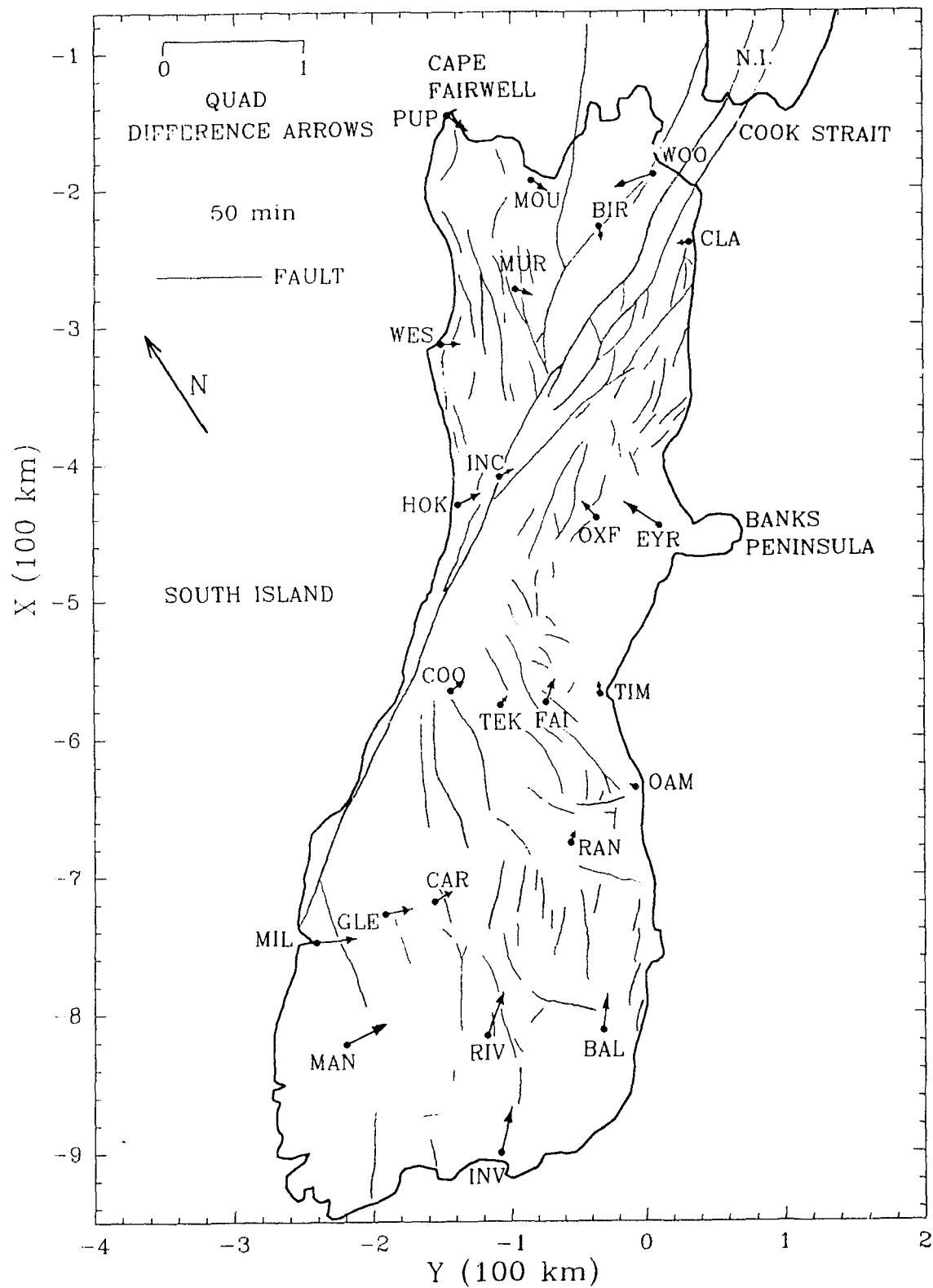


Figure 7.20: The quadrature difference arrows on South Island at 50 min period.

the responses at some periods, e.g. at 15, 20, 25 min for the in-phase component at BIR. At site CLA, the competing responses appear to be those of the array of parallel faults to the left and the nearby off shore conductive structures to the east associated with the Hikurangi Trench and the Pacific Plate subduction (postulated sediment wedge between the east coast and the trench). The in-phase arrows at 5 min point towards the trench, then with increasing period rotate clockwise somewhat, then reverse rotation to again point directly towards the trench at 80 min (Figs. 7.17, 7.19 and J.1-J.5). The quadrature arrow, on the other hand points inland to the array of parallel faults at periods up to 50 min, then at 80 min has rotated counter-clockwise by 90° . With a further increase in period the arrow would be expected to also point directly towards the trench.

At MUR, the site between a pair of faults that converge to a fork nearby, and about 40 km to the left of the major Alpine Fault, the quadrature arrows at 10 and 50 min (Figs. 7.18 and 7.20) consistently point towards the Alpine Fault, as might be expected. The in-phase arrow also has this direction (Figs. 7.17 and 7.19) up to 25 min period, but then begins to rotate clockwise to point northward at long periods, perhaps also responding to a segmented subducted Pacific Plate at depth.

The difference arrow responses at WES (near the cape on the west coast), may have limited validity due to considerable mutual coupling of the enhanced current of the cape effect and the conductive inland fault. However, the quadrature arrows at periods greater than 10 min do consistently point inland (Figs. 7.18, 7.20, and J.1-J.5) towards the array of faults roughly parallel to the coast as might be expected, whereas the in-phase components tend to point parallel to the coast then rotate to point seaward at long periods.

At HOK (near the bay coastline) the mutual coupling should be less of a problem than at WES. The main structures somewhat inland are the major Alpine Fault and a narrow strip of Haast Schist between the sedimentary basin and the large Torlesse rock area (Fig. 7.12). At periods of 15 to 50 min, the quadrature arrow (Figs. 7.20 and J.2-J.4) points towards the Alpine Fault and the rock boundaries, whereas the in-phase arrow (as was the case for site WES) again has a component parallel to the coast.

At INC (about 40 km inland), a site just to the left of the Alpine Fault, the quadrature arrow for periods less than 50 min (Figs. 7.18, J1-J4) points directly towards the Alpine and Hope Faults as expected, while the in-phase arrow for periods of 50 min (and greater) has rotated counter-clockwise to point seaward, as was the case at sites WES and HOK near the coast. This behaviour of the difference arrow at INC, a site far enough inland so as not be seriously affected by mutual coupling, might in fact indicate a conductive anomaly off shore. Since INC is situated right at the boundary of the large sedimentary basin (Fig. 7.12) that extends seaward, the off shore conductor could very well be this sedimentary basin.

The behaviour of the arrows at site OXF (about 50 km from EYR, the site discussed in detail in section 7.2.2) is almost identical to that of the arrows at EYR. That is, both the in-phase and quadrature arrows at all periods point northward to the Alpine and Hope Faults and the nearby minor faults parallel to the latter. Since the behaviour of the arrows at EYR, based on the Chamalaun and McKnight (1993) data set discussed here, is completely consistent with the behaviour of those of Kellett et al. (1988) presented in section 7.2.2, the responses at both OXF and EYR will not be discussed further here.

The sites COO, TEK, FAI, and TIM lie along a profile across the island approximately at the narrow mid-island section. At the three inland sites (first three named), the in-phase and quadrature arrows at 5 min (Fig. J.1) all point to the right directly towards nearby minor faults. The arrows at COO are showing the competing response of the Alpine Fault and the sedimentary basin to the left and perhaps the structure associated with the edge of the axial tectonic belt to the right (Fig. 7.12). At long periods the in-phase arrow has rotated to point to the left (Figs. 7.19 and J.5), opposite to that at short periods, while the quadrature arrow continues to point to the right at periods up to 50 min (Fig. 7.20), but at 80 min (Fig. J.5) has rotated counter-clockwise by about 90° . At still longer periods it should align its direction with that of the in-phase arrow. The behaviour of the arrows at each of TEK and FAI is very similar to that at COO, with the main difference that the arrow magnitudes are generally somewhat smaller at TEK and FAI, and perhaps rotate to point towards the Alpine Fault and the sedimentary basin at somewhat longer periods than was the case at COO, since the sedimentary basin to the right (boundary between FAI and TIM) too would be contributing to the responses. The responses at TIM (over the sedimentary basin, but near its border), though small, are still rather puzzling in that the in-phase arrows tend to point roughly parallel to the coast, while the quadrature arrows tend to point inland to the left at most periods.

The sites MIL, GLE, CAR, RAN and OAM in the southern region lie along a profile across roughly the widest section of the island. The arrows at MIL (near the west coast) may have limited validity due to mutual coupling effects associated with the very nearby ocean, sedimentary basin, Alpine Fault, and the complex

rock structure. The in-phase arrows at MIL for the entire period range $T=5-80$ min (Figs. 7.17, 7.19, and J.1-J.5), point in the south-west direction, as though the components to the left and right have cancelled, and the resultant response is that associated with the subduction zone at the southwestern tip of the island, where the Indian Plate is believed to be subducting beneath the Pacific Plate. The quadrature arrows at MIL, however, reverse direction from pointing towards the ocean at the short periods of 5 and 10 min (Figs. J.1 and 7.18) to pointing inland at 15 min and longer periods (Figs. J.2-J.5). It is puzzling that the directions of the quadrature arrows at MIL at long periods are roughly opposite to those of the in-phase arrows. But if valid, the arrows at long period may indicate that the induction in the eastward sloping Alpine Fault beneath the site, and a conductive interface between the schist and the Don Mountain rocks to the east, have greater importance than that of the offshore sedimentary basin to the west.

At GLE, CAR, RAN and OAM, the small in-phase and quadrature arrows at 10 min (Figs. 7.17 and 7.18) can be accounted for in part by the competing responses of the nearby array of minor faults and the sedimentary basin near the east coast, and at GLE, CAR and RAN in part by the underlying conductive Haast Schist rock, and at OAM in part by the conductive sedimentary basin (Fig. 7.12). With increasing period, the in-phase arrows at GLE and CAR increase in length, and at the long periods of $T=50$ and 80 min (Figs. 7.19 and J.5), point westward towards the boundary between the schist and the Dun Mountain rocks, while the quadrature arrows point eastward towards the nearby faults. At RAN and OAM (near the east coast), both the in-phase and quadrature arrows are essentially zero at 10 min (Figs. 7.17 and 7.18), as though the responses of the nearby multiple faults and the

sedimentary basin roughly cancel at these two sites. This seems to be also the case at the long period of 50 min (Figs. 7.19 and 7.20), except for the in-phase response at OAM, possibly due to the effect of unwanted mutual coupling at this coastal site.

At MAN, RIV and BAL (in the southern region of the island), both the in-phase and quadrature arrows at periods up to 25 min (Figs. 7.17, 7.18 and J.1-J.4) are seen to point towards the interface between the more conductive schist and the less conductive Dun Mountain rocks (Fig. 7.12). At the long period of 50 min (Figs. 7.19 and 7.20), the quadrature arrows at MAN, RIV and BAL are seen to point towards the boundary and the bulk of the conductive schist region. The in-phase arrows at MAN and BAL, however, at 50 min point seaward. These two sites are relatively near the cape coast line, and thus as explained earlier, the difference arrows here would show the effects of mutual coupling.

At INV (the southern tip of South Island) both the in-phase and quadrature arrow responses at the short periods of 5-10 min are small (Figs. 7.17, 7.18, and J.1). The site INV is located directly over a sedimentary basin (Southern Basins Province in Fig. 5.8) which could in part account for the observed small responses at short periods. With increasing period both the in-phase and quadrature arrows increase in length, reaching maximum responses at 50 min, as though pointing inland towards the conductive interface between the Haast Schist and Dun Mountain rocks (Fig. 7.12). The significant arrow responses at long periods (while the responses at short periods are negligible) may indicate that the sedimentary basin onland at the southern tip of the island is not very deep, so that at long periods the induction at the boundary becomes more important.

Although the interpretation of the difference arrow responses at some coastal sites must remain tenuous due to the effects of mutual coupling, the arrows at many sites do clearly show the responses of the conductive structures such as major and minor faults, sedimentary basins, and conductive regions associated with adjacent rock types, tears in the subducting plate, and the plate boundaries.

7.5 Chapter Summary

Analogue model induction arrow response curves along 16 traverses over the New Zealand laboratory analogue model were used to obtain the in-phase and quadrature induction arrows at 96 field sites. Since the New Zealand islands are relatively narrow, the coast effect is seen to be important at all sites. Further, at various sites near the complex coastline, the arrow responses clearly show the cape effects (East Cape, Cape Egmont, Banks Peninsula), the bay effects (Bay of Plenty, Hawke Bay, North and South Taranaki Bights), and the current channelling effects (Cook Strait). The difference arrows (field arrows minus analogue model arrows) at most sites in the survey region generally show the responses of the conductive geological and tectonic structures not included in the analogue model simulation.

The Midha (1979) and Ingham (1985a, 1985b, 1987, 1988b) Field Sites

The comparison of the analogue model and the field site (Midha and Ingham measurements) induction arrows at 35 sites on North Island for a range of periods $T=5-80$ min demonstrates the large role the ocean has in the observed field responses. The discrepancies between the model and field site (Midha, 1979)

induction arrows in the northern region of North Island support the hypothesis put forward by Midha (1979) of a NW-SE trending conductive structure both onland and offshore the north coast beneath the Bay of Plenty. The differences in the behaviour of the model and field arrows (Ingham, 1985a, b, 1987) in the Cape Egmont region could in part be attributed to the conductive structure postulated by Ingham (1987) to lie at about 40 km depth beneath the north-western part of North Island, and in part to the deep Wanganui sedimentary basin in this region. The model arrows in the southern tip region of North Island generally show larger responses than the field site arrows (Ingham, 1988b), and the model arrows rotate from pointing towards Cook Strait to pointing more directly towards the deep ocean off the east coast at a shorter period than is the case for the field site arrows. Such discrepancies may in part be attributed to tears in the subducting Pacific Plate (Robinson, 1986) beneath the southern end of North Island, as well as to the many major and minor faults in this region.

The Kellett et al. (1988) Eyrewell Field Site

The in-phase and quadrature model, field site and the difference induction arrows (field site arrows minus analogue model arrows) are discussed for periods $T=5-80$ min at the Eyrewell Observatory (EYR) near Christchurch on South Island. The model arrows clearly show the ocean coast effect. The in-phase model arrow shows a maximum length at about 15 min pointing towards the peninsular cape, while the quadrature arrow rotates from pointing away from the ocean at short periods to pointing towards the ocean at longer periods. The in-phase and quadrature difference arrows at EYR, consistently pointing northward towards the local minor faults and the more distant Alpine and Marlborough Faults for a wide period

range, are consistent with that predicted by the analogue model study of the responses of conductive faults as presented in Chapter 4. Expanding on the earlier interpretation of Kellett et al. (1988) that current channelling to Cook Strait could account for the observed geomagnetic fields, the present work shows that in addition to the effects of current channelling, induction in the conductive faulted region to the north provides an important component.

The Bromley (1979) Field Sites

The in-phase and quadrature difference arrow responses at 10 min period for 26 sites (Bromley, 1979) in the Southern Alps region on South Island are discussed. The difference arrows at many sites clearly show the responses of the nearby major and minor faults, as well as the responses of sedimentary basins in the survey region. The in-phase, as well as the quadrature difference arrows at two sites in particular (REE and INA) situated near the White Creek Fault, but on either side of the fault do point towards each other, and thus point towards the conductive fault. This is supported by the observation in the analogue model study of a conductive fault in Chapter 4, showing the arrows on either side pointing towards the fault, with the direction reversing directly over the fault. At another particular site (AIK), between the roughly parallel Alpine and Hope Faults, the in-phase difference arrow at 10 min points towards the Alpine Fault, while the quadrature arrow at this same period points away from the Alpine Fault. This induction arrow behaviour is predicted by the model study of a pair of parallel major-minor faults in Chapter 4, in that the in-phase and quadrature arrows at a given location between a pair of faults reverse directions at different periods. At sites (GOE, DUN, SPR) over the sedimentary basins, the difference arrows are seen to be very small as would be expected for induction arrows over a good conductor.

The Chamalaun and McKnight (1993) Field Sites

On the North Island of New Zealand, the difference arrows at sites HAM, WHK, GIS and TAU show the responses of the Central Volcanic Region, in addition to the responses of major (Wellington Fault) and minor faults nearby. The arrows at WHK, OHA and MAS also show the responses of the postulated (Robinson, 1986, Reyners, 1983) tears in the subducting Pacific Plate, as well as the response of the postulated (Midha, 1979) NW-SE trending conductor beneath the Bay of Plenty, particularly at long periods. The arrows at GIS and NAP near the east coast point towards the axis of the negative gravity anomaly, which has been interpreted as being associated with the subduction of the Pacific Plate. On South Island, the difference arrows at many sites, including OXF and EYR, show the responses of the major (Alpine and Marlborough Fault system) and minor faults, in addition to the many sedimentary basins. The arrow responses at GLE, MAN, RIV and BAL appear to show that the electrical conductivity contrasts between the conductive Haast Schist and adjoining resistive rocks do play a role in the observed geomagnetic responses.

In summary, although the interpretation of the difference arrows at some of the coastal sites in New Zealand must remain tenuous due to the effects of mutual coupling, the arrows at many of the 96 sites in this complex region have been successfully interpreted in terms of the geological and tectonic structures.

Chapter VIII

SUMMARY AND CONCLUSIONS

Since a fairly detailed summary is provided at the end of each chapter in the body of this dissertation, only a very brief summary, followed by suggestions for further work, will be given here.

Laboratory analogue models simulating finite length single and pairs of parallel conductive faults near an ocean coastline were studied to determine the induction arrow responses for a range of periods. Model measurements were also carried out for models of the ocean and the faults separately in order to examine the validity of removing the ocean responses through a vector subtraction. Empirical curves of the induction arrow responses for a range of parameters (e.g. fault depths, fault separation distances, inducing field periods, etc) applicable to the interpretation of geomagnetic field measurements are provided.

A laboratory analogue model of New Zealand was constructed and magnetic field measurements were carried out for a detailed grid of traverses for a wide range of periods. In-phase and quadrature induction arrow components were used to examine the coast effect responses for selected traverses over the model. The analogue model induction arrow responses were used to remove the coast effect components present in geomagnetic field site measurements through a simple vector subtraction of the model arrows from the field site arrows. The resulting difference arrows at 96 sites (both coastal and inland New Zealand) were interpreted

in terms of the responses of a range of conductive structures (conductive faults, sedimentary basins, geology, and subducting plate structure) in the field site survey region.

Recommended further work might include additional analogue model studies of fault models other than those included in the present work. In particular, the response of a non-vertical fault, such as the Alpine Fault that is believed to slope towards the east coast at an angle of up to 45° relative to the vertical, should be studied. It would be of interest in this case to examine the responses for a range of angles for both long and short faults. Further, since some sites in New Zealand were found to be situated near an array of parallel short and long faults, model studies similar to those carried out in the present work, but for models of three or more faults would be of interest. As well, responses of models that simulate a segmented subducting plate too would have application. The results of further studies of this nature would permit a more definitive interpretation at some sites in New Zealand, as well as have application to geomagnetic field studies in other geologically complex coastal regions.

REFERENCES

- Agarwal, A.K. and Weaver, J.T., 1989. Regional electromagnetic induction around the Indian Peninsula and Sri Lanka: a three-dimensional numerical model study using the thin sheet approximation. *Phys. Earth Planet. Inter.*, **54**, 320-331.
- Agarwal, A.K. and Dosso, H.W., 1990. On the behaviour of the induction arrows over a buried conductive plate — a numerical model study. *Phys. Earth Planet. Inter.*, **60**, 265-277.
- Agarwal, A.K. and Dosso, W.H., 1993. The characteristic periods of the induction arrows for a conductive-resistive interface—a numerical model study. *Phys. Earth Planet. Inter.*, **76**, 67-74.
- Agarwal, A.K. and Weaver, J.T., 1989. Regional electromagnetic induction around the Indian peninsula and Sri Lanka; a three-dimensional numerical model study using the thin sheet approximation. *Phys. Earth Planet. Inter.*, **54**, 320-331.
- Agarwal, A.K. and Weaver, J.T., 1993. Inversion of the COPROD2 data by a method of modelling. *J. Geomag. Geoelectr.*, **45**, 969-983.
- Agarwal, A.K., Poll, H.E. and Weaver, J.T., 1993. One- and two-dimensional inversion of magnetotelluric data in continental regions. *Phys. Earth Planet. Inter.*, **81**, 155-176.
- Arabasz, W.J. and Robinson, R., 1976. Microseismicity and geologic structure in the northern South Island, New Zealand. *N.Z. J. Geol. Geophys.*, **19**, 569-601.

- Arora, B.R. and Adam, A., 1992. Anomalous directional behaviour of induction arrows above elongated conductive structures and its possible causes. *Phys. Earth Planet. Inter.*, **74**, 183-190.
- Auld, D.R., Dosso, S.E., Oldenburg, D.W. and Law, L.K., 1992. Monitoring temporal change in conductivity in the central Vancouver Island region, an area with past large earthquakes. *Can. J. Earth Sci.*, **29**, 601-608.
- Bannister, S.C., 1988. Microseismicity and velocity structure in the Hawkes Bay region, New Zealand: fine structure of the subducting Pacific plate. *Geophysical Journal*, **95**, 45-62.
- Bapat, V.J., Segawa, J., Honkura, Y. and Tarits, P., 1993. Numerical estimation of the sea effect on the distribution of induction arrows in the Japanese island arc. *Phys. Earth Planet. Inter.*, **81**, 215-229.
- Barnes, P.M., 1990. Provenance of Cretaceous accretionary wedge sediments: the Mangapokia Formation, Wairarapa, New Zealand. *N.Z. J. Geol. Geophys.*, **33**, 125-135.
- Beanland, S., 1994. Field trip to the Wellington and Wairarapa Faults, compiled by S. Beanland. IASPEI 94, Wellington, New Zealand.
- Boerner, D.E., 1992. Controlled source electromagnetic deep sounding: theory, results and correlation with natural source results. *Surveys in Geophysics*, **13**, 435-488.
- Boteler, D.H., Kaiser, A.B. and Ingham, M.R., 1987. Direct observation of channelling of induced currents. *Geophys. J.R. Astro. Soc.*, **88**, 529-534.
- Brjunelli, B.Je., Dobrovolskaya, M.A., Kovtun, A.A. and Kuznetsov, N.S., 1969. In: *Methods of Investigating the Structure of the Earth's Crust and Upper Mantle*. Izd. Nauka, Moscow, p. 125.

- Bromley, C.J., 1979. Geomagnetic depth sounding and magneto-telluric survey of the Southern Alps. M.Sc. Thesis, Victoria University of Wellington, Wellington, New Zealand.
- Cagniard, L., 1953. Basic theory of the magneto-telluric method of geophysical prospecting. *Geophys.*, **8**, 605-635.
- Campbell, J.K., 1992. Field trip guides, edited by J.K. Campbell. Geological Society of New Zealand Miscellaneous Publication 63B, ISBN 0-908678-27-4.
- Campbell, W.H. and Schiffmacher, E.R., 1988. Upper mantle electrical conductivity for seven subcontinental regions of the Earth. *J. Geomag. Geoelectr.*, **40**, 1387-1406.
- Carter, L., Lewis, K.B. and Davey, F., 1988. Faults in Cook Strait and their bearing on the structure of central New Zealand. *N.Z. J. Geol. Geophys.*, **31**, 431-446.
- Cashman, S.M., Kelsey, H.M., Erdman, C.F., Cutten, H.N.C. and Berryman, K.R., 1992. Strain partitioning between structural domains in the forearc of the Hikurangi subduction zone, New Zealand. *Tectonics*, **11**, No.2, 242-257.
- Cerv, V. and Pek, J., 1990. Modelling and analysis of electromagnetic fields in 3D inhomogeneous media. *Surveys in Geophysics*, **11**, 205-229.
- Chamalaun, F.H. and McKnight, J.D., 1993. A New Zealand wide magnetometer array study. *J. Geomag. Geoelectr.*, **45**, 741-759.
- Chan, G.H., Dosso, H.W. and Law, L.K., 1981a. An analogue model study of electromagnetic induction for cape and bay coastlines. *Phys. Earth Planet. Inter.*, **25**, 167-176.

- Chan, E., Dosso, H.W. and Nienaber, W., 1981b. An analogue model study of electromagnetic induction in the Queen Charlotte Island region. *J. Geomagn. Geoelectr.*, **33**, 587-605.
- Chan, E., Dosso, H.W., Law, L.K., Auld, D.R. and Nienaber, W., 1983. Electromagnetic induction in the Queen Charlotte Island region : analogue model and field station results. *J. Geomagn. Geoelectr.*, **35**, 501-516.
- Charters, R.A., Dosso, H.W., Best, M.E. and Nienaber, W., 1989. Inductive coupling for a conductive dyke in a resistive Earth. *Phys. Earth Planet. Inter.*, **54**, 140-148.
- Chave, A.D. and Booker, J.R., 1987. Electromagnetic induction studies. *Rev. Geophys.*, **25**, 989-1003.
- Chen, J., Dosso, H.W. and Nienaber, W., 1989. Laboratory Electromagnetic Model Results for the EMSLAB Region. *J. Geophys. Res.*, **94**, 14167-14172.
- Chen, P.F. and Fung, P.C.W., 1985. Significance of the sign changing of the imaginary arrows in geomagnetic induction investigation. *Geophys. J.R. Astron. Soc.*, **80**, 257-263.
- Chen, P.F. and Fung, P.C.W., 1987. On the behaviour of the imaginary Parkinson arrows near the anomalous conductor-host medium interface. *Phys. Earth Planet. Inter.*, **50**, 195-198.
- Chouteau, M., 1985. Magnetotelluric measurements in La Malbaie area (Quebec): the anomalous vertical magnetic field. *Can. J. Earth Sci.*, **22**, 1530-1536.
- Christoffel, D.A. and Linford, J.G., 1968. The magnetotelluric method for locating major geological features and its application in the Wairarapa. *N. Z. J. Geol. Geophys.*, **11**, 66-77.

- Clowes, R.M., Green, A.G., Yorath, C.J., Kanasewich, E.R., West, G.F. and Garland, G.D., 1984. Lithoprobe—a national program for studying the third dimension of geology. *Journal of the Canadian Society of Exploration Geophysicists*, **20**, No.1, 23-39.
- Clowes, R.M., Cook, F.A., Green, A.G., Keen, C.E., Ludden, J.N., Percival, J.A., Quinlan, G.M. and West, G.F., 1992. Lithoprobe: new perspectives on crustal evolution. *Canadian Journal of Earth Sciences*, **29**, 1813-1864.
- Constable, S.C., Parker, R.L. and Constable, C.G., 1987. Occam's Inversion: a practical algorithm for generating smooth models from EM sounding data. *Geophysics*, **52**, 289-300.
- Constable, S.C., 1990. Marine electromagnetic induction studies. *Surveys in Geophysics*, **11**, 303-327.
- Cowan, H., 1994. Field guide to New Zealand active tectonics - IASPEI 94, compiled by H. Cowan. The Royal Society of New Zealand, Miscellaneous Series 27.
- Czochanska, Z., Sheppard, C.M., Weston, R.J. and Woolhouse, A.D., 1987. A biological marker study of oil and sediments from the west coast, South Island, New Zealand. *N. Z. J. Geol. Geophys.*, **30**, 1-17.
- Darby, D. J. and Beanland, S., 1992. Possible source models for the 1855 Wairarapa earthquake, New Zealand. *J. Geophys. Res.*, **97**, 12375-12389.
- Davey, F.J. and Smith, E.G.C., 1983. The tectonic setting of the Fiordland region, south-west New Zealand. *Geophys. J.R. Astron. Soc.*, **72**, 23-38.
- Dawson, T.W. and Weaver, J.T., 1979. Three-dimensional induction in a non-uniform thin sheet at the surface of a uniformly conducting earth. *Geophys. J. R. Astro. Soc.*, **59**, 445-462.

- DeLaurier, J.M., Auld, D.R and Law, L.K., 1983. The geomagnetic response across the continental margin off Vancouver Island: comparison of results from numerical modelling and field data. *J. Geomag. Geoelectr.*, **35**, 517-528.
- Dosso, H.W., 1966a. A plane wave analogue model for studying electromagnetic variations. *Can. J. Phys.*, **44**, 67-80.
- Dosso, H.W., 1966b. Analogue model measurements for electromagnetic variations near vertical faults and dykes. *Can. J. Earth Sci.*, **3**, 287-303.
- Dosso, H.W., 1966c. The electric and magnetic fields at the surface of a flat conducting earth in the near field of an oscillating line current. *Can. J. Phys.*, **44**, 1923-1931.
- Dosso, H.W., 1969. Analogue model study of electromagnetic variations over an anisotropic conductor. *J. Geomag. Geoelectr.*, **21**, 647-653.
- Dosso, H.W., 1973. A review of analogue model studies of the coast effect. *Phys. Earth Planet. Inter.*, **7**, 294-302.
- Dosso, H.W., Agarwal, A.K. and Chen, J., 1992. EM induction in the Vancouver Island region: 3D numerical, Analogue model, and field site results. *PAGEOPH*, **138**, 193-206.
- Dosso, H.W., Chan, G.H. and Nienaber, W., 1986. An analogue model study of EM induction for an island near bay and cape coastlines. *Phys. Earth Planet. Inter.*, **42**, 178-183.
- Dosso, H.W., Chen, J. and Nienaber, W., 1990. Comparison of Analogue Model and Field Station EM Responses on Southern Vancouver Island. *Phys. Earth Planet. Inter.*, **60**, 18-24.

- Dosso, H.W. and Jacobs, J.A., 1968. Analogue model measurements of electromagnetic variations in the near field of an oscillating line current. *Can. J. Earth Sci.*, **5**, 23-29.
- Dosso, H.W. and Meng, M., 1992. The coast effect response in geomagnetic field measurements. *Phys. Earth Planet. Inter.*, **70**, 39-56.
- Dosso, H.W., Nienaber, W. and Hutton, V.R.S., 1980a. An analogue model study of electromagnetic induction in the British Isles region. *Phys. Earth Planet. Inter.*, **22**, 68-85.
- Dosso, H.W., Nienaber, W., Wright, J.A., Greenhouse, J.P. and Bailey, R.C., 1980b. An analogue model study of electromagnetic induction in the eastern coastal region of North America. *Phys. Earth Planet. Inter.*, **23**, 13-30.
- Dosso, H.W., Nienaber, W. and Parkinson, W.D., 1985. An Analogue Model study of Electromagnetic induction in the Tasmania region. *Phys. Earth Planet. Inter.*, **39**, 118-133.
- Dosso, H.W. and Nienaber, W., 1986. A laboratory electromagnetic model study of the Juan de Fuca plate region. *Phys. Earth Planet. Inter.*, **43**, 34-46.
- Dosso, H.W., Nienaber, W. and Chen, J., 1989. Laboratory electromagnetic modelling of the subducting Juan de Fuca Plate. *Phys. Earth Planet. Inter.*, **53**, 221-227.
- Dosso, S.E. and Oldenburg, D.W., 1991. Magnetotelluric appraisal using simulated annealing. *Geophys. J. Int.*, **106**, 379-385.
- Duckworth, K., 1987. Lithologically discordant resistivity and IP anomalies associated with hydrocarbons in the Rocky Mountain foothills of Alberta, Canada. *Expl. Geophys.*, **18**, 31-34.
- EOS, Vol. **74**, No.28, p.316-317. July 13, 1993.

- EMSLAB, 1989. Special Issue of Journal of Geophysical Research devoted to the EMSLAB experiment (14 papers). *J. Geophys. Res.*, **94**, 14093-14283.
- Everett J.E. and Hyndman R.D., 1967. Geomagnetic variation and electrical conductivity structure in south-western Australia. *Phys. Earth Planet. Interiors*, **1**, 24-34
- Fainberg, E.B., Pankratov, O.V. and Singer, B.Sh., 1993. Thin sheet modelling of subsurface and deep inhomogeneities. *Geophys. J. Int.*, **113**, 144-154.
- Fischer, G. and LeQuang, B.V., 1981. Topography and minimization of the standard deviation in one-dimensional magnetotelluric modelling. *Geophys. J. R. Astr. Soc.*, **67**, 279-292.
- Fischer, G. and Weaver, J.T., 1986. Theoretical investigations of the ocean-coast effect at a passive continental margin. *Phys. Earth Planet. Inter.*, **42**, 246-254.
- Frischknecht, F.C., 1971. Electromagnetic scale modelling. in *Electromagnetic Probing in Geophysics*, edited by Wait, J.R., The Golem Press, Boulder, Colorado.
- Gill, P.J. and MacDonald, W.J.P., 1967. Large scale earth resistivity experiment in New Zealand. *Nature*, **216**, 1195-1197.
- Gough, D.I., 1989. Magnetometer array studies, Earth structure, and tectonic processes. *Reviews of Geophysics*, **27**, 141-157.
- Gough, D.I., 1992. Electromagnetic exploration for fluids in the Earth's crust. *Earth Sci. Rev.*, **32**, 3-18.
- Gough, D.I. and Ingham, M.R., 1983. Interpretation methods for magnetometer arrays. *Rev. Geophys. Space Phys.*, **21**, 805-827.

- Gregori, G.P. and Lanzerotti, L.J., 1980. Geomagnetic Depth Sounding by Induction Arrow Representation: A Review. *Rev. Geophys. Space Phys.*, **18**, 203-209.
- Gregori, G.P. and Lanzerotti, L.J. and Meloni, A., 1982. Reply. *Rev. Geophys. Space Phys.*, **20**, 523-528.
- Grindley, G.W., 1978. Alpine schist belt-Haast to Wanganui rivers, south Westland. in *The Geology of New Zealand, Volume 1*. Chief editor: R.P.Suggate, Government Printer, Wellington, New Zealand.
- Groom, R. W. and Bailey, R.C., 1989. Decomposition of magnetotelluric impedance tensors in the presence of local three-dimensional galvanic distortion. *J. Geophys. Res.*, **94**, 1913-1925.
- Groom, R.W. and Bahr, K., 1992. Corrections for near surface effects: decomposition of the magnetotelluric impedance tensor and scaling corrections for regional resistivities: a tutorial. *Surveys in Geophysics*, **13**, 341-379.
- Haak, V. and Hutton, V.R.S., 1986. Electrical resistivity in continental lower crust. *Geol. Soc. London, Spec. Publ.*, **24**, 35-49.
- Hatherton, T., 1970. Upper mantle inhomogeneity beneath New Zealand: surface manifestations. *J. Geophys. Res.*, **75**, 269-284.
- Heard, G.J., Dosso, H.W., Nienaber, W. and Lokken, J.E., 1983. The electromagnetic response of the Assistance Bay region. *J. Geomagn. Geoelectr.*, **35**, 529-5451.
- Heard, G.J., Dosso, H.W., Nienaber, W. and Lokken, J.E., 1985. Laboratory analogue modelling of the Schumann resonance source field. *Phys. Earth Planet. Inter.*, **39**, 178-181.

- Hebert, D., Dosso, H.W. and Nienaber, W., Wright, J.A., 1983a. Analogue model study of electromagnetic induction in the Newfoundland region. *Phys. Earth Planet. Inter.*, **32**, 65-84.
- Hebert, D., Wright, J.A., Dosso, H.W. and Nienaber, W., 1983b. Comparison of analogue model and field station results for the Newfoundland region. *J. Geomagn. Geoelectr.*, **35**, 673-682.
- Heinson, G.S. and Lilley, F.E.M., 1993. An application of thin-sheet electromagnetic modelling to the Tasman Sea. *Phys. Earth Planet. Inter.*, **81**, 231-251.
- Hibbs, R.D., Jones, F.W., Ramaswamy, V. and Dosso, H.W., 1978. Electromagnetic analogue model measurements and finite-difference numerical calculations of the responses of a conducting slab to three different source fields. *Phys. Earth Planet. Inter.*, **16**, 327-340.
- Hjelt, S.E., 1988. Regional EM studies in the 80's. *Surveys in Geophysics*, **9**, 349-387.
- Hjelt, S.E. and Korja, T., 1993. Lithospheric and upper-mantle structures, results of electromagnetic soundings in Europe. *Phys. Earth Planet. Inter.*, **79**, 137-177.
- Hu, W.B., Nienaber, W. and Dosso, H.W., 1983. Laboratory model magnetic field for the Hainan Island region. *J. Geomagn. Geoelectr.*, **35**, 683-692.
- Hu, W.B., Dosso, H.W. and Nienaber, W., 1984. Analogue model magnetic field responses of an ocean channel, and island and a seamount in the Hainan Island region. *J. Geophys.*, **55**, 222-227.
- Hu, W.B., Dosso, H.W. and Nienaber, W., 1986. Model magnetic field responses of an ocean channel, an island, and a seamount for two polarizations. *Annales Geophysicae*, **4**, 165-172.

- Hu, W.B., Nienaber, W. and Dosso, H.W., 1989. Vertical magnetic field response of a seamount. *Phys. Earth Planet. Inter.*, **54**, 135-139.
- Hurst, A.W., 1974. Magnetic effects in volcanic regions. Ph.D. Thesis, Victoria University of Wellington, New Zealand.
- Ingham, M.R., 1985a. Magnetovariational measurements in the Cook Strait region of New Zealand. *Phys. Earth Planet. Inter.*, **39**, 182-193.
- Ingham, M.R., 1985b. Magnetotelluric measurements in the Wellington region. *N.Z. J. Geol. Geophys.*, **28**, 397-404.
- Ingham, M.R., 1987. Lower crustal and upper mantle electrical conductivity contrasts in the central North Island of New Zealand. *Phys. Earth Planet. Inter.*, **49**, 304-313.
- Ingham, M.R., 1988a. The use of invariant impedances in magnetotelluric interpretation. *Geophysical J.* **92**, 165-169.
- Ingham, M.R., 1988b. A magnetotelluric and magnetovariational traverse across the New Zealand subduction zone. *Geophys. J.R. Astron. Soc.*, **92**, 495-504.
- Ingham, M.R., 1991. Electrical conductivity structure of the Broadlands-Ohaaki geothermal field, New Zealand. *Phys. Earth Planet. Inter.*, **66**, 62-75.
- Jiracek, G.R., 1990. Near-surface and topographic distortion in electromagnetic induction. *Surveys in Geophysics*, **11**, 163-203.
- Jones, A.G., 1981a. Comment on "Geomagnetic depth sounding by induction arrow representation : A review" by G.P. Gregori and L. J. Lanzerotti. *Rev. Geophys. Space Phys.*, **19**, 687-688.
- Jones, A.G., 1981b. Geomagnetic induction studies in Scandinavia—II. Geomagnetic depth sounding, induction vectors and coast effect. *J. Geophysics*, **50**, 23-36.

- Jones, A.G., 1983. The problem of current channelling: a critical review. *Geophysical Surveys*, **6**, 79-122.
- Jones, A.G., 1986. Parkinson's pointers' potential perfidy ! *Geophys. J.R. Astr. Soc.*, **87**, 1215-1224.
- Jones, A.G. and Craven, J.A., 1990. The North American Central Plains conductivity anomaly and its correlation with gravity, magnetics, seismic, and heat flow data in the Province of Saskatchewan. *Phys. Earth Planet. Inter.*, **60**, 169-194.
- Jones, A.G., 1987. MT and reflection: an essential combination. *Geophys. J.R. Astron. Soc.*, **89**, 7-18.
- Jones, A.G., 1992. Electrical conductivity of the continental lower crust. In: D.M. Fountain, R.J. Arculus and R.W. Kay (editors), Elsevier, Amsterdam, pp. 81-143.
- Jones, A.G., Kurtz, R.D., Boerner, D.E., Craven, J.A. and McNeice, G.W., 1992. Electromagnetic constraints on strike-slip fault geometry--The Fraser River fault system. *Geology*, **20**, 561-564.
- Jones, A.G., 1993. Electromagnetic images of modern and ancient subduction zones. *Tectonophysics*, **219**, 29-45.
- Kaikkonen, P., 1986. Numerical electromagnetic modeling including studies of characteristic dimensions: a review. *Surveys in Geophysics*, **8**, 301-337.
- Kamp, P.J.J., 1984. Neogene and Quaternary extent and geometry of the subducted Pacific Plate beneath North Island, New Zealand: implications for Kaikoura tectonics. *Tectonophysics*, **108**, 241-266.

- Kamp, P.J.J and Hegarty, K.A., 1989. Multigenitic gravity couple across a modern convergent margin: inheritance from Cretaceous asymmetric extension. *Geophysical J.*, **96**, 33-41.
- Kang, S, Dosso, H.W. and Ogunade, S.O., 1993. Electromagnetic induction in South-west Nigeria: analogue model and field results. *J. Geomag. Geoelectr.*, **45**, 805-816.
- Katz, H.R., 1979. Alpine uplift and subsidence of foredeeps. In: Walcott, R.I.; Cresswell, M.M. ed. *The origin of the Southern Alps. Bulletin of the Royal Society of New Zealand* **18**, 121-130.
- Kayal, J.R., 1984. Microseismicity and tectonics at the Indian/Pacific plate boundary: south-east Wellington province, New Zealand. *Geophys. J. R. Astr. Soc.*, **77**, 567-592.
- Keller, G.V., Pritchard, J.I., Jacobson, J.J. and Harthill, N., 1984. Megasource time-domain electromagnetic sounding methods. *Geophysics*, **49**, 993-1009.
- Kellett, R.L., Ferguson, I.J. and Lilley, R.E.M., 1988. Magnetic field fluctuations at the Eyrewell Observatory, Christchurch, New Zealand. *N.Z. J. Geol. Geophys.*, **31**, 87-93.
- Kurtz, R.D., DeLaurier, J.M. and Gupta, J.C., 1986. A magnetotelluric sounding across Vancouver Island sees the subducting Juan de Fuca plate. *Nature*, **321**, 596-599.
- Kurtz, R.D., Macnae, J.C. and West, G.F., 1989. A controlled-source, time-domain electromagnetic survey over an upthrust section of Archean crust in the Kapuskasing Structural Zone. *Geophys. J. Int.*, **99**, 195-203.

- Kurtz, R.D., DeLaurier, J.M. and Gupta, J.C., 1990. The electrical conductivity distribution beneath Vancouver Island: a region of active plate subduction. *J. Geophys. Res.*, **95**, 10929-10946.
- Lawrie, J.A., 1965. Directions of geomagnetic fluctuations near coastlines. *N. Z. J. Geol. Geophys.*, **8**, 869-884.
- Lilley, F.E.M. and Arora, B.R., 1982. The sign convention for quadrature Parkinson arrows in geomagnetic induction studies. *Rev. Geophys. Space Phys.*, **20**, 513-518.
- Lilley, F.E.M., Filloux, J.H., Ferguson, I.J., Bindoff, N.L. and Mulhearn, P.J., 1989. The Tasman project of seafloor magnetotelluric exploration: experiment and observation. *Phys. Earth Planet. Inter.*, **53**, 405-421.
- Macnae, J.D. and Lamontagne, Y., 1987. Imaging quasi-layered conductive structures by simple processing of TEM data. *Geophysics*, **52**, 545-554.
- McCaig, A.M., 1988. Deep fluid circulation in fault zones. *Geology*, **16**, 867-870.
- McGeary, S., 1989. Reflection seismic evidence for a Moho offset beneath the Walls Boundary strike-slip fault. *Geological Society of London Journal*, **146**, 261-269.
- McKirdy, D. McA., Weaver, J.T. and Dawson, T.W., 1985. Induction in a thin sheet of variable conductance at the surface of a stratified earth--II: three-dimensional theory. *Geophys. J.R. Astron. Soc.*, **80**, 177-194.
- Meng, Z. and Dosso, H.W., 1990. An analogue model study of EM induction in the Japan--Korea--China region. *Phys. Earth Planet. Inter.*, **62**, 246-256.
- Meng, Z., Dosso, H.W. and Nienaber, W., 1990. An analogue model study of EM induction in the North China--Korea coastal region. *Phys. Earth Planet. Inter.*, **60**, 25-39.

- Midha, R.K., 1979. Geoelectromagnetic induction studies in the North Island Volcanic Region, New Zealand. Ph.D. Thesis, Victoria University of Wellington, New Zealand, 342 pp.
- Miles, T. and Dosso, H.W., 1979. A laboratory analogue model study of ocean-wave induced magnetic field for cases of non-uniform depths and sea-land interfaces. *Phys. Earth Planet. Inter.*, **19**, 12-20.
- Miles, T. and Dosso, H.W., 1980. An analogue model study of ocean-wave induced magnetic field variations near a coastline. *J. Geomagn. Geoelectr.*, **32**, 151-154.
- Miles, T., Dosso, H.W. and NG, T.P., 1977. An analogue model for studying magnetic variations induced by ocean waves. *Phys. Earth Planet. Inter.*, **14**, 137-142.
- Morisson, H.F., Clarke, A.J., Hansen, W.D. and Becker, A., 1982. A versatile EM scale modelling system (SEG 1981 annual meeting abstracts). *Geophysics*, **47**, 435.
- Nekut, A. and Spies, B.R., 1989. Petroleum exploration using controlled source electromagnetic methods. *Proc. IEEE* **77**, 338-362.
- Niblett, E.R. and Sayn-Wittgenstein, C., 1960. Variations of electrical conductivity with depth by the magnetotelluric method. *Geophysics*, **25**, 998-1008.
- Nienaber, W., Dosso, H.W., Law, L.K., Jones, F.W. and Ramaswamy, V., 1976. An analogue model study of electromagnetic induction for island-continent ocean channels. *Phys. Earth Planet. Inter.*, **13**, 169-183.
- Nienaber, W., Dosso, H.W., Law, L.K., Jones, F.W., and Ramaswamy, V., 1977a. An analogue model study of electromagnetic induction for island-continent ocean channels for the H polarization. *Phys. Earth Planet. Inter.*, **15**, 69-76.

- Nienaber, W., Dosso, H.W., Law, L.K., Jones, F.W. and Ramaswamy, V., 1977b.
Studies of electromagnetic induction for island-continent ocean channels with applications to Vancouver Island. *Acta. Geodaet., Geophys. et Montanist. Acad. Sci. Hung.*, 12, 187-190.
- Nienaber, W., Dosso, H.W., Law, L.K., Jones, F.W. and Ramaswamy, V., 1979a.
An analogue model study of electromagnetic induction in the Vancouver Island region. *J. Geomagn. Geoelectr.*, 31, 115-132.
- Nienaber, W., Dosso, H.W., Law, L.K., Jones, F.W. and Ramaswamy, V., 1979b.
Electromagnetic induction in the Vancouver Island region — field station and analogue model results. *J. Geomagn. Geoelectr.*, 31, 599-613.
- Nienaber, W., Dosso, H.W., Law, L.K. and Jones, F.W., 1980. Electromagnetic induction in the Vancouver Island region. *J. Geomagn. Geoelectr.*, 32, 45-49.
- Nienaber, W., Dosso, H.W. and Hutton, V.R.S., 1981. Electromagnetic induction in the British Isles region: analogue model and field station results. *Phys. Earth Planet. Inter.*, 27, 122-132.
- Nienaber, W., Hibbs, R.D., Dosso, H.W. and Law, L.K., 1982. An estimate of the conductivity structure for the Vancouver Island region from geomagnetic results. *Phys. Earth Planet. Inter.*, 27, 300-305.
- Nienaber, W., Hebert D. and Dosso, H.W., 1983. Induction Arrows for a Buried Conducting Plate. *Phys. Earth Planet. Inter.*, 32, 306-311.
- Ogunade, S.O., Ramaswamy, V. and Dosso, H.W., 1974. Electromagnetic responses of a conducting sphere buried in a conducting earth. *J. Geomagn. Geoelectr.*, 26, 417-427.

- Ogunade, S.O. and Dosso, H.W., 1977. Subsurface electromagnetic response of a conducting sphere embedded in the lower layer of a two-layer earth. *Acta. Geodaet., Geophys. et Montanist. Acad. Sci. Hung.*, **12**, 311-314.
- Ogunade, S.O. and Dosso, H.W., 1980. The inductive response of a horizontal conducting cylinder buried in a uniform earth for a uniform inducing field. *Geophysical Prospecting*, **28**, 601-609.
- Ogunade, S.O. and Dosso, H.W., 1981. The response of a horizontal conducting cylinder embedded in a uniform earth for uniform and line current sources. *PAGEOPH*, **119**, 51-58.
- Oldenburg, D.W. and Ellis, R.G., 1993. Effective inversion of magnetotelluric data in two dimensions. *Physics of the Earth and Planetary Interiors*, **81**, 177-200.
- Olm, M.C. and Frischknecht, F.C., 1982. EM scale model study of the dual frequency differencing technique (SEG 1981 annual meeting abstracts). *Geophysics*, **47**, 436.
- Parker, R.L., 1980. The inverse problem of electromagnetic induction: existence and construction of solutions based on incomplete data. *J. Geophys. Res.*, **85b**, 4421-4428.
- Parkinson, W.D., 1959. Direction of rapid geomagnetic fluctuation. *Geophys. J.R. Astr. Soc.*, **2**, 1-14.
- Parkinson, W.D., 1962. The influence of continents and oceans on geomagnetic variations. *Geophys. J.R. Astron. Soc.*, **6**, 441-449.
- Parkinson, W.D. and Jones, F.W., 1979. The geomagnetic coast effect. *Rev. Geophys. Space Phys.*, **17**, No. 8, 1999-2015.

- Parkinson, W.D., Hermanto, R., Sayers, J., Bindoff, N.L., Dosso, H.W. and Nienaber, W., 1988. The Tamar conductivity anomaly. *Phys. Earth Planet. Inter.*, **52**, 8-22.
- Pillans, B., 1986. A late Quaternary uplift map for North Island, New Zealand, in *Recent Crustal Movements of the Pacific Region*, ed. Reilly, W.I., Bull. R. Soc. N.Z., Wellington, New Zealand.
- Price, A.T., 1949. The introduction of electric currents in non-uniform thin sheets and shells. *Q.J. Mech. Appl. Math.*, **2**; 283-310.
- Pu, X.H., Agarwal, A.K. and Weaver, J.T., 1993. Magnetic Field Solutions of E-polarization induction problems. *J. Geomag. Geoelectr.*, **45**, 859-872.
- Raiche, A., 1993. Modelling and inversion — progress, problems, and challenges. *Surveys in Geophysics*, in press.
- Ramaswamy, V. and Dosso, H.W., 1973. Locating a horizontal magnetic dipole buried in a 2-layer earth. *Electronics Letters*, **9**, No.4.
- Ramaswamy, V. and Dosso, H.W., 1975. Effect of a conducting overburden on the fields of a buried dipole source. *Can. J. Phys.*, **53**, 598-609.
- Ramaswamy, V. and Dosso, H.W., 1977. The response of a conducting cylinder to the inducing fields of various sources. *J. Geomag. Geoelec.*, **29**, 181-189.
- Ramaswamy, V. and Dosso, H.W., 1978. Analogue model measurements for a horizontal magnetic dipole embedded within a conducting medium. *Phys. Earth Planet. Inter.*, **17**, 295-299.
- Ramaswamy, V., Dosso, H.W. and Weaver, J.T., 1972. Horizontal magnetic dipole embedded in a two-layer conducting medium. *Can. J. Phys.*, **50**, 607-616.

- Ramaswamy, V., Nienaber, W., Dosso, H.W., Jones, F.W. and Law, L.K., 1975.
Numerical and analogue model results for electromagnetic induction for an island situated near a coastline. *Phys. Earth Planet. Inter.*, **11**, 81-90.
- Ramaswamy, V., Nienaber, W., Dosso, H.W., Jones, F.W. and Law, L.K., 1977.
Comments on the "Numerical and analogue model results for electromagnetic induction for an island situated near a coastline". *Phys. Earth Planet. Inter.*, **14**, 28-30.
- Ramaswamy, V., Jones, F.W., Dosso, H.W. and Nienaber, W., 1980. A comparison of numerical, analogue model, and field-station vertical magnetic-fields for the Vancouver Island region. *Phys. Earth Planet. Inter.*, **22**, 60-67.
- Rankin, D., 1962. The magnetotelluric effect on a dike. *Geophysics*, **27**, 666-676.
- Rankin, D., Garland, G.D. and Vozoff, K., 1965. An analog model for the magnetotelluric effect. *J. Geophys. Res.*, **70**, 1939-1945.
- Reilly, W. I., 1978. Gravity anomalies. in *The Geology of New Zealand*, Volume 1. Chief editor: R.P. Suggate, Government Printer, Wellington, New Zealand.
- Reyners, M., 1983. Lateral segmentation of the subducted plate at the Hikurangi Margin, New Zealand: seismological evidence. *Tectonophysics*, **96**, 203-223.
- Reyners, M., 1989. New Zealand seismicity 1964-87: an interpretation. *N.Z. J. Geol. Geophys.*, **32**, 307-315.
- Reyners, M., Gledhill, K. and Waters, D., 1991. Tearing of the subducted Australian plate during the Te Anau, New Zealand, earthquake of 1988 June 3. *Geophys. J. Int.*, **104**, 105-115.
- Roberts, R. G., 1986. Global electromagnetic induction. *Surveys in Geophysics*, **8**, 339-374.

- Robinson, R., 1986. Seismicity, structure and tectonics of the Wellington region, New Zealand. *Geophys. J.R. Astr. Soc.*, **87**, 379-409.
- Rokityansky, I.I., 1982. Geoelectromagnetic investigation of the earth's crust and mantle. Springer, Berlin, 287 pp.
- Schmucker, U., 1970. Anomalies of geomagnetic variations in the southwestern United States. *Bull. Scripps Inst. Oceanography, University of California*. **13**, 1-165.
- Schmucker, U., 1983. Anomalies of geomagnetic variations in the southwestern United States. *Bull. Scripps Inst. Oceanography*, **13**, University of California Press, California.
- Schnegg, P.A., Le Quang, B.V., Fisher, G. and Weaver, J.T., 1983. Audio-magnetotelluric study of a structure with a reverse fault. *J. Geomagn. Geoelectr.*, **35**, 653-671.
- Schnegg, P.A., Fischer, G., Le Quang, B.V. and Weaver, J.T., 1986. Investigation of a buried vertical fault with natural and controlled source AMT. *Annales Geophysicae*, **4**, B, 2, 139-144.
- Schwarz, G., 1990. Electrical conductivity of the Earth's crust and upper mantle. *Surveys in Geophysics*, **11**, 133-161.
- Sinclair G., 1948. Theory of Models of Electromagnetic Systems. *Proc. I.R.E.*, **36**, 1364-1370.
- Singer, B.S.H., 1992. Correction for distortions of magnetotelluric fields: limits of validity of the static approach. *Surveys in Geophysics*, **13**, 309-340.
- Skokan, C.K. and Anderson, H. T., 1991. Deep long-offset transient electromagnetic surveys for crustal studies in the U.S.A. *Phys. Earth Planet. Inter.*, **66**, 39-50.

- Smith, E.G.C., Stern, T. and Reyners, M., 1989. Subduction and back-arc activity at the Hikurangi convergent margin, New Zealand. *PAGEOPH*, **129**, 203-231.
- Smith, J.T. and Booker, J.R., 1991. Rapid inversion of two and three-dimensional magnetotelluric data. *J. Geophys. Res.*, **96**, 3905-3922.
- Smith, W., 1994. Private communication.
- Stern, T.A. and Davey, F.J., 1987. A seismic investigation of the crustal and upper mantle structure within the Central Volcanic Region of New Zealand. *N.Z. J. Geol. Geophys.*, **30**, 217-231.
- Strack, K. M., 1984. The deep transient electromagnetic sounding technique: first field test in Australia. *Explor. Geophys.*, **15**, 251-259.
- Suggate, R.P., 1978. The main movements. in *The Geology of New Zealand*, Volume 2. Chief editor: R.P. Suggate, Government Printer, Wellington, New Zealand.
- The EMSLAB Group, 1988. The EMSLAB electromagnetic sounding experiment. *EOS*, **69**, No. 7, pages 89, 98-99.
- Thomson, D.J., Ramaswamy, V. and Dosso, H.W., 1972. Model measurements of electromagnetic variations near a coastline for localized source fields. *J. Geomagn. Geoelectr.*,
- Thornton, J., 1993. Field guide to New Zealand geology. Reed Publishing Group (NZ) Ltd., Auckland, New Zealand.
- Towle, J.N., 1980. Observations of direct current concentration on the eastern Sierran Front: evidence for shallow crustal conductors on the eastern Sierran Front and beneath the Coso Range. *J. Geophys. Res.*, **85**, 2484-2490.

- Trevino, E.G. and Edwards, R.N., 1983. Electromagnetic soundings in the sedimentary basin of southern Ontario. *Geophysics*, **48**, 311-330.
- Utada, H., Hamano, Y. and Yukutake, T., 1986. A two-dimensional conductivity model across central Japan. *J. Geomag. Geoelectr.*, **38**, 447-473.
- Vasseur, G. and Weidelt, P., 1977. Bimodal electromagnetic induction in non-uniform thin sheets with an application to the northern Pyrenean induction anomaly. *Geophys. J.R. Astron. Soc.*, **51**, 669-690.
- Velikhov, Ye. P., Zhamaletdinov, A.A., Belkov, I.V., Gorhunov, G.I., Hjelt, S.E., Lisin, A.S., Vanyan, L.L., Zhdanov, M.S., Demidova, T.A., Korja, T., Kirillov, S.K., Kuksa, Yu. I., Poltanov, A. Ye., Tokarev, A.D. and Yevstigneyev, V.V., 1986. Electromagnetic studies on the Kola Peninsula and in northern Finland by means of powerful controlled source. *Journal of Geodynamics*, **5**, 237-256.
- Vozoff, K., 1986. Magnetotelluric methods. Soc. Explor. Geophys. Reprint Ser. No. 5, Publ. by Soc. Expl. Geophys., Tulsa, Okla., ISBN 0-931830-36-2.
- Walcott, R.I., 1978. Present tectonics and Late Cenozoic evolution of New Zealand. *Geophys. J. R. Astro. Soc.*, **52**, 137-164.
- Walcott, R.I., 1987. Geodetic strain and the deformational history of the North Island of New Zealand during the late Cainozoic. *Phil. Trans. R. Soc. Lond.*, **A 321**, 163-181.
- Ward, S.H., 1967. Electromagnetic theory for geophysical applications. in *Mining Geophysics: Vol. 2, Theory*, SEG, Tulsa, pp. 10-196.
- Ward, S.H., 1983. Controlled source electrical methods for deep exploration. *Geophysical surveys*, **6**, 137-152.

- Weaver, J.T., 1973. Induction in a layered plane earth by uniform and non-uniform source fields. *Phys. Earth Planet. Inter.*, **7**, 266-281.
- Brewitt-Taylor, C.R. and Weaver, J.T., 1976. On the finite difference solution of two-dimensional induction problems. *Geophys. J. R. astr. Soc.*, **47**, 375-396.
- Weaver, J.T., 1982. Regional induction in Scotland: an example of three-dimensional numerical modelling using the thin sheet approximation. *Phys. Earth Planet. Inter.*, **28**, 161-180.
- Weaver, J.T., 1987. The mathematic solution of the geomagnetic coast effect. *Proceedings of the Conference on Applied Mathematics (in honour of Prof. A.A. Ashour), Cairo University (Egypt), Cairo*, pp. 1-34.
- Weaver, J.T. and Agarwal, A.K., 1991. Is addition of induction vectors meaningful? *Phys. Earth Planet. Inter.*, **65**, 267-275.
- Wiese, H., 1962. Geomagnetische Tiefentellurik Teil II: Die Streichrichtung der Untergrundstrukturen des elektrischen Widerstandes, erschlossen aus geomagnetischen Variationen. *Geofis. Pura Appl.*, **52**, 83-103.
- Wolf, D., 1982. Comment on 'Geomagnetic depth sounding by induction arrow representation: a review' by G.P. Gregori and L.J. Lanzerotti. *Rev. Geophys. Space Phys.*, **20**, 519-521.
- Wolf, D., 1983. Inductive coupling between idealized conductors and its significance for the geomagnetic coast effect. *J. Geophys.*, **52**, 22-33.

APPENDIX A
MODEL INDUCTION ARROW RESPONSES FOR FAULTS
PARALLEL TO AN OCEAN COASTLINE

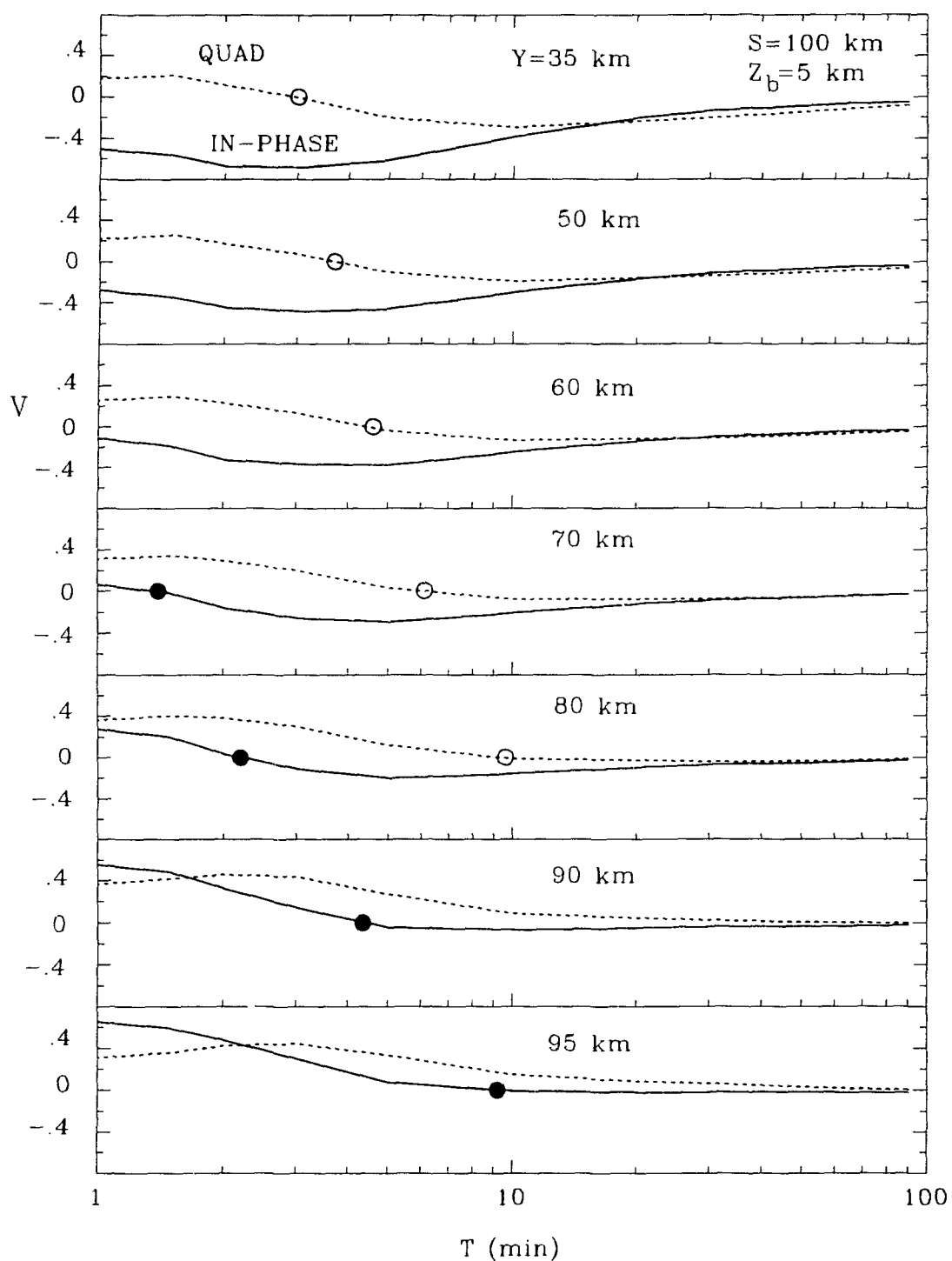


Figure A.1: The in-phase and quadrature induction arrow responses as a function of period for selected locations at distances $Y=35-95$ km from the coastline for $S=100$ km for the fault depth $Z_b=5$ km. The closed and open circles indicate the zero response periods T_0 for the in-phase and quadrature components respectively.

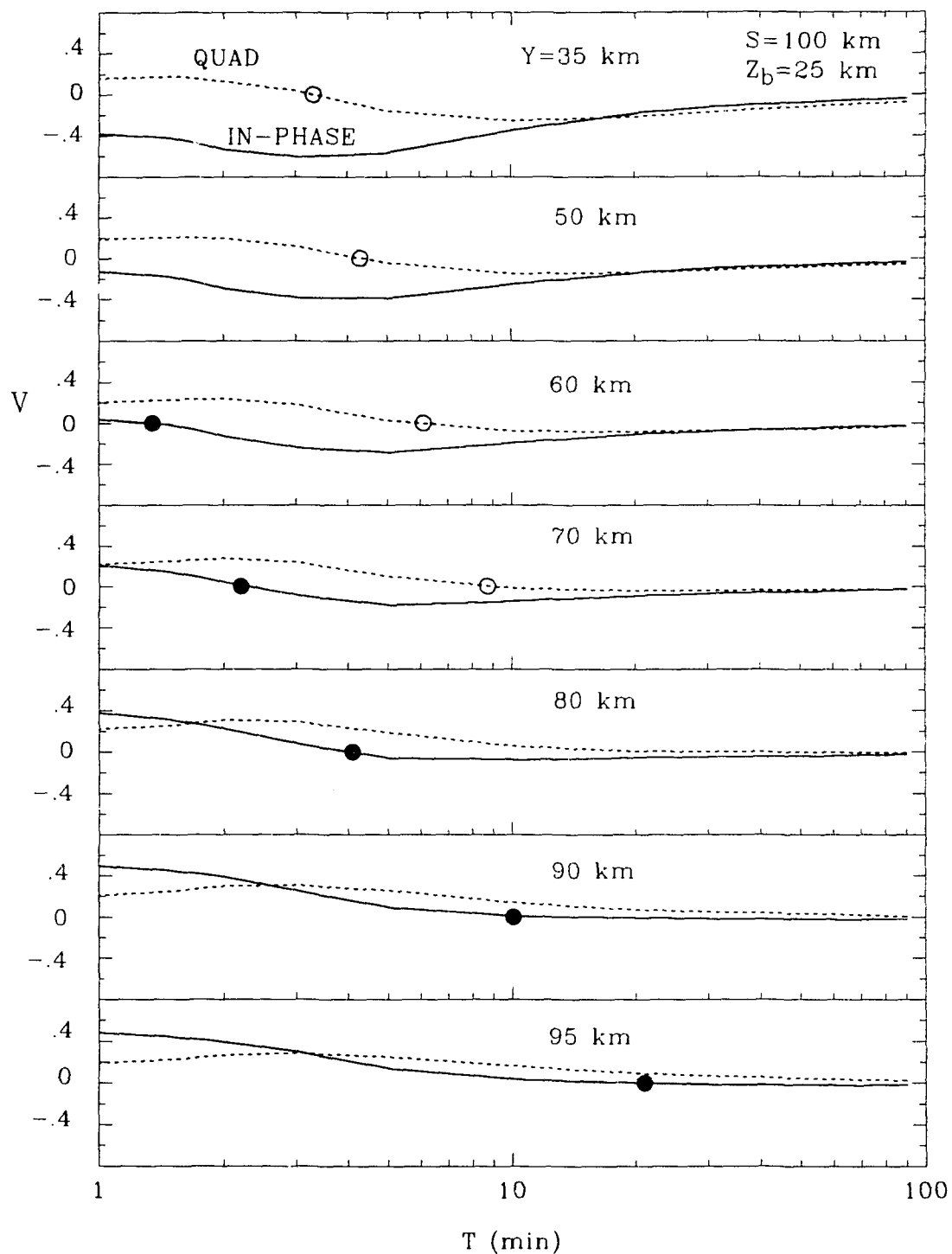


Figure A.2: The in-phase and quadrature induction arrow responses as a function of period for selected locations at distances $Y=35-95$ km from the coastline for $S=100$ km for the fault depth $Z_b=25$ km. The closed and open circles indicate the zero response periods T_0 for the in-phase and quadrature components respectively.

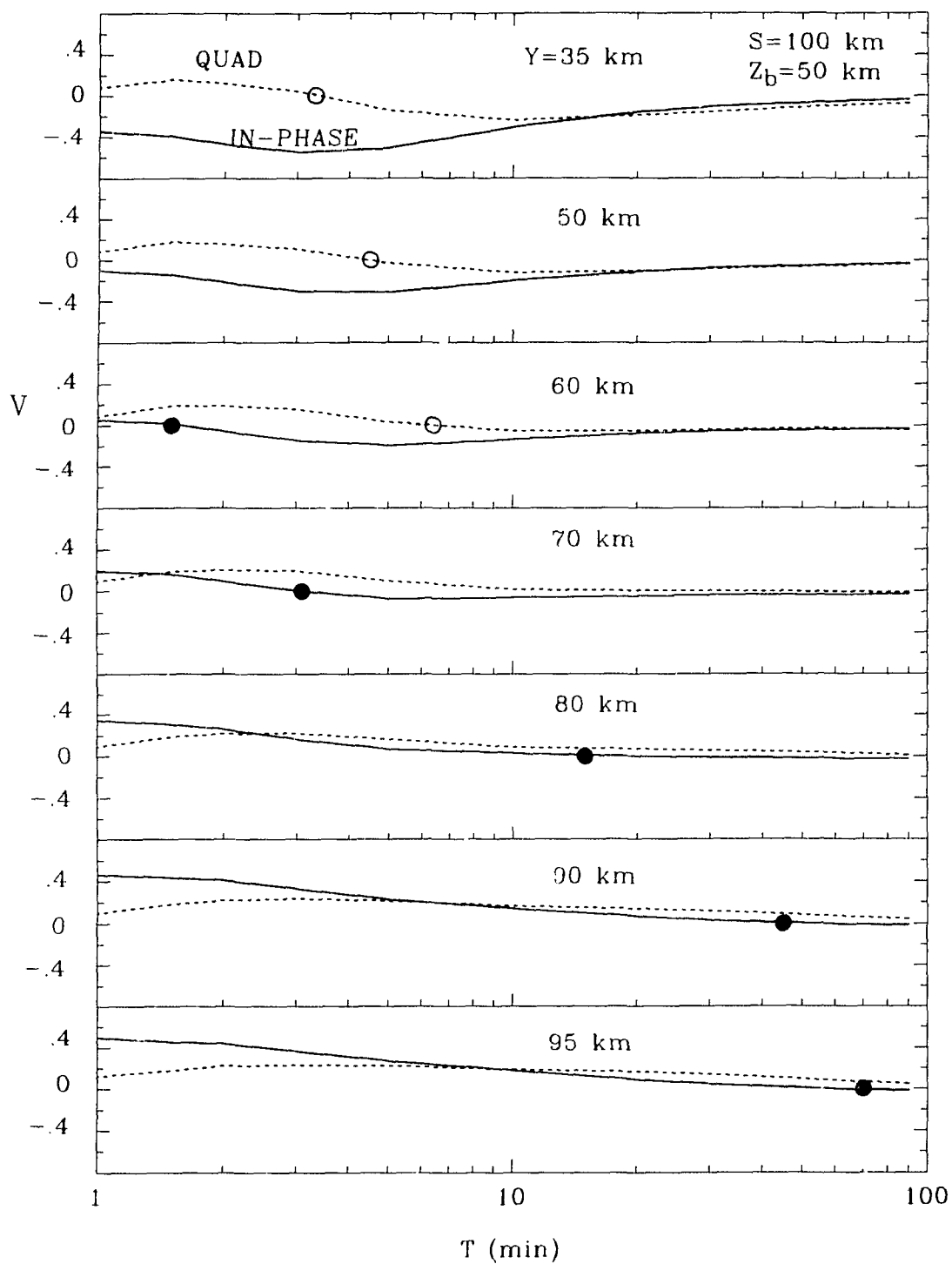


Figure A.3: The in-phase and quadrature induction arrow responses as a function of period for selected locations at distances $Y=35-95$ km from the coastline for $S=100$ km for the fault depth $Z_b=50$ km. The closed and open circles indicate the zero response periods T_0 for the in-phase and quadrature components respectively.

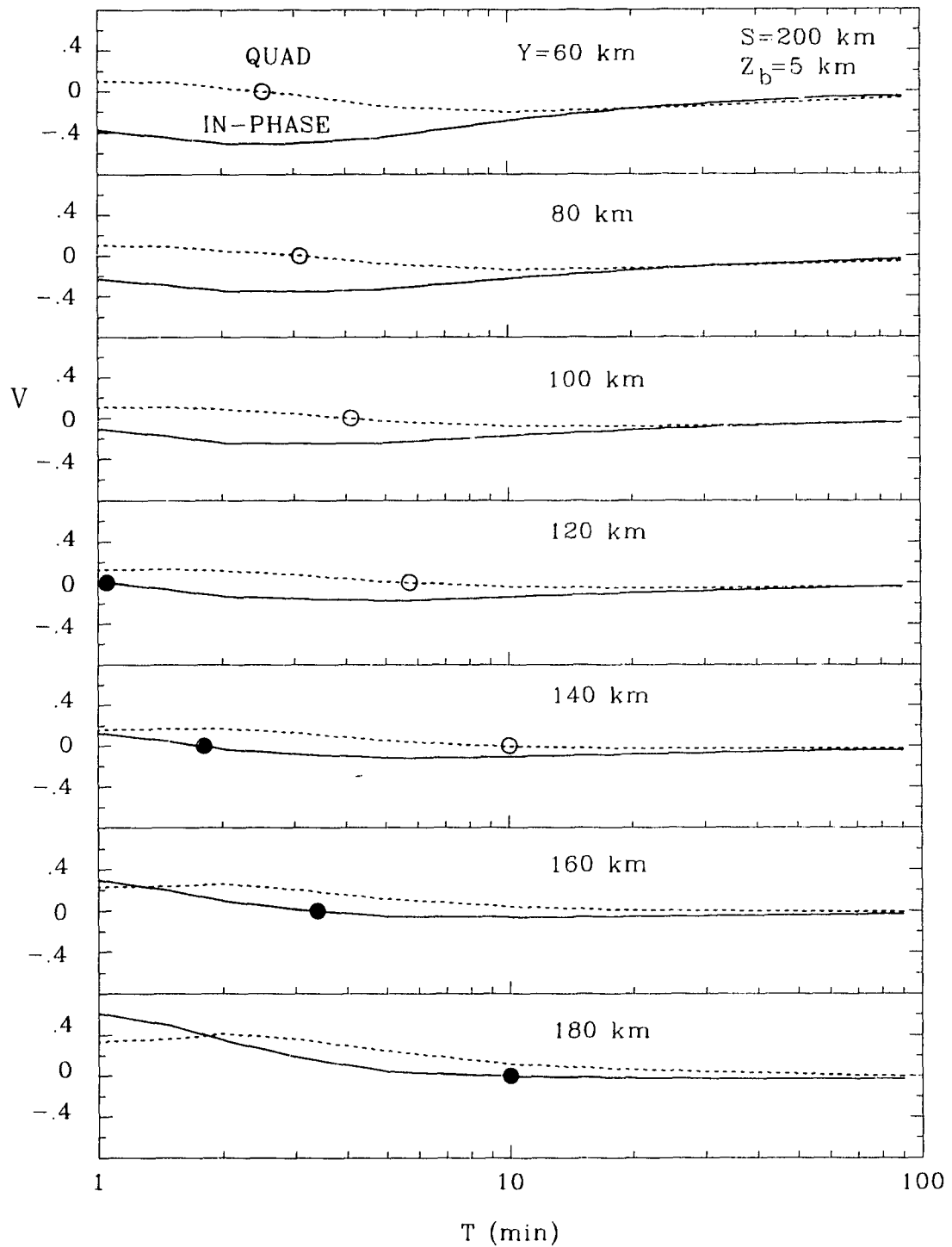


Figure A.4: The in-phase and quadrature induction arrow responses as a function of period for selected locations at distances $Y=60-180$ km from the coastline for $S=200$ km for the fault depth $Z_b=5$ km. The closed and open circles indicate the zero response periods T_0 for the in-phase and quadrature components respectively.

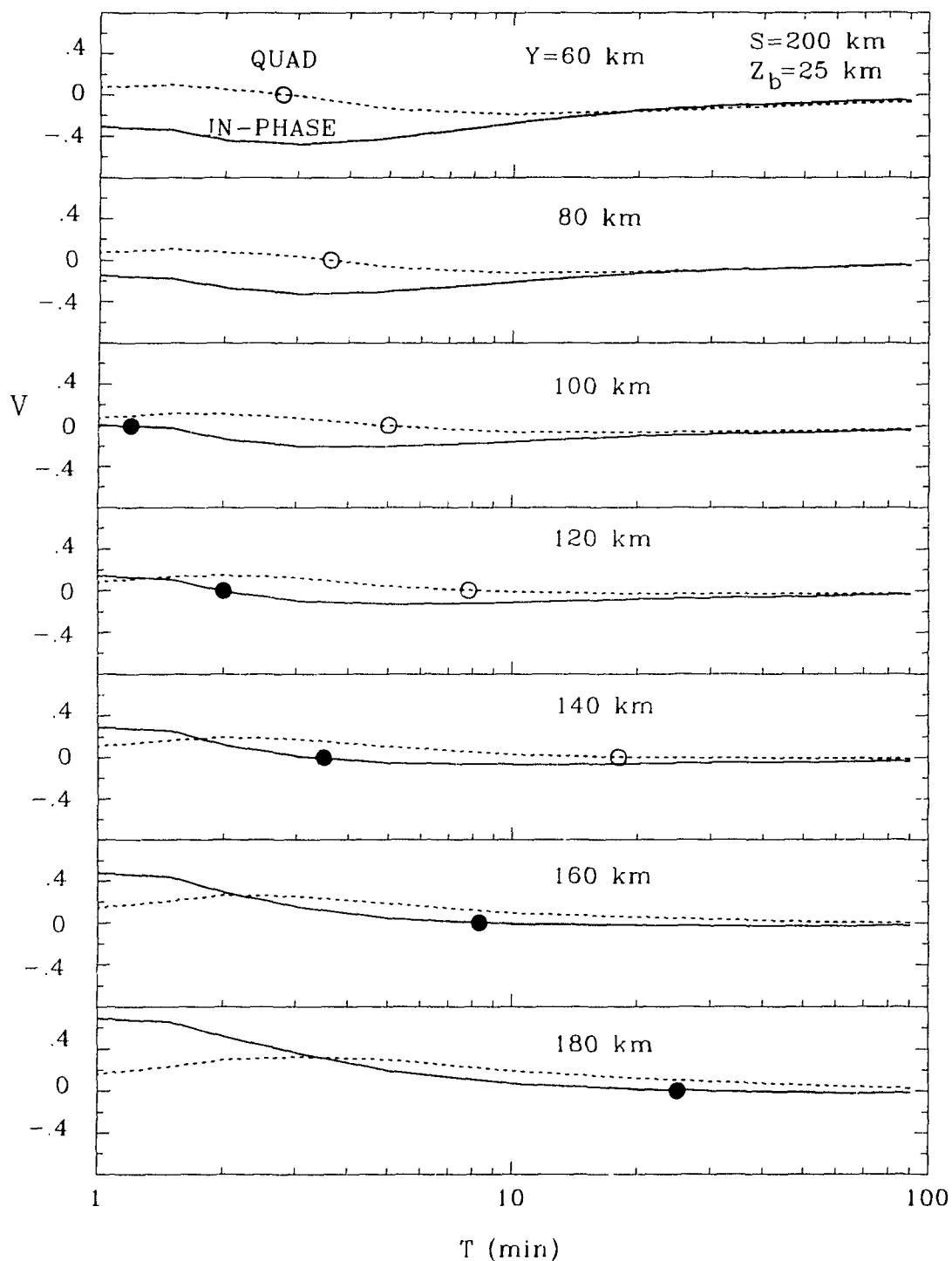


Figure A.5: The in-phase and quadrature induction arrow responses as a function of period for selected locations at distances $Y=60-180$ km from the coastline for $S=200$ km for the fault depth $Z_b=25$ km. The closed and open circles indicate the zero response periods T_0 for the in-phase and quadrature components respectively.

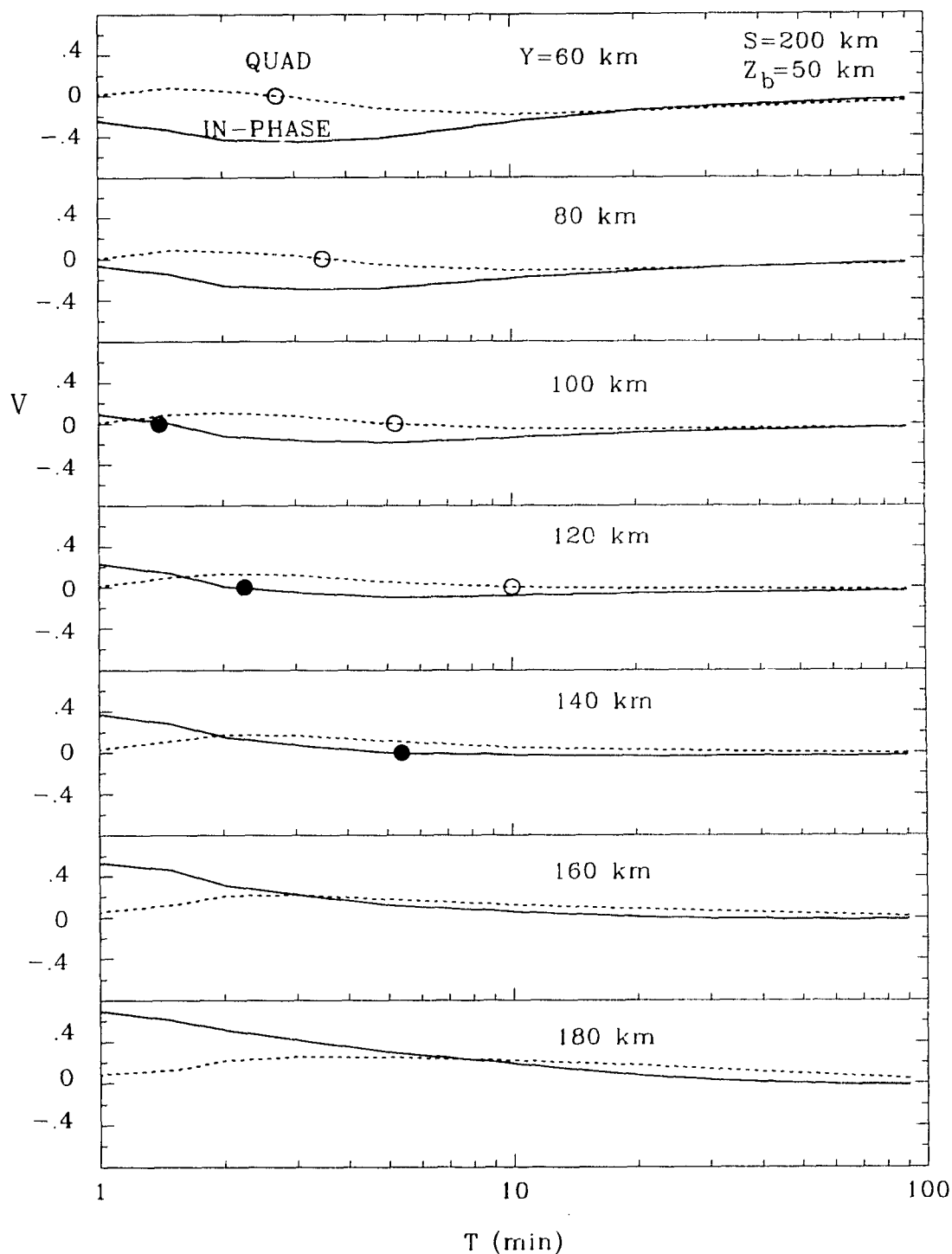


Figure A.6: The in-phase and quadrature induction arrow responses as a function of period for selected locations at distances $Y=60-180$ km from the coastline for $S=200$ km for the fault depth $Z_b=50$ km. The closed and open circles indicate the zero response periods T_0 for the in-phase and quadrature components respectively.

APPENDIX B
MODEL INDUCTION ARROW RESPONSES FOR SINGLE FAULTS

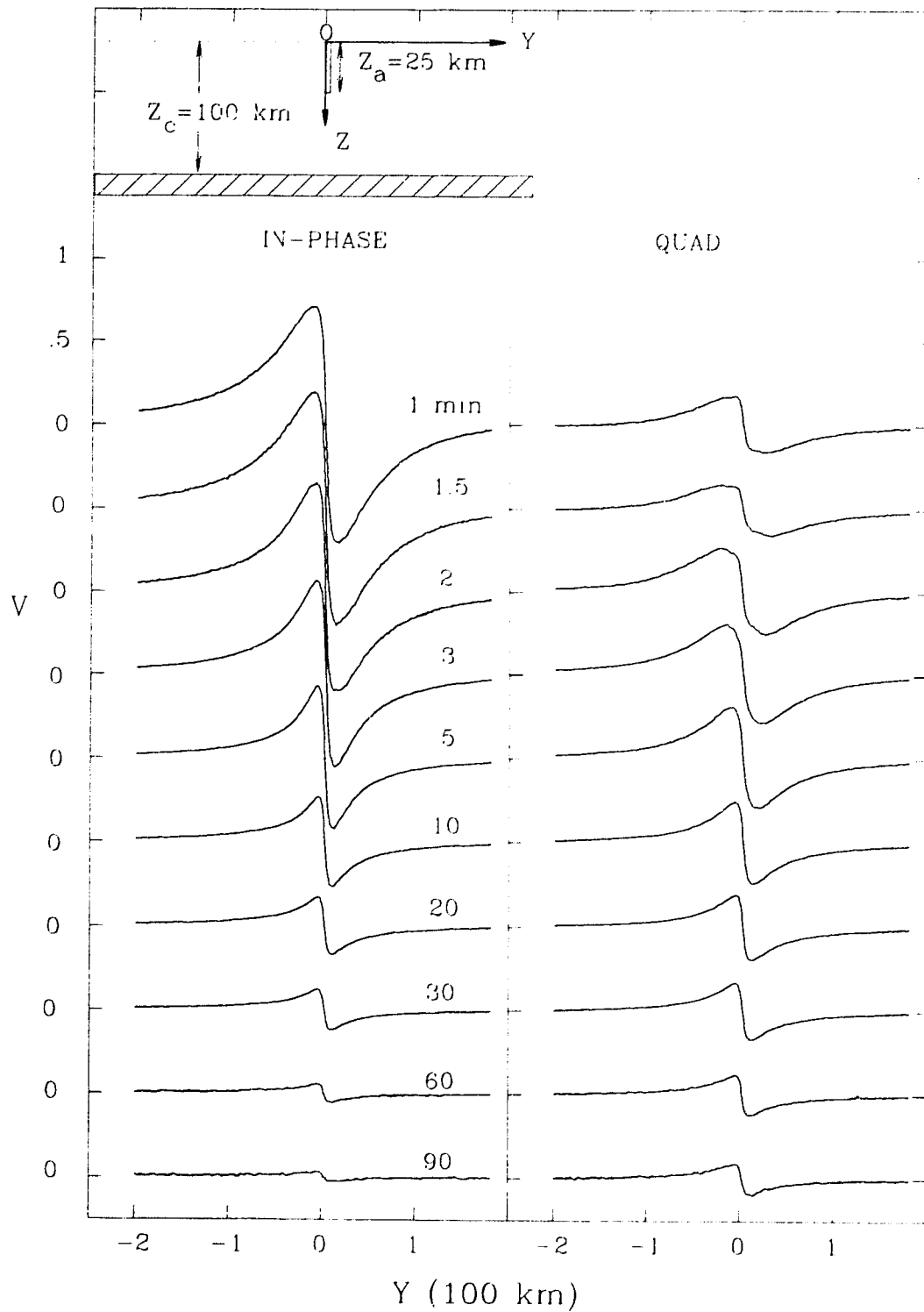


Figure B.1: The in-phase and quadrature induction arrow responses V along a traverse perpendicular to the fault for periods of 1–90 min for a 25 km depth conductive fault underlain by a conductive substratum.

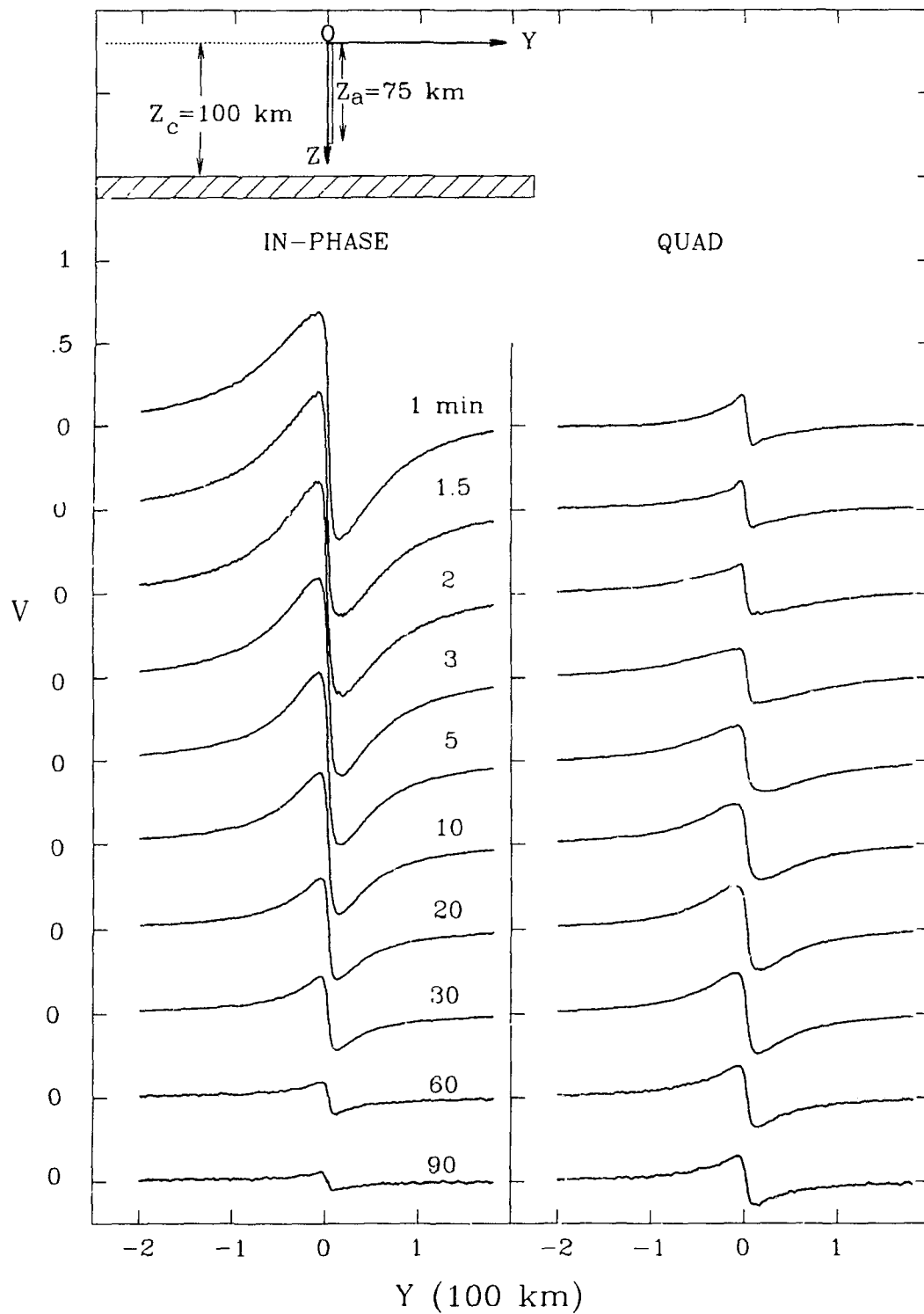


Figure B.2: The in-phase and quadrature induction arrow responses V along a traverse perpendicular to the fault for periods of 1–90 min for a 75 km depth conductive fault underlain by a conductive substratum.

APPENDIX C
MODEL INDUCTION ARROW RESPONSES FOR PAIRS OF
PARALLEL FAULTS

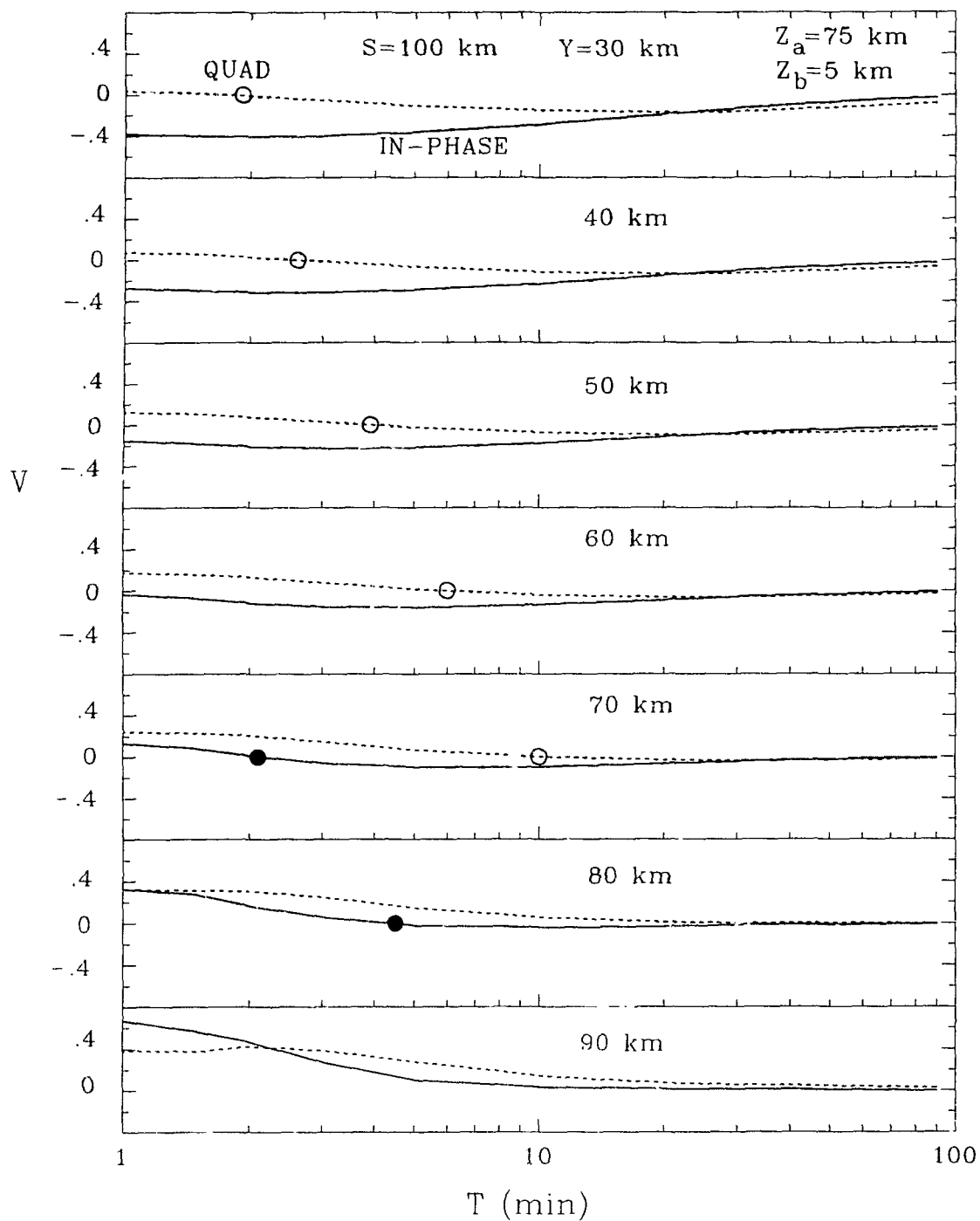


Figure C.1: The in-phase and quadrature induction arrow responses as a function of period for selected locations at distances $Y=30-90$ km from the major fault ($Z_a = 75$ km) for $S=100$ km for $Z_b = 5$ km. The closed and open circles indicate the zero response periods T_0 for the in-phase and quadrature components respectively.

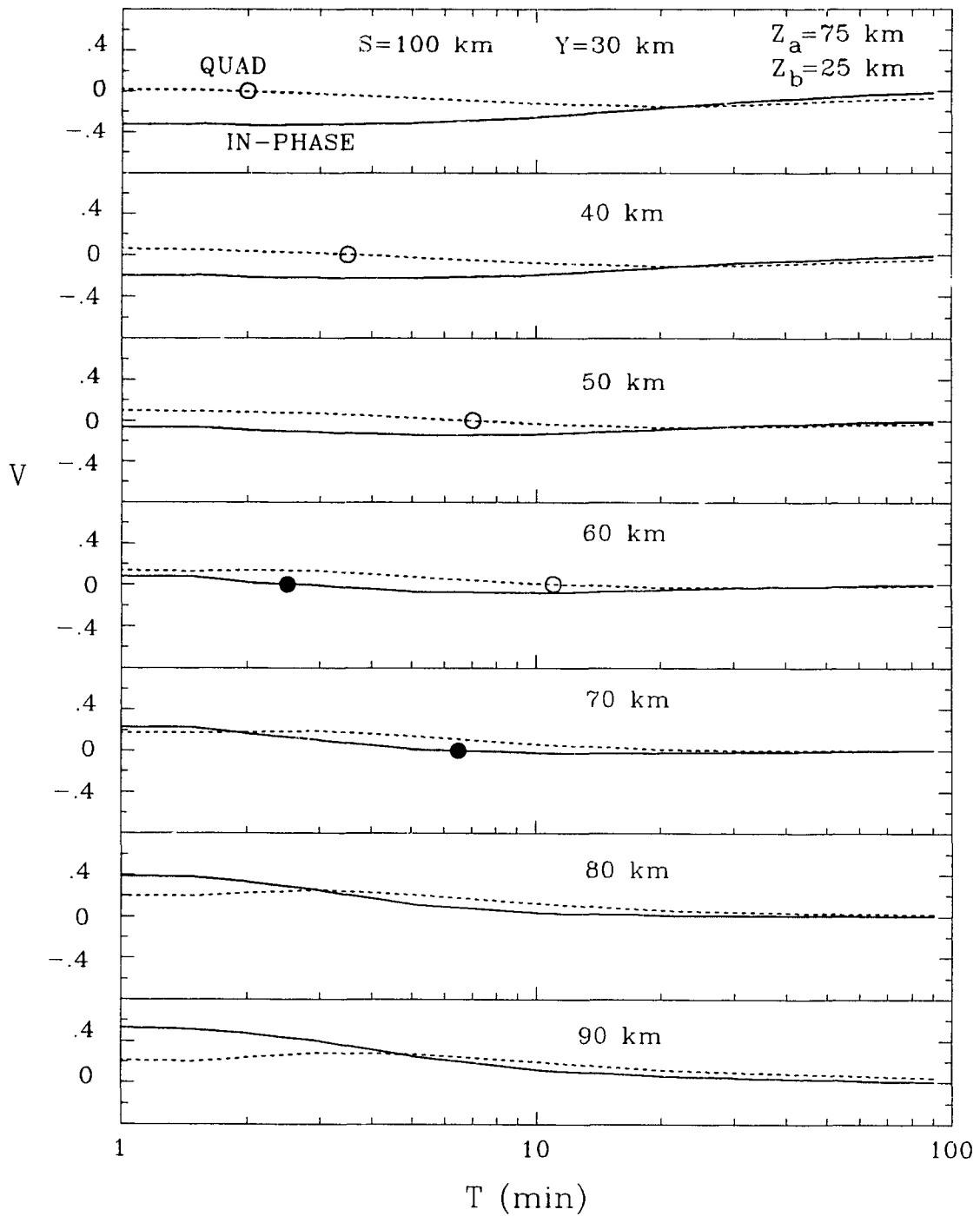


Figure C.2: The in-phase and quadrature induction arrow responses as a function of period for selected locations at distances $Y=30-90$ km from the major fault ($Z_a=75$ km) for $S=100$ km for $Z_b=25$ km. The closed and open circles indicate the zero response periods T_0 for the in-phase and quadrature components respectively.

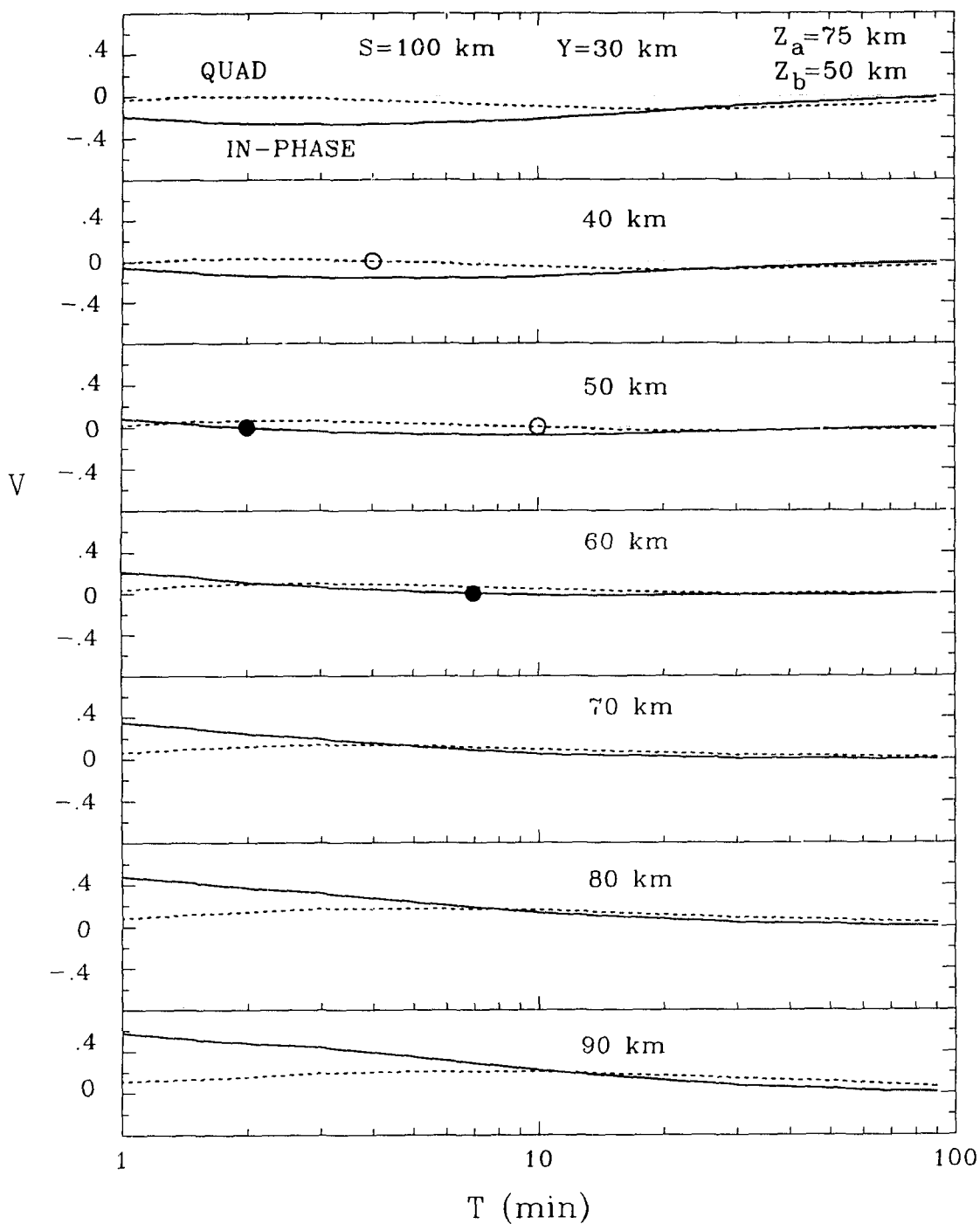


Figure C.3: The in-phase and quadrature induction arrow responses as a function of period for selected locations at distances $Y=30-90$ km from the major fault ($Z_a=75$ km) for $S=100$ km for $Z_b=50$ km. The closed and open circles indicate the zero response periods T_0 for the in-phase and quadrature components respectively.

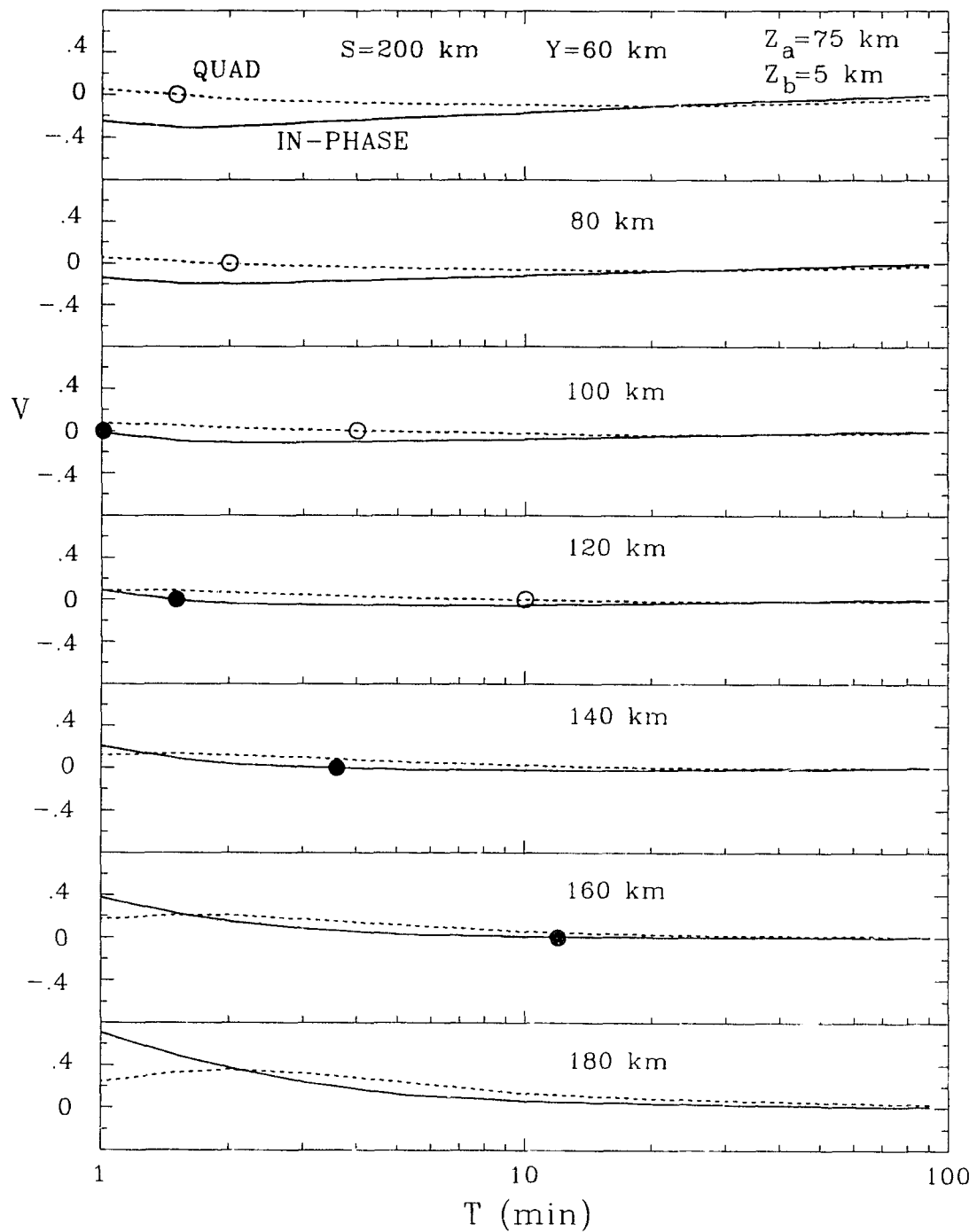


Figure C.4: The in-phase and quadrature induction arrow responses as a function of period for selected locations at distances $Y=60-180$ km from the major fault ($Z_a=75$ km) for $S=200$ km for $Z_b=5$ km. The closed and open circles indicate the zero response periods T_0 for the in-phase and quadrature components respectively.

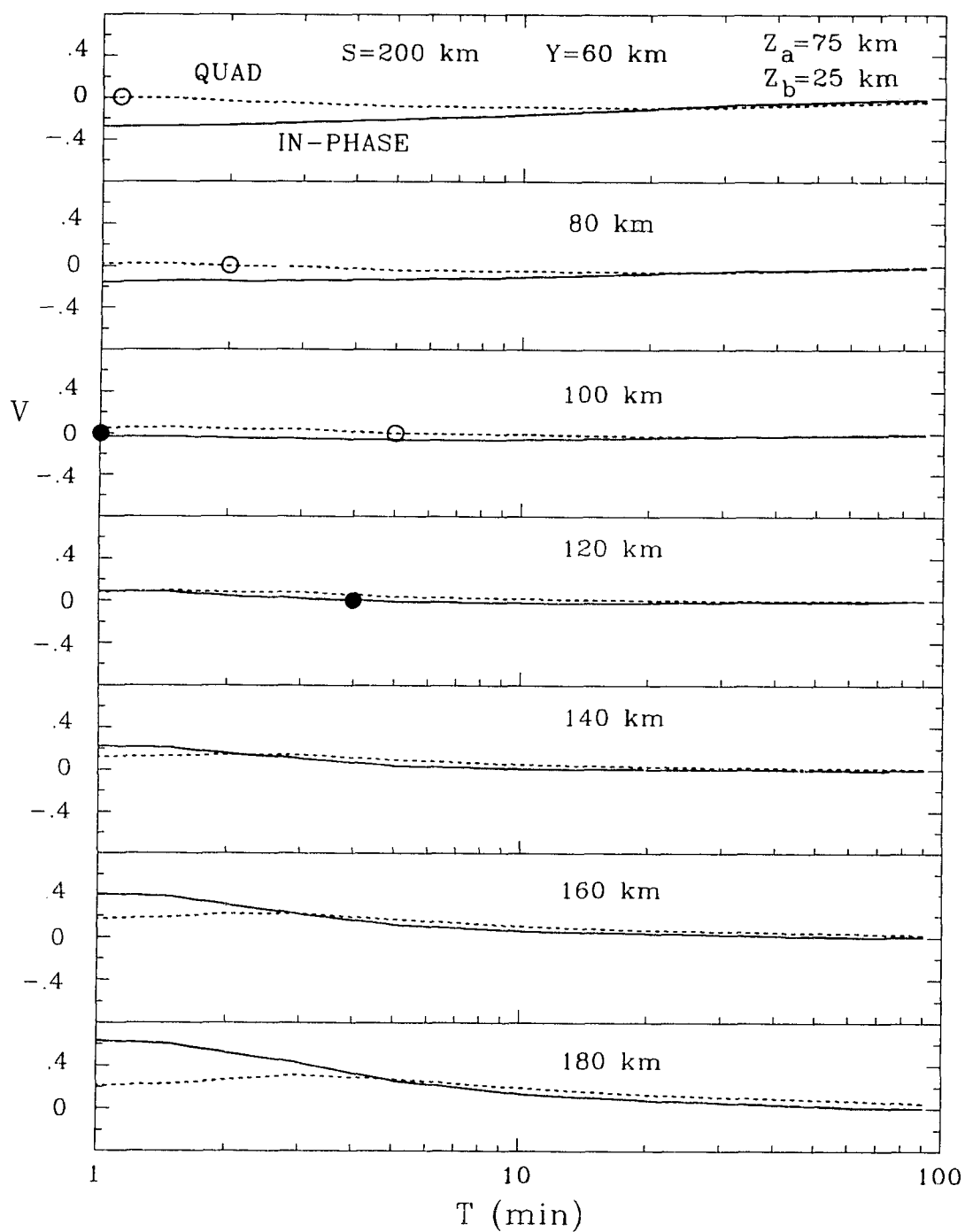


Figure C.5: The in-phase and quadrature induction arrow responses as a function of period for selected locations at distances $Y=60-180$ km from the major fault ($Z_a=75$ km) for $S=200$ km for $Z_b=25$ km. The closed and open circles indicate the zero response periods T_0 for the in-phase and quadrature components respectively.

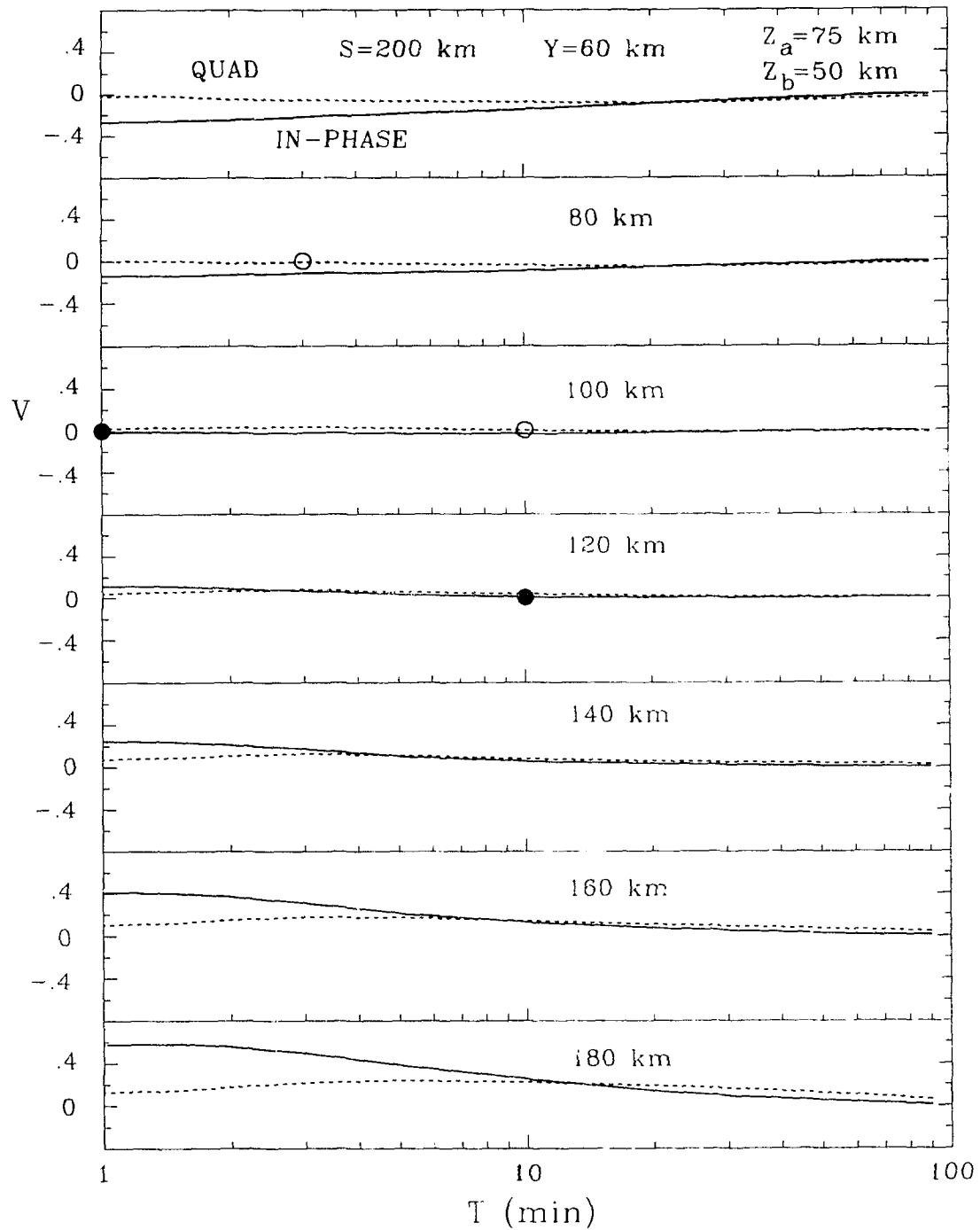


Figure C.6: The in-phase and quadrature induction arrow responses as a function of period for selected locations at distances $Y=60-180$ km from the major fault ($Z_a=75$ km) for $S=200$ km for $Z_b=50$ km. The closed and open circles indicate the zero response periods T_0 for the in-phase and quadrature components respectively.

APPENDIX D
MODEL B_x , B_y AND B_z COMPONENTS FOR X- AND
Y-POLARIZATIONS

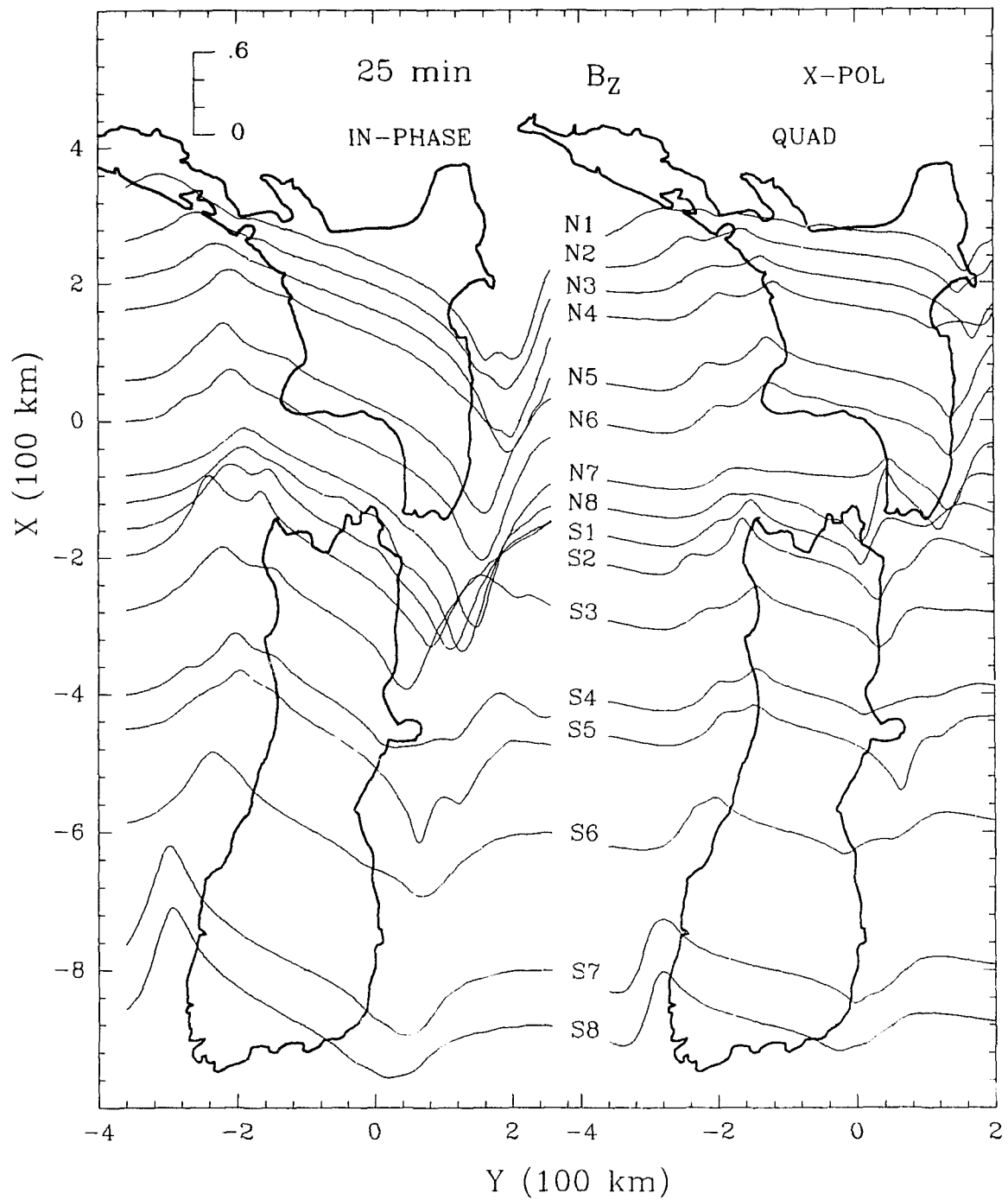


Figure D.1: The in-phase and quadrature B_z along traverses over the model at 25 min for X-polarization.

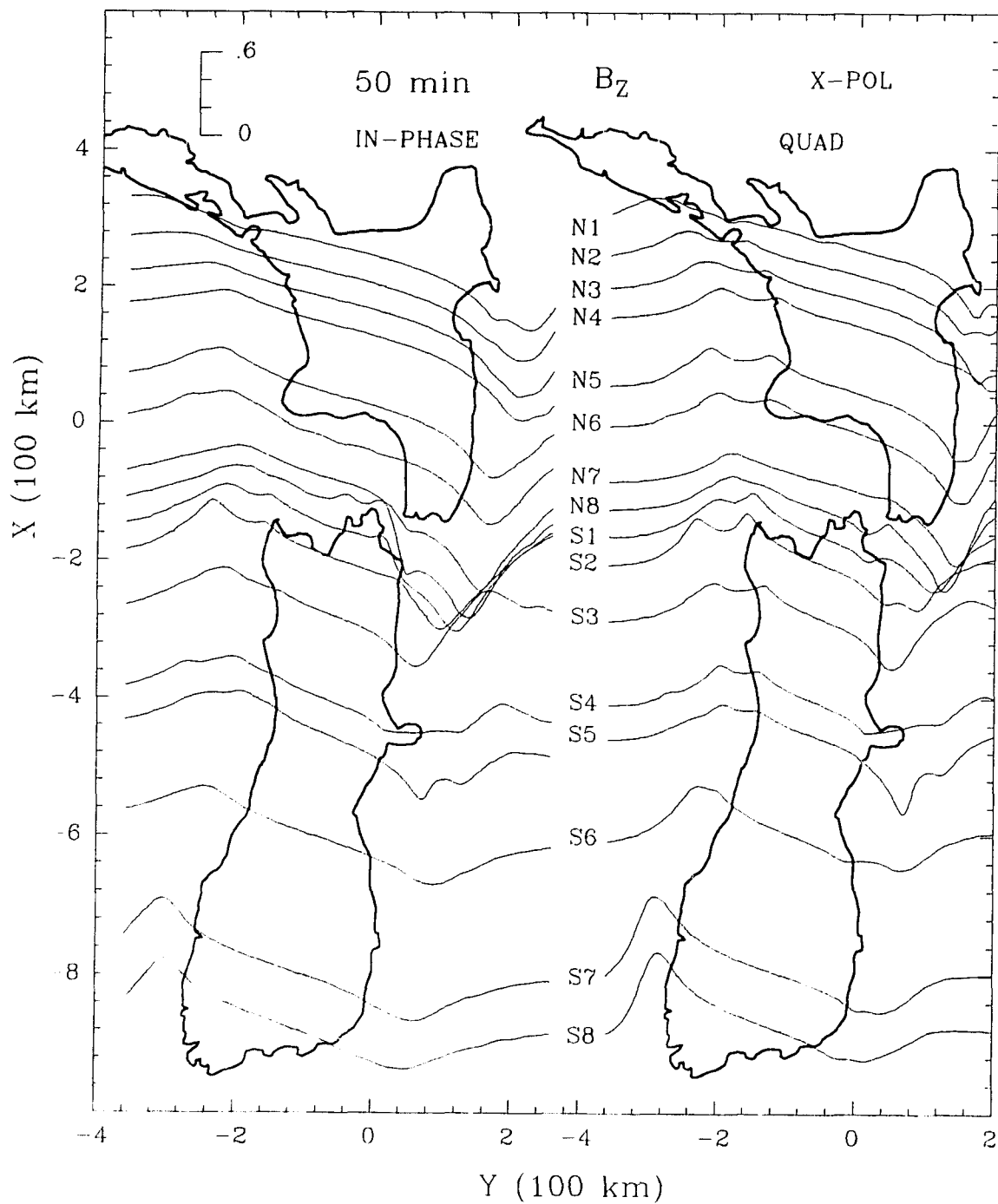


Figure 5.2: The in-phase and quadrature B_z along traverses over the model 50 min for X-polarization.

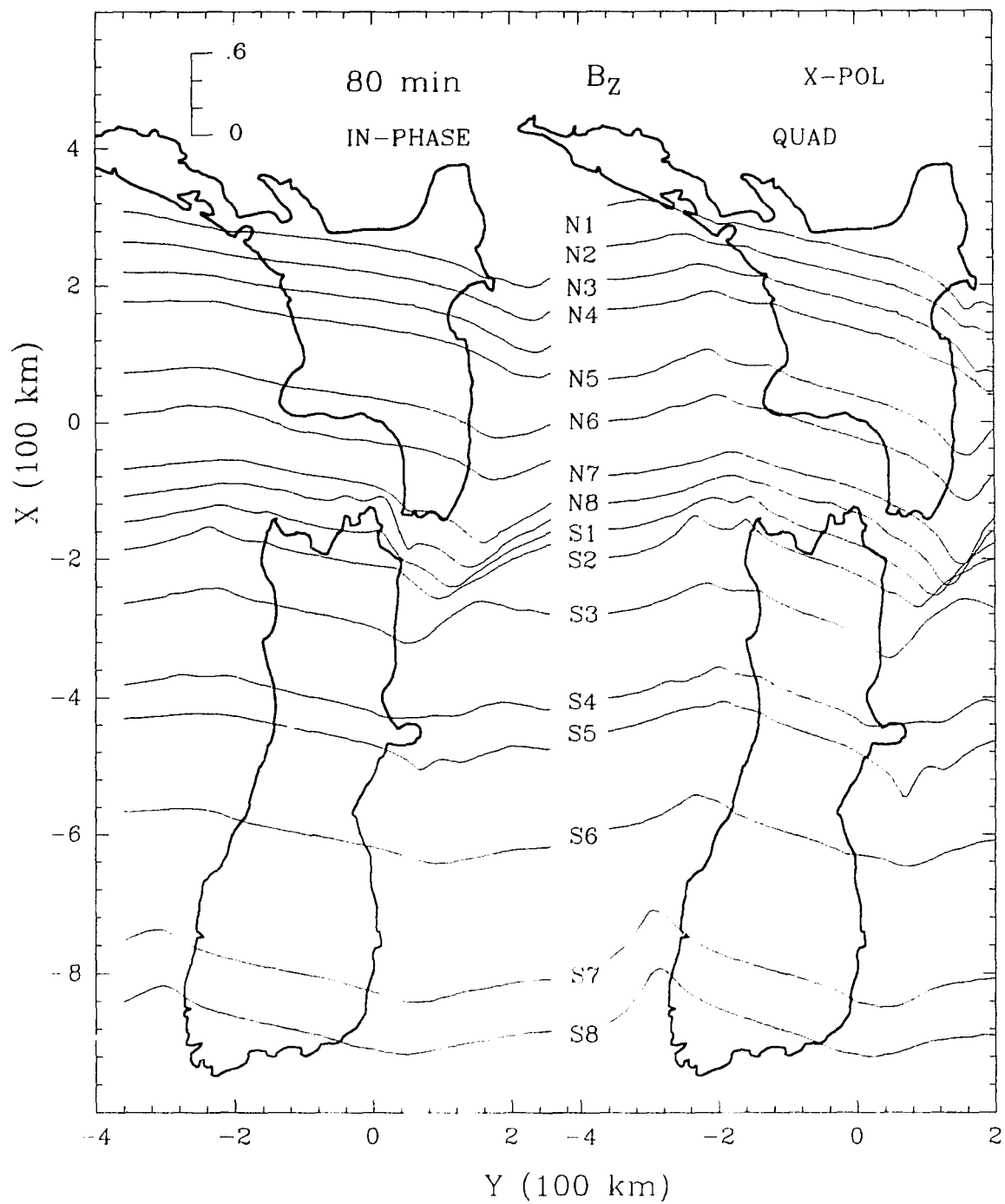


Figure D.3: The in-phase and quadrature B_z along traverses over the model at 80 min for X-polarization.

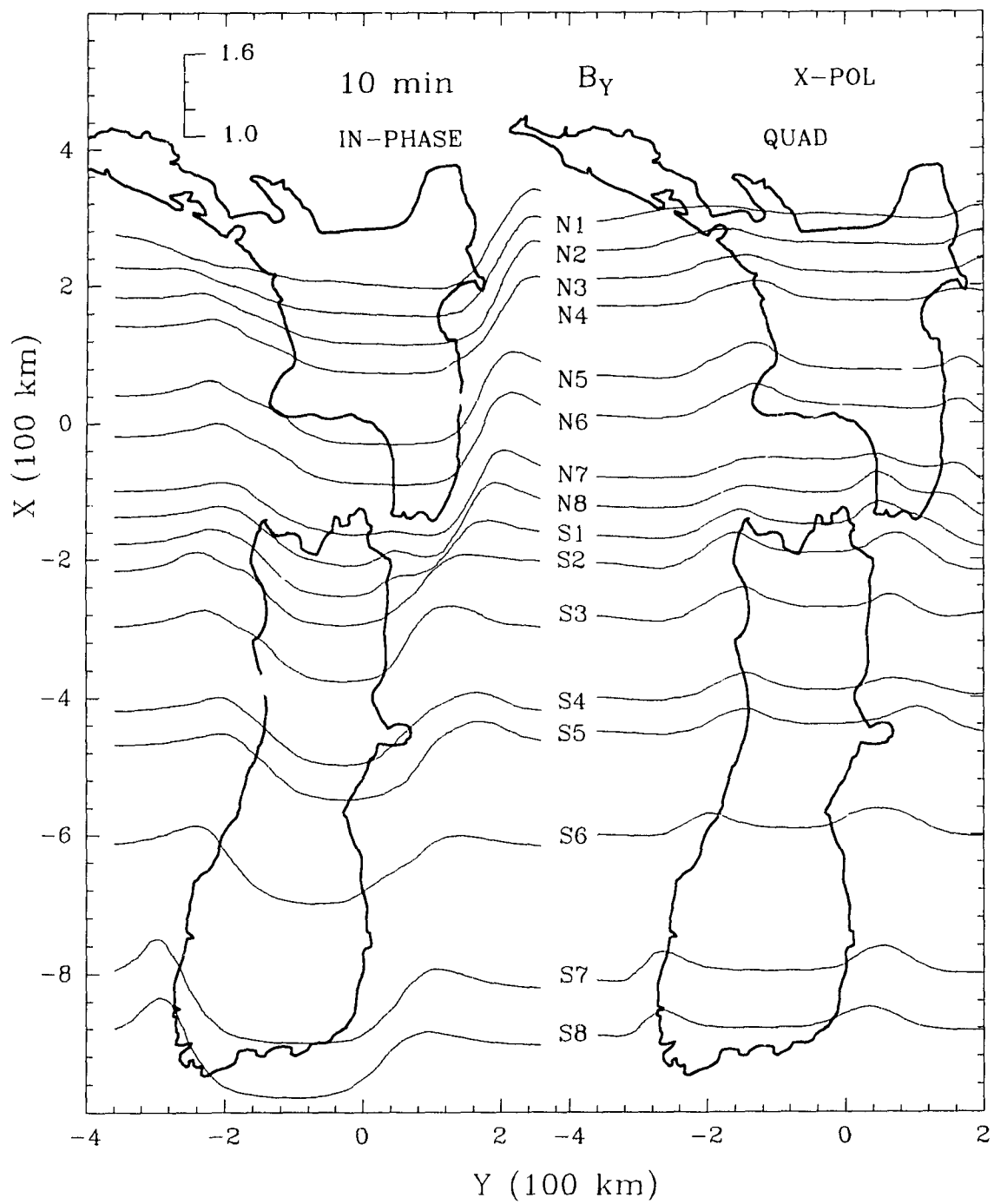


Figure D.4: The in-phase and quadrature B_y along traverses over the model at 10 min for X-polarization.

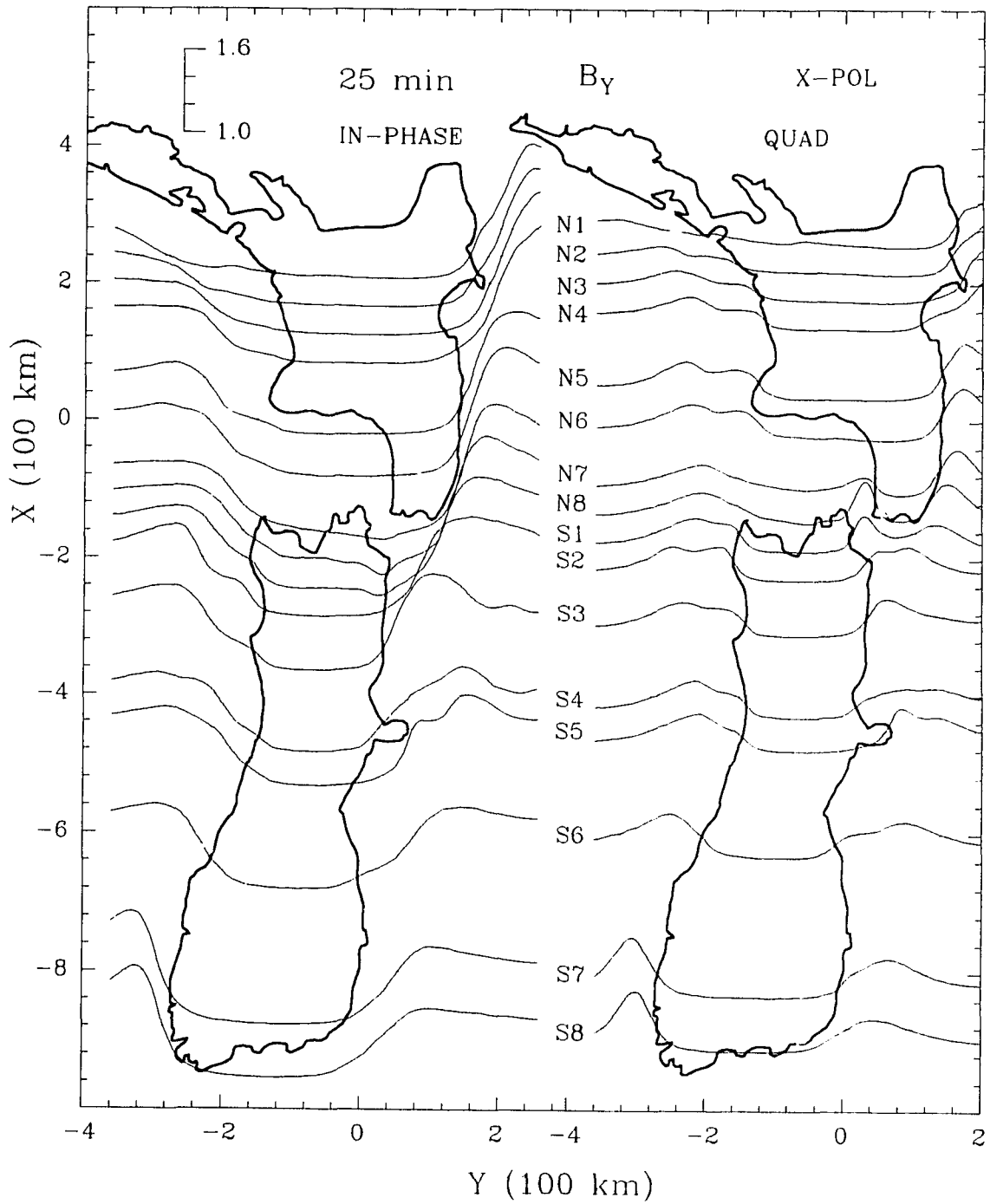


Figure D.5: The in-phase and quadrature B_y along traverses over the model at 25 min for X-polarization.

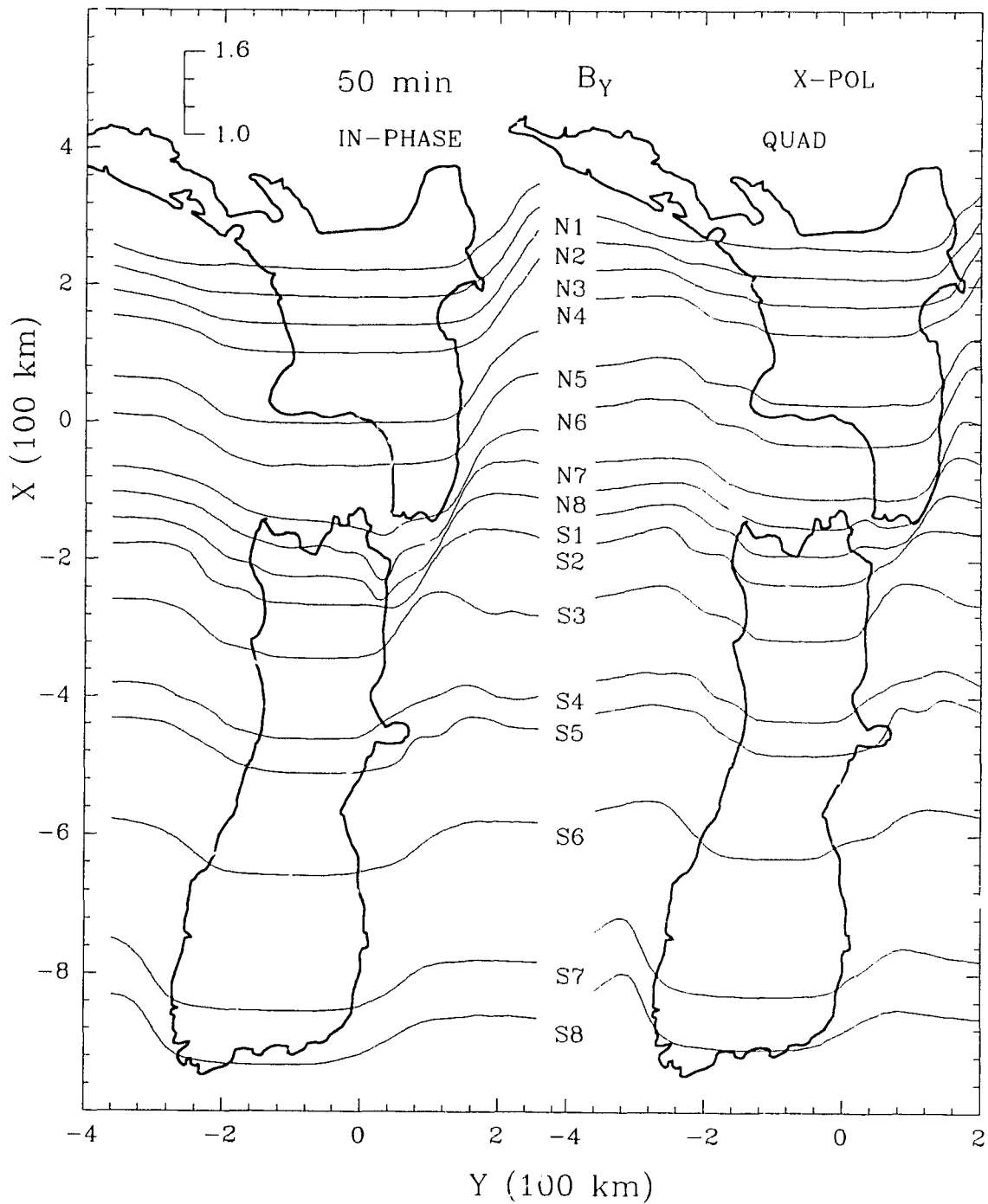


Figure D.6: The in-phase and quadrature B_y along traverses over the model at 50 min for X-polarization.

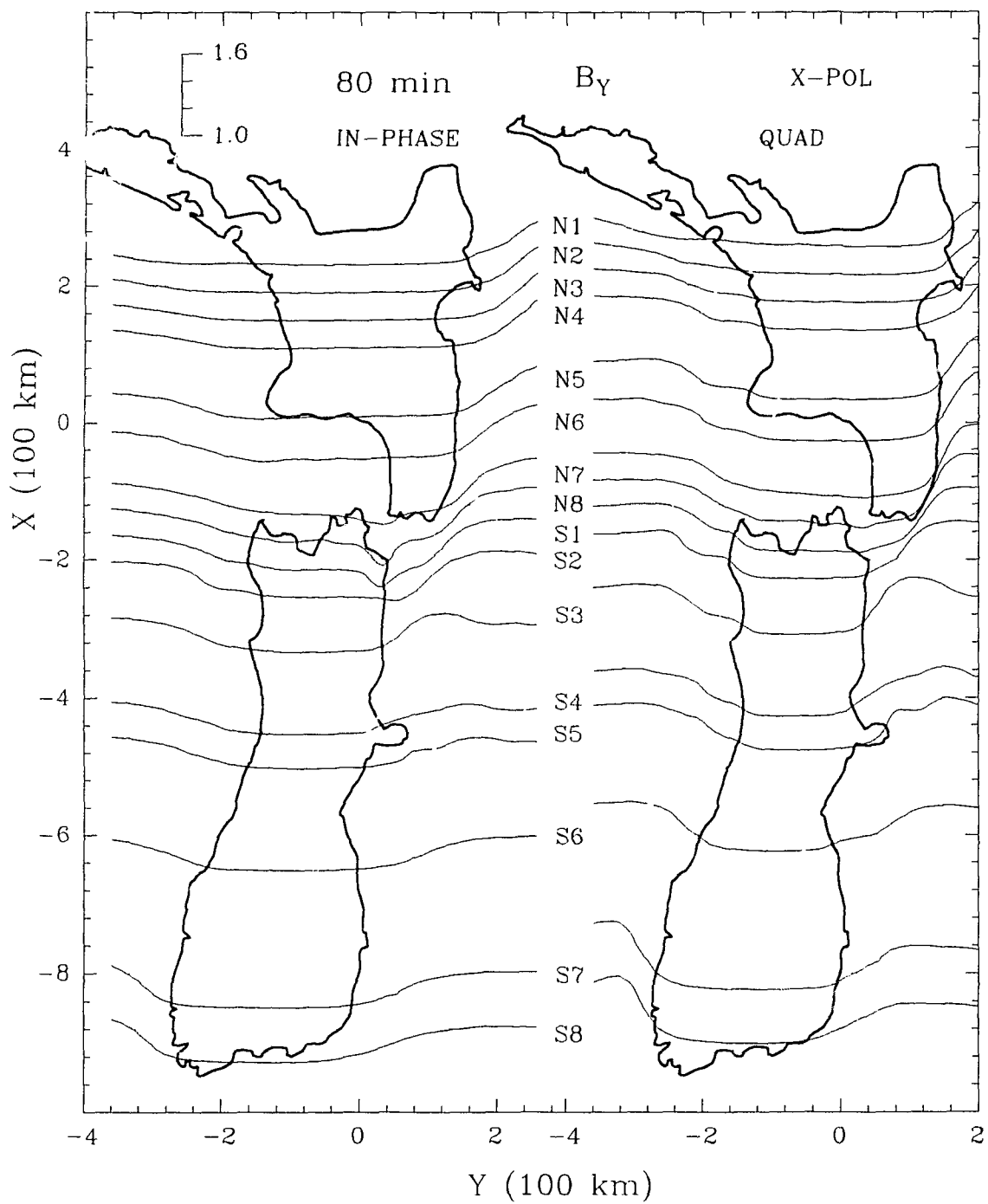


Figure D.7: The in-phase and quadrature B_y along traverses over the model at 80 min for X-polarization.

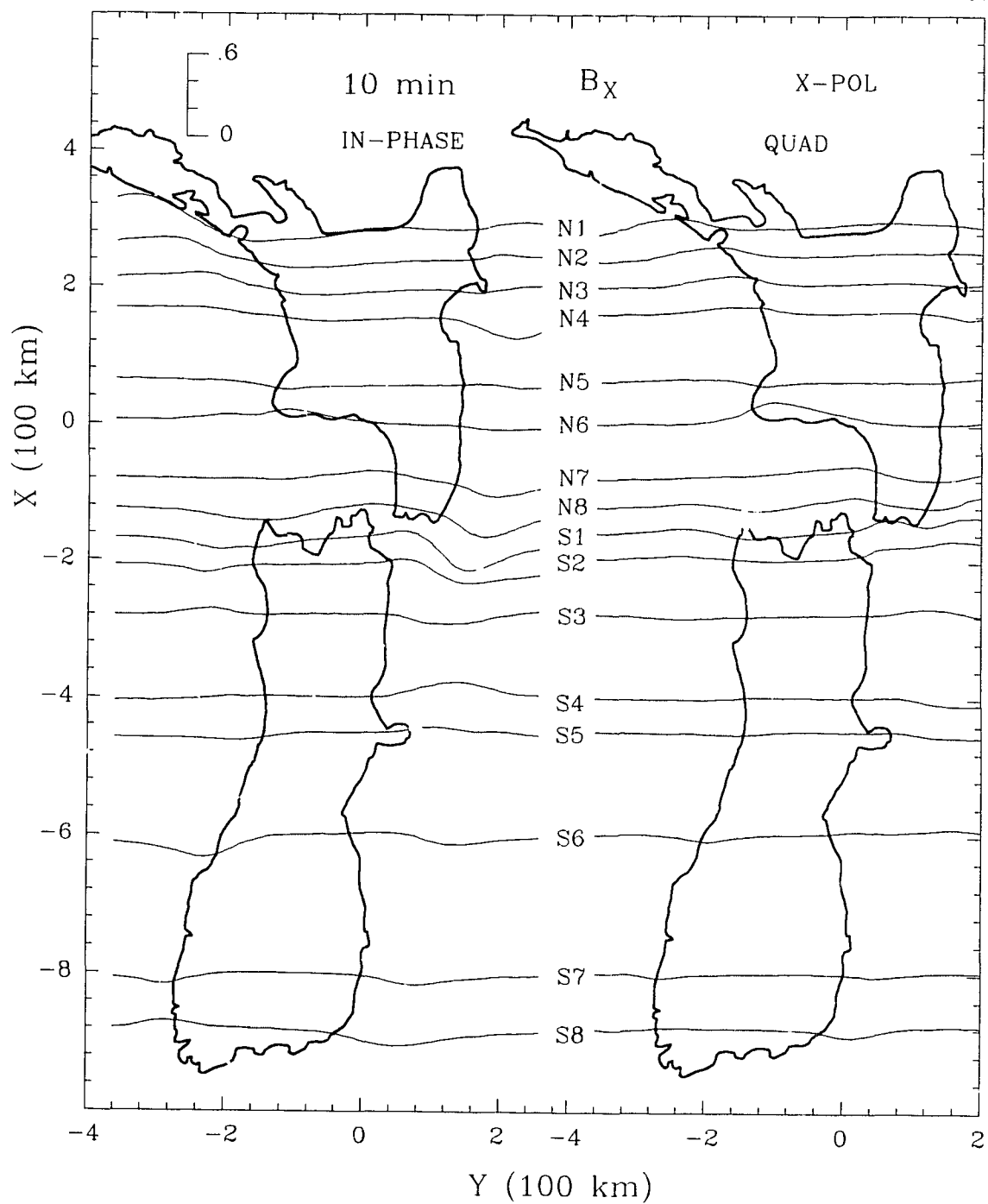


Figure D.8: The in-phase and quadrature B_x along traverses over the model at 10 min for X-polarization.

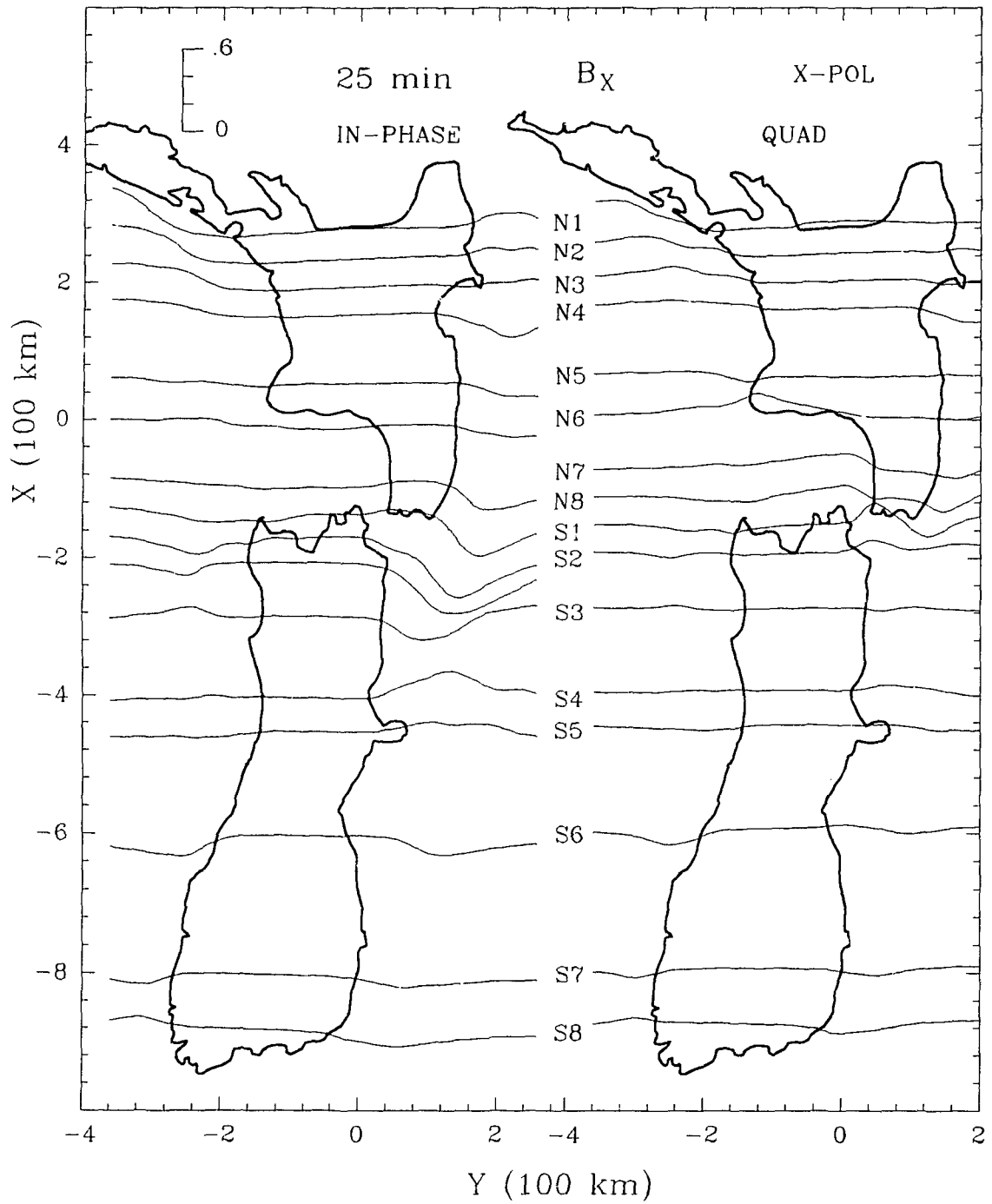


Figure D.9: The in-phase and quadrature B_x along traverses over the model at 25 min for X-polarization.

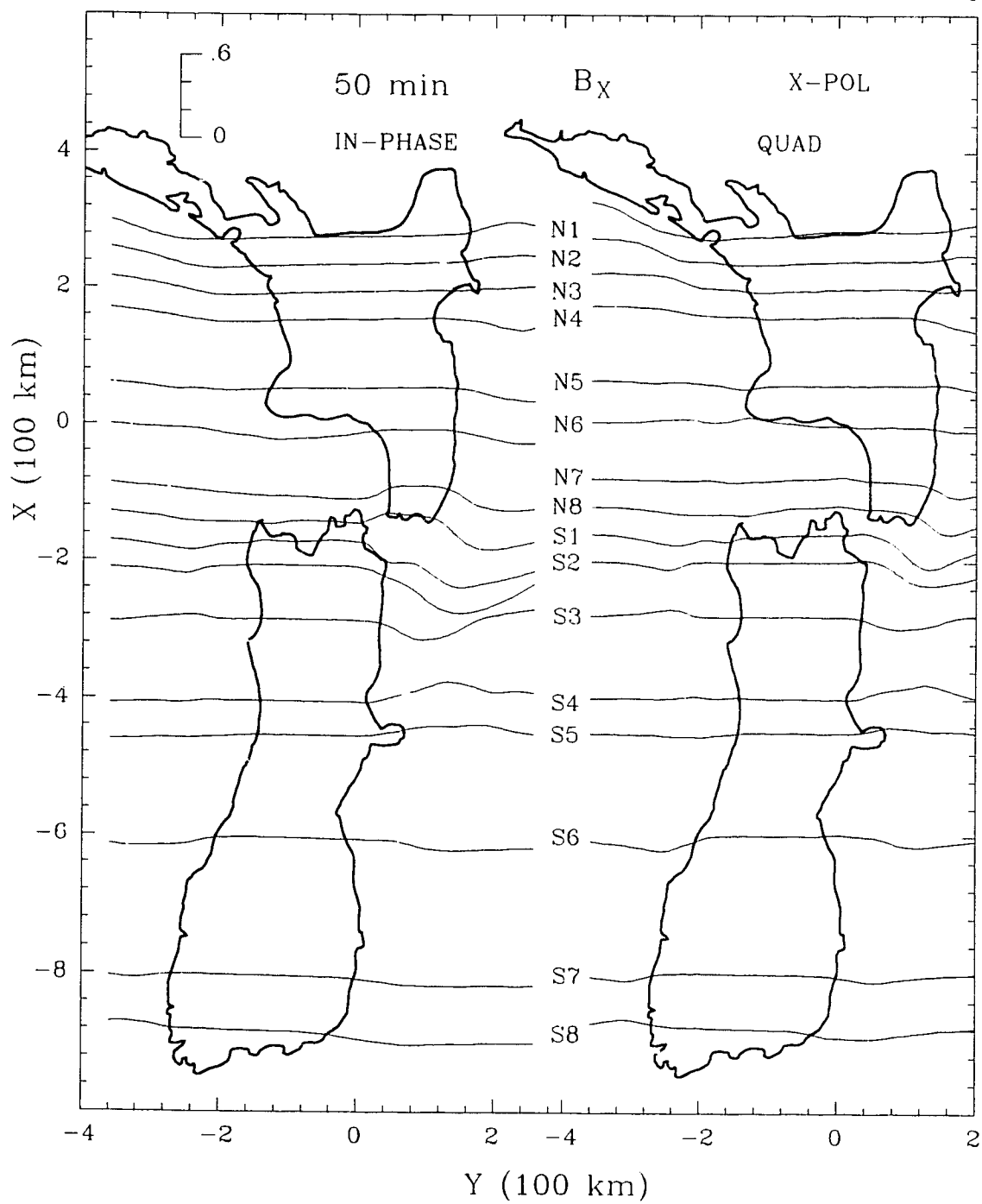


Figure D.10: The in-phase and quadrature B_x along traverses over the model at 50 min for X-polarization.

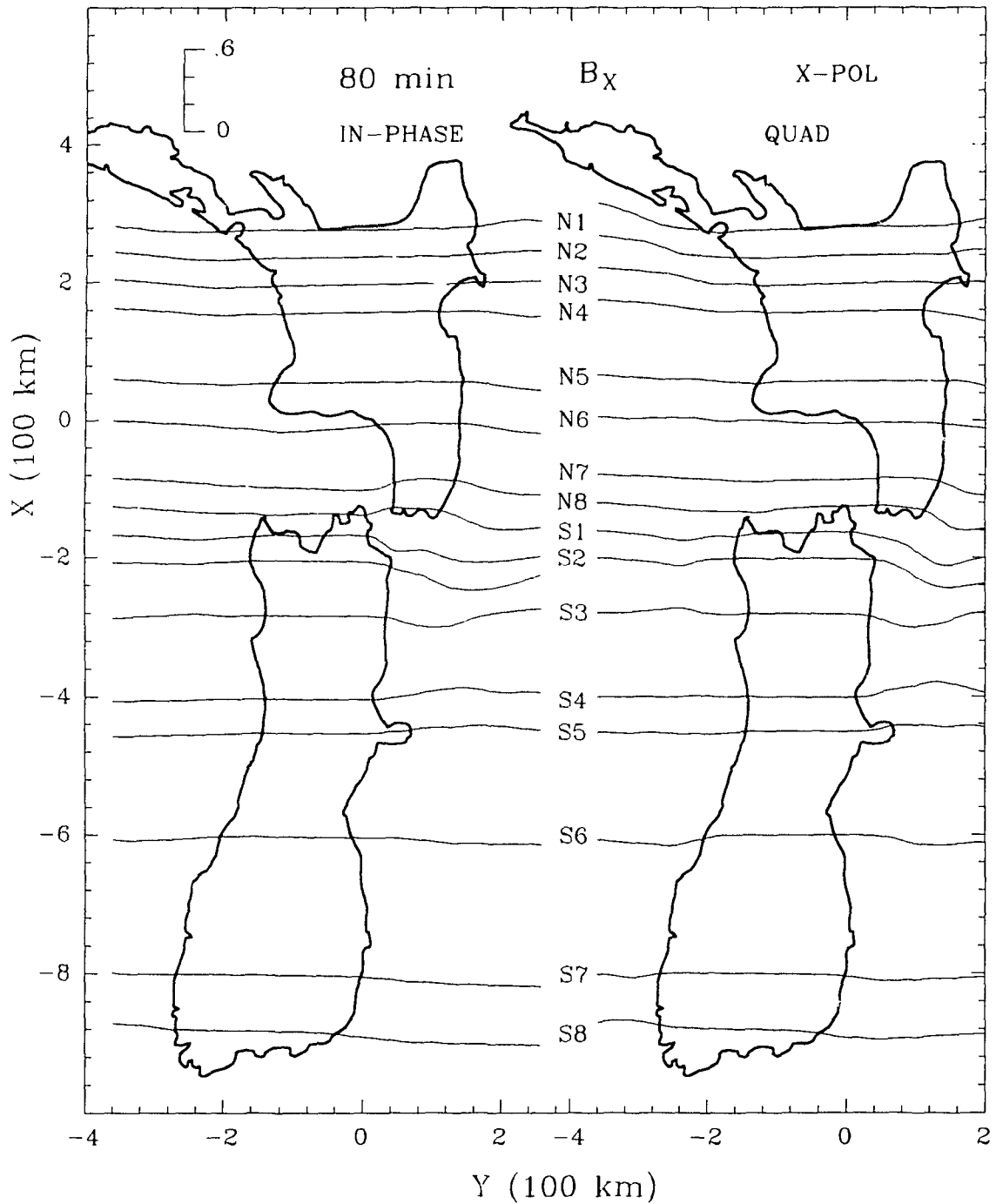


Figure D.11: The in-phase and quadrature B_x along traverses over the model at 80 min for X-polarization.

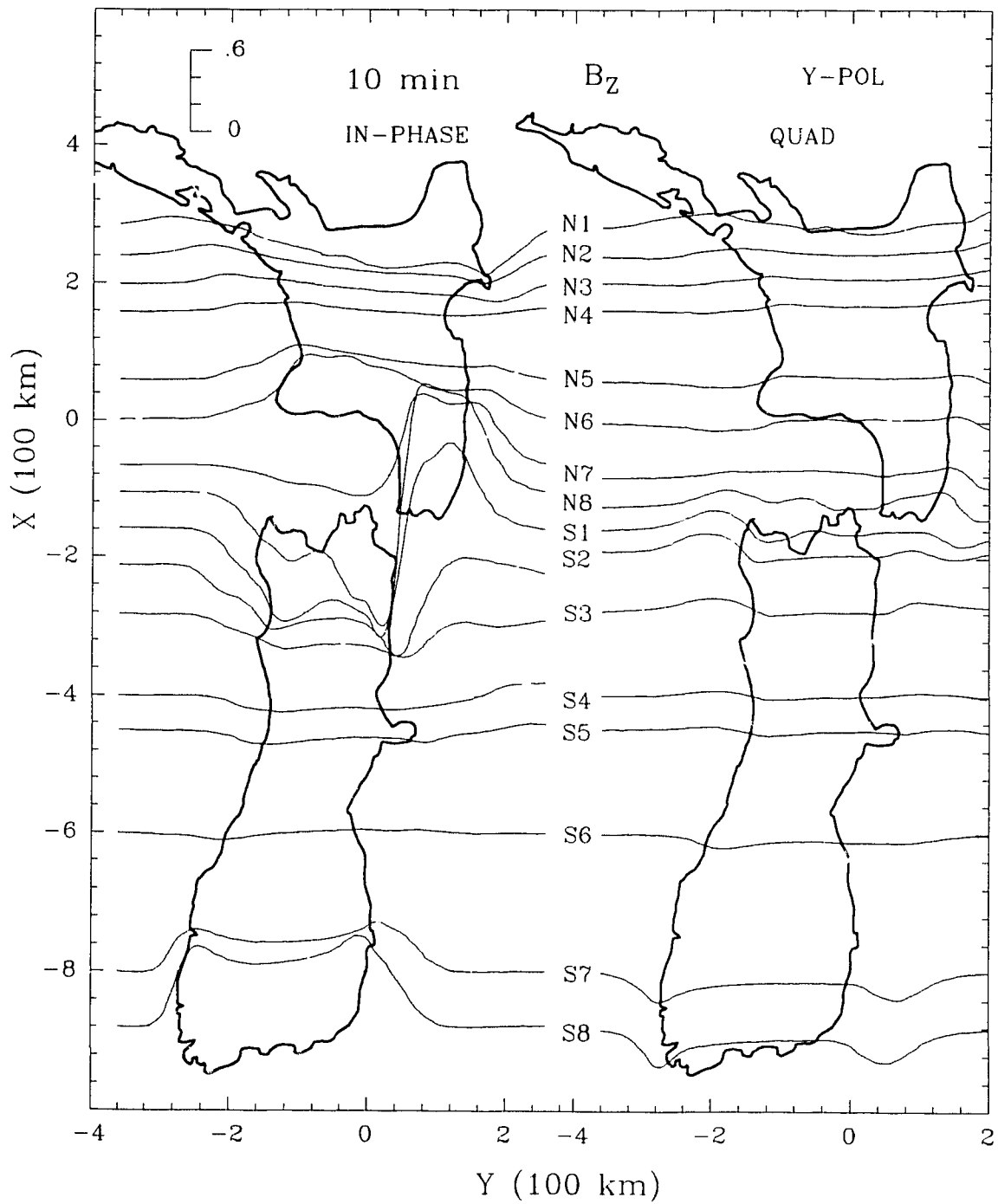


Figure D.12: The in-phase and quadrature B_z along traverses over the model at 10 min for Y-polarization.

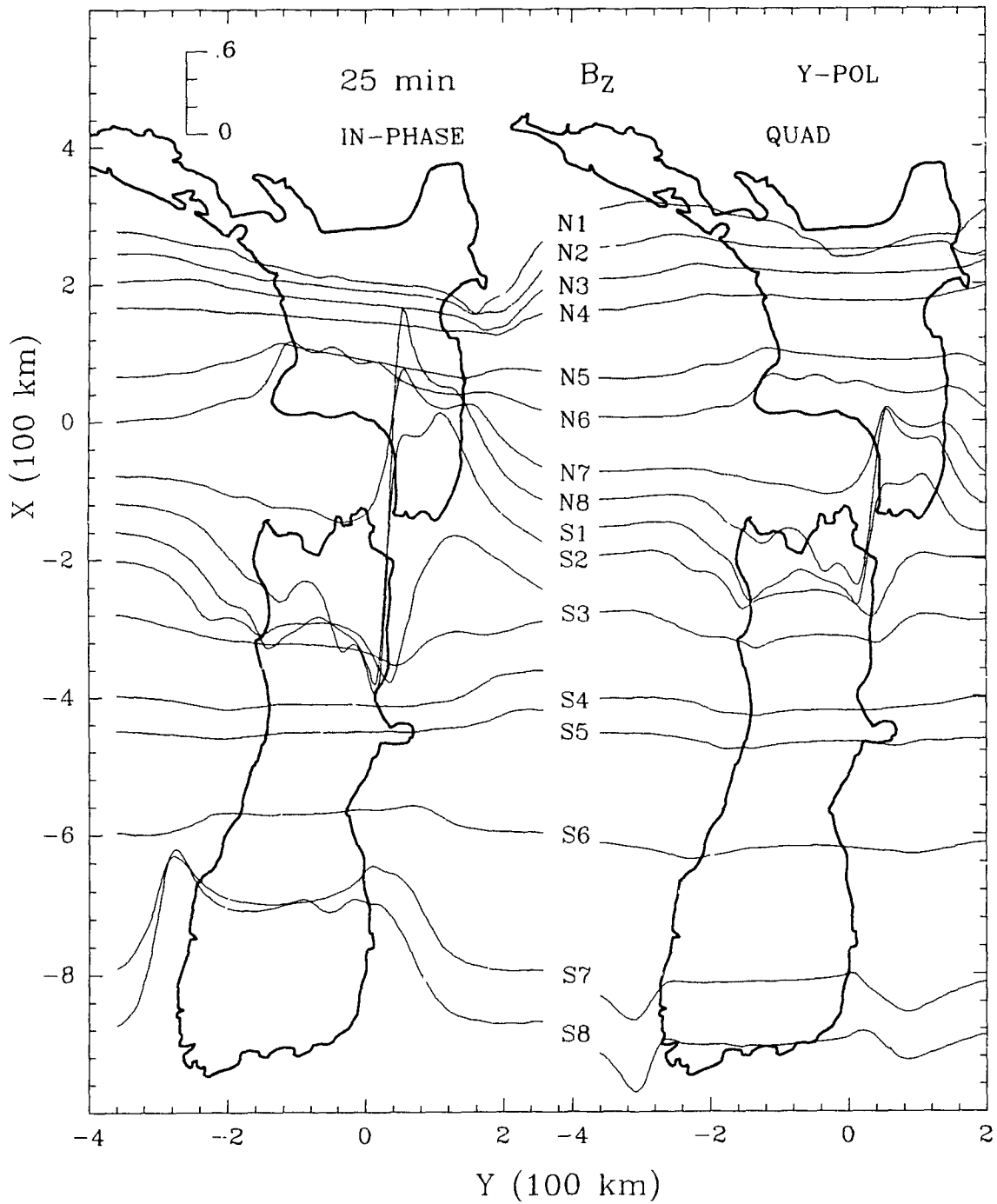


Figure D.13: The in-phase and quadrature B_z along traverses over the model at 25 min for Y-polarization.

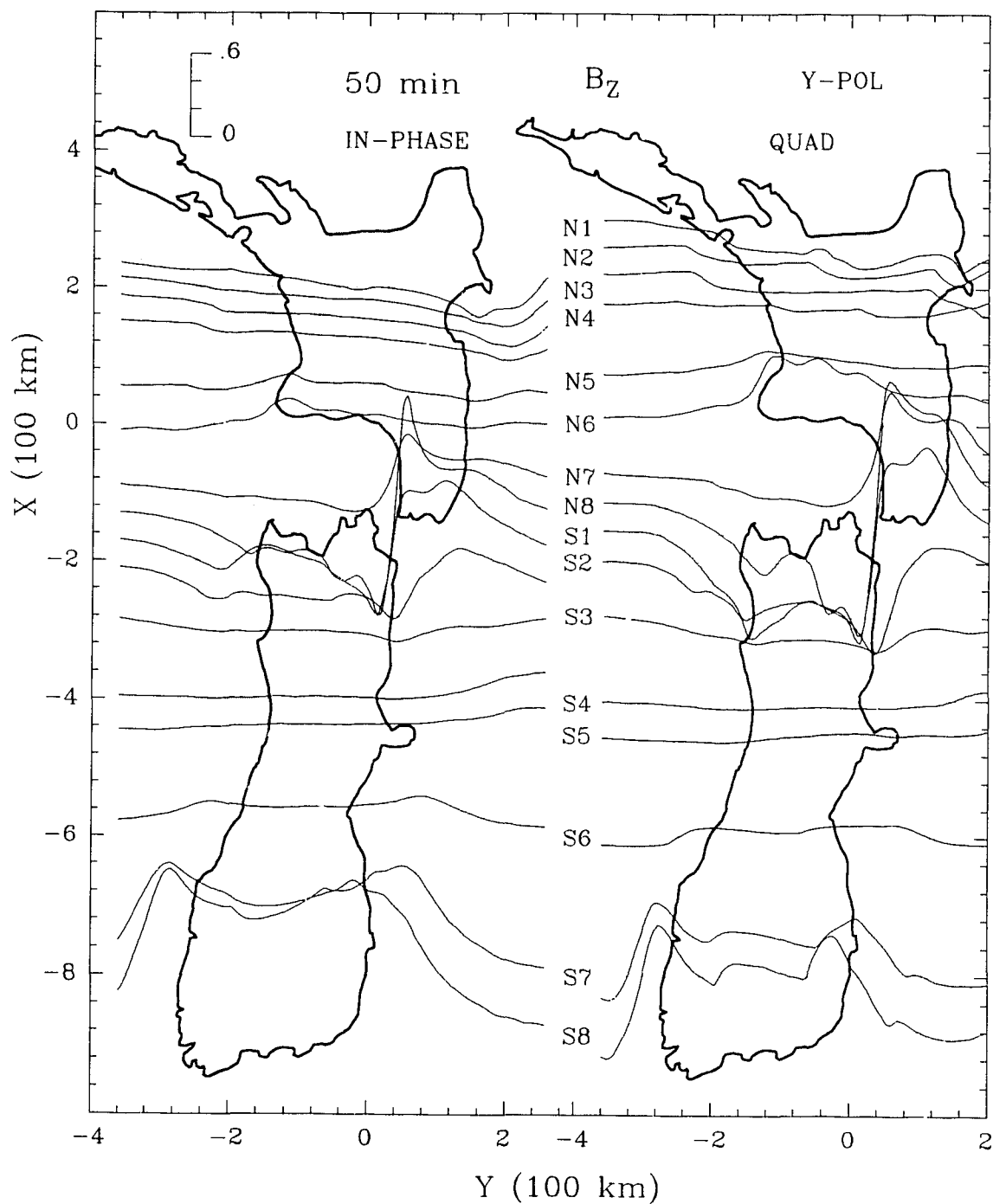


Figure D.14: The in-phase and quadrature E_z along traverses over the model at 50 min for Y-polarization.

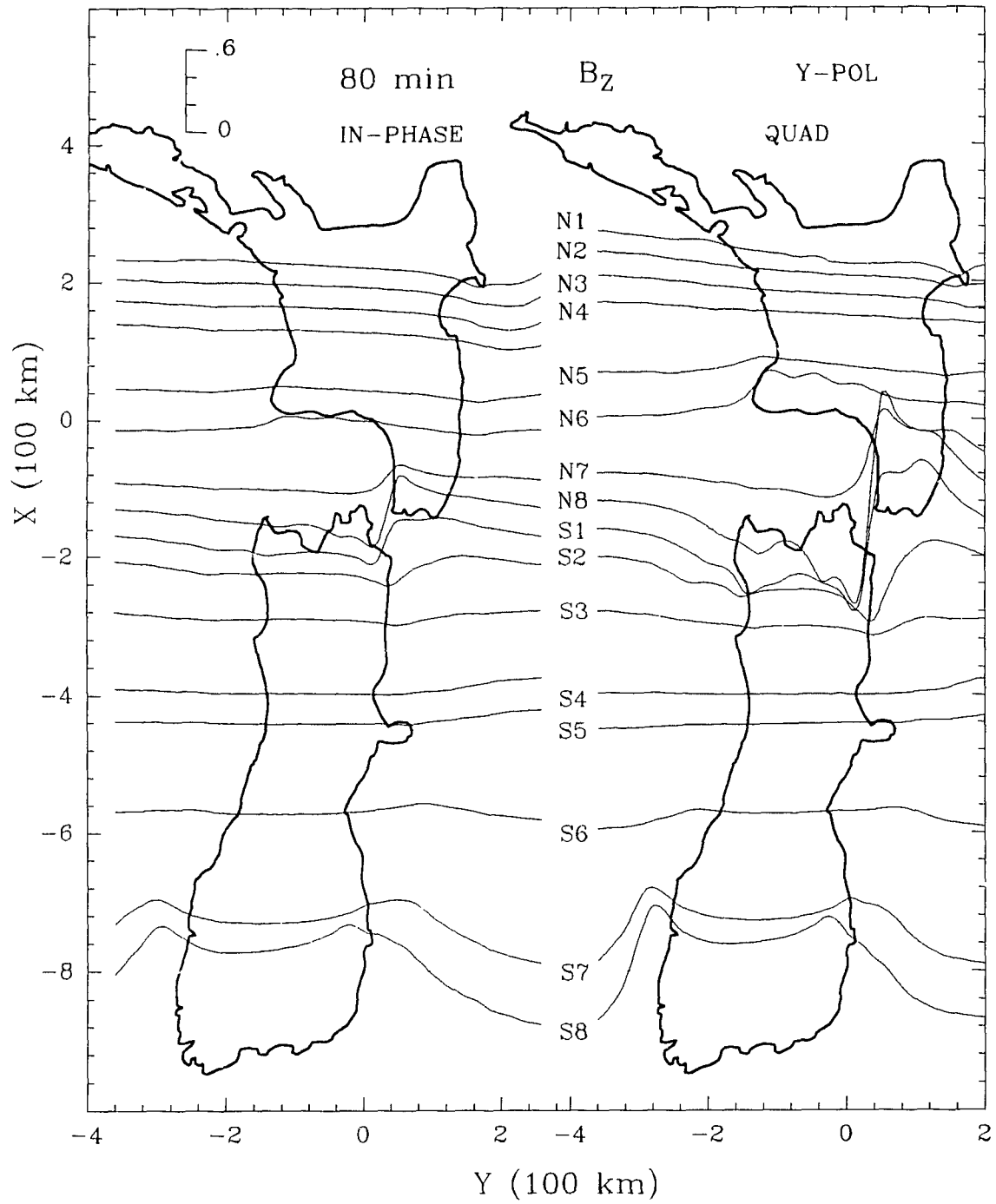


Figure D.15: The in-phase and quadrature B_z along traverses over the model at 80 min for Y-polarization.

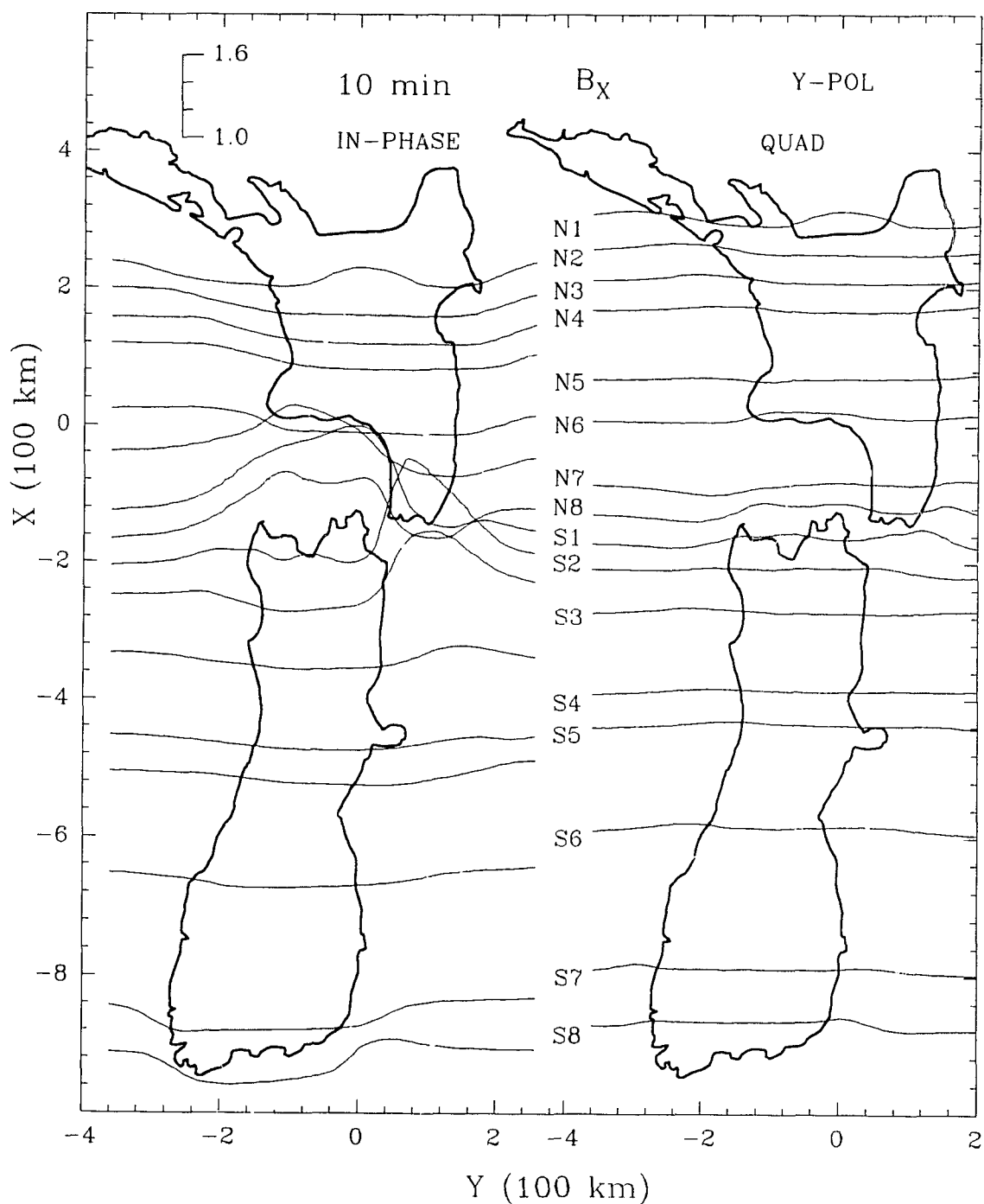


Figure D.16: The in-phase and quadrature B_x along traverses over the model at 10 min for Y-polarization.

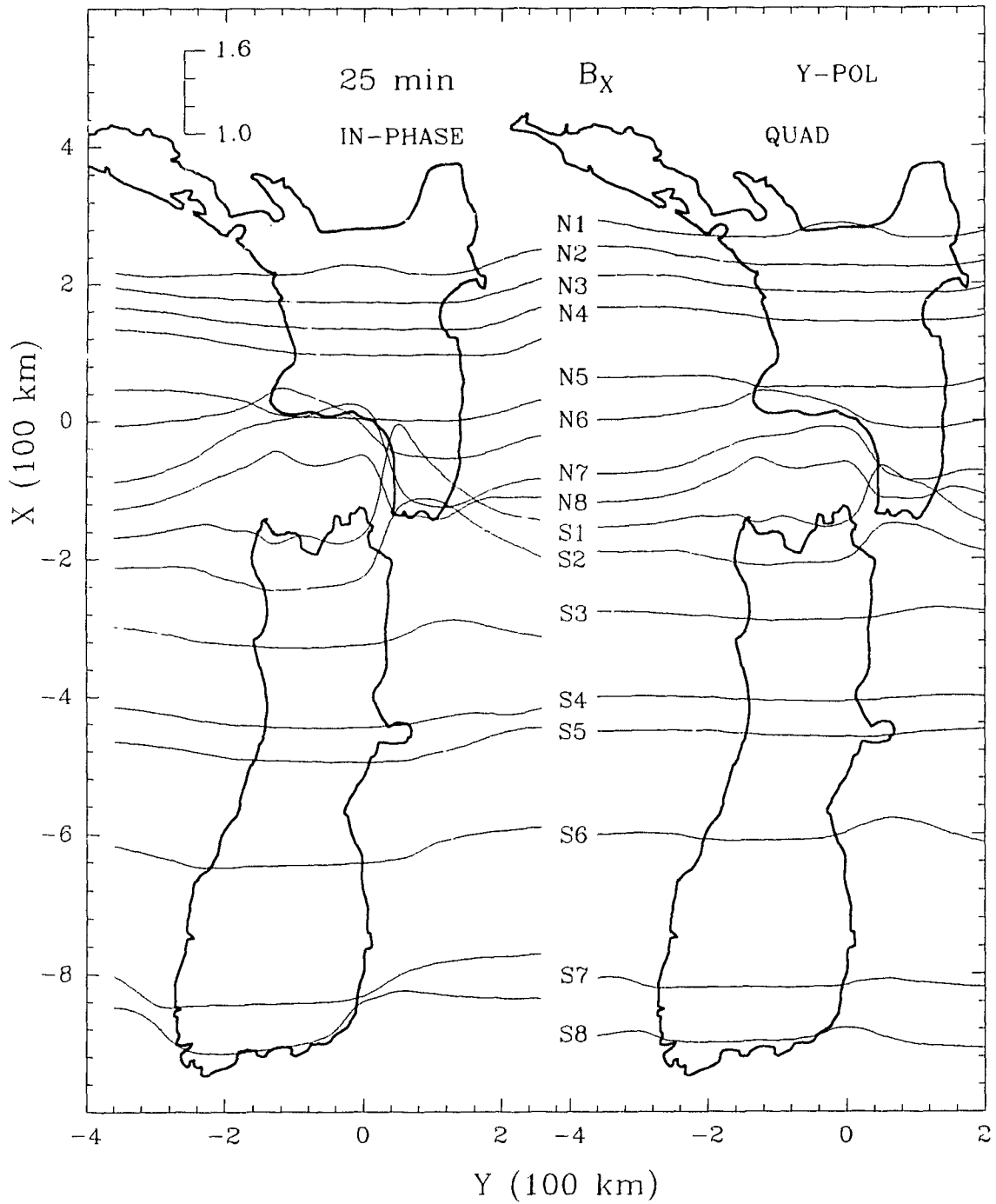


Figure D.17: The in-phase and quadrature B_x along traverses over the model at 25 min for Y-polarization.

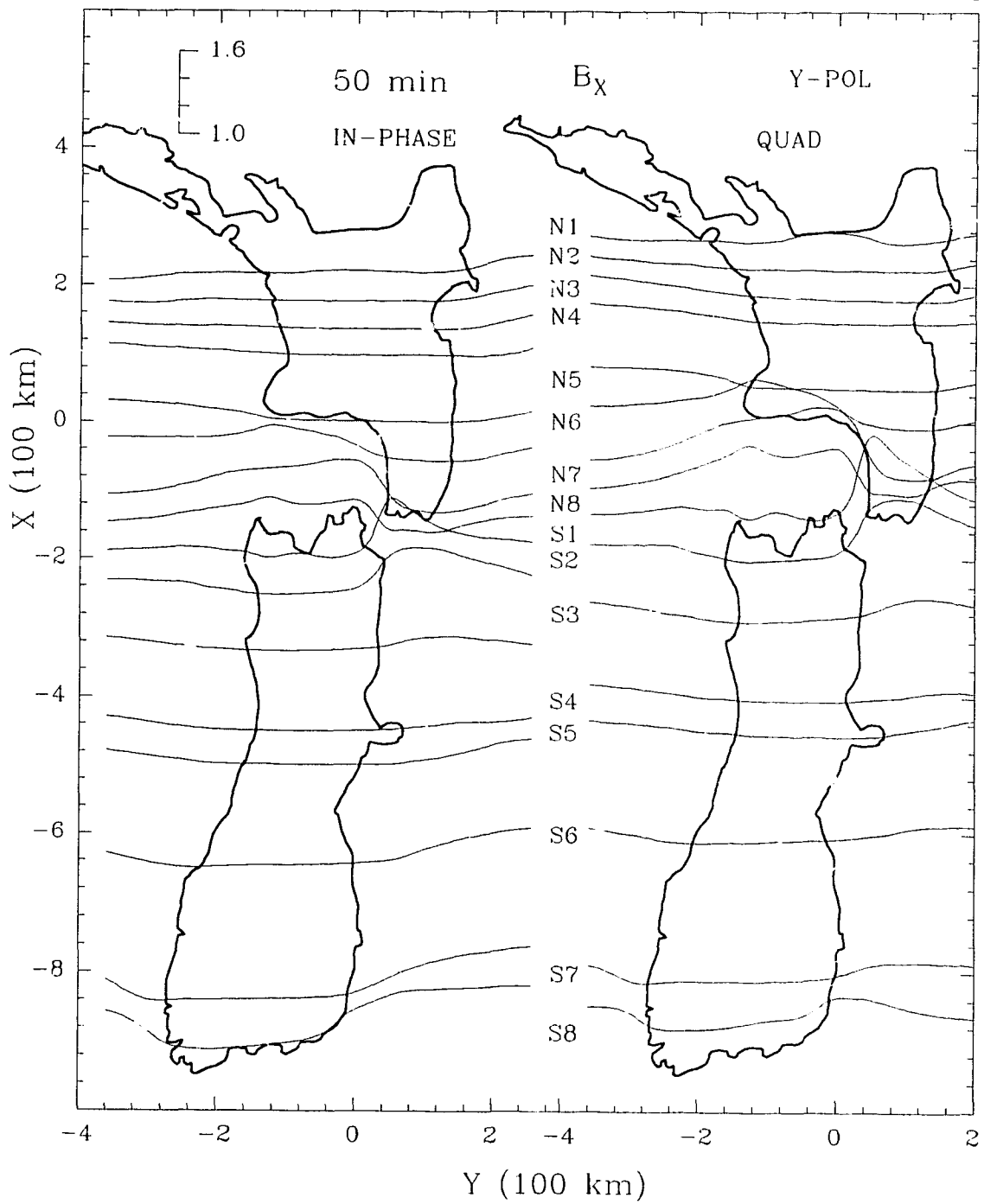


Figure D.18: The in-phase and quadrature B_x along traverses over the model at 50 min for Y-polarization.

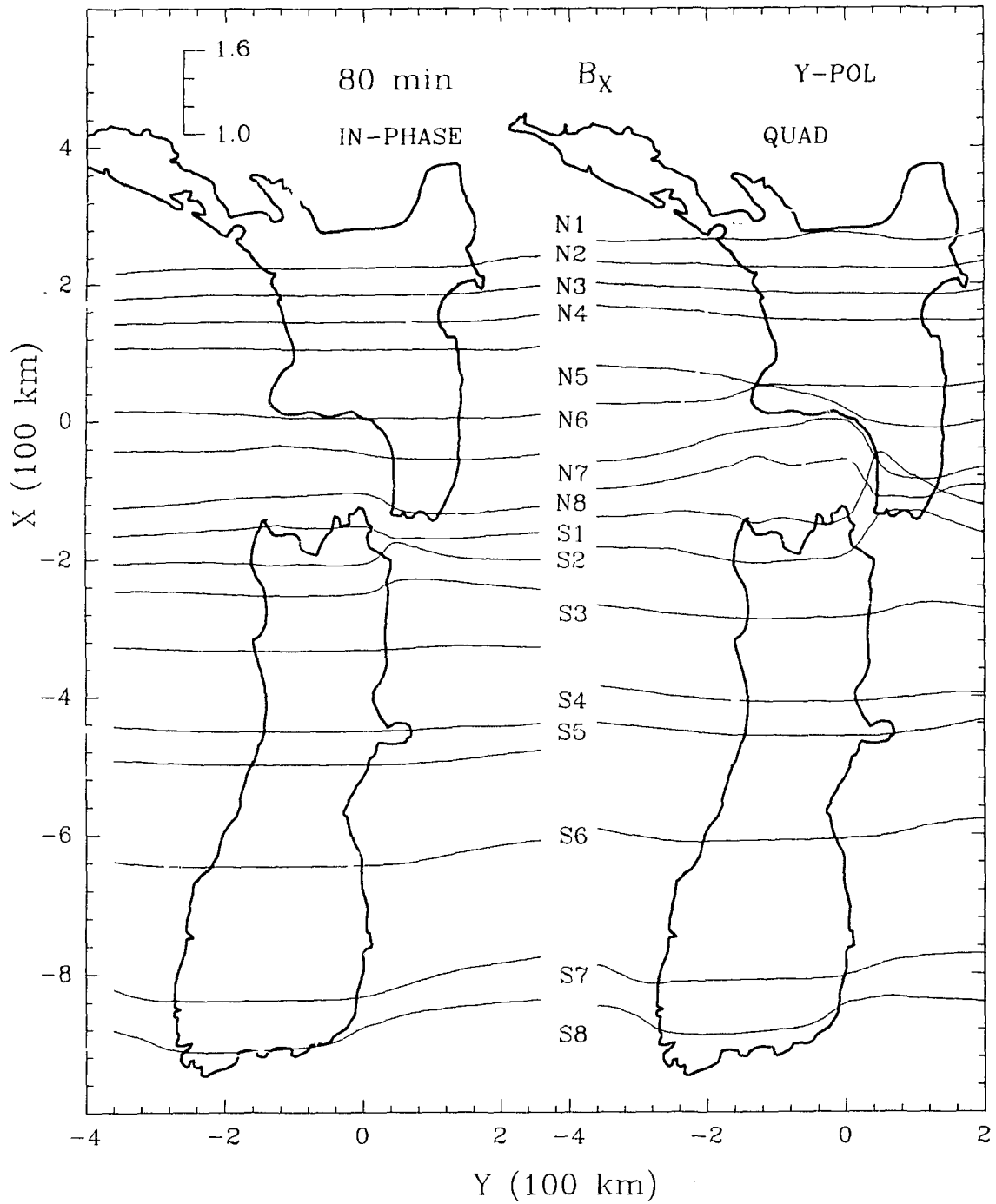


Figure D.19: The in-phase and quadrature B_x along traverses over the model at 80 min for Y-polarization.

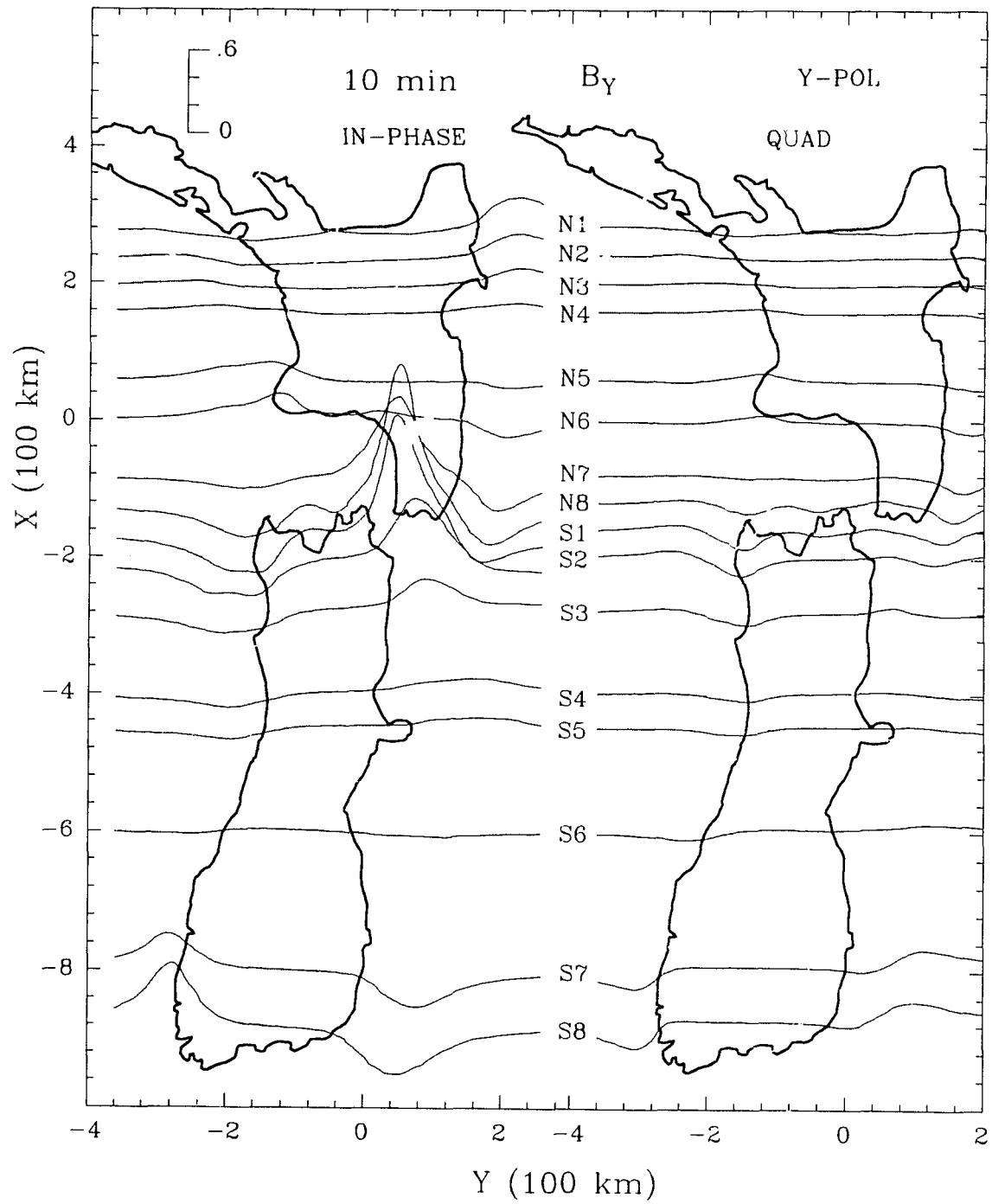


Figure D.20: The in-phase and quadrature B_y along traverses over the model at 10 min for Y-polarization.

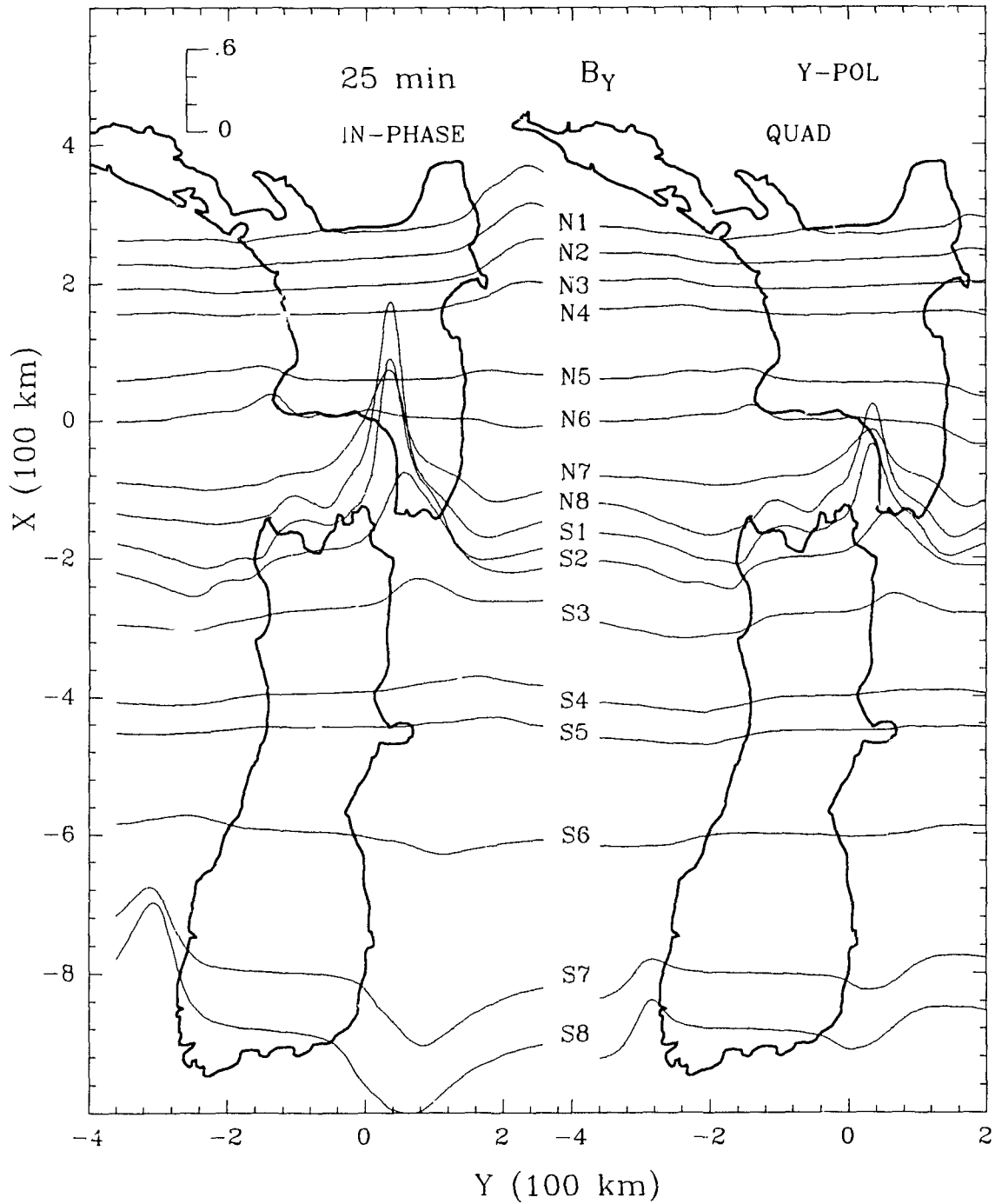


Figure D.21: The in-phase and quadrature B_y along traverses over the model at 25 min for Y-polarization.

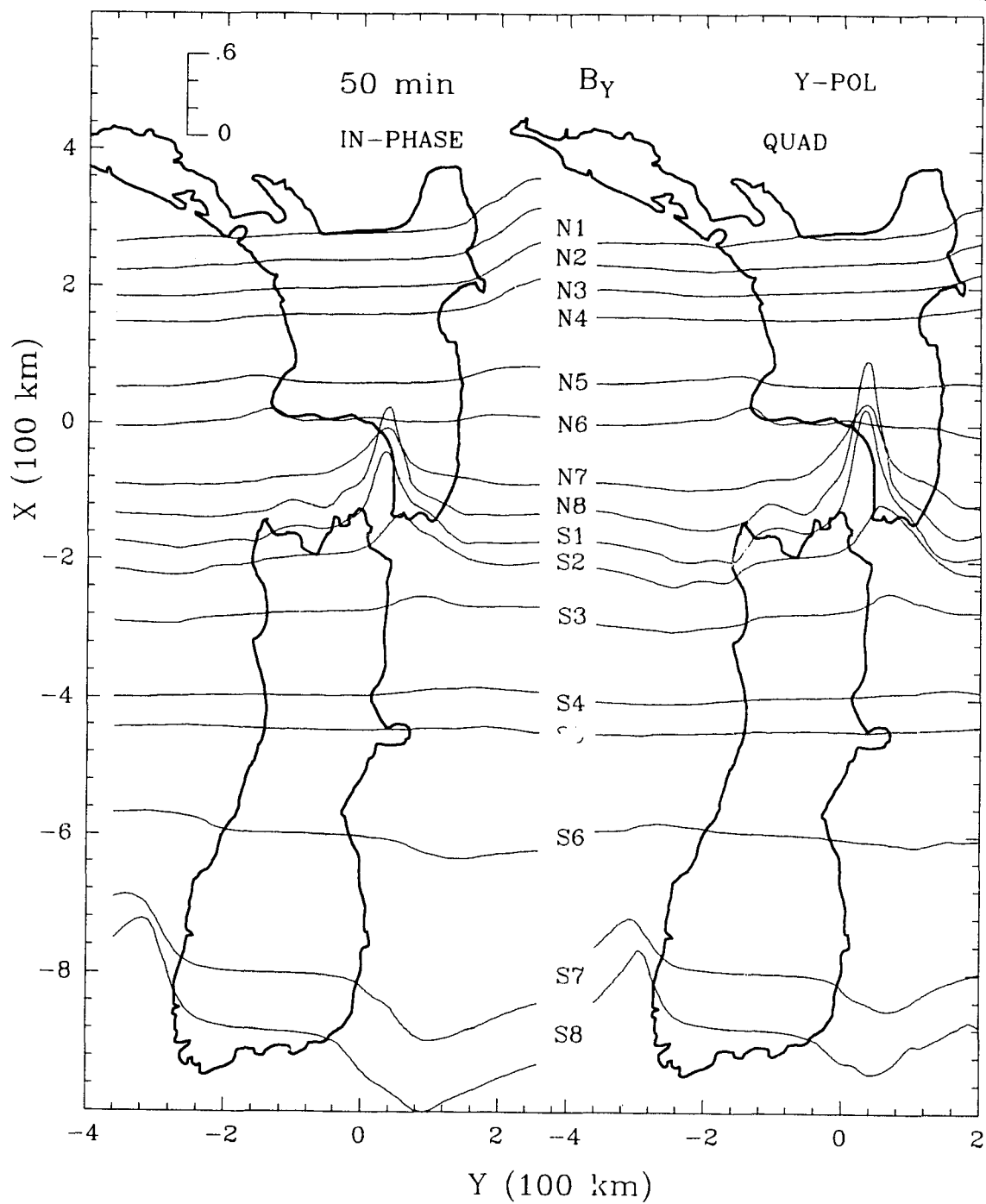


Figure D.22: The in-phase and quadrature B_y along traverses over the model at 50 min for Y-polarization.

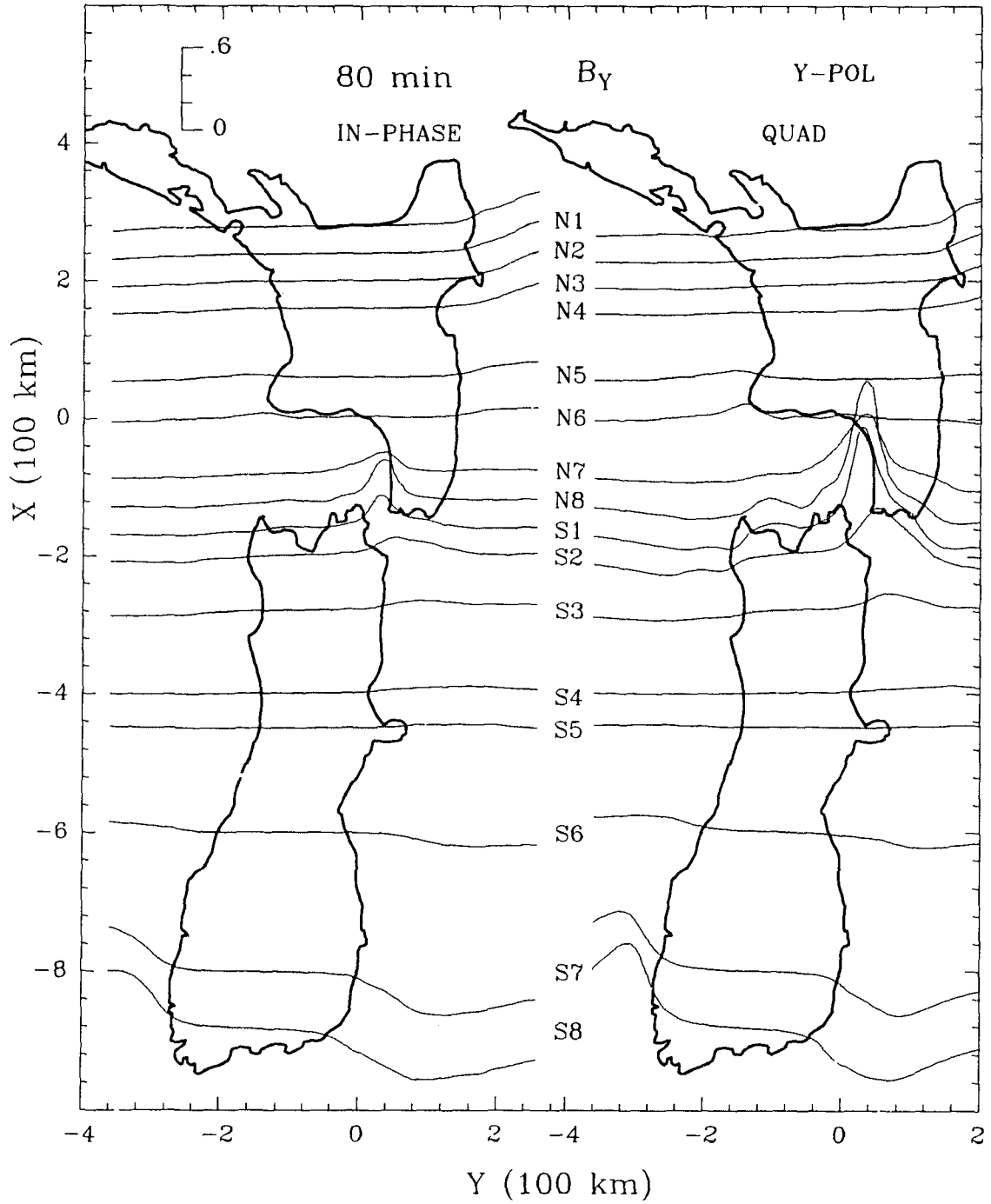


Figure D.23: The in-phase and quadrature B_y along traverses over the model at 80 min for Y-polarization.

APPENDIX E
MODEL INDUCTION ARROW V_X AND V_Y RESPONSE CURVES

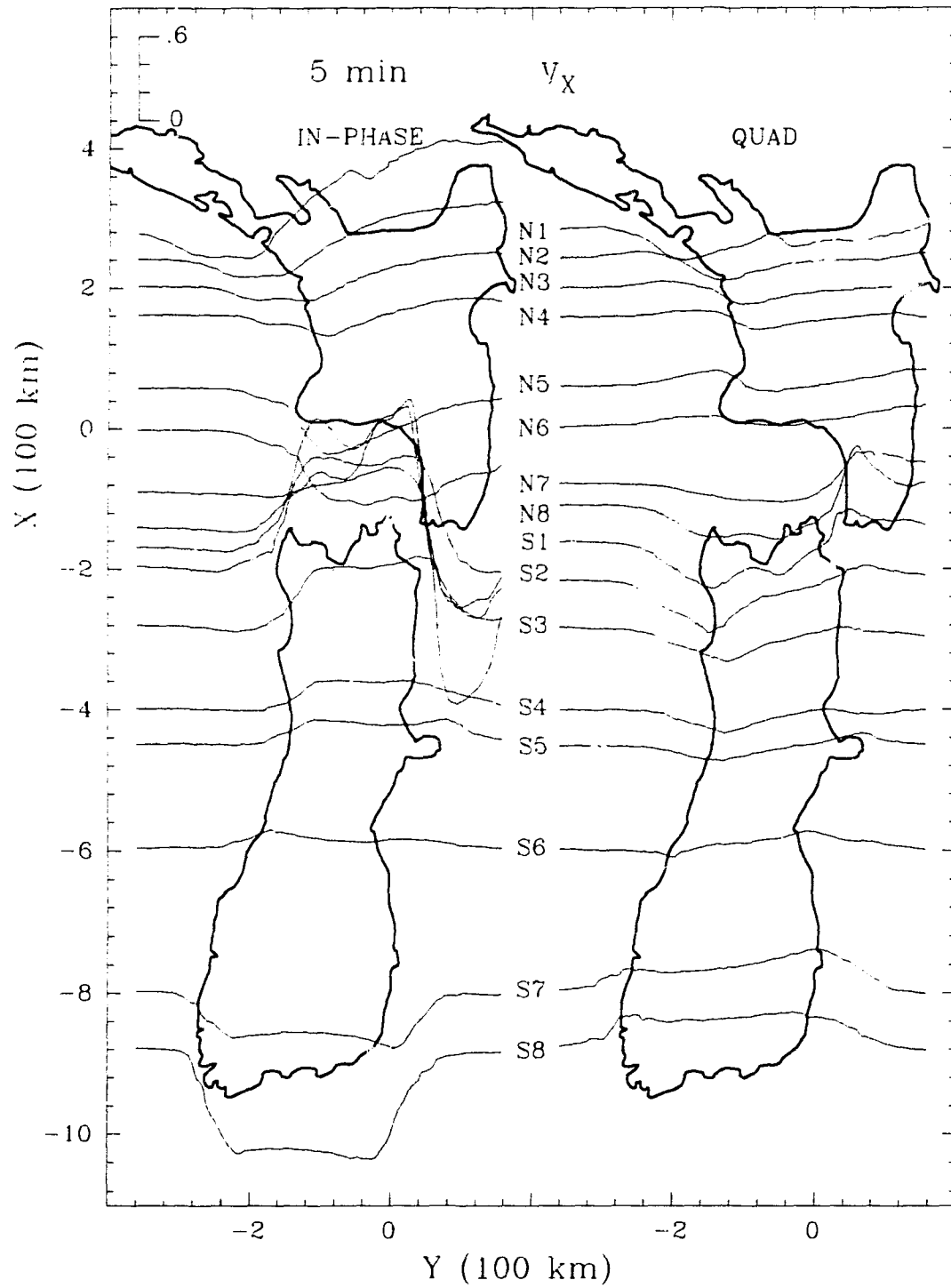


Figure E.1: The in-phase and quadrature V_x (x-component of the induction arrow V) response curves at 5 min for traverses over the model.

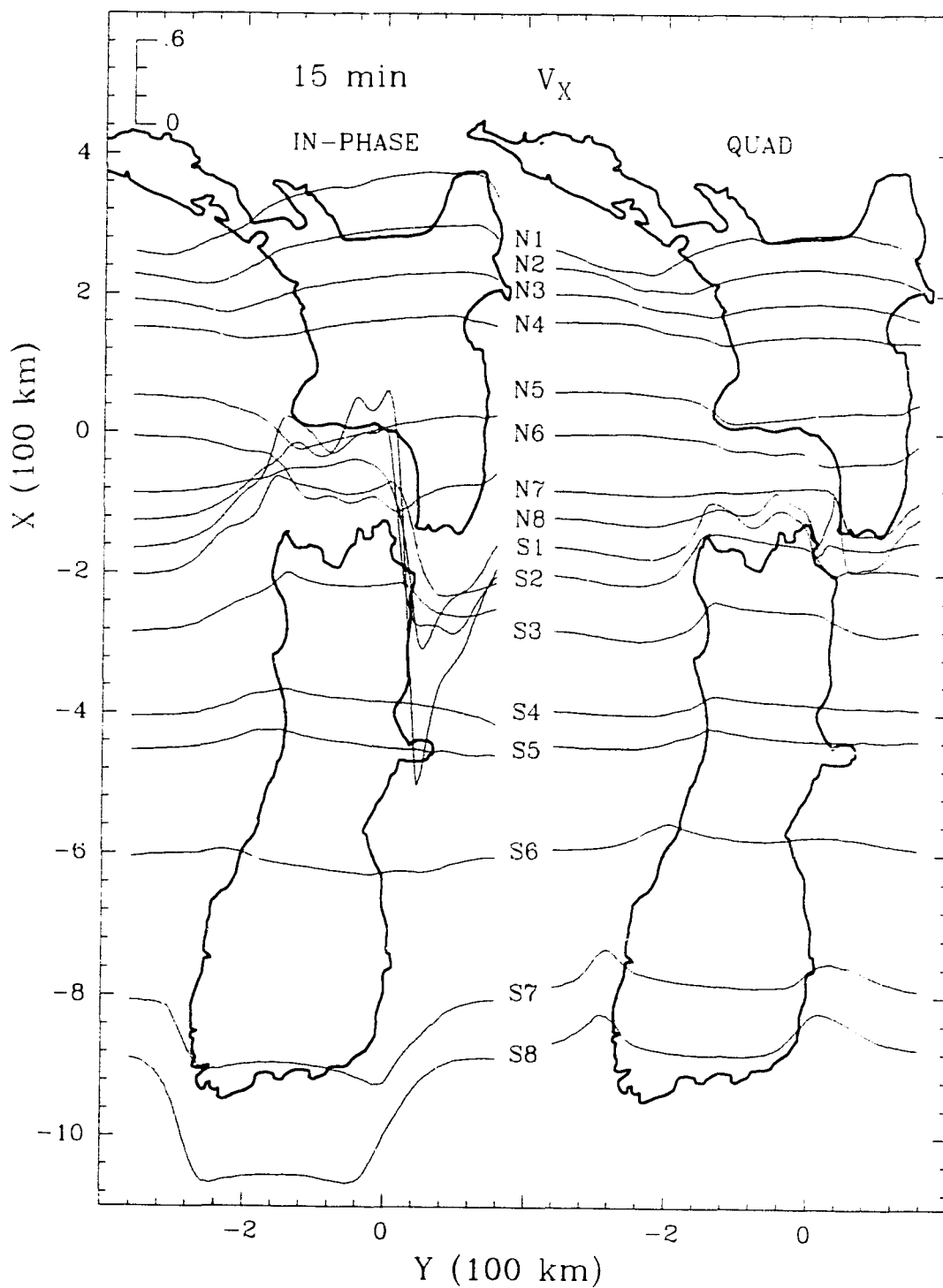


Figure E.2: The in-phase and quadrature V_x (x-component of the induction arrow V) response curves at 15 min for traverses over the model.

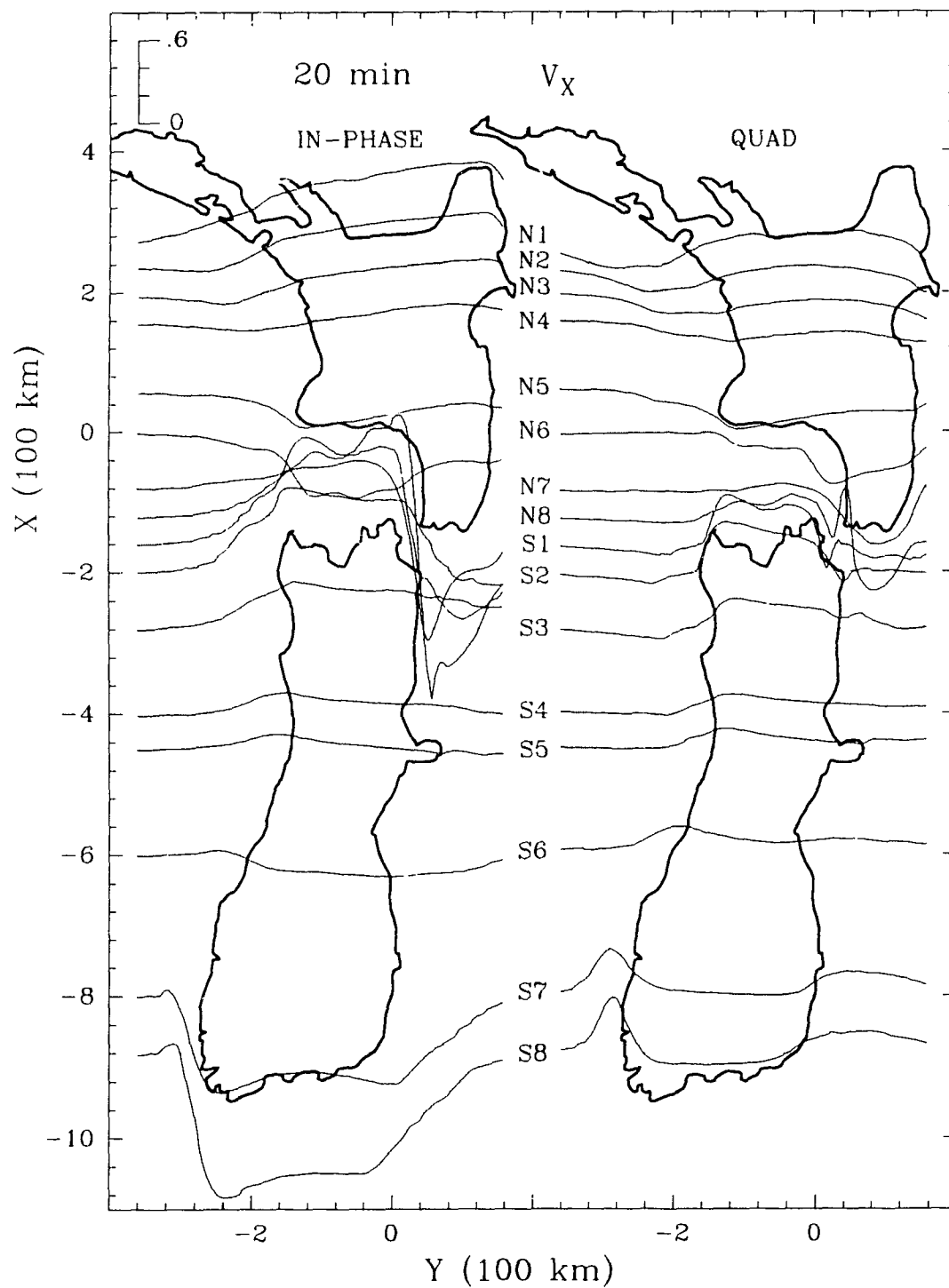


Figure E.3: The in-phase and quadrature V_x (x-component of the induction arrow V) response curves at 20 min for traverses over the model.

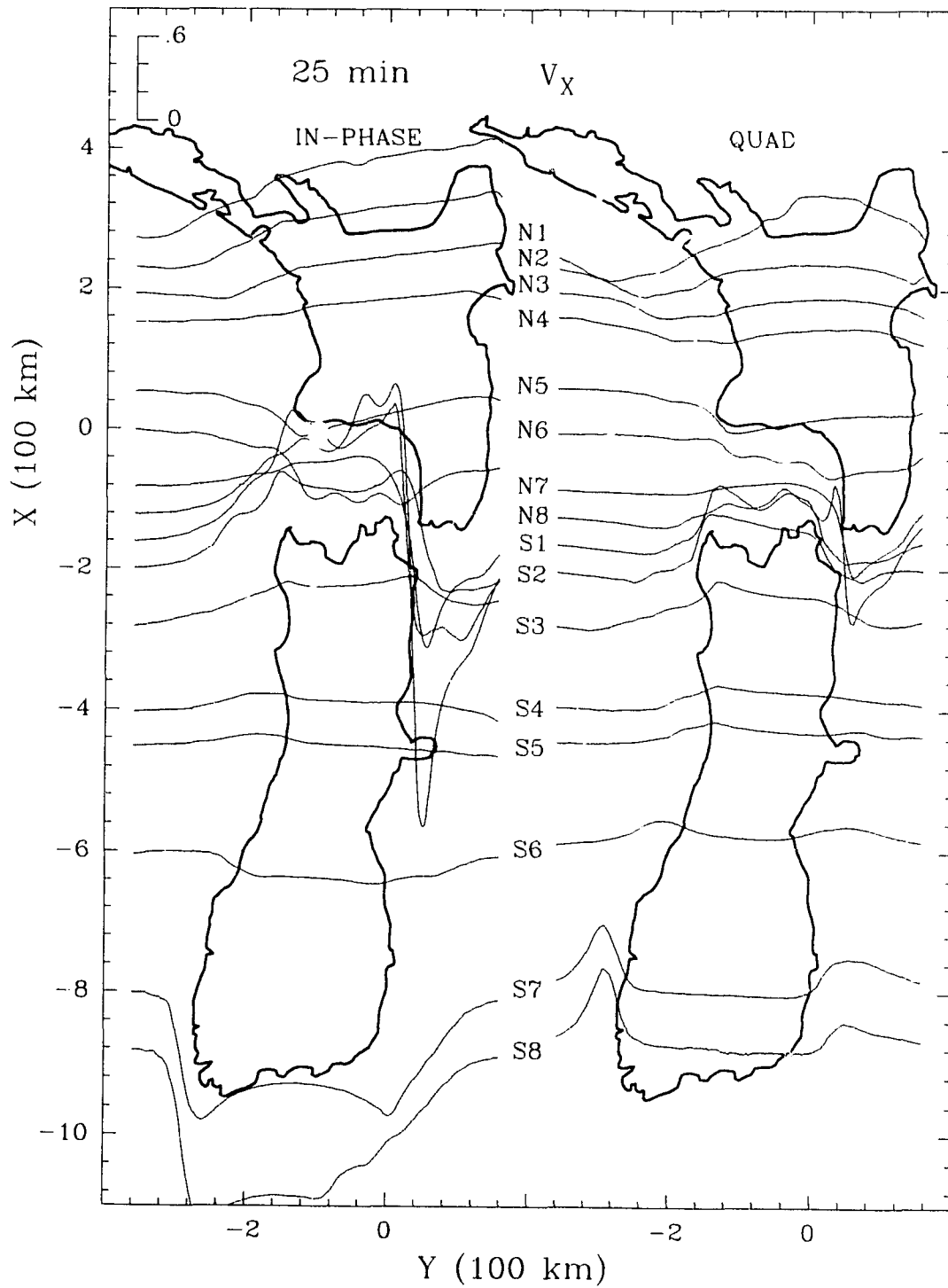


Figure E.4: The in-phase and quadrature V_x (x-component of the induction arrow V) response curves at 25 min for traverses over the model.

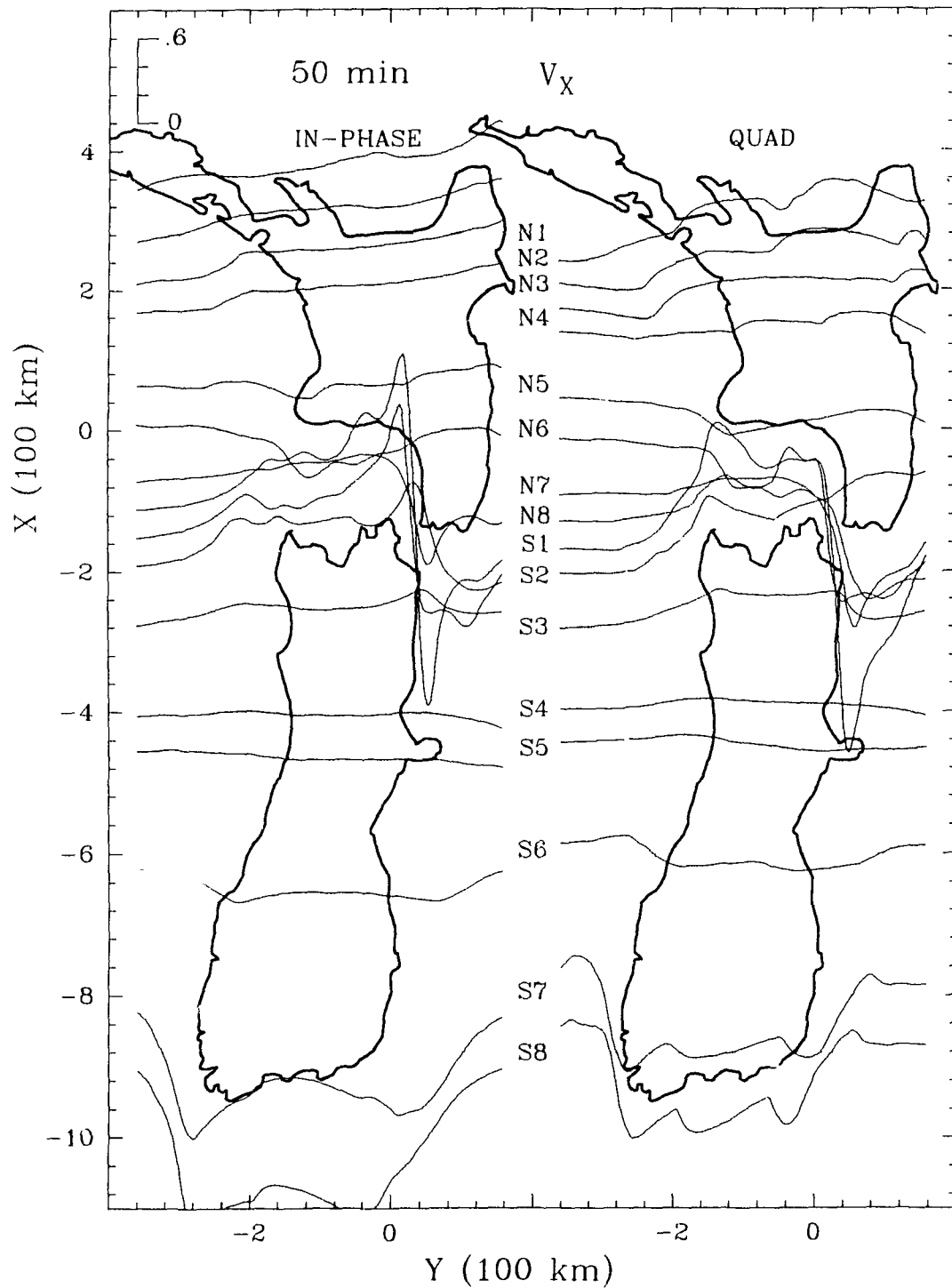


Figure E.5: The in-phase and quadrature V_x (x-component of the induction arrow V) response curves at 50 min for traverses over the model.

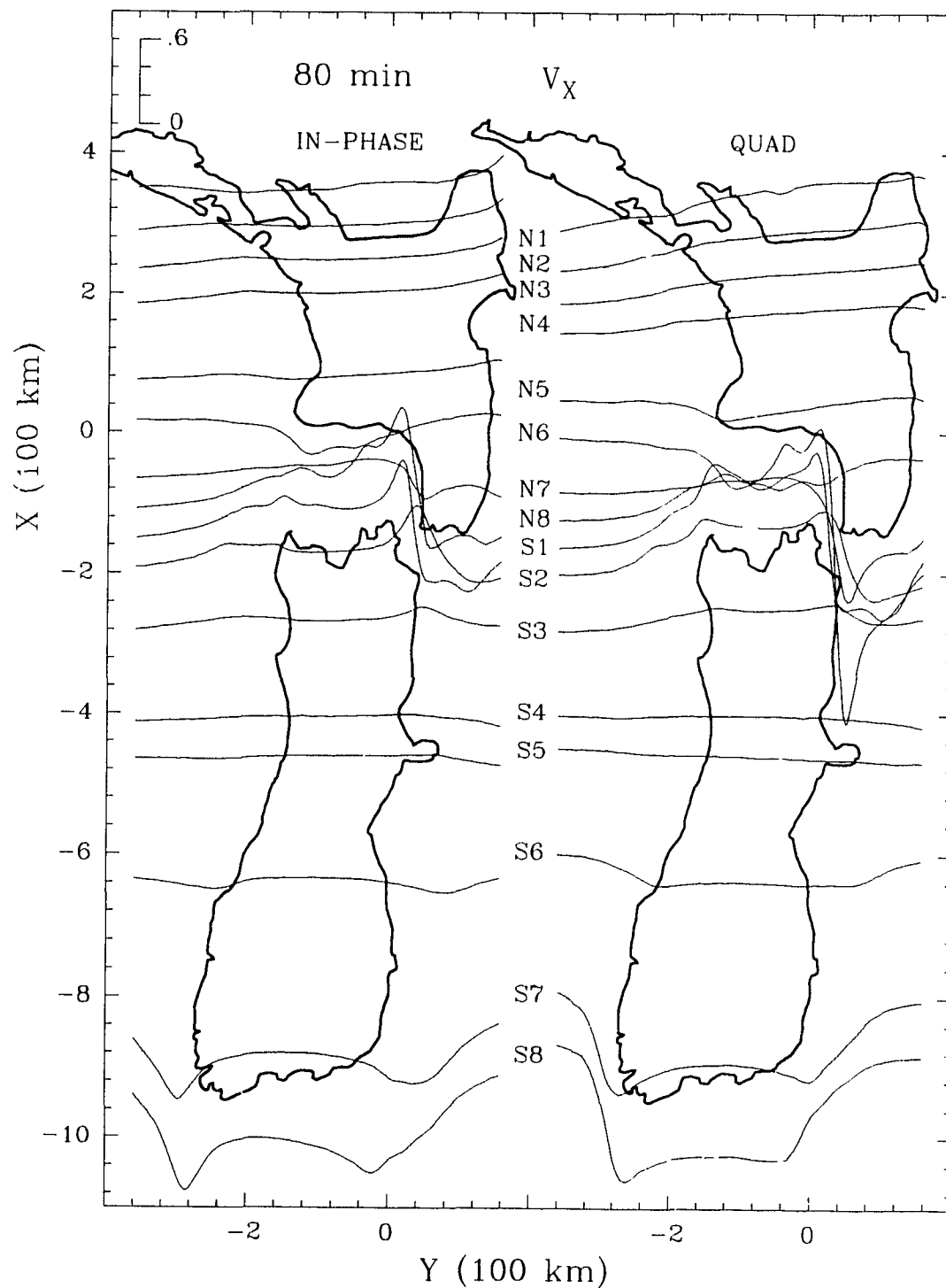


Figure E.6: The in-phase and quadrature V_x (x-component of the induction arrow V) response curves at 80 min for traverses over the model.

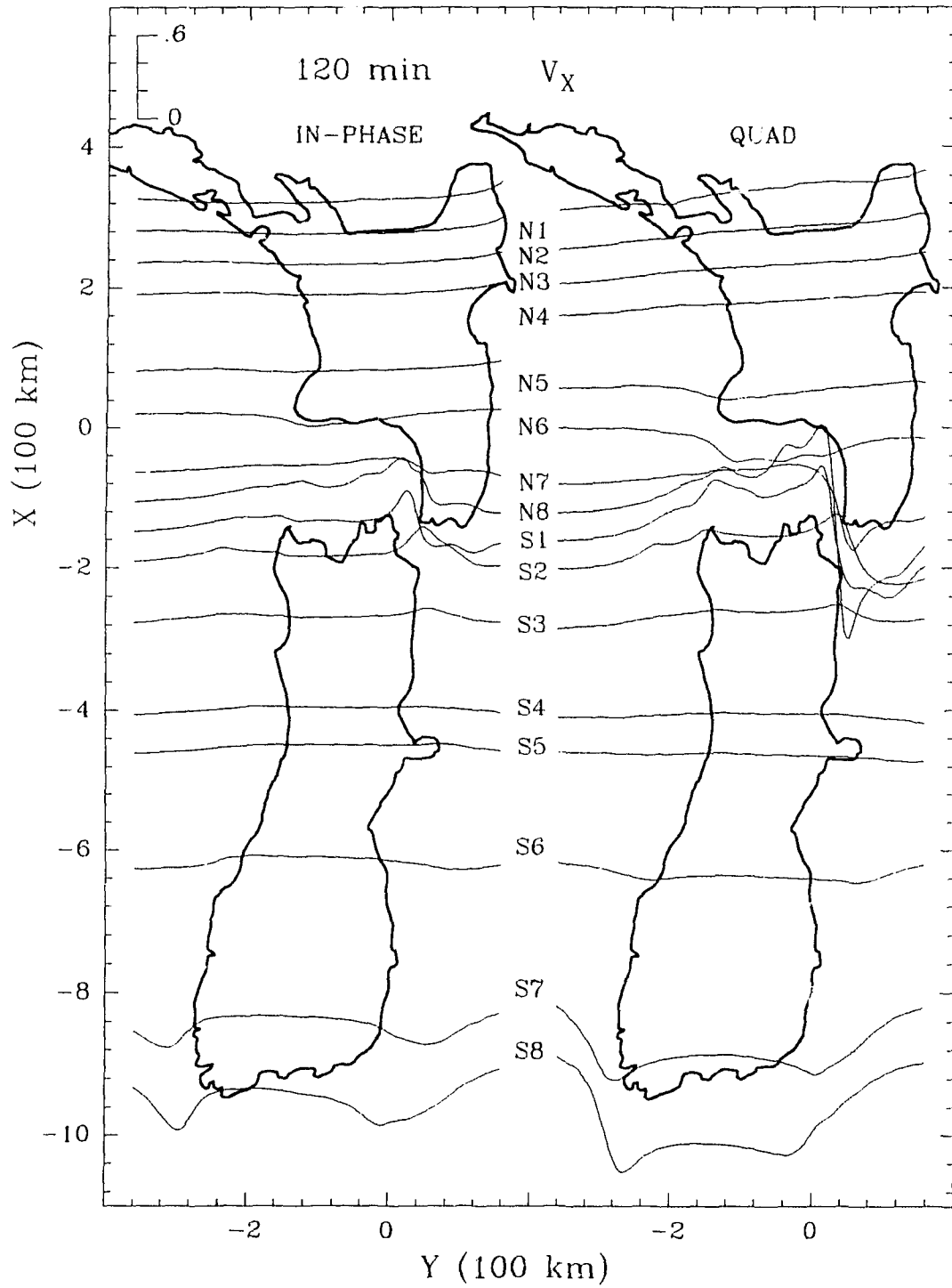


Figure E.7: The in-phase and quadrature V_x (x-component of the induction arrow V) response curves at 120 min for traverses over the model.

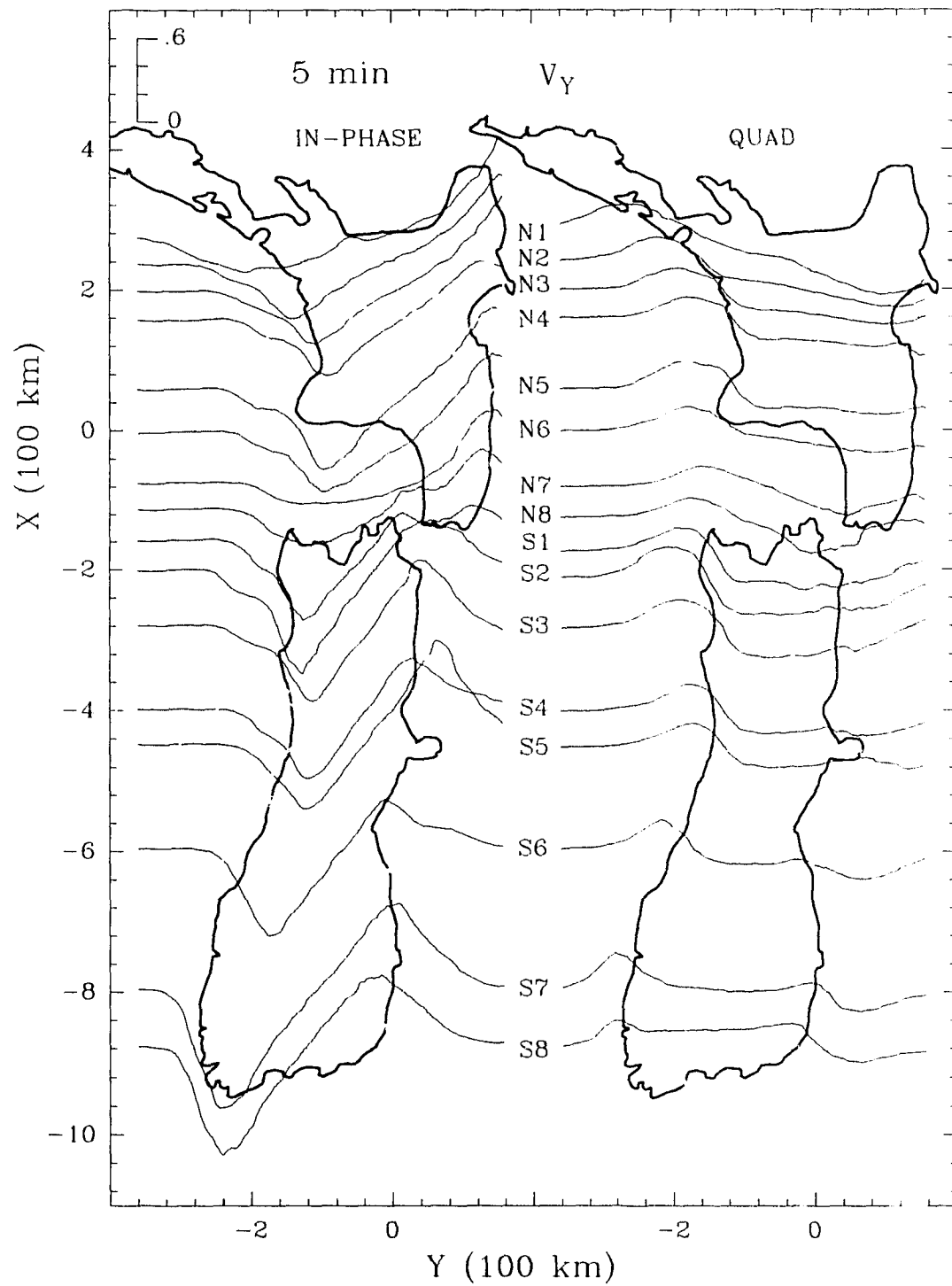


Figure E.8: The in-phase and quadrature V_y (y -component of the induction arrow V) response curves at 5 min for traverses over the model.

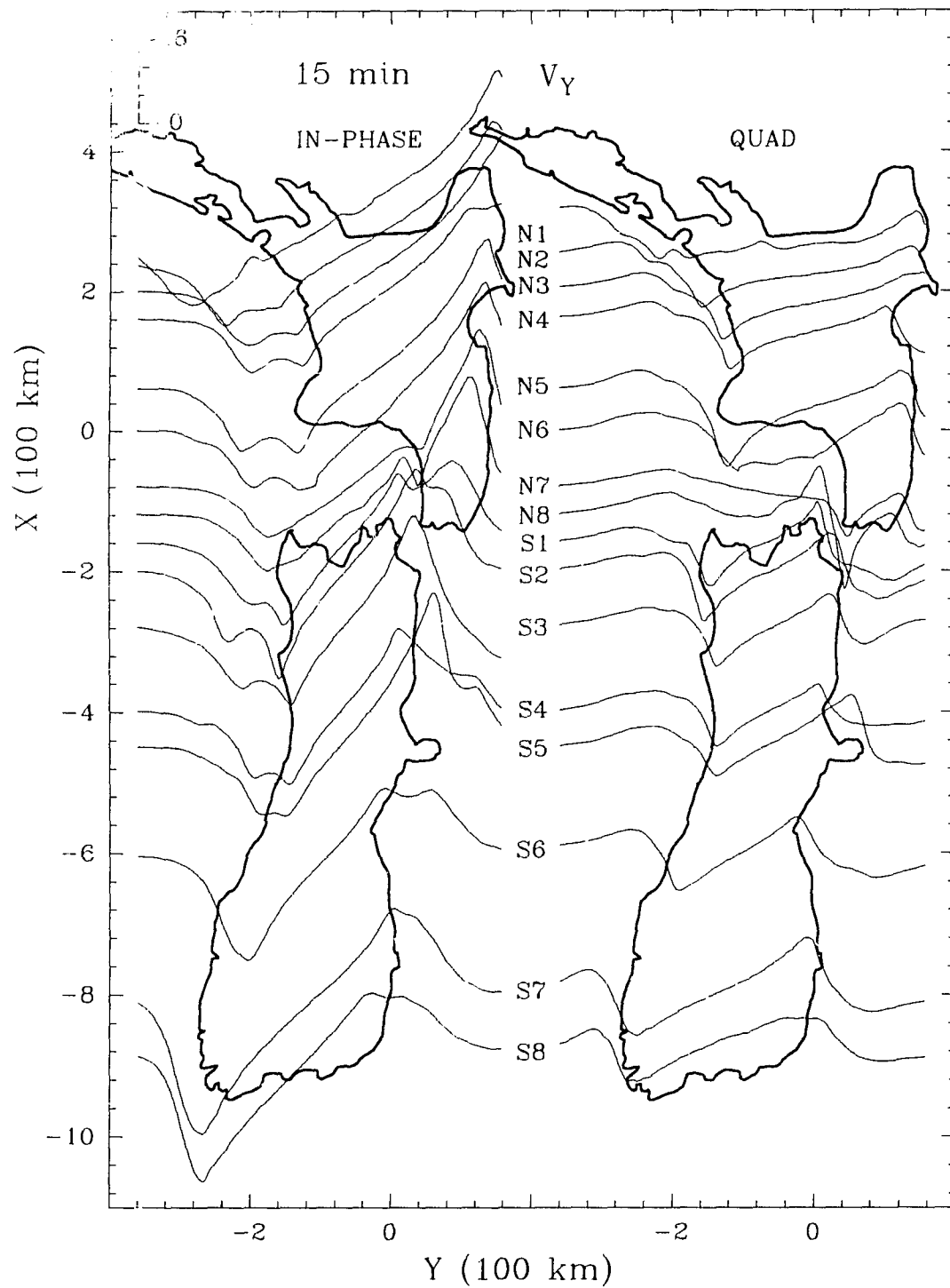


Figure E.9: The in-phase and quadrature V_y (y-component of the induction arrow V) response curves at 15 min for traverses over the model.

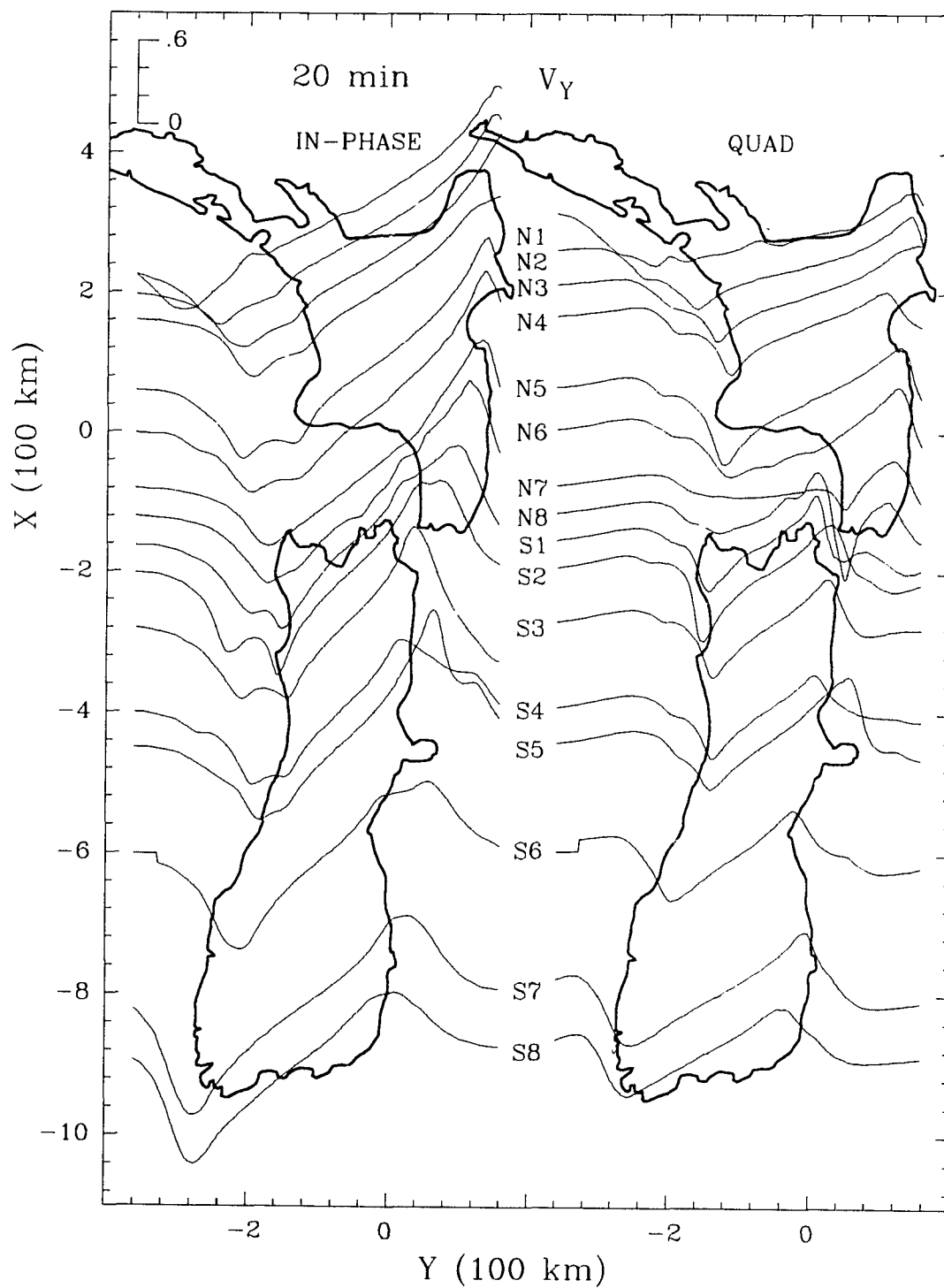


Figure E.10: The in-phase and quadrature V_y (y-component of the induction arrow V) response curves at 20 min for traverses over the model.

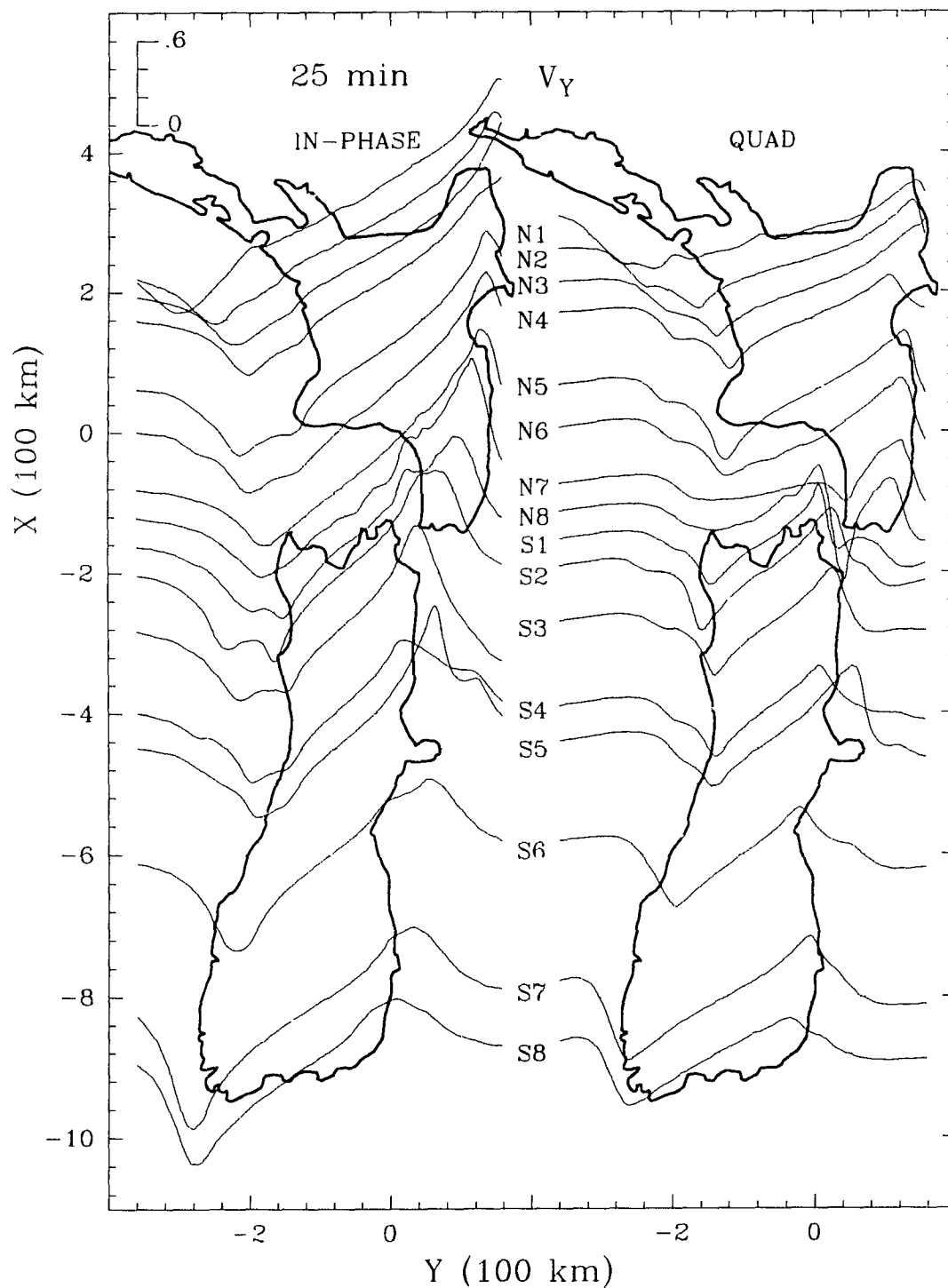


Figure E.11: The in-phase and quadrature V_y (y-component of the induction arrow V) response curves at 25 min for traverses over the model.

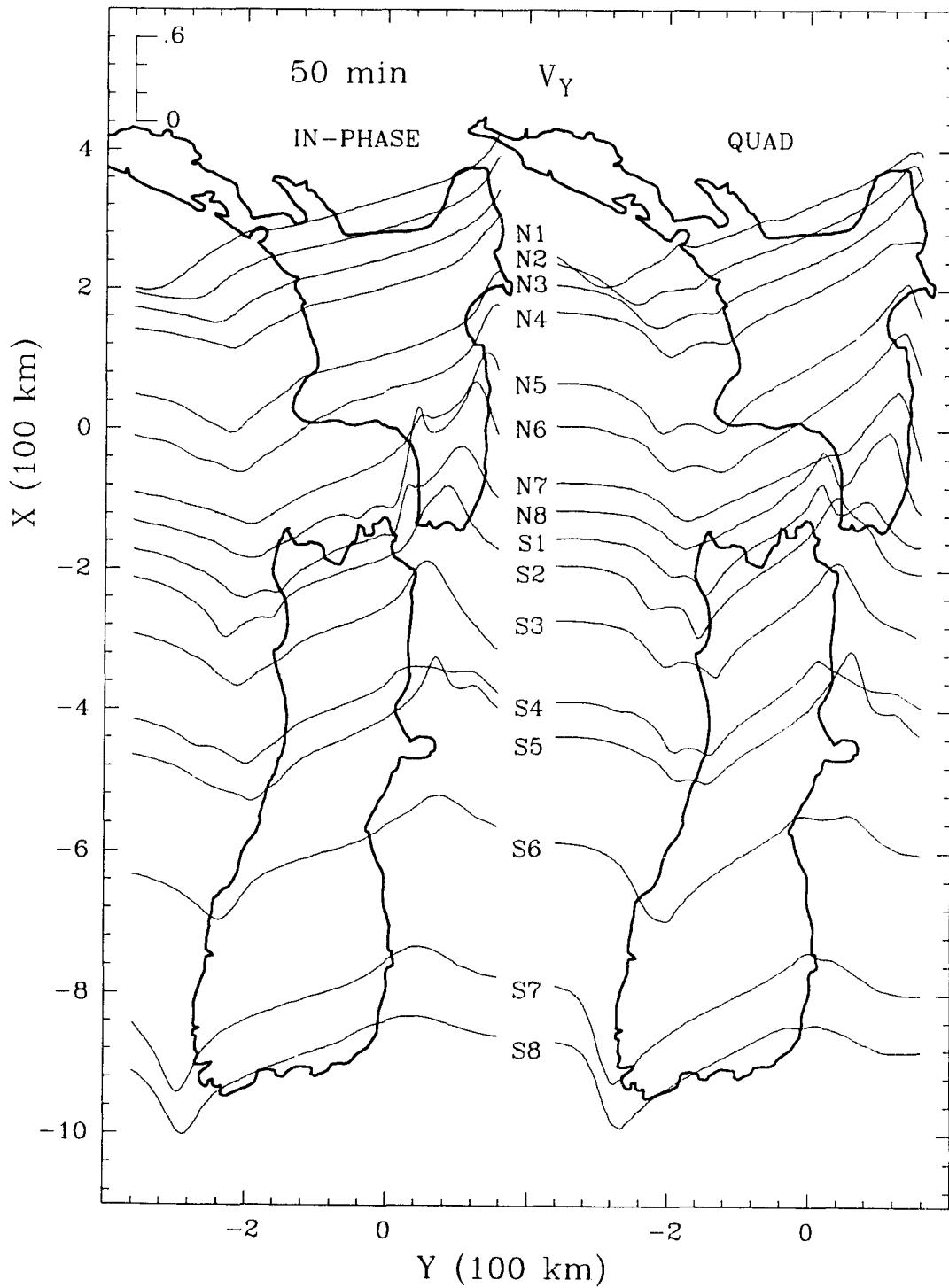


Figure E.12: The in-phase and quadrature V_y (y -component of the induction arrow V) response curves at 50 min for traverses over the model.

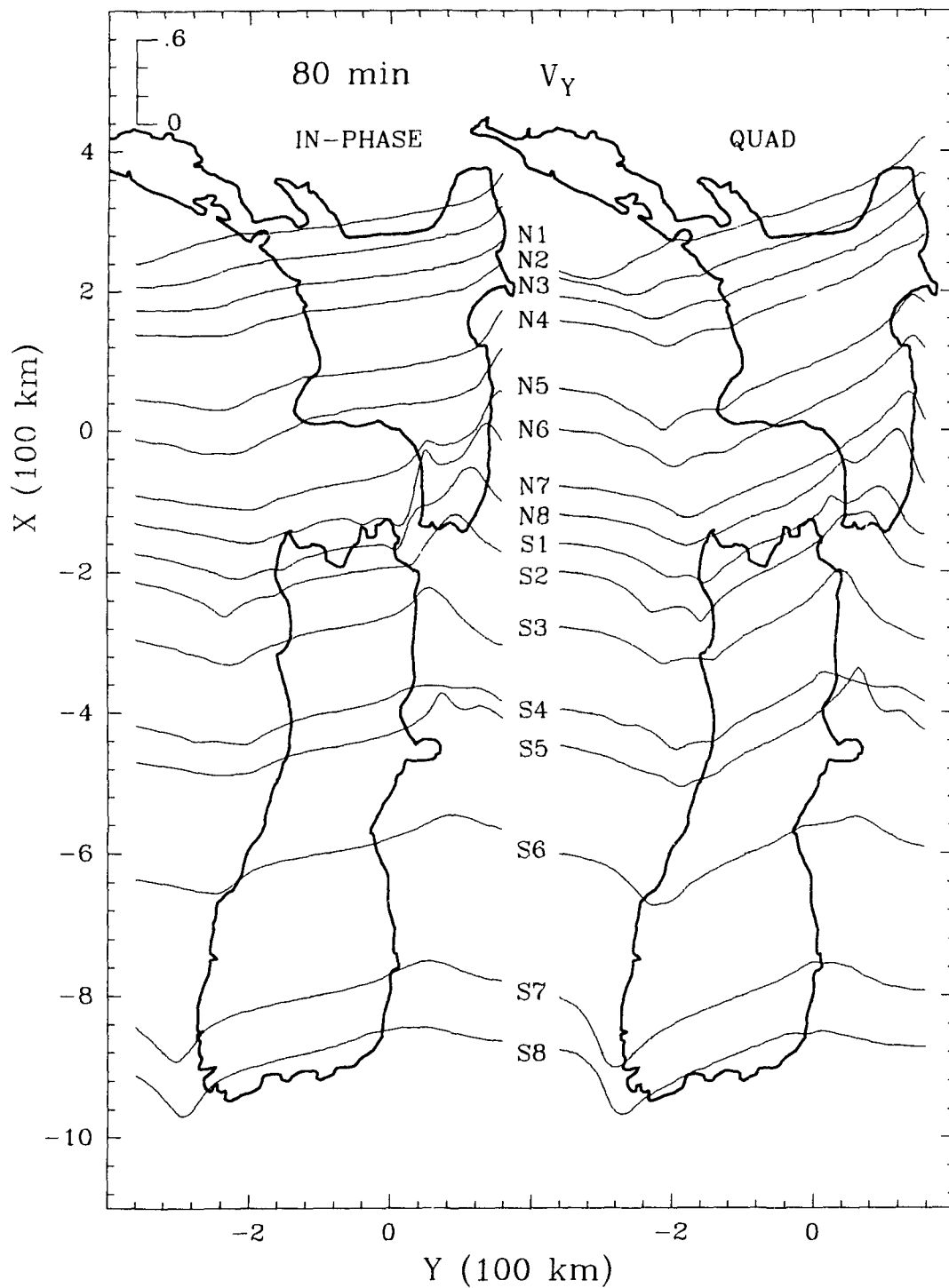


Figure E.13: The in-phase and quadrature V_y (y-component of the induction arrow V) response curves at 80 min for traverses over the model.

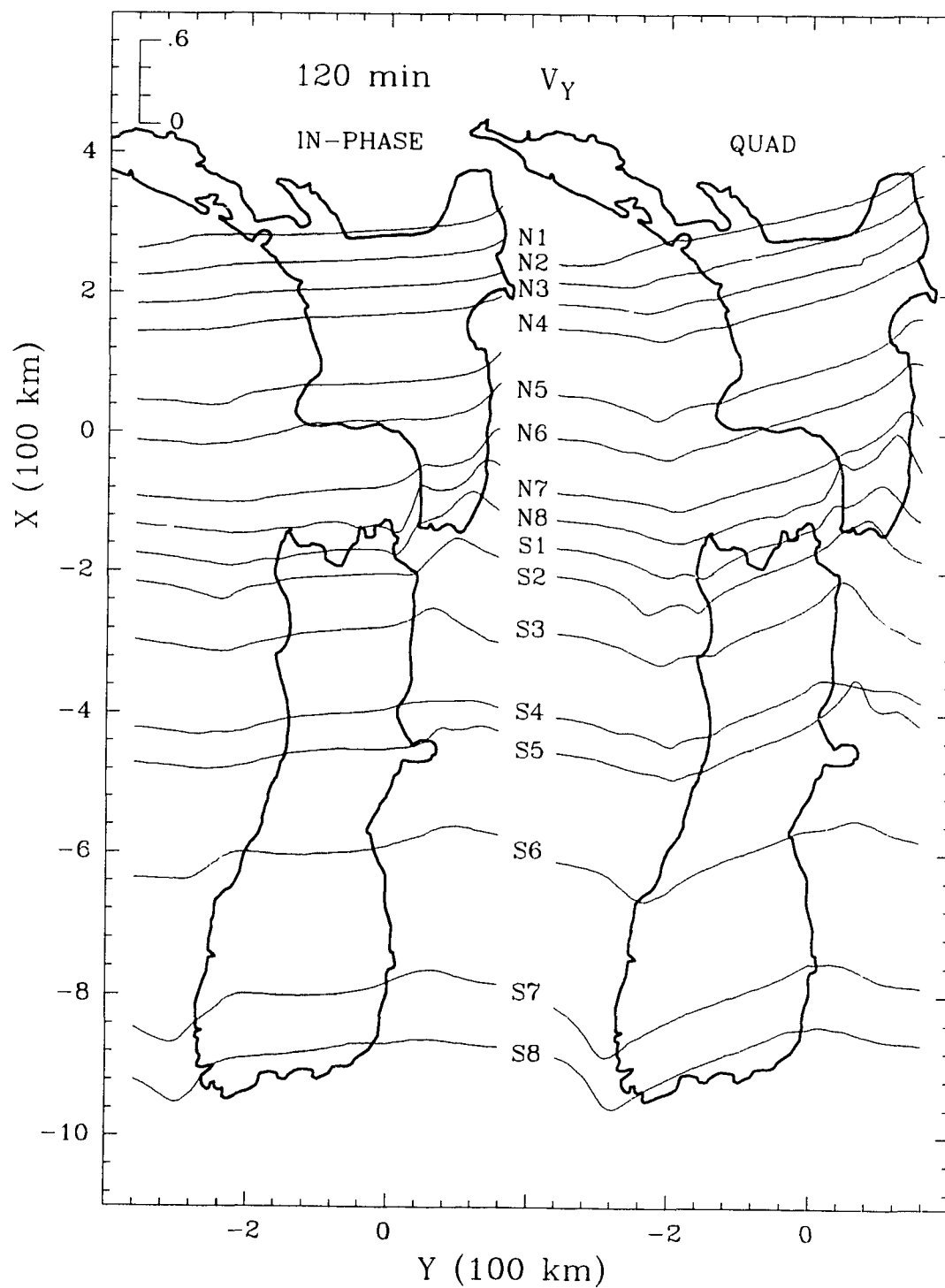


Figure E.14: The in-phase and quadrature V_y (y -component of the induction arrow V) response curves at 120 min for traverses over the model.

APPENDIX F
FIELD SITE (CHAMALAUN AND MCKNIGHT, 1993) INDUCTION
ARROW COMPONENTS AS A FUNCTION OF PERIOD AT 34
SITES

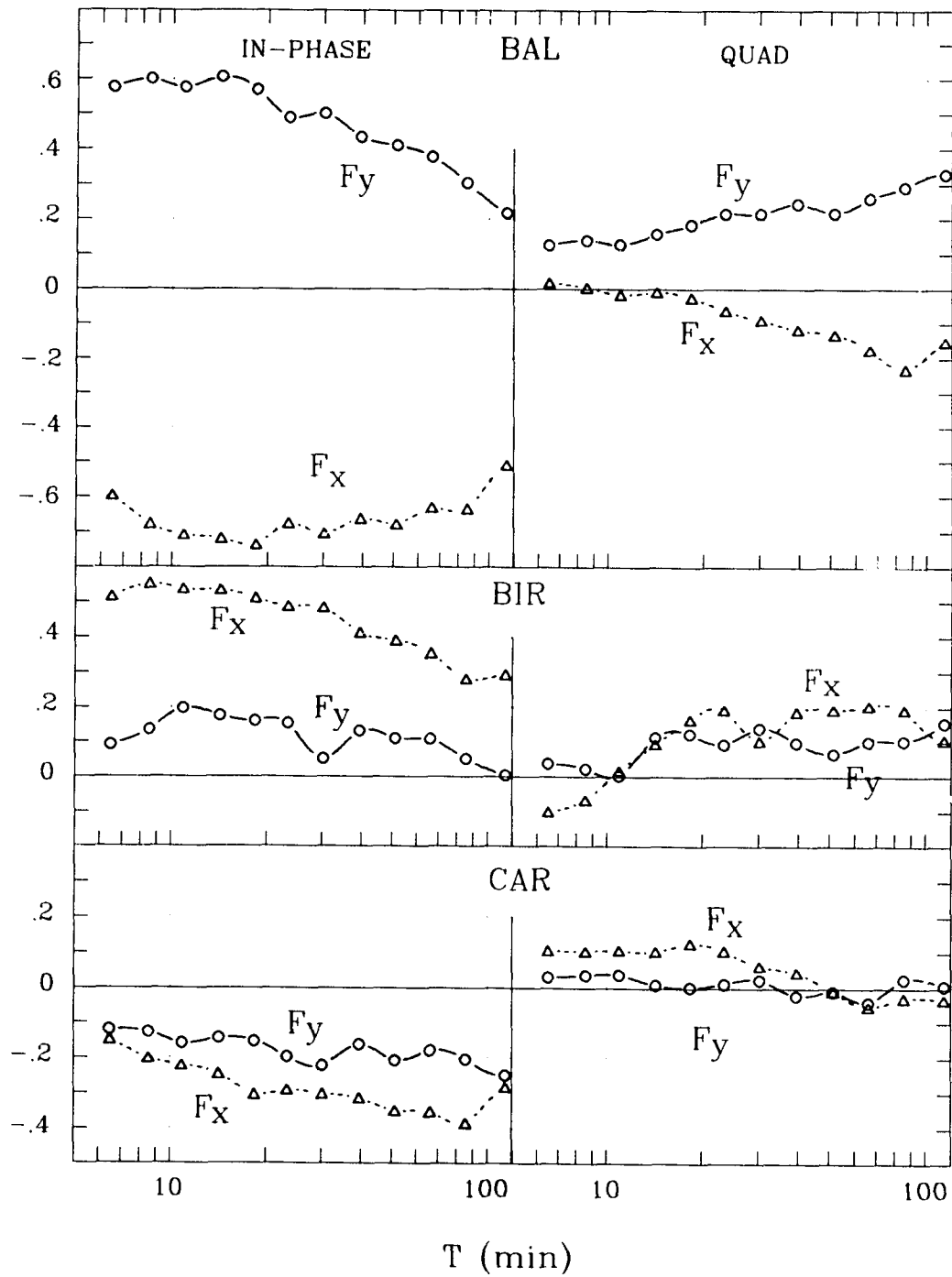


Figure F.1: The x- and y-components of the field site induction arrows as a function of period at BAL, BIR and CAR.

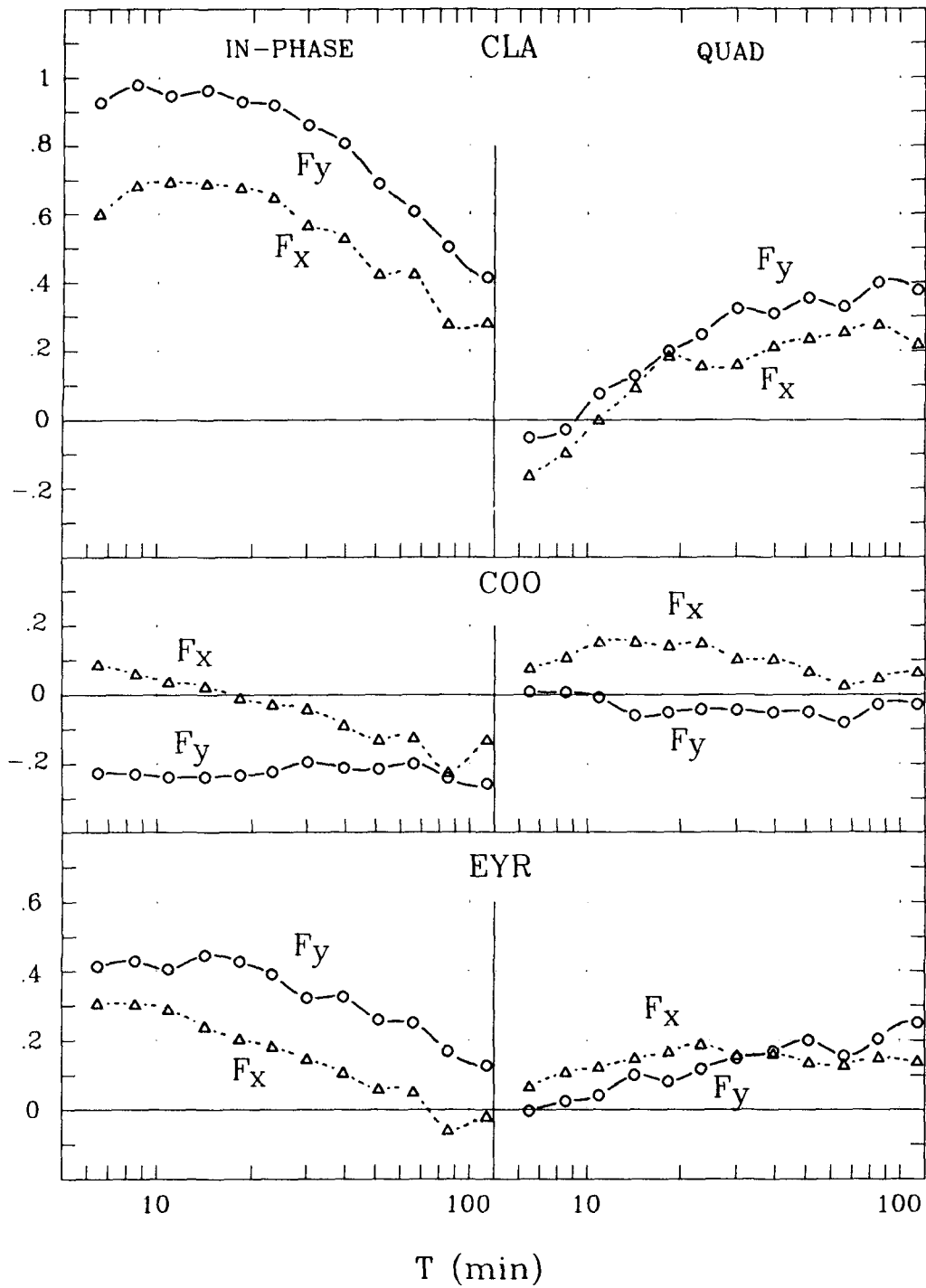


Figure F.2: The x- and y-components of the field site induction arrows as a function of period at CLA, COO and EYR.

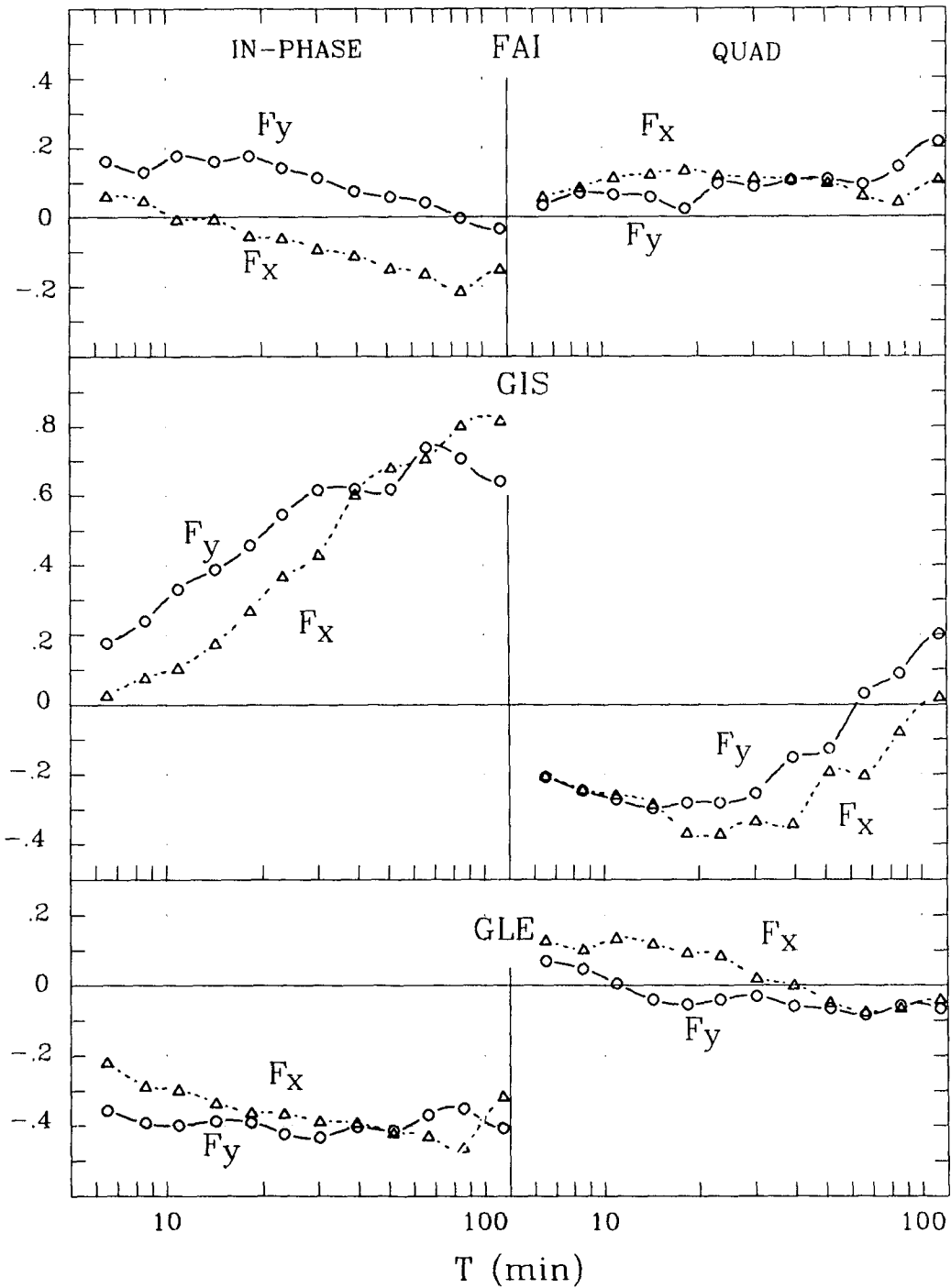


Figure F.3: The x- and y-components of the field site induction arrows as a function of period at FAI, GIS and GLE.

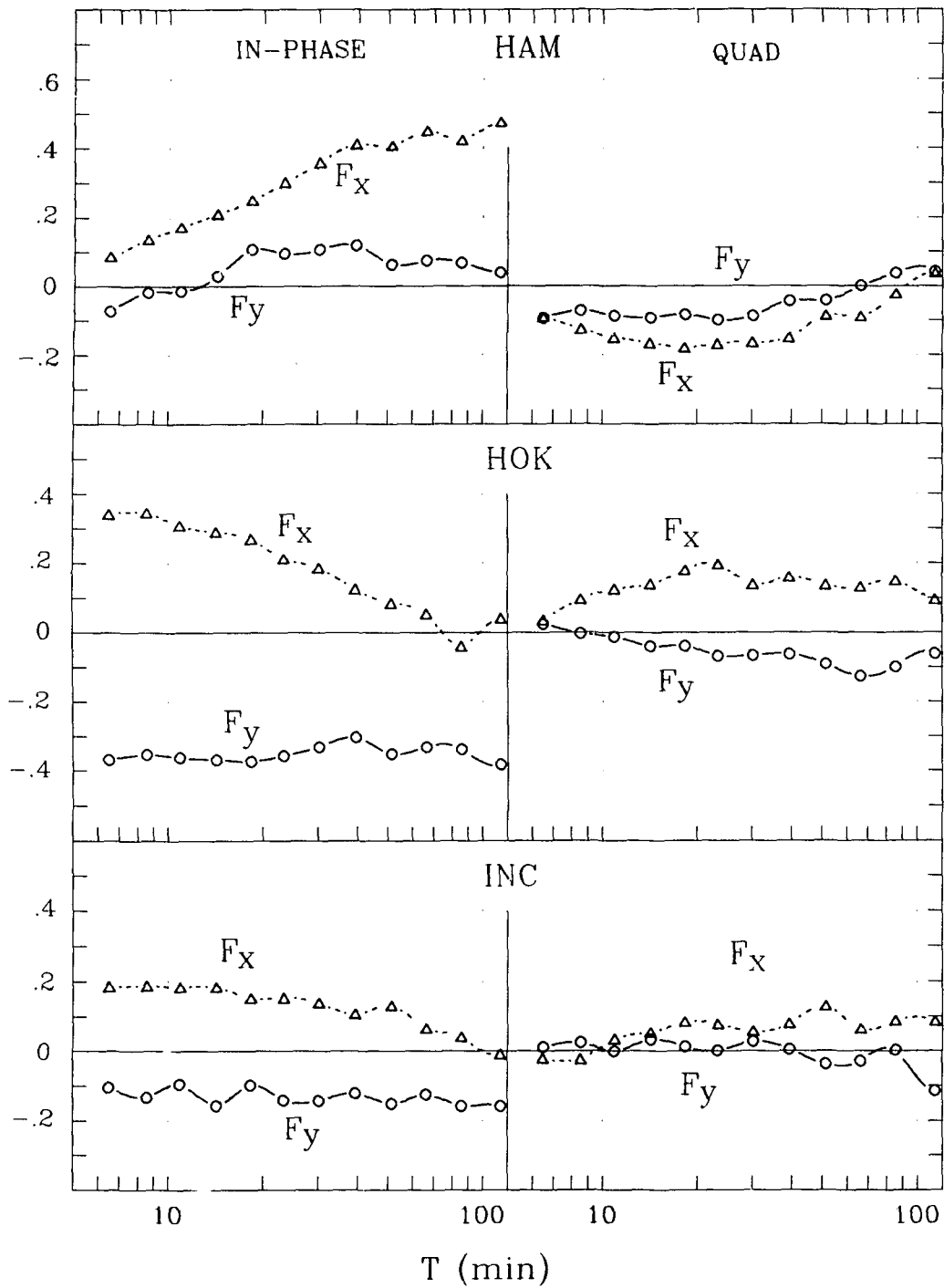


Figure F.4: The x- and y-components of the field site induction arrows as a function of period at HAM, HOK and INC.

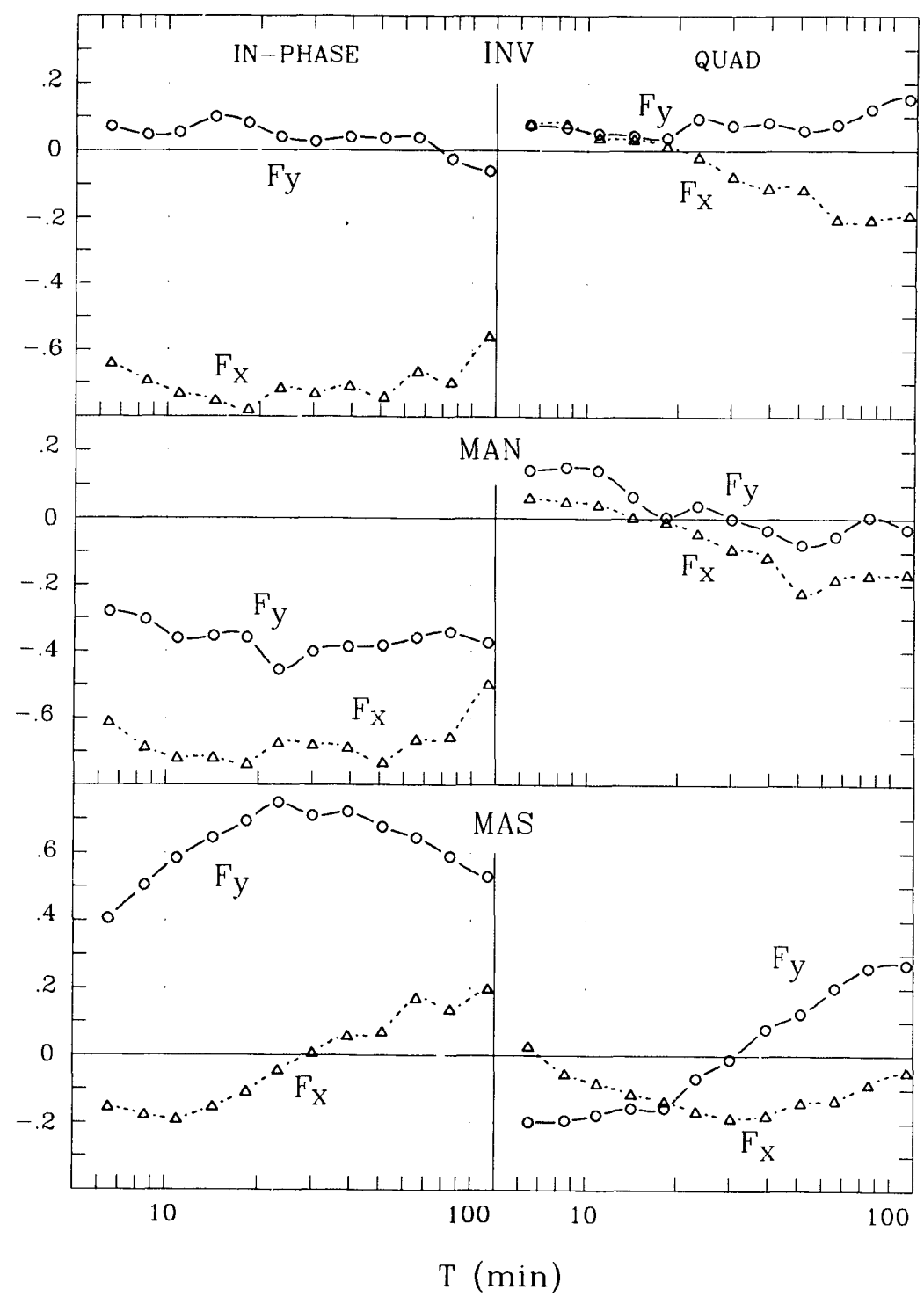


Figure F.5: The x- and y-components of the field site induction arrows as a function of period at INV, MAN and MAS.

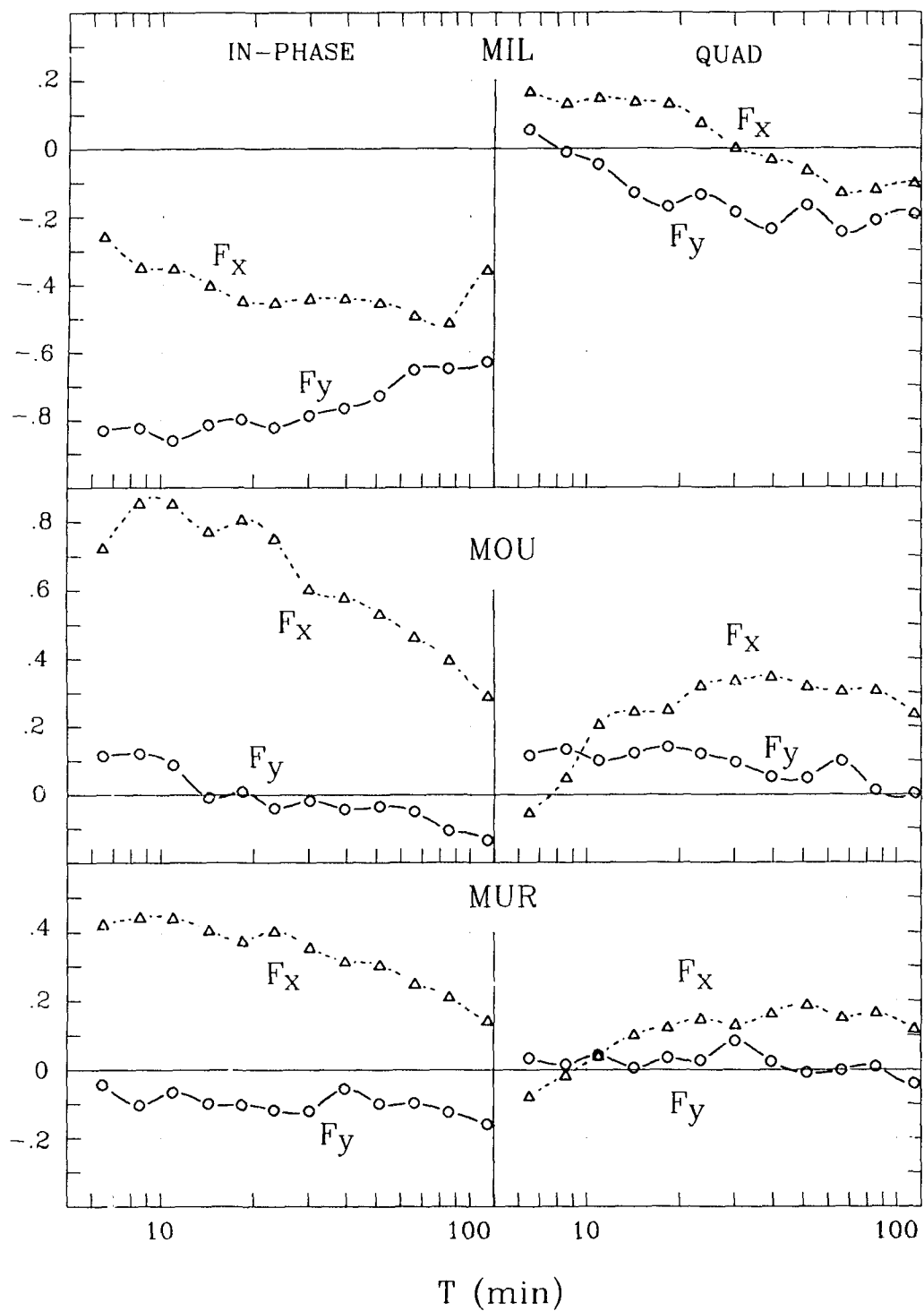


Figure F.6: The x- and y-components of the field site induction arrows as a function of period at MIL, MOU and MUR.

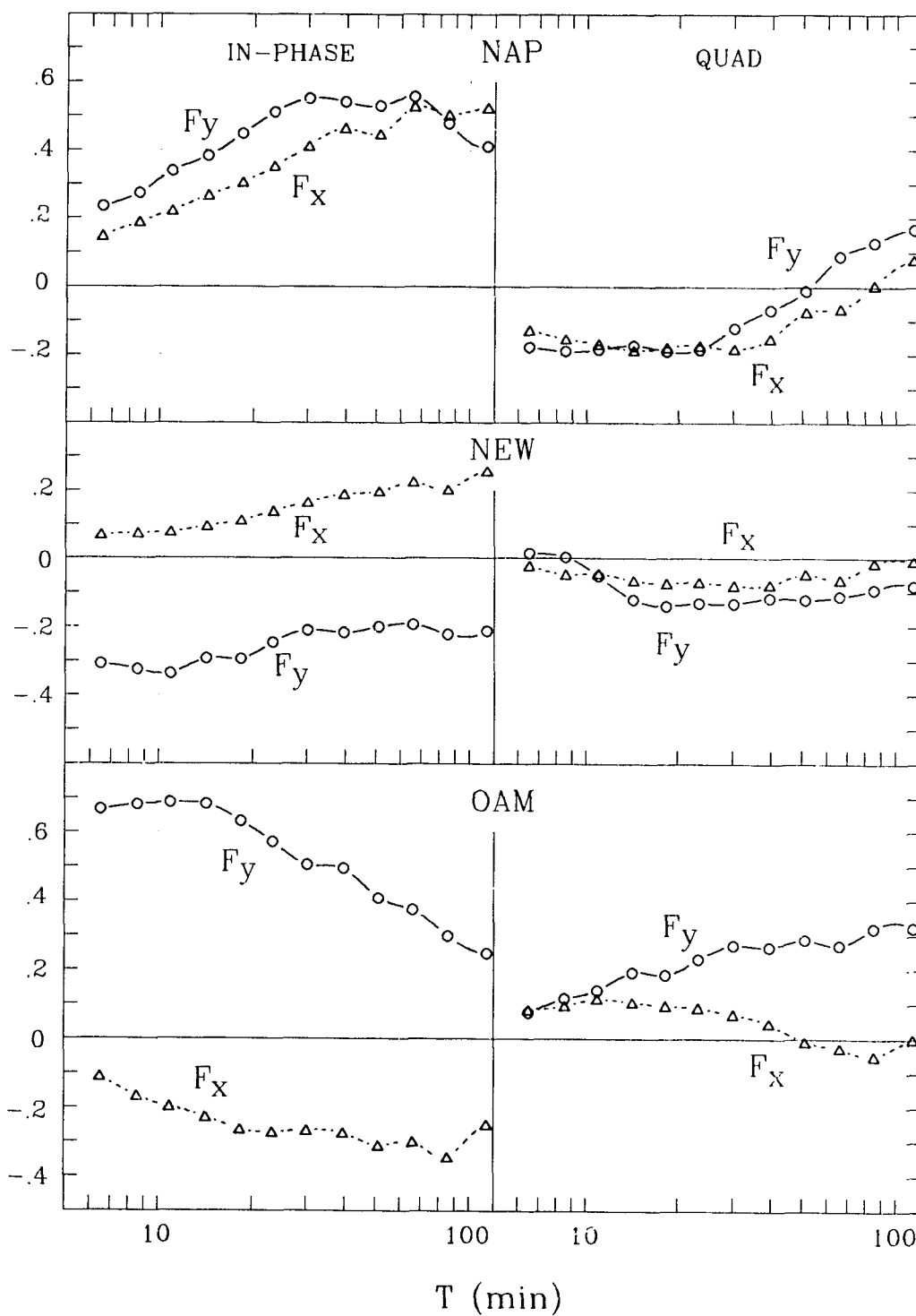


Figure F.7: The x- and y-components of the field site induction arrows as a function of period at NAP, NEW and OAM.

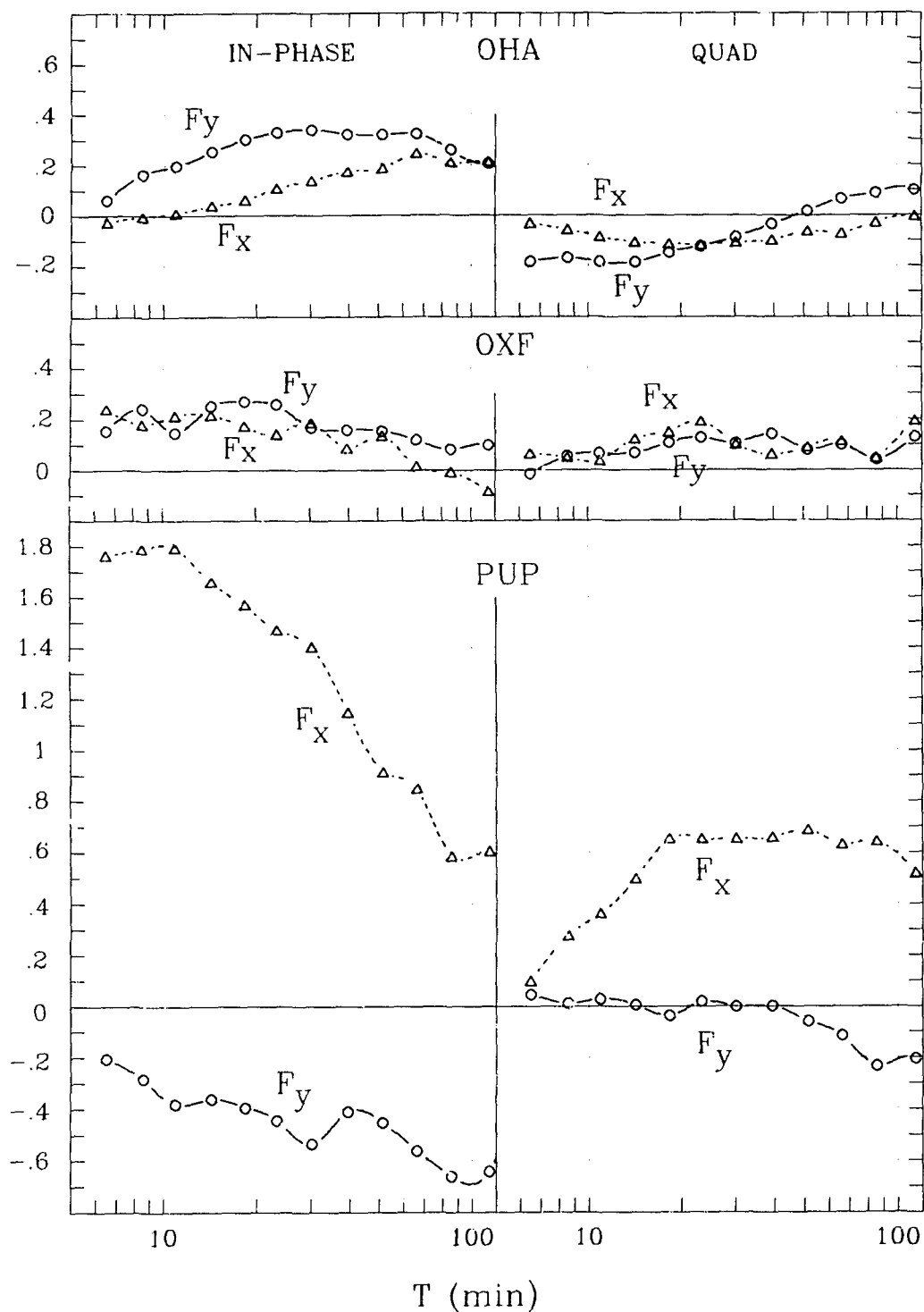


Figure F.8: The x- and y-components of the field site induction arrows as a function of period at OHA, OXF and PUP.

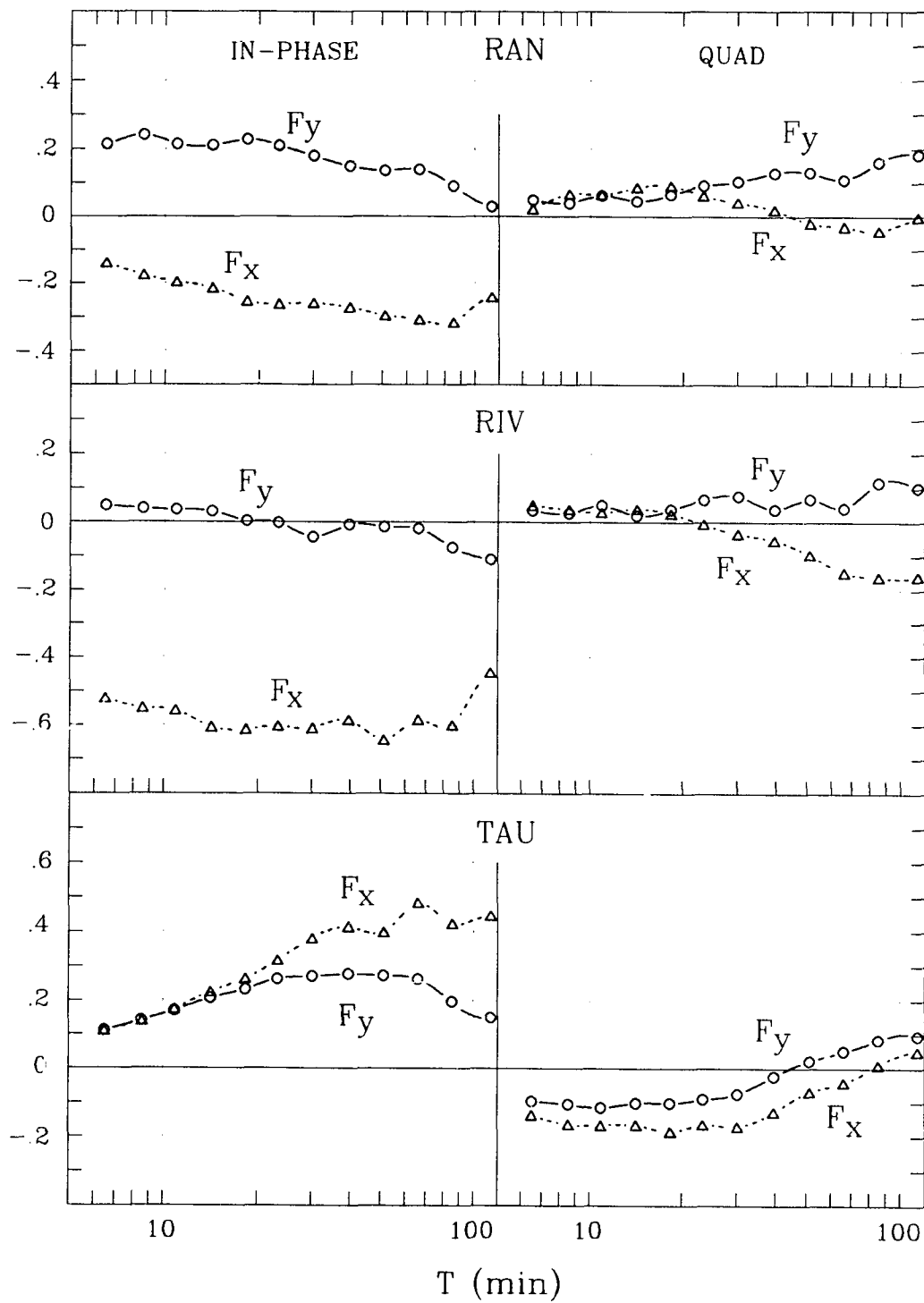


Figure F.9: The x- and y-components of the field site induction arrows as a function of period at RAN, RIV and TAU.

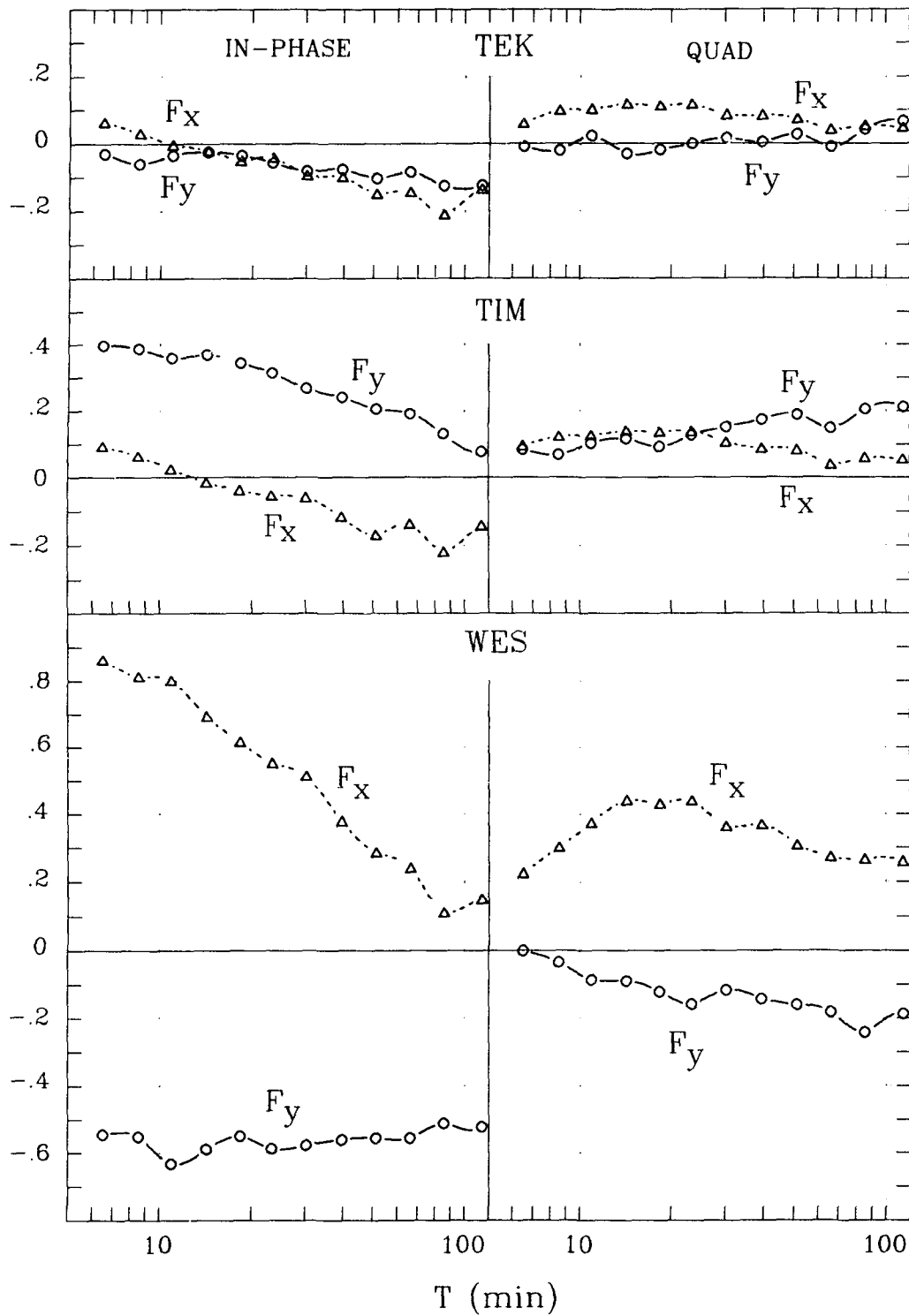


Figure F.10: The x- and y-components of the field site induction arrows as a function of period at TEK, TIM and WES.

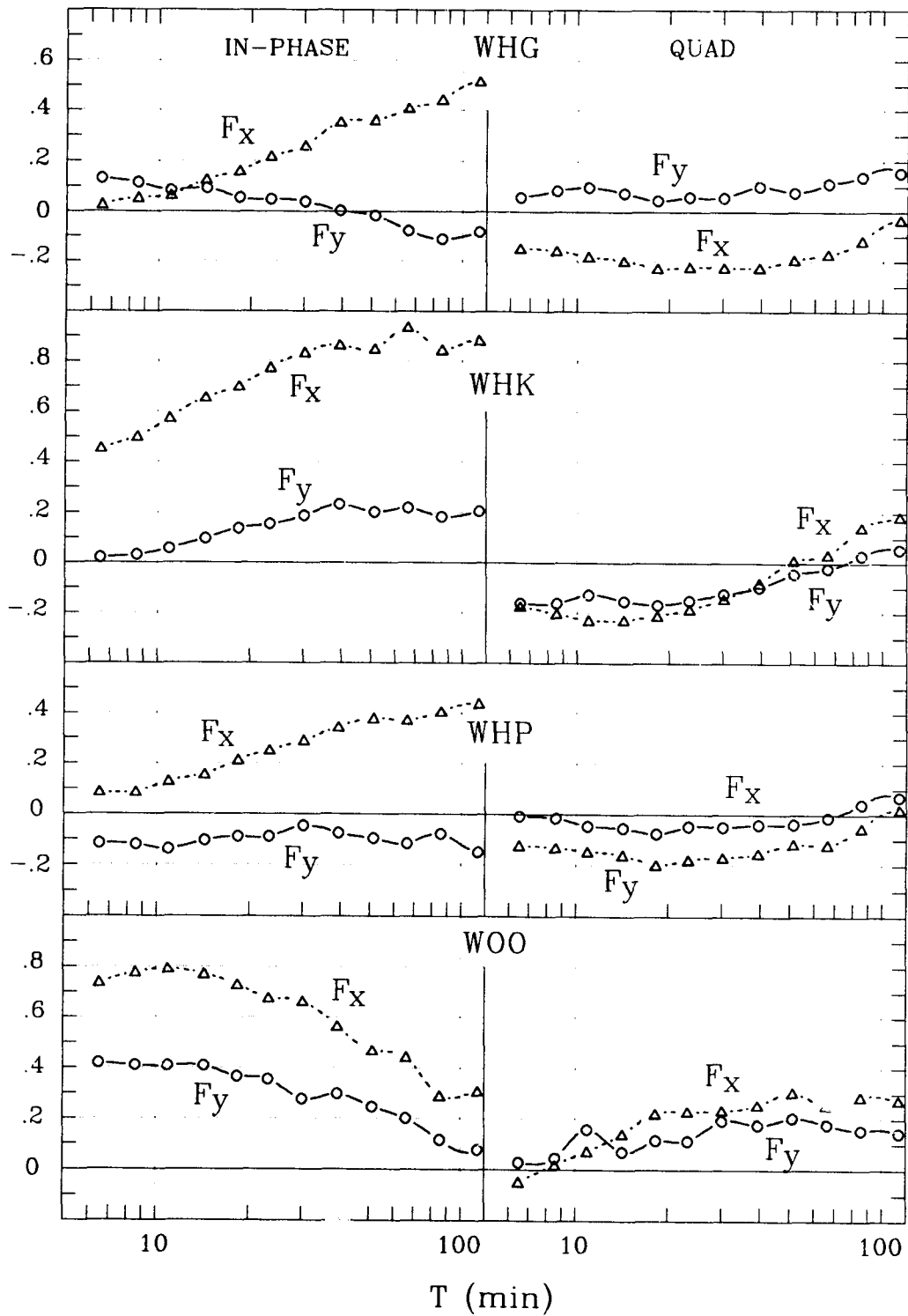


Figure F.11: The x- and y-components of the field site induction arrows as a function of period at WHG, WHK, WHP and WOO.

APPENDIX G
ANALOGUE MODEL INDUCTION ARROW COMPONENTS AS A
FUNCTION OF PERIOD AT 34 SITES.

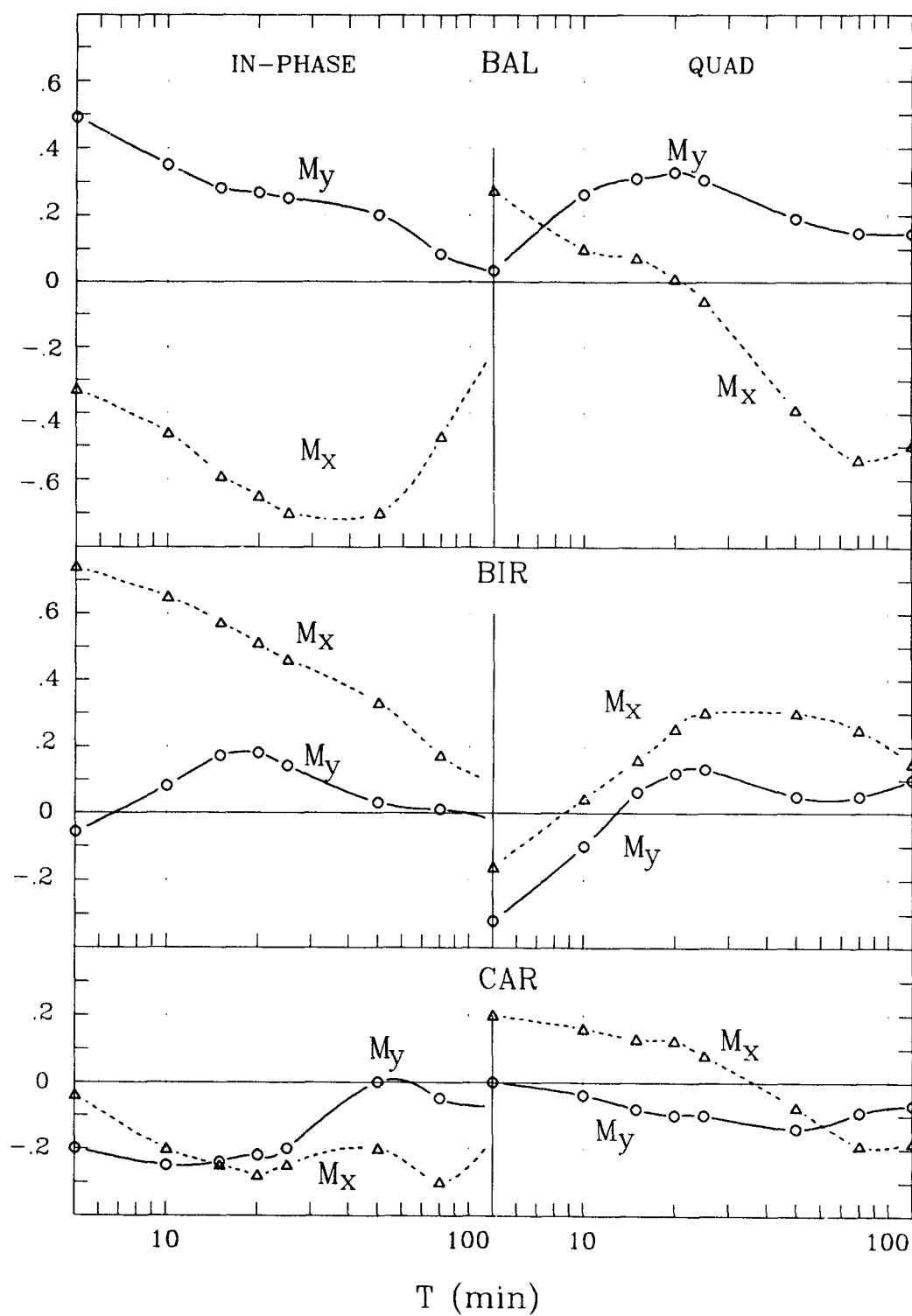


Figure G.1: The x- and y-components of the analogue model induction arrows as a function of period at sites BAL, BIR and CAR.

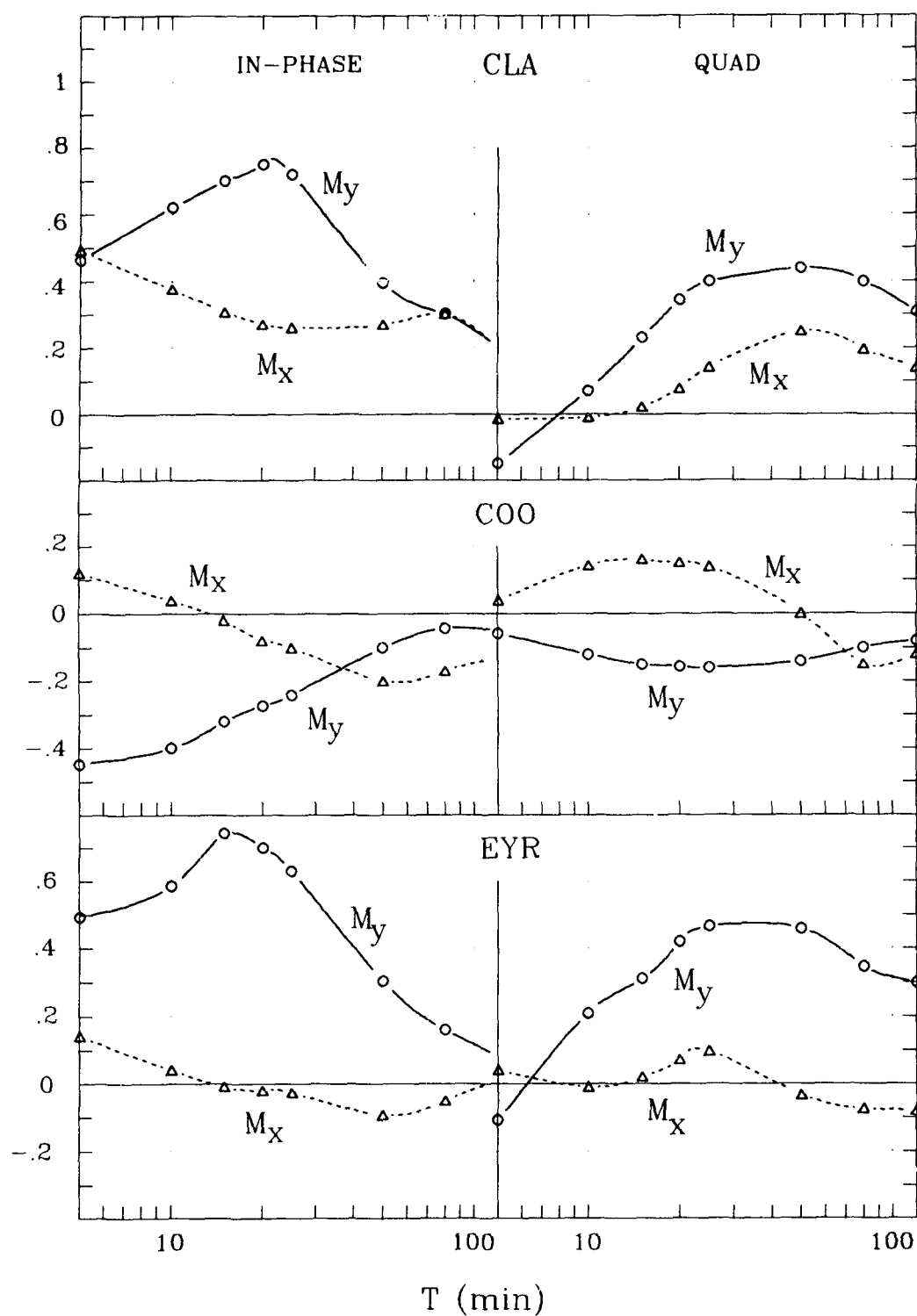


Figure G.2: The x- and y-components of the analogue model induction arrows as a function of period at sites CLA, CJO and EYR.

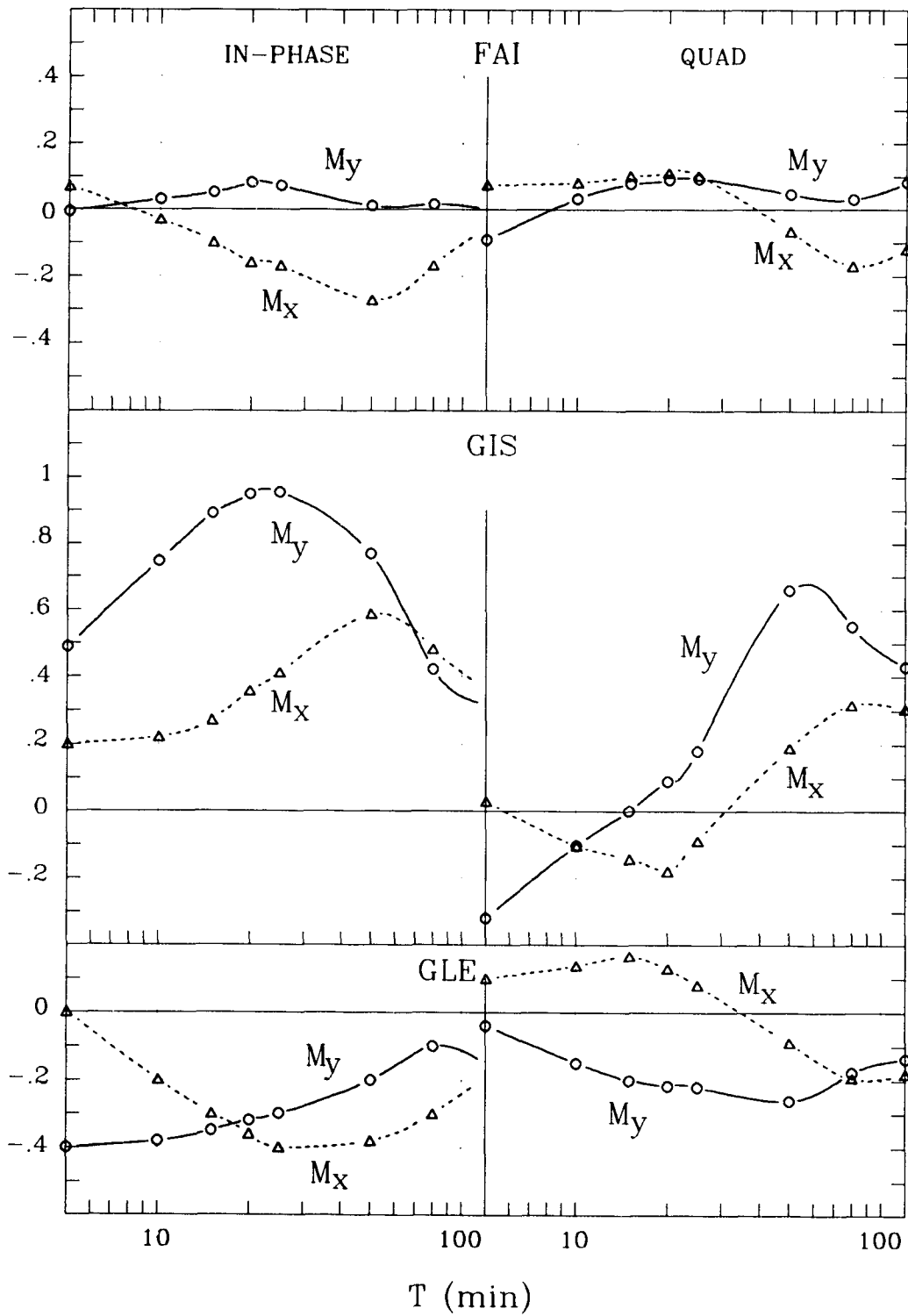


Figure G.3: The x- and y-components of the analogue model induction arrows as a function of period at sites FAI, GIS and GLE.

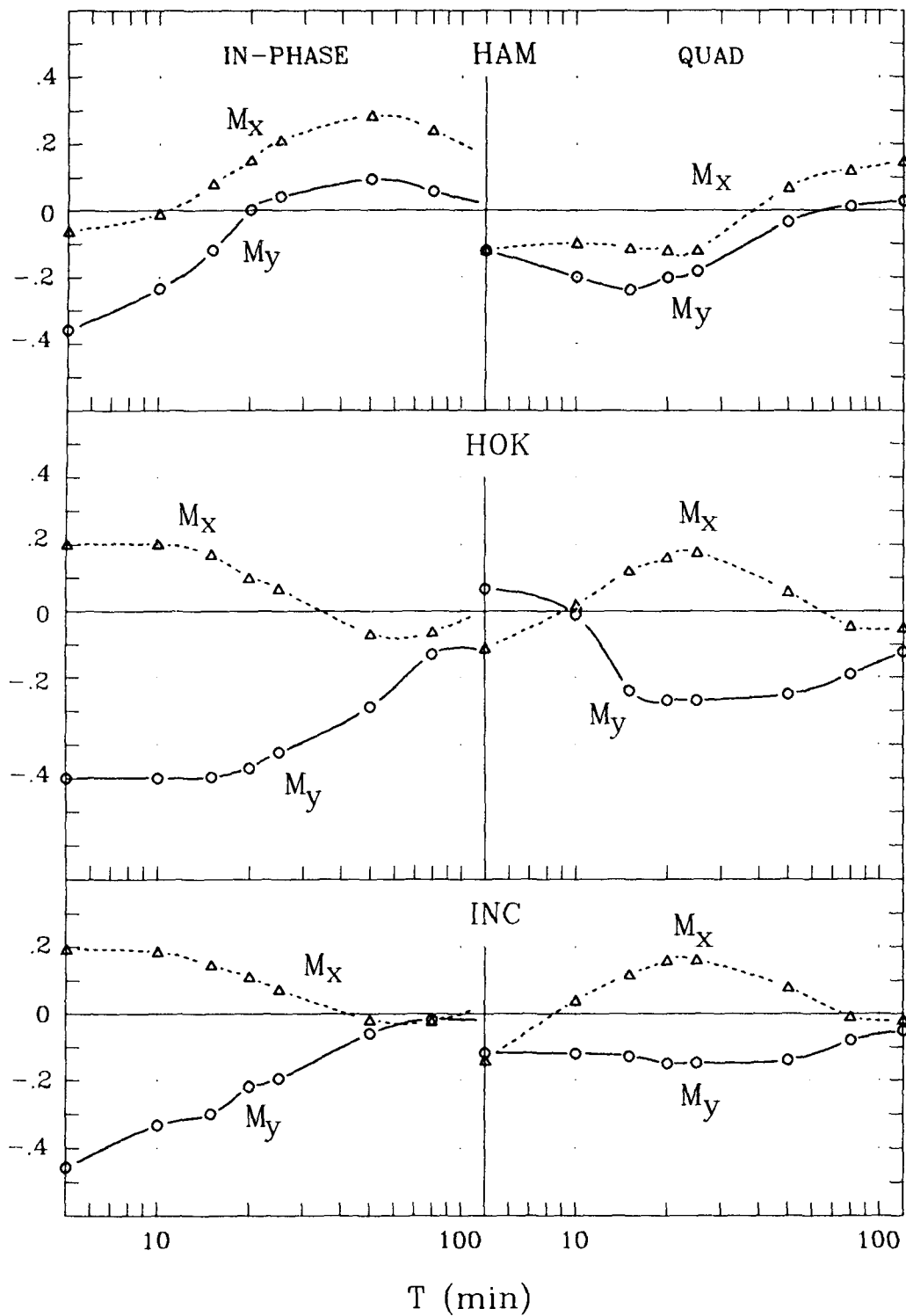


Figure G.4: The x- and y-components of the analogue model induction arrows as a function of period at sites HAM, HOK and INC.

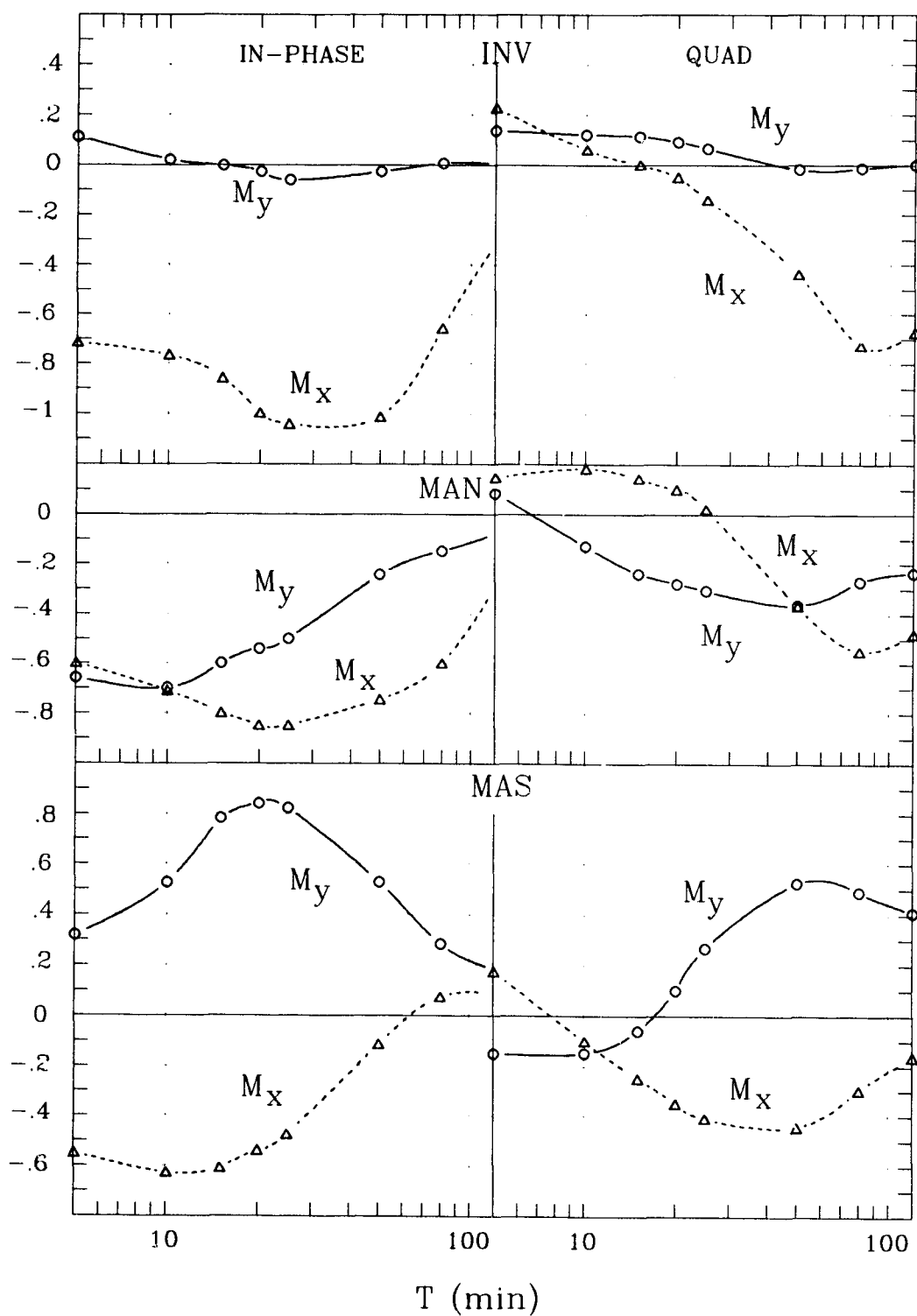


Figure G.5: The x- and y-components of the analogue model induction arrows as a function of period at sites INV, MAN and MAS.

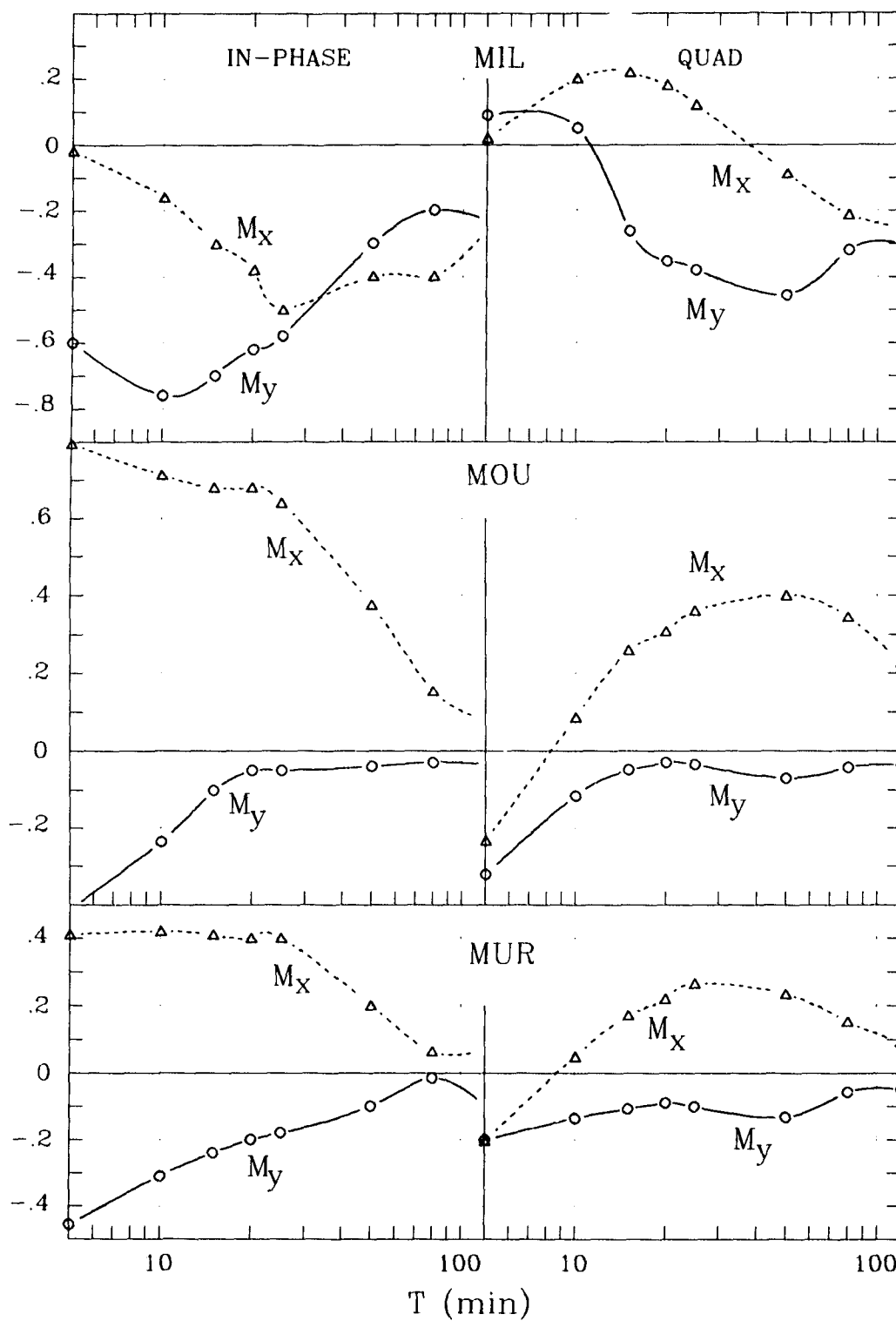


Figure G.6: The x- and y-components of the analogue model induction arrows as a function of period at sites MIL, MOU and MUR.

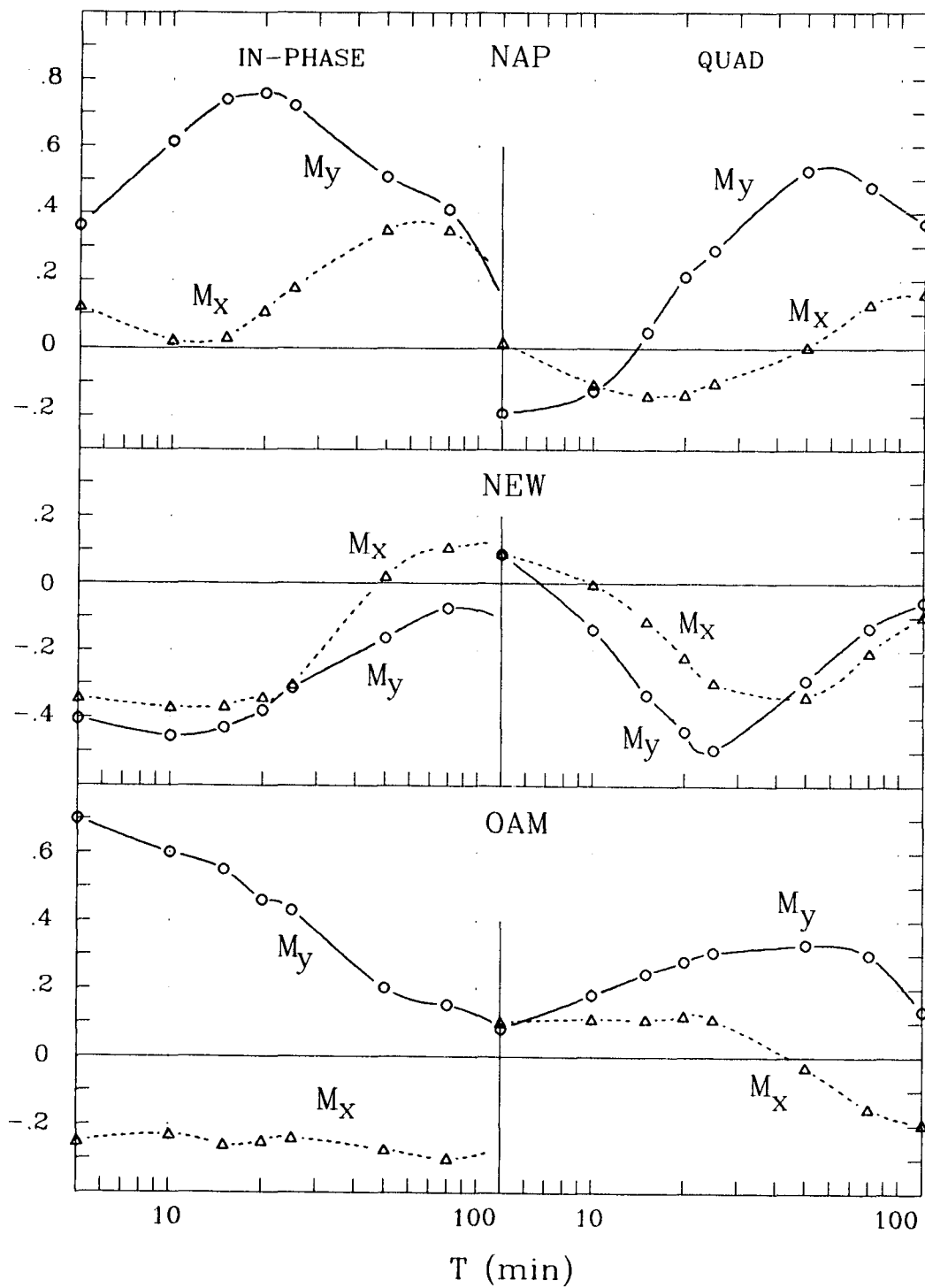


Figure G.7: The x- and y-components of the analogue model induction arrows as a function of period at sites NAP, NEW and OAM.

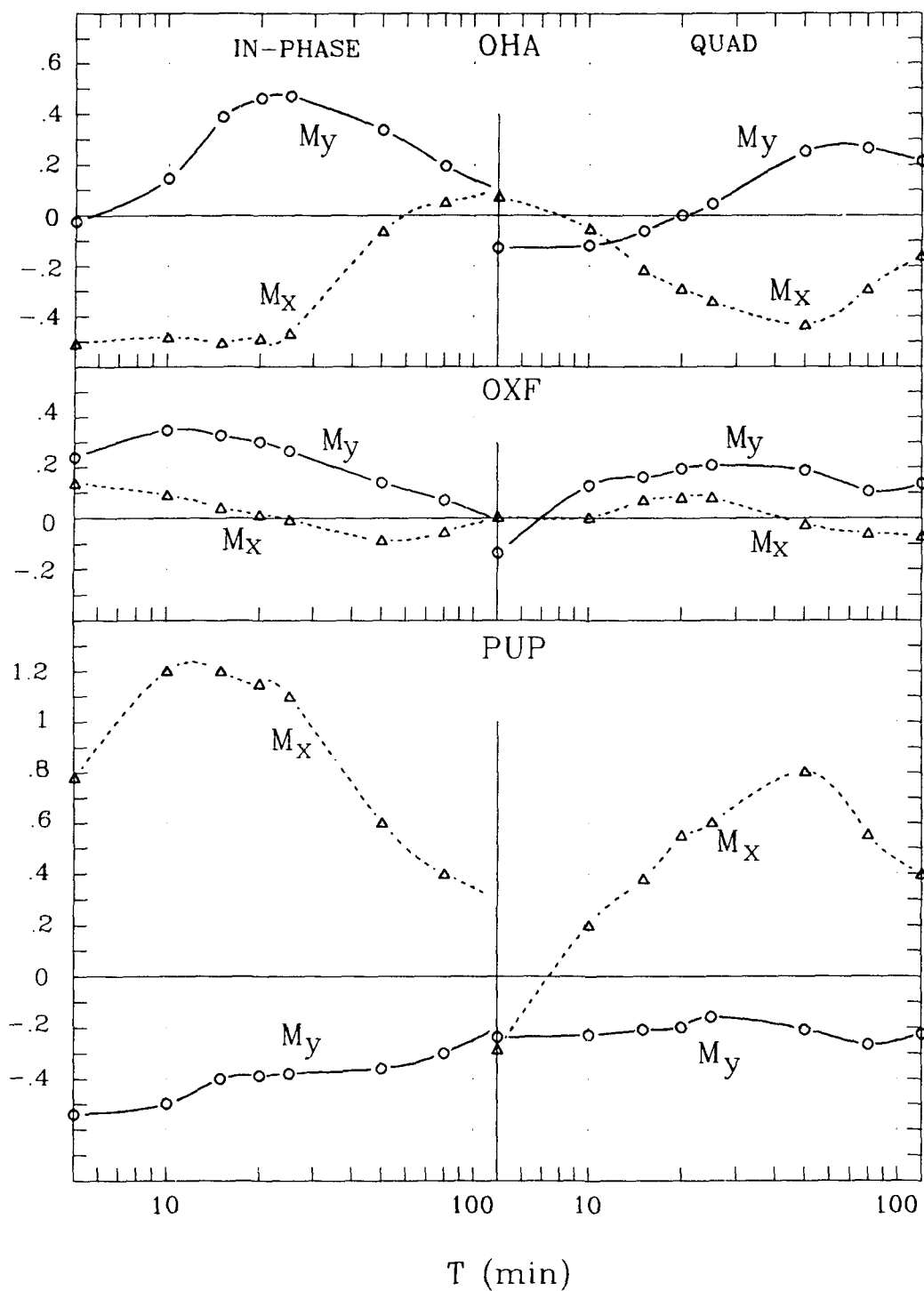


Figure G.8: The x- and y-components of the analogue model induction arrows as a function of period at sites OHA, OXF and PUP.

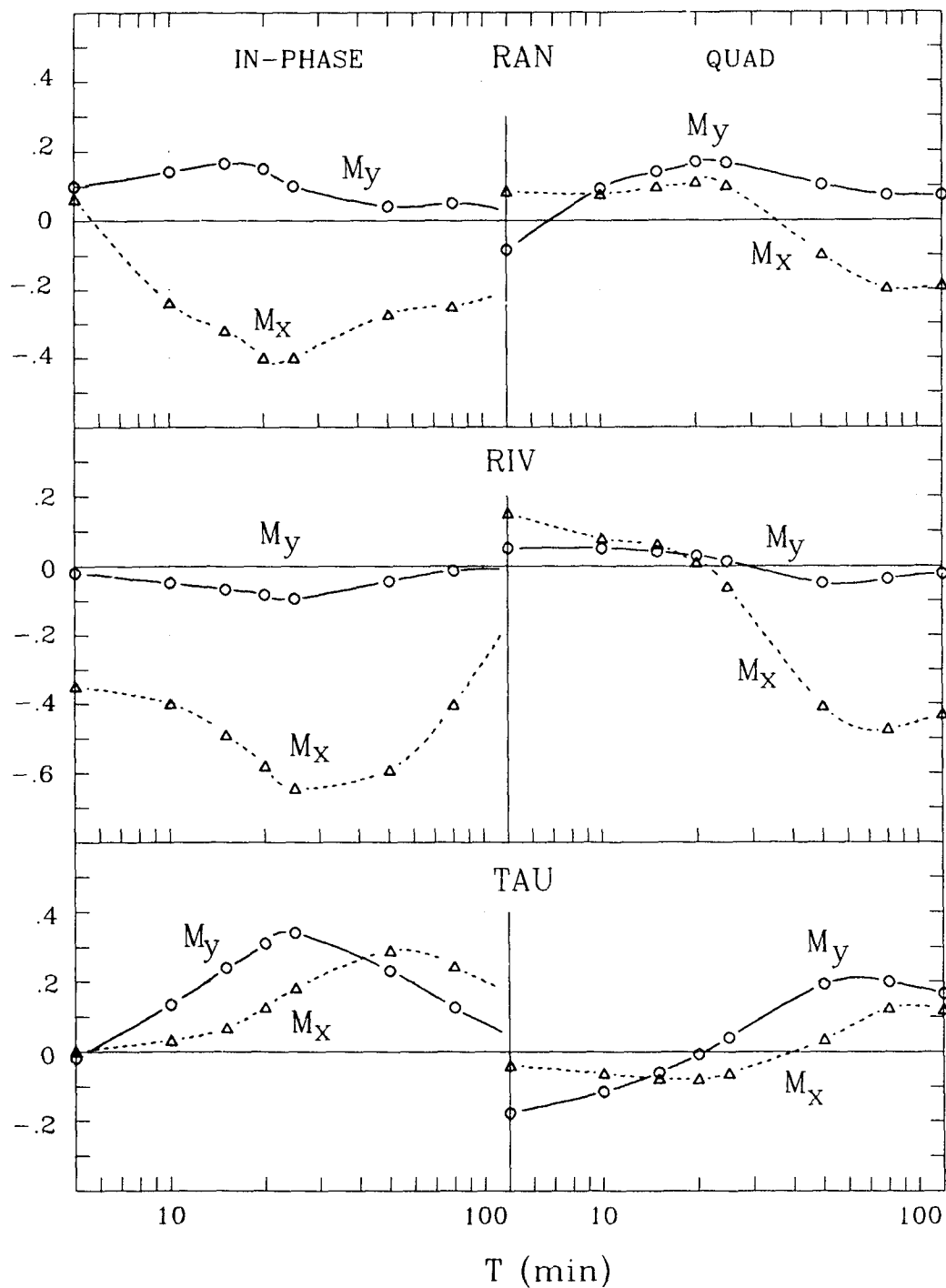


Figure G.9: The x- and y-components of the analogue model induction arrows as a function of period at sites RAN, RIV and TAU.

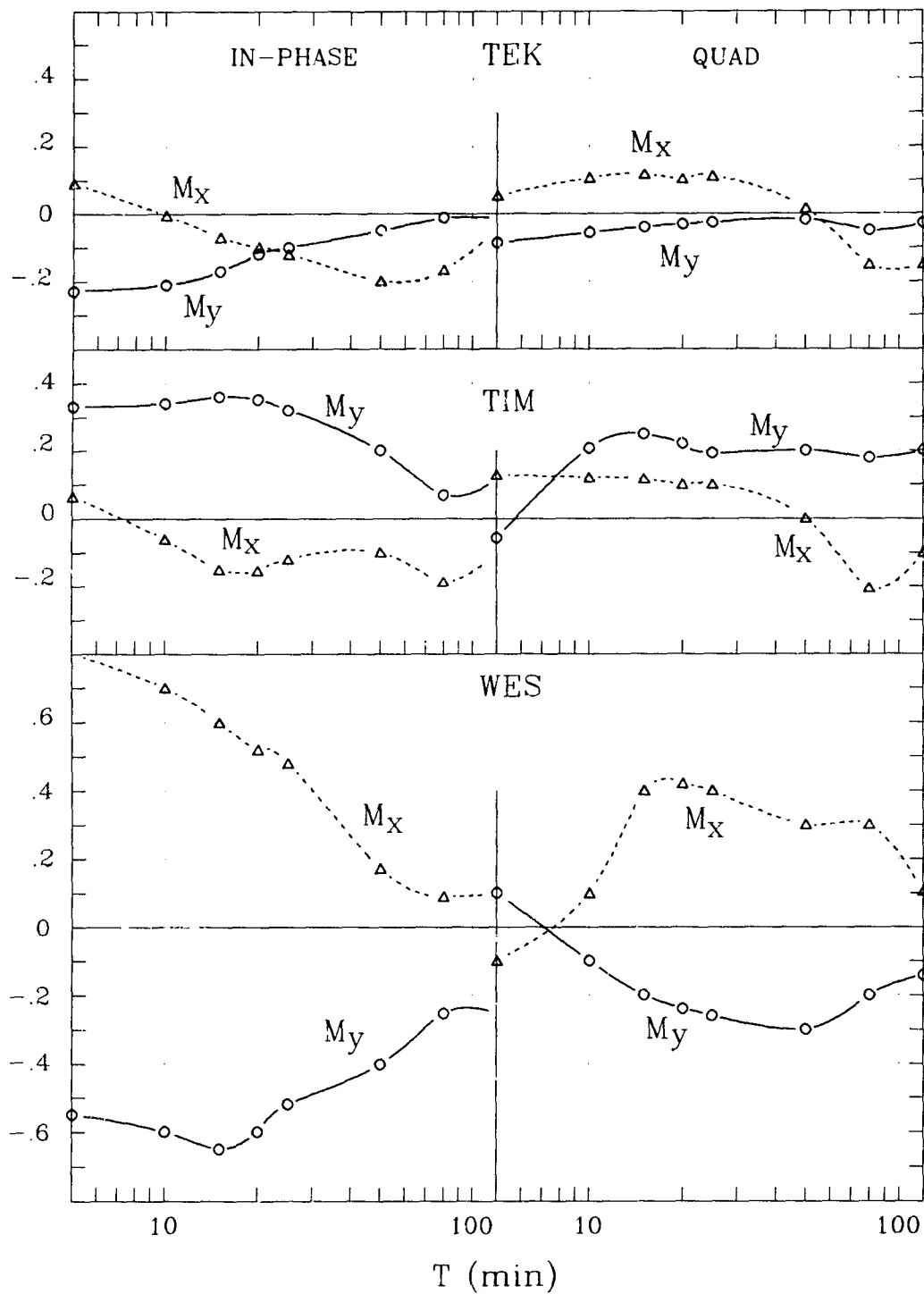


Figure G.10: The x- and y-components of the analogue model arrows as a function of period at sites TEK, TIM and WES.

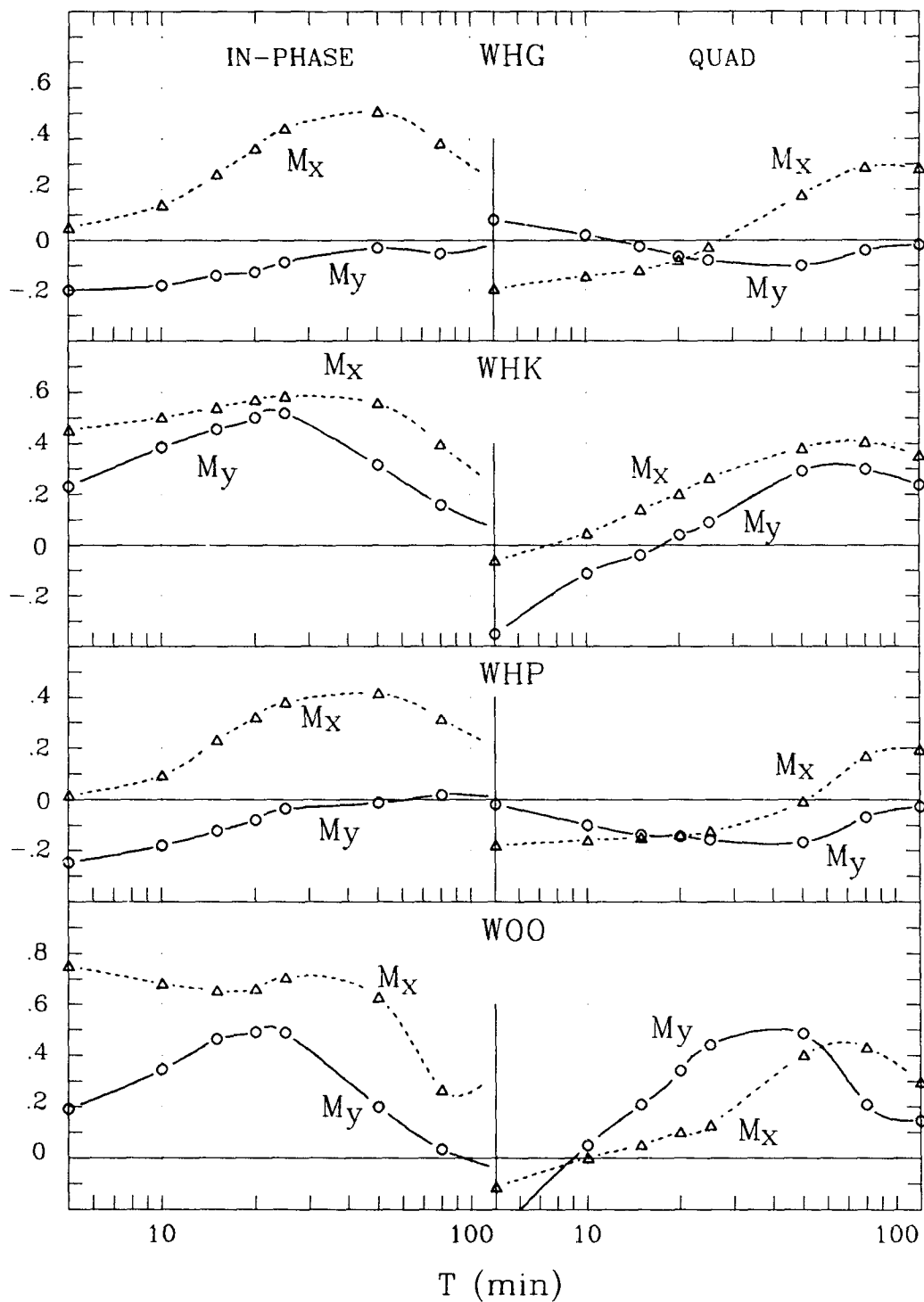


Figure G.11: The x- and y-components of the analogue model induction arrows as a function of period at sites WHG, WHK, WHP and W00.

APPENDIX H
DIFFERENCE INDUCTION ARROW COMPONENTS (DX AND
DY) AS A FUNCTION OF PERIOD AT THE 34 SITES OF
CHAMALAUN AND MCKNIGHT, 1993

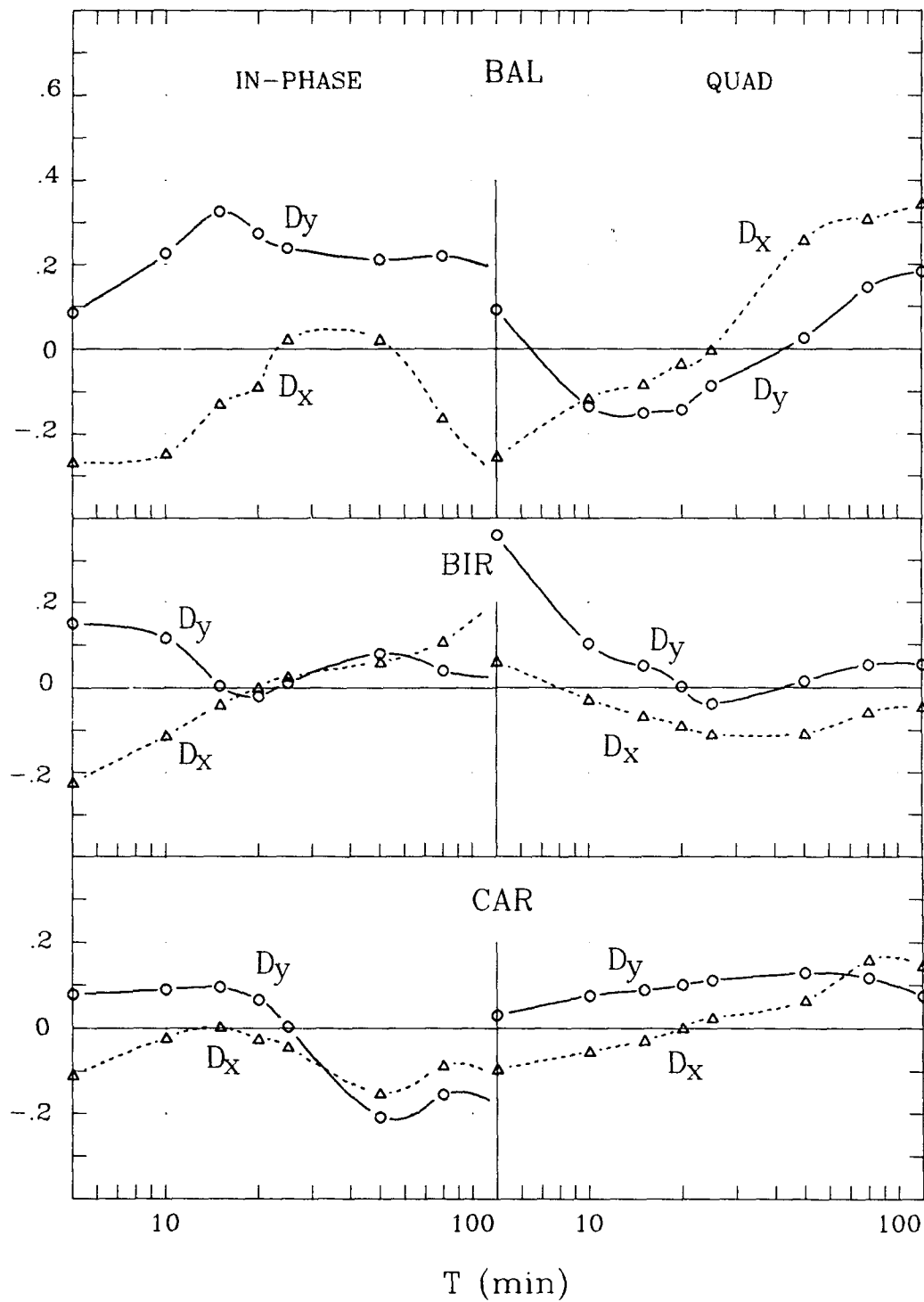


Figure H.1: The x- and y-components of the difference induction arrows as a function of period at sites BAL, BIR and CAR.

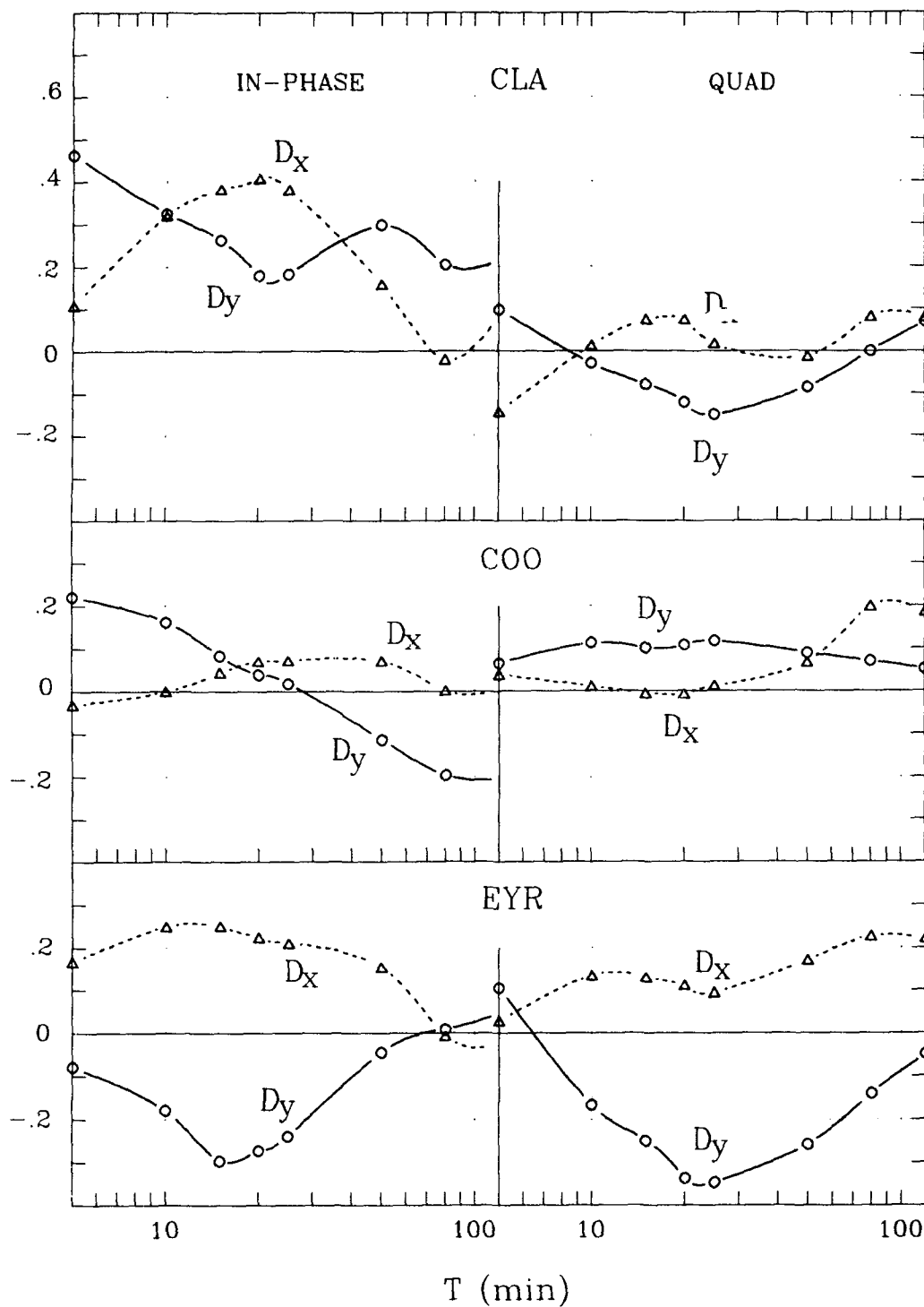


Figure H.2: The x- and y-components of the difference induction arrows as a function of period at sites CLA, COO, EYR.

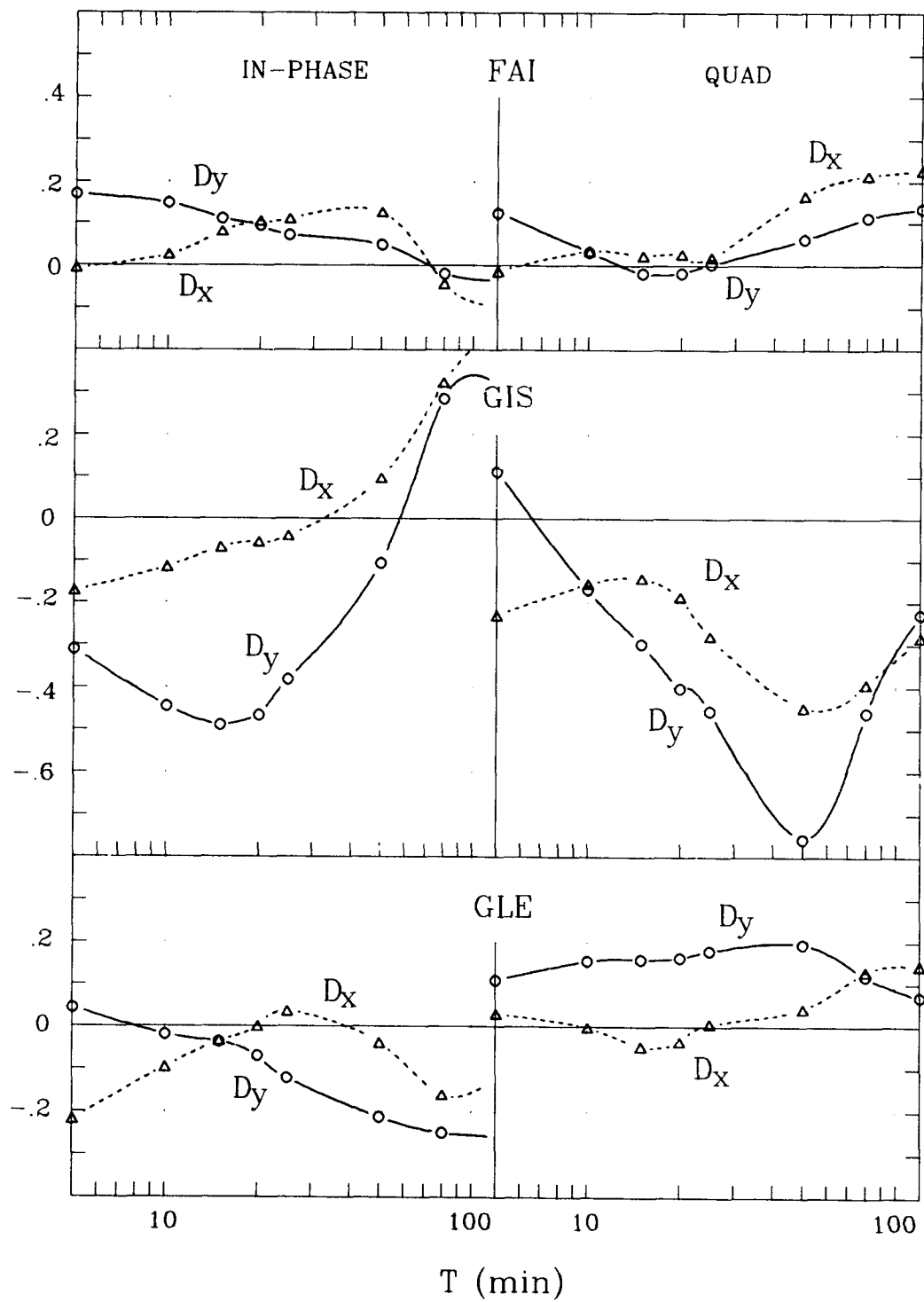


Figure H.3: The x- and y-components of the difference induction arrows as a function of period at sites FAI, GIS and GLE.

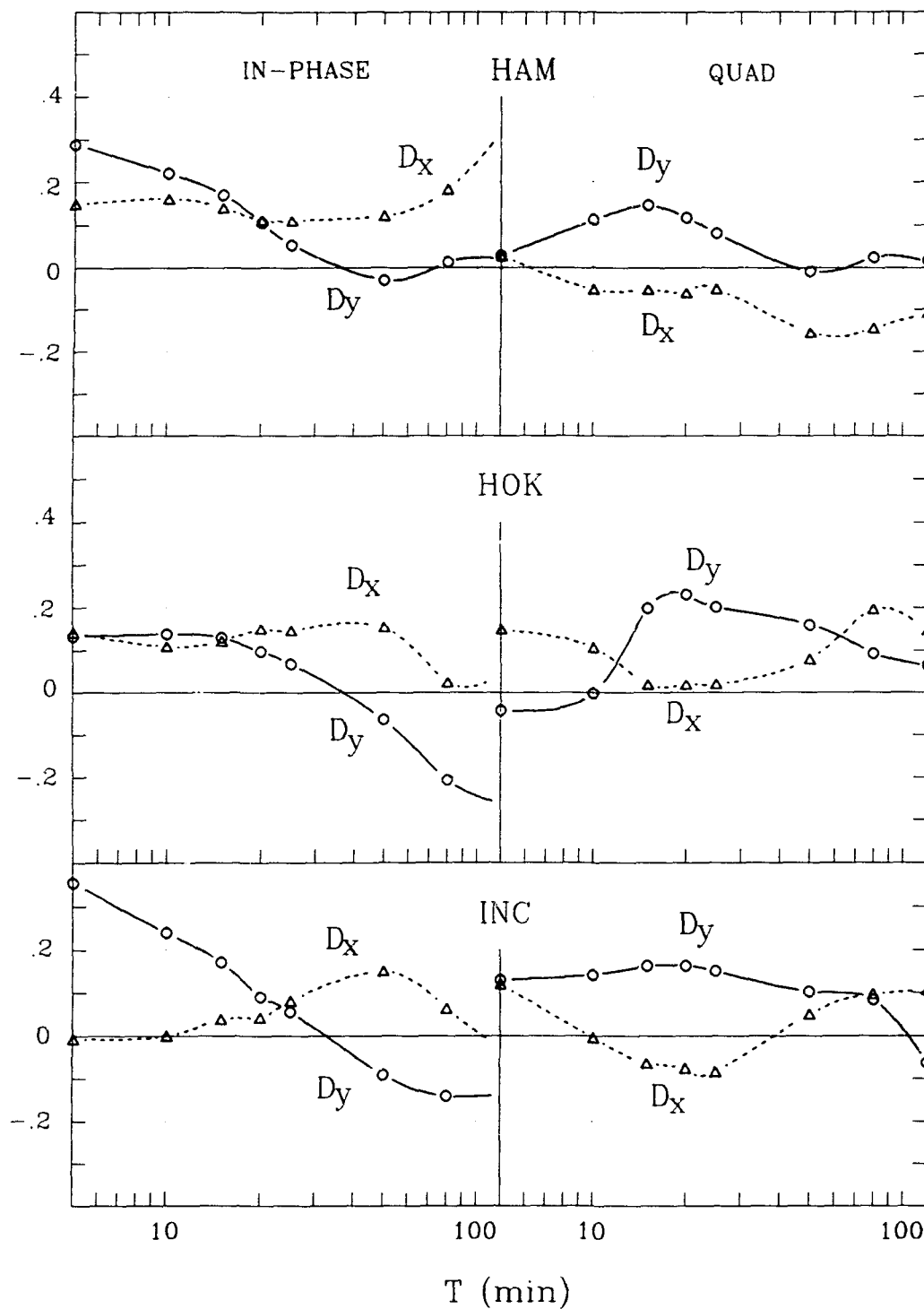


Figure H.4 The x- and y-components of the difference induction arrows as a function of period at sites HAM, HOK and INC.

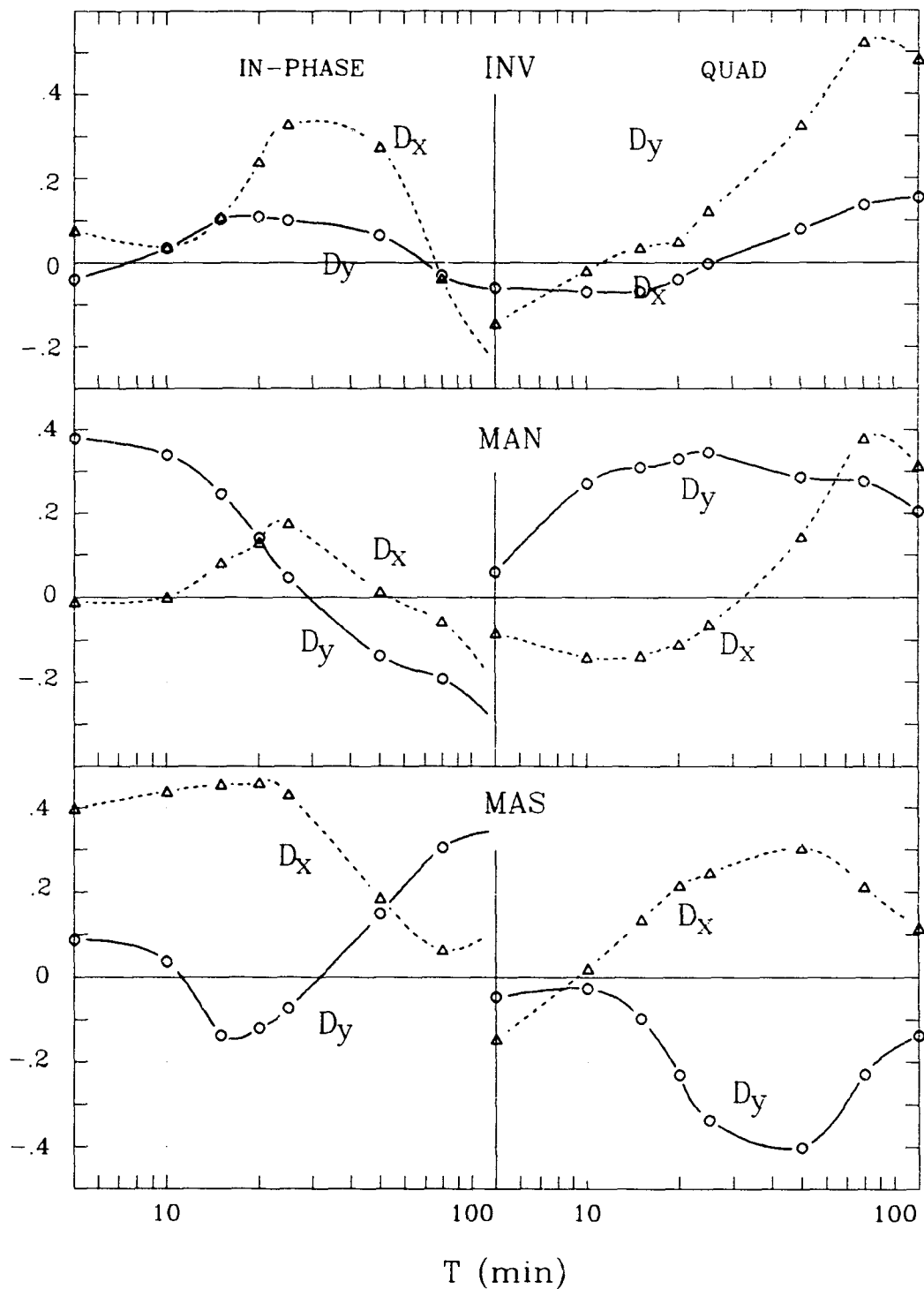


Figure H.5: The x- and y-components of the difference induction arrows as a function of period at sites INV, MAN and MAS.

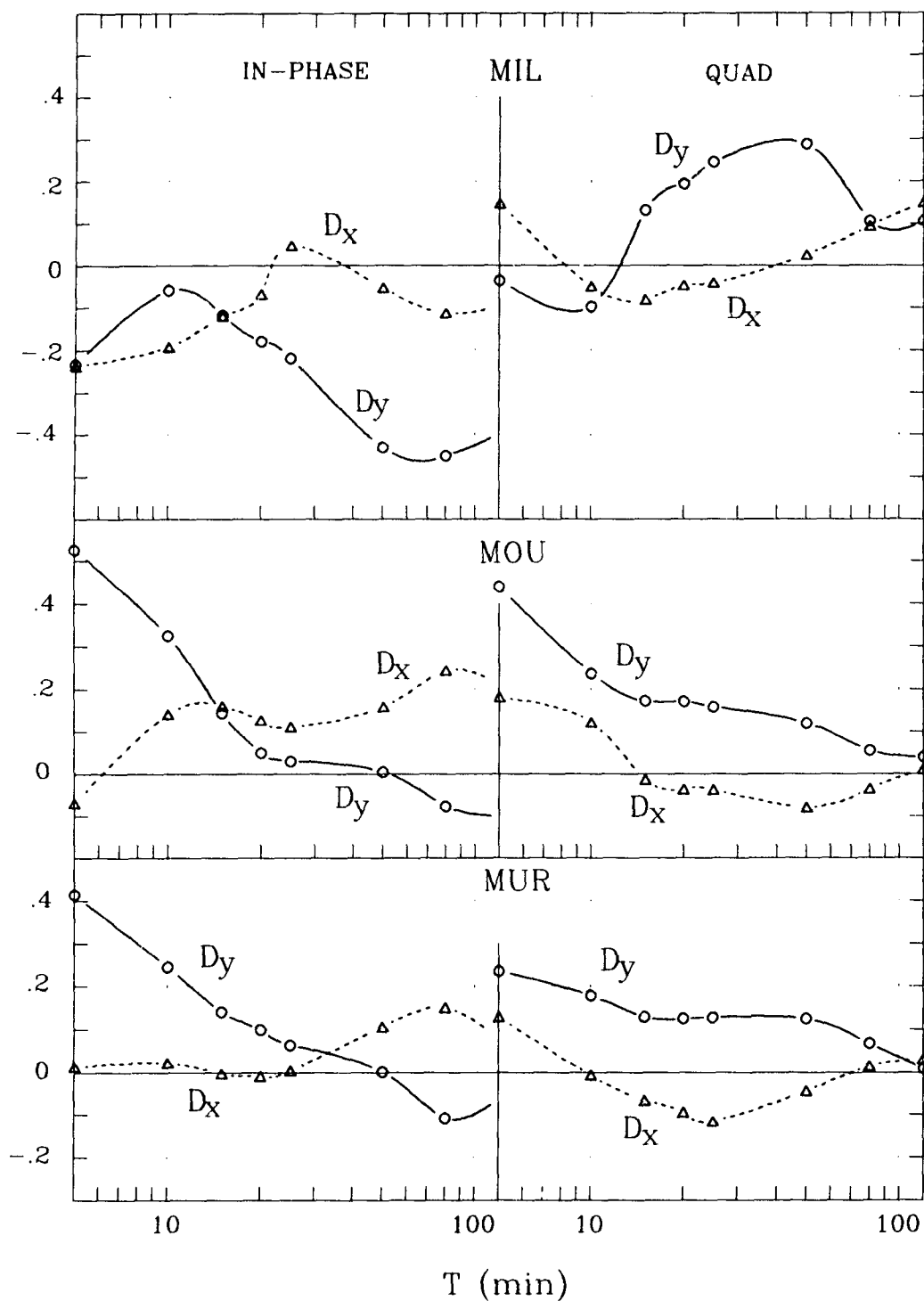


Figure H.6: The x- and y-components of the difference induction arrows as a function of period at sites MIL, MOU and MUR.

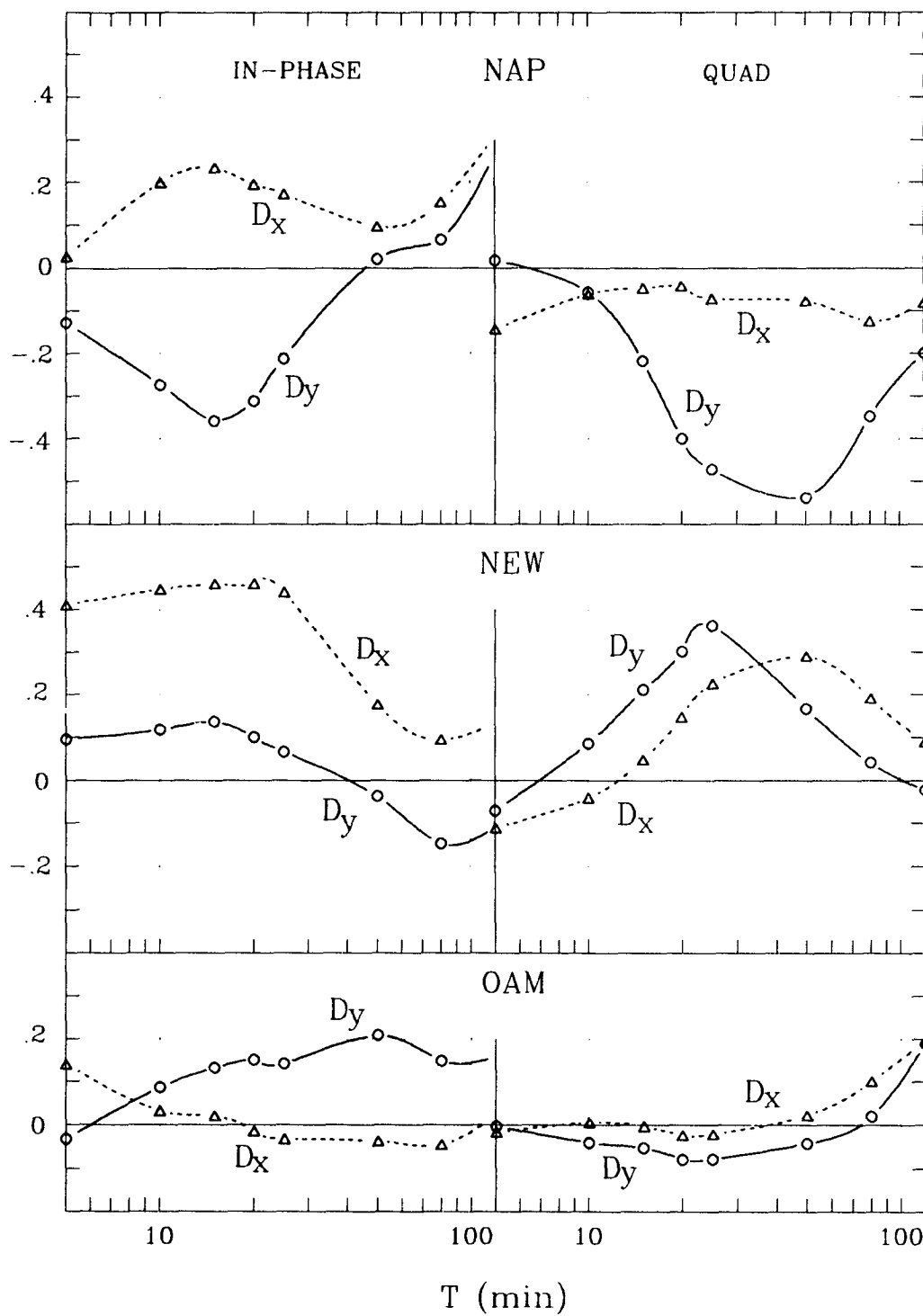


Figure H.7: The x- and y-components of the difference induction arrows as a function of period at sites NAP, NEW and OAM.

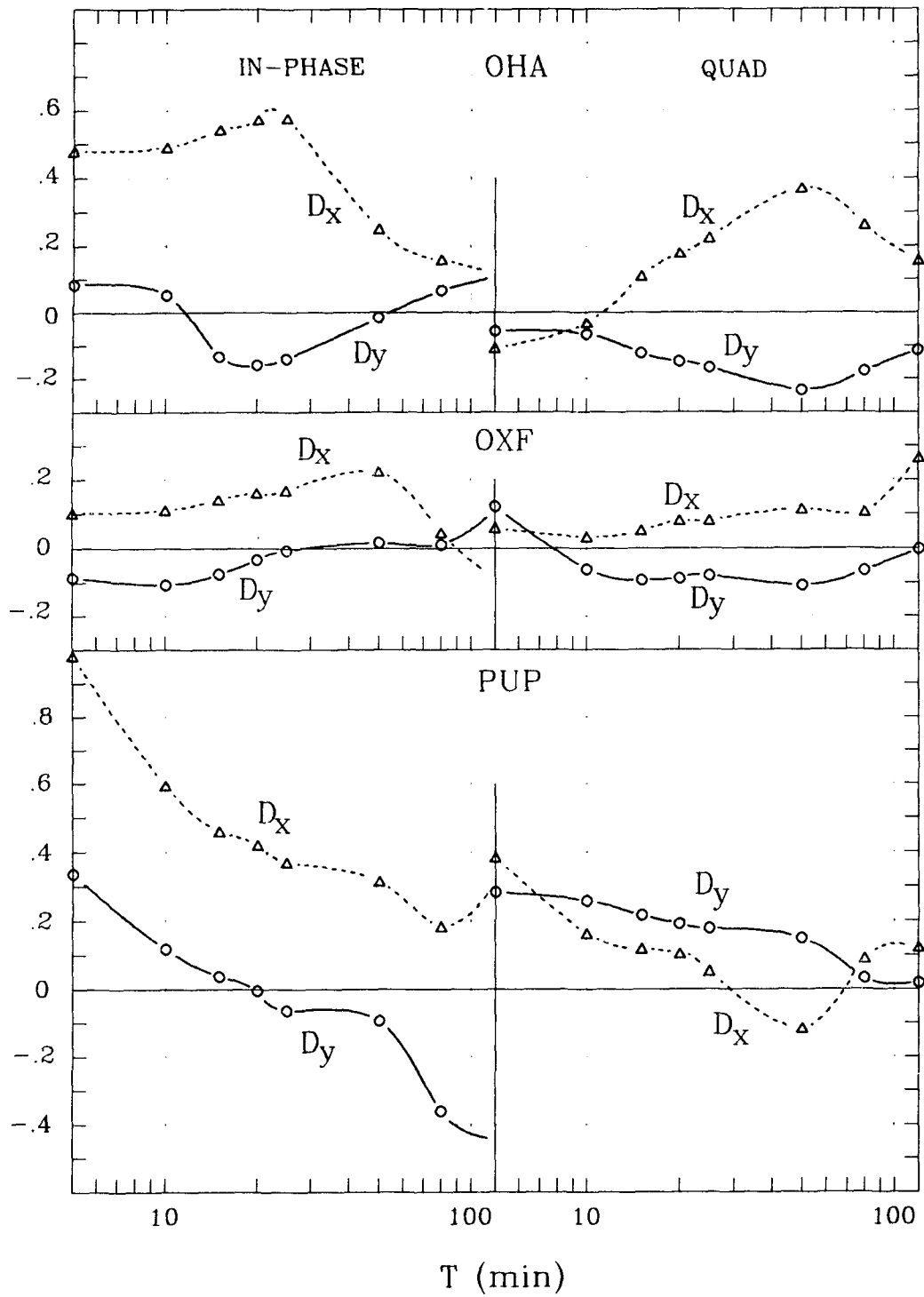


Figure H.8: The x- and y-components of the difference induction arrows as a function of period at sites OHA, OXF and PUP.

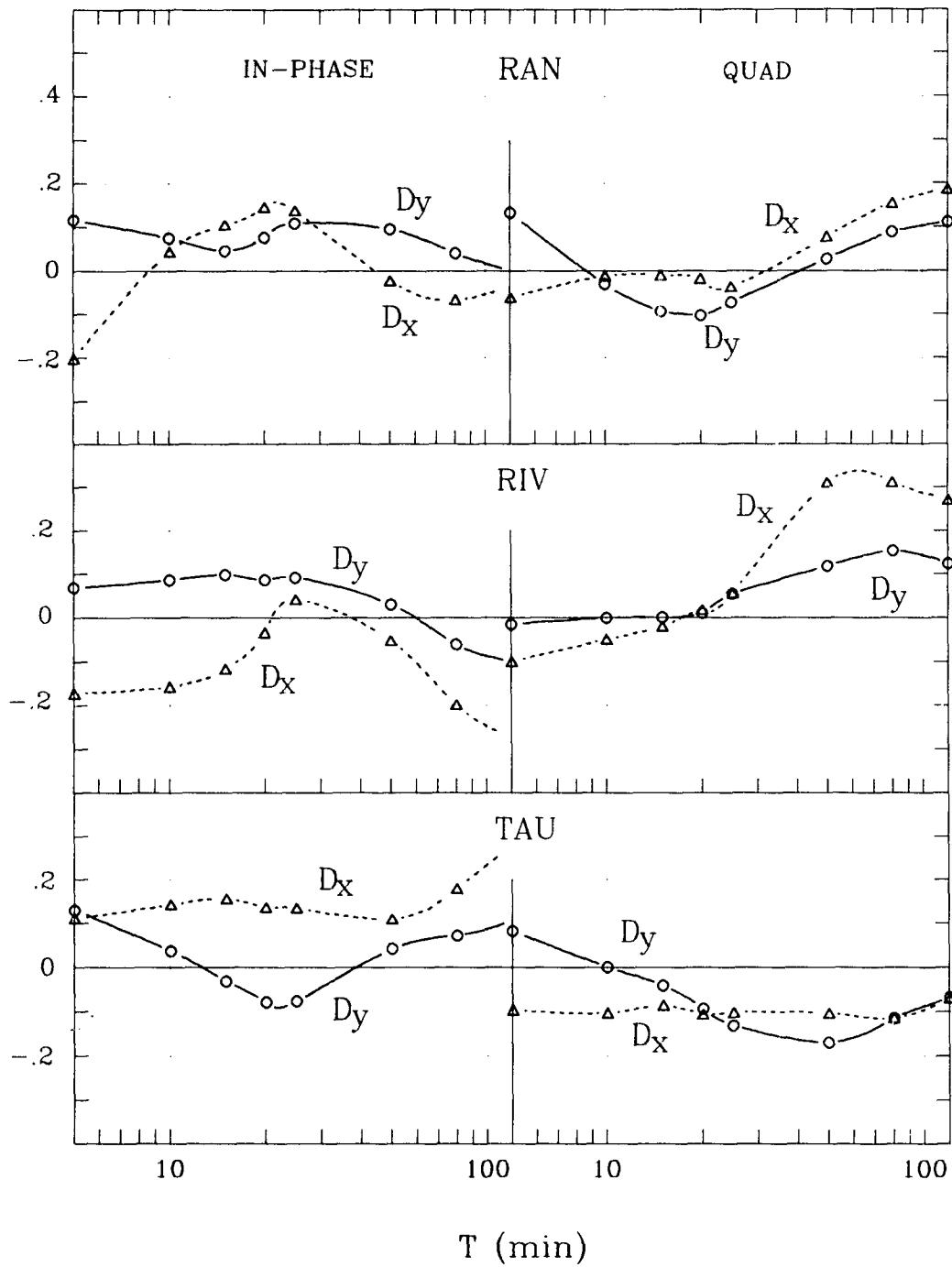


Figure H.9: The x- and y-components of the difference induction arrows as a function of period at sites RAN, RIV and TAU.

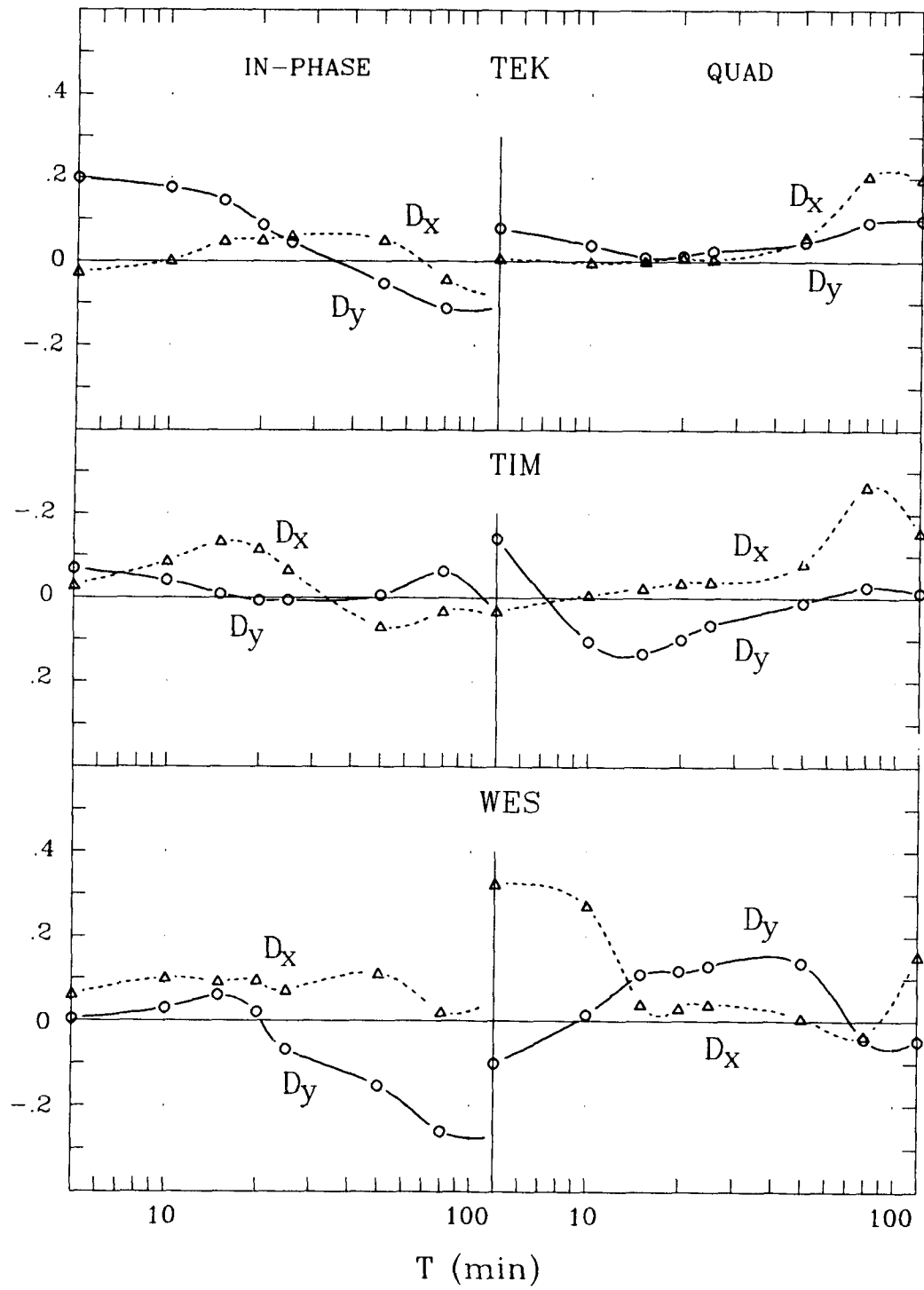


Figure H.10: The difference induction arrow components as a function of period at sites TEK, TIM and WES.

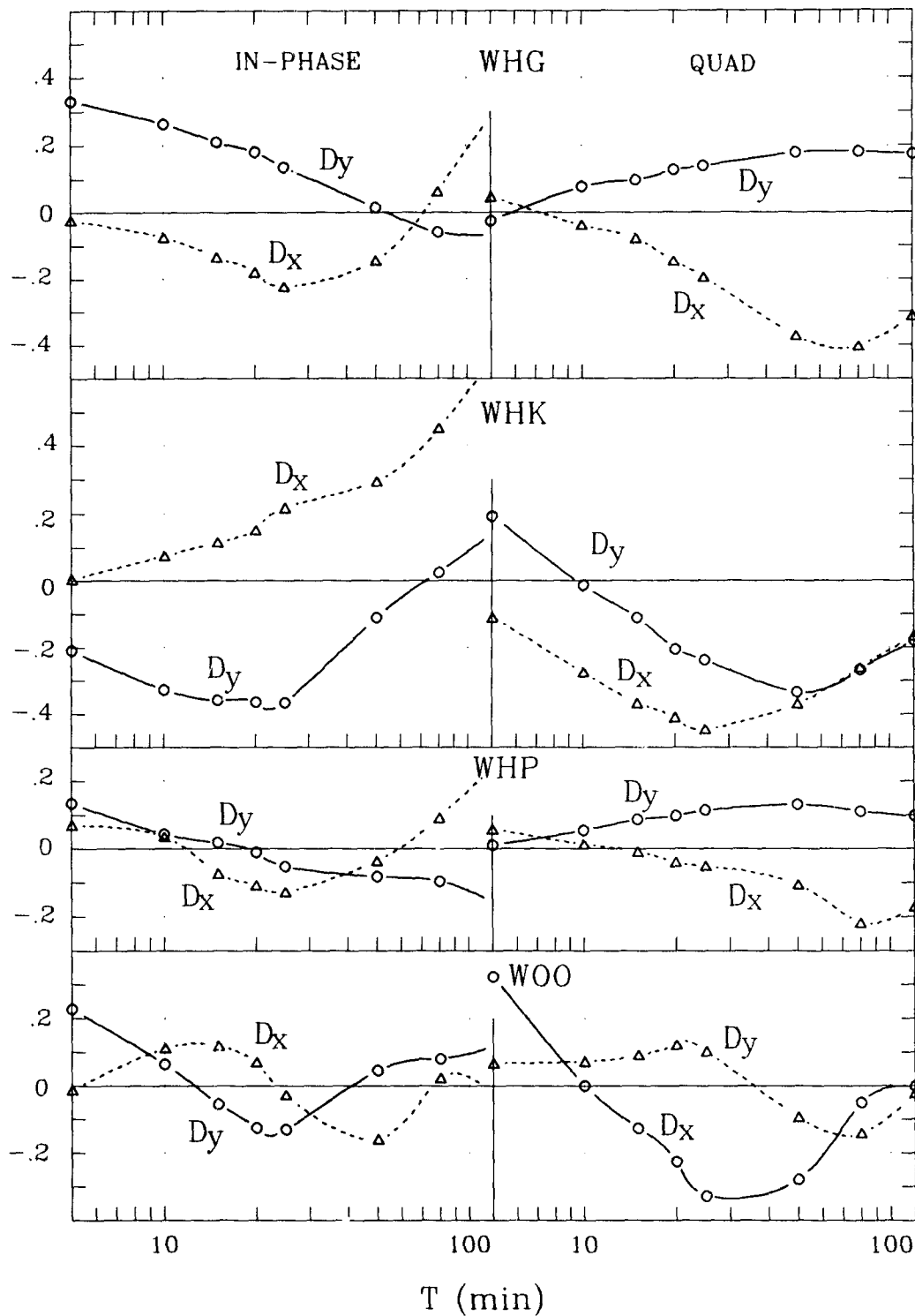


Figure H.11: The x- and y-components of the difference induction arrows as a function of period at sites WHG, WHK, WHP and WOO.

APPENDIX I
ANALOGUE MODEL AND FIELD SITE (CHAMALAUN AND
MCKNIGHT, 1993) INDUCTION ARROWS AT 34 SITES

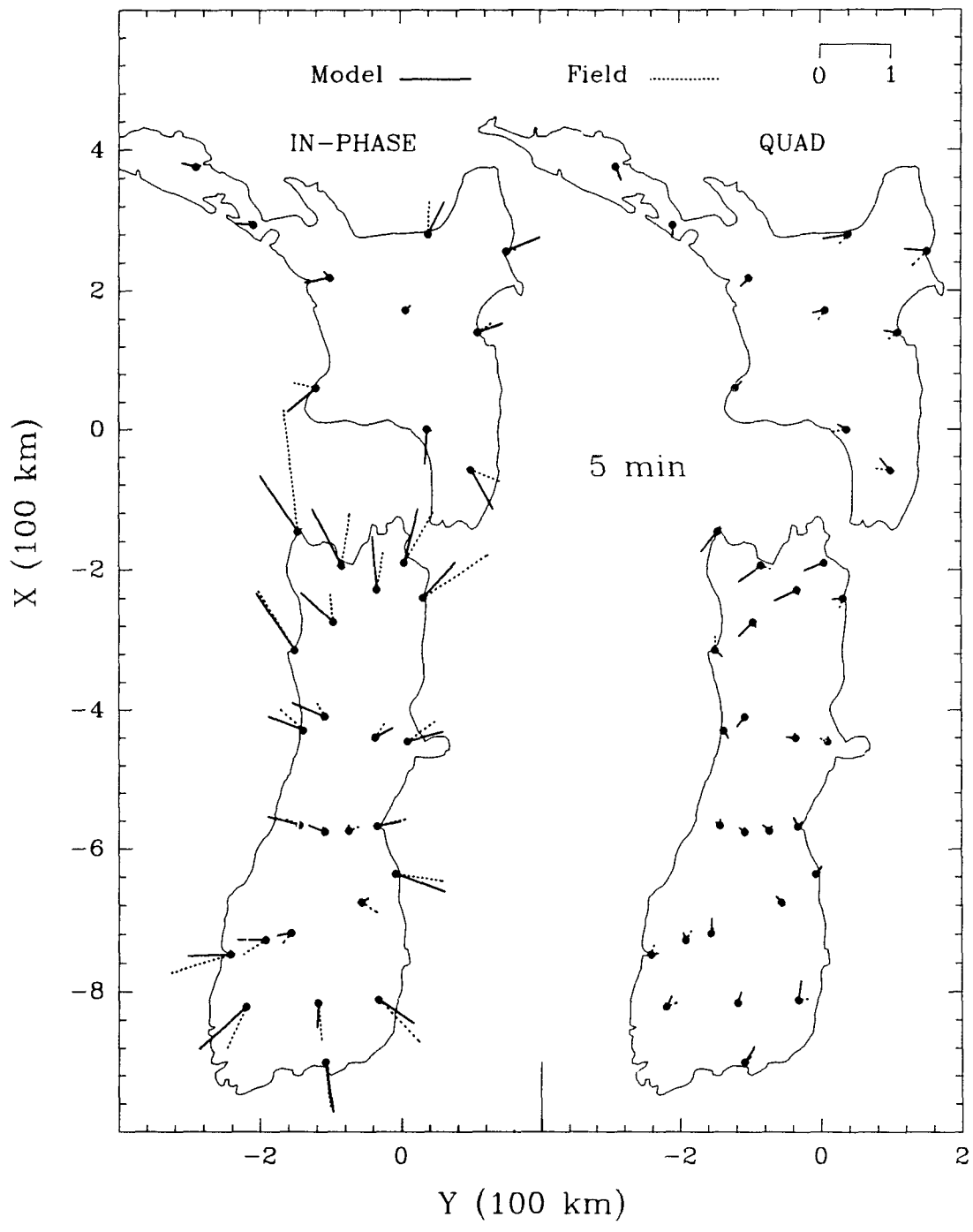


Figure I.1: The in-phase and quadrature model and field site (Chamalaun and McKnight, 1993) induction arrows at 5 min.

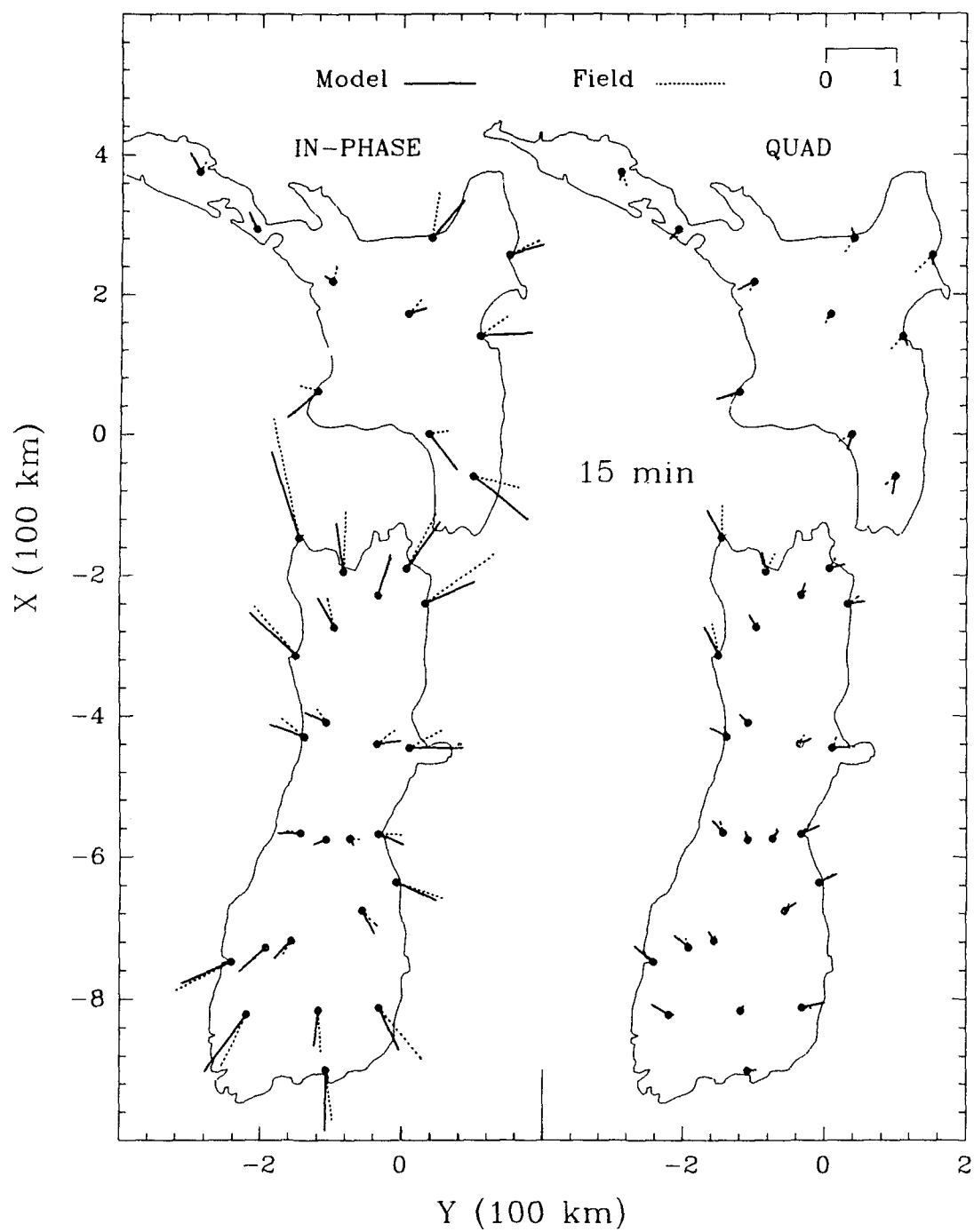


Figure I.2: The in-phase and quadrature model and field site (Chamalaun and McKnight, 1993) induction arrows at 15 min.

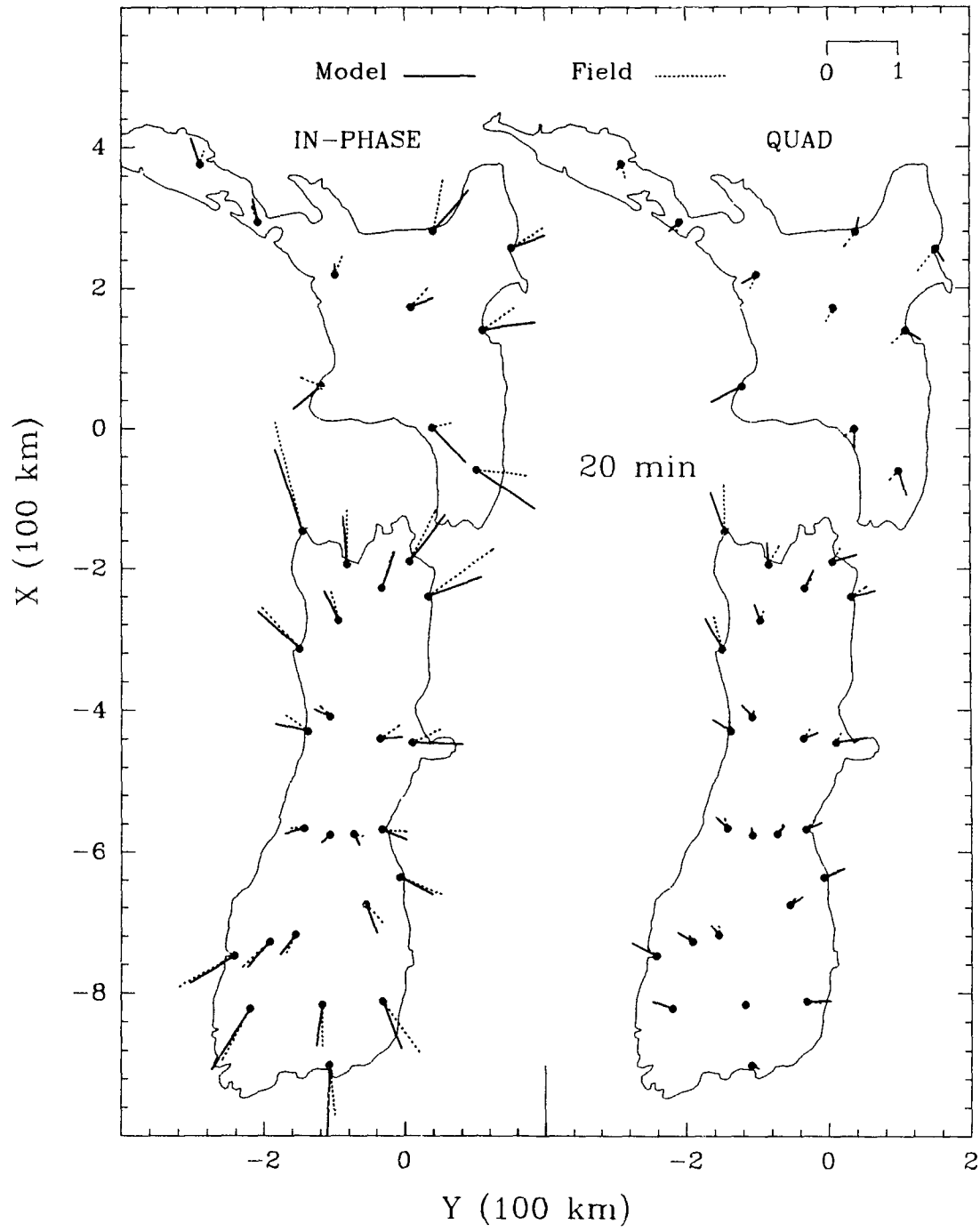


Figure I.3: The in-phase and quadrature model and field site (Chamalaun and McKnight, 1993) induction arrows at 20 min.

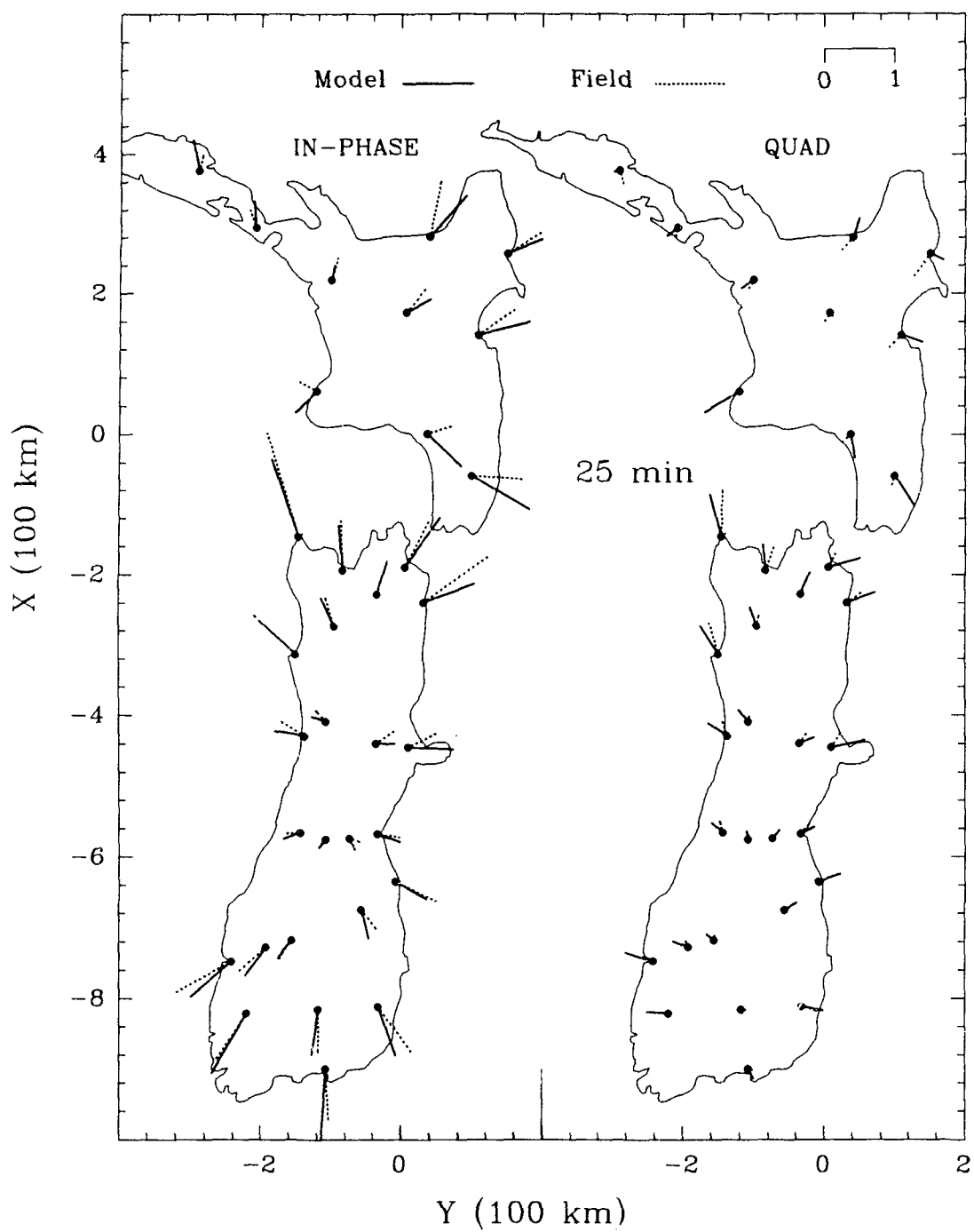


Figure I.4: The in-phase and quadrature model and field site (Chamalaun and McKnight, 1993) induction arrows at 25 min.

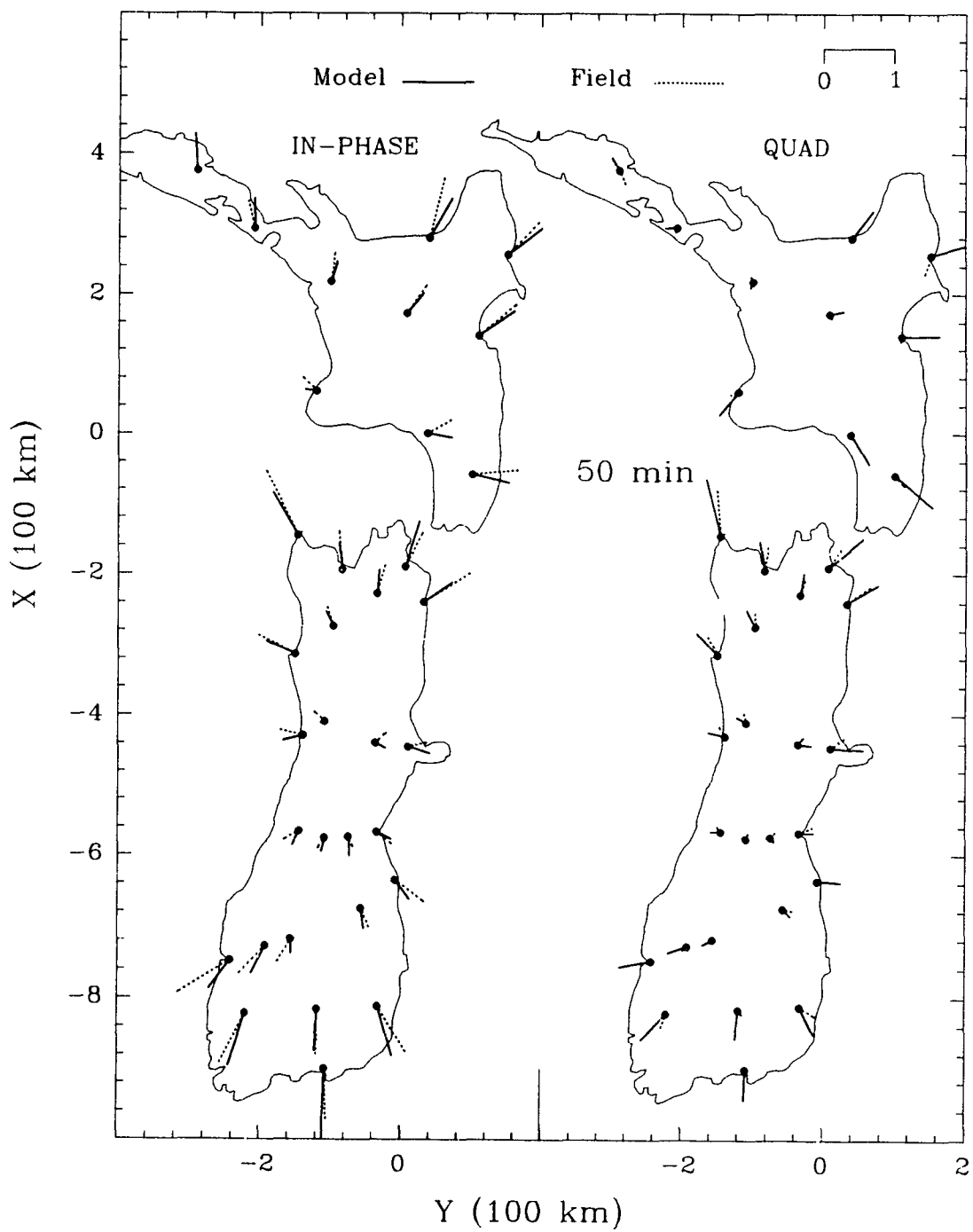


Figure 1.5: The in-phase and quadrature model and field site (Chamalaun and McKnight, 1993) induction arrows at 50 min.

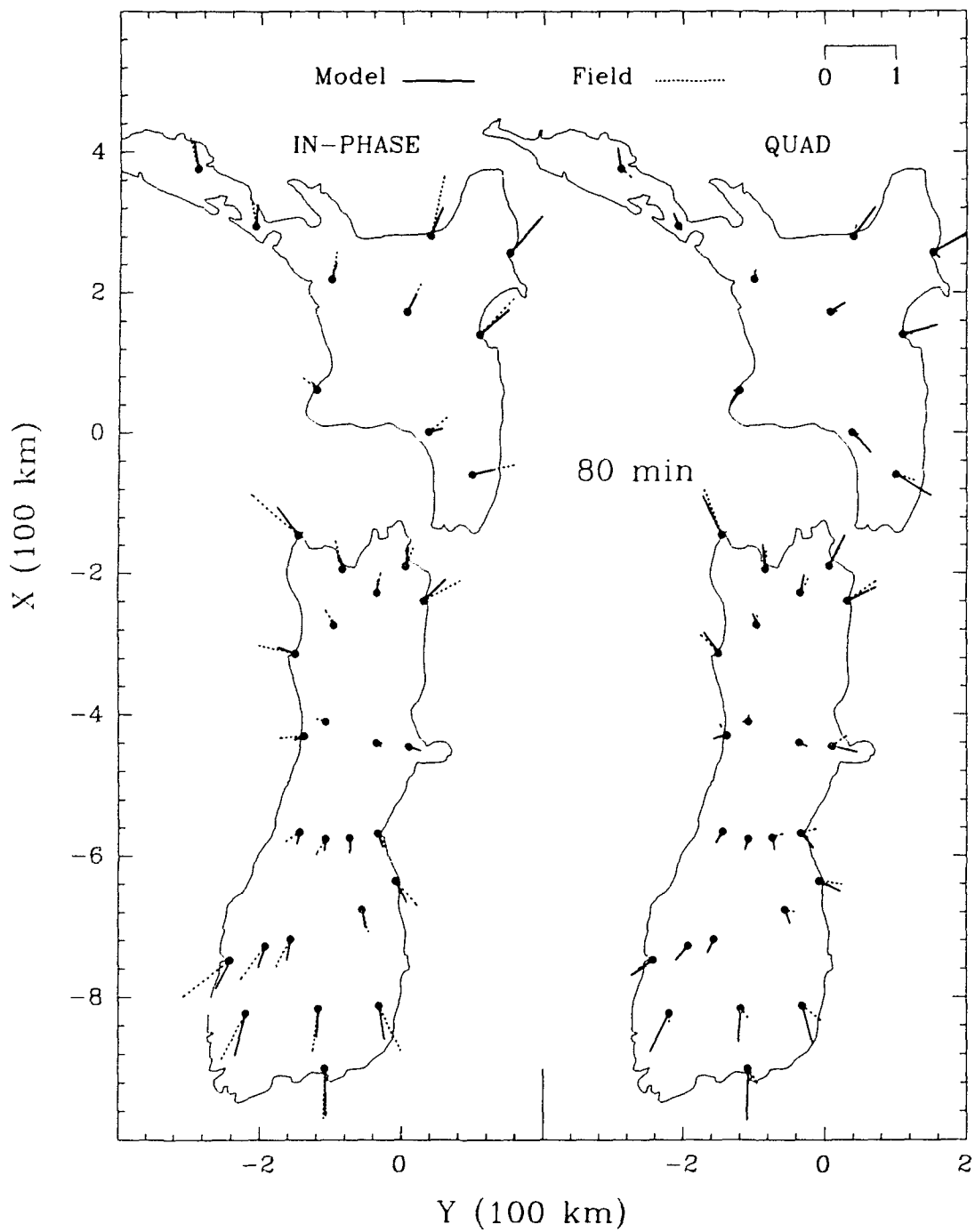


Figure I.6: The in-phase and quadrature model and field site (Chamalaun and McKnight, 1993) induction arrows at 80 min.

APPENDIX J
DIFFERENCE INDUCTION ARROWS AT THE 34 SITES OF
CHAMALAUN AND MCKNIGHT (1993)

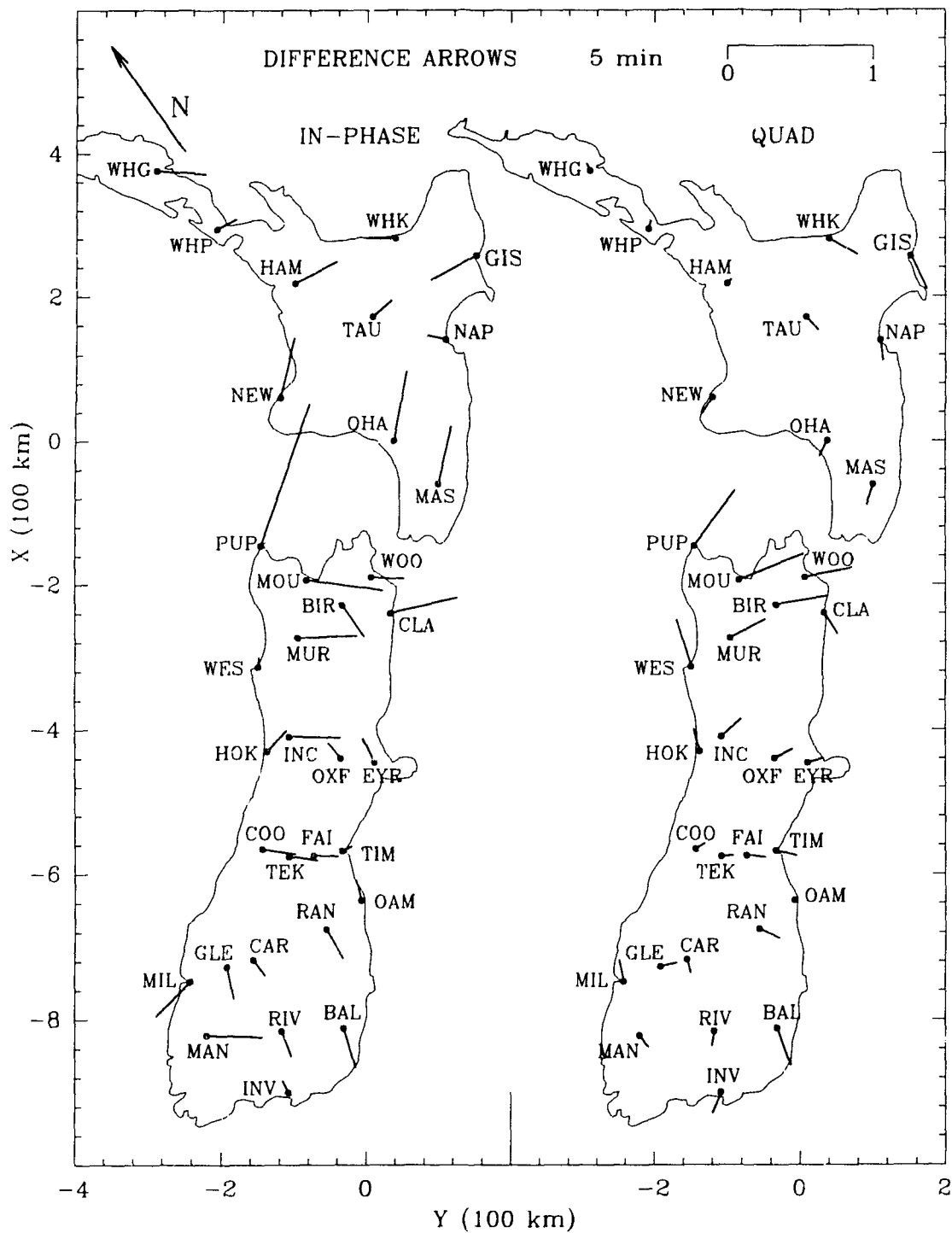


Figure J.1: The in-phase and quadrature difference induction arrows at 34 sites at 5 min period.

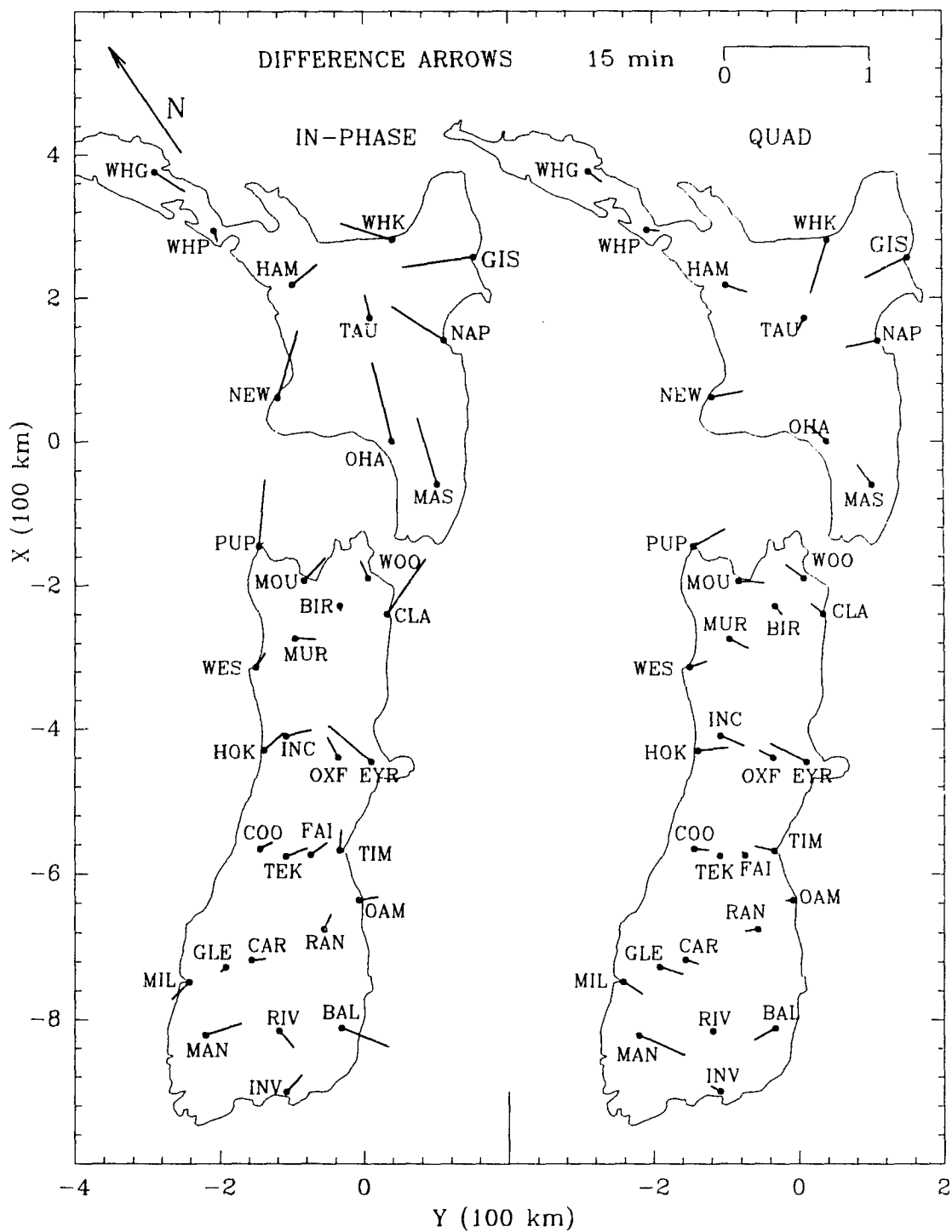


Figure J.2: The in-phase and quadrature difference induction arrows at 34 sites at 15 min period.

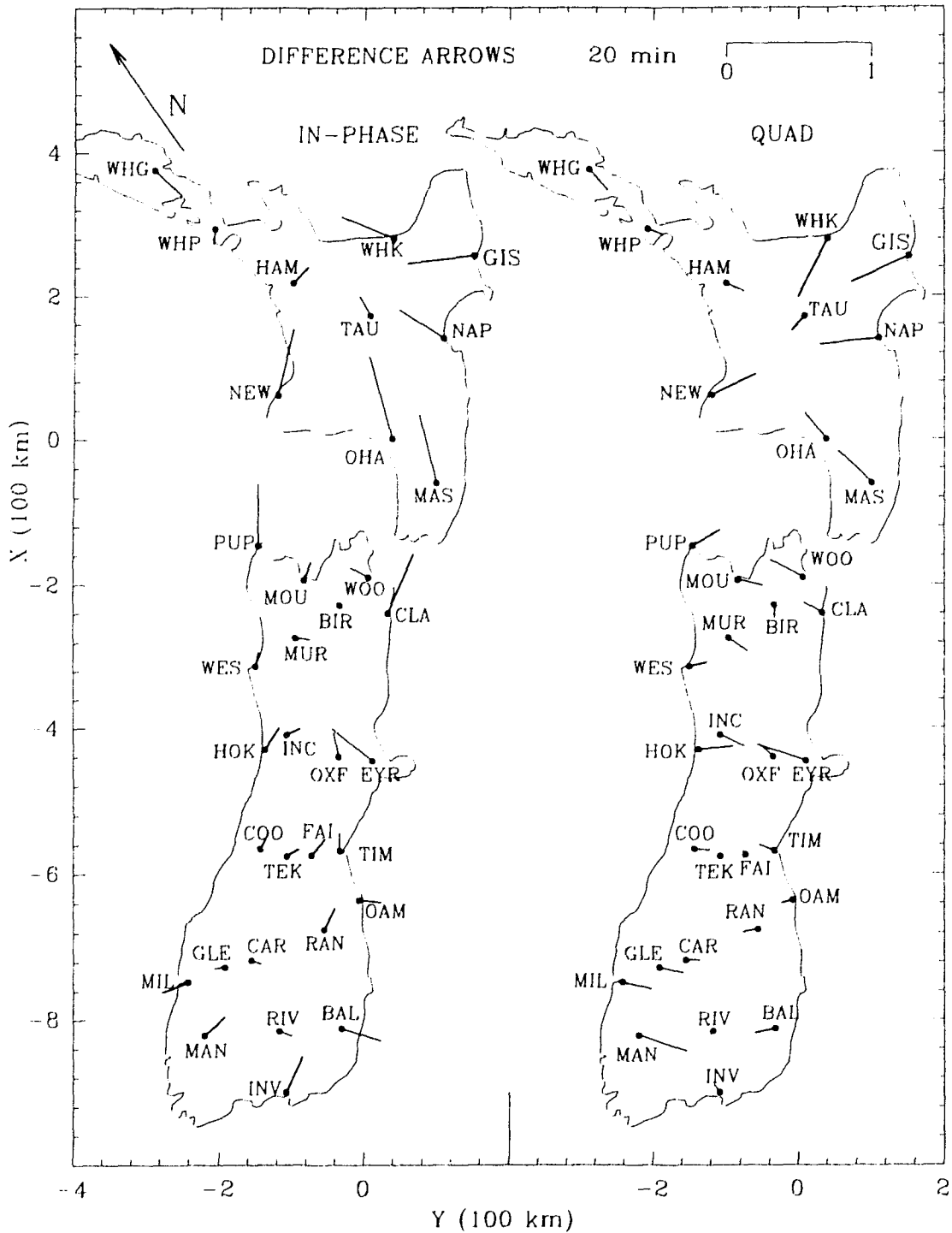


Figure J.3: The in-phase and quadrature difference induction arrows at 34 sites at 20 min period.

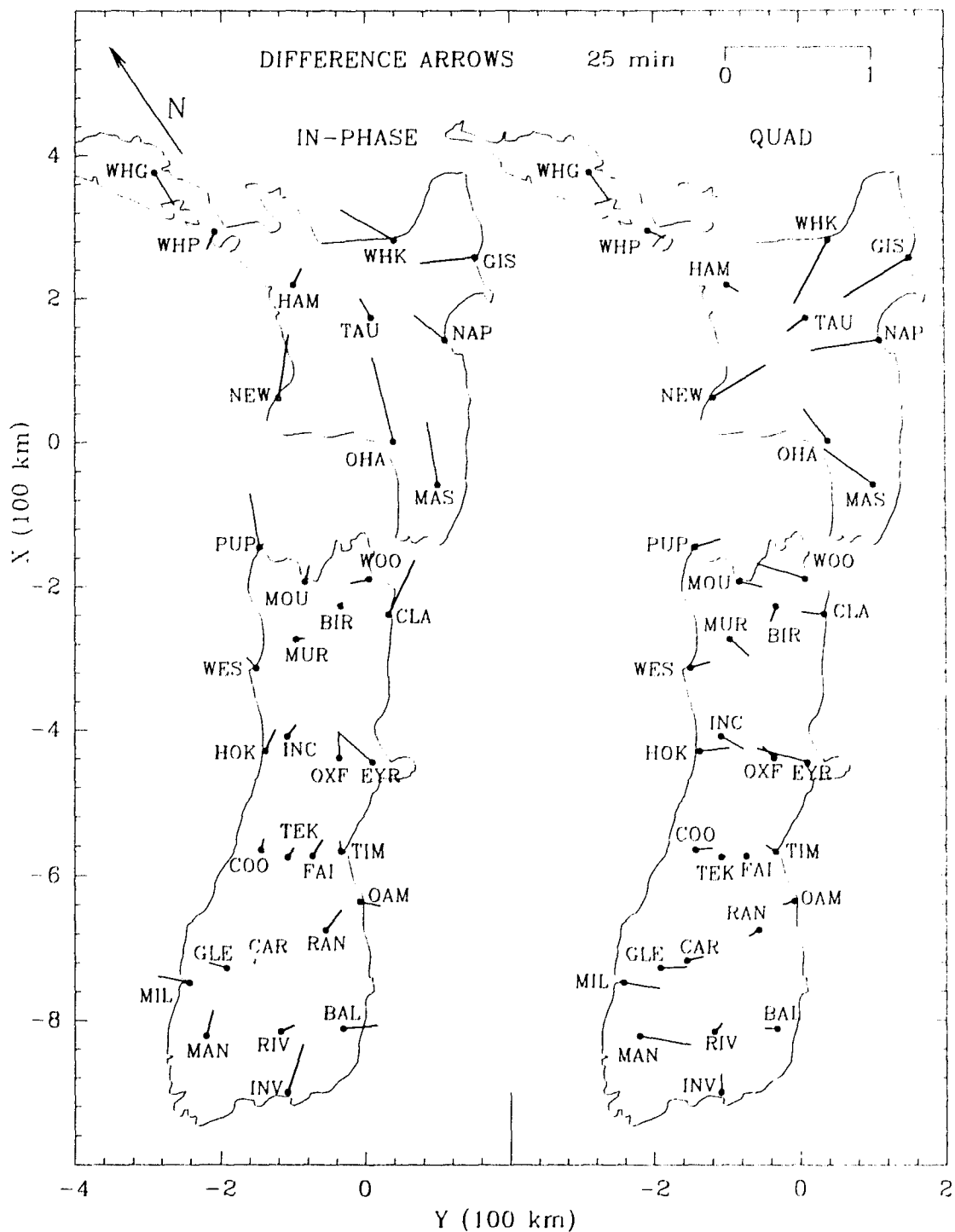


Figure J.4: The in-phase and quadrature difference induction arrows at 34 sites at 25 min period.

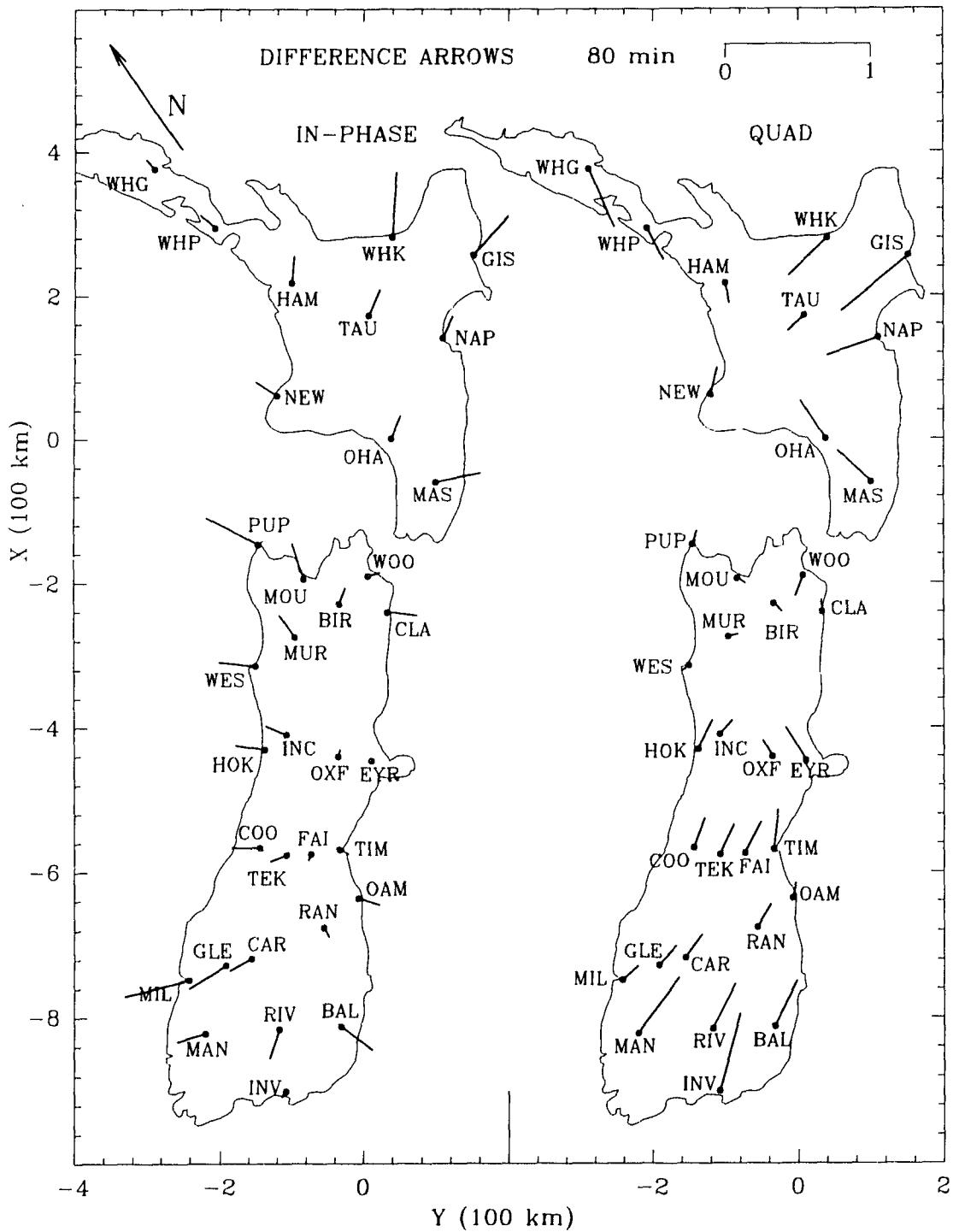


Figure J.5: The in-phase and quadrature difference induction arrows at 34 sites at 80 min period.

CURRICULUM VITAE

Name: JIE CHEN
Date of Birth: March 21, 1957
Place of Birth: Shanghai, P.R. China

DEGREES:

| | |
|---|------|
| M.Sc., Physics, University of Victoria, B.C., Canada | 1988 |
| B.Sc., Physics, Shanghai Teachers University, Shanghai, China | 1982 |

AWARDS:

| | |
|--|-----------|
| Graduate Teaching Fellowship, University of Victoria | 1992-1994 |
| University of Victoria Fellowship | 1986-1992 |
| The Charles S. Humphrey Graduated Student Award | 1986-1989 |

PUBLICATIONS:

CHEN, Jie, Dosso, H.W. and Ingham, M.R., 1993. Electromagnetic induction in the New Zealand South Island. *Phys. Earth Planet. Inter.*, **81**, 253-260.

Dosso, H.W., Agarwal, A.K. and CHEN, Jie, 1992. EM induction in the Vancouver Island region: 3D numerical, analogue model, and field site results. *PAGEOPH.*, **138**, 193-206.

CHEN, Jie, Dosso, H.W. and Ingham, M.R., 1990. Electromagnetic induction in New Zealand: analogue model and field results. *Phys. Earth Planet. Inter.*, **62**, 257-270.

Dosso, H.W., CHEN, Jie and Nienaber, W., 1990. Comparison of analogue model and field station EM responses on southern Vancouver Island. *Phys. Earth Planet. Inter.*, **60**, 18-24.

CHEN, Jie, Dosso, H.W. and Nienaber, W., 1989. Laboratory electromagnetic model results for the EMSLAB region. *J. Geophys. Res.*, **94**, 14167-14172.

Dosso, H.W., Nienaber, W. and CHEN, Jie, 1989. Laboratory electromagnetic modelling of the subducting Juan de Fuca Plate. *Phys. Earth Planet. Inter.*, **53**, 221-227.

PAPER PRESENTED AT SCIENTIFIC MEETINGS:

CHEN, Jie, Kang, S. and Dosso, H.W., 1993. EM induction for embedded elongated conductors. The 19th Annual General Meeting of the Canadian Geophysical Union (Banff, Canada).

CHEN, Jie, Dosso, H.W. and Ingham, M.R., 1992. EM induction in the New Zealand South Island: analogue model and field results. The 11th Workshop on EM Induction in the Earth and Moon (Wellington, New Zealand).

CHEN, Jie, 1991. EM induction in New Zealand--analogue and field results. The 38th Annual Pacific Northwest Regional Meeting of the American Geophysical Union (Washington State University Tri-Cities, USA).

CHEN, Jie, Dosso, H.W. and Ingham, M.R., 1990. Electromagnetic induction in New Zealand--laboratory model and field studies. The 10th Workshop on EM Induction in the Earth and Moon (Ensenada, Mexico).

CHEN, Jie, Dosso, H.W. and Nienaber, W., 1987. Analogue modelling of the EMSLAB region. International Union of Geodesy and Geophysics XIX General Assembly (Vancouver, British Columbia, Canada).

Dosso, H.W., CHEN, Jie and Nienaber, W., 1987. Electromagnetic induction in the Vancouver Island region. International Union of Geodesy and Geophysics XIX General Assembly (Vancouver, British Columbia, Canada).

CHEN, Jie, Nienaber, W. and Dosso, H.W., 1986. Electromagnetic induction in the Pacific north-west coastal region. American Geophysical Union (San Francisco, USA).

Dosso, H.W., Nienaber, W. and CHEN, Jie, 1986. A model study of the EM response of Juan de Fuca region. The 8th Workshop on EM Induction in the Earth and Moon (Switzerland).

PARTIAL COPYRIGHT LICENSE

I hereby grant the right to lend my thesis or dissertation (the title of which is shown below) to users of the University of Victoria Library, and to make single copies only for such users of in response to a request from the library of any other university, or similar institution, on its behalf or for one of its users. I further agree that permission for extensive copying of this thesis for scholarly purposes may be granted by me or a member of the University designated by me. It is understood that copying or publication of this thesis for financial gain shall not be allowed without my written permission.

Title of Thesis

Electromagnetic Induction in the New Zealand Region

Author _____ signature _____

Jie Chen

name

May 26, 1994

date